THE UNIVERSITY
of ADELAIDE

Advanced Nano-Array Catalysts for Electrochemical Energy Conversion Reactions

Jinlong Liu

School of Chemical Engineering

A thesis submitted for the degree of Doctor of Philosophy

The University of Adelaide

March 2018

Table of Contents

Abstract

The development of next-generation energy technologies, such as water-alkali electrolysers and rechargeable metal-air batteries, provides a highly desirable path forward sustainable energy by converting electricity derived from renewable sources in the form of chemical energy, thus allowing for reducing the dependence on conventional fossil fuels as well as the greenhouse gases emissions thereof. Typically, such promising energy systems require precious metal based catalysts (e.g. Pt, RuO_2 and IrO_2) to improve the sluggish kinetics of related reaction processes, such as hydrogen evolution reaction (HER) and oxygen evolution reaction (OER). However, their high cost, low abundance, and poor stability greatly restrict the large-scale practical applications. Therefore, it is of paramount importance to explore earth-abundant, efficient, and robust alternatives. To this end, this thesis aims to design and synthesize a series of self-supported nanoarrays as advanced electrocatalysts for electrochemical energy conversion reactions.

The first aspect of this thesis is to identify the pH-dependence of the HER mechanism for a rational design of functional nanocomposite with interfacial synergy. A Ru/MoS_2 hybrid, consisting of Ru nanoparticles modified defect-rich MoS_2 nanosheets arrays with strong interfacial interaction vertically aligned on carbon paper, was assembled via a simple we-chemical method. By a comprehensive comparison of the HER behaviours in alkaline and acidic media, along with HER mechanism analysis based on Tafel slopes, a pH-dependent synergy on Ru/MoS_2 interface was demonstrated, whereby Ru facilitates water dissociation and nearby MoS_2 accelerates hydrogen recombination into molecular hydrogen in alkaline electrolyte. Due to the synergistic effect, the resulting Ru/MoS_2 electrode exhibited superior alkaline HER activity (10 mA cm^{-2} at -13 mV in 1.0 M KOH) to commercial 20 wt.% Pt/C catalyst and almost all Ru-based and MoS_2-based electrocatalysts.

The second aspect of this thesis focuses on enhancing the conductivity and stability of NiFe-based materials as highly efficient and durable electrocatalysts towards the OER. Well-defined single-crystalline Fe-doped $Ni(OH)_2$ nanoflake arrays were grown on nickel foam (Fe-Ni(OH)$_2$/NF) by a facile hydrothermal reaction. It is discovered that the as-fabricated Fe-Ni(OH)$_2$/NF featured unique physiochemical properties, namely, strong electronic interaction between Fe^{3+} and Ni^{2+} species, good electrical conductivity, and robust structure, in favour of improved OER activity and long-term operation. As a result, it achieved remarkable OER performance in 1.0 M KOH, even outperforming benchmark IrO_2 catalyst. Furthermore, self-

activation during prolonged test, which reflected by a dramatically reduced overpotential from 267 mV to 235 mV to afford 10 mA cm^{-2} after 75 h cycling, was correlated with increased active oxyhydroxide species, making it very attractive for practical application.

The third aspect of this thesis aims to develop effective bifunctional electrocatalysts for both the HER and OER in order to realize overall water splitting. NiFe-based oxides are known as one of the best OER electrocatalysts, yet their HER activity is usually unsatisfactory. Combining component manipulation with nanostructure engineering, sulfur-incorporated NiFe$_2$O$_4$ nanosheets composed of ultra-small nanoparticles (~2 nm) were deposited on nickel foam through a simple thiourea-assisted electrodeposition. Benefitting from the homogeneous sulphur doping and hierarchical structure, the as-obtained S-NiFe$_2$O$_4$/NF electrode showed fascinating OER and HER activities for overall water splitting under alkaline and neutral conditions. Besides, according to previous theoretical studies, NiO is proposed to be a bifunctional promotor for RuO$_2$ towards alkaline water electrolysis, because potential-induced interfacial synergy between NiO and RuO$_2$ could maximize the rate of both the OER and HER. Specifically, NiO-derived NiOOH can reinforce the oxygen binding energy for enhanced OER at the anode, and NiO is able to promote water dissociation for improved HER on RuO$_2$-derived Ru at the cathode. The proof-of-concept studies were carried out by preparing porous nanosheet arrays consisting of strongly coupled NiO and RuO$_2$ nanoparticles grown on nickel foam. As expected, the as-designed RuO$_2$/NiO/NF electrode displayed significantly higher OER and HER performance with a cell voltage of 1.5 V to deliver 10 mA cm^{-2} in 1.0 M KOH, while the PtC/NF||IrO$_2$/NF couple needed 1.56 V. Moreover, the self-consistent interpretation of the OER and HER Tafel slopes supported the interfacial bifunctional synergy. These strategies might be extended to a wide range of electrocatalytic systems, thereby opening a new dimension for constructing higher-performance electrocatalysts.

Declaration

I declare that this is my original work that contains no material previously written or published, in whole or in part, by another person, or material which has been accepted for the award of any other degree or diploma in my name at any university or any other educational institution, except where due acknowledgment has been made in the thesis. Any contribution made to the co-authored works by others, with whom I have worked at The University of Adelaide or elsewhere, is clearly stated and acknowledged in the text. Also, I certify that no part of this work will be used in the future under my name for any purposes, without the prior approval of The University of Adelaide.

I grant the University Library the right to archive and to make available my thesis, in whole or part for loan and photocopying, subject to the provisions of the Copyright Act 1968.

I acknowledge that copyright of published works contained in this thesis resides with the copyright holders of those works, where copyright permissions have been obtained to reproduce published materials in this thesis.

I give permission for the electronic copy of my thesis to be made available online, via the University's digital research repository, the Library Search and also through web search engines, unless permission has been granted by the University to forbid access for a period of time.

Name of Candidate: Jinlong Liu

Signature:

Date: 1 / 03 / 2018

3

Acknowledgments

This thesis can come to fruition only with the kind support and assistance of many people. I would like to extend my sincere thanks to all of them.

First and foremost, I owe my deepest gratitude to my principle supervisor, Prof. Shizhang Qiao, who has been supportive throughout my PhD study with his patience, enthusiasm, and immense knowledge. Without his continuous guidance and valuable suggestion concerning this work, this thesis would hardly have been completed. I also want to thank my co-supervisors, A/Prof. Bo Jin, Dr. Yao Zheng, and Dr. Yan Jiao, for their insightful comments and useful advices during my research and paper writing.

It is a great pleasure to express my heartfelt appreciation to those who contributed directly to some material characterizations: Dr. Tao Ling of Tianjin University, Mr. Zhenyu Wang and Prof. Zhouguang Lu of South University of Science and Technology, for transmission electron microscopy analyses; Dr. Youhong Tang of Flinders University, for X-ray photoelectron spectroscopy tests; and Prof. Christopher Sumby of The University of Adelaide, for X-ray diffraction tests. I have benefited greatly from their generous helps and passionate discussions.

I am deeply indebted to all colleagues in Prof. Qiao's group at The University of Adelaide: Dr. Sheng Chen, Dr. Jingjing Duan, Dr. Ruifeng Zhou, Dr. Jingrun Ran, Dr. Lin Xiong, Dr. Bita Bayatsarmadi, Dongdong Zhu, Fangxi Xie, Anthony Vasileff, Lei Liu, Yongqiang Zhao, Chao Ye, Xuesi Wang, Huanyu Jin, Chaochen Xu, Xing Zhi, Jieqiong Shan, Xin Liu, Mohammad Ziaur Rahman, for the technological assistance, for the enlightening discussions, and for all the fun we have had in the last three years.

Special thanks go to Officers Michelle Fitton and Sue Earle, and Analytical Services Co-ordinator Dr. Qiuhong Hu, School of Chemical Engineering, for their administrative helps; Microscopists Mr. Ken Neubauer and Dr. Ashley Slattery, and Microanalysis Specialist Dr. Sarah Gilbert, Adelaide Microscopy, for technical supports.

I would also like to acknowledge The University of Adelaide and Australia Research Council (ARC) for the financial support.

Finally, I am grateful to all my families and friends in China and Australia for their long time support, encouragement, and unconditional love. They were always there cheering me up and stood by me through the good times and bad.

Chapter 1: Introduction

1.1 Significance of the project

The foreseeable energy and environmental crises, associated with the increasing depletion of fossil fuels and accelerated greenhouse effect, have stimulated unprecedented drive to develop renewable and clean energy technologies.[1−6] Particularly, water electrocatalysis provides a highly comprehensive solution by producing hydrogen as a clean energy carrier.[7−9] However, such technology requires efficient catalysts to improve the reaction rate of involved electrochemical processes (i.e., hydrogen evolution reaction (HER) at cathode and oxygen evolution reaction (OER) at anode) and reduce energy input by lowering their overpotentials.[10] Although noble metal based catalysts are regarded as state-of-the-art electrocatalysts for these energy conversion reactions, such as Pt for the HER and RuO_2 or IrO_2 for the OER,[11] they often suffer from high cost, low abundance, and poor durability mainly due to dissolution and vulnerability to impurities/poisonings, which greatly limit their commercial applications.[12,13] Therefore, it is urgent yet challenging to develop earth-abundant, efficient, and robust alternatives for a sustainable energy future.[10,14−16]

1.2 Research objectives

The major goals of this thesis are to get deeper insights into the mechanisms of key electrochemical reactions (HER and OER), and guides rational design and controllable synthesis of a series of advanced nanostructured electrocatalysts towards high-performance water-alkali electrolysers. Specifically, the objectives of this thesis are:

- *To fabricate* a new catalyst model beyond $Pt/Ni(OH)_2$ based on Ru nanoparticles modified defect-rich MoS_2 nanosheets with well-defined interfaces for highly efficient alkaline HER;

- *To identify* the pH-dependent synergy on Ru/MoS_2 interface by a comprehensive comparison of alkaline and acidic HER behaviours and mechanism analysis based on Tafel slopes;

- *To investigate* single-crystalline Fe-doped $Ni(OH)_2$ nanoflake arrays as an improved OER electrocatalyst to overcome the low conductivity and poor durability associated with NiFe-based materials;

- *To reveal* the self-activation of NiFe-based OER catalysts during prolonged operation through electrochemical measurements and microanalyses;

- *To tune* the chemical composition and nanostructure of $NiFe_2O_4$ nanosheets by S incorporation and confined growth through thiourea-assisted electrodeposition for overall water splitting in alkaline and neutral pH;
- *To optimize* the parameters of thiourea-assisted electrodeposition and extend the method as a general strategy to construct ultra-small nanoparticles built nanosheets;
- *To design* a bifunctional electrocatalyst using NiO as the co-catalyst for RuO_2 towards superior overall water splitting in alkaline solution;
- *To understand* the origins of both enhanced OER and HER activities from the synergetic effects on RuO_2/NiO interface at different potentials.

1.3 Thesis outline

This thesis is partial outcomes of my PhD research presented in the form of journal publications. The chapters in this thesis are presented in the following sequence:

- *Chapter 1* introduces the significance of the project and outlines the research objectives and key contributions to the field of electrocatalysis.
- *Chapter 2* reviews the literatures covering the recent advances of self-supported earth-abundant nanoarrays as promising electrocatalysts for energy conversion reactions.
- *Chapter 3* devotes the identification of pH-dependent synergy on Ru/MoS_2 interface: a comparison of alkaline and acidic hydrogen evolution.
- *Chapter 4* investigates free-standing single-crystalline NiFe-hydroxide nanoflake arrays: a self-activated and robust electrocatalyst for oxygen evolution.
- *Chapter 5* studies $S-NiFe_2O_4$ ultra-small nanoparticle built nanosheets for efficient water splitting in alkaline and neutral pH.
- *Chapter 6* develops NiO as a bifunctional promotor for RuO_2 towards superior overall water splitting.
- *Chapter 7* presents the conclusions and perspectives for future work on design, synthesis, and applications of nanostructured electrocatalysts.

1.4 References

[1]   Seh Z.W.; Kibsgaard J.; Dickens C.F.; Chorkendorff I.; Nørskov J.K.; Jaramillo T.F. Combining theory and experiment in electrocatalysis: insights into materials design. Science 2017, 355, eaad4998.

[2]   Aricò A.S.; Srinivasan S.; Antonucci V. DMFCs: from fundamental aspects to technology development. Fuel Cells 2001, 1, 133−161.

[3]   Cheng F.; Chen J. Metal-air batteries: from oxygen reduction electrochemistry to cathode catalysts. Chem. Soc. Rev. 2012, 41, 2172−2192.

[4]   Benson E.E.; Kubiak C.P.; Sathrum A.J.; Smieja J.M. Electrocatalytic and homogeneous approaches to conversion of CO_2 to liquid fuels. Chem. Soc. Rev. 2009, 38, 89−99.

[5]   Guo C.; Ran J.; Vasileff A.; Qiao S.-Z. Rational design of electrocatalysts and photo(electro)catalysts for nitrogen reduction to ammonia (NH_3) under ambient conditions. Energy Environ. Sci. 2018, 11, 45−56.

[6]   Liu J.; Zhu D.; Guo C.; Vasileff A.; Qiao S.-Z. Design strategies toward advanced MOF-derived electrocatalysts for energy-conversion reactions. Adv. Energy Mater. 2017, 7, 1700518.

[7]   Gong M.; Wang D.-Y.; Chen C.-C.; Hwang B.-J.; Dai H. A mini review on nickel-based electrocatalysts for alkaline hydrogen evolution reaction. Nano Res. 2016, 9, 28−46.

[8]   Koper M.T.M. Hydrogen electrocatalysis: A basic solution. Nat. Chem. 2013, 5, 255−256.

[9]   Anantharaj S.; Ede S.R.; Sakthikumar K.; Karthick K.; Mishra S.; Kundu S. Recent trends and perspectives in electrochemical water splitting with an emphasis on sulfide, selenide, and phosphide catalysts of Fe, Co, and Ni: A review. ACS Catal. 2016, 6, 8069−8097.

[10] Roger I.; Shipman M.A.; Symes M.D. Earth-abundant catalysts for electrochemical and photoelectrochemical water splitting. Nat. Rev. Chem. 2017, 1, 0003.

[11] McCrory C.C.L.; Jung S.; Ferrer I.M.; Chatman S.M.; Peters J.C.; Jaramillo T.F. Benchmarking hydrogen evolving reaction and oxygen evolving reaction electrocatalysts for solar water splitting devices. J. Am. Chem. Soc. 2015, 137, 4347−4357.

[12] Zou X.; Zhang Y. Noble metal-free hydrogen evolution catalysts for water splitting. Chem. Soc. Rev. 2015, 44, 5148−5180.

[13] Suen N.-T.; Hung S.-F.; Quan Q.; Zhang N.; Xu Y.-J.; Chen H.M. Electrocatalysis for the oxygen evolution reaction: recent development and future perspectives. Chem. Soc. Rev. 2017, 46, 337−365.

[14] Hou Y.; Zhuang X.; Feng X. Recent advances in earth-abundant heterogeneous electrocatalysts for photoelectrochemical water splitting. Small Methods 2017, 1, 1700090.

[15] Jamesh M.I. Recent progress on earth abundant hydrogen evolution reaction and oxygen evolution reaction bifunctional electrocatalyst for overall water splitting in alkaline media. J. Power Sources 2016, 333, 213−236.

[16] Faber M.S.; Jin S. Earth-abundant inorganic electrocatalysts and their nanostructures for energy conversion applications. Energy Environ. Sci. 2014, 7, 3519−3542.

Chapter 2: Literature Review

2.1 Introduction

This chapter reviews the recent progress of advanced electrocatalysts based on self-supported earth-abundant nanoarrays in terms of their synthetic methodologies, applications, and prospective. Specifically, typical synthetic methods (e.g., template directed synthesis, hydro/solvothermal method, electrochemical deposition, etc.) are summarized to construct nanoarrays with tuneable component, morphology, and structure. As high-performance electrocatalysts for a wide range of energy conversion processes, they are highlighted to replace precious metal based catalysts (e.g., Pt, IrO_2 and RuO_2) for a series of electrochemical reactions (e.g., oxygen reduction reaction (ORR), oxygen evolution reaction (OER), hydrogen evolution reaction (HER), CO_2 reduction reaction (CRR), nitrogen reduction reaction (NRR), urea oxidation reaction (URR)) as well as energy devices (e.g., rechargeable metal-air batteries and water-alkali electrolysers). Finally, we discuss remaining challenges and the prospective of exploring improved earth-abundant electrocatalysts related to self-supported nanoarrays.

2.2 Self-Supported Earth-Abundant Nanoarrays as Efficient and Robust Electrocatalysts for Energy-Related Reactions

This section is included as it appears as a journal paper published by **Jinlong Liu**, Dongdong Zhu, Yao Zheng, Anthony Vasileff, and Shi-Zhang Qiao, Self-Supported Earth-Abundant Nanoarrays as Efficient and Robust Electrocatalysts for Energy-Related Reactions, *ACS Catalysis*, 2018, submitted.

Statement of Authorship

Title of Paper	Self-supported Earth-abundant Nanoarrays as Efficient and Robust Electrocatalysts for Energy-related Reactions
Publication Status	☐ Published ☐ Accepted for Publication ☑ Submitted for Publication ☐ Unpublished and Unsubmitted work written in manuscript style
Publication Details	Jinlong Liu, Dongdong Zhu, Yao Zheng, Anthony Vasileff, and Shi-Zhang Qiao, Self-supported Earth-abundant Nanoarrays as Efficient and Robust Electrocatalysts for Energy-related Reactions, ACS Catalysis, 2018, to be submitted.

Principal Author

Name of Principal Author (Candidate)	Jinlong Liu		
Contribution to the Paper	Manuscript drafting.		
Overall percentage (%)			
Certification:	This paper reports on original research I conducted during the period of my Higher Degree by Research candidature and is not subject to any obligations or contractual agreements with a third party that would constrain its inclusion in this thesis. I am the primary author of this paper.		
Signature		Date	4/02/2018

Co-Author Contributions

By signing the Statement of Authorship, each author certifies that:

i. the candidate's stated contribution to the publication is accurate (as detailed above);

ii. permission is granted for the candidate in include the publication in the thesis; and

iii. the sum of all co-author contributions is equal to 100% less the candidate's stated contribution.

Name of Co-Author	Dongdong Zhu		
Contribution to the Paper	Discussion of research organization and manuscript revision.		
Signature		Date	4/02/2018

Name of Co-Author	Yao Zheng		
Contribution to the Paper	Discussion of research organization and manuscript revision.		
Signature		Date	5 Feb 2018

Name of Co-Author	Anthony Vasileff
Contribution to the Paper	Assistance with manuscript editing and polishing.
Signature			Date	05/02/2018

Name of Co-Author	Shi-Zhang Qiao
Contribution to the Paper	Supervision of the work and manuscript evaluation.
Signature			Date	15/02/2018

Self-supported Earth-abundant Nanoarrays as Efficient and Robust Electrocatalysts for Energy-Related Reactions

Jinlong Liu,[†] Dongdong Zhu,[†] Yao Zheng,[†] Anthony Vasileff,[†] and Shi-Zhang Qiao[,†,‡]*

[†]School of Chemical Engineering, The University of Adelaide, Adelaide, SA 5005, Australia

[‡]School of Materials Science and Engineering, Tianjin University, Tianjin 300072, P.R. China

ABSTRACT: The replacement of precious metal-based catalysts with earth-abundant alternatives for a diverse range of electrochemical applications is of great importance for next-generation energy technologies. Many self-supported earth-abundant nanoarrays have emerged as state-of-the-art electrocatalysts due to their fascinating structures and electrochemical properties. Herein, we present recent advances made towards developing self-supported earth-abundant nanoarrays for a wide range of energy conversion processes. First, we summarize the different synthetic methods used to construct nanoarrays and tune their compositions, morphologies, and structures. Then, we highlight their application and performance as catalysts for various energy-related reactions. We also discuss their ability to perform as bifunctional electrocatalysts in energy devices. Finally, we conclude with the challenges and prospects in this promising field, where further exploration into these materials will facilitate the development of next-generation energy technologies.

1. INTRODUCTION

Our growing demand for fossil fuels (e.g. coal, petroleum, and natural gas) is accelerating their depletion and causing significant environmental issues due to the associated emission of carbon dioxide (CO_2).[1–3] For the sustainable development of society, it is necessary to address our dependency on fossil fuels and develop alternative energy sources.[3,4] One of the most promising solutions is the conversion of small molecules (e.g. water, CO_2, and nitrogen) into valuable fuels and chemicals (e.g., hydrogen, hydrocarbons, and ammonia) via electrochemical approaches using renewable energy (e.g. solar, wind, and hydroelectric power).[5] However, these technologies usually involve kinetically sluggish reactions, such as the oxygen reduction reaction (ORR), oxygen evolution reaction (OER), alkaline hydrogen evolution reaction (HER), CO_2 reduction reaction (CRR), nitrogen reduction reaction (NRR), and urea oxidation reaction (UOR).[5] Therefore, the main goal in this field is to develop high-performance electrocatalysts for these electrochemical reactions with improved activity, selectivity, and durability.

Generally, the benchmark electrocatalysts for these reactions are based on precious metals. For example, platinum (Pt) is regarded as the best electrocatalyst for the ORR and HER,[6,7] and iridium dioxide (IrO_2) is considered the benchmark catalyst for the OER.[8] Over the past decade, tremendous efforts have been devoted to developing alternative electrocatalysts based on earth-abundant materials.[9–13] In particular, advances in nanotechnology and materials chemistry have greatly contributed to the emergence of a series of nanostructured materials for advanced electrocatalysis. This is largely because nanostructure engineering has proven to be an effective strategy for increasing the active sites density within materials.[12,13] Although most nanostructured catalysts have exhibited better electrochemical performance compared to their bulk forms, conventional nanoparticle powders still suffer from several issues. Firstly, the coating of an active material on a current collector (i.e. the general preparation of a working electrode) is a time-consuming and complicated procedure.[14] Meanwhile, it requires the

11

assistance of binders, which often impede electrolyte access to the active sites and increase contact resistance.[15] Secondly, nanoparticles are inclined to aggregate due to their high surface energies, leading to extensive "dead" volume.[16,17] Thirdly, carbon materials like Vulcan XC72 are added as conductive supports to improve conductivity and electron transport to active sites. However, for anodic processes (e.g. ORR and OER), dissolution of the carbon support hinders continuous operation of the catalyst as the equilibrium potential for carbon oxidation ($C + H_2O \rightarrow CO_2 + 4H^+ + 4e^-$) is only +0.207 V.[18-20] For the OER or HER, the activity and stability of active materials can also be affected by bubble formation which can cause delamination from the support.[14,21] As a result, it is desirable to integrate nanostructured electrocatalysts into various conductive substrates as self-supported and binder-free electrodes.

Self-supported nanoarrays based on earth-abundant elements are very attractive because: (1) different synthetic methods (e.g. template directed synthesis, hydro/solvothermal methods, electrochemical deposition) to controllably construct nanostructure arrays on substrates are well-established and avoid the need for electrode additives (i.e. binders and carbon black);[22-27] (2) vertically-aligned nanoarrays can offer large electrochemical surface area, and the spacing between nanoarrays can allow for effective electrolyte access to the active sites;[28-30] (3) in-situ growth of nanoarrays on conductive substrates enables rapid charge transfer between the current collector and active sites, and simultaneously prevents the active materials from delaminating;[14,30,31] (4) optimization of electrochemical properties can be achieved by tuning the composition, morphology, and structure of the nanoarrays on different substrates;[32-34] (5) the utilization of earth-abundant elements can significantly reduce the cost of resultant technologies and expedite their commercialization.[11-13,35] Due to these advantages, many self-supported earth-abundant nanoarrays in the literature have exhibited significant catalytic efficiency and stability towards the above reactions, and have even outperformed noble-metal benchmarks. Further, some examples exhibit bifunctional properties, such as ORR/OER and

OER/HER, for practical application in specific energy systems (e.g. rechargeable metal-air batteries and water-alkali electrolyzers).

At present, some high-quality reviews on nanostructured electrocatalysts for specific applications have been reported.[36–41] However, few of them have exclusively focused on self-supported earth-abundant nanoarrays for advanced electrocatalysis in energy-related reactions. Moreover, with the advancement of various nanotechnologies and the application of these nanoarrays in new research fields (e.g. CRR and NRR) and energy devices, new progress has been made in very recent years. Accordingly, an updated review on self-supported nanoarrays for electrocatalysis is required and will hopefully promote further development within the field. In this review, we summarize recent development of self-supported earth-abundant nanoarrays as prospective electrocatalysts for energy conversion and storage. Specifically, we first briefly introduce various synthetic methods used for fabricating well-defined nanoarrays. Then, we discuss recently developed nanoarray electrocatalysts for the ORR, OER, HER, CRR, NRR, and UOR. Here, we also highlight some nanostructured arrays utilized as multifunctional catalysts in practical energy devices. Finally, we discuss the challenges and opportunities in this research field related to designing more advanced electrocatalysts for large-scale applications.

2. SYNTHETIC METHODS OF SELF-SUPPORTED NANOARRAYS

In order to optimize the electrochemical performance of self-supported nanoarrays, it is necessary to manipulate their composition, morphology, size, and microstructure through various synthesis strategies.[42,43] In turn, the relationship between physicochemical properties and resultant electrocatalytic behavior can provide useful guidance for optimizing the synthetic parameters. Typically, nanoarrays (e.g. nanowires, nanorods, nanotubes, nanoflakes, and nanosheets) are fabricated on conductive substrates (e.g. metal mesh, metal plate, metal foam, carbon paper, carbon cloth, fluorine-doped tin oxide (FTO), etc.) via bottom-up methods.

Herein, we mainly introduce several synthetic methods that have been widely employed to grow well-defined nanoarrays, including template directed synthesis, hydro/solvothermal methods, and electrochemical deposition. Note that the construction of nanostructure array electrocatalysts often involves multiple steps through the combination of different synthesis methods.

2.1 Template Directed Synthesis

Template directed synthesis is a very effective strategy for constructing highly ordered 1D nanoarrays (e.g. nanowires, nanotubes, and nanorods).[22,42,44−51] Anodic aluminium oxide (AAO) is widely employed as a controllable hard template in the preparation of nanostructured arrays.[42,44,45,48] As illustrated in Figure 1a, Hideki et al. fabricated highly ordered metal nanohole arrays using a two-step replication of the honeycomb structure of AAO.[44] Despite the relatively complicated synthesis procedures involved in the deposition onto the substrates and then removal of the template, it is an effective way of controlling the diameter, length, and interspace of grown 1D nanoarrays.[42,44,45] For instance, Zhang et al. used AAO templates with a pore diameter of 20 nm to fabricate Ni-Cu composite nanowire arrays (average diameter of about 20 nm and length of more than 1 μm) on gold substrates by potentiostatic control and a pulsed deposition technique.[42] Similarly, pure Cu and Ni nanowire arrays were also synthesized by AAO template directed electrodeposition.[42] By using an AAO template with different pore length and diameter, they reported Sn nanotube arrays with an inner diameter of 210 ± 60 nm and average length of up to 60 μm.[48] Following the same template directed synthesis, many transition metals and transition metal composite 1D nanoarrays have been successfully prepared.[52−54] In addition, well-aligned carbon nanotubes (CNTs) arrays have also been synthesized with the assistance of AAO templates through CVD or carbonization of pre-deposited carbon precursors like glucose.[46,47] Therefore, AAO has been demonstrated as a versatile template to direct the growth of various 1D nanoarrays.

In addition to AAO, other templates, such as ZnO and Si arrays, have been widely utilized in the synthesis of nanoarrays in recent years.[22,49−51] In this regard, Ling and co-workers recently prepared CoO nanoarrays on carbon fiber paper (CFP) using an ion-exchange process with ZnO templates.[51] Specifically, ZnO nanoarrays with tailorable pore length were first grown on CFP via hydrothermal reaction. Following, the as-prepared ZnO nanoarrays on CFP were calcinated in a furnace under Ar gas flow with $CoCl_2$ powder upstream. During the calcination process, the ZnO nanoarrays were converted into CoO nanoarrays through cation exchange with the $CoCl_2$. ZnO templates can also be prepared on conductive substrates by simple electrodeposition and serve as a template for nanotube arrays.[49] In the pursuit of highly ordered and tunable nanoarrays, Si templates have been developed because Si nanoarrays can be precisely tailored by photolithography.[22,50] As an example, Liu et al. fabricated heteroatom doped carbon nanorods in regularly aligned arrays using ordered Si nanoarray templates (Figure 1b).[22,50] Owing to their ease of preparation and controllable properties, these newly emerged templates provide numerous opportunities to construct well-defined nanoarrays.

Notably, the majority of current nanoarray templates are based on 1D nanomaterials. However, it is highly preferable to explore general and versatile template directed strategies for preparing nanoarrays with multi-dimensional nanostructures. To this end, metal oxide and hydroxide 1D/2D nanoarrays on different substrates have been reported and can be utilized as self-sacrificing templates. Cai et al. successfully demonstrated such a template directed strategy to fabricate metal oxide@MOF hybrid arrays (nanowalls and nanorods) as illustrated in Figure 1c.[23] CoO nanowall or nanorod arrays were first deposited on a specific substrate (e.g. Ti foil, Cu foil, and conductive glass). Next, the corresponding CoO arrays were converted in situ to metal-organic framework (MOF) arrays in the presence of suitable ligands. Moreover, the obtained metal oxide@MOF hybrid arrays could be thermally transformed to hybrid metal oxide@porous carbon arrays with the original structure being well-preserved. This strategy is

15

quite general and controllable and therefore provides new opportunities to expand template synthesis.

2.2 Hydro/Solvothermal Method

Hydro/solvothermal methods are a simple synthesis technique used to produce various nanoarrays on different substrates with fine structures. Unlike template directed synthesis which involves complicated operations, hydro/solvothermal synthesis makes it possible to readily grow self-supported nanoarrays with "one-pot" reactions. In most cases, the added substrate induces heterogeneous nucleation which assures the uniform deposition of nanoarrays, whereas the absence of a substrate might result in severe aggregation because of fast nucleation and crystal growth. For example, Shang et al. studied vertical WS_2 nanosheets arrays grown on oxidized carbon fiber using a one-pot hydrothermal process and applied as efficient 3D electrocatalysts.[55] In contrast, bulk WS_2 was obtained using the same preparation procedure but in the absence of the carbon fiber substrate. So far, a series of earth-abundant nanoarrays, consisting of transition metal hydroxides,[56] oxides,[57,58] sulphides,[24,55,59,60] and selenides,[61,62] have been synthesized by hydro/solvothermal methods.

Interestingly, under hydro/solvothermal conditions, some metal substrates can not only act as support for the growth of nanoarrays, but also provide a metal source to obtain desired nanomaterials. Taking common Ni foam for example, the surface Ni is able to dissolve and re-precipitate by an acidic hydrothermal treatment, forming ultrathin $Ni(OH)_2$ nanosheet arrays on the Ni foam.[56] As shown in Figure 2a, Tian el al. proposed a dissolution-precipitation mechanism to explain the in-situ hydrothermal growth of $Ni(OH)_2$ nanosheet arrays.[56] As another example, Yang and co-workers fabricated self-supported MoS_2-Ni_3S_2 heteronanorod arrays on Ni foam.[24] Figure 2b illustrates the hydrothermal growth process. As shown, the hydrothermal reaction between Ni foam substrate and ammonium heptamolybdate tetrahydrate (AHM) first generated $NiMoO_4$ nanorods. As the reaction progressed, the $NiMoO_4$ nanorods

reacted with thioacetamide (TAA) to produce Ni_3S_2 nanorod arrays decorated with MoS_2 nanosheets. In this regard, hydro/solvothermal methods have the unique advantage of facilitating in-situ synthesis of nanoarray materials.

Although hydro/solvothermal methods are able to control the morphology of nanomaterials, a major shortcoming associated with this method is its limitation in tuning the composition, which is mainly confined to transition metal oxides, hydroxides, and sulphides described above. To overcome this, post-treatment of the precursors obtained from hydro/solvothermal reactions plays an essential role in component manipulation. Currently, thermal treatments, such as nitrogenization,[63,64] phosphorization,[25,34,65,66] and selenation,[66-68] have been broadly adopted to modify material composition. As presented in Figure 2c, Li et al. reported the synthesis of Fe-doped Ni_2P nanosheet arrays guided by this strategy.[25] Specifically, NiFe precursor arrays were first prepared using a hydrothermal method, which was further treated in Ar under high temperature using Na_2HPO_2 as P source to accomplish phosphorization.[25] Inspired by such synthesis strategies, nanoarrays based on transition metal carbides, nitrides, phosphides, and selenides have been developed as novel electrocatalysts.

2.3 Electrochemical Deposition

Electrochemical deposition is another versatile synthesis method for the growth of self-supported earth-abundant nanoarrays on different substrates. In this approach, nanostructured arrays are able to deposit on conductive substrates in a very short time (from tens of seconds to several minutes) due to the ability of the applied electric field to facilitate the diffusion of precursor ions for fast deposition. In addition to rapid synthesis, another advantage of electrochemical deposition is its ability to controllably produce desired chemical compounds. This is because electrode potential is the most versatile redox agent and can be strong enough to drive almost all chemical reactions. Consequently, electrochemical deposition has been

frequently adopted to prepare all kinds of transition metals and their compounds, including transition metal hydroxides,[69] oxides,[70] sulphides,[71] selenides,[72] and phosphides.[73]

Of note, typical synthesis of phosphide-based arrays involves two steps, i.e. preparation of the precursor and subsequent phosphorization as shown in Figure 2c. However, electrochemical deposition enables the direct synthesis of well-defined phosphide nanoarrays. For instance, Zhu et al. fabricated CoP mesoporous nanorod arrays on Ni foam via a one-step potentiostat electrodeposition (Figure 3a).[26] In the electrodeposition, a constant potential of -0.8 V vs. Ag/AgCl was applied on the Ni foam in an electrolyte solution containing 25 mM $CoCl_2$ and 0.5 M NaH_2PO_2, which drove the redox between Co^{2+} and $H_2PO_2^-$ to generate CoP. Besides being able to directly manipulate the composition, it also allows for further modification to the electrodeposited nanoarrays by additional electrochemical treatment. As illustrated in Figure 3b, Yang et al. reported an amorphous cobalt-borate nanosheet array on a Ti mesh (Co-Bi/Ti) which was synthesized using in situ electrochemical tuning of electrodeposited α-$Co(OH)_2$ nanoarrays (α-$Co(OH)_2$/Ti).[27] In this method, transformation of the nanoarrays was realized by cyclic voltammetry in 0.1 M KBi ($K_2B_4O_7 \cdot 4H_2O$, pH = 9.2).[27] In addition, electrodeposition is an effective approach to precisely modify self-supported nanoarrays with functional materials, thus modulating the interfacial electronic structures for improved activity. Using electrodeposition (a potentiostatic deposition at -1.0 V vs Ag/AgCl for 15 s in 3mM $Fe(NO_3)_3 \cdot 9H_2O$), Shang et al. recently studied hydrothermally prepared V-doped nickel sulphide nanowires supported on Ni foam (NiVS/NF) and uniformly decorated with Fe hydroxide films (eFe/NiVS/NF; Figure 3c).[74] The resultant eFe/NiVS/NF was applied as an electrocatalyst for the OER and exhibited significant activity and stability Therefore, electrochemical deposition is an ideal synthetic method for the construction of nanoarrays with desired composition.

Furthermore, electrochemical deposition allows for the tailoring of physicochemical properties (e.g. morphology and structure) of deposited nanoarrays by controlling the applied potential/current density and electrodeposition time. In this direction, our group recently developed a thiourea-assisted electrodeposition method to fabricate ultra-small nanoparticle built S-NiFe$_2$O$_4$ nanosheets on nickel foam (S-NiFe$_2$O$_4$/NF), and the effects of applied potential and electrodeposition on the morphology and structure of the resultant S-NiFe$_2$O$_4$/NF were systematically investigated.[75] Specifically, appropriate applied potential is critical to compromise nucleation and crystal growth for the growth of well-defined S-NiFe$_2$O$_4$ nanosheets. Under low overpotentials, fast nucleation took place and generated dense small S-NiFe$_2$O$_4$ nanosheets. While under high overpotentials, fast crystal growth occurred and caused severe aggregation of S-NiFe$_2$O$_4$ nanoparticles. With an optimized potential, electrodeposition time was also studied to achieve the optimal loading of S-NiFe$_2$O$_4$ nanosheets. In general, the loading of active materials is proportional to the electrodeposition time, and too little or too much loading of a catalyst will reduce catalytic performance. It was found that prolonged reaction time caused excessive electrodeposition in the spaces among S-NiFe$_2$O$_4$ nanosheets and the structure's porosity was lost. Therefore, optimal activity, morphology, structure, and mass loading of electrocatalysts prepared via electrochemical deposition is achieved using moderate applied potentials and reaction times.

2.4 Other Synthesis Methods

In addition to the common synthetic methods discussed above, approaches such as chemical vapor deposition (CVD) and traditional wet chemical methods have also been reported to synthesize self-supported nanoarrays.[76,77] In fact, some of the post-thermal treatments (e.g. nitrogenization, phosphorization, and selenation) can be considered CVD methods. However, direct CVD methods are capable of producing nanoarrays on various substrates. For instance, Chen et al. synthesized vertically aligned core-shell MoO$_2$/MoSe$_2$ nanosheet arrays on different

substrates (SiO$_2$/Si and carbon cloth) by a continuous two-step CVD method.[76] In the first CVD process, MoO$_3$ and H$_2$ gas were employed as precursors to grow MoO$_2$ nanosheet arrays. Afterwards, a MoSe$_2$ outer layer was formed on the as-grown MoO$_2$ nanosheet arrays by annealing in Se vapor. CVD has also been applied to grow carbon nanoarrays on metal (e.g. Fe, Co, and Ni) substrates. Despite the advantages of CVD, it should be noted that CVD equipment and operation are highly specialized, which to some extent limit its proliferation as a large-scale technique.

In traditional wet chemical methods, self-supported nanoarrays can also be obtained through the redox reaction between some substrates and precursor solutions.[77,78] As an example, Zhang et al. used a wet chemical approach to synthesize Cu(OH)$_2$ nanotube arrays on Cu foil via the oxidation of the Cu foil surface to Cu(OH)$_2$ by ammonium persulfate.[77] The advantages of traditional wet chemical methods lie in its simplicity, mild synthesis conditions, and high yield. Nevertheless, it relies greatly on the suitable redox reaction involving specific substrates.

3. APPLICATIONS IN ELECTROCHEMICAL REACTIONS

Self-supported nanoarrays have exhibited fascinating catalytic properties for a wide range of energy conversion reactions due to their conductivity, abundant active sites, and robust construction. The diversity of earth-abundant nanoarrays also creates ample opportunities to screen more advanced catalysts for certain electrochemical reactions. Until now, self-supported earth-abundant nanoarrays have driven considerable progress in the field of electrocatalysis. In this section, they are highlighted as state-of-the-art electrocatalysts towards multiple frontier reactions including the ORR, OER, HER, CRR, NRR with emphasis on their replacement of precious metal-based electrocatalysts.

3.1 Oxygen Reduction Reaction (ORR)

The ORR is a multi-step electrochemical process with sluggish kinetics. It involves either a four proton-coupled electron transfer to directly reduce oxygen to H$_2$O (in acidic solution) and

OH$^-$ (in alkaline solution) or a two proton-coupled electron pathway with H$_2$O$_2$ (in acidic solution) and HO$_2^-$ (in alkaline solution) as the intermediate species. In fuel cells and metal-air batteries, ORR electrocatalysts which facilitate a direct four-electron pathway are preferred and generally achieve higher catalytic efficiency. According to the Sabatier principle, an optimal ORR catalyst should bind oxygen neither too strongly nor too weakly. In theory, a plot of ORR activity for a variety of close-packed metals as a function of their oxygen binding energy yields a volcano framework, where Pt resides close to the volcano peak. Experimentally, Pt demonstrates the best ORR activity out of all pure metal electrocatalysts, and is thus regarded as the benchmark ORR catalyst. However, the high cost, inadequate stability (Pt agglomeration, dissolution, detachment, sintering, and corrosion of carbon support materials), and low tolerance to various impurities (e.g. methanol and CO) severely restrict the ubiquitous utilization of Pt-based ORR electrocatalysts. In an effort to reduce Pt usage, the rational design and fabrication of earth-abundant ORR catalysts with activity comparable (or even superior) to Pt-based catalysts provides a worthy challenge. Among them, many self-supported nanoarrays based on metal oxides, doped carbon materials, and their composites have been identified as promising ORR electrocatalysts which facilitate four-electron mechanism.

Until now, various metal oxides have been reported as ORR electrocatalysts, of which, spinel structured metal oxides like Co$_3$O$_4$ have drawn significant attention due to their appealing catalytic properties. As a representative spinel cubic crystal, Co$_3$O$_4$ contains both Co^{2+} and Co^{3+} ions, with Co^{2+} occupying an eighth of the tetrahedral sites and Co^{3+} occupying a half of the octahedral sites. For the ORR, it has been proven that the Co^{3+} in octahedral sites are the active sites. Accordingly, Co$_3$O$_4$-based materials should be synthesized with maximum exposure of active octahedral Co^{3+} sites in order to maximize ORR performance. At the same time, efforts should be made to improve the poor intrinsic conductivity of pristine Co$_3$O$_4$ and ensure fast electron transfer. In this area, Tong et al. demonstrated self-supported mesoporous

Ni-doped Co_3O_4 nanowire arrays which addressed these two issues.[79] The nanowire architecture and mesoporous structure (Figure 4a−c) expedited the kinetics by shortening the transport/diffusion distance for both electrons and reactant ions. More notably, Ni doping caused the resultant Co_3O_4 nanowires to be enriched with Co^{3+} species at the surface and enhanced conductivity. In 0.1 M KOH electrolyte, the Ni-doped Co_3O_4 nanowire arrays showed remarkable ORR activity with a half-wave potential ($E_{1/2}$) of ~0.86 V and a diffusion-limiting current density of ~5.76 mA cm^{-2}, even outperforming commercial 20 wt.% Pt/C (~0.85 V, 5.42 mA cm^{-2}, Figure 4d). Moreover, it also exhibited excellent long-term stability with strong tolerance to both methanol and CO (Figure 4e and 4f), implying superior comprehensive performance for practical applications. This study indicates that self-supported nanoarrays based on earth-abundant metal oxides have huge potential as a class of highly efficient ORR electrocatalysts.

Another category of state-of-the-art ORR electrocatalyst comparable to Pt catalysts is doped carbon nanomaterial arrays. Using an AAO template route, She et al. fabricated N-doped microporous carbonaceous nanotube arrays as high-performance ORR catalyst, which displayed comparable activity and superior durability to commercial Pt/C.[80] By a facile one-step pyrolysis of N, P-containing resin in the presence of Ni foam, Zhu et al. reported self-supported N and P dual-doped carbon nanotube arrays for highly efficient oxygen reduction.[81] Likewise, the as-synthesized N, P-dual-doped carbon nanotube arrays achieved comparable ORR activity and much better stability with stronger tolerance to methanol and CO compared to Pt/C. Normally, the origin of ORR activity for doped carbon nanomaterials is attributed to the N species, especially pyridinic N and graphitic N, because they can effectively polarize the pristine carbon matrix. Consequently, these N-species induce an electron-donor effect to activate nearby carbon atoms for electrocatalysis. Accordingly, structure engineering of carbon nanomaterial arrays provides further opportunities to explore Pt-free ORR catalysts.

Self-supported nanoarrays also create possibilities to design electrode architectures with better gas diffusion for higher-performance ORR. During the ORR process, fast gas diffusion is essential to assure continues oxygen supply to active sites as the diffusion of oxygen in aqueous solution is slow. Therefore, the ORR preferentially occurs at a three-phase (i.e., oxygen, electrolyte, and catalyst) contact point (TPCP), where sufficient oxygen can be provided due to the fast diffusion rate. Yet the direct loading of powdery catalysts like Pt/C on commonly used Teflon-treated carbon fiber paper (TCFP) is unfavourable for creating enough TPCP, and binders like poly(tetrafluoroethylene) (PTFE) can have an adverse effect on conductivity. Inspired by these considerations, Lu et al. fabricated porous cobalt-incorporated N-doped carbon nanotube arrays on carbon fiber paper with subsequent PTFE modification (PTFE-CoNCNT-CFP, Figure 5a−d), leading to simultaneously accelerated electron transport and oxygen diffusion.[82] Surprisingly, despite its later ORR onset potential compared to Pt/C, the integrated PTFE-CoNCNT-CFP electrode with "superaerophilic" properties displayed a faster increase in current density, which exceeded the Pt/C in 6 M KOH when the potential was more negative than 0.68 V vs. RHE (Figure 5e). Again, as a Pt-free catalyst, PTFE-CoNCNT-CFP possessed excellent stability during prolonged operation (Figure 5f). In this case, it can be seen that tailoring electrode architecture with self-supported nanoarrays is extremely advantageous when optimizing ORR performance.

3.2 Oxygen Evolution Reaction (OER)

As the reverse reaction of the ORR, the OER is another four electron-proton coupled reaction. Similarly, it is a very important process in many energy conversion devices, such as water electrolyzers and rechargeable metal-air batteries. Like the ORR, the OER is a multiple electron-proton transfer process which has very sluggish kinetics, and requires a large overpotential to overcome the kinetic barrier.[83,84] Since the most investigated OER electrocatalysts are metal oxides, an OER volcano plot has been built for a vast variety of metal

oxides,[85] which predict RuO_2 and IrO_2 to be the most active for the OER. This is also shown by experimental evidence, where RuO_2 and IrO_2 have been found as the two best OER catalysts. Hence, they are considered as the benchmark OER electrocatalysts. Unfortunately, under harsh oxidizing potentials, both of them (especially RuO_2) suffer from high dissolution rate forming RuO_4 and IrO_4^{2-}.[86-88] Issues with their stability, together with their high cost and carbon support corrosion, inhibits their practical applications. To replace Ru- and Ir-based OER catalysts, a large number of self-supported nanoarrays based on earth-abundant candidates, including transition metal (e.g., Fe, Co, Ni, Mn, etc.) hydroxides, oxides, sulphides, selenides, nitrides, phosphides, borides, carbon-based materials, and their composites, have been developed (Table 1).

With respect to earth-abundant OER catalysts, one key problem is finding stable materials that can withstand corrosion from both the electrolyte and the high oxidizing potentials. Among the above mentioned OER candidates, some transition metal hydroxides and oxides exhibit good corrosion resistance in alkaline conditions. Particularly, nickel-based hydroxides and oxides possess high stability. Further, it was discovered that the presence of Fe ions in nickel hydroxides and oxides can dramatically boost catalytic activity by lowering the OER overpotential. So NiFe hydroxides and oxides are one of the most promising OER catalysts at present.[89] Meanwhile, nickel substrates like Ni foam also possess both excellent corrosion resistance and electric conductivity. Therefore, numerous NiFe-based nanoarrays have been grown on Ni substrates to construct more advanced OER catalysts.[90] For example, Lu et al. prepared amorphous mesoporous NiFe composite nanosheet arrays on Ni foam (Figure 6a and 6b) as an OER electrode by a facile one-step electrodeposition.[21] Impressively, the as-prepared electrode showed remarkable alkaline OER activity (Figure 6c−e), with a low onset overpotential of 200 mV and a large current density of 1000 mA cm^{-2} at overpotential of 270 mV. Moreover, the turnover frequency (TOF) results showed that the intrinsic OER activity of

the NiFe composite (0.075 s^{-1}) was about three times that of commercial 20 wt% It/C (0.027 s^{-1}). In Figure 6f, excellent prolonged stability was further observed on the as-obtained NiFe composite nanosheet arrays. In addition to NiFe-related nanoarrays, many other self-supported nanoarrays based on transition metal hydroxides and oxides have also been explored as efficient and robust OER electrocatalysts. Examples include Co_3O_4C nanowire arrays on Cu foil,[140] Ni-substituted Co_3O_4 nanowire array on Ni foam,[28] α-Fe_2O_3 nanorod arrays on carbon cloth,[169] CuO nanowire@Co_3O_4 ultrathin nanosheet core-shell arrays on carbon fibers,[32] $NiCo_2O_4$ nanowire arrays on FTO glass plate,[170] and $NiCo_2O_4$@Ni-Co-Ci core shell nanowire arrays on carbon cloth.[164]

Beyond transition metal hydroxides and oxides, self-supported nanoarrays based on other transition metal compounds (e.g. sulphides, selenides, nitrides, borides, and phosphides) have emerged as another type of attractive OER catalysts. Using a one-pot hydrothermal method, Chen et al. reported NiS nanosheet arrays supported in stainless steel mesh for OER electrocatalysis.[60] The resultant catalyst exhibited a low overpotential of 297 mV to deliver 11 mA cm^{-2} and a small Tafel slope of 47 mV dec^{-1}.[60] Similar sulphides and selenides nanoarrays, such as Ni_3S_2/MoS_x nanosheet arrays on Ni foam and Co_3Se_4 nanowire arrays on Co foam,[31,61] can be prepared by facile hydrothermal reactions between precursor solution and selected substrates. Spinel-structured $MnCo_2S_4$ nanowire arrays reported as efficient OER catalysts in alkaline conditions were grown on Ti mesh through the hydrothermal growth of $MnCo_2O_4$ nanowire array precursor and subsequent sulfidization.[91] Using the same two-step strategy, Zn-doped $CoSe_2$ nanosheet arrays on carbon fabric,[92] Ni-substituted cobalt borate nanowire arrays on carbon cloth,[93] Fe-doped Ni_2P nanosheet arrays on carbon cloth,[94] Fe-Ni phosphide nanoparticle-stack arrays on Ni foam,[29] CoN nanowire arrays on Ni Foam,[95] have been synthesized and investigated as highly efficient catalysts for the OER. Different from metal hydroxides and oxides, metal sulphides, selenides, nitrides, borides, and phosphides are

thermodynamically less stable, and many recent reports have found that they are oxidized to corresponding metal hydroxides/oxides in OER environments (at least on the surface). Therefore, it is likely that the generated metal hydroxides/oxides are the real active OER catalysts. According to Jin's advocacy, these unstable materials should be called OER "precatalysts" instead of OER catalysts.[96] Of course, there are still many unresolved questions surrounding the effect of these precatalysts on OER performance. Therefore, further work is required in order to better understand the catalytic dynamics of these metal compounds.

Carbon-based materials have also shown considerable OER activity due to their good conductivity and synergistic coupling effects from multiple heteroatoms (e.g. N, P, B, and S). Very recently, Zhu et al. reported N and P co-doped carbon nanofibers grown on carbon paper (NPC-CP) via a two-step method (i.e. electrochemical polymerization of aniline and subsequent carbonization; Figure 7a).[97] As a self-supported OER electrocatalyst (Figure 7b and 7c), the as-obtained NPC-CP was employed directly as the working electrode, and exhibited a low overpotential to afford 10 mA cm^{-2} at 310 mV (η_{10} = 310 mV), which was comparable to the IrO$_2$ benchmark (Figure 7d). From corresponding Tafel plots in Figure 7e, NPC-CP also displayed a smaller Tafel slope (87.7 mV dec^{-1}) than IrO$_2$ (92.1 mV dec^{-1}), single N-doped carbon nanofibers on carbon paper (NC-CP, 105.3 mV dec^{-1}), and pristine carbon paper (CP, 131.8 mV dec^{-1}), indicating its superior OER kinetics. After 12 h chronoamperometric operation at 1.54 V vs. RHE, NPC-CP showed a slight current attenuation of 6.6%, while the OER current decay of IrO$_2$ was up to 27.1% (Figure 7f), demonstrating the exceptional stability of the integrated electrode over powdery electrocatalysts coated on conductive substrates. Density functional theory calculations revealed that the enhanced OER activity originated from the synergistic effect between the N, P dopants and the carbon matrix. Note that compared with N-doped carbon, P-doped carbon, pristine carbon, and IrO$_2$, N, P-doped carbon was found to have the smallest onset overpotential as shown in the volcano plots in Figure 7g. Therefore,

engineering self-supported carbonaceous nanoarrays with multiple heteroatom doping provides further strategies for developing synergistically enhanced OER catalysts.

3.3 Hydrogen Evolution Reaction (HER)

Hydrogen has relatively high energy density and is increasingly becoming more feasible as a source of sustainable fuel. This fuel can be produced by water electrolysis, in which the OER occurs on the anode and the HER takes place on the cathode. As a two-electron transfer reaction, the HER has faster kinetics than the OER, but efficient and robust HER electrocatalysts are still required. In the HER volcano plot, Pt is the nearest catalyst to the peak and therefore is also the benchmark electrocatalyst for the HER.[98] Nevertheless, the scarcity and high price hinder the large-scale application of Pt-based HER catalysts. However, the HER activity of Pt is usually about $2-3$ orders of magnitude lower in alkaline media than in acidic solutions, yet the efficiency of water electrolyzers in alkaline electrolyte is higher than that in acidic media. Therefore, it is significant to explore highly efficient and earth-abundant alternative catalysts towards alkaline HER. In light of the advantages of self-supported electrocatalysts, various nanoarrays based on transition metal chalcogenides, phosphides, nitrides, etc. are of particular interest for HER applications due to their appealing performance (Table 2).

Ever since it was theoretically determined that the hydrogen adsorption free energy (ΔG_H) of MoS_2 was close to that of Pt, and the experimental identification of the MoS_2 active edge sites for electrochemical hydrogen evolution, transition metal chalcogenides have been extensively utilized to catalyze the HER. Technically, vertically aligned MoS_2 or its analogous nanosheet arrays can maximally expose the active edge sites for enhanced HER activity. As expected, many self-supported Mo-related chalcogenides nanoarrays, including vertically aligned MoS_2/$MoSe_2$ nanosheet arrays on diverse substrates (i.e. glassy carbon, quartz, and oxidized silicon),[99] MoS_2 nanosheet arrays on Mo meshes,[100] and hierarchical Ni-Mo-S nanosheets on carbon fiber cloth,[101] have shown significantly improved HER performance. In

27

particular, Xing et al. synthesized core/shell structured MoS$_2$@Ni nanosheet arrays vertically aligned on carbon cloth (MoS$_2$@Ni/CC, Figure 8a) which achieved significant HER activity and stability in alkaline media.[102] In 1.0 M KOH, MoS$_2$@Ni/CC exhibited a small onset potential of 30 mV and an η_{10} of 91 mV (Figure 8b). To drive a current density of 200 mA cm^{-2}, MoS$_2$@Ni/CC only needed an overpotential of 253 mV, much less than that of Pt/C (395 mV). As shown in Figure 8c, it also showed significant improvement to HER activity and durability in neutral pH electrolyte. The enhancements are presumably assigned to the synergy between MoS$_2$ and Ni. The success of Mo-based chalcogenides has also driven the exploration of other transition metal chalcogenide nanoarrays for advanced alkaline HER electrocatalysts, such as CoS$_2$ nanopyramid arrays on carbon fiber,[103] CoS$_2$ nano-pine-tree arrays on carbon fiber,[104] CoS$_{2x}$Se$_{(1-x)}$ nanowire arrays on carbon fiber,[105] and Ni$_3$S$_2$ nanosheet arrays on Ni foam.[106].

Apart from chalcogenides, recent years have seen important advances in transition metal phosphides and nitrides towards the exploration of low-cost and durable HER catalysts. For example, Tang et al. reported free-standing ternary Fe$_{0.5}$Co$_{0.5}$P nanowire arrays on carbon cloth (Fe$_{0.5}$Co$_{0.5}$P/CC), which showed Pt-like activity with a very small η_{10} of 37 mV and excellent stability in 0.5 M H$_2$SO$_4$ (Figure 8d−f).[107] DFT calculations showed that Fe doping in CoP could tune the ΔG_H to optimize hydrogen adsorption. Similarly, Zn-doped CoP nanowall arrays on Ti mesh (Zn$_{0.08}$Co$_{0.92}$P/TM) and Mn-doped CoP nanosheet arrays on Ti mesh (Mn-Co-P/Ti) were developed very recently as Pt-like HER electrocatalysts in a wider pH range of 0−14.[108,109] These examples show the effectiveness of transition metal doping for improving the overall HER activity of bi-metal phosphides. Transition metal nitrides are also known for their Pt-like HER performance with various advantageous properties like high electrical conductivity, good corrosion resistance, and excellent stability. As an example, Ren et al. synthesized self-supported porous WN nanowire arrays on carbon cloth (WN NW/CC, Figure 8g) via a clean

plasma-assisted nitridation method.[110] The as-synthesized WN NW/CC displayed an η_{10} of 130 mV and a Tafel slope of 59.6 mV dec^{-1} in 1.0 M KOH, producing higher HER current density than that of Pt foil at overpotentials greater than 200 mV (Figure 8h and 8i). Undoubtedly, the great progress made towards developing these advanced HER catalysts will further increase the commercial potential of hydrogen fuel.

3.4 CO$_2$ Reduction Reaction (CRR)

The conversion of CO$_2$ into valuable fuels and chemicals using the CRR has received renewed interest in recent years due to the increasing environmental and energy security issues surrounding conventional fossil fuels.[111−113] Unlike the electrochemical reactions discussed above, the CRR is a much more complex proton-coupled multi-step process that involves two, four, six, eight or even more electrons, leading to a vast number of possible products (e.g. CO, HCOOH, HCHO, CH$_3$OH, CH$_4$, and CH$_3$CH$_2$OH). Due to these complicated reaction pathways and the stability of the CO$_2$ molecule, the kinetics of the CRR are very sluggish. Although the CRR has been studied for several decades, the development of CRR electrocatalysts is still in its infancy, especially in terms of products selectivity. According to their major CRR products, conventional metal catalysts have been classified into three groups: (1) Au, Ag, Zn for CO production; (2) Sn, Hg, Pb for HCOOH production; (3) Cu for hydrocarbon and alcohol production. Conventional CRR catalysts face low Faradaic efficiencies due to competition from the more favorable HER in aqueous electrolyte. Therefore, developing highly active CRR electrocatalysts with high selectivity is a major challenge in this field.

Recently emerged nanostructured CRR electrocatalysts, including transition metals, transition metal oxides, transition metal chalcogenides, carbon materials,[114] and their nanocomposites, have shown to possess high CRR activity and selectivity, primarily owing to the high-density of exposed active sites and unique nano-size effects. Among them, a few self-

supported nanoarrays are particularly outstanding with significant CRR performances. For example, Liu et al. reported highly ordered N-doped nanodiamond/Si rod array (NDD/Si RA) using template directed synthesis (Figure 9a and 9b).[50] The NDD/Si RA prepared at relatively low temperature (NDD$_L$/Si RA) was highly selective in reducing CO_2 to acetate over formate at a low onset potential of -0.36 V vs. RHE, and the total FE reached 91.2$-$91.8% at -0.8 to -1.0 V vs. RHE (Figure 9c). Moreover, the production rates for acetate and formate were found to be positively correlated with the N content, and it was found that the N-sp^{3}C species were responsible for the high CRR activity. The CRR pathway was further investigated by electrokinetic data and in situ infrared spectroscopy which found that the likely pathway is: $CO_2 \rightarrow CO_2^{\cdot-} \rightarrow (COO)_2^{\cdot} \rightarrow CH_3COO^-$. Recently, Bi nanoflakes were designed and directly deposited on Cu substrates by a novel pulsed electrochemical method, which achieved a FE towards $HCOO^-$ of ~100% at -0.6 V vs. RHE (Figure 9d$-$f).[115] The numerical simulation indicated that the sharp edge and corner sites of the Bi nanoflakes are beneficial for the CRR because these sites can create strong local electric fields which enhance catalytic activity. Meanwhile, it was found that the thinner the nanoflakes, the stronger the electric field formed on the edge and corner sites. This example shows how nanostructuring and nano-size effects can affect electrocatalysis and provides insightful guidance for designing more advanced CRR catalysts. From these case studies and the lessons learnt from other electrochemical processes, constructing self-supported earth-abundant nanoarrays for CRR appears promising and warrants further development.

3.5 Nitrogen Reduction Reaction (NRR)

The NRR for ammonia (NH_3) synthesis is conventionally conducted via the Haber-Bosch process which requires high purity hydrogen, high temperatures (500$-$600 ºC), and high pressures (200$-$500 atm).[116] In contrast, electrocatalytic synthesis of NH_3 using renewable energy (e.g. sunlight and wind) at ambient conditions uses little energy and is environmentally

benign.[117] Like the CRR, electrochemical NRR involves multiple proton-coupled electron transfer steps and multiple intermediates. As the N≡N bond is much more stable than the C=O bond in CO_2, the NRR suffers from extremely sluggish kinetics, which often needs higher overpotentials to drive the reaction. Under these circumstances, it is likely that the competing HER becomes more prominent. Therefore, current NRR electrocatalysts usually exhibit poor activity and low selectivity, and it is highly significant to consider these issues in their design.

Until now, different materials, including metals (e.g. Pt, Au, Ru, Cu, Ti, Ni),[118−122] transition metal oxides (e.g. Fe_2O_3),[123] carbon based materials (e.g. polyaniline),[124] have been applied as NRR electrocatalysts. Since electrochemical NRR has attracted relatively less attention, few self-supported earth-abundant nanoarrays have been reported for it. Nevertheless, among current NRR electrocatalysts, Ni has shown the most promising activity. Kim and co-workers employed a Ni wire (Ø 1 mm × 3 cm, Nilaco Co.) as a NRR electrocatalyst in 0.1 M LiCl/ethylenediamine (EDA) electrolyte, which afforded a FE towards NH_3 of 17.2%.[122] This result is one of the highest among all reported NRR electrocatalysts given that most exhibit a FE toward NH_3 below 5%. It is believed that developing self-supported nanoarrays based on earth-abundant metals like Ni will create new opportunities for the electrochemical NRR. On the other hand, theoretical DFT studies provide another important way to screen efficient NRR electrocatalysts. For example, transition metal nitrides (e.g., VN and ZrN) are predicted to catalyze the NRR efficiently at low overpotentials and suppress the HER.[125,126] In this respect, Li et al. studied nitrogen fixation over GaN nanowires arrays assisted by Ru clusters with low atomicity (Figure 10a−c).[116] Among pure GaN materials with different doping levels and forms, the n-type GaN NWs exhibited the highest activity for NH_3 generation (Figure 10d). As shown in Figure 10e, surface modification of n-type GaN NWs with Ru at an optimized loading of 5 wt% could significantly improve the NH_3 synthesis rate. The optimized Ru@n-GaN NWs with 5 wt% Ru achieved an average NH_3 generation rate of 120 μmol h^{-1} g^{-1} as well as good cycle

stability (Figure 10f). With these insights as an initial step towards rational catalyst design, more and more breakthroughs can be expected in this underexplored field.

3.6 Urea Oxidation Reaction (UOR)

Self-supported earth-abundant nanoarrays are also promising electrocatalysts for other electrochemical reactions such as the urea oxidation reaction (UOR). The UOR is an important half reaction in urea-rich wastewater processing and direct urea fuel cells.[127,128] Being a six-electron transfer reaction with slow kinetics, more efficient electrocatalysts are necessary to lower the energy barrier and reduce the overpotentials required.[129] Benefitting from a large amount of active sites, good electrical conductivity, and robust structure, various Ni foam supported Ni-based nanoarrays, such as α-Ni(OH)$_2$ nanotubes,[130] mesoporous NiO nanosheets,[131] NiMoO$_4 \cdot$xH$_2$O nanosheets,[132] and Ni nanowires,[133] have emerged as a class of state-of-the-art electrocatalysts for the UOR. It is noted that the unique UOR activity of Ni-based catalysts is closely related to the Ni^{2+}/Ni^{3+} oxidation states, whereby the formed Ni^{3+} is responsible for oxidizing the urea.[129,134] Recently, Tang et al. reported Se-Ni(OH)$_2$-shelled NiSe nanowires vertically grown Ni foam as a superior UOR electrocatalyst (Figure 11 a−c).[135] The resultant catalyst required a very low potential of 0.366 V vs. saturated calomel electrode (SCE) to deliver 100 mA cm^{-2} in alkaline electrolyte (Figure 11d and 11e), exceeding all reported noble-metal-free UOR catalysts to date. Furthermore, DFT analysis showed that the Se-Ni(OH)$_2$ shell could lower the CO$_2$ adsorption/desorption barrier over pristine Ni(OH)$_2$ and enhance the reaction kinetics (Figure 11f and 11g). Hence, combining nanostructure engineering and surface modification offers a more effective strategy to assembling enhanced UOR catalysts.

4. BIFUNCTIONAL ELECTROCATALYSIS IN ENERGY DEVICES

All the electrochemical reactions that we have discussed so far are the half reactions of an overall energy system. However, real energy systems involve two different electrochemical

processes. For example, rechargeable metal-air batteries involve the ORR and OER, and water-alkali electrolyzers involve the OER and HER. In order to simplify these energy devices, it is highly desirable to explore bifunctional electrocatalysts. Particularly, to realize reversible energy conversion in rechargeable metal-air batteries, the electrocatalyst is required to be active for both the ORR and OER. To this end, electrocatalysts with bifunctional ability are traditionally prepared by mixing two powdery catalysts like benchmark Pt/C and IrO_2/C in a certain ratio (e.g. mass ratio of 1:1) and then depositing them on a current collector. Regardless of the complexity of operating such a catalyst, it is difficult to fully utilize them because one catalyst component is not operating while the other is. Therefore, developing bifunctional electrocatalysts with both ORR and OER activity can effectively address these issues. In the case of water-alkali electrolyzers, although different OER and HER electrocatalysts can be coupled to realize overall water splitting, the use of catalysts with bifunctional OER and HER electrocatalysis allows for device simplification. Accordingly, the concept of bifunctional electrocatalysts has been extensively developed and many self-supported earth-abundant nanoarrays with bifunctional electrocatalysis have been applied to these two well-studied energy devices.

4.1 Rechargeable Metal-Air Batteries

Rechargeable metal-air batteries, such as Li-air batteries and Zn-air batteries, are extremely attractive as energy storage devices with high energy density.[136,137] In theory, Li-air batteries have a specific energy density of 3862 W h kg^{-1} and Zn-air batteries can store up to 1084 W h kg^{-1}, whereas the practical energy density of commercial Li-ion batteries is less than 200 W h kg^{-1}.[138] Typically, a rechargeable metal-air battery consists of three key components: metal anode, cathode with catalysts, and electrolyte. Since the cathode with catalysts (also called the oxygen or air electrode) plays a vital role in improving the overall battery performance, it is essential to explore highly active and durable bifunctional electrocatalysts to promote oxygen

33

electrocatalysis, namely ORR and OER.[139] From the above section, it can be seen that two kinds of materials (i.e. transition metal oxides and carbon based materials) can serve as both ORR and OER catalysts. Indeed, this has been demonstrated by recent studies focusing on transition metal oxides and carbon-based materials as bifunctional catalysts for the ORR and OER.[140–143]

Transition metal oxides, especially Ni and Co related oxides, have shown promising bifunctional electrocatalysis for the ORR and OER in alkaline electrolyte. As self-supported nanoarrays can provide abundant active sites and rapid electrolyte/gas diffusion, nanostructured Ni- and Co-based arrays have been designed as superior oxygen electrodes. For example, Ling et al. reported carbon fiber paper supported single-crystal CoO nanorods (SC CoO NRs) with oxygen vacancies on pyramidal nanofacets introduced via surface structure engineering.[51] Amazingly, the as-synthesized SC CoO NRs displayed superior ORR and OER performances to Pt and RuO_2 catalysts, respectively. For the ORR, it exhibited an onset potential of 0.96 V vs. RHE, a half-wave potential of 0.85 V vs. RHE, a Tafel slope of 47 mV dec^{-1}, and an ORR current retention of 97% after 10 h operation. Regarding the OER, it showed an η_{10} of 330 mV and a Tafel slope of 44 mV dec^{-1}. As suggested by DFT calculations, surface oxygen defects on the SC CoO NRs enabled optimal adsorption on intermediates in the ORR/OER pathway. Wu and co-workers demonstrated CoO mesoporous nanowire arrays on Ni foam as a high-performance cathode for Li-O_2 batteries.[144] Owing to the advantageous electrode configuration and high intrinsic ORR/OER activity, the CoO nanoarrays achieved a high specific capacity of over 4800 mAh g_{CoO}^{-1} and prolonged durability of 50 cycles during 500 h.[144] In addition to CoO, self-supported spinel $NiCo_2O_4$ nanoarrays are also prospective oxygen cathode materials for Li-air batteries.[145,146]

Well-known as metal-free catalysts with bifunctional ORR/OER electrocatalysis and excellent electrical conductivity, N-doped carbon materials have been utilized as another type

of oxygen cathode in Li-air batteries. Li et al. prepared vertically aligned carbon nanotube arrays (CNTAs) on carbon fiber paper and investigated the as-prepared electrode as the air cathode in rechargeable hybrid Li-air batteries with 0.5 M LiOH and 0.5 M LiNO$_3$ as the catholyte.[147] The hybrid Li-air battery with CNTAs exhibited a discharge capacity of 710 A h kg^{-1} based on the carbon cathode and a specific energy of 2057 W h kg^{-1}, outperforming other hybrid Li-air batteries with Pt, MnO$_2$, and graphene cathodes. This superior performance was attributed to the N-doping and rich surface defects on the exposed graphene edges. The CNTAs also showed good stability for the ORR/OER during 63 h charge-discharge cycling tests. Shui and co-workers reported an oxygen electrode composed of vertically aligned N-doped coral-like carbon nanofiber (VA-NCCF) arrays (Figure 12a−c).[148] Due to its unique microstructure, the VA-NCCF showed favorable oxygen/electron transfer, and the assembled Li-O$_2$ battery displayed an energy efficiency up to 90% in a full discharge/charge cycle and a small discharge/charge potential gap of only 0.3 V (Figure 12d). Meanwhile, an impressively high specific capacity up to 1000 mAh g^{-1} was observed after 150 discharge/charge cycles. As a result, structure engineering of hierarchical heteroatom doped carbon nanoarrays offers a significant strategy to design more efficient bifunctional catalysts.

In addition to Li-air batteries, self-supported nanoarrays based on transition metal oxides and carbon materials have also been used as cathodes for Zn-air batteries. For instance, Lee et al. fabricated mesoporous Co$_3$O$_4$ nanowire arrays directly grown on stainless steel mesh as a bifunctional air electrode for rechargeable Zn-air batteries.[149] The resultant electrodes demonstrated considerable activity and stability with charge and discharge potential retentions of 97% and 94%, respectively, during long-term cycling for 600 h.[149] Recently, Li et al. reported N-doped carbon nanotube arrays on Ni foam as a bifunctional oxygen electrode for rechargeable Zn-air batteries, achieving a high discharge voltage of 1.02 V and low charge voltage of 1.98 V at 5 mA cm^{-2}.[150] Hybrid bifunctional nanoarrays based on Co$_3$O$_4$ and N-

doped carbon nanotubes (NCNT) hold greater potential in developing higher-performance cathodes for rechargeable Zn-air batteries.[143] A study by Fu et al. designed self-supported hair-like Co_3O_4-NCNT arrays directly grown on a flexible stainless-steel mesh (Figure 12e−g).[151] Using the Co_3O_4-NCNT/SS as air electrodes, the assembled Zn-air battery exhibited a high energy density of 847.6 W h kg^{-1} and a remarkable cycling durability over 500 h at a current density of 25 mA cm^{-2} (Figure 12h). This progress shows the potential of self-supported earth-abundant nanoarrays as bifunctional cathodes for rechargeable metal-air batteries.

4.2 Water-Alkali Electrolyzers

Water electrolysis enables the storage of electricity from renewable sources (e.g. sunlight, wind, waterpower) in the form of chemical energy (i.e. H_2 and O_2). This stored energy can be utilized at any time when energy is not being produced, overcoming the issues of intermittency associated with these energy sources. The H_2 produced is a clean fuel and is important in the production of many industrial chemicals. To reduce the cost and energy input of water-alkali electrolyzers for their large-scale commercialization, many highly efficient and robust catalysts based on inexpensive earth-abundant materials are being keenly pursued to replace the Pt-based catalysts for the HER and Ir-based catalysts for the OER. Various transition metal compounds (especially oxides, chalcogenides, nitrides, and phosphides) have been explored as bifunctional electrocatalysts to meet this challenge due to their intrinsic properties for both the HER and OER (Table S3). Particularly, self-supported nanoarrays represent one of the most advanced electrocatalysts for overall water splitting due to the fascinating structural and electronic properties.

During overall water splitting, the energy loss largely originates from the high OER overpotential. To screen efficient bifunctional catalysts for water-alkali electrolyzers, one obvious strategy is to develop state-of-the-art earth-abundant OER candidates and simultaneously improve their HER performance. With this in mind, our group has recently

developed some self-supported nanoarrays based on transition metal oxides towards superior overall alkaline water electrolysis, because they are regarded as a class of the most active OER catalysts. For example, hollow Co_3O_4 microtube arrays with hierarchical porosity have been grown on Ni foam (Figure 13a) through an electrochemical self-templating strategy.[152] The bifunctional Co_3O_4 microtube arrays delivered a current density of 10 mA cm^{-2} at a cell voltage of 1.63 V in 1.0 M KOH, comparable to the integrated performance of Pt/C and IrO_2/C (Figure 13b). More recently, S-$NiFe_2O_4$ ultra-small nanoparticle built nanosheets on Ni foam have been synthesized though a facile confined growth strategy with the assistance of thiourea.[75] By virtue of favorable 3D hierarchical structure with abundant active sites, high electrical conductivity and rapid mass transfer, it required only 1.65 and 1.95 V to afford 10 mA cm^{-2} for overall water splitting in alkaline and neutral pH. Intriguingly, Cai et al. developed a general, simple, and controllable template-directed strategy to assembly well-aligned metal-organic framework (MOF) arrays and derived self-supporting electrodes for water splitting.[23] Using ZIF-67 nanowire arrays as precursors, Ni@CoO@Co/N-doped porous carbon arrays were obtained which displayed a HER η_{10} of 190 mV with a Tafel slope of 98 mV dec^{-1} and an OER η_{10} of 309 mV with a Tafel slope of 53 mV dec^{-1}. Accordingly, self-supported transition metal oxide nanoarrays serve as important platforms for efficient water-alkali electrolyzers.

Self-supported metal chalcogenide, nitride, and phosphide nanoarrays have also recently emerged as a novel class of bifunctional electrocatalysts for overall water splitting in alkaline electrolytes. Feng et al. studied $\{\bar{2}10\}$ high-index faceted Ni_3S_2 nanosheet arrays on Ni foam (Figure 13c) as HER/OER electrocatalysts by combining experimental investigations with theoretical calculations.[59] The hydrothermally grown Ni_3S_2/NF afforded a current density of 10 mA cm^{-2} in 1.0 M KOH at an overpotential of 223, 260, and 530 mV for the HER, OER, and overall water splitting, respectively (Figure 13d−f). The correlation of experimental results and computational analysis confirmed that the excellent catalytic activity originated from the

synergistic catalytic effects from its nanosheet arrays and exposed $\{\bar{2}10\}$ high-index facets. As illustrated in Figure 2b, Yang reported the hydrothermal synthesis of MoS_2-Ni_3S_2 heteronanorod arrays on Ni foam.[24] Owing to its self-supported hierarchical structure, the resulting electrode achieved enhanced kinetics and activity for the HER, OER, and overall water electrolysis, requiring a low cell voltage (1.50 V) to produce 10 mA cm^{-2} in 1.0 M KOH. In the case of nitride nanoarrays, Jiang et al. reported vertically aligned Fe_2NiN nanoplate arrays on Ni foam as a bifunctional electrocatalyst which needed 1.65 V to deliver 10 mA cm^{-2} in 1.0 M KOH.[63] Reports have also shown that metal phosphides possess bifunctional electrocatalysis. For example, a series of self-supported nanoarrays based on Fe, Co, and Ni phosphides displayed superior overall water splitting performance compared to benchmark Pt/C‖IrO$_2$ (or Ir/C) couples. Notably, Duan et al. fabricated Fe and O doped Co_2P grown on Ni foam via the cation and anion manipulation of metal phosphides. The optimized dual-doped Co_2P required only η_{10} of 335.5 mV to drive overall alkaline water splitting, superior to state-of-the-art Pt/C‖IrO$_2$ counterparts (491.5 mV).[34] Further, Li and co-workers investigated Fe-doped Ni_2P nanosheet arrays as another mixed phosphide for both the HER and OER.[25] The $(Ni_{0.33}Fe_{0.67})_2P$ displayed optimal HER and OER activities and reached 10 mA cm^{-2} for overall water splitting at a cell voltage as low as 1.49 V, implying the high intrinsic bifunctional activity of mixed phosphide nanoarrays. According to Jin's editorial,[96] transition metal chalcogenides, nitrides, and phosphides are strictly precatalysts to OER catalysts, whereas they can work efficiently to catalyze both the OER and HER. Given their better apparent electrocatalytic performance, we believe that the extension of self-supported nanoarrays will accelerate the development of more advanced catalysts for water-alkali electrolyzers.

5. CONCLUSIONS AND PROSPECTS

During the last decade, remarkable progress has been made in the field of self-supported earth-abundant nanoarrays, from their synthesis to their application as promising electrocatalysts for

next generation energy technologies. Although many specifically designed nanoarrays have achieved satisfactory electrocatalysis for certain energy conversion reactions, there are still some challenges when considering utilization of the electrocatalysts in this research area. First, the majority of current studies are guided by performance-oriented trial-and-error approaches, yet the rational design of advanced catalysts is severely limited by the fundamental understanding of related reaction mechanisms, especially the elucidation of active sites and reaction pathways.[5] A clear understanding of these things would enable us to consciously tailor the components, morphologies, and structures of targeted materials, aiming to improve the activity and selectivity of resultant catalysts. Good examples of this progression are MoS_2 and heteroatom doped graphene as considerable advances have been achieved during the last few years in their computational modelling.[153-155] However, from the material synthesis perspective, combining the knowledge obtained from computational studies with experiments greatly depends on the precise control of composition and structure (at the nano-level) of the final materials. Therefore, developing more effective synthetic methods with component manipulation, morphology control, and structure engineering creates a significant challenge to be overcome.[43] To better understand the relationship between experimental results and theoretical calculations, in situ characterization techniques are indispensable for discovering the correlations between physicochemical properties and electrocatalytic performances. Accordingly, extensive exploration of in situ characterizations, such as in situ XAESE,[156,157] XPS,[158] Raman spectroscopy,[159] infrared spectroscopy,[50] and TEM,[160] is anticipated to guide future catalyst design. Finally, some of the more recently pursued reactions like the CRR and NRR have a profound place in a sustainable energy future, but remain underexplored. Therefore, more research efforts are needed to seek breakthroughs in these frontiers of electrocatalysis. It is likely that expanding the strategy of self-supported nanoarrays to more

39

earth-abundant candidates will lead to significant progress for the CRR, NRR, and related energy devices.

In summary, here we have presented the various synthesis methods of self-supported earth-abundant nanoarrays and their application in a wide range of electrochemical reactions and energy devices. Emerged as efficient and robust alternatives to precious metal electrocatalysts, various nanoarrays based on earth-abundant compounds have been highlighted in different energy conversion reactions (i.e. ORR, OER, HER, CRR, NRR, and UOR) and energy devices (i.e. rechargeable metal-air batteries and water-alkali electrolyzers). Although the community still faces some challenges, continuous development of relevant fields, particularly in theoretical computation and materials science, will create many new opportunities to explore more advanced electrocatalysts in the future. We believe that sustainable development based on next generation clean energy technologies can be eventually realized through further efforts in this exciting field of self-supported earth-abundant nanoarrays.

AUTHOR INFORMATION

Corresponding Author

*E-mail: s.qiao@adelaide.edu.au.

ORCID

Shi-Zhang Qiao: 0000-0002-4568-8422

Notes

The authors declare no competing financial interest.

REFERENCES

(1) Arakawa, H.; Aresta, M.; Armor, J. N.; Barteau, M. A.; Beckman, E. J.; Bell, A. T.; Bercaw, J. E.; Creutz, C.; Dinjus, E.; Dixon, D. A.; et al. Catalysis Research of Relevance to Carbon Management: Progress, Challenges, and Opportunities. *Chem. Rev.* **2001**, *101*, 953−996.

(2) Friedlingstein, P.; Andrew, R. M.; Rogelj, J.; Peters, G. P.; Canadell, J. G.; Knutti, R.; Luderer, G.; Raupach, M. R.; Schaeffer, M.; van Vuuren, D. P.; et al. Persistent Growth of CO_2 Emissions and Implications for Reaching Climate Targets. *Nat. Geosci.* **2014**, *7*, 709−715.

(3) Lewis, N. S.; Nocera, D. G. Powering the Planet: Chemical Challenges in Solar Energy Utilization. *Proc. Natl. Acad. Sci.* **2006**, *103*, 15729−15735.

(4) Olah, G. A.; Prakash, G. K. S.; Goeppert, A. Anthropogenic Chemical Carbon Cycle for a Sustainable Future. *J. Am. Chem. Soc.* **2011**, *133*, 12881−12898.

(5) Seh, Z. W.; Kibsgaard, J.; Dickens, C. F.; Chorkendorff, I.; Nørskov, J. K.; Jaramillo, T. F. Combining Theory and Experiment in Electrocatalysis: Insights into Materials Design. *Science* **2017**, *355*, eaad4998.

(6) Liu, J.; Jiao, M.; Lu, L.; Barkholtz, H. M.; Li, Y.; Wang, Y.; Jiang, L.; Wu, Z.; Liu, D.-j.; Zhuang, L.; et al. High Performance Platinum Single Atom Electrocatalyst for Oxygen Reduction Reaction. *Nat. Commun.* **2017**, *8*, 15938.

(7) Cheng, N.; Stambula, S.; Wang, D.; Banis, M. N.; Liu, J.; Riese, A.; Xiao, B.; Li, R.; Sham, T.-K.; Liu, L.-M.; et al. Platinum Single-Atom and Cluster Catalysis of the Hydrogen Evolution Reaction. *Nat. Commun.* **2016**, *7*, 13638.

(8) Lee, Y.; Suntivich, J.; May, K. J.; Perry, E. E.; Shao-Horn, Y. Synthesis and Activities of Rutile IrO_2 and RuO_2 Nanoparticles for Oxygen Evolution in Acid and Alkaline Solutions. *J. Phys. Chem. Lett.* **2012**, *3*, 399−404.

(9) Jamesh, M. I. Recent Progress on Earth Abundant Hydrogen Evolution Reaction and Oxygen Evolution Reaction Bifunctional Electrocatalyst for Overall Water Splitting in Alkaline Media. *J. Power Sources* **2016**, *333*, 213−236.

(10) Zhu, Y. P.; Guo, C.; Zheng, Y.; Qiao, S.-Z. Surface and Interface Engineering of Noble-Metal-Free Electrocatalysts for Efficient Energy Conversion Processes. *Acc. Chem. Res.* **2017**, *50*, 915−923.

(11) Du, P.; Eisenberg, R. Catalysts Made of Earth-Abundant Elements (Co, Ni, Fe) for Water Splitting: Recent Progress and Future Challenges. *Energy Environ. Sci.* **2012**, *5*, 6012−6021.

(12) Xia, W.; Mahmood, A.; Liang, Z.; Zou, R.; Guo, S. Earth-Abundant Nanomaterials for Oxygen Reduction. *Angew. Chem. Int. Ed.* **2016**, *55*, 2650−2676.

(13) Faber, M. S.; Jin, S. Earth-Abundant Inorganic Electrocatalysts and their Nanostructures for Energy Conversion Applications. *Energy Environ. Sci.* **2014**, *7*, 3519−3542.

(14) Ma, T. Y.; Dai, S.; Qiao, S. Z. Self-Supported Electrocatalysts for Advanced Energy Conversion Processes. *Mater. Today* **2016**, *19*, 265−273.

(15) Weber, A. Z.; Kusoglu, A. Unexplained Transport Resistances for Low-Loaded Fuel-Cell Catalyst Layers. *J. Mater. Chem. A* **2014**, *2*, 17207−17211.

(16) Li, L.; Hu, L.; Li, J.; Wei, Z. Enhanced Stability of Pt Nanoparticle Electrocatalysts for Fuel Cells. *Nano Res.* **2015**, *8*, 418−440.

(17) Luo, F.; Liao, S.; Dang, D.; Zheng, Y.; Xu, D.; Nan, H.; Shu, T.; Fu, Z. Tin and Silicon Binary Oxide on the Carbon Support of a Pt Electrocatalyst with Enhanced Activity and Durability. *ACS Catal.* **2015**, *5*, 2242−2249.

(18) Eastwood, B. J.; Christensen, P. A.; Armstrong, R. D.; Bates, N. R. Electrochemical Oxidation of a Carbon Black Loaded Polymer Electrode in Aqueous Electrolytes. *J. Solid State Electrochem.* **1999**, *3*, 179−186.

(19) Shao, Y.; Yin, G.; Gao, Y. Understanding and Approaches for the Durability Issues of Pt-Based Catalysts for PEM Fuel Cell. *J. Power Sources* **2007**, *171*, 558−566.

(20) Katsounaros, I.; Cherevko, S.; Zeradjanin, A. R.; Mayrhofer, K. J. J. Oxygen Electrochemistry as a Cornerstone for Sustainable Energy Conversion. *Angew. Chem. Int. Ed.* **2014**, *53*, 102−121.

(21) Lu, X.; Zhao, C. Electrodeposition of Hierarchically Structured Three-Dimensional Nickel–Iron Electrodes for Efficient Oxygen Evolution at High Current Densities. *Nat. Commun.* **2015**, *6*, 6616.

(22) Liu, Y.; Chen, S.; Quan, X.; Zhao, H.; Yu, H.; Zhang, Y. Tuning the Electrochemical Properties of a Boron and Nitrogen Codoped Nanodiamond Rod Array to Achieve High Performance for both Electro-Oxidation and Electro-Reduction. *J. Mater. Chem. A* **2013**, *1*, 14706−14712.

(23) Cai, G.; Zhang, W.; Jiao, L.; Yu, S.-H.; Jiang, H.-L. Template-Directed Growth of Well-Aligned MOF Arrays and Derived Self-Supporting Electrodes for Water Splitting. *Chem* **2017**, *2*, 791−802.

(24) Yang, Y.; Zhang, K.; Lin, H.; Li, X.; Chan, H. C.; Yang, L.; Gao, Q. MoS_2–Ni_3S_2 Heteronanorods as Efficient and Stable Bifunctional Electrocatalysts for Overall Water Splitting. *ACS Catal.* **2017**, *7*, 2357−2366.

(25) Li, Y.; Zhang, H.; Jiang, M.; Zhang, Q.; He, P.; Sun, X. 3D Self-Supported Fe-Doped Ni_2P Nanosheet Arrays as Bifunctional Catalysts for Overall Water Splitting. *Adv. Funct. Mater.* **2017**, *27*, 1702513.

(26) Zhu, Y.-P.; Liu, Y.-P.; Ren, T.-Z.; Yuan, Z.-Y. Self-Supported Cobalt Phosphide Mesoporous Nanorod Arrays: A Flexible and Bifunctional Electrode for Highly Active Electrocatalytic Water Reduction and Oxidation. *Adv. Funct. Mater.* **2015**, *25*, 7337−7347.

(27) Yang, L.; Liu, D.; Hao, S.; Kong, R.; Asiri, A. M.; Zhang, C.; Sun, X. A Cobalt-Borate Nanosheet Array: An Efficient and Durable Non-Noble-Metal Electrocatalyst for Water Oxidation at Near Neutral pH. *J. Mater. Chem. A* **2017**, *5*, 7305−7308.

(28) Lu, B.; Cao, D.; Wang, P.; Wang, G.; Gao, Y. Oxygen Evolution Reaction on Ni-Substituted Co_3O_4 Nanowire Array Electrodes. *Int. J. Hydrogen Energy* **2011**, *36*, 72−78.

(29) Zhang, B.; Lui, Y. H.; Zhou, L.; Tang, X.; Hu, S. An Alkaline Electro-Activated Fe-Ni Phosphide Nanoparticle-Stack Array for High-Performance Oxygen Evolution under Alkaline and Neutral Conditions. *J. Mater. Chem. A* **2017**, *5*, 13329−13335.

(30) Wang, X.; Zheng, Y.; Yuan, J.; Shen, J.; Hu, J.; Wang, A.-j.; Wu, L.; Niu, L. Porous NiCo Diselenide Nanosheets Arrayed on Carbon Cloth as Promising Advanced Catalysts Used in Water Splitting. *Electrochim. Acta* **2017**, *225*, 503−513.

(31) Xu, Y.-Z.; Yuan, C.-Z.; Chen, X.-P. One-Pot Synthesis Nickel Sulfide/Amorphous Molybdenum Sulfide Nanosheets Array on Nickel Foam as a Robust Oxygen Evolution Reaction Electrocatalyst. *J. Solid State Chem.* **2017**, *256*, 124−129.

(32) Li, X.; Du, X.; Ma, X.; Wang, Z.; Hao, X.; Abudula, A.; Yoshida, A.; Guan, G. CuO Nanowire@Co3O4 Ultrathin Nanosheet Core-Shell Arrays: An Effective Catalyst for Oxygen Evolution Reaction. *Electrochim. Acta* **2017**, *250*, 77−83.

(33) Ren, X.; Ge, R.; Zhang, Y.; Liu, D.; Wu, D.; Sun, X.; Du, B.; Wei, Q. Cobalt-Borate Nanowire Array as a High-Performance Catalyst for Oxygen Evolution Reaction in Near-Neutral Media. *J. Mater. Chem. A* **2017**, *5*, 7291−7294.

(34) Duan, J.; Chen, S.; Vasileff, A.; Qiao, S. Z. Anion and Cation Modulation in Metal Compounds for Bifunctional Overall Water Splitting. *ACS Nano* **2016**, *10*, 8738−8745.

(35) Tahir, M.; Pan, L.; Idrees, F.; Zhang, X.; Wang, L.; Zou, J.-J.; Wang, Z. L. Electrocatalytic Oxygen Evolution Reaction for Energy Conversion and Storage: A Comprehensive Review. *Nano Energy* **2017**, *37*, 136−157.

(36) Zhang, F.; Qi, L. Recent Progress in Self-Supported Metal Oxide Nanoarray Electrodes for Advanced Lithium-Ion Batteries. *Adv. Sci.* **2016**, *3*, 1600049.

(37) Morales-Guio, C. G.; Stern, L.-A.; Hu, X. Nanostructured Hydrotreating Catalysts for Electrochemical Hydrogen Evolution. *Chem. Soc. Rev.* **2014**, *43*, 6555−6569.

(38) Asefa, T. Metal-Free and Noble Metal-Free Heteroatom-Doped Nanostructured Carbons as Prospective Sustainable Electrocatalysts. *Acc. Chem. Res.* **2016**, *49*, 1873−1883.

(39) Kuang, M.; Zheng, G. Nanostructured Bifunctional Redox Electrocatalysts. *Small* **2016**, *12*, 5656−5675.

(40) Luc, W.; Jiao, F. Nanoporous Metals as Electrocatalysts: State-of-the-Art, Opportunities, and Challenges. *ACS Catal.* **2017**, *7*, 5856−5861.

(41) Zhang, L.; Zhao, Z.-J.; Gong, J. Nanostructured Materials for Heterogeneous Electrocatalytic CO_2 Reduction and their Related Reaction Mechanisms. *Angew. Chem. Int. Ed.* **2017**, *56*, 11326−11353.

(42) Zhang, H.-M.; Guo, Y.-G.; Wan, L.-J.; Bai, C.-L. Novel Electrocatalytic Activity in Layered Ni-Cu Nanowire Arrays. *Chem. Commun.* **2003**, *0*, 3022−3023.

(43) Liu, J.; Zhu, D.; Guo, C.; Vasileff, A.; Qiao, S.-Z. Design Strategies toward Advanced MOF-Derived Electrocatalysts for Energy-Conversion Reactions. *Adv. Energy Mater.* **2017**, *7*, 1700518.

(44) Masuda, H.; Fukuda, K. Ordered Metal Nanohole Arrays Made by a Two-Step Replication of Honeycomb Structures of Anodic Alumina. *Science* **1995**, *268*, 1466−1468.

(45) Sander, M. S.; Prieto, A. L.; Gronsky, R.; Sands, T.; Stacy, A. M. Fabrication of High-Density, High Aspect Ratio, Large-Area Bismuth Telluride Nanowire Arrays by Electrodeposition into Porous Anodic Alumina Templates. *Adv. Mater.* **2002**, *14*, 665−667.

(46) Zhang, X. Y.; Zhang, L. D.; Li, G. H.; Zhao, L. X. Template Synthesis of Well-Graphitized Carbon Nanotube Arrays. *Mater. Sci. Eng. A* **2001**, *308*, 9−12.

(47) Wen, Z.; Wang, Q.; Li, J. Template Synthesis of Aligned Carbon Nanotube Arrays using Glucose as a Carbon Source: Pt Decoration of Inner and Outer Nanotube Surfaces for Fuel-Cell Catalysts. *Adv. Funct. Mater.* **2008**, *18*, 959−964.

(48) Guo, Y. G.; Hu, J. S.; Zhang, H. M.; Liang, H. P.; Wan, L. J.; Bai, C. L. Tin/Platinum Bimetallic Nanotube Array and its Electrocatalytic Activity for Methanol Oxidation. *Adv. Mater.* **2005**, *17*, 746−750.

(49) Ding, L.-X.; Li, G.-R.; Wang, Z.-L.; Liu, Z.-Q.; Liu, H.; Tong, Y.-X. Porous Ni@Pt Core-Shell Nanotube Array Electrocatalyst with High Activity and Stability for Methanol Oxidation. *Chem. Eur. J.* **2012**, *18*, 8386−8391.

(50) Liu, Y.; Chen, S.; Quan, X.; Yu, H. Efficient Electrochemical Reduction of Carbon Dioxide to Acetate on Nitrogen-Doped Nanodiamond. *J. Am. Chem. Soc.* **2015**, *137*, 11631−11636.

(51) Ling, T.; Yan, D.-Y.; Jiao, Y.; Wang, H.; Zheng, Y.; Zheng, X.; Mao, J.; Du, X.-W.; Hu, Z.; Jaroniec, M.; et al. Engineering Surface Atomic Structure of Single-Crystal Cobalt (II) Oxide Nanorods for Superior Electrocatalysis. *Nat. Commun.* **2016**, *7*, 12876.

(52) Zhao, G.-Y.; Xu, C.-L.; Guo, D.-J.; Li, H.; Li, H.-L. Template Preparation of Pt–Ru and Pt Nanowire Array Electrodes on a Ti/Si Substrate for Methanol Electro-Oxidation. *J. Power Sources* **2006**, *162*, 492−496.

(53) Li, R.; Zhang, P.; Huang, Y.; Chen, C.; Chen, Q. Facile Approach to Prepare Pd Nanoarray Catalysts within Porous Alumina Templates on Macroscopic Scales. *ACS Appl. Mater. Interfaces* **2013**, *5*, 12695−12700.

(54) Shi, L.; Pei, C.; Xu, Y.; Li, Q. Template-Directed Synthesis of Ordered Single-Crystalline Nanowires Arrays of Cu_2ZnSnS_4 and $Cu_2ZnSnSe_4$. *J. Am. Chem. Soc.* **2011**, *133*, 10328−10331.

(55) Shang, X.; Yan, K.-L.; Liu, Z.-Z.; Lu, S.-S.; Dong, B.; Chi, J.-Q.; Li, X.; Liu, Y.-R.; Chai, Y.-M.; Liu, C.-G. Oxidized Carbon Fiber Supported Vertical WS_2 Nanosheets Arrays as Efficient 3D Nanostructure Electrocatalyts for Hydrogen Evolution Reaction. *Appl. Surf. Sci.* **2017**, *402*, 120−128.

(56) Tian, J.; Xing, Z.; Chu, Q.; Liu, Q.; Asiri, A. M.; Qusti, A. H.; Al-Youbi, A. O.; Sun, X. PH-Driven Dissolution-Precipitation: A Novel Route toward Ultrathin $Ni(OH)_2$ Nanosheets Array on Nickel Foam as Binder-Free Anode for Li-Ion Batteries with Ultrahigh Capacity. *CrystEngComm* **2013**, *15*, 8300−8305.

(57) Zhao, Y.; Chang, C.; Teng, F.; Zhao, Y.; Chen, G.; Shi, R.; Waterhouse, G. I. N.; Huang, W.; Zhang, T. Defect-Engineered Ultrathin δ-MnO_2 Nanosheet Arrays as Bifunctional Electrodes for Efficient Overall Water Splitting. *Adv. Energy Mater.* **2017**, *7*, 1700005.

(58) Chen, Y.-Y.; Zhang, Y.; Zhang, X.; Tang, T.; Luo, H.; Niu, S.; Dai, Z.-H.; Wan, L.-J.; Hu, J.-S. Self-Templated Fabrication of $MoNi_4$/MoO_{3-x} Nanorod Arrays with Dual Active Components for Highly Efficient Hydrogen Evolution. *Adv. Mater.* **2017**, *29*, 1703311.

(59) Feng, L.-L.; Yu, G.; Wu, Y.; Li, G.-D.; Li, H.; Sun, Y.; Asefa, T.; Chen, W.; Zou, X. High-Index Faceted Ni_3S_2 Nanosheet Arrays as Highly Active and Ultrastable Electrocatalysts for Water Splitting. *J. Am. Chem. Soc.* **2015**, *137*, 14023−14026.

(60) Chen, J. S.; Ren, J.; Shalom, M.; Fellinger, T.; Antonietti, M. Stainless Steel Mesh-Supported NiS Nanosheet Array as Highly Efficient Catalyst for Oxygen Evolution Reaction. *ACS Appl. Mater. Interfaces* **2016**, *8*, 5509−5516.

(61) Li, W.; Gao, X.; Xiong, D.; Wei, F.; Song, W.-G.; Xu, J.; Liu, L. Hydrothermal Synthesis of Monolithic Co_3Se_4 Nanowire Electrodes for Oxygen Evolution and Overall Water Splitting with High Efficiency and Extraordinary Catalytic Stability. *Adv. Energy Mater.* **2017**, *7*, 1602579.

(62) Tang, C.; Cheng, N.; Pu, Z.; Xing, W.; Sun, X. NiSe Nanowire Film Supported on Nickel Foam: An Efficient and Stable 3D Bifunctional Electrode for Full Water Splitting. *Angew. Chem. Int. Ed.* **2015**, *54*, 9351−9355.

(63) Jiang, M.; Li, Y.; Lu, Z.; Sun, X.; Duan, X. Binary Nickel-Iron Nitride Nanoarrays as Bifunctional Electrocatalysts for Overall Water Splitting. *Inorg. Chem. Front.* **2016**, *3*, 630−634.

(64) Xie, L.; Qu, F.; Liu, Z.; Ren, X.; Hao, S.; Ge, R.; Du, G.; Asiri, A. M.; Sun, X.; Chen, L. In Situ Formation of a 3D Core/Shell Structured Ni$_3$N@Ni-Bi Nanosheet Array: An Efficient Non-Noble-Metal Bifunctional Electrocatalyst toward Full Water Splitting under Near-Neutral Conditions. *J. Mater. Chem. A* **2017**, *5*, 7806−7810.

(65) Lv, C.; Peng, Z.; Zhao, Y.; Huang, Z.; Zhang, C. The Hierarchical Nanowires Array of Iron Phosphide Integrated on a Carbon Fiber Paper as an Effective Electrocatalyst for Hydrogen Generation. *J. Mater. Chem. A* **2016**, *4*, 1454−1460.

(66) Liu, K.; Wang, F.; Shifa, T. A.; Wang, Z.; Xu, K.; Zhang, Y.; Cheng, Z.; Zhan, X.; He, J. An efficient ternary CoP$_{2x}$Se$_{2(1-x)}$ Nanowire Array for Overall Water Splitting. *Nanoscale* **2017**, *9*, 3995−4001.

(67) Wang, F.; Li, Y.; Shifa, T. A.; Liu, K.; Wang, F.; Wang, Z.; Xu, P.; Wang, Q.; He, J. Selenium-Enriched Nickel Selenide Nanosheets as a Robust Electrocatalyst for Hydrogen Generation. *Angew. Chem. Int. Ed.* **2016**, *55*, 6919−6924.

(68) Lee, C.-P.; Chen, W.-F.; Billo, T.; Lin, Y.-G.; Fu, F.-Y.; Samireddi, S.; Lee, C.-H.; Hwang, J.-S.; Chen, K.-H.; Chen, L.-C. Beaded Stream-Like CoSe$_2$ Nanoneedle Array for Efficient Hydrogen Evolution Electrocatalysis. *J. Mater. Chem. A* **2016**, *4*, 4553−4561.

(69) Ma, X.; Li, X.; Jagadale, A. D.; Hao, X.; Abudula, A.; Guan, G. Fabrication of Cu(OH)$_2$@NiFe-Layered Double Hydroxide Catalyst Array for Electrochemical Water Splitting. *Int. J. Hydrogen Energy* **2016**, *41*, 14553−14561.

(70) V. Manzano, C.; Caballero-Calero, O.; Hormeño, S.; Penedo, M.; Luna, M.; Martín-González, M. S. ZnO Morphology Control by Pulsed Electrodeposition. *J. Phys. Chem. C* **2013**, *117*, 1502−1508.

(71) Sun, Y.; Liu, C.; Grauer, D. C.; Yano, J.; Long, J. R.; Yang, P.; Chang, C. J. Electrodeposited Cobalt-Sulfide Catalyst for Electrochemical and Photoelectrochemical Hydrogen Generation from Water. *J. Am. Chem. Soc.* **2013**, *135*, 17699−17702.

(72) Zhang, L.; Liu, B.; Zhang, N.; Ma, M. Electrosynthesis of Co_3O_4 and $Co(OH)_2$ Ultrathin Nanosheet Arrays for Efficient Electrocatalytic Water Splitting in Alkaline and Neutral Media. *Nano Res.* **2017**, *11*, 323−333.

(73) Han, G.-Q.; Li, X.; Liu, Y.-R.; Dong, B.; Hu, W.-H.; Shang, X.; Zhao, X.; Chai, Y.-M.; Liu, Y.-Q.; Liu, C.-G. Controllable Synthesis of Three Dimensional Electrodeposited Co-P Nanosphere Arrays as Efficient Electrocatalysts for Overall Water Splitting. *RSC Adv.* **2016**, *6*, 52761−52771.

(74) Shang, X.; Yan, K.-L.; Lu, S.-S.; Dong, B.; Gao, W.-K.; Chi, J.-Q.; Liu, Z.-Z.; Chai, Y.-M.; Liu, C.-G. Controlling Electrodeposited Ultrathin Amorphous Fe Hydroxides Film on V-Doped Nickel Sulfide Nanowires as Efficient Electrocatalyst for Water Oxidation. *J. Power Sources* **2017**, *363*, 44−53.

(75) Liu, J.; Zhu, D.; Ling, T.; Vasileff, A.; Qiao, S.-Z. S-$NiFe_2O_4$ Ultra-Small Nanoparticle Built Nanosheets for Efficient Water Splitting in Alkaline and Neutral pH. *Nano Energy* **2017**, *40*, 264−273.

(76) Chen, X.; Liu, G.; Zheng, W.; Feng, W.; Cao, W.; Hu, W.; Hu, P. Vertical 2D MoO_2/$MoSe_2$ Core–Shell Nanosheet Arrays as High-Performance Electrocatalysts for Hydrogen Evolution Reaction. *Adv. Funct. Mater.* **2016**, *26*, 8537−8544.

(77) Zhang, W.; Wen, X.; Yang, S.; Berta, Y.; Wang, Z. L. Single-Crystalline Scroll-Type Nanotube Arrays of Copper Hydroxide Synthesized at Room Temperature. *Adv. Mater.* **2003**, *15*, 822−825.

(78) Hou, C.-C.; Fu, W.-F.; Chen, Y. Self-Supported Cu-Based Nanowire Arrays as Noble-Metal-Free Electrocatalysts for Oxygen Evolution. *ChemSusChem* **2016**, *9*, 2069−2073.

(79) Tong, X.; Xia, X.; Guo, C.; Zhang, Y.; Tu, J.; Fan, H. J.; Guo, X.-Y. Efficient Oxygen Reduction Reaction Using Mesoporous Ni-Doped Co_3O_4 Nanowire Array Electrocatalysts. *J. Mater. Chem. A* **2015**, *3*, 18372−18379.

(80) She, X.; Yang, D.; Jing, D.; Yuan, F.; Yang, W.; Guo, L.; Che, Y. Nitrogen-Doped One-Dimensional (1D) Macroporous Carbonaceous Nanotube Arrays and their Application in Electrocatalytic Oxygen Reduction Reactions. *Nanoscale* **2014**, *6*, 11057−11061.

(81) Zhu, J.; Jiang, S. P.; Wang, R.; Shi, K.; Shen, P. K. One-Pot Synthesis of a Nitrogen and Phosphorus-Dual-Doped Carbon Nanotube Array as a Highly Effective Electrocatalyst for the Oxygen Reduction Reaction. *J. Mater. Chem. A* **2014**, *2*, 15448−15453.

(82) Lu, Z.; Xu, W.; Ma, J.; Li, Y.; Sun, X.; Jiang, L. Superaerophilic Carbon-Nanotube-Array Electrode for High-Performance Oxygen Reduction Reaction. *Adv. Mater.* **2016**, *28*, 7155−7161.

(83) Suen, N.-T.; Hung, S.-F.; Quan, Q.; Zhang, N.; Xu, Y.-J.; Chen, H. M. Electrocatalysis for the Oxygen Evolution Reaction: Recent Development and Future Perspectives. *Chem. Soc. Rev.* **2017**, *46*, 337−365.

(84) Cheng, Y.; Jiang, S. P. Advances in Electrocatalysts for Oxygen Evolution Reaction of Water Electrolysis-from Metal Oxides to Carbon Nanotubes. *Prog. Nat. Sci.* **2015**, *25*, 545−553.

(85) Man, I. C.; Su, H.-Y.; Calle-Vallejo, F.; Hansen, H. A.; Martínez, J. I.; Inoglu, N. G.; Kitchin, J.; Jaramillo, T. F.; Nørskov, J. K.; Rossmeisl, J. Universality in Oxygen Evolution Electrocatalysis on Oxide Surfaces. *ChemCatChem* **2011**, *3*, 1159−1165.

(86) Kötz, R.; Lewerenz, H. J.; Stucki, S. XPS Studies of Oxygen Evolution on Ru and RuO_2 Anodes. *J. Electrochem. Soc.* **1983**, *130*, 825−829.

(87) Kötz, R.; Neff, H.; Stucki, S. Anodic Iridium Oxide Films: XPS-Studies of Oxidation State Changes and O_2-Evolution. *J. Electrochem. Soc.* **1984**, *131*, 72−77.

(88) Fabbri, E.; Habereder, A.; Waltar, K.; Kotz, R.; Schmidt, T. J. Developments and Perspectives of Oxide-Based Catalysts for the Oxygen Evolution Reaction. *Catal. Sci. Technol.* **2014**, *4*, 3800−3821.

(89) Gong, M.; Dai, H. A Mini Review of NiFe-Based Materials as Highly Active Oxygen Evolution Reaction Electrocatalysts. *Nano Res.* **2015**, *8*, 23−39.

(90) Zhao, Z.; Wu, H.; He, H.; Xu, X.; Jin, Y. Self-Standing Non-Noble Metal (Ni-Fe) Oxide Nanotube Array Anode Catalysts with Synergistic Reactivity for High-Performance Water Oxidation. *J. Mater. Chem. A* **2015**, *3*, 7179−7186.

(91) Zhang, X.; Si, C.; Guo, X.; Kong, R.; Qu, F. A $MnCo_2S_4$ Nanowire Array as an Earth-Abundant Electrocatalyst for an Efficient Oxygen Evolution Reaction under Alkaline Conditions. *J. Mater. Chem. A* **2017**, *5*, 17211−17215.

(92) Dong, Q.; Wang, Q.; Dai, Z.; Qiu, H.; Dong, X. MOF-Derived Zn-Doped $CoSe_2$ as an Efficient and Stable Free-Standing Catalyst for Oxygen Evolution Reaction. *ACS Appl. Mater. Interfaces* **2016**, *8*, 26902−26907.

(93) Ma, M.; Qu, F.; Ji, X.; Liu, D.; Hao, S.; Du, G.; Asiri, A. M.; Yao, Y.; Chen, L.; Sun, X. Bimetallic Nickel-Substituted Cobalt-Borate Nanowire Array: An Earth-Abundant Water Oxidation Electrocatalyst with Superior Activity and Durability at Near Neutral pH. *Small* **2017**, *13*, 1700394.

(94) Wang, J.; Ma, X.; Qu, F.; Asiri, A. M.; Sun, X. Fe-Doped Ni_2P Nanosheet Array for High-Efficiency Electrochemical Water Oxidation. *Inorg. Chem.* **2017**, *56*, 1041−1044.

(95) Zhang, Y.; Ouyang, B.; Xu, J.; Jia, G.; Chen, S.; Rawat, R. S.; Fan, H. J. Rapid Synthesis of Cobalt Nitride Nanowires: Highly Efficient and Low-Cost Catalysts for Oxygen Evolution. *Angew. Chem. Int. Ed.* **2016**, *55*, 8670−8674.

(96) Jin, S. Are Metal Chalcogenides, Nitrides, and Phosphides Oxygen Evolution Catalysts or Bifunctional Catalysts? *ACS Energy Lett.* **2017**, *2*, 1937−1938.

(97) Zhu, Y. P.; Jing, Y.; Vasileff, A.; Heine, T.; Qiao, S.-Z. 3D Synergistically Active Carbon Nanofibers for Improved Oxygen Evolution. *Adv. Energy Mater.* **2017**, *7*, 1602928.

(98) Greeley, J.; Jaramillo, T. F.; Bonde, J.; Chorkendorff, I.; Nørskov, J. K. Computational High-Throughput Screening of Electrocatalytic Materials for Hydrogen Evolution. *Nat. Mater.* **2006**, *5*, 909.

(99) Kong, D.; Wang, H.; Cha, J. J.; Pasta, M.; Koski, K. J.; Yao, J.; Cui, Y. Synthesis of MoS_2 and $MoSe_2$ Films with Vertically Aligned Layers. *Nano Lett.* **2013**, *13*, 1341−1347.

(100) Xu, Y.; Zheng, C.; Wang, S.; Hou, Y. 3D Arrays of Molybdenum Sulphide Nanosheets on Mo Meshes: Efficient Electrocatalysts for Hydrogen Evolution Reaction. *Electrochim. Acta* **2015**, *174*, 653−659.

(101) Miao, J.; Xiao, F.-X.; Yang, H. B.; Khoo, S. Y.; Chen, J.; Fan, Z.; Hsu, Y.-Y.; Chen, H. M.; Zhang, H.; Liu, B. Hierarchical Ni-Mo-S Nanosheets on Carbon Fiber Cloth: A Flexible Electrode for Efficient Hydrogen Generation in Neutral Electrolyte. *Sci. Adv.* **2015**, *1*, e1500259.

(102) Xing, Z.; Yang, X.; Asiri, A. M.; Sun, X. Three-Dimensional Structures of MoS_2@Ni Core/Shell Nanosheets Array toward Synergetic Electrocatalytic Water Splitting. *ACS Appl. Mater. Interfaces* **2016**, *8*, 14521−14526.

(103) Zhang, H.; Li, Y.; Zhang, G.; Xu, T.; Wan, P.; Sun, X. A Metallic CoS_2 Nanopyramid Array Grown on 3D Carbon Fiber Paper as an Excellent Electrocatalyst for Hydrogen Evolution. *J. Mater. Chem. A* **2015**, *3*, 6306−6310.

(104) Kim, J. Y.; Han, S.; Bang, J. H. Cobalt Disulfide Nano-Pine-Tree Array as a Platinum Alternative Electrocatalyst for Hydrogen Evolution Reaction. *Mater. Lett.* **2017**, *189*, 97−100.

(105) Liu, K.; Wang, F.; Xu, K.; Shifa, T. A.; Cheng, Z.; Zhan, X.; He, J. $CoS_{2x}Se_{2(1−x)}$ Nanowire Array: An Efficient Ternary Electrocatalyst for the Hydrogen Evolution Reaction. *Nanoscale* **2016**, *8*, 4699−4704.

(106) Tang, C.; Pu, Z.; Liu, Q.; Asiri, A. M.; Luo, Y.; Sun, X. Ni_3S_2 Nanosheets Array Supported on Ni foam: A Novel Efficient Three-Dimensional Hydrogen-Evolving Electrocatalyst in both Neutral and Basic Solutions. *Int. J. Hydrogen Energy* **2015**, *40*, 4727−4732.

(107) Tang, C.; Gan, L.; Zhang, R.; Lu, W.; Jiang, X.; Asiri, A. M.; Sun, X.; Wang, J.; Chen, L. Ternary $Fe_xCo_{1−x}P$ Nanowire Array as a Robust Hydrogen Evolution Reaction Electrocatalyst with Pt-Like Activity: Experimental and Theoretical Insight. *Nano Lett.* **2016**, *16*, 6617−6621.

(108) Liu, T.; Liu, D.; Qu, F.; Wang, D.; Zhang, L.; Ge, R.; Hao, S.; Ma, Y.; Du, G.; Asiri, A. M.; et al. Enhanced Electrocatalysis for Energy-Efficient Hydrogen Production over CoP Catalyst with Nonelectroactive Zn as a Promoter. *Adv. Energy Mater.* **2017**, *7*, 1700020.

(109) Liu, T.; Ma, X.; Liu, D.; Hao, S.; Du, G.; Ma, Y.; Asiri, A. M.; Sun, X.; Chen, L. Mn Doping of CoP Nanosheets Array: An Efficient Electrocatalyst for Hydrogen Evolution Reaction with Enhanced Activity at All pH Values. *ACS Catal.* **2017**, *7*, 98−102.

(110) Ren, B.; Li, D.; Jin, Q.; Cui, H.; Wang, C. A Self-Supported Porous WN Nanowire Array: An Efficient 3D Electrocatalyst for the Hydrogen Evolution Reaction. *J. Mater. Chem. A* **2017**, *5*, 19072−19078.

(111) Zhu, D. D.; Liu, J. L.; Qiao, S. Z. Recent Advances in Inorganic Heterogeneous Electrocatalysts for Reduction of Carbon Dioxide. *Adv. Mater.* **2016**, *28*, 3423−3452.

(112) Liu, J.; Guo, C.; Vasileff, A.; Qiao, S. Nanostructured 2D Materials: Prospective Catalysts for Electrochemical CO_2 Reduction. *Small Methods* **2016**, *1*, 1600006.

(113) Hou, J.; Cheng, H.; Takeda, O.; Zhu, H. Three-Dimensional Bimetal-Graphene-Semiconductor Coaxial Nanowire Arrays to Harness Charge Flow for the Photochemical Reduction of Carbon Dioxide. *Angew. Chem. Int. Ed.* **2015**, *54*, 8480−8484.

(114) Sharma, P. P.; Wu, J.; Yadav, R. M.; Liu, M.; Wright, C. J.; Tiwary, C. S.; Yakobson, B. I.; Lou, J.; Ajayan, P. M.; Zhou, X.-D. Nitrogen-Doped Carbon Nanotube Arrays for High-Efficiency Electrochemical Reduction of CO_2: On the Understanding of Defects, Defect Density, and Selectivity. *Angew. Chem. Int. Ed.* **2015**, *54*, 13701−13705.

(115) Kim, S.; Dong, W. J.; Gim, S.; Sohn, W.; Park, J. Y.; Yoo, C. J.; Jang, H. W.; Lee, J.-L. Shape-Controlled Bismuth Nanoflakes as Highly Selective Catalysts for Electrochemical Carbon Dioxide Reduction to Formate. *Nano Energy* **2017**, *39*, 44−52.

(116) Li, L.; Wang, Y.; Vanka, S.; Mu, X.; Mi, Z.; Li, C.-J. Nitrogen Photofixation over III-Nitride Nanowires Assisted by Ruthenium Clusters of Low Atomicity. *Angew. Chem. Int. Ed.* **2017**, *56*, 8701−8705.

(117) Guo, C. X.; ran, j.; Vasileff, A.; Qiao, S. Rational Design of Electrocatalysts and Photo(electro)catalysts for Nitrogen Reduction to Ammonia (NH_3) under Ambient Conditions. *Energy Environ. Sci.* **2018**, *11*, 45−56.

(118) Lan, R.; Irvine, J. T. S.; Tao, S. Synthesis of Ammonia Directly from Air and Water at Ambient Temperature and Pressure. *Sci. Rep.* **2013**, *3*, 1145.

(119) Bao, D.; Zhang, Q.; Meng, F.-L.; Zhong, H.-X.; Shi, M.-M.; Zhang, Y.; Yan, J.-M.; Jiang, Q.; Zhang, X.-B. Electrochemical Reduction of N_2 under Ambient Conditions for Artificial N_2 Fixation and Renewable Energy Storage Using N_2/NH_3 Cycle. *Adv. Mater.* **2017**, *29*, 1604799.

(120) Kordali, V.; Kyriacou, G.; Lambrou, C. Electrochemical Synthesis of Ammonia at Atmospheric Pressure and Low Temperature in a Solid Polymer Electrolyte Cell. *Chem. Commun.* **2000**, *0*, 1673−1674.

(121) Tsuneto, A.; Kudo, A.; Sakata, T. Lithium-Mediated Electrochemical Reduction of High Pressure N_2 to NH_3. *J. Electroanal. Chem.* **1994**, *367*, 183−188.

(122) Kim, K.; Yoo, C.-Y.; Kim, J.-N.; Yoon, H. C.; Han, J.-I. Electrochemical Synthesis of Ammonia from Water and Nitrogen in Ethylenediamine under Ambient Temperature and Pressure. *J. Electrochem. Soc.* **2016**, *163*, F1523−F1526.

(123) Chen, S.; Perathoner, S.; Ampelli, C.; Mebrahtu, C.; Su, D.; Centi, G. Electrocatalytic Synthesis of Ammonia at Room Temperature and Atmospheric Pressure from Water and Nitrogen on a Carbon-Nanotube-Based Electrocatalyst. *Angew. Chem. Int. Ed.* **2017**, *56*, 2699−2703.

(124)   Köleli, F.; Röpke, T. Electrochemical Hydrogenation of Dinitrogen to Ammonia on a Polyaniline Electrode. *Appl. Catal. B* **2006**, *62*, 306−310.

(125)   Abghoui, Y.; Skúlasson, E. Transition Metal Nitride Catalysts for Electrochemical Reduction of Nitrogen to Ammonia at Ambient Conditions. *Procedia Comput. Sci.* **2015**, *51*, 1897−1906.

(126)   Abghoui, Y.; Garden, A. L.; Howalt, J. G.; Vegge, T.; Skúlason, E. Electroreduction of N_2 to Ammonia at Ambient Conditions on Mononitrides of Zr, Nb, Cr, and V: A DFT Guide for Experiments. *ACS Catal.* **2016**, *6*, 635−646.

(127)   Chen, S.; Duan, J.; Vasileff, A.; Qiao, S. Z. Size Fractionation of Two-Dimensional Sub-Nanometer Thin Manganese Dioxide Crystals towards Superior Urea Electrocatalytic Conversion. *Angew. Chem. Int. Ed.* **2016**, *55*, 3804−3808.

(128)   Zhu, D.; Guo, C.; Liu, J.; Wang, L.; Du, Y.; Qiao, S.-Z. Two-Dimensional Metal-Organic Frameworks with High Oxidation States for Efficient Electrocatalytic Urea Oxidation. *Chem. Commun.* **2017**, *53*, 10906−10909.

(129)   Boggs, B. K.; King, R. L.; Botte, G. G. Urea Electrolysis: Direct Hydrogen Production from Urine. *Chem. Commun.* **2009**, *0*, 4859−4861.

(130)   Ji, R.-Y.; Chan, D.-S.; Jow, J.-J.; Wu, M.-S. Formation of Open-Ended Nickel Hydroxide Nanotubes on three-Dimensional Nickel Framework for Enhanced Urea Electrolysis. *Electrochem. Commun.* **2013**, *29*, 21−24.

(131)   Wu, M.-S.; Lin, G.-W.; Yang, R.-S. Hydrothermal Growth of Vertically-Aligned Ordered Mesoporous Nickel Oxide Nanosheets on Three-Dimensional Nickel Framework for Electrocatalytic Oxidation of Urea in Alkaline Medium. *J. Power Sources* **2014**, *272*, 711−718.

(132)   Liang, Y.; Liu, Q.; Asiri, A. M.; Sun, X. Enhanced Electrooxidation of Urea Using $NiMoO_4 \cdot xH_2O$ Nanosheet Arrays on Ni Foam as Anode. *Electrochim. Acta* **2015**, *153*, 456−460.

(133)   Guo, F.; Ye, K.; Cheng, K.; Wang, G.; Cao, D. Preparation of Nickel Nanowire Arrays Electrode for Urea Electro-Oxidation in Alkaline Medium. *J. Power Sources* **2015**, *278*, 562−568.

(134) Wu, M.-S.; Ji, R.-Y.; Zheng, Y.-R. Nickel Hydroxide Electrode with a Monolayer of Nanocup Arrays as an Effective Electrocatalyst for Enhanced Electrolysis of Urea. *Electrochim. Acta* **2014**, *144*, 194−199.

(135) Tang, C.; Zhao, Z. L.; Chen, J.; Li, B.; Chen, L.; Li, C. M. Se-Ni(OH)$_2$-Shelled Vertically Oriented NiSe Nanowires as a Superior Electrocatalyst toward Urea Oxidation Reaction of Fuel Cells. *Electrochim. Acta* **2017**, *248*, 243−249.

(136) Girishkumar, G.; McCloskey, B.; Luntz, A. C.; Swanson, S.; Wilcke, W. Lithium−Air Battery: Promise and Challenges. *J. Phys. Chem. Lett.* **2010**, *1*, 2193−2203.

(137) Li, Y.; Dai, H. Recent Advances in Zinc-Air Batteries. *Chem. Soc. Rev.* **2014**, *43*, 5257−5275.

(138) Lee, J.-S.; Tai Kim, S.; Cao, R.; Choi, N.-S.; Liu, M.; Lee, K. T.; Cho, J. Metal–Air Batteries with High Energy Density: Li–Air versus Zn–Air. *Adv. Energy Mater.* **2011**, *1*, 34−50.

(139) Liu, Z.-Q.; Cheng, H.; Li, N.; Ma, T. Y.; Su, Y.-Z. ZnCo$_2$O$_4$ Quantum Dots Anchored on Nitrogen-Doped Carbon Nanotubes as Reversible Oxygen Reduction/Evolution Electrocatalysts. *Adv. Mater.* **2016**, *28*, 3777−3784.

(140) Ma, T. Y.; Dai, S.; Jaroniec, M.; Qiao, S. Z. Metal–Organic Framework Derived Hybrid Co$_3$O$_4$-Carbon Porous Nanowire Arrays as Reversible Oxygen Evolution Electrodes. *J. Am. Chem. Soc.* **2014**, *136*, 13925−13931.

(141) Zheng, Y.; Jiao, Y.; Zhu, Y.; Cai, Q.; Vasileff, A.; Li, L. H.; Han, Y.; Chen, Y.; Qiao, S.-Z. Molecule-Level g-C$_3$N$_4$ Coordinated Transition Metals as a New Class of Electrocatalysts for Oxygen Electrode Reactions. *J. Am. Chem. Soc.* **2017**, *139*, 3336−3339.

(142) Jin, C.; Lu, F.; Cao, X.; Yang, Z.; Yang, R. Facile Synthesis and Excellent Electrochemical Properties of NiCo$_2$O$_4$ Spinel Nanowire Arrays as a Bifunctional Catalyst for the Oxygen Reduction and Evolution Reaction. *J. Mater. Chem. A* **2013**, *1*, 12170−12177.

(143) Tian, W.; Li, H.; Qin, B.; Xu, Y.; Hao, Y.; Li, Y.; Zhang, G.; Liu, J.; Sun, X.; Duan, X. Tuning the Wettability of Carbon Nanotube Arrays for Efficient Bifunctional Catalysts and Zn-Air Batteries. *J. Mater. Chem. A* **2017**, *5*, 7103−7110.

(144)   Wu, B.; Zhang, H.; Zhou, W.; Wang, M.; Li, X.; Zhang, H. Carbon-Free CoO Mesoporous Nanowire Array Cathode for High-Performance Aprotic Li–O$_2$ Batteries. *ACS Appl. Mater. Interfaces* **2015**, *7*, 23182−23189.

(145)   Liu, W.-M.; Gao, T.-T.; Yang, Y.; Sun, Q.; Fu, Z.-W. A Hierarchical Three-Dimensional NiCo$_2$O$_4$ Nanowire Array/Carbon Cloth as an Air Electrode for Nonaqueous Li-Air Batteries. *Phys. Chem. Chem. Phys.* **2013**, *15*, 15806−15810.

(146)   Lu, F.; Cao, X.; Wang, Y.; Jin, C.; Shen, M.; Yang, R. A Hierarchical NiCo$_2$O$_4$ Spinel Nanowire Array as an Electrocatalyst for Rechargeable Li-Air Batteries. *RSC Adv.* **2014**, *4*, 40373−40376.

(147)   Li, Y.; Huang, Z.; Huang, K.; Carnahan, D.; Xing, Y. Hybrid Li-Air Battery Cathodes with Sparse Carbon Nanotube Arrays Directly Grown on Carbon Fiber Papers. *Energy Environ. Sci.* **2013**, *6*, 3339−3345.

(148)   Shui, J.; Du, F.; Xue, C.; Li, Q.; Dai, L. Vertically Aligned N-Doped Coral-like Carbon Fiber Arrays as Efficient Air Electrodes for High-Performance Nonaqueous Li–O$_2$ Batteries. *ACS Nano* **2014**, *8*, 3015−3022.

(149)   Lee, D. U.; Choi, J.-Y.; Feng, K.; Park, H. W.; Chen, Z. Advanced Extremely Durable 3D Bifunctional Air Electrodes for Rechargeable Zinc-Air Batteries. *Adv. Energy Mater.* **2014**, *4*, 1301389.

(150)   Li, Z.; Shao, M.; Yang, Q.; Tang, Y.; Wei, M.; Evans, D. G.; Duan, X. Directed Synthesis of Carbon Nanotube Arrays Based on Layered Double Hydroxides toward Highly-Efficient Bifunctional Oxygen Electrocatalysis. *Nano Energy* **2017**, *37*, 98−107.

(151)   Fu, J.; Hassan, F. M.; Li, J.; Lee, D. U.; Ghannoum, A. R.; Lui, G.; Hoque, M. A.; Chen, Z. Flexible Rechargeable Zinc-Air Batteries through Morphological Emulation of Human Hair Array. *Adv. Mater.* **2016**, *28*, 6421−6428.

(152)   Zhu, Y. P.; Ma, T. Y.; Jaroniec, M.; Qiao, S. Z. Self-Templating Synthesis of Hollow Co$_3$O$_4$ Microtube Arrays for Highly Efficient Water Electrolysis. *Angew. Chem. Int. Ed.* **2017**, *56*, 1324−1328.

(153)   Hinnemann, B.; Moses, P. G.; Bonde, J.; Jørgensen, K. P.; Nielsen, J. H.; Horch, S.; Chorkendorff, I.; Nørskov, J. K. Biomimetic Hydrogen Evolution: MoS$_2$ Nanoparticles as Catalyst for Hydrogen Evolution. *J. Am. Chem. Soc.* **2005**, *127*, 5308−5309.

(154)   Hong, X.; Chan, K.; Tsai, C.; Nørskov, J. K. How Doped MoS_2 Breaks Transition-Metal Scaling Relations for CO_2 Electrochemical Reduction. *ACS Catal.* **2016**, *6*, 4428-4437.

(155)   Jiao, Y.; Zheng, Y.; Davey, K.; Qiao, S.-Z. Activity Origin and Catalyst Design Principles for Electrocatalytic Hydrogen Evolution on Heteroatom-Doped Graphene. *Nat. Energy* **2016**, *1*, 16130.

(156)   Gorlin, Y.; Lassalle-Kaiser, B.; Benck, J. D.; Gul, S.; Webb, S. M.; Yachandra, V. K.; Yano, J.; Jaramillo, T. F. In Situ X-ray Absorption Spectroscopy Investigation of a Bifunctional Manganese Oxide Catalyst with High Activity for Electrochemical Water Oxidation and Oxygen Reduction. *J. Am. Chem. Soc.* **2013**, *135*, 8525−28534.

(157)   Lassalle-Kaiser, B.; Merki, D.; Vrubel, H.; Gul, S.; Yachandra, V. K.; Hu, X.; Yano, J. Evidence from in Situ X-ray Absorption Spectroscopy for the Involvement of Terminal Disulfide in the Reduction of Protons by an Amorphous Molybdenum Sulfide Electrocatalyst. *J. Am. Chem. Soc.* **2015**, *137*, 314−2321.

(158)   Ali-Löytty, H.; Louie, M. W.; Singh, M. R.; Li, L.; Sanchez Casalongue, H. G.; Ogasawara, H.; Crumlin, E. J.; Liu, Z.; Bell, A. T.; Nilsson, A.; et al. Ambient-Pressure XPS Study of a Ni–Fe Electrocatalyst for the Oxygen Evolution Reaction. *J. Phys. Chem. C* **2016**, *120*, 2247−22253.

(159)   Deng, Y.; Yeo, B. S. Characterization of Electrocatalytic Water Splitting and CO_2 Reduction Reactions Using In Situ/Operando Raman Spectroscopy. *ACS Catal.* **2017**, *7*, 7873−27889.

(160)   Hodnik, N.; Dehm, G.; Mayrhofer, K. J. J. Importance and Challenges of Electrochemical in Situ Liquid Cell Electron Microscopy for Energy Conversion Research. *Acc. Chem. Res.* **2016**, *49*, 2015−22022.

(161)   Zhou, T.; Cao, Z.; Wang, H.; Gao, Z.; Li, L.; Ma, H.; Zhao, Y. Ultrathin Co-Fe Hydroxide Nanosheet Arrays for Improved Oxygen Evolution during Water Splitting. *RSC Adv.* **2017**, *7*, 22818−22824.

(162)   Zhang, R.; Wang, Z.; Hao, S.; Ge, R.; Ren, X.; Qu, F.; Du, G.; Asiri, A. M.; Zheng, B.; Sun, X. Surface Amorphization: A Simple and Effective Strategy toward Boosting the Electrocatalytic Activity for Alkaline Water Oxidation. *ACS Sustainable Chem. Eng.* **2017**, *5*, 8518−8522.

(163) Ge, R.; Ren, X.; Ji, X.; Liu, Z.; Du, G.; Asiri, A. M.; Sun, X.; Chen, L. Benzoate Anion-Intercalated Layered Cobalt Hydroxide Nanoarray: An Efficient Electrocatalyst for the Oxygen Evolution Reaction. *ChemSusChem* **2017**, *10*, 4004−4008.

(164) Ge, R.; Ma, M.; Ren, X.; Qu, F.; Liu, Z.; Du, G.; Asiri, A. M.; Chen, L.; Zheng, B.; Sun, X. NiCo$_2$O$_4$@Ni-Co-Ci Core-Shell Nanowires Array as an Efficient Electrocatalyst for Water Oxidation at Near-Neutral pH. *Chem. Commun.* **2017**, *53*, 7812−7815.

(165) Hao, S.; Yang, Y. Water Splitting in Near-Neutral Media: Using Homologous Mn-Co-Based Nanowires Array as Complementary Electrocatalysts. *J. Mater. Chem. A* **2017**, *5*, 12091−12095.

(166) Ge, R.; Du, H.; Tao, K.; Zhang, Q.; Chen, L. Cobalt-Borate Nanoarray: An Efficient and Durable Electrocatalyst for Water Oxidation under Benign Conditions. *ACS Appl. Mater. Interfaces* **2017**, *9*, 15383−15387.

(167) Ge, R.; Ren, X.; Qu, F.; Liu, D.; Ma, M.; Hao, S.; Du, G.; Asiri, A. M.; Chen, L.; Sun, X. Three-Dimensional Nickel–Borate Nanosheets Array for Efficient Oxygen Evolution at Near-Neutral pH. *Chem. Eur. J.* **2017**, *23*, 6959−6963.

(168) Yang, Q.; Li, T.; Lu, Z.; Sun, X.; Liu, J. Hierarchical Construction of an Ultrathin Layered Double Hydroxide Nanoarray for Highly-Efficient Oxygen Evolution Reaction. *Nanoscale* **2014**, *6*, 11789−11794.

(169) Liu, Q.; Asiri, A. M.; Sun, X. Hematite Nanorods Array on Carbon Cloth as an Efficient 3D Oxygen Evolution Anode. *Electrochem. Commun.* **2014**, *49*, 21−24.

(170) Yu, X.; Sun, Z.; Yan, Z.; Xiang, B.; Liu, X.; Du, P. Direct Growth of Porous Crystalline NiCo$_2$O$_4$ Nanowire Arrays on a Conductive Electrode for High-Performance Electrocatalytic Water Oxidation. *J. Mater. Chem. A* **2014**, *2*, 20823−20831.

(171) Zhou, H.; Yu, F.; Liu, Y.; Sun, J.; Zhu, Z.; He, R.; Bao, J.; Goddard, W. A.; Chen, S.; Ren, Z. Outstanding Hydrogen Evolution Reaction Catalyzed by Porous Nickel Diselenide Electrocatalysts. *Energy Environ. Sci.* **2017**, *10*, 1487−1492.

(172) Xu, H.; Jiang, Z.; Zhang, H.; Liu, L.; Fang, L.; Gu, X.; Wang, Y. New Efficient Electrocatalyst for the Hydrogen Evolution Reaction: Erecting a V$_2$Se$_9$@Poly(3,4-ethylenedioxythiophene) Nanosheet Array with a Specific Active Facet Exposed. *ACS Energy Lett.* **2017**, *2*, 1099−1104.

(173) Liu, M.; Yang, L.; Liu, T.; Tang, Y.; Luo, S.; Liu, C.; Zeng, Y. Fe_2P/Reduced Graphene Oxide/Fe_2P Sandwich-Structured Nanowall Arrays: A High-Performance Non-Noble-Metal Electrocatalyst for Hydrogen Evolution. *J. Mater. Chem. A* **2017**, *5*, 8608−8615.

(174) Ouyang, C.; Wang, X.; Wang, S. Phosphorus-Doped CoS_2 Nanosheet Arrays as Ultra-Efficient Electrocatalysts for the Hydrogen Evolution Reaction. *Chem. Commun.* **2015**, *51*, 14160−14163.

(175) Zhou, W.; Zhou, Y.; Yang, L.; Huang, J.; Ke, Y.; Zhou, K.; Li, L.; Chen, S. N-Doped Carbon-Coated Cobalt Nanorod Arrays Supported on a Titanium Mesh as Highly Active Electrocatalysts for the Hydrogen Evolution Reaction. *J. Mater. Chem. A* **2015**, *3*, 1915−1919.

(176) Hou, J.; Sun, Y.; Cao, S.; Wu, Y.; Chen, H.; Sun, L. Graphene Dots Embedded Phosphide Nanosheet-Assembled Tubular Arrays for Efficient and Stable Overall Water Splitting. *ACS Appl. Mater. Interfaces* **2017**, *9*, 24600−24607.

(177) Zhang, Q.; Zhang, C.; Liang, J.; Yin, P.; Tian, Y. Orthorhombic α-NiOOH Nanosheet Arrays: Phase Conversion and Efficient Bifunctional Electrocatalysts for Full Water Splitting. *ACS Sustainable Chem. Eng.* **2017**, *5*, 3808−3818.

(178) Libin, Y.; Honglan, Q.; Chengxiao, Z.; Xuping, S. An Efficient Bifunctional Electrocatalyst for Water Splitting Based on Cobalt Phosphide. *Nanotechnology* **2016**, *27*, 23LT01.

(179) Yu, J.; Li, Q.; Chen, N.; Xu, C.-Y.; Zhen, L.; Wu, J.; Dravid, V. P. Carbon-Coated Nickel Phosphide Nanosheets as Efficient Dual-Electrocatalyst for Overall Water Splitting. *ACS Appl. Mater. Interfaces* **2016**, *8*, 27850−27858.

(180) Fang, W.; Liu, D.; Lu, Q.; Sun, X.; Asiri, A. M. Nickel Promoted Cobalt Disulfide Nanowire Array Supported on Carbon Cloth: An Efficient and Stable Bifunctional Electrocatalyst for Full Water Splitting. *Electrochem. Commun.* **2016**, *63*, 60−64.

(181) Liang, Y.; Liu, Q.; Luo, Y.; Sun, X.; He, Y.; Asiri, A. M. $Zn_{0.76}Co_{0.24}S$/CoS_2 Nanowires Array for Efficient Electrochemical Splitting of Water. *Electrochim. Acta* **2016**, *190*, 360−364.

(182) Liu, D.; Lu, Q.; Luo, Y.; Sun, X.; Asiri, A. M. $NiCo_2S_4$ Nanowires Array as an Efficient Bifunctional Electrocatalyst for Full Water Splitting with Superior Activity. *Nanoscale* **2015**, *7*, 15122−15126.

(183) Ouyang, C.; Wang, X.; Wang, C.; Zhang, X.; Wu, J.; Ma, Z.; Dou, S.; Wang, S. Hierarchically Porous Ni$_3$S$_2$ Nanorod Array Foam as Highly Efficient Electrocatalyst for Hydrogen Evolution Reaction and Oxygen Evolution Reaction. *Electrochim. Acta* **2015**, *174*, 297−301.
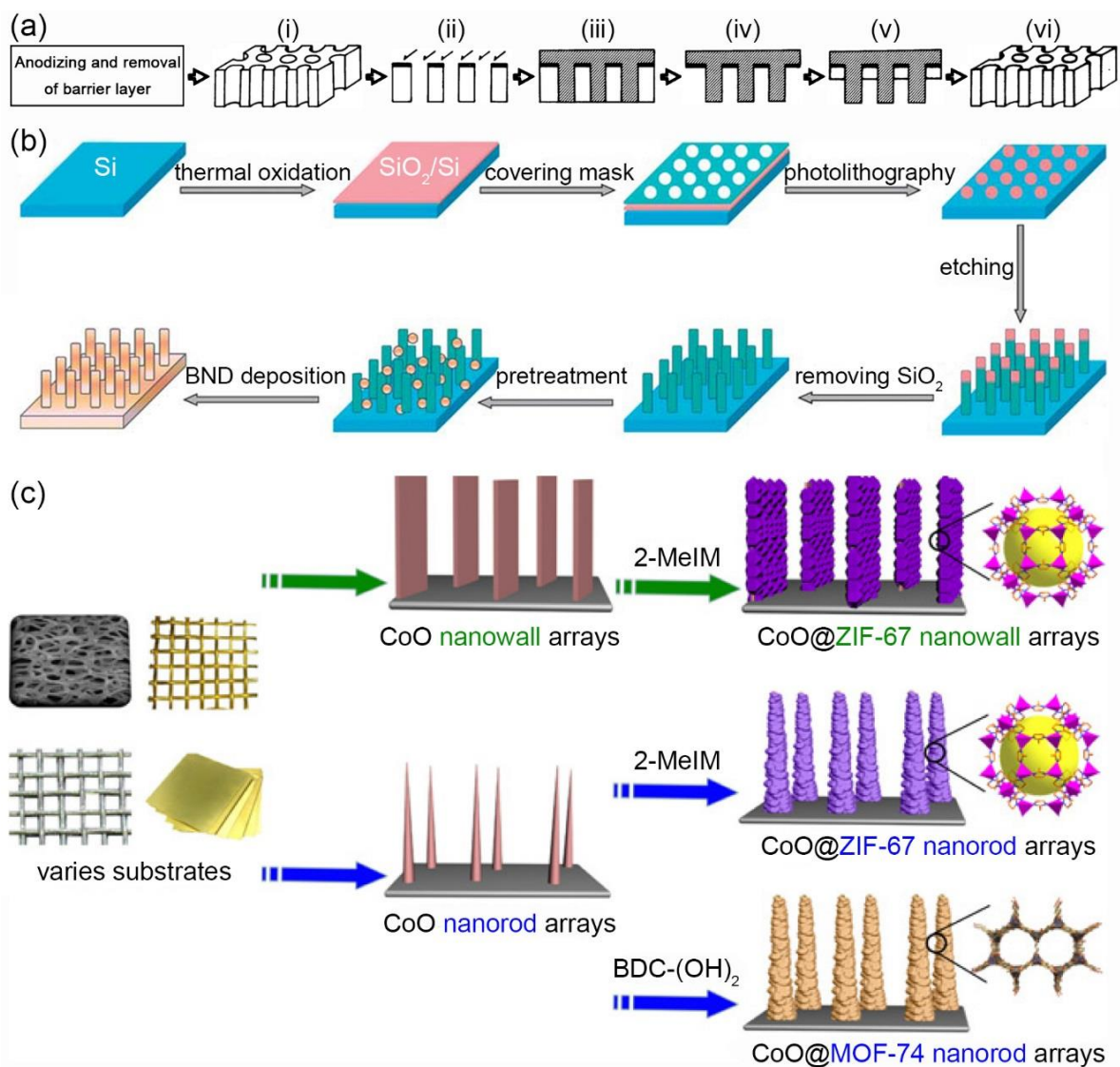
Figure 1. (a) Schematic diagram of the process for the fabrication of the metal nanohole array: (i) porous alumina with through holes (mother structure), (ii) metal deposition with vacuum evaporation, (iii) injection and polymerization of methylmethacrylate, (iv) poly(methyl methacrylate) negative type, (v) electroless metal deposition, and (vi) metal hole array. Adapted with permission from ref.[44] Copyright 1995, American Association for the Advancement of Science. (b) The procedures for VA-BND/Si RA preparation. Reproduced with permission from ref.[22] Copyright 2013, The Royal Society of Chemistry. (c) Schematic illustration showing the fabrication of different metal oxide@MOF hybrid arrays onto various substrates. Reproduced with permission from ref.[23] Copyright 2017, Elsevier.
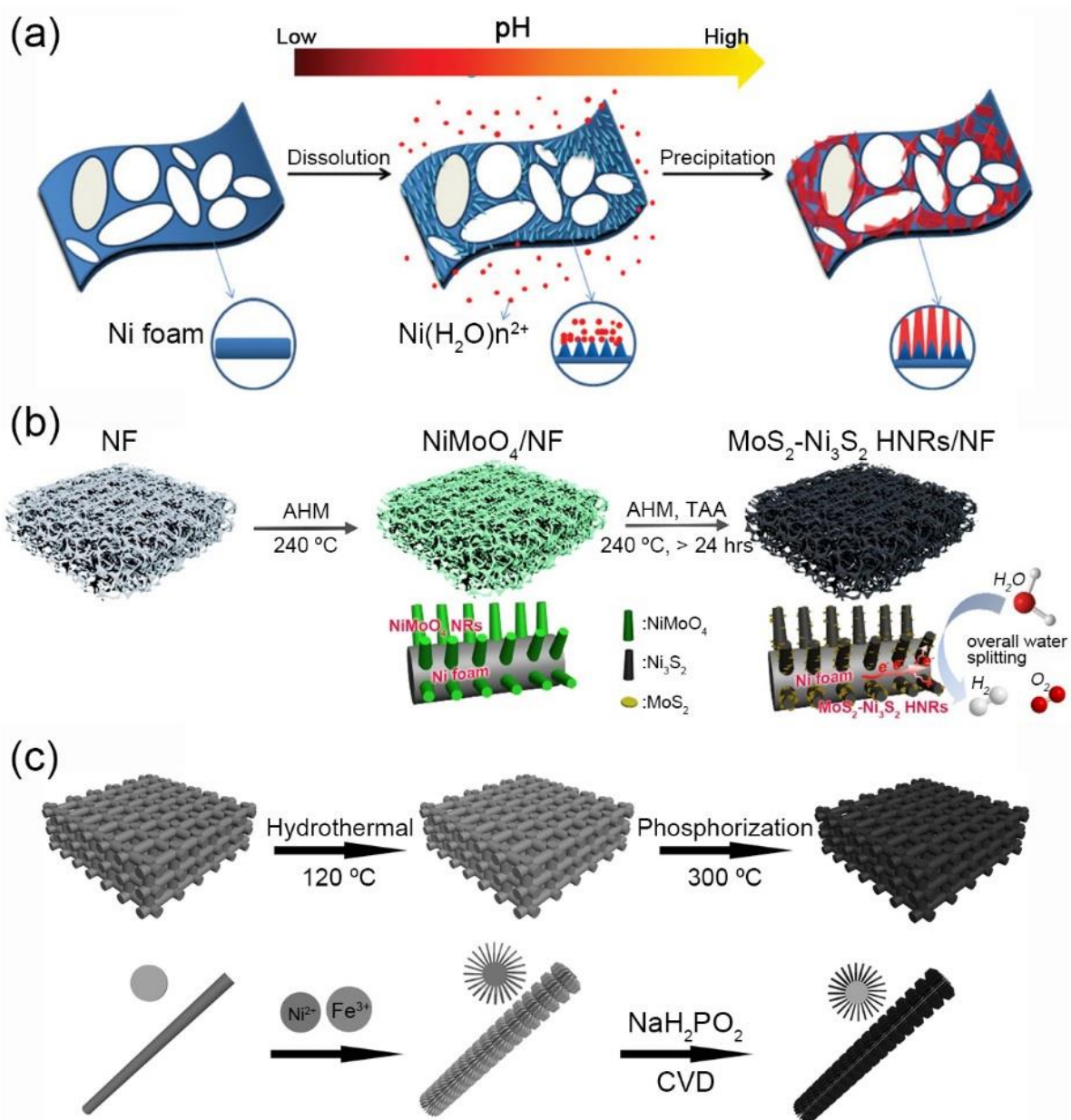
Figure 2. (a) Schematic diagram illustrating the pH-driven, dissolution-precipitation based growth of Ni(OH)$_2$ on the NF. Reproduced with permission from ref.[56] Copyright 2013, The Royal Society of Chemistry. (b) Illustration of the fabrication of heterostructured MoS$_2$-Ni$_3$S$_2$ HNRs/NF composites. Reproduced with permission from ref.[24] Copyright 2017, American Chemical Society. (c) Schematic illustration of the synthesis process of Fe-doped Ni$_2$P nanosheet arrays. Reproduced with permission from ref.[25] Copyright 2017, WILEY-VCH.
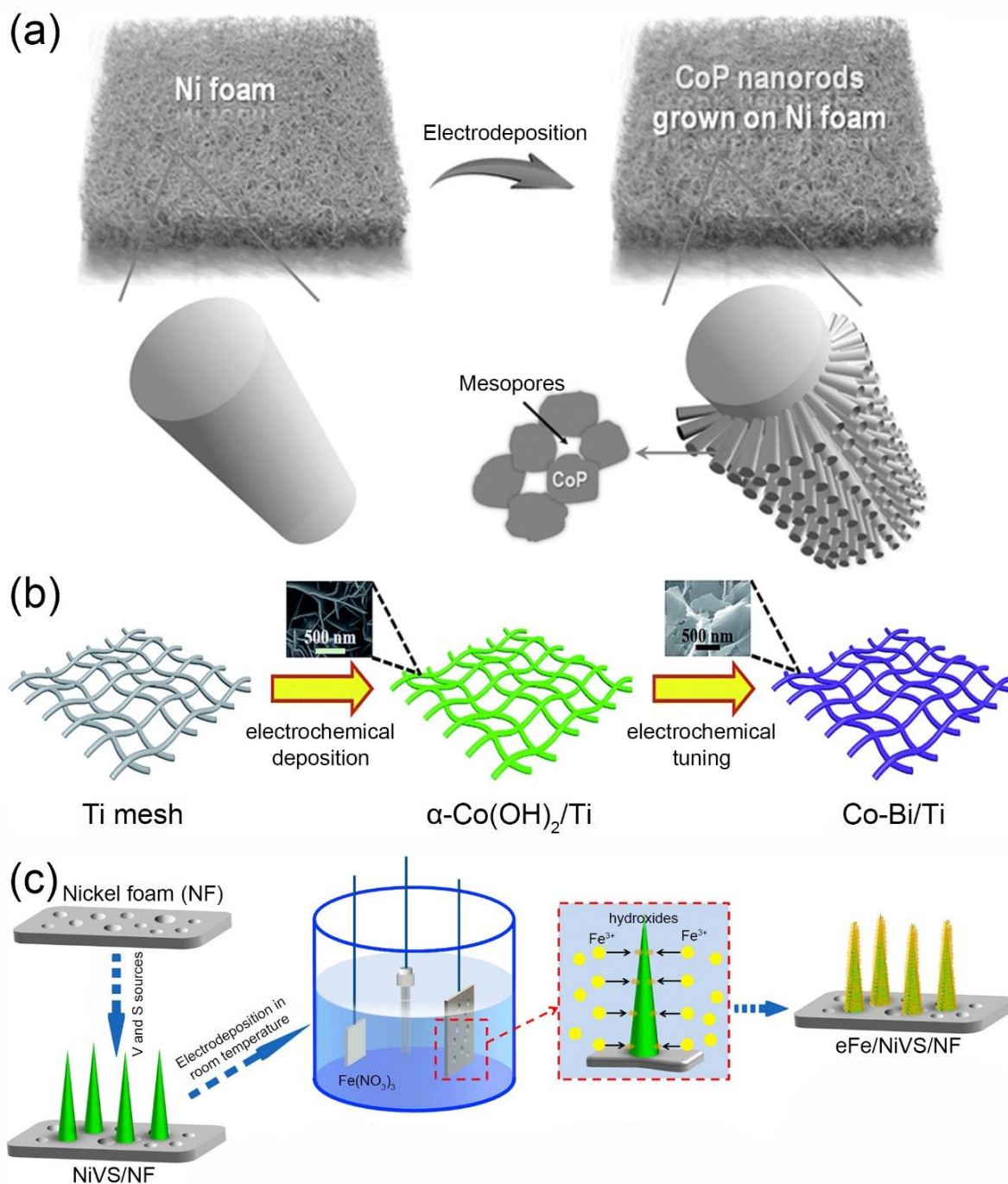
Figure 3. (a) Schematic illustration of the fabrication of CoP mesoporous nanorods arrays. Reproduced with permission from ref.[26] Copyright 2015, WILEY-VCH. (b) Schematic illustration of the preparation process of Co-Bi/Ti. Reproduced with permission from ref.[27] Copyright 2017, The Royal Society of Chemistry. (c) Schematically synthesis of eFe/NiVS/NF through electrodeposition. Reproduced with permission from ref.[74] Copyright 2017, Elsevier.
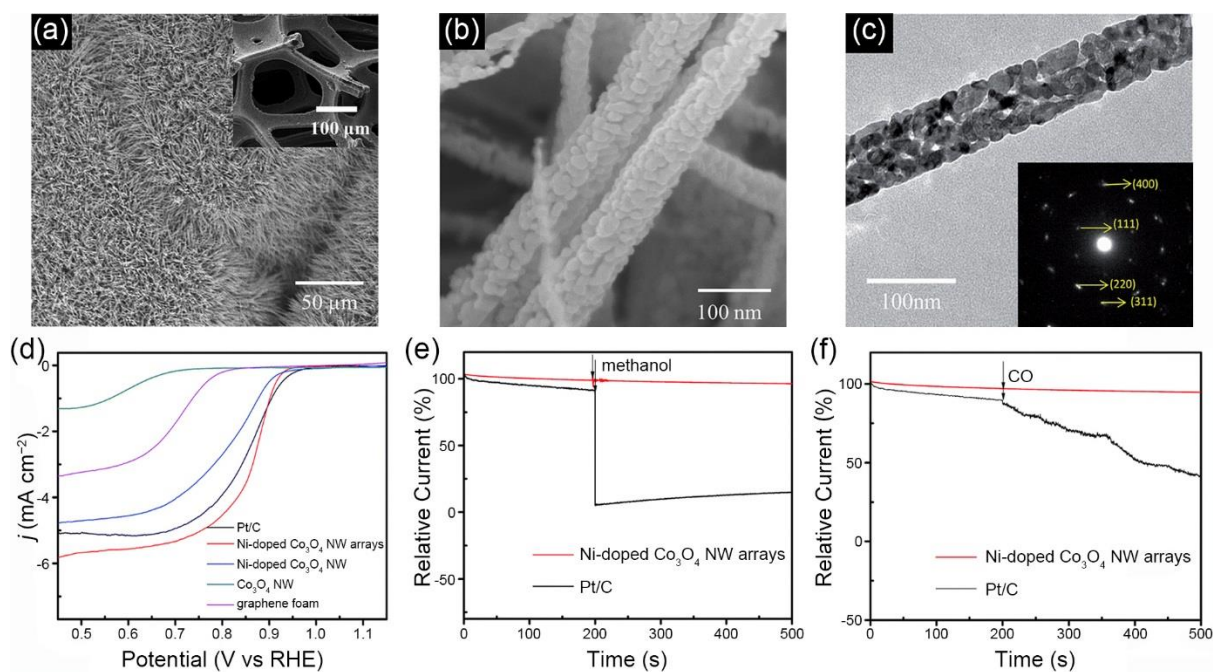
Figure 4. (a, b) SEM images of the Ni-doped Co_3O_4 NW arrays. (c) Typical TEM image of the Ni-doped Co_3O_4. (d) RDE voltammograms at 10 mV s^{-1} for different electrodes in an O_2-saturated 0.1 M KOH solution at a rotation rate of 1600 rpm. (e, f) Chronoamperometric responses of the Ni-doped Co_3O_4 NW arrays and Pt/C in O_2-saturated 0.1 M KOH with the addition of 3 M methanol and CO after about 200 s at 0.765 V. Reproduced with permission from ref.[79] Copyright 2015, The Royal Society of Chemistry.
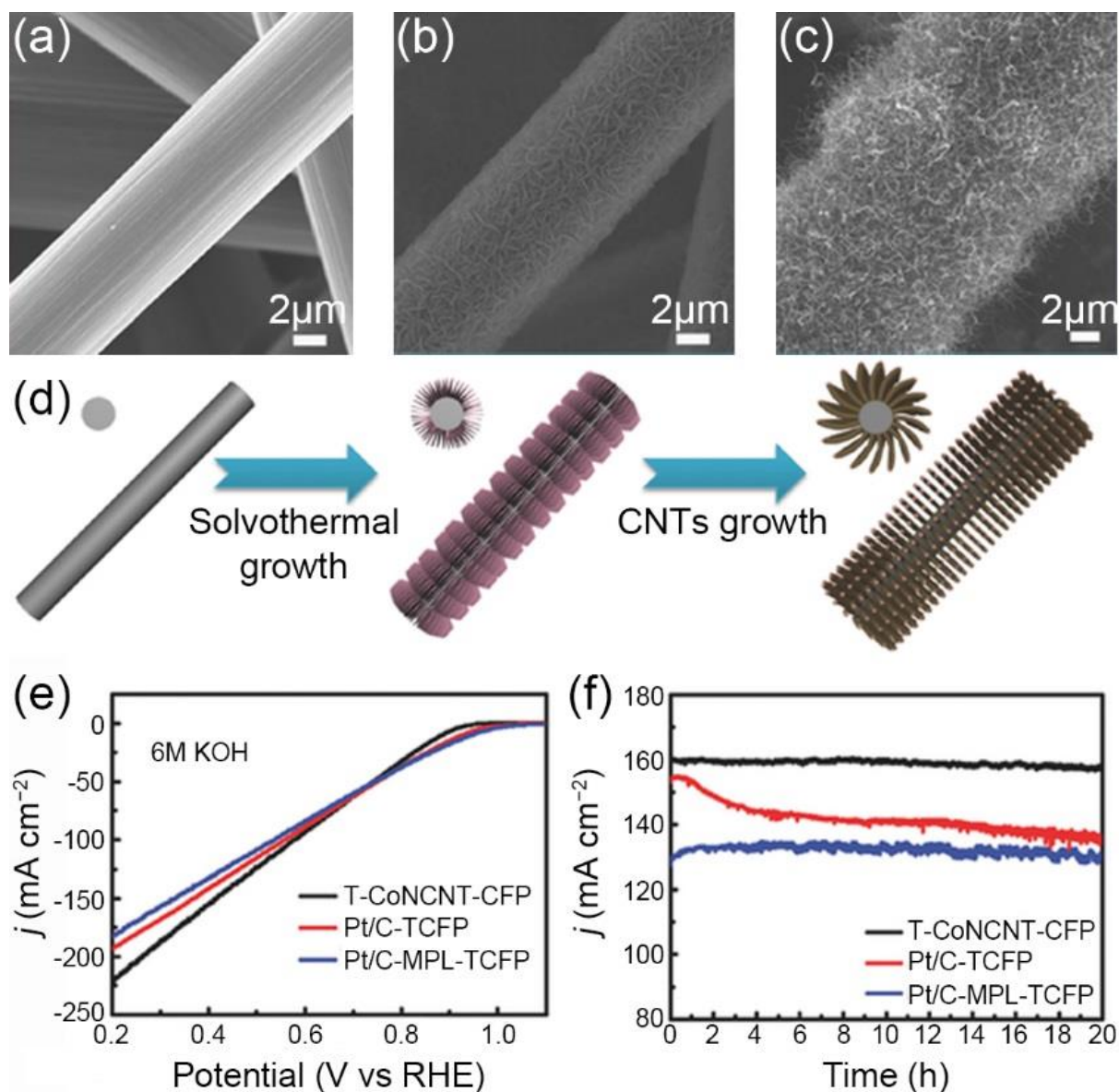
Figure 5. SEM images of (a) CFP, (b) $Co(OH)_2$ nanosheet arrays on CFP, and (c) CoNCNTs arrays on CFP. (d) Schematic illustration of the fabrication procedure of CoNCNTs on CFP. (e) ORR polarization curves of the three electrodes in oxygen-bubbled 6M KOH solution without IR-correction, the T-CoNCNT-CFP electrode shows the fastest current density increase, result in higher ORR current densities than commercial Pt/C electrodes under high overpotentials. (f) Stability testing of the three electrodes under high current densities, a stable and high current density is observed on the T-CoNCNT-CFP electrode, manifesting a prominent ORR stability. Reproduced with permission from ref.[82] Copyright 2016, WILEY-VCH.
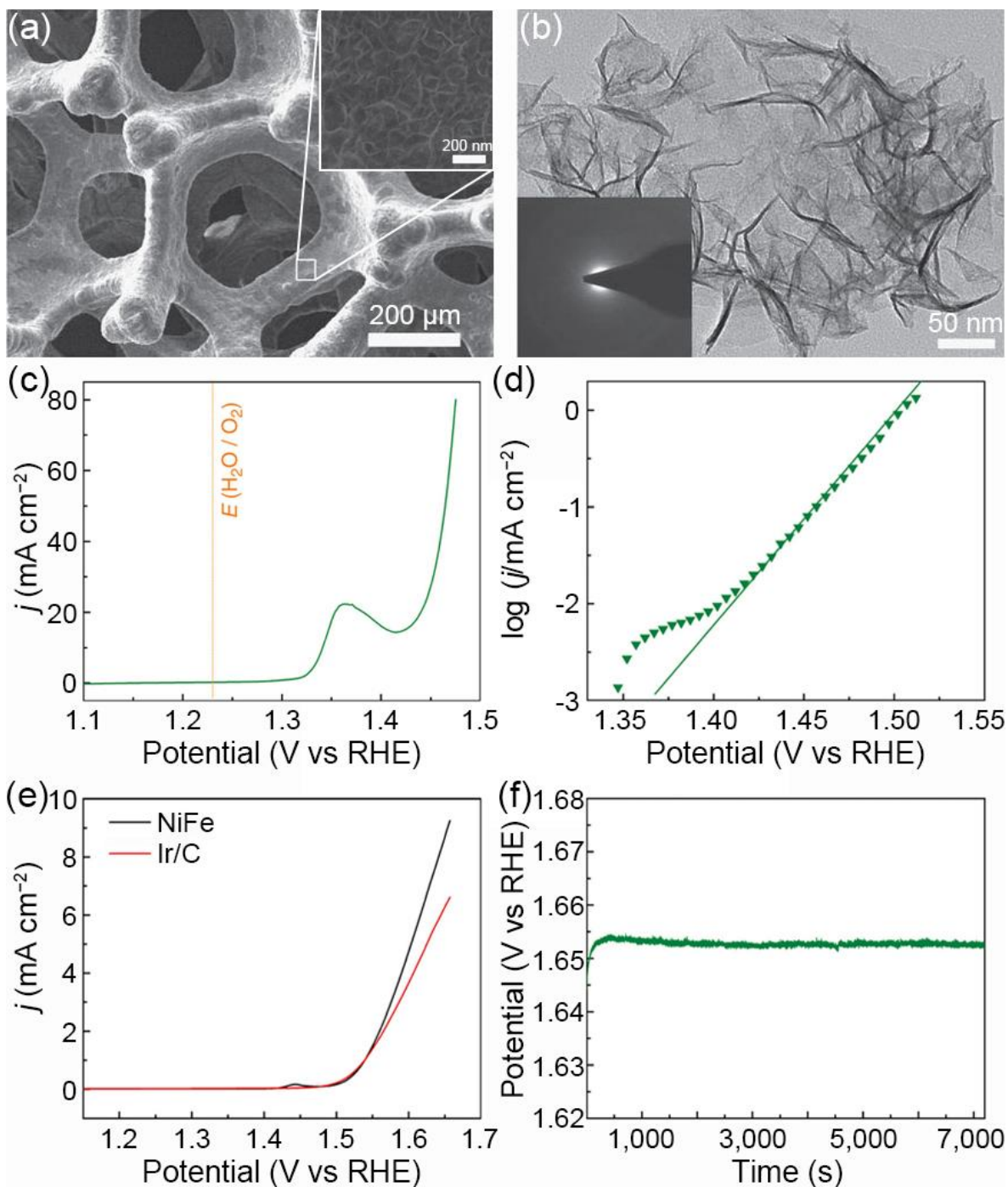
Figure 6. (a) SEM image of the NiFe/NF electrode (inset shows the high-resolution SEM image of the selected area). (b) TEM image of NiFe nanosheets scratched off from the NiFe/NF (inset shows the corresponding selected area diffraction pattern). (c) The OER polarization curve of NiFe/NF in 10 M KOH at 5 mV s^{-1} with 75% iR compensation. (d) The Tafel plot of NiFe/NF in 10 M KOH at 0.1 mV s^{-1} with 95% iR compensation. (e) The first OER polarization curves obtained with the NiFe- and Ir/C-coated GC electrodes, respectively. (f) The chronopotentiometry curve of NiFe/NF in 10 M KOH with a constant current density of 500 mA cm^{-2}. Reproduced with permission from ref.[21] Copyright 2015, Nature Publishing Group.
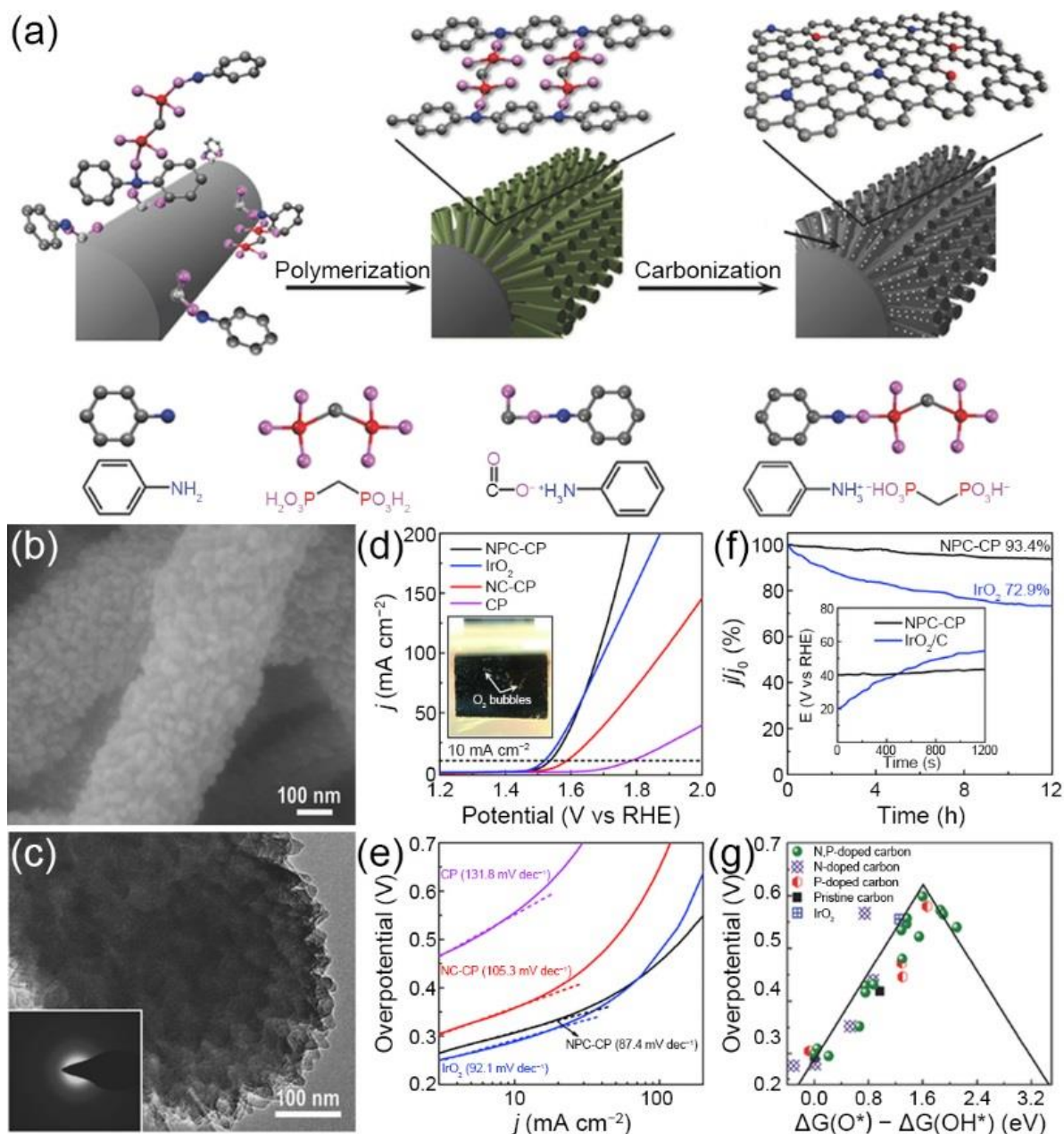
Figure 7. (a) Schematic illustration of direct growth of N and P-doped carbon nanofibers on carbon paper. (b) SEM and (c) TEM images of NPC-CP (inset in panel (c) shows the corresponding SAED pattern. (d) OER curves and (e) Tafel plots of NPC-CP, NC-CP, IrO$_2$, and pristine CP in O$_2$-satuated 1M KOH (scan rate: 2 mV s^{-1}). (f) Chronoamperometric responses of NPC-CP and IrO$_2$ at a constant potential of 1.54 V (inset in panel (d) shows the corresponding chronopotentiometric response curves with the constant current density held at 10 mA cm^{-2}). (g) Volcano plots of OER overpotential versus the difference between the adsorption energy of O* and OH*, that is, ΔG(O*) − ΔG(OH*), for the simulated carbon structures. Reproduced with permission from ref.[97] Copyright 2017, WILEY-VCH.
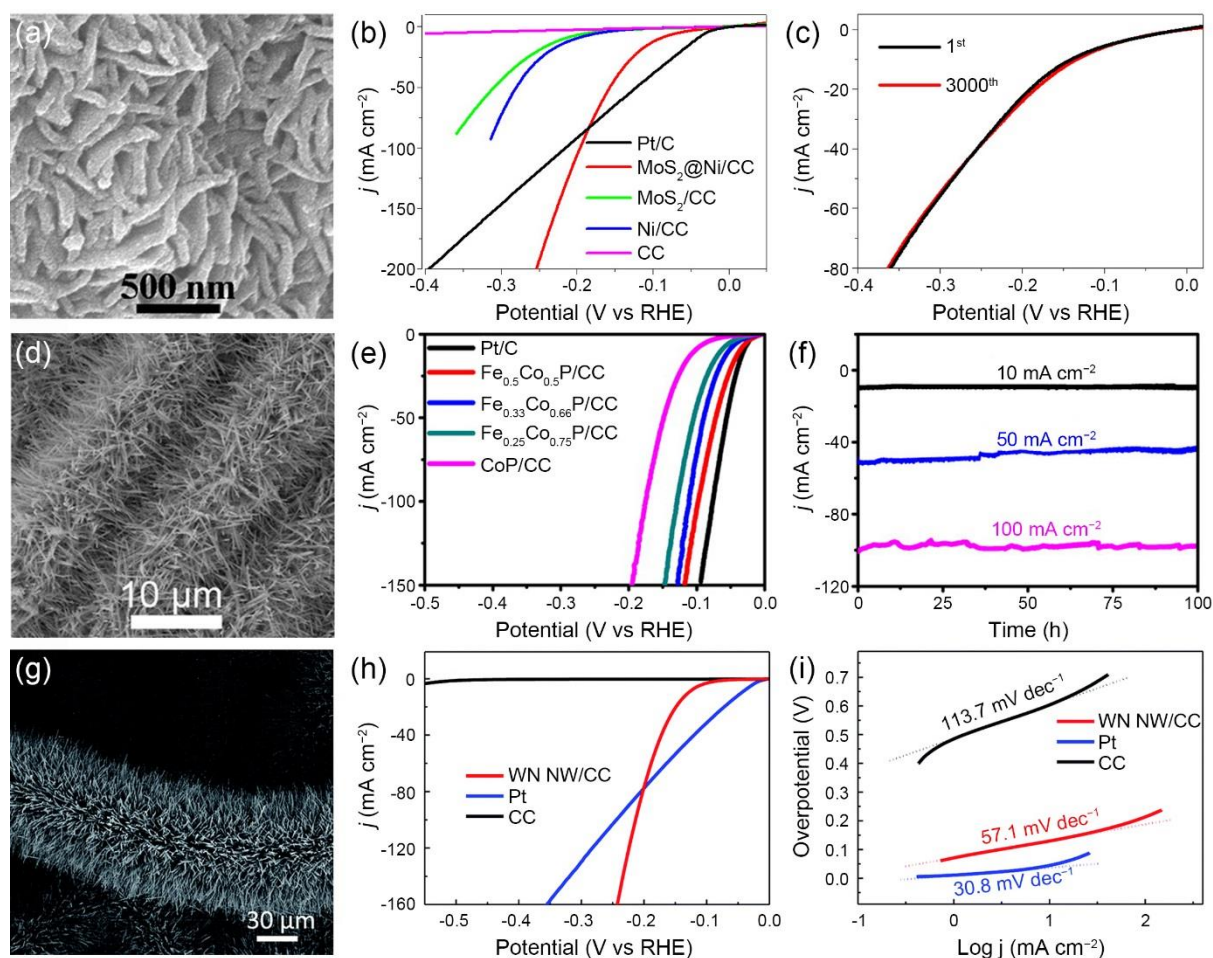
Figure 8. (a) SEM image of MoS₂@Ni/CC. (b) Polarization curves of MoS₂@Ni/CC, MoS₂/CC, Ni/CC, Pt/C, and bare CC in 1.0 M KOH solution with a scan rate of 5 mV s⁻¹. (c) Polarization curves of MoS₂@Ni/CC in 1.0 M PBS. Reproduced with permission from ref.[102] Copyright 2016, American Chemical Society. (d) SEM image of $Fe_{0.5}Co_{0.5}P/CC$. (e) LSV curves for Pt/C on CC, bare CC, and $Fe_xCo_{1-x}P/CC$ with a scan rate of 2 mV s⁻¹ for HER. (f) Time-dependent current density curves of $Fe_{0.5}Co_{0.5}P/CC$ at fixed overpotentials of 37, 72, and 98 mV to drive 10, 50, and 100 mA cm⁻², respectively. Reproduced with permission from ref.[107] Copyright 2016, American Chemical Society. (g) SEM image of WN NW/CC. (h) Polarization curves and (i) corresponding Tafel plots of WN NW/CC in comparison with those of Pt and CC and in 1 M KOH. Reproduced with permission from ref.[110] Copyright 2017, The Royal Society of Chemistry.

67
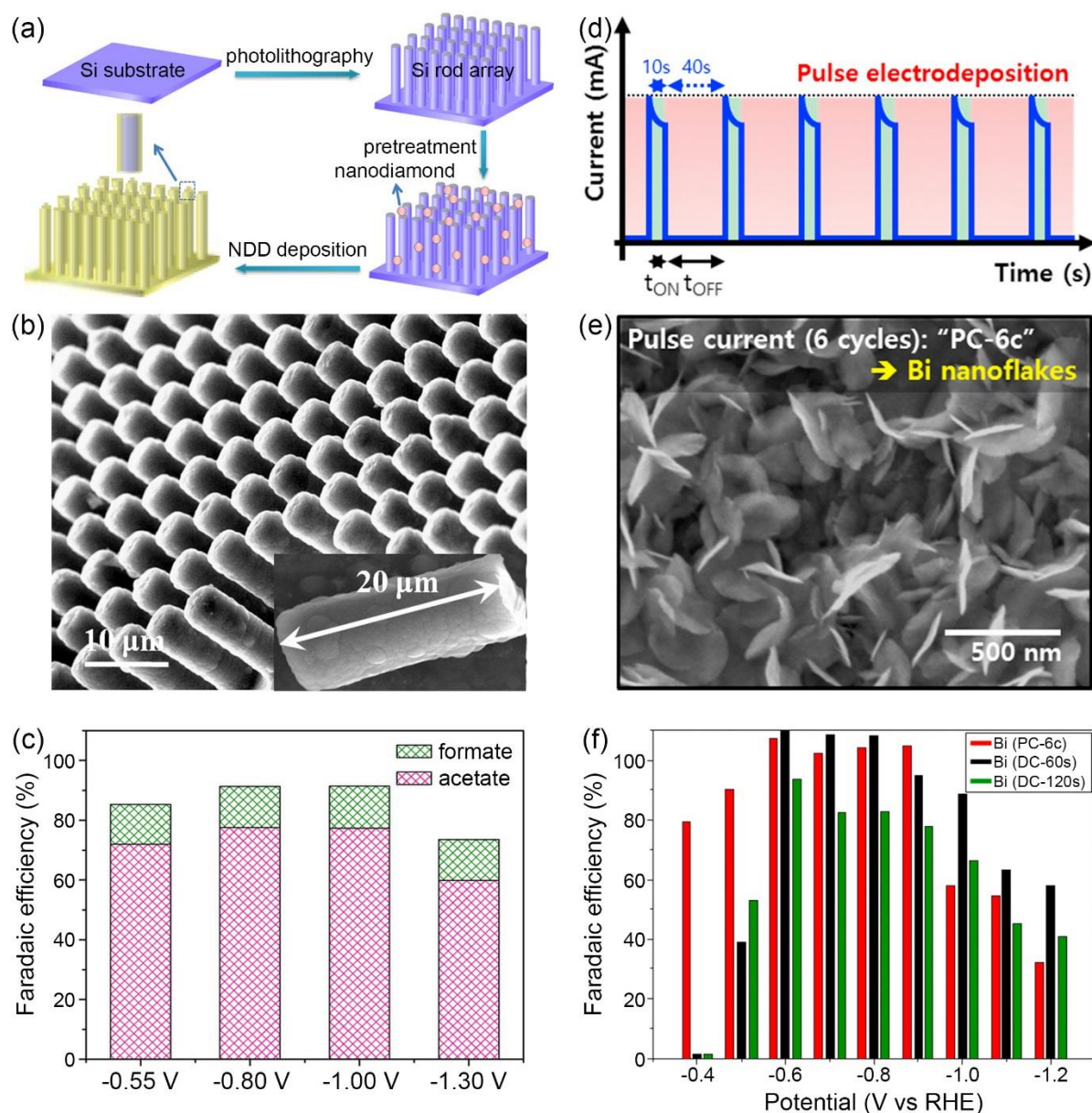
Figure 9. (a) Schematic illustration of the process for NDD/Si RA preparation. (b) SEM image of NDD_L/Si RA. (c) Faradaic efficiency for acetate and formate production for electrochemical reduction of CO_2 on NDD_L/Si RA electrode at -0.55 to -1.30 V (CO_2 saturated 0.5 M $NaHCO_3$ solution). Reproduced with permission from ref.[50] Copyright 2015, American Chemical Society. (d) Transient current curve of pulse electrodeposition. (e) SEM image of Bi nanoflakes grown by pulse-current 6 cycles. (f) $HCOO^-$ Faradaic efficiency of PC-6c, DC-60s and DC-120s deposited Bi films in CO_2-purged 0.1 M $KHCO_3$ electrolyte. Reproduced with permission from ref.[115] Copyright 2017, Elsevier.
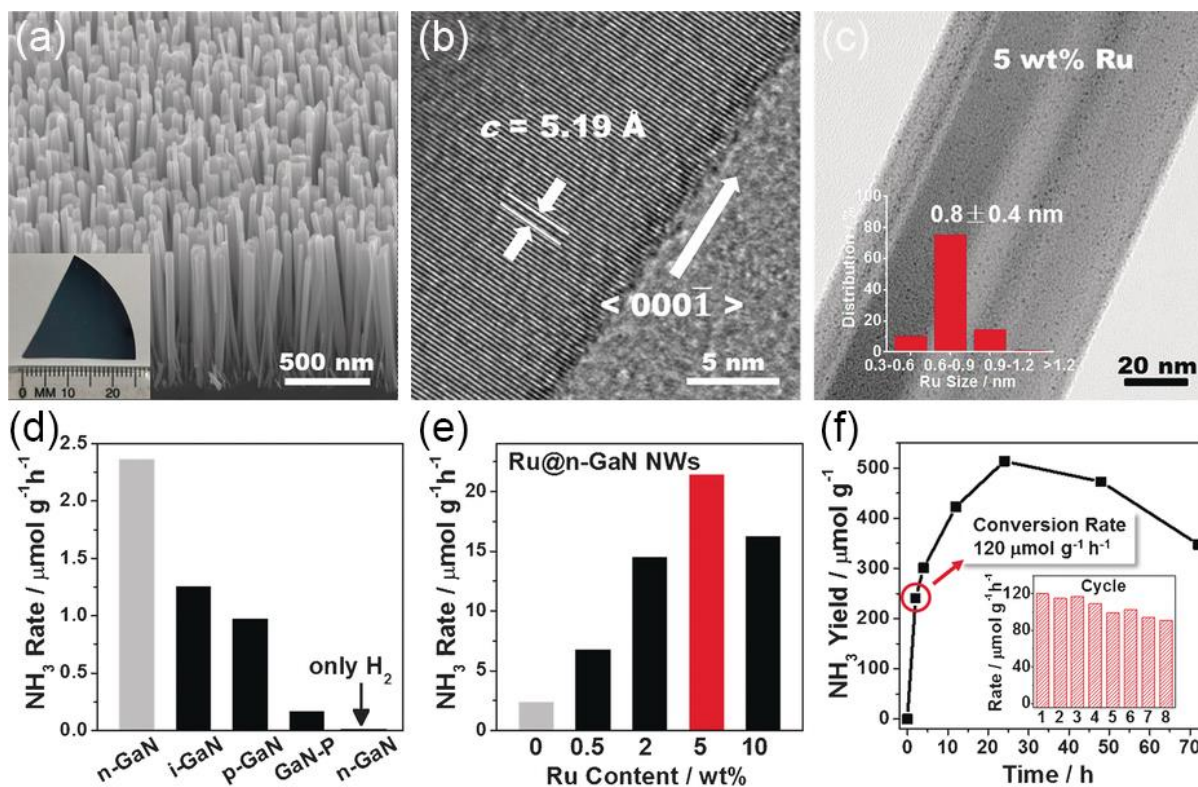
Figure 10. (a) 45° tilted SEM and (b) TEM images of the as-synthesized GaN NWs. Inset (a) shows the sample size. (c) TEM image of 5 wt% Ru-modified GaN NWs. Inset plot (c) shows diameter distribution of Ru clusters. NH_3 generation rate over (d) pure GaN materials with different doping levels and forms (24 h), (e) Plots of NH_3 release as a function of time over the optimized 5 wt% Ru-loaded n-GaN NWs under UV irradiation. Inset: reusability of Ru@n-GaN (2h for each cycle). Reproduced with permission from ref.[116] Copyright 2017, WILEY-VCH.

69
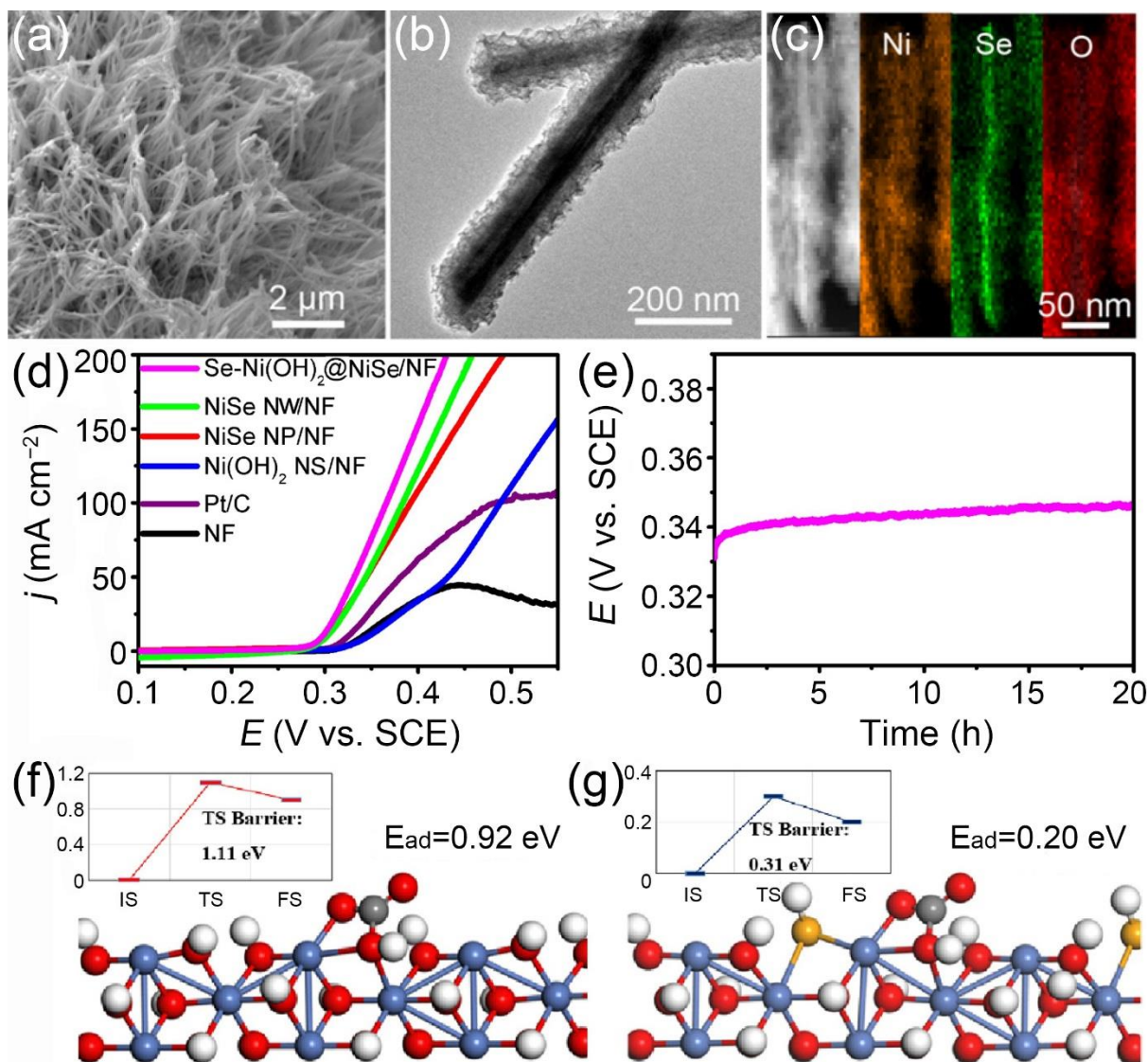
Figure 11. (a) FESEM image for Se-Ni(OH)$_2$@NiSe/NF. (b) TEM image for Se-Ni(OH)$_2$@NiSe core-shell nanowires. (c) STEM image and EDX elemental mapping for Ni, Se, and O for NiSe nanowire. (d) LSV curves for different electrodes toward 0.33 M urea with a scan rate of 5 mV s^{-1}. (e) Chronopotentiometric curve of Se-Ni(OH)$_2$@NiSe/NF with current density of 100 mA cm^{-2}. The schematic of CO$_2$ adsorption on the (f) pristine and (g) Se-Ni(OH)$_2$ (110) surface, in which the insets display the energy profile of the desorption process, IS, TS and FS represent the initial state (adsorption), transition state and final state (desorption). C, O, O, Se and Ni atoms are colored grey, red, white, yellow and blue, respectively. Reproduced with permission from ref.[135] Copyright 2017, Elsevier.
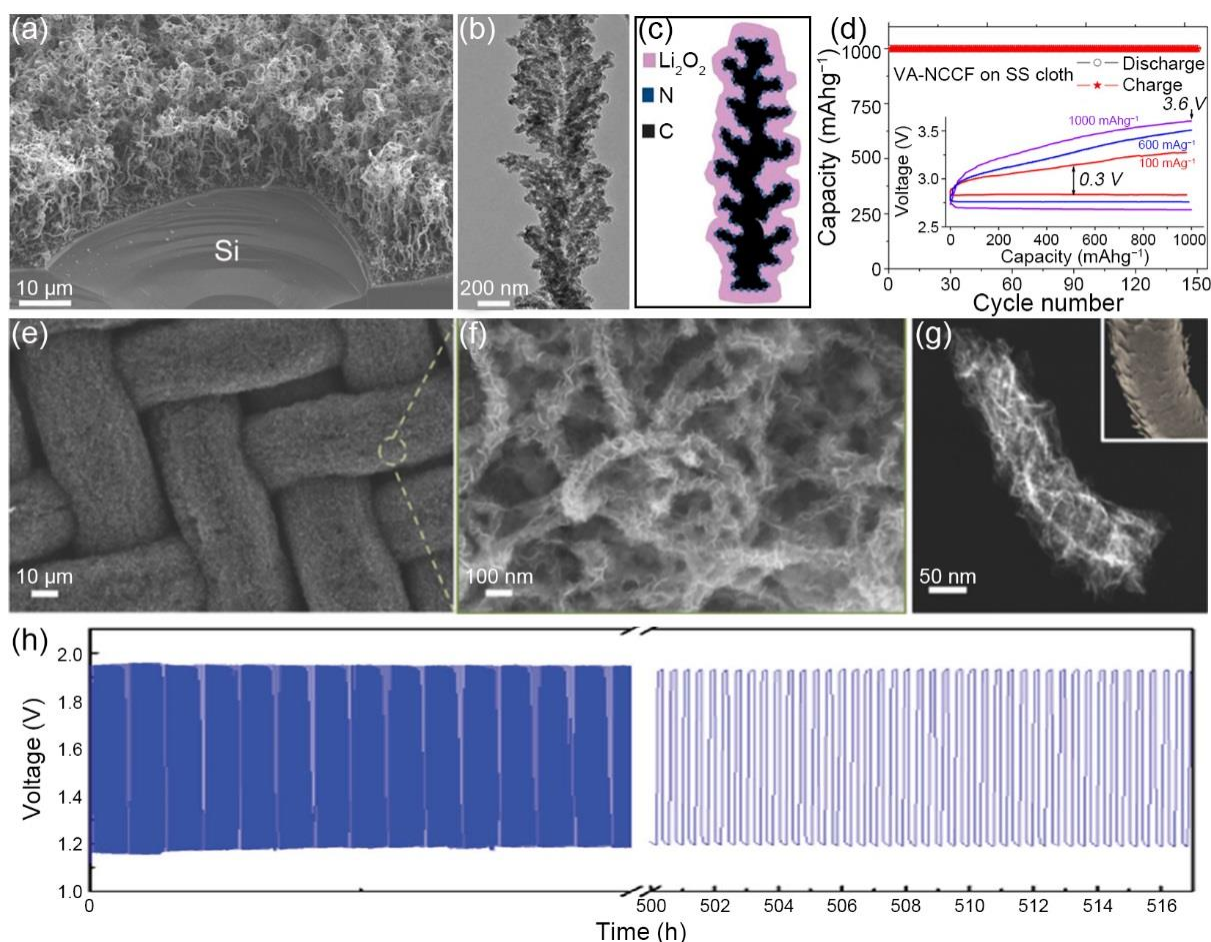
Figure 12. (a) SEM image of a VA-NCCF array grown by CVD. (b) TEM image of an individual VA-NCCF. (c) The sketch of Li_2O_2 grown on a coral-like carbon fiber, which has an advantage to tightly hold the Li_2O_2 deposit by the rugged surface. (d) Cycling performance of the VA-NCCF array on the SS cloth substrate (inset in (d) shows rate performance of the VA-NCCF electrode under current densities of 100, 600, and 1000 mA g^{-1}). Reproduced with permission from ref.[148] Copyright 2014, American Chemical Society. (e, f) SEM images of the Co_3O_4-NCNT/SS air electrode. (g) TEM image of the individual Co_3O_4-NCNT (inset in (g) shows the petal-like (spinous) scale patterns of human hair). (h) Galvanostatic charge-discharge cycling at a current density of 25 mA cm^{-2} with each cycle being 20 min. Reproduced with permission from ref.[151] Copyright 2016, WILEY-VCH.
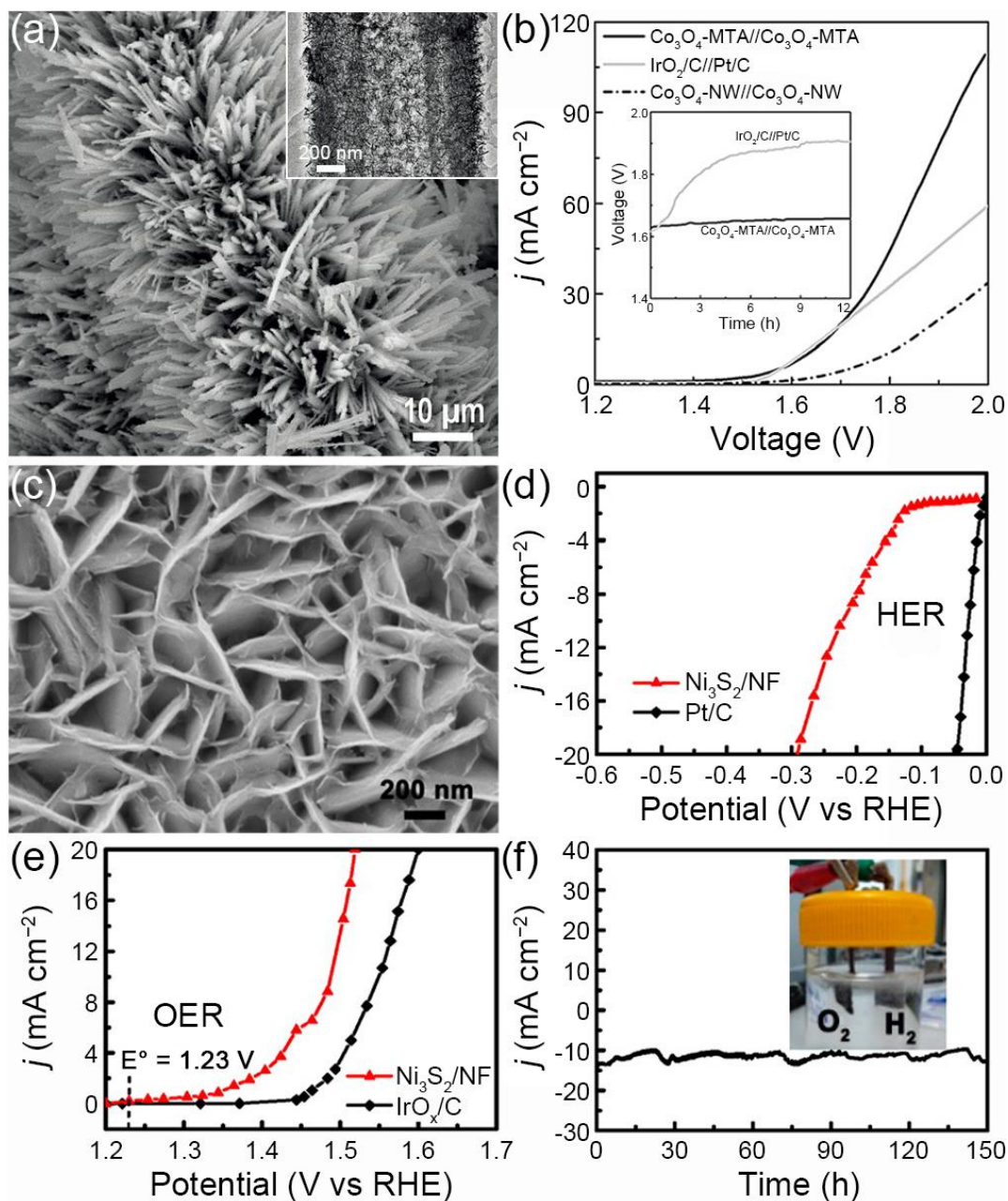
Figure 13. (a) SEM image of Co_3O_4-MTA (inset shows the TEM image of an individual Co_3O_4-MTA). (b) LSV curves of a two-electrode alkaline electrolyzer with Co_3O_4-MTA//Co_3O_4-MTA and Pt/C//IrO_2/C (inset in (b) shows galvanostatic water splitting at a stationary current density of 10 mA cm^{-2} for 12 h for Co_3O_4-MTA//Co_3O_4-MTA and Pt/C//IrO_2/C). Reproduced with permission from ref.[152] Copyright 2017, WILEY-VCH. (c) SEM image of the Ni_3S_2/NF. (d) HER and (e) OER steady-state current density as a function of applied voltage in alkaline media (pH 14) over Ni_3S_2/NF. (f) I−t curve at pH 14 at an applied potential of 1.76 V for an electrolyzer with both Ni_3S_2/NF anode and cathode (inset shows the generation of H_2 and O_2 bubbles on the Ni_3S_2/NF electrodes). Reproduced with permission from ref.[59] Copyright 2015, American Chemical Society.

72

Table 1. The performance of recent self-supported nanoarrays for the OER.

Catalyst	Substrate	Electrolyte	η_{onset} (mV)	η_{10} (mV)	Tafel slope (mV dec^{-1})	Ref.	Year
Fe-doped Ni$_2$P nanosheet	Carbon cloth	1.0 M KOH	190	$\eta_{50}=215$	48	94	2017
Ni$_3$S$_2$/MoS$_x$ nanosheet	Ni foam	1.0 M KOH	165	215	67.5	31	2017
Co$_{0.7}$Fe$_{0.3}$(OH)$_x$ nanosheet	Cu foam	1.0 M KOH	220	245	62.4	161	2017
Ni$_{0.7}$Co$_{0.3}$Se$_2$ nanosheet	Carbon cloth	1.0 M KOH	-	258	42.3	30	2017
CuO nanowire@Co$_3$O$_4$ nanosheet	Carbon paper	1.0 M KOH	-	258	72	32	2017
NiO@Ni-Bi nanosheet	Carbon cloth	1 M KOH	-	290	71	162	2017
Benzoate-Co(OH)$_2$ nanobelt	Ni foam	1.0 M KOH	-	$\eta_{50}=291$	78	163	2017
NiCo$_2$O$_4$@Ni-Co-Ci nanowire	Carbon cloth	1.0 M KHCO$_3$	-	309	91	164	2017
N, P-doped carbon nanofiber	Carbon paper	1 M KOH	280	310	87.4	97	2017
MnCo$_2$O$_4$ nanowire	Ti mesh	1.0 M KOH	-	$\eta_{50}=325$	115	91	2017
eFe/NiVS nanowire	Ni foam	1.0 M KOH	-	$\eta_{100}=325$	75	74	2017
Mn-Co-Bi nanowire	Carbon cloth	0.5 M K-Bi	-	366	193	165	2017
Ni-Co-Bi nanowire	Carbon cloth	0.1 M K-Bi	-	388	142	93	2017
Co-Bi nanowire	Carbon cloth	0.1 M K-Bi	-	411	131	166	2017
Co-Bi nanowire	Ti mesh	0.1 M K-Bi	-	420	195	33	2017
Ni-Bi nanosheet	Ti mesh	0.1 M K-Bi	-	430	276	167	2017
Co-Bi nanosheet	Ti mesh	0.1 M K-Bi	-	469	138	27	2017
Cu(OH)$_2$ nanorod@NiFe-LDH nanosheet	Carbon paper	1.0 M KOH	-	283	88	69	2016
CoN nanowire	Ni foam	1 M KOH	-	290	70	95	2016
NiS nanosheet	Stainless steel mesh	0.1 M KOH	-	$\eta_{11}=297$	47	60	2016
Zn-doped CoSe$_2$ nanosheet	Carbon fabric	1 M KOH	117	356	88	92	2016
Cu(OH)$_2$ nanowire	Cu foil	0.1 M NaOH	395	430	86	78	2016
NiCoFe LDH nanowire	Ni foam	1.0 M KOH	233	$\eta_{80}=257$	53	168	2014
Co$_3$O$_4$C nanowire	Cu foil	0.1 M KOH	240	290	70	140	2014
α-Fe$_2$O$_3$ nanorod	Carbon cloth	0.1 M KOH	330	420	52	169	2014
NiCo$_2$O$_4$ nanowire	FTO	1.0 M KOH	290	540	90	170	2014

Table 2. The performance of recent self-supported nanoarrays for the HER.

Catalyst	Substrate	Electrolyte	η_{onset} (mV)	η_{10} (mV)	Tafel slope (mV dec^{-1})	Ref.	Year
MoNi$_4$/MoO$_{3-x}$ nanorod	Ni foam	1.0 M KOH	5	17	36	[58]	2017
Zn$_{0.08}$Co$_{0.92}$P nanowall	Ti mech	0.5 M H$_2$SO$_4$	-	39	39	[108]	2017
		1.0 M KOH	-	67	-		
Mn-doped CoP nanosheet	Ti mesh	0.5 M H$_2$SO$_4$	-	49	55	[109]	2017
		1.0 M KOH	-	76	52		
		1.0 M PBS	-	86	82		
NiSe$_2$ nanosheet	Ni foam	0.5 M H$_2$SO$_4$	-	57	43	[171]	2017
CoP$_{1.37}$Se$_{0.63}$ nanowire	Carbon fiber	0.5 M H$_2$SO$_4$	-	70	54	[66]	2017
		1.0 M KOH	-	98	74		
V$_2$Se$_9$@PEDOT nanosheet	Ni foam	0.5 M H$_2$SO$_4$	-	72	36.5	[172]	2017
Fe$_2$P@rGO nanowall	Ti plate	0.5 M H$_2$SO$_4$	41	101	55.2	[173]	2017
Ni$_{0.7}$Co$_{0.3}$Se$_2$ nanosheet	Carbon cloth	0.5 M H$_2$SO$_4$	-	108	31.6	[30]	2017
CoS$_2$ nano-pine-tree	Carbon fiber	0.5 M H$_2$SO$_4$	-	114	58	[104]	2017
WN nanowire	Carbon cloth	0.5 M H$_2$SO$_4$	79	134	59.6	[110]	2017
		1.0 M KOH	60	130	57.1		
Ni$_3$N nanosheet	Carbon cloth	1.0 M KOH	-	136	-		2017
WS$_2$ nanosheet	Carbon fiber	0.5 M H$_2$SO$_4$	-	278	99	[55]	2017
MnCo$_2$O$_4$ nanowire	Carbon cloth	0.5 M K-Bi	-	293	-	[165]	2017
Fe$_{0.5}$Co$_{0.5}$P	Carbon cloth	0.5 M H$_2$SO$_4$	-	37	30	[107]	2016
FeP nanowire	Carbon fiber	0.5 M H$_2$SO$_4$	-	$\eta_{20}=45$	53	[65]	2016
		1.0 M KOH	-	$\eta_{20}=221$	134		
MoS$_2$@Ni	Carbon cloth	1.0 M KOH	30	91	89	[102]	2016
Se-enriched NiSe$_2$ nanosheet	Carbon fiber	H$_2$SO$_4$ (pH $\approx$ 0.67)	71	117	32	[67]	2016
CoSe$_2$ nanoneedle	Ti foil	0.5 M H$_2$SO$_4$	-	$\eta_{20}=125$	48.5	[68]	2016
CoS$_{2x}$Se$_{2(1-x)}$ nanowire	Carbon fiber	0.5 M H$_2$SO$_4$	-	129.5	44	[105]	2016
MoO$_2$/MoSe$_2$ nanosheet	Carbon cloth	0.5 M H$_2$SO$_4$	63	181	49.1	[76]	2016
CoS$_2$/P nanosheet	Carbon paper	0.5 M H$_2$SO$_4$	25	67	50	[174]	2015
CoS$_2$ nanopyramid	Carbon fiber	0.5 M H$_2$SO$_4$	61	70	70.1	[103]	2015
Co@NC nanorod	Ti mesh	0.5 M H$_2$SO$_4$	56	106	78.2	[175]	2015
MoS$_2$ nanosheet	Mo mesh	0.5 M H$_2$SO$_4$	120	160	46	[100]	2015
Ni-Mo-S nanosheet	Carbon fiber	0.5 M PBS	132	200	85.3	[101]	2015
Ni$_3$S$_2$ nanosheet	Ni foam	1.0 M KOH	180	220	108	[106]	2015

Table 3. The performance of recent bifunctional nanoarrays for overall water splitting.

| Catalysts	Substrate	Electrolyte	HER η_{onset} (mV)	HER η_{10} (mV)	HER Tafel slope (mV dec^{-1})	OER η_{onset} (mV)	OER η_{10} (mV)	OER Tafel slope (mV dec^{-1})	E_{10} (V)	Ref.	Year
$(Ni_{0.33}Fe_{0.67})_2P$ nanosheet	Ni foam	1.0 M KOH	-	$\eta_{50}=214$	-	-	$\eta_{50}=230$	55.9	1.49	[25]	2017
MoS_2-Ni_3S_2 HNRs	Ni foam	1.0 M KOH	31	98	61	195	249	57	1.50	[24]	2017
GDs/$Co_{0.8}Ni_{0.2}P$	Cu mesh	1.0 M KOH	-	$\eta_{15}=93$	51	230	$\eta_{15}=287$	50	1.54	[176]	2017
Co_3Se_4 nanowire	Co foam	1.0 M KOH	-	179	72	-	~240	44	1.59	[61]	2017
δ-MnO_2 nanosheet	Ni foam	1.0 M KOH	-	197	62	-	320	40	-	[57]	2017
Hollow Co_3O_4 microtube	Ni foam	1.0 M KOH	100	$\eta_{20}=190$	98	290	$\eta_{150}=360$	84	1.63	[152]	2017
CoO@CoNC nanorod	Ni foam	1.0 M KOH	-	190	98	-	309	53	-	[23]	2017
S-$NiFe_2O_4$ nanosheet	Ni foam	1.0 M KOH	29	138	61.3	-	267	36.7	1.65	[75]	2017
		1.0 M PBS	-	197	81.3	-	494	118.1	1.95		
α-NiOOH nanosheet	Ni foam	1.0 M KOH	170	282	119.1	260	266	76.3	1.66	[177]	2017
Ni_3N@Ni-Bi nanosheet	Ti mesh	0.5 M K-Bi	-	265	190	-	382	82	1.95	[64]	2017
CoFePO nanowire	Ni foam	1.0 M KOH	-	87.5	38.1	-	274.5	51.7	1.564	[34]	2016
CoP	Ti mesh	1.0 M KOH	-	72	65	-	310	87	1.64	[178]	2016
Fe_2Ni_2N nanoplate	Ni foam	1.0 M KOH	110	180	101	200		34	1.65	[63]	2016
C@Ni_8P_3 nanosheet	Ni foam	1.0 M KOH	-	144	59	-	267	51	1.65	[179]	2016
$Ni_{2.3\%}$-CoS_2 nanowire	Carbon cloth	1.0 M KOH	136	$\eta_{100}=231$	106	297	$\eta_{100}=370$	119	1.66	[180]	2016
$Zn_{0.76}Co_{0.24}S$/CoS_2 nanowire	Ti mesh	1.0 M KOH	170	$\eta_{20}=238$	164	316	$\eta_{20}=330$	79	1.66	[181]	2016
CoP nanorod	Ni foam	1.0 M KOH	~0	54	51	270	290	65	1.62	[26]	2015
NiSe nanowire	Ni foam	1.0 M KOH	-	96	120	-	$\eta_{20}=270$	64	1.63	[62]	2015
$NiCo_2O_4$ nanowire	Carbon cloth	1.0 M KOH	230	$\eta_{100}=305$	141	270	$\eta_{100}=340$	89	1.68	[182]	2015
Ni_3S_2 nanosheet	Ni foam	1.0 M KOH	-	223		-	260		$E_{13}=1.76$	[59]	2015
Ni_3S_2 nanorod	Ni foam	1.0 M KOH	-	200	107	-	217	163	-	[183]	2015

Table of contents:

Self-supported earth-abundant nanoarrays have emerged as the most promising electrocatalysts for various energy conversion reactions and devices due to their unique structures and fascinating electrochemical properties. Recent progress on their synthetic methods and applications for different energy-related processes and practical devices are presented.

Keywords: self-supported nanoarray, earth-abundant electrocatalyst, synthetic method, energy-related reaction, bifunctional electrocatalysis

Jinlong Liu, Dongdong Zhu, Yao Zheng, Anthony Vasileff, and Shi-Zhang Qiao

Title: Self-supported Earth-abundant Nanoarrays as Efficient and Robust Electrocatalysts for Energy-Related Reactions

TOC graphic
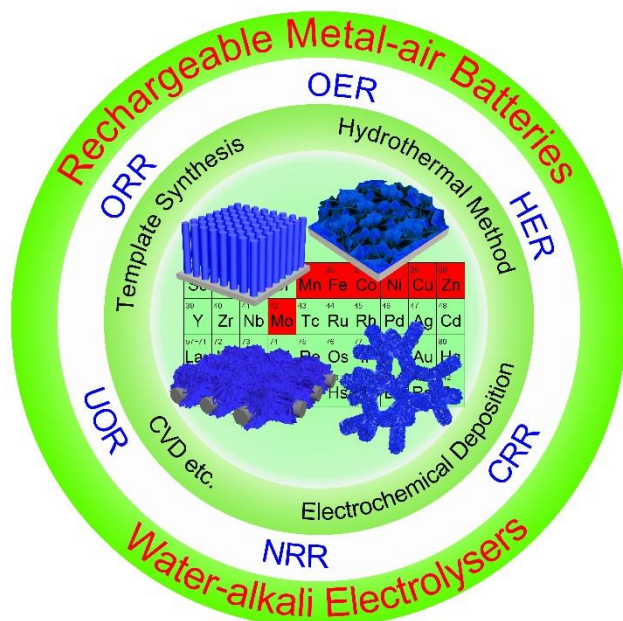
Chapter 3: Identification of pH-Dependent Synergy on Ru/MoS$_2$ Interface: A Comparison of Alkaline and Acidic Hydrogen Evolution

3.1 Introduction and Significance

Understanding the HER mechanism at molecular level plays a critical role in rational design of advanced HER electrocatalysts. The discovery of significantly enhanced HER activity on Pt/Ni(OH)$_2$ catalysts provides some evidences for water dissociation as an essential step in alkaline HER, where Ni(OH)$_2$ can effectively cleave the HO−H bond. To obtain more insights into the HER mechanism, it is necessary to develop more general catalyst models that are stable under both alkaline and acidic conditions. In this chapter, a new catalyst, consisting of Ru nanoparticles on defect-rich MoS$_2$ nanosheets vertically aligned on carbon paper, was designed and fabricated, and its HER behaviours in alkaline and acidic solutions were investigated and compared. It was found that the Ru/MoS$_2$ exhibited remarkable catalytic activity in 1.0 M KOH, while no improved HER activity was observed in 0.5 M H$_2$SO$_4$, demonstrating pH-dependent synergy for the HER. The highlights in this study include:

1. A new model catalyst based on Ru and MoS$_2$ was rationally designed and successfully synthesized by a facile wet-chemical method, in which Ru facilitates the dissociation of water and MoS$_2$ accelerates the recombination of hydrogen intermediates into molecular hydrogen towards synergistically improved alkaline HER.

2. The resultant Ru/MoS$_2$/CP achieved remarkable activity and durability for the alkaline HER, with an onset overpotential close to zero, an extremely low η_{10} at 13 mV, favourable kinetics, near ideal Faradaic efficiency (~100%), and considerable structural and chemical stability for long-term operation, which far exceeded previous reports on MoS$_2$-based and Ru-based electrocatalysts, even outperformed commercial Pt catalyst in alkaline media.

3. The pH-dependent synergy on Ru/MoS$_2$ interface was identified for the first time through a comparison of intrinsic HER activities in alkaline and acidic media, and the interfacial synergy for enhanced HER rate was further verified by the self-consistent Tafel slopes from experiment results and theoretical calculations.

3.2 Identification of pH-Dependent Synergy on Ru/MoS$_2$ Interface: A Comparison of Alkaline and Acidic Hydrogen Evolution

This chapter is included as it appears as a journal paper published by **Jinlong Liu**, Yao Zheng, Dongdong Zhu, Anthony Vasileff, Tao Ling and Shi-Zhang Qiao, Identification of pH-Dependent Synergy on Ru/MoS$_2$ Interface: A Comparison of Alkaline and Acidic Hydrogen Evolution, *Nanoscale*, 2017, 9, 16616−16621.

Statement of Authorship

Title of Paper	Identification of pH-dependent synergy on Ru/MoS$_2$ interface: a comparison of alkaline and acidic hydrogen evolution
Publication Status	☑ Published ☐ Accepted for Publication ☐ Submitted for Publication ☐ Unpublished and Unsubmitted work written in manuscript style
Publication Details	Jinlong Liu, Yao Zheng, Dongdong Zhu, Anthony Vasileff, Tao Ling and Shi-Zhang Qiao, Identification of pH-dependent synergy on Ru/MoS$_2$ interface: a comparison of alkaline and acidic hydrogen evolution, Nanoscale, 2017, 9, 16616–16621.

Principal Author

Name of Principal Author (Candidate)	Jinlong Liu
Contribution to the Paper	Research plan, material synthesis, most of the characterizations and data analysis, electrochemical measurements, and manuscript drafting.
Overall percentage (%)	
Certification:	This paper reports on original research I conducted during the period of my Higher Degree by Research candidature and is not subject to any obligations or contractual agreements with a third party that would constrain its inclusion in this thesis. I am the primary author of this paper.
Signature	Date 4/02/2018

Co-Author Contributions

By signing the Statement of Authorship, each author certifies that:

   i.   the candidate's stated contribution to the publication is accurate (as detailed above);

   ii.   permission is granted for the candidate in include the publication in the thesis; and

   iii.   the sum of all co-author contributions is equal to 100% less the candidate's stated contribution.

Name of Co-Author	Yao Zheng
Contribution to the Paper	Discussion of research plan, data analysis, and manuscript revision.
Signature	Date 5 Feb 2018

Name of Co-Author	Dongdong Zhu
Contribution to the Paper	Assistance with HER testing and analysis.
Signature	Date 4/02/2018

Name of Co-Author	Anthony Vasileff			
Contribution to the Paper	Assistance with manuscript editing and polishing.			
Signature			Date	05/02/2018

Name of Co-Author	Tao Ling			
Contribution to the Paper	Assistance with TEM characterization.			
Signature			Date	04/02/2018

Name of Co-Author	Shi-Zhang Qiao			
Contribution to the Paper	Supervision of the work, data interpretation, and manuscript evaluation.			
Signature			Date	15/02/2018

Check for updates

Identification of pH-dependent synergy on Ru/MoS₂ interface: a comparison of alkaline and acidic hydrogen evolution†

Jinlong Liu,[a] Yao Zheng,[a] Dongdong Zhu,[a] Anthony Vasileff, [ID][a] Tao Ling [ID][b] and Shi-Zhang Qiao [ID] *[a,b]

Engineering bifunctional interfaces for enhanced alkaline hydrogen evolution reaction (HER) kinetics is achieved by rational coupling of Ru nanoparticles and defect-rich MoS₂ nanosheets *via* a simple wet-chemical method. Comprehensive material characterizations, especially high-resolution transmission electron microscopy, reveal well-defined interfaces between both components, leading to interfacial synergy whereby Ru expedites water dissociation and nearby defect-rich MoS₂ enables favorable hydrogen adsorption for recombination into H₂. The designed Ru/MoS₂ material demonstrates remarkable catalytic activity towards alkaline HER (−13 mV at −10 mA cm⁻²) with stable operation after 12 h or 1000 cycles, which is superior to almost all Ru-based and MoS₂-based electrocatalysts and even outperforms commercial 20 wt% Pt/C at overpotentials larger than −78 mV in alkaline media. No improved HER activity is observed for Ru/MoS₂ in acidic electrolyte (−96 mV at −10 mA cm⁻²), which is even inferior to Ru/CP (−78 mV at −10 mA cm⁻²). The correlation between alkaline and acidic HER results confirms that the intrinsic HER activity of this material originates from the desired synergistic effect under alkaline conditions.

Photoelectrochemical water splitting in alkaline or neutral media has attracted renewed interest to produce high-purity hydrogen fuel for hydrogen-based energy devices like hydrogen fuel cells.[1,2] Such techniques greatly rely on the development of efficient catalysts to increase reaction rate and reduce the required energy input.[1–3] In particular, the higher efficiency of water electrolyzers in alkaline electrolyte over those in acidic media makes it more significant to explore improved electrocatalysts for alkaline water splitting.[4] Fundamentally, the binding energy of the hydrogen intermediate, being the hydrogen–metal bond energy ($E_{M–H}$) or the hydrogen adsorption free energy (ΔG_{H*}),[5,6] is considered to be the activity descriptor for the cathodic hydrogen evolution reaction (HER) in hydrolysis. As proposed by Parsons and Gerischer, the optimal catalyst for the HER must bind atomic hydrogen (H_{ads}) neither too strongly nor too weakly.[7,8] Under acidic conditions, this descriptor explains HER activities on various catalyst surfaces very well from analytical, experimental, and computational perspectives.[9] However, for common phenomena, such as the significantly lower HER activity of Pt in alkaline media compared to in acidic media, it is inadequate.[10] As a result, there is debate whether ΔG_{H*} can be the sole descriptor for the HER rate over the whole pH range.[2,11–13] Some pioneering works reported by Markovic *et al.* indicate that the HER activity of Pt in alkaline can be enhanced significantly by modification with Ni(OH)₂ as an OH⁻-adsorption promoter *via* a facilitated water dissociation process.[11] Additionally, Koper *et al.* found that the rate of interfacial water reorganization was increased by the addition of a submonolayer of Ni(OH)₂ to the Pt(111) surface, which enhanced overall HER kinetics.[12] Although this interfacial engineering strategy provides some evidence for the contribution of water dissociation towards the reaction rate of hydrogen evolution and presents new insight to understanding the mechanism of alkaline HER, current models are mainly limited to precious Pt and Ni(OH)₂ couples.[11,12] However, in order to validate this new theory on the synergistic effect between water dissociation and hydrogen adsorption towards alkaline HER performance, more general cases are required. In addition, it is likely that the interfacial synergy is pH-dependent due to different reaction pathways under alkaline and acidic conditions. Hence, the comparison of alkaline and acidic HER activity may provide evidence for this synergistic effect whereby the effect should not be apparent in acidic media due to the lack of the initial water dissociation process. Unfortunately, previous studies based on model catalyst Pt/Ni(OH)₂ have not taken this into consideration, likely due to the instability of Ni(OH)₂ in acidic electrolyte.

To this end, the design of a novel bifunctional system, that is stable in both alkaline and acidic environments, is needed with the aim of confirming this pH-dependent interfacial synergy

[a]School of Chemical Engineering, The University of Adelaide, Adelaide, SA 5005, Australia. E-mail: s.qiao@adelaide.edu.au
*[b]School of Materials Science and Engineering, Tianjin University, Tianjin, 300072, P.R. China*
†Electronic supplementary information (ESI) available: Experimental section, supplementary figures, tables, notes, and movie. See DOI: 10.1039/c7nr06111k

and developing a Pt-free catalyst for superior alkaline HER. Among various alternatives to Pt, MoS_2 has been theoretically identified as having a favourable ΔG_{H^*} close to zero (ΔG_{H^*} = +0.08 eV on the unsaturated Mo and/or S edges).[14] Therefore, some MoS_2-based electrocatalysts have exhibited promising HER activity in acidic media,[15–17] but still suffer from sluggish HER kinetics in alkaline conditions. This is mainly due to their poor water dissociation ability.[18] Recently, both spectroscopic characterization and computational techniques have indicated that Ru possesses the greatest water dissociation capability, and strongest (electro)chemical adsorptions of H and OH amongst almost all of the precious metals (Pt, Rh, Ir, Pd, Au, etc.).[19–22] Accordingly, it is proposed that if synergy does exist at the interface of a bifunctional system in alkaline electrolyte, the coupling of Ru and MoS_2 with tailored interfacial structure is desirable for the optimization of energetics for both water dissociation and hydrogen adsorption. In such a model, Ru would greatly facilitate water dissociation, and the nearby unsaturated Mo and/or S atoms of MoS_2 would rapidly capture reactive hydrogen atoms and prompt their combination into molecular H_2. This kind of functionality would realize a synergistic effect on the interfacial reactivity for overall hydrogen evolution in alkaline electrolyte. In comparison, no synergistic effect can be observed on the Ru/MoS_2 interface with the absence of water dissociation step during acidic HER. Nevertheless, it remains a great challenge to manipulate the well-defined Ru/MoS_2 interface with abundant exposure of unsaturated Mo/S sites, as conventional MoS_2 basal planes are inactive for hydrogen adsorption.

Inspired by these hypotheses, herein, we present the design and fabrication of such bifunctional system, composed of Ru nanoparticles decorated on defect-rich MoS_2 nanosheets vertically aligned on carbon paper (Ru/MoS_2/CP). The Ru/MoS_2 heterostructures feature well-defined interfaces between Ru nanoparticles and defect-rich MoS_2 nanosheets. As a result, Ru/MoS_2/CP exhibits excellent alkaline HER performance, even superior to commercial 20 wt% Pt/C, as well as almost all reported Ru-based and MoS_2-based electrocatalysts. A series of controlled electrochemical tests identify that the intrinsic alkaline HER activity of Ru/MoS_2/CP likely originates from the interfacial synergy between the two active components to promote both water dissociation and hydrogen adsorption processes. In contrast, Ru/MoS_2/CP shows no better HER activity than Ru/CP and commercial 20 wt% Pt/C in acidic conditions, further demonstrating the pH-dependence of the interfacial synergy. This work may provide solid evidence for the importance of water dissociation in alkaline HER processes based on alternative systems beyond Pt.

As illustrated in Fig. 1a, Ru/MoS_2/CP was synthesized via hydrothermal growth of vertically aligned MoS_2 nanosheets on carbon paper and subsequent chemical modification with Ru from impregnation and calcination. By means of hydrothermal reaction, pre-cleaned carbon paper was fully covered by vertically aligned MoS_2 nanosheets with a highly developed interconnected structure (Fig. S1†). Notably, under hydrothermal conditions, oxygen can be effectively incorporated into the
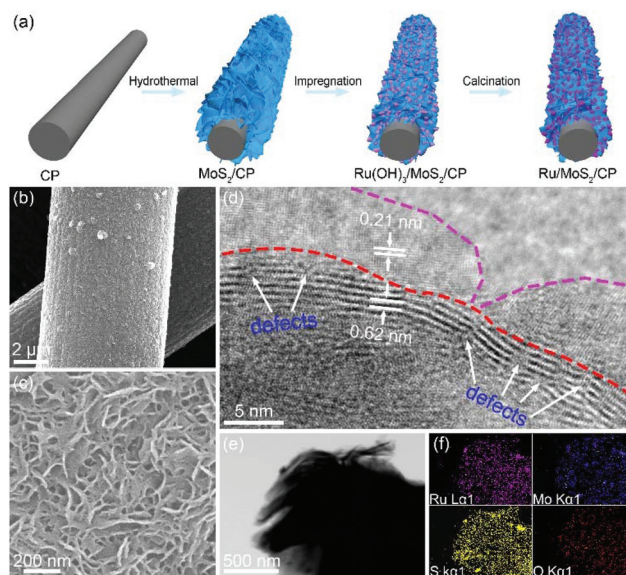
Fig. 1 (a) Schematic illustration of the synthesis process of Ru/MoS_2/CP. (b, c) SEM, (d) HRTEM, (e) HADDF-STEM images and (f) corresponding element mapping of Ru/MoS_2/CP.

MoS_2 to enhance intrinsic conductivity (Fig. S2a and b†).[23] Excess thiourea was introduced to create defect-rich MoS_2 nanosheets (Fig. S2c and d†), as additional thiourea can be adsorbed on primary nanocrystallites to prevent their regular crystal growth.[24] Subsequently, the obtained MoS_2/CP was immersed in 5 mM $RuCl_3$ solution to modify MoS_2 with Ru $(OH)_3$, which was further reduced by H_2 under calcination to obtain Ru/MoS_2/CP. As can be seen in the scanning electron microscope images (SEM, Fig. 1b and c), Ru/MoS_2/CP shows identical morphology to MoS_2/CP, except that the MoS_2 nanosheet planes are decorated with homogeneous Ru nanoparticles, resulting in a rougher MoS_2 nanosheet surface. By comparison, the Ru deposited on CP in Ru/CP formed wrinkled agglomerates (Fig. S3†). From high-resolution transmission electron microscope imaging (HRTEM, Fig. 1d), the Ru/MoS_2 heterostructure shows an obvious interface with close contact between Ru nanoparticles and MoS_2 nanosheets, where the lattice fringes with interlayer distances of 0.21 and 0.62 nm correspond to the (002) plane of hexagonal Ru and (002) plane of hexagonal MoS_2, respectively. It is found that the Ru nanoparticles are approximately 10 nm in size (Fig. 1d and Fig. S4†). Perpendicular to the MoS_2 nanosheet planes, many defects (e.g. dislocation, vacancy, and distortion) are evident, offering plenty of active sites for reinforced interfacial synergy. It is worth noting that Ru/MoS_2/CP possessed more and larger defects across MoS_2 planes compared with bare MoS_2, which is probably a result of the corrosive effect of $RuCl_3$. Furthermore, the high-angle annular dark field scanning TEM (HAADF-STEM) image and corresponding elemental mapping analyses (Fig. 1e and f) indicated the homogeneous distribution of Ru, Mo, S, and O throughout the nanosheet network, suggesting the uniform decoration of Ru nano-

particles and the successful incorporation of O in MoS_2 nanosheets. According to these results and previous studies,[11,21,23,24] $Ru/MoS_2/CP$ likely offers improved alkaline HER activity and increased conductivity due to its large amount of active sites, strong interfacial synergy, and O-incorporation.

For further structural and chemical analyses, X-ray diffraction (XRD) and X-ray photoelectron spectroscopy (XPS) characterizations were carried out. Following the hydrothermal reaction, in the absence of CP, pure MoS_2 nanosheets display an XRD pattern that can be indexed to hexagonal MoS_2 (Fig. S5a,† JCPDS card no. 73-1508). Fig. S5b† shows the XRD pattern of $Ru/MoS_2/CP$. Aside from the characteristic peaks arising from MoS_2 and CP (graphite, JCPDS no. 75-2078), the two peaks centred at 43.9° and 77.9° can be assigned to hexagonal Ru (JCPDS no. 06-0663), in accordance with the results discussed above. Also, the XPS survey spectrum of $Ru/MoS_2/CP$ shows distinct signals of Mo, S, O, Ru, and C (Fig. S6†). As shown in Fig. 2a, the spin–orbit peaks in the Mo 3d region are fitted to four peaks. Specifically, the peaks located at 229 and 232 eV are attributed to the Mo^{IV} $3d_{5/2}$ and Mo^{IV} $3d_{3/2}$, respectively, while the peaks centred at 232.8 and 235.8 eV are ascribed to the Mo^{VI} $3d_{5/2}$ and Mo^{VI} $3d_{3/2}$, respectively. This implies the coexistence of Mo^{IV} and Mo^{VI} in the product material.[25,26] The S 2p region (Fig. 2b) exhibits the representative peaks of S $2p_{3/2}$ and S $2p_{1/2}$ with binding energies at 161.7 and 163.9 eV, respectively, suggesting a −2 valence of S.[23] The O 1s spectrum is deconvoluted into three peaks centred at 530.5, 531.3, and 532 eV, which are assigned to Mo–O bonds, carbon–oxygen species, and adsorbed water, respectively (Fig. 2c).[23,27] The presence of Mo–O bonds strongly support O-incorporation in MoS_2 nanosheets. In the Ru 3d spectrum of $Ru/MoS_2/CP$ (Fig. 2d), two spin–orbit peaks, that is, Ru $3d_{5/2}$ and Ru $3d_{3/2}$,

are observed at 280.3 and 284.4 eV with an interval of 4.1 eV, indicating the metallic state of Ru.[28] Due to the proximity of binding energy for Ru $3d_{3/2}$ and C 1s, the Ru $3d_{3/2}$ is further divided into four peaks. Among them, the peaks at 284.6, 285.7, and 288.4 eV correspond to C–C, C–O, and C=O, respectively.[29] All these results further validate O-incorporation and Ru-decoration of MoS_2 nanosheets in the resultant $Ru/MoS_2/CP$.

The electrochemical performance of the $Ru/MoS_2/CP$, together with control groups including PtC/CP, Ru/CP, MoS_2/CP, and pristine MoS_2, were evaluated in a typical three-electrode cell setup with 1.0 M KOH electrolyte. Fig. 3a shows their linear sweep voltammetry (LSV) curves towards cathodic HER. As expected, $Ru/MoS_2/CP$ exhibited much improved alkaline HER activity compared to bare MoS_2, MoS_2/CP, and Ru/CP, achieving the lowest onset overpotential (η_{onset} = ~0 mV, ESI Note 1†) comparable to PtC/CP. More impressively, $Ru/MoS_2/CP$ requires an overpotential of only −13 mV to produce a current density of −10 mA cm^{-2}, which is −347, −181, and −22 mV less than that of bare MoS_2, MoS_2/CP, and Ru/CP, respectively. This value is much smaller than many other recently reported electrocatalysts, such as $Co_{0.68}Fe_{0.32}P$ (−116 mV)[30] and Mo_xC-IOL (−117 mV).[31] As far as is known, this overpotential is also superior to almost all previously reported electrocatalysts based on Ru or MoS_2 under alkaline and/or acidic conditions (Tables S1 and S2†). Moreover, the current density of $Ru/MoS_2/CP$ increases sharply with more negative potentials, even surpassing PtC/CP when the potential decreases further than −0.078 V vs. RHE. The corresponding Tafel plots show that $Ru/MoS_2/CP$ has a small Tafel slope (ESI Note 1†) of −60 mV dec^{-1} (Fig. 3b), suggesting its favourable reaction kinetics.
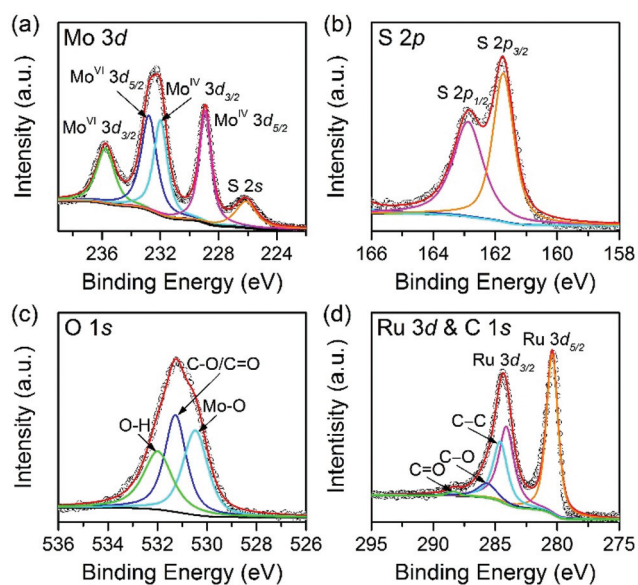

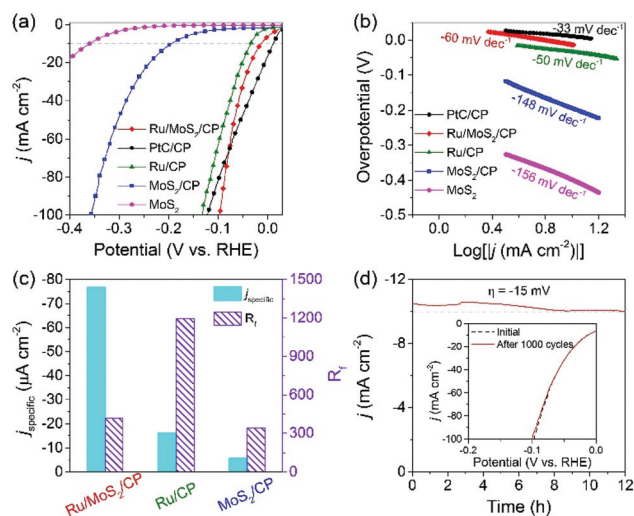Fig. 2 High-resolution XPS spectra of (a) Mo 3d, (b) S 2p, (c) O 1s, and (d) Ru 3d & C 1s of $Ru/MoS_2/CP$.

Fig. 3 (a) Polarization curves of $Ru/MoS_2/CP$ electrode in 1.0 M KOH, along with PtC/CP, Ru/CP, MoS_2/CP, and MoS_2 for comparison. (b) Corresponding Tafel plots. (c) Comparison of $j_{specific}$ and R_f for $Ru/MoS_2/$CP, MoS_2/CP, and Ru/CP in 1.0 M KOH. (d) Chronoamperometric curve of $Ru/MoS_2/CP$ electrode at an overpotential of −15 mV. Inset presents HER polarization curves recorded before and after 1000 potential sweeps in 1.0 M KOH.

Considering that overall HER activity is determined by the intrinsic activity and the number of electrocatalyst active sites,[32] it is necessary to estimate the catalytically active surface area for revealing the synergistic effect in Ru/MoS$_2$/CP. In this regard, the double-layer capacitance (C_{dl}), which is generally proportional to the catalytically active surface area,[33,34] was investigated using cyclic voltammetry (CV, Fig. S7 and ESI Note 2†). From the scan-rate dependent CVs, the C_{dl} of Ru/MoS$_2$/CP, Ru/CP, and MoS$_2$/CP are 25, 71.6, and 20.6 mF cm^{-2}, respectively, which matches well with the C_{dl} estimated by electrochemical impedance spectroscopy (EIS, Fig. S8†) within an error range of ±10% (ESI Note 3†). Thus, the roughness factor (R_f) and specific alkaline HER current density ($j_{specific}$) of various samples were evaluated as illustrated in ESI Note 2.† As presented in Fig. 3c, although Ru modification in Ru/MoS$_2$/CP contributes somewhat to increasing its R_f in comparison to MoS$_2$/CP, Ru/MoS$_2$/CP exhibits the highest $j_{specific}$ by decoupling the geometric effect. As a result, the significant enhancement in activity of Ru/MoS$_2$/CP for alkaline HER is most likely associated with its high intrinsic activity originating from its interfacial synergy.

The long-term operating durability of the Ru/MoS$_2$/CP electrode under alkaline conditions was assessed using chronoamperometry and CV techniques (Fig. 3d). Notably, the chronoamperometric curve of the Ru/MoS$_2$/CP electrode shows negligible attenuation during 12 h of operation, and no obvious potential shift was observed in LSV curves after 1000 CV cycles. It was found that the initial morphology and steady chemical states of Ru/MoS$_2$/CP were preserved after long-term operation (Fig. S9 and S10†), indicating good structural and chemical stability. Accordingly, the strong coupling of Ru/MoS$_2$/CP offers structural and chemical stability for practical operation. To evaluate the Faradaic efficiency, evolved H$_2$ gas was measured quantitatively using gas chromatography (GC), and the amount of measured H$_2$ strongly agrees with theoretical predictions (Fig. S11†). This reflects a near 100% Faradaic efficiency for Ru/MoS$_2$/CP towards alkaline HER.

From a reaction pathway standpoint, the proposed interfacial synergy between Ru and MoS$_2$ for enhanced alkaline HER can be explained indirectly by comparing the HER activities of various electrocatalysts with those under acidic conditions, as acidic HER is predominately correlated with hydrogen adsorption ability without the need for water dissociation. Fig. 4a gives the LSV curves of various electrodes in 0.5 M H$_2$SO$_4$ electrolyte. It can be seen that Ru/MoS$_2$/CP exhibits poorer HER activity than that of Ru/CP and PtC/CP. In terms of the overpotential at −10 mA cm^{-2} (η_{10}, Fig. 4b), the η_{10} of Ru/MoS$_2$/CP and Ru/CP increase to −96 and −78 mV, respectively. In contrast, bare MoS$_2$ and MoS$_2$/CP achieve considerably smaller η_{10} under acidic conditions. This comparison unambiguously demonstrates that Ru is more capable of dissociating water to promote subsequent hydrogen adsorption and recombination on MoS$_2$, resulting in significantly enhanced HER kinetics in alkaline solution. Consequently, this study provides substantiating evidence for the synergistic effect of Ru/MoS$_2$/CP towards alkaline HER through the coupling of water dissociation on Ru and hydrogen adsorption on MoS$_2$.
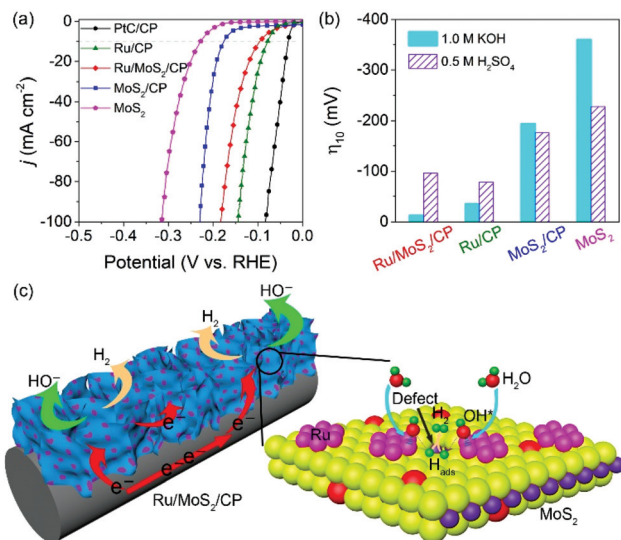
Fig. 4 (a) Polarization curves of Ru/MoS$_2$/CP, PtC/CP, Ru/CP, MoS$_2$/CP, and MoS$_2$ electrodes in 0.5 M H$_2$SO$_4$. (b) Comparison of the overpotential values required to afford a current density of −10 mA cm^{-2} under basic and acidic conditions. (c) Schematic illustration of interfacial synergy between Ru and MoS$_2$ for enhanced alkaline HER.

With the establishment of physical structure and electrochemical properties, the outstanding performance of Ru/MoS$_2$/CP for alkaline HER can be ascribed to its rationally designed composition with favourable electrode configuration, as schematically illustrated in Fig. 4c. Firstly, the highly conductive CP promotes fast electron transport to the MoS$_2$ nanosheet arrays,[29,35] and O-incorporation and Ru-decoration facilitate the effective charge transfer to active sites, leading to a highly improved capability of delivering electrons (Fig. S8†).[23] Secondly, the vertically aligned MoS$_2$ nanosheets are able to expose more edge sites as active centres.[35,36] Meanwhile, the "inert" MoS$_2$ nanosheet planes are activated by a large amount of defects and Ru modification, allowing for the exposure of numerous in-plane active sites. Thirdly, and most importantly, the reaction kinetics for alkaline HER are significantly improved by the interfacial synergy between Ru nanoparticles and defect-rich MoS$_2$ nanosheets. As highlighted in Fig. 4c, Ru can efficiently dissociate a water molecule into an OH$^−$ ion and an intermediate H$_{ads}$. Nearby unsaturated Mo and/or S atoms can then immediately absorb the generated H$_{ads}$ and promote their recombination into H$_2$, which can also be verified by HER mechanism analysis using the Tafel slopes of Ru/MoS$_2$/CP at low and high overpotentials (Fig. S12 and ESI Note 4†). Additionally, the unique porous structure among vertically aligned MoS$_2$ nanosheets facilitates rapid access of the electrolyte to the reaction sites, the release of evolved H$_2$ (Movie S1†), and the diffusion of OH$^−$.[37] Collectively, these features contribute to the fascinating HER activity on Ru/MoS$_2$/CP in alkaline electrolyte. Furthermore, the excellent structural and chemical stability of Ru/MoS$_2$/CP provide durability for long-term operation.

Conclusions

In summary, nanostructured Ru/MoS$_2$ nanosheets, featuring strong interfacial interactions between Ru metal nanoparticles and defect-rich MoS$_2$ nanosheets, have been directly grown on carbon paper. The self-supported Ru/MoS$_2$/CP electrode exhibits superior activity and favourable kinetics towards alkaline HER, which can be attributed to the significant interfacial synergy between Ru and MoS$_2$, allowing for accelerated water dissociation on Ru nanoparticles and rapid hydrogen adsorption on nearby defect-rich MoS$_2$ nanosheets for efficient recombination into H$_2$. Moreover, it also shows excellent long-term durability with robust structural and chemical stability under alkaline electrolyte, making it attractive for practical application. Comparison of the intrinsic alkaline and acidic HER activity of the Ru/MoS$_2$/CP identifies a pH-dependence of the interfacial synergy, thereby establishing a more solid basis for the bifunctional theory. From a more fundamental point of view, the interface engineering strategy developed in this work can provide new perspectives in the design of more advanced electrocatalysts for photoelectrochemical water splitting and water-alkali electrolyzers.

Conflicts of interest

The authors declare no competing financial interest.

Acknowledgements

Notes and references

1 K. Zeng and D. Zhang, *Prog. Energy Combust. Sci.*, 2010, **36**, 307–326.
2 M. T. M. Koper, *Nat. Chem.*, 2013, **5**, 255–256.
3 N. Danilovic, R. Subbaraman, D. Strmcnik, K. C. Chang, A. P. Paulikas, V. R. Stamenkovic and N. M. Markovic, *Angew. Chem., Int. Ed.*, 2012, **51**, 12495–12498.
4 M. Schalenbach, G. Tjarks, M. Carmo, W. Lueke, M. Mueller and D. Stolten, *J. Electrochem. Soc.*, 2016, **163**, F3197–F3208.
5 S. Trasatti, *J. Electroanal. Chem. Interfacial Electrochem.*, 1972, **39**, 163–184.
6 J. K. Nørskov, T. Bligaard, A. Logadottir, J. R. Kitchin, J. G. Chen, S. Pandelov and U. Stimming, *J. Electrochem. Soc.*, 2005, **152**, J23–J26.
7 R. Parsons, *Trans. Faraday Soc.*, 1958, **54**, 1053–1063.
8 H. Gerischer, *Bull. Soc. Chim. Belg.*, 1958, **67**, 506–527.
9 Y. Zheng, Y. Jiao, M. Jaroniec and S. Z. Qiao, *Angew. Chem., Int. Ed.*, 2015, **54**, 52–65.
10 W. Sheng, H. A. Gasteiger and Y. Shao-Horn, *J. Electrochem. Soc.*, 2010, **157**, B1529–B1536.
11 R. Subbaraman, D. Tripkovic, D. Strmcnik, K. C. Chang, M. Uchimura, A. P. Paulikas, V. Stamenkovic and N. M. Markovic, *Science*, 2011, **334**, 1256–1260.
12 I. Ledezma-Yanez, W. D. Z. Wallace, P. Sebastián-Pascual, V. Climent, J. M. Feliu and M. T. M. Koper, *Nat. Energy*, 2017, **2**, 17031.
13 J. Zheng, W. Sheng, Z. Zhuang, B. Xu and Y. Yan, *Sci. Adv.*, 2016, **2**, e1501602.
14 B. Hinnemann, P. G. Moses, J. Bonde, K. P. Jørgensen, J. H. Nielsen, S. Horch, I. Chorkendorff and J. K. Nørskov, *J. Am. Chem. Soc.*, 2005, **127**, 5308–5309.
15 Y. Yan, B. Xia, Z. Xu and X. Wang, *ACS Catal.*, 2014, **4**, 1693–1705.
16 X. Y. Yu, Y. Feng, Y. Jeon, B. Guan, X. W. Lou and U. Paik, *Adv. Mater.*, 2016, **28**, 9006–9011.
17 X. Y. Yu, L. Yu and X. W. Lou, *Small Methods*, 2017, **1**, 1600020.
18 J. Zhang, T. Wang, P. Liu, S. Liu, R. Dong, X. Zhuang, M. Chen and X. Feng, *Energy Environ. Sci.*, 2016, **9**, 2789–2793.
19 J. Greeley and M. Mavrikakis, *Nat. Mater.*, 2004, **3**, 810–815.
20 G. S. Karlberg, *Phys. Rev. B: Condens. Matter*, 2006, **74**, 153414.
21 Y. Zheng, Y. Jiao, Y. Zhu, L. H. Li, Y. Han, Y. Chen, M. Jaroniec and S. Z. Qiao, *J. Am. Chem. Soc.*, 2016, **138**, 16174–16181.
22 J. Mahmood, F. Li, S. M. Jung, M. S. Okyay, I. Ahmad, S. J. Kim, N. Park, H. Y. Jeong and J. B. Baek, *Nat. Nanotechnol.*, 2017, **12**, 441–446.
23 J. Xie, J. Zhang, S. Li, F. Grote, X. Zhang, H. Zhang, R. Wang, Y. Lei, B. Pan and Y. Xie, *J. Am. Chem. Soc.*, 2013, **135**, 17881–17888.
24 J. Xie, H. Zhang, S. Li, R. Wang, X. Sun, M. Zhou, J. Zhou, X. W. Lou and Y. Xie, *Adv. Mater.*, 2013, **25**, 5807–5813.
25 C. Wang, B. Tian, M. Wu and J. Wang, *ACS Appl. Mater. Interfaces*, 2017, **9**, 7084–7090.
26 Y. Yang, K. Zhang, H. Lin, X. Li, H. C. Chan, L. Yang and Q. Gao, *ACS Catal.*, 2017, **7**, 2357–2366.
27 A. Bagri, C. Mattevi, M. Acik, Y. J. Chabal, M. Chhowalla and V. B. Shenoy, *Nat. Chem.*, 2010, **2**, 581–587.
28 C. D. Wagner, W. M. Riggs, L. E. Davis and J. F. Moulder, in *Handbook of X-ray Photoelectron Spectroscopy: A Reference Book of Standard Data for Use in X-ray Photoelectron Spectroscopy*, ed. G. E. Muilenberg, Physical Electronics Division, Perkin-Elmer Corp., Eden Prairie, 1979, ch. 106, p. 106.
29 A. Li, Y. Hu, M. Yu, X. Liu and M. Li, *Int. J. Hydrogen Energy*, 2017, **42**, 9419–9427.
30 F. Li, Y. Bu, Z. Lv, J. Mahmood, G. F. Han, I. Ahmad, G. Kim, Q. Zhong and J. B. Baek, *Small*, 2017, 1701167, DOI: 10.1002/smll.201701167.
31 F. Li, X. Zhao, J. Mahmood, M. S. Okyay, S. M. Jung, I. Ahmad, S. J. Kim, G. F. Han, N. Park and J. B. Baek, *ACS Nano*, 2017, **11**, 7527–7533.

32 Z. W. Seh, J. Kibsgaard, C. F. Dickens, I. Chorkendorff, J. K. Nørskov and T. F. Jaramillo, *Science*, 2017, **355**, eaad4998.

33 J. Kibsgaard, Z. Chen, B. N. Reinecke and T. F. Jaramillo, *Nat. Mater.*, 2012, **11**, 963–969.

34 Y. Yin, J. Han, Y. Zhang, X. Zhang, P. Xu, Q. Yuan, L. Samad, X. Wang, Y. Wang, Z. Zhang, P. Zhang, X. Cao, B. Song and S. Jin, *J. Am. Chem. Soc.*, 2016, **138**, 7965–7972.

35 H. Yu, X. Yu, Y. Chen, S. Zhang, P. Gao and C. Li, *Nanoscale*, 2015, **7**, 8731–8738.

36 D. Kong, H. Wang, J. J. Cha, M. Pasta, K. J. Koski, J. Yao and Y. Cui, *Nano Lett.*, 2013, **13**, 1341–1347.

37 Z. Lu, W. Zhu, X. Yu, H. Zhang, Y. Li, X. Sun, X. Wang, H. Wang, J. Wang, J. Luo, X. Lei and L. Jiang, *Adv. Mater.*, 2014, **26**, 2683–2687.

Supporting Information

Identification of pH-dependent synergy on Ru/MoS$_2$ interface: a comparison of alkaline and acidic hydrogen evolution

Jinlong Liu,[a] Yao Zheng,[a] Dongdong Zhu,[a] Anthony Vasileff,[a] Tao Ling[b] and Shi-Zhang Qiao*[ab]

[a]School of Chemical Engineering, University of Adelaide, Adelaide, SA 5005, Australia.
[b]School of Materials Science and Engineering, Tianjin University, Tianjin 300072, China

Corresponding Author: Shi-Zhang Qiao, E-mail address: s.qiao@adelaide.edu.au

1. Experimental Section

1.1 Materials

All chemicals (analytical reagent grade) used in this work, including $(NH_4)_6Mo_7O_{24}\cdot4H_2O$, $NaH_2PO_2\cdot4H_2O$, thiourea, urea, KOH, H_2SO_4, Pt/C (20 wt.% of Pt on Vulcan XC72), Nafion (15 wt.%) were purchased from Sigma-Aldrich and used without further purification. Carbon paper (CP, AvCarb MGL 190, Product Code: 1594008) was bought from FuelCellStore. Ultra-pure water (18.2 MΩ·cm, PURELAB Option-Q) was used in all experiments.

1.2 Synthesis of Electrocatalysts

Preparation of MoS₂/CP: A piece of CP (2 cm × 4 cm) was washed thoroughly with ethanol, 0.5 M H_2SO_4, and water in sequence under sonication for 1 h each time. The vertically aligned MoS_2 nanosheets were grown on the cleaned CP via a facile hydrothermal approach. Typically, $(NH_4)_6Mo_7O_{24}\cdot4H_2O$ (0.088 g), thiourea (0.163 g), $NaH_2PO_2\cdot4H_2O$ (0.023 g) were added into 35 mL of deionized water under magnetic stirring to obtain a precursor solution, which was then transferred to a Teflon-lined stainless autoclave (50 mL) with a piece of pre-cleaned CP. Subsequently, the autoclave was kept in a preheated oven at 180 ℃ for 24 h. After the autoclave cooled down naturally to ambient temperature, the sample was collected and rinsed with deionized water several times, and then dried in a vacuum oven at 60 ℃ overnight.

Preparation of Ru/MoS₂/CP: The obtained MoS_2/CP was completely immersed into 20 mL of $RuCl_3$ aqueous solution (5 mM) for 24 h. The product was collected and dried using compressed N_2 at ambient temperature. To obtain the final product, the sample was then heated to 250 ℃ in a tube furnace at a rate of 2 ℃ min^{-1} and held at that temperature for 2 h under H_2/Ar flow. For the as-prepared Ru/MoS_2/CP, the mass increment of CP was about 1.0 mg cm^{-2}. XPS quantification analysis revealed that the atomic percentage of Ru in Ru/MoS_2 was ~15 at.%, which converts to a Ru mass percentage of about 10%. Accordingly, the Ru loading for Ru/MoS_2/CP was ~0.1 mg cm^{-2}.

Preparation of MoS₂: Bare MoS_2 was synthesized via a hydrothermal approach similar to that of MoS_2/CP. Specifically, $(NH_4)_6Mo_7O_{24}\cdot4H_2O$ (1.236 g), thiourea (2.284 g), $NaH_2PO_2\cdot4H_2O$ (0.318 g) were added into 35 mL of deionized water under magnetic stirring to obtain a precursor solution, which was then transferred to a Teflon-lined stainless autoclave (50 mL) without CP. Subsequently, the autoclave was kept in a preheated oven at 180 ℃ for 24 h. After the autoclave cooled down naturally to ambient temperature, the resultant precipitates were

collected by centrifugation, washed with deionized water several times, and then dried in a vacuum oven at 60 ºC overnight.

Preparation of Ru/CP: A piece of pre-cleaned CP was completely immersed in 20 mL of RuCl$_3$ aqueous solution (5 mM) for 24 h. The following procedure was the same as the preparation of Ru/MoS$_2$/CP. For the as-prepared Ru/CP, the mass increment of CP was ~0.31 mg cm^{-2}, which was attributed to the Ru loading.

Preparation of PtC/CP: 5 mg of 20 wt.% Pt/C was dispersed in 2 mL of ethanol containing 0.15 wt.% of Nafion under ultrasound for 1 h. Next, 200 μL of the Pt/C dispersion was loaded onto a piece of pre-cleaned CP (1 cm × 1 cm) to obtain the PtC/CP electrode.

1.3 Characterizations

The morphology, structure, and chemical composition of the samples were characterized by field emission scanning electron microscopy (SEM, QUANTA 450) equipped with energy dispersive spectrometer (EDS), transmission electron microscopy (TEM, Tecnai G2 Spirit and JEOL 2100 Cryo) equipped with EDS, powder X-ray diffractometer (XRD, Cu-target Bruker D8 Advance), X-ray photoelectron spectroscopy (XPS, ESCALab250).

1.4 Electrochemical Measurements

Electrochemical measurements were performed on a 760D (CH Instruments, Inc., USA) in a standard three-electrode glass cell (Pine Research Instruments, USA). 1 cm × 1 cm Ru/MoS$_2$/CP, MoS$_2$/CP, Ru/CP, and PtC/CP were directly used as the working electrode. For MoS$_2$, a glassy carbon rotating disk electrode (RDE, diameter: 5 mm) was employed. Specifically, 5 mg of MoS$_2$ was dispersed in 2 mL of ethanol containing 0.15 wt.% of Nafion under sonication for 1 h. 40 μL of the catalyst ink (2 mg mL^{-1}) was loaded onto the RDE (0.196 cm^2) serving as the working electrode. A carbon rod and an Ag/AgCl (4 M KCl) electrode were used as the counter electrode and the reference electrode, respectively. All potentials were referenced to the reversible hydrogen electrode (RHE) using the following equation: E(RHE) = E(Ag/AgCl) + 0.205 + 0.059 × pH. All the electrolytes were purged with N$_2$ for 30 min before measurements to remove dissolved O$_2$. The linear sweep voltammetry (LSV) curves were collected with a scan rate of 5 mV s^{-1}. Electrochemical impedance spectroscopy (EIS) was measured in the frequency range from 0.1 Hz to 100 kHz with an amplitude of 5 mV. The double-layer capacitance (C$_{dl}$) and roughness factor (R$_f$) of various samples were evaluated from the capacitance of the double-layer at the electrode-electrolyte interface using cyclic voltammetry (CV) in a small potential range of 0.15−0.25 V vs. RHE. IR compensation of

polarization curves was performed using the solution resistance (R_s) estimated from EIS measurements. The long-term stability test was carried out by chronoamperometric measurement and repetitive CV scans in a potential window from 0 to −0.35 V vs. RHE (refer to IR-uncompensated values). The evolved H_2 was analyzed using gas chromatograph (GC, Clarus 480, PerkinElmer, USA with Ar as a carrier gas and 5 Å molecular sieve column).

2. Supplementary Figures
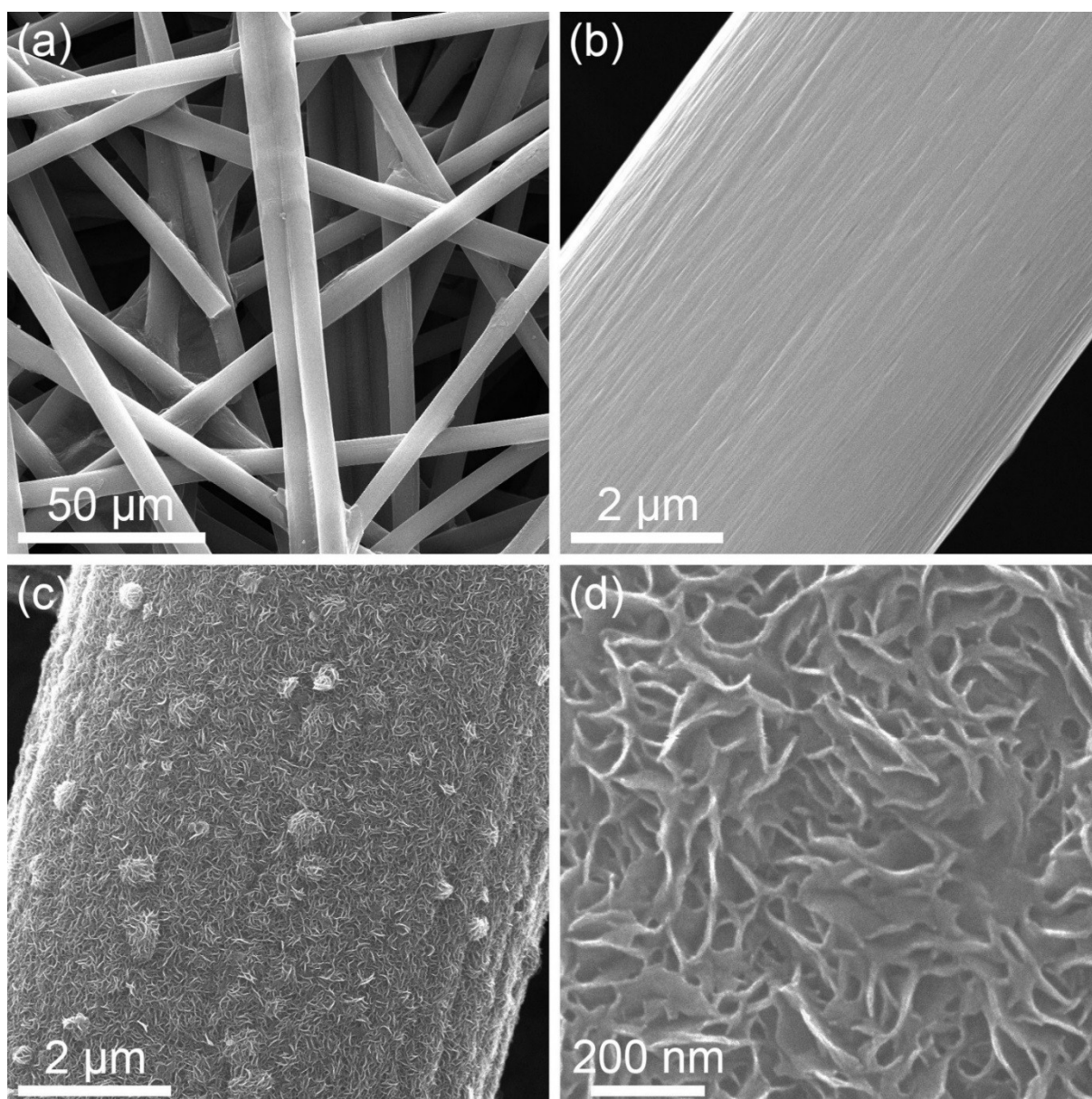
Fig. S1 (a,b) SEM images of pre-cleaned carbon paper (CP) with clean surface. (c,d) SEM images of MoS_2/CP, showing the full and homogeneous coverage of CP by vertically aligned MoS_2 nanosheets.
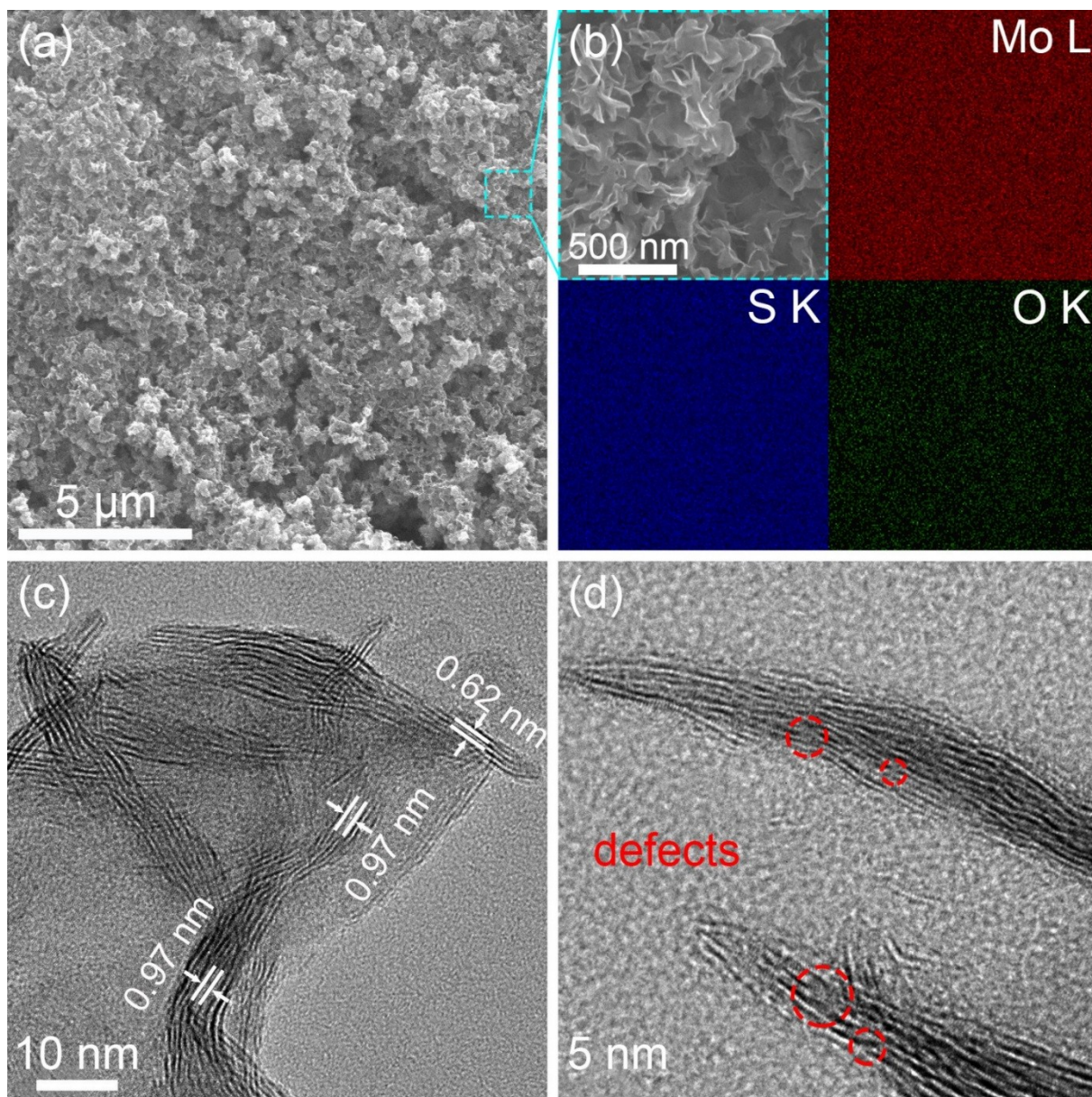
Fig. S2 (a) SEM image of MoS$_2$. (b) Magnified SEM image and corresponding element mapping of MoS$_2$ for the selected area. (c) HRTEM image of few-layer MoS$_2$ nanosheets. The well-defined interplanar distance of 0.62 nm corresponds to (002) planes of hexagonal MoS$_2$, while the large distance of 0.97 nm indicates the appearance of enlarged interlayers, which agrees with previous reports.[1] (d) Cross-sectional HRTEM image of MoS$_2$ nanosheets. Selected areas, indicated by red dashed circles, show the presence of defects in the MoS$_2$ nanosheets.
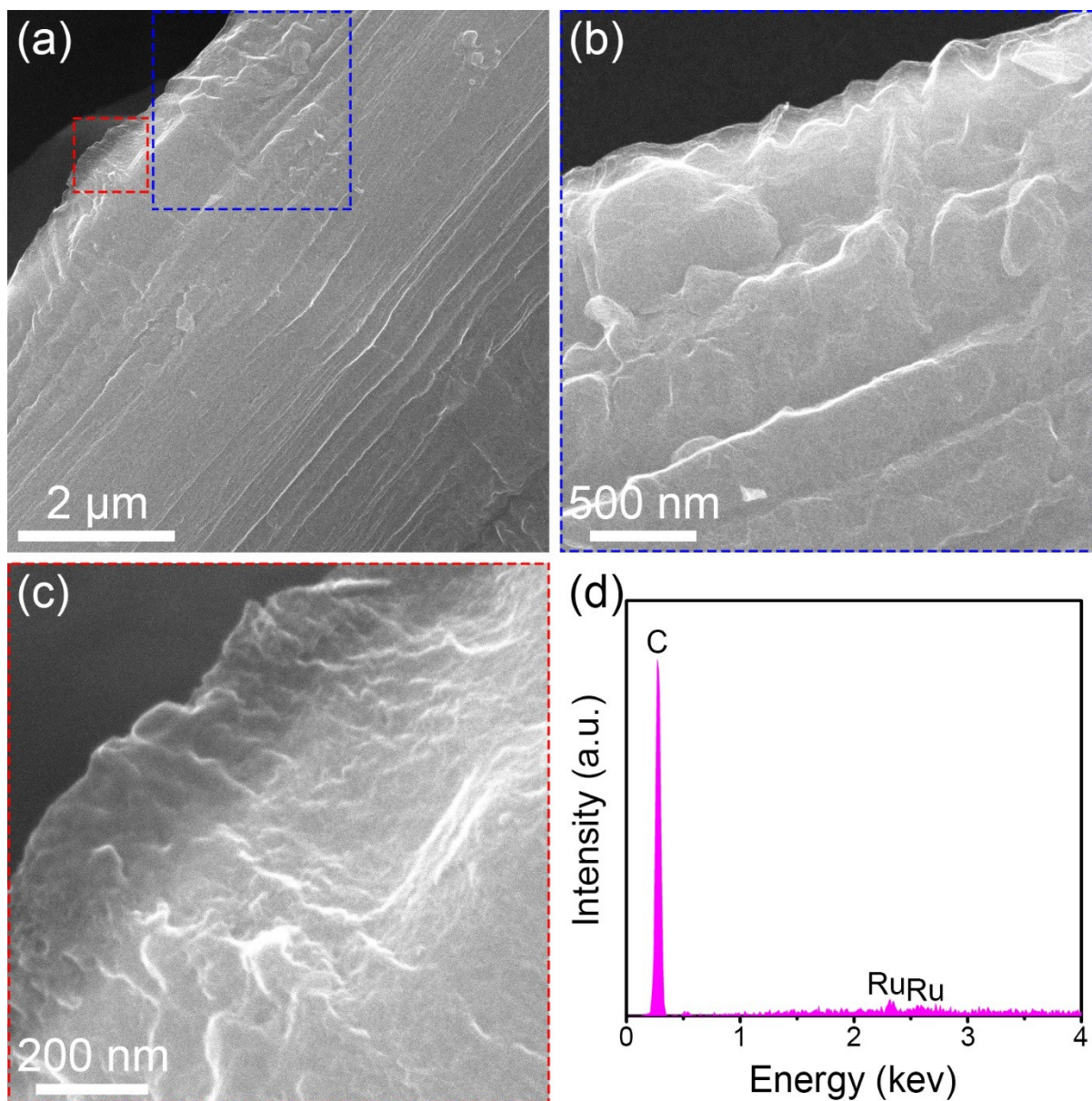
Fig. S3 (a) SEM image of Ru/CP. (b,c) Magnified SEM images of Ru/CP for selected areas, showing the wrinkled Ru on CP. (d) EDS spectrum of Ru/CP containing C and Ru.
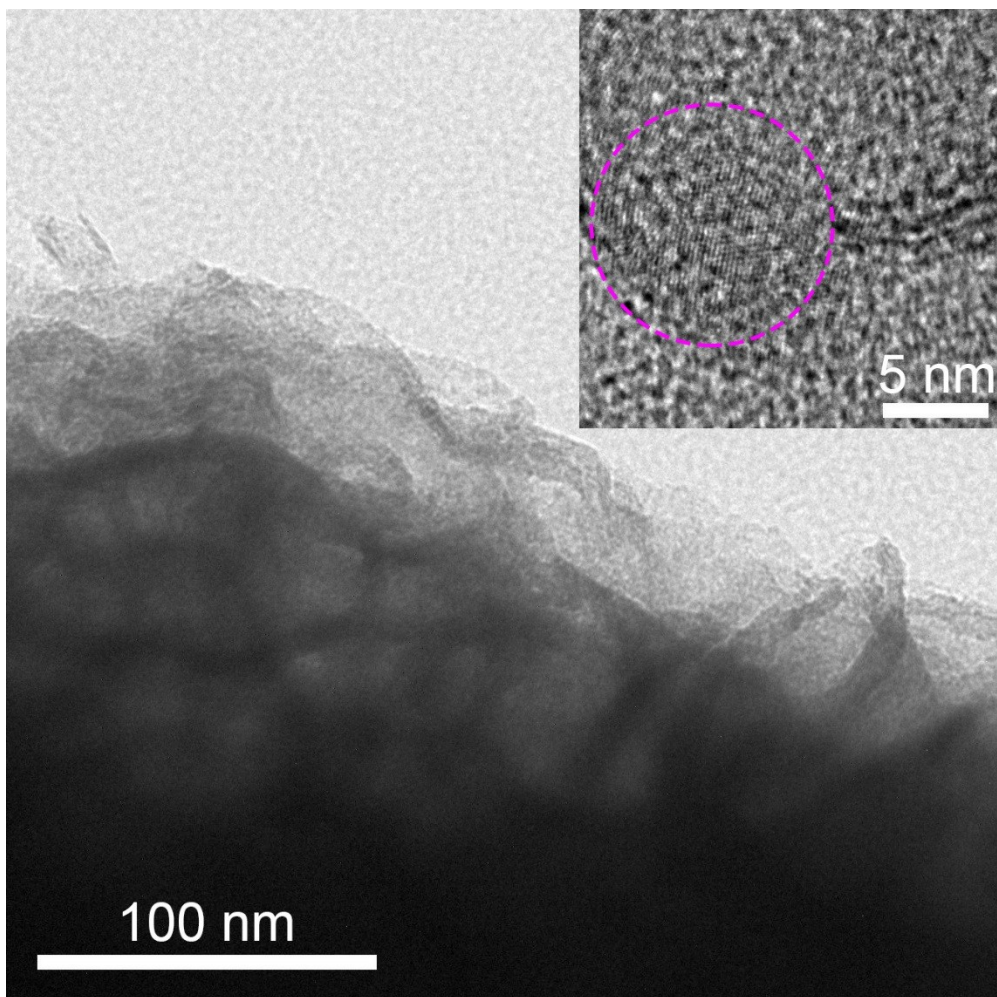
Fig. S4 TEM image of Ru/MoS$_2$. Inset HRTEM image shows an individual Ru nanoparticle of about 10 nm in size.
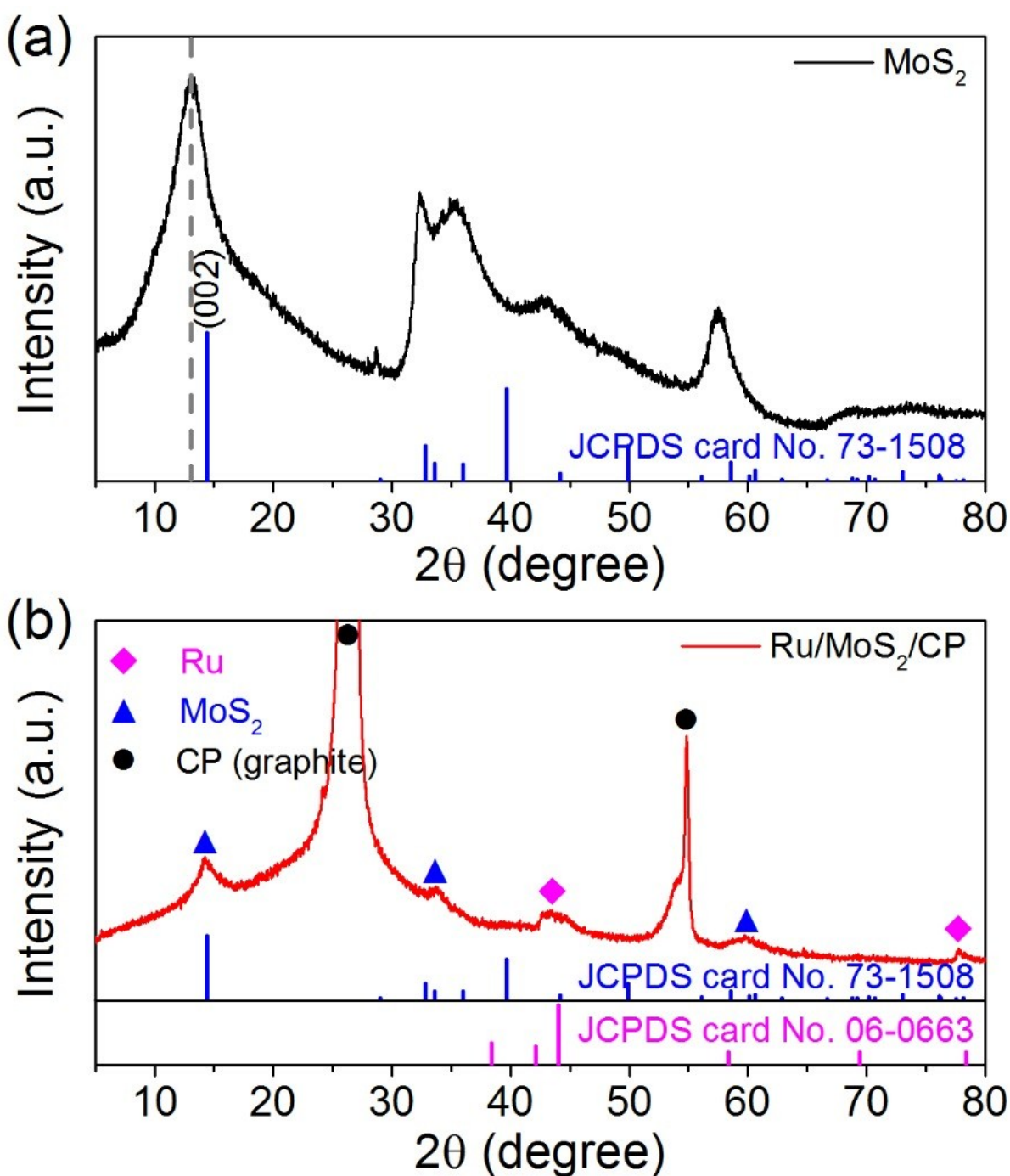
Fig. S5 XRD patterns of (a) bare MoS_2 and (b) $Ru/MoS_2/CP$. The standard patterns of the hexagonal MoS_2 (JCPDS card No. 73-1508) and the hexagonal Ru (JCPDS card No. 06-0663) are given as references. In the XRD pattern of bare MoS_2, the shift of the (002) peak to a lower angle indicates the expansion of partial interlayers, matching well with HRTEM observation (Fig. S2c). According to Xie et al.'s report, thermal treatment (> 232 ℃) could lead to a structural conversion to the thermodynamically stable $2H\text{-}MoS_2$.[1] For this reason, the XRD pattern of $Ru/MoS_2/CP$ shows no shift of the (002) peak of MoS_2, which can be further confirmed by its HRTEM result without enlarged interlayers (Fig. 1d).
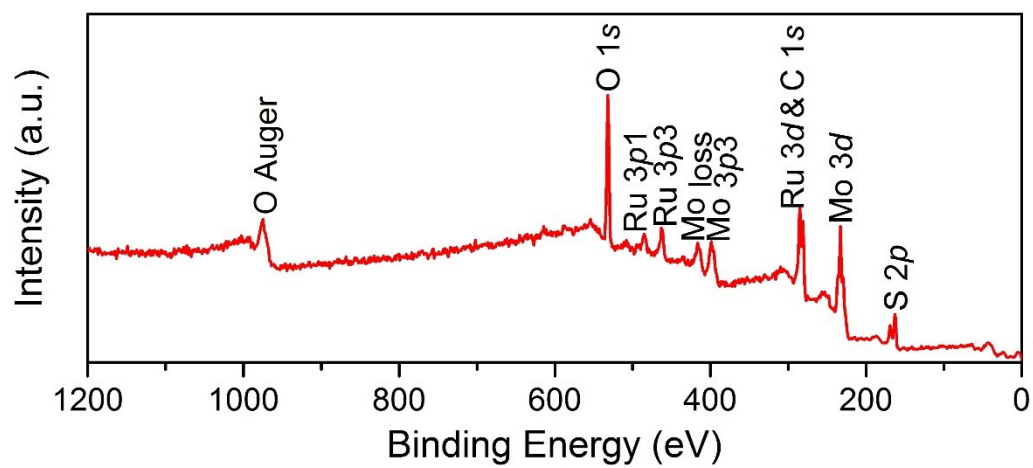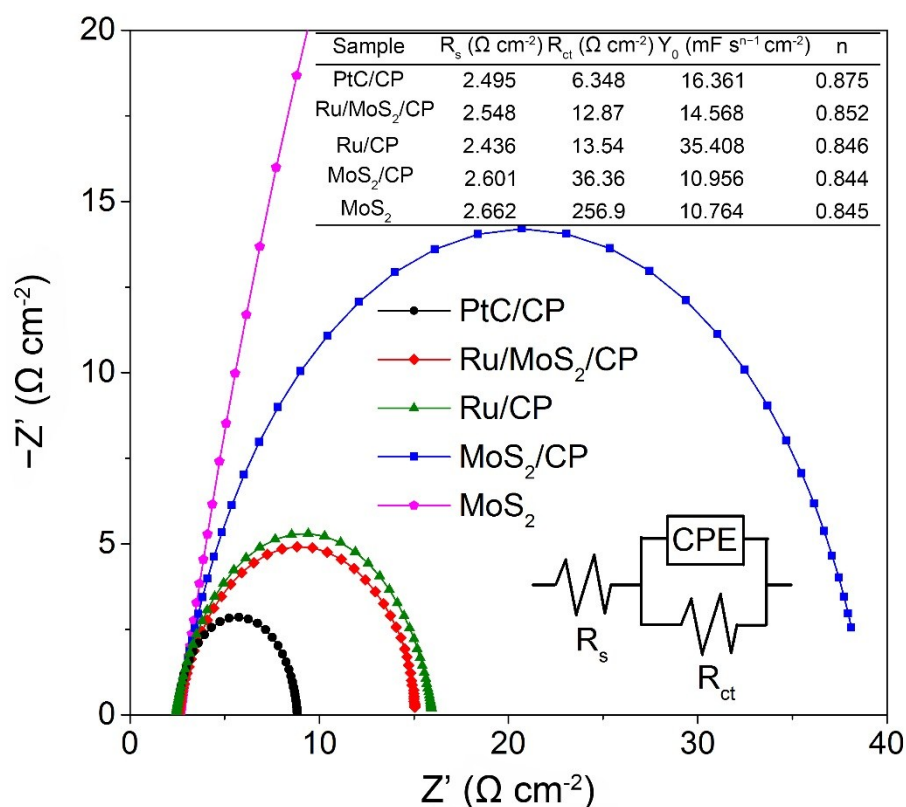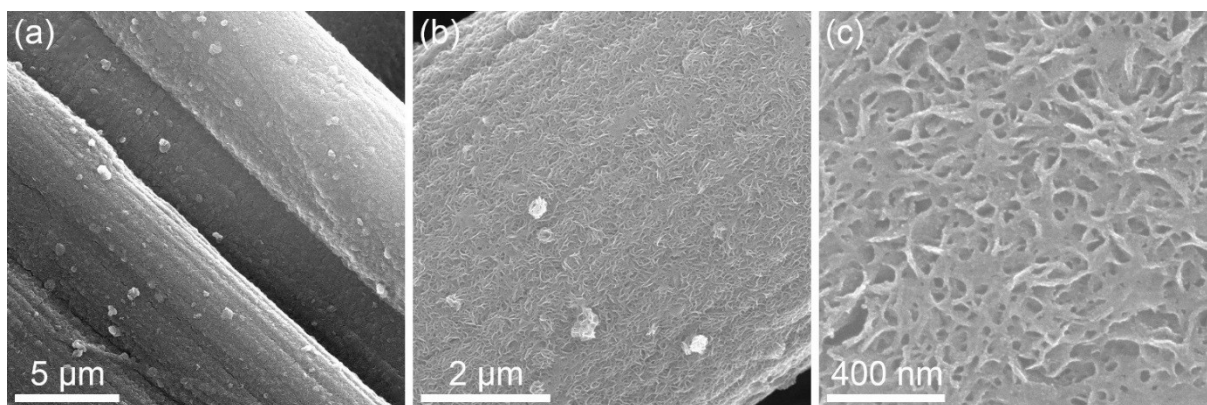
Fig. S6 XPS survey spectrum of Ru/MoS$_2$/CP.
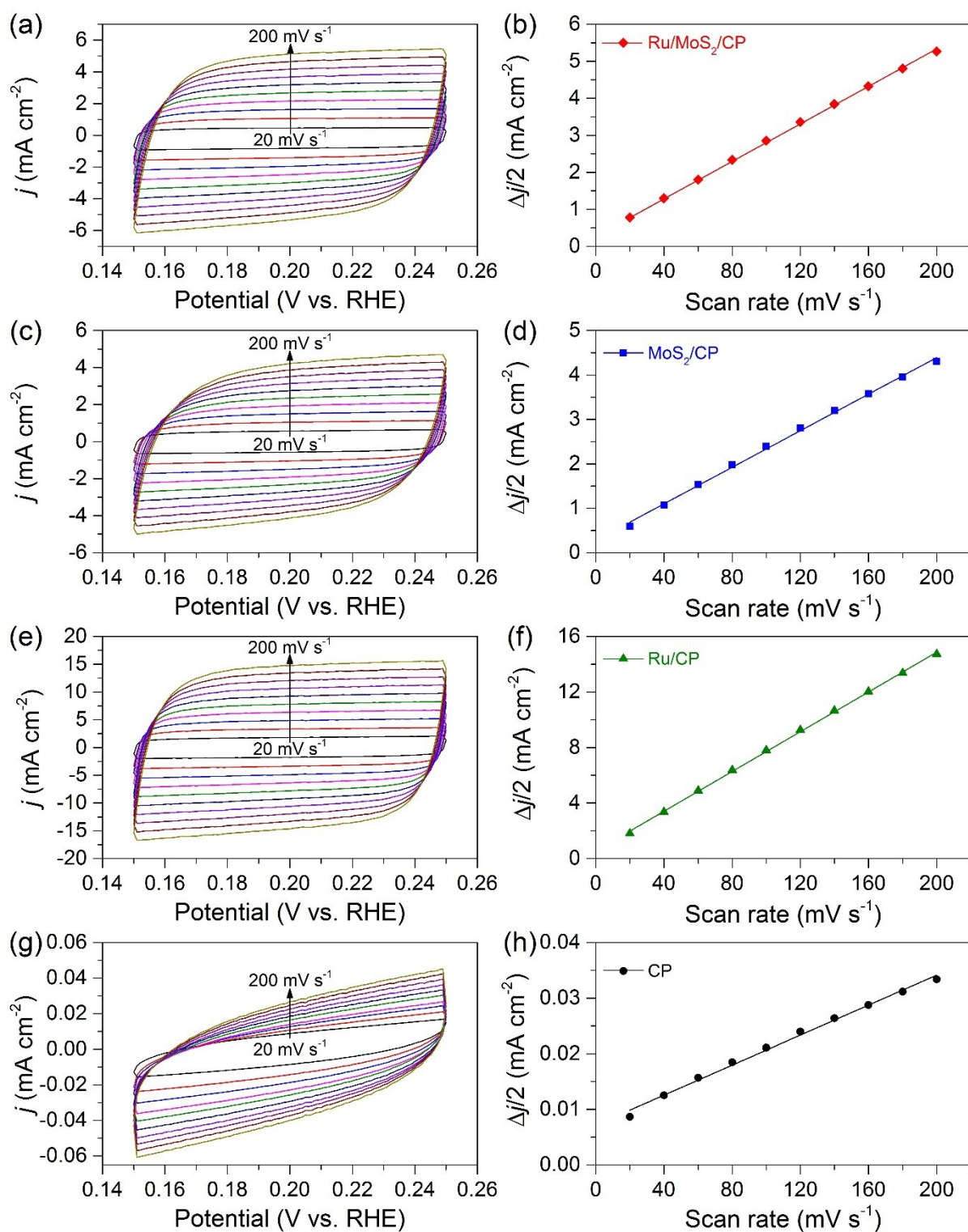
Fig. S7 CV curves and corresponding capacitive current densities at +0.20 V vs. RHE against scan rate for Ru/MoS₂/CP (a,b), MoS₂/CP (c,d), Ru/CP (e,f) and CP (g,h).

Sample	R_s (Ω cm^{-2})	R_{ct} (Ω cm^{-2})	Y_0 (mF s^{n-1} cm^{-2})	n
PtC/CP	2.495	6.348	16.361	0.875
Ru/MoS$_2$/CP	2.548	12.87	14.568	0.852
Ru/CP	2.436	13.54	35.408	0.846
MoS$_2$/CP	2.601	36.36	10.956	0.844
MoS$_2$	2.662	256.9	10.764	0.845

Fig. S8 Nyquist plots for Ru/MoS$_2$/CP, PtC/CP, Ru/CP, MoS$_2$/CP, and MoS$_2$ electrodes, measured at –0.05 V vs. RHE in 1.0 M KOH. Insets are the equivalent circuit and simulated parameters, where R_s, R_{ct}, Y_0 and n are the solution resistance, charge-transfer resistance, and the parameters of a constant phase element (CPE), respectively. The solid lines present the fitted curves.

It was found that bare MoS$_2$ possesses the highest charge transfer resistance (R_{ct}, up to 256.9 Ω cm^{-2}), as the resistivity through the basal planes is approximately 2200 times higher than along the planes for MoS$_2$ nanosheets.[2] For MoS$_2$/CP, the R_{ct} decreases significantly due to the fast electron transfer along CP and the intimate contact between CP and vertically aligned MoS$_2$ nanosheets. This result is consistent with previous studies.[3,4] Interestingly, Ru/CP displays the smallest R_s, which is likely attributed to the metallic character of Ru and its direct contact with CP. It is clear that Ru/MoS$_2$/CP exhibits a small R_{ct} of 12.87 Ω cm^{-2}, indicating favourable electrode kinetics for alkaline HER. In addition to the conductive CP framework, the Ru-decoration and O-incorporation ensure better conductivity along and through the planes of the MoS$_2$ nanosheets.

Fig. S9 (a−c) SEM images of Ru/MoS$_2$/CP electrode after long-term operation.
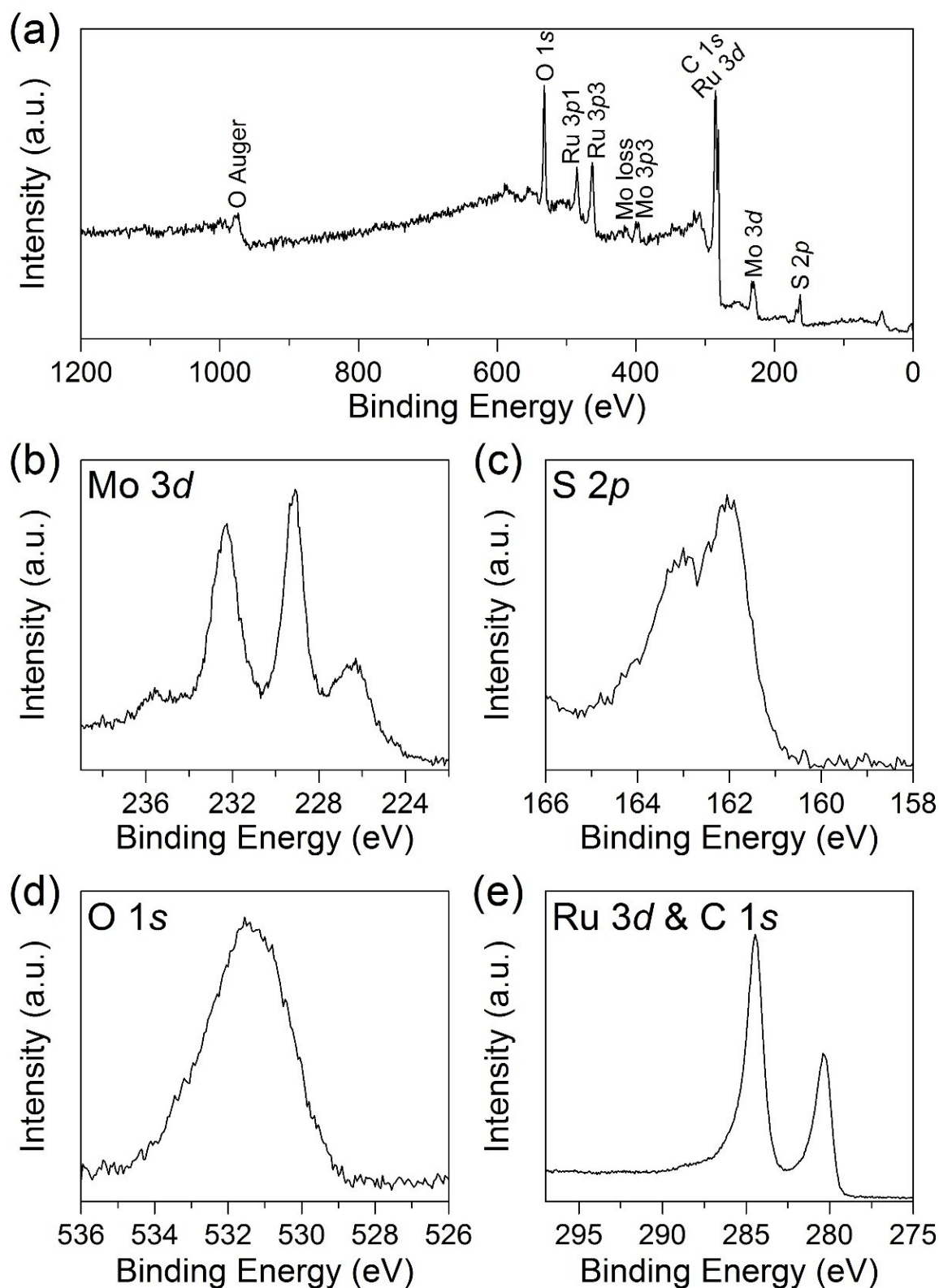
Fig. S10 (a) XPS survey spectrum and high-resolution XPS spectra of (b) Mo 3d, (c) S 2p, (d) O 1s, and (e) Ru 3d & C 1s of Ru/MoS$_2$/CP electrode after long-term operation.
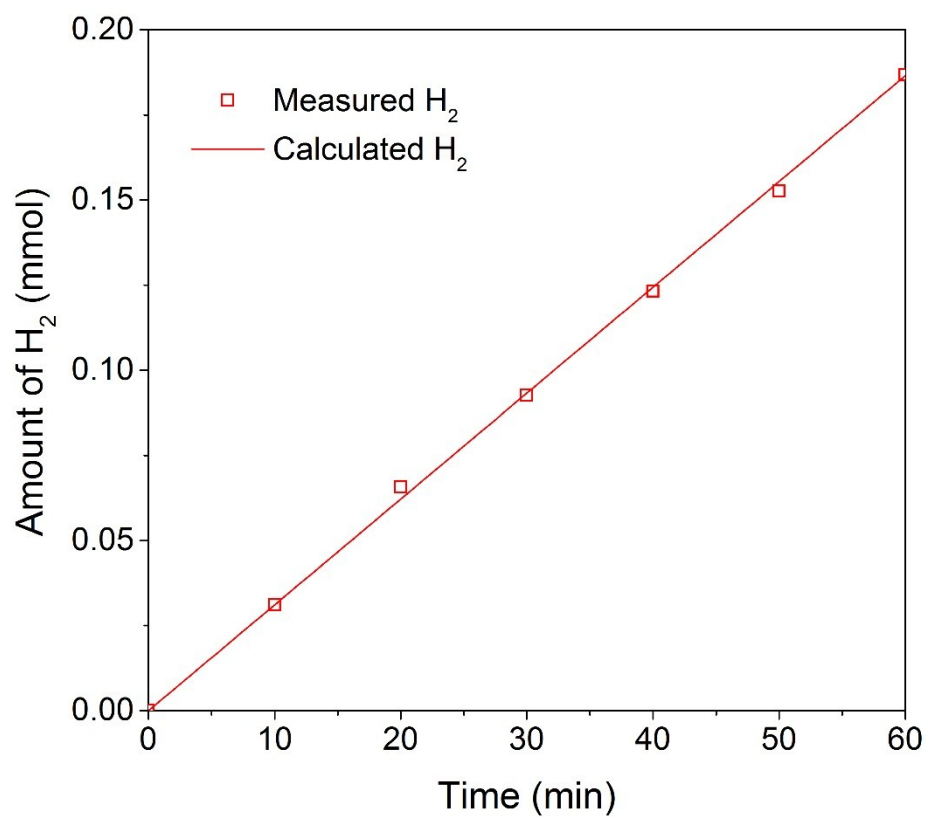
Fig. S11 The amount of H_2 experimentally measured and theoretically calculated versus time for alkaline HER of Ru/MoS$_2$/CP at a current density of -10 mA cm^{-2}.
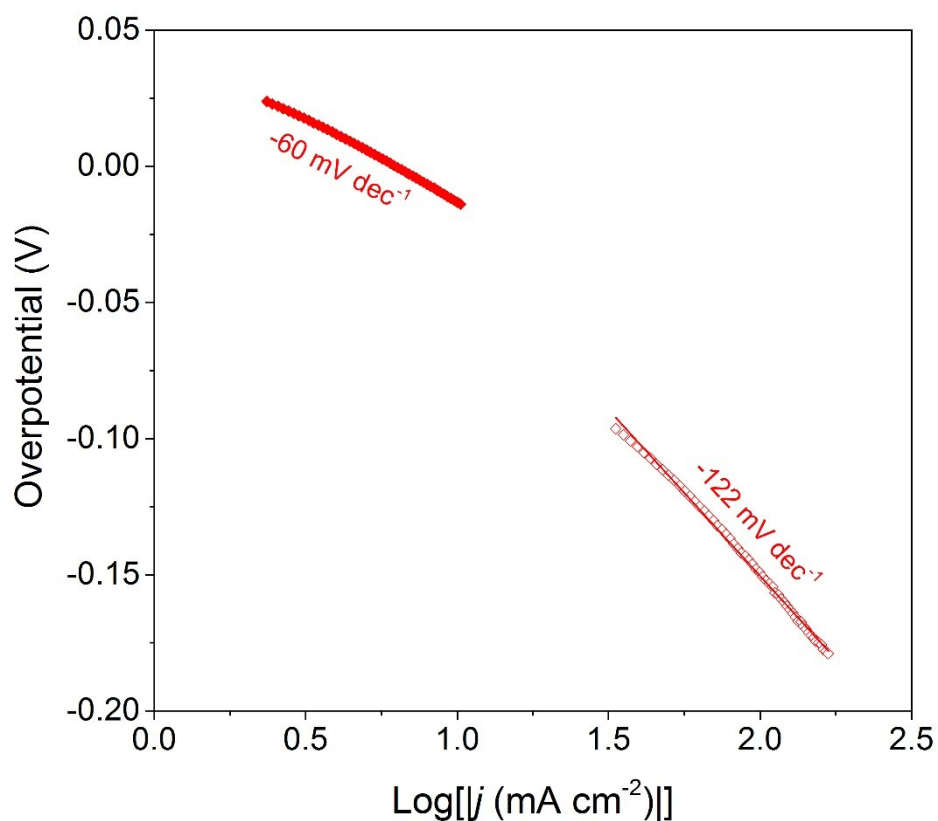
Fig. S12 Tafel plots of Ru/MoS$_2$/CP at low (solid squares) and high (open squares) potentials.

3. Supplementary Tables

Table S1. Comparison of Ru-based electrocatalysts for HER.

Catalyst	Electrode	Electrolyte	η_{onset} (mV)	η_{10} (mV)	Tafel slope (mV dec^{-1})	Ref.	Year
Ru/MoS$_2$	Carbon paper	1 M KOH	0	−13	−60	This work	
Ru@C$_2$N	Glassy carbon	1 M KOH	-	−17	−38	5	2017
Ru-MoO$_2$	Glassy carbon	1 M KOH	-	−29	−31	6	2017
Co-Ru-Pt	Carbon paste	0.5 M H$_2$SO$_4$	-	−73.1 @ 4 mA cm^{-2}	−30.4	7	2017
Ru/C$_3$N$_4$/C	Glassy carbon	1 M KOH	-	−79	-	8	2016
Ru/GLC	Glassy carbon	0.5 M H$_2$SO$_4$	−3	−35	−46	9	2016
Ru/SiNW-42.9	Glassy carbon	0.5 M H$_2$SO$_4$	-	−200	−81	10	2015
GCE-S-GNs-1000-CB-Ru	Glassy carbon	0.5 M H$_2$SO$_4$	0[a]	−75[a]	−61	11	2015

[a] Values estimated from polarization curve found in corresponding Ref.

Table S2. Comparison of MoS$_2$-based electrocatalysts for HER.

Catalyst	Electrode	Electrolyte	η_{onset} (mV)	η_{10} (mV)	Tafel slope (mV dec^{-1})	Ref.	Year
Ru/MoS$_2$	Carbon paper	1 M KOH	0	−13	−59.7	This work	
MoS$_2$-Ni$_3$S$_2$ HNRs/NF	Nickel foam	1 M KOH	−31	−98	−61	12	2017
MoS$_2$|NiS|MoO$_3$	Ti sheet	1 M KOH	−36	−91	−54.5	13	2017
(MoS$_2$)$_{0.6}$(SnO$_2$)$_{0.4}$/rGO	Glassy carbon	0.5 M H$_2$SO$_4$	-	−263±5	−50.8	14	2017
O-MoS2	Carbon cloth	0.5 M H$_2$SO$_4$	-	−258	−57	15	2017
MoS$_{2(1-x)}$Se$_{2x}$(HD)/CNTs	Carbon nanofibers	0.5 M H$_2$SO$_4$	−54	−150	−144	16	2017
Co$_2$Mo$_9$S$_{26}$	FTO	0.5 M H$_2$SO$_4$	-	−260	−64	17	2017
1T/2H MoS$_2$	Glassy carbon	0.5 M H$_2$SO$_4$	-	−234	−46	18	2017
Coral MoS$_2$@GQDs	Glassy carbon	0.5 M H$_2$SO$_4$	−95	−120	−40	19	2017
MoS$_2$ QDs@GS 3:1	Glassy carbon	0.5 M H$_2$SO$_4$	−94	−140	−68	20	2017
C-1TMoS$_2$	Glassy carbon	0.5 M H$_2$SO$_4$	−113	−156	−42.7	21	2017
MoS$_2$@CNTs-5	Glassy carbon	0.5 M H$_2$SO$_4$	-	−62	−49	4	2017
MoS$_2$/Ni$_3$S$_2$	Nickel foam	1 M KOH	−50	−110	−83.1	22	2016
NiS$_2$-MoS$_2$	Ti foil	1 M KOH	−76	-	−70	23	2016
MoS$_2$@Ni/CC	Carbon cloth	1 M KOH	−30	−91	−89	24	2016
HF-MoSP	Glassy carbon	0.5 M H$_2$SO$_4$ 1 M KOH	−29 −42	−108 −119	−76 −85	25	2016
Pt/MoS$_2$/CC	Carbon cloth	0.5 M H$_2$SO$_4$	0	−18	−49	26	2016
Pt/MoS$_2$	Mo foil	0.5 M H$_2$SO$_4$	-	−60[a]	-	27	2016
N-MoS$_2$-3	Glassy carbon	0.5 M H$_2$SO$_4$	−37	−46	−47	28	2016
Se-GL-MoS$_2$/G	Glassy carbon	0.5 M H$_2$SO$_4$	−102	−185[a]	−50	29	2016
Sn-FL-MoS$_2$/G	Glassy carbon	0.5 M H$_2$SO$_4$	−134	−250[a]	−54	30	2016
Co-MoS$_2$/G-3	Glassy carbon	0.5 M H$_2$SO$_4$	−142	−194	−44.3	31	2016
Cu$_7$S$_4$@MoS$_2$	Glassy carbon	0.5 M H$_2$SO$_4$	-	−133	−48	32	2016
CoS$_2$-MoS$_2$/CNTs	Glassy carbon	0.5 M H$_2$SO$_4$	−70	−180[a]	−67	33	2016
Ni$_2$P/MoS$_2$	Glassy carbon	0.5 M H$_2$SO$_4$	−75	−190[a]	−76	34	2016
MoS$_2$-W3	Glassy carbon	0.5 M H$_2$SO$_4$	−200	−260	−45.1	35	2016
Co-FL-MoS$_2$/NG	Glassy carbon	0.5 M H$_2$SO$_4$	−90	−175[a]	−59	36	2016
MoSSe@rGO	Glassy carbon	0.5 M H$_2$SO$_4$	-	−153	−51	37	2016
Ni-MoS$_2$	Glassy carbon	0.5 M H$_2$SO$_4$	−200	−305[a]	−47	38	2016
P-1T-MoS$_2$	Glassy carbon	0.5 M H$_2$SO$_4$	-	−153	−43	39	2016
O-MoS$_2$/rGO	Glassy carbon	0.5 M H$_2$SO$_4$	−100	-	−40	40	2016
MoS$_2$/N-RGO-180	Glassy carbon	0.5 M H$_2$SO$_4$	−5	−56	−41.3	41	2016
CoMoS$_3$	Glassy carbon	0.5 M H$_2$SO$_4$	−112	−171	−56.9	42	2016
CoMoS-2-C	Glassy carbon	0.5 M H$_2$SO$_4$	−90	−135	−50	43	2015
MoS$_2$/CoSe$_2$	Glassy carbon	0.5 M H$_2$SO$_4$	−11	−68	−36	44	2015

MoS$_2$ composite (NMP)	Glassy carbon	0.5 M H$_2$SO$_4$	−120	−250[a]	−69	45	2015
H-MoS$_2$	Glassy carbon	0.5 M H$_2$SO$_4$	−50	−167	−70	46	2015
Co$_9$S$_8$@MoS$_2$/CNFs	Glassy carbon	0.5 M H$_2$SO$_4$	−64	−190	−110	47	2015
[Mo$_2$S$_{12}$]$^{2-}$	Glassy carbon	0.5 M H$_2$SO$_4$	-	−161	−39	48	2015
Se-doped MoS$_2$	Glassy carbon	0.5 M H$_2$SO$_4$	−140	−280[a]	−55	49	2015
IF-Re$_x$Mo$_{1-x}$S$_2$	Glassy carbon	0.5 M H$_2$SO$_4$	−70	−250	−136	50	2015
Pt-MoS$_2$	Glassy carbon	0.1 M H$_2$SO$_4$	-	−140[a]	−96	51	2015
CoS$_2$@MoS$_2$	Ti foil	0.5 M H$_2$SO$_4$	−44	−110.5	−57.3	52	2015
ET&IE MoS$_2$	Glassy carbon	0.5 M H$_2$SO$_4$	−103	−149	−49	53	2015
NG-Mo	Graphene film	0.1 M H$_2$SO$_4$	-	−140.6	−105	54	2015
MoS$_2$ QDs	Glassy carbon	0.5 M H$_2$SO$_4$	−210	−300[a]	−60	55	2015
MWCNTs@Cu@MoS$_2$	Glassy carbon	0.5 M H$_2$SO$_4$	−146	−184	−62	56	2015
MoS$_x$-NCNT	Glassy carbon	0.5 M H$_2$SO$_4$	−75	−110	−40	57	2014
MoP|S	Ti foil	0.5 M H$_2$SO$_4$	-	−64	−50	58	2014
MoS$_2$ film	Ti foil	0.5 M H$_2$SO$_4$	−150	-	−51	59	2014
1 L MoS$_2$@NPG	Nanoporous Au	0.5 M H$_2$SO$_4$	−118	−226	−46	60	2014
O-MoS$_2$ (S 180)	Glassy carbon	0.5 M H$_2$SO$_4$	−120	−180[a]	−55	1	2013
1T-MoS$_2$	Glassy carbon	0.5 M H$_2$SO$_4$	-	−187	−43	61	2013
MoS$_2$/RGO	Glassy carbon	0.5 M H$_2$SO$_4$	-	−150[a]	−41	62	2011

[a] Values estimated from polarization curves found in corresponding Ref.

4. Supplementary Notes

Supplementary Note 1. Definition of overpotential and Tafel slope

According to classic electrochemistry books,[63,64] the overpotential (η) is defined as the difference between the actual applied potential (E) and the reversible potential (E_r) of the reaction:

$\eta = E - E_r$

For the HER, E_r is 0 V vs. RHE. As a result, HER η equals to the actual applied potential E, which is always a negative quantity. Moreover, according to the Tafel equation ($\eta = a + b \cdot \log|j|$), the HER Tafel slope b determined from the Tafel plot (η vs. $\log|j|$) should also be negative. Note that presenting the data in this way is consistent with electrochemistry conventions.

Note that much of the literature have not paid attention to the definitions and reported HER η and Tafel slope in absolute values. To practice correct notations, the electrochemistry research community should adopt the strict attitude towards electrochemical quantities.

Supplementary Note 2. Double-layer capacitance, roughness factor, and intrinsic alkaline HER activity

Sample	C_{dl} (mF cm^{-2})[a]	R_f[b]	j @ −0.05 V vs. RHE (mA cm^{-2})	$j_{specific}$ @ −0.05 V vs. RHE (μA cm^{-2})[c]
Ru/MoS$_2$/CP	25	416.7	−31.98	−76.75
Ru/CP	71.6	1193.3	−19.22	−16.11
MoS$_2$/CP	20.6	343.3	−1.93	−5.62

[a] C_{dl} is estimated by applying the equation: $C_{dl} = \dfrac{\Delta j}{2 \cdot v} = \dfrac{(j_a - j_c)}{2 \cdot v}$,[65] where j_a and j_c are the anodic and cathodic current density, respectively, recorded at a potential of +0.20 V vs. RHE, and v is the scan rate (Fig. S7).

[b] According to the Ref. 66, an ideal plane electrode has a C_{dl} of 60 μF cm^{-2}, and R_f can be calculated using the equation: $R_f = \dfrac{C_{dl}}{60} \times 1000$.

[c] According to the Ref. 67 and 68, $j_{specific}$ is calculated by the equation: $j_{specific} = \dfrac{j}{R_f}$, where j is the HER current density at a potential of −0.05 V vs. RHE.

Supplementary Note 3. C_{dl} measured by EIS

The parameters (i.e., R_s, R_{ct}, Y_0, and n) from the EIS measurement using the applied equivalent circuit can be used to calculate C_{dl} according to the following equation:[65,68–70]

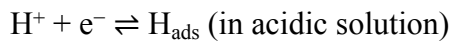$$C_{dl} = [Y_0(\frac{1}{R_s} + \frac{1}{R_{ct}})^{(n-1)}]^{\frac{1}{n}}$$

As shown in the below table, the C_{dl} values estimated by EIS match well with those obtained from the scan rate-dependent CVs (within an error range of ±10%).

Sample	R_s (Ω cm^{-2})	R_{ct} (Ω cm^{-2})	Y_0 (mF s^{n-1} cm^{-2})	n	C_{dl} (mF cm^{-2})
Ru/MoS$_2$/CP	2.548	12.87	14.568	0.852	26.45
Ru/CP	2.436	13.54	35.408	0.846	77.34
MoS$_2$/CP	2.601	36.36	10.956	0.844	20.09

Supplementary Note 4. HER mechanism and Tafel slope

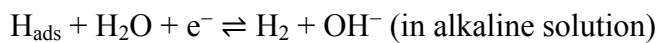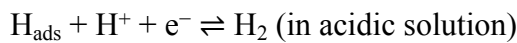Regarding the HER mechanism, two possible reaction pathways have been proposed.[71,72] (i) The first step is to form electrochemically adsorbed hydrogen (H_{ads}, Volmer reaction):

$H^+ + e^- \rightleftharpoons H_{ads}$ (in acidic solution)

$H_2O + e^- \rightleftharpoons H_{ads} + OH^-$ (in alkaline solution)

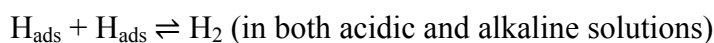$$b = \frac{-2.303 \cdot R \cdot T}{\beta \cdot F} \approx -120 \; mV \; dec^{-1}$$

where R is the ideal gas constant, T is the absolute temperature, $\beta \approx 0.5$ is the symmetry coefficient, and F is the Faraday constant.

A different reaction step in the next pathway leads to a different HER mechanism. To be specific, (ii) the formed H_{ads} undergoes an electrochemical desorption step (Heyrovsky reaction):

$H_{ads} + H^+ + e^- \rightleftharpoons H_2$ (in acidic solution)

$H_{ads} + H_2O + e^- \rightleftharpoons H_2 + OH^-$ (in alkaline solution)

$$b = \frac{-2.303 \cdot R \cdot T}{(1 + \beta) \cdot F} \approx -40 \; mV \; dec^{-1}$$

or a recombination step (Tafel reaction)

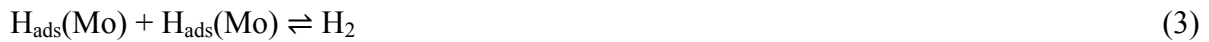$H_{ads} + H_{ads} \rightleftharpoons H_2$ (in both acidic and alkaline solutions)

$$b = \frac{-2.303 \cdot R \cdot T}{2 \cdot F} \approx -30 \; mV \; dec^{-1}$$

For Ru/MoS$_2$/CP in this work, its Tafel slope in 1.0 M KOH was found to be −60 mV dec^{-1}. In fact, a Tafel slope of about −60 mV dec^{-1} is commonly observed on Ru-based HER

catalysts.[73–78] It can be explained by a formal kinetics approach in two cases: (i) the Heyrovsky mechanism is operative and the adsorption of the reaction intermediate H_{ads} proceeds under Temkin conditions in the range of intermediate surface coverages $0.2 < \theta < 0.8$;[77,79] (ii) the mechanism involves a surface chemical rearrangement step $H_{ads}(A) \rightarrow H_{ads}(B)$ as the rate-determining step (RDS), which features the surface sites A and B having different energy levels.[68,75,78,79] The latter case supports the proposed hypothesis on the synergy between Ru and MoS_2. Accordingly, the following HER mechanism is predicted:

$$H_2O + e^- \rightleftharpoons H_{ads}(Ru) + OH^- \tag{1}$$

$$H_{ads}(Ru) \rightarrow H_{ads}(Mo) \tag{2}$$

$$H_{ads}(Mo) + H_{ads}(Mo) \rightleftharpoons H_2 \tag{3}$$

If Step 2 representing the surface diffusion of H_{ads} from the Ru sites to the nearby unsaturated Mo atoms of MoS_2 is the RDS, the overall reaction rate is equal to:

$$-j = 2 \cdot F \cdot k_2 \cdot \theta(Ru) \cdot (1 - \theta(MoS_2)) \tag{4}$$

where $k_{\pm i}$ is the rate constant of step i in the forward (+) or backward (−) direction and θ the fractional occupancy of H-adsorption sites on Ru or MoS_2. If we assume that the Volmer step (Step 1) preceding the RDS is in quasi-equilibrium at low overpotentials, we obtain the following equation:

$$k_1 \cdot (1 - \theta(Ru)) \cdot e^{-\frac{\beta_1 \cdot F \cdot E}{R \cdot T}} = k_{-1} \cdot c(OH^-) \cdot \theta(Ru) \cdot e^{\frac{(1 - \beta_1) \cdot F \cdot E}{R \cdot T}} \tag{5}$$

where β is the symmetry factor. Since $\theta(Ru)$ is close to 0 at low overpotentials, it can be approximated that $(1-\theta(Ru)) \rightarrow 1$. In that case from Eq. 5, we obtain:

$$\theta(Ru) = \frac{k_1}{k_{-1}} \cdot \frac{1}{c(OH^-)} \cdot e^{-\frac{F \cdot E}{R \cdot T}} \tag{6}$$

Now, by replacing $\theta(Ru)$ in the rate law of the total reaction (Eq. 4), we get:

$$-j = 2 \cdot F \cdot k_2 \cdot \frac{k_1}{k_{-1}} \cdot \frac{1}{c(OH^-)} \cdot e^{-\frac{F \cdot E}{R \cdot T}} \tag{7}$$

For T = 298 K, the Tafel slope is:

$$b = -\frac{2.303 \cdot R \cdot T}{F} = -60 \, mV \, dec^{-1} \tag{8}$$

Given that the theoretical Tafel slope is identical to the observed one on Ru/MoS$_2$/CP (-60 mV dec^{-1}), such a result further supports the interfacial synergy between Ru and MoS$_2$ towards improve alkaline HER kinetics.

Notably, the aforementioned mechanism could apply to Ru/MoS$_2$/CP only at low overpotentials when $\theta \rightarrow 0$ (at overpotentials lower than -25 mV according to Fig. 3b). At higher overpotentials, i.e. at higher current densities, where $\theta \rightarrow 1$, the reaction pathway involving Step 2 as the RDS reaches a reaction limiting current density,[79] and H desorption from the Ru sites dominantly proceeds through the Heyrovsky step:

$$H_{ads}(Ru) + H_2O + e^- = H_2 + OH^- \tag{9}$$

Under such conditions, the overall reaction rate is then given by:

$$-j = 2 \cdot F \cdot k_2 \cdot e^{-\frac{\beta_1 \cdot F \cdot E}{R \cdot T}} \tag{10}$$

For T = 298 K, assuming $\beta_1 = 0.5$, the theoretical Tafel slope is:

$$b = -\frac{2.303 \cdot R \cdot T}{\beta_1 \cdot F} = -120 \; mV \; dec^{-1} \tag{11}$$

To this end, we also calculated the Tafel slope of Ru/MoS$_2$/CP at higher overpotentials, as presented in Fig. S12. A Tafel slope of -122 mV dec^{-1} is observed on Ru/MoS$_2$/CP at high overpotentials, which is also consistent with the theoretically calculated slope. All these results further demonstrate the proposed alkaline HER mechanism on Ru/MoS$_2$/CP.

5. Supplementary Movie

Movie S1. The self-supported Ru/MoS$_2$/CP electrode is directly employed as the working electrode in a typical three-electrode cell setup using 1.0 M KOH as the electrolyte. H$_2$ bubbles are visibly observed on the Ru/MoS$_2$/CP electrode at an overpotential of -15 mV. When the overpotential increases from -15 to -100 mV, the evolution rate of H$_2$ bubbles increases significantly, and the generated bubbles release quickly without obvious adherence on the electrode. No visible peeling of the active material from the electrode can be observed, reflecting remarkable structural robustness of the as-synthesized electrode.

6. References

1   J. Xie, J. Zhang, S. Li, F. Grote, X. Zhang, H. Zhang, R. Wang, Y. Lei, B. Pan and Y. Xie, *J. Am. Chem. Soc.*, 2013, **135**, 17881−17888.

2   H. Tributsch, *Ber. Bunsen-Ges.*, 1977, **81**, 361−369.

3   H. Yu, X. Yu, Y. Chen, S. Zhang, P. Gao and C. Li, *Nanoscale*, 2015, **7**, 8731−8738.

4   A. Li, Y. Hu, M. Yu, X. Liu and M. Li, *Int. J. Hydrogen Energy*, 2017, **42**, 9419−9427.

5   J. Mahmood, F. Li, S. M. Jung, M. S. Okyay, I. Ahmad, S. J. Kim, N. Park, H. Y. Jeong and J. B. Baek, *Nat. Nanotechnol.*, 2017, **12**, 441−446.

6   P. Jiang, Y. Yang, R. Shi, G. Xia, J. Chen, J. Su and Q. Chen, *J. Mater. Chem. A*, 2017, **5**, 5475−5485.

7   J. V. Medina-Flores, A. Manzo-Robledo, J. M. Mora-Hernández and E. M. Arce Estrada, *Int. J. Hydrogen Energy*, 2017, **42**, 38−45.

8   Y. Zheng, Y. Jiao, Y. Zhu, L. H. Li, Y. Han, Y. Chen, M. Jaroniec and S. Z. Qiao, *J. Am. Chem. Soc.*, 2016, **138**, 16174−16181.

9   Z. Chen, J. Lu, Y. Ai, Y. Ji, T. Adschiri and L. Wan, *ACS Appl. Mater. Interfaces*, 2016, **8**, 35132−35137.

10   L. Zhu, Q. Cai, F. Liao, M. Sheng, B. Wu and M. Shao, *Electrochem. Commun.*, 2015, **52**, 29−33.

11   R. K. Shervedani and A. Amini, *Carbon*, 2015, **93**, 762−773.

12   Y. Yang, K. Zhang, H. Lin, X. Li, H. C. Chan, L. Yang and Q. Gao, *ACS Catal.*, 2017, **7**, 2357−2366.

13   C. Wang, B. Tian, M. Wu and J. Wang, *ACS Appl. Mater. Interfaces*, 2017, **9**, 7084−7090.

14   S. Ravula, C. Zhang, J. B. Essner, J. D. Robertson, J. Lin and G. A. Baker, *ACS Appl. Mater. Interfaces*, 2017, **9**, 8065−8074.

15   X. Shang, W. H. Hu, X. Li, B. Dong, Y. R. Liu, G. Q. Han, Y. M. Chai and C. G. Liu, *Electrochim. Acta*, 2017, **224**, 25−31.

16   H. Yang, T. Zhang, H. Zhu, M. Zhang, W. Wu and M. Du, *Int. J. Hydrogen Energy*, 2017, **42**, 1912−1918.

17   I. Roger, R. Moca, H. N. Miras, K. G. Crawford, D. A. J. Moran, A. Y. Ganin and M. D. Symes, *J. Mater. Chem. A*, 2017, **5**, 1472−1480.

18   D. Wang, X. Zhang, S. Bao, Z. Zhang, H. Fei and Z. Wu, *J. Mater. Chem. A*, 2017, **5**, 2681−2688.

19   B. Guo, K. Yu, H. Li, R. Qi, Y. Zhang, H. Song, Z. Tang, Z. Zhu and M. Chen, *ACS Appl. Mater. Interfaces*, 2017, **9**, 3653−3660.

20   W. Li, F. Li, X. Wang, Y. Tang, Y. Yang, W. Gao and R. Li, *Appl. Surf. Sci.*, 2017, **401**, 190−197.

21 Y. Li, L. Wang, S. Zhang, X. Dong, Y. Song, T. Cai and Y. Liu, *Catal. Sci. Technol.*, 2017, **7**, 718−724.

22 J. Zhang, T. Wang, D. Pohl, B. Rellinghaus, R. Dong, S. Liu, X. Zhuang and X. Feng, *Angew. Chem. Int. Ed.*, 2016, **55**, 6702−6707.

23 T. An, Y. Wang, J. Tang, W. Wei, X. Cui, A. M. Alenizi, L. Zhang and G. Zheng, *J. Mater. Chem. A*, 2016, **4**, 13439−13443.

24 Z. Xing, X. Yang, A. M. Asiri and X. Sun, *ACS Appl. Mater. Interfaces*, 2016, **8**, 14521−14526.

25 A. Wu, C. Tian, H. Yan, Y. Jiao, Q. Yan, G. Yang and H. Fu, *Nanoscale*, 2016, **8**, 11052−11059.

26 Y. Luo, D. Huang, M. Li, X. Xiao, W. Shi, M. Wang, J. Su and Y. Shen, *Electrochim. Acta*, 2016, **219**, 187−193.

27 A. Jagminas, A. Naujokaitis, R. Žalnėravičius, V. Jasulaitiene and G. Valušis, *Appl. Surf. Sci.*, 2016, **385**, 56−62.

28 W. Xiao, P. Liu, J. Zhang, W. Song, Y. P. Feng, D. Gao and J. Ding, *Adv. Energy Mater.*, 2017, **7**, 1602086.

29 L. Ma, L. Xu, W. Lin, Q. Li, X. Xu, X. Zhou and H. Li, *Adv. Powder Technol.*, 2016, **27**, 2153−2160.

30 L. Ma, L. Xu, X. Zhou, X. Xu, J. Luo and L. Zhang, *Colloids Surf. A*, 2016, **509**, 140−148.

31 J. Ye, W. Chen, S. Xu, Z. Yu and S. Hou, *RSC Adv.*, 2016, **6**, 104925−104932.

32 J. Xu, J. Cui, C. Guo, Z. Zhao, R. Jiang, S. Xu, Z. Zhuang, Y. Huang, L. Wang and Y. Li, *Angew. Chem. Int. Ed.*, 2016, **55**, 6502−6505.

33 Y. R. Liu, W. H. Hu, X. Li, B. Dong, X. Shang, G. Q. Han, Y. M. Chai, Y. Q. Liu and C. G. Liu, *Appl. Surf. Sci.*, 2016, **384**, 51−57.

34 Y. R. Liu, W. H. Hu, X. Li, B. Dong, X. Shang, G. Q. Han, Y. M. Chai, Y. Q. Liu and C. G. Liu, *Appl. Surf. Sci.*, 2016, **383**, 276−282.

35 J. N. He, Y. Q. Liang, J. Mao, X. M. Zhang, X. J. Yang, Z. D. Cui, S. L. Zhu, Z. Y. Li and B. B. Li, *J. Electrochem. Soc.*, 2016, **163**, H299−H304.

36 L. Ma, L. Xu, X. Xu, X. Zhou, J. Luo and L. Zhang, *Mater. Sci. Eng. B*, 2016, **212**, 30−38.

37 B. Konkena, J. Masa, W. Xia, M. Muhler and W. Schuhmann, *Nano Energy*, 2016, **29**, 46−53.

38 D. Wang, X. Zhang, Y. Shen and Z. Wu, *RSC Adv.*, 2016, **6**, 16656−16661.

39 Y. Yin, J. Han, Y. Zhang, X. Zhang, P. Xu, Q. Yuan, L. Samad, X. Wang, Y. Wang, Z. Zhang, P. Zhang, X. Cao, B. Song and S. Jin, *J. Am. Chem. Soc.*, 2016, **138**, 7965−7972.

40 A. Liu, L. Zhao, J. Zhang, L. Lin and H. Wu, *ACS Appl. Mater. Interfaces*, 2016, **8**, 25210−25218.

41 Y. J. Tang, Y. Wang, X. L. Wang, S. L. Li, W. Huang, L. Z. Dong, C. H. Liu, Y. F. Li and Y. Q. Lan, *Adv. Energy Mater.*, 2016, **6**, 1600116.

42 L. Yu, B. Y. Xia, X. Wang and X. W. Lou, *Adv. Mater.*, 2016, **28**, 92−97.

43 X. Dai, K. Du, Z. Li, M. Liu, Y. Ma, H. Sun, X. Zhang and Y. Yang, *ACS Appl. Mater. Interfaces*, 2015, **7**, 27242−27253.

44 M. R. Gao, J. X. Liang, Y. R. Zheng, Y. F. Xu, J. Jiang, Q. Gao, J. Li and S. H. Yu, *Nat. Commun.*, 2015, **6**, 5982.

45 S. Xu, D. Li and P. Wu, *Adv. Funct. Mater.*, 2015, **25**, 1127−1136.

46 J. Zhang, S. Liu, H. Liang, R. Dong and X. Feng, *Adv. Mater.*, 2015, **27**, 7426−7431.

47 H. Zhu, J. Zhang, R. Yanzhang, M. Du, Q. Wang, G. Gao, J. Wu, G. Wu, M. Zhang, B. Liu, J. Yao and X. Zhang, *Adv. Mater.*, 2015, **27**, 4752−4759.

48 Z. Huang, W. Luo, L. Ma, M. Yu, X. Ren, M. He, S. Polen, K. Click, B. Garrett, J. Lu, K. Amine, C. Hadad, W. Chen, A. Asthagiri and Y. Wu, *Angew. Chem. Int. Ed.*, 2015, **54**, 15181−15185.

49 X. Ren, Q. Ma, H. Fan, L. Pang, Y. Zhang, Y. Yao, X. Ren and S. Liu, *Chem. Commun.*, 2015, **51**, 15997−16000.

50 M. Chhetri, U. Gupta, L. Yadgarov, R. Rosentsveig, R. Tenne and C. N. R. Rao, *Dalton Trans.*, 2015, **44**, 16399−16404.

51 J. Deng, H. Li, J. Xiao, Y. Tu, D. Deng, H. Yang, H. Tian, J. Li, P. Ren and X. Bao, *Energy Environ. Sci.*, 2015, **8**, 1594−1601.

52 H. Zhang, Y. Li, T. Xu, J. Wang, Z. Huo, P. Wan and X. Sun, *J. Mater. Chem. A*, 2015, **3**, 15020−15023.

53 M. R. Gao, M. K. Y. Chan and Y. Sun, *Nat. Commun.*, 2015, **6**, 7493.

54 S. Chen, J. Duan, Y. Tang, B. Jin and S. Z. Qiao, *Nano Energy*, 2015, **11**, 11−18.

55 D. Gopalakrishnan, D. Damien, B. Li, H. Gullappalli, V. K. Pillai, P. M. Ajayan and M. M. Shaijumon, *Chem. Commun.*, 2015, **51**, 6293−6296.

56 F. Li, J. Li, X. Lin, X. Li, Y. Fang, L. Jiao, X. An, Y. Fu, J. Jin and R. Li, *J. Power Sources*, 2015, **300**, 301−308.

57 D. J. Li, U. N. Maiti, J. Lim, D. S. Choi, W. J. Lee, Y. Oh, G. Y. Lee and S. O. Kim, *Nano Lett.*, 2014, **14**, 1228−1233.

58 J. Kibsgaard and T. F. Jaramillo, *Angew. Chem. Int. Ed.*, 2014, **53**, 14433−14437.

59 Z. Lu, W. Zhu, X. Yu, H. Zhang, Y. Li, X. Sun, X. Wang, H. Wang, J. Wang, J. Luo, X. Lei and L. Jiang, *Adv. Mater.*, 2014, **26**, 2683−2687.

60 Y. Tan, P. Liu, L. Chen, W. Cong, Y. Ito, J. Han, X. Guo, Z. Tang, T. Fujita, A. Hirata and M. W. Chen, *Adv. Mater.*, 2014, **26**, 8023−8028.

61 M. A. Lukowski, A. S. Daniel, F. Meng, A. Forticaux, L. Li and S. Jin, *J. Am. Chem. Soc.*, 2013, **135**, 10274−10277.

62 Y. Li, H. Wang, L. Xie, Y. Liang, G. Hong and H. Dai, *J. Am. Chem. Soc.*, 2011, **133**, 7296−7299.

63 E. Gileadi, *Electrode Kinetics for Chemists, Chemical Engineers and Materials Scientists*, Wiley-VCH, New York, 1993.

64 A. J. Bard and L. R. Faulkner, *Electrochemical Methods: Fundamentals and Applications*, Wiley, New York, 2rd Edition, 2000.

65 C. C. L. McCrory, S. Jung, J. C. Peters and T. F. Jaramillo, *J. Am. Chem. Soc.*, 2013, **135**, 16977−16987.

66 S. Levine and A. L. Smith, *Discuss. Faraday Soc.*, 1971, **52**, 290−301.

67 B. M. Jović, V. D. Jović, U. Č. Lačnjevac, L. Gajić-Krstajić and N. V. Krstajić, *Int. J. Hydrogen Energy*, 2015, **40**, 10480−10490.

68 B. M. Jović, V. D. Jović, U. Č. Lačnjevac, S. I. Stevanović, J. Kovač, M. Radović and N. V. Krstajić, *J. Electroanal. Chem.*, 2016, **766**, 78−86.

69 G. J. Brug, A. L. G. van den Eeden, M. Sluyters-Rehbach and J. H. Sluyters, *J. Electroanal. Chem. Interfacial Electrochem.*, 1984, **176**, 275−295.

70 D. Lin and A. Lasia, *J. Electroanal. Chem.*, 2017, **785**, 190−195.

71 B. E. Conway and B. V. Tilak, *Electrochim. Acta*, 2002, **47**, 3571−3594.

72 Y. Zheng, Y. Jiao, M. Jaroniec and S. Z. Qiao, *Angew. Chem. Int. Ed.*, 2015, **54**, 52−65.

73 M. Fleischmann and M. Grenness, *J. Chem. Soc., Faraday Trans. 1*, 1972, **68**, 2305−2315.

74 V. S. Bagotzky, A. M. Skundin and E. K. Tuseeva, *Electrochim. Acta*, 1976, **21**, 29−36.

75 I. M. Kodintsev and S. Trasatti, *Electrochim. Acta*, 1994, **39**, 1803−1808.

76 A. C. Tavares and S. Trasatti, *Electrochim. Acta*, 2000, **45**, 4195−4202.

77 U. Č. Lačnjevac, B. M. Jović, V. D. Jović, V. R. Radmilović and N. V. Krstajić, *Int. J. Hydrogen Energy*, 2013, **38**, 10178−10190.

78 U. Č. Lačnjevac, V. V. Radmilović, V. R. Radmilović and N. V. Krstajić, *Electrochim. Acta*, 2015, **168**, 178−190.

79 A. Kahyarian, B. Brown and S. Nesic, *J. Electrochem. Soc.*, 2017, **164**, H365−H374.

Chapter 4: Free-Standing Single-Crystalline NiFe-Hydroxide Nanoflake Arrays: A Self-Activated and Robust Electrocatalyst for Oxygen Evolution

4.1 Introduction and Significance

NiFe-based materials, especially NiFe-hydroxide, have stimulated great interest in electrocatalysis, due to their appealing OER activity as a class of earth-abundant and noble-metal-free electrocatalysts. However, conventional powdery NiFe-hydroxide catalysts with inferior structural properties suffer from low conductivity and poor stability, which is detrimental for practical applications. In this chapter, a strategy comprising the construction of self-supported single-crystalline nanoarrays is proposed to address these issues. Due to its advantageous electrode configuration and unique electronic structure, the developed Fe-Ni(OH)$_2$/NF electrode achieves superior activity and excellent stability towards the OER, making it attractive substitute of expensive IrO$_2$ catalysts. The highlights in this study include:

1. A simple dissolution-precipitation hydrothermal process was developed to produce single-crystalline Fe-Ni(OH)$_2$ nanoflake arrays grown vertically on nickel foam (Fe-Ni(OH)$_2$/NF), leading to a self-supported electrode with rational configuration that bypassed disadvantages associated with powder catalysts (e.g., elaborate electrode preparation, high contact resistance, and exfoliation off of substrates).

2. The as-obtained Fe-Ni(OH)$_2$/NF exhibited higher OER activity and more favourable kinetics than benchmark IrO$_2$/NF, and many recently reported OER electrocatalysts under alkaline electrolyte. More impressively, it shows significant stability and further enhanced activity during long-term operation, affording 10 mA cm^{-2} at a decreased overpotential from 267 mV to 235 mV after 75 h cycling.

3. The outstanding electrochemical performance was correlated to several aspects: (i) increased intrinsic OER activity related to the strong electronic interaction between Fe^{3+} and Ni^{2+} species; (ii) enhanced electrical conductivity for rapid charge transport; (iii) improved mass transfer and bubble release due to the vertically aligned nanoflake arrays; (iv) chemical stability and structural robustness originating from the single-crystalline structure as well as the self-supported electrode configuration.

4.2 Free-Standing Single-Crystalline NiFe-Hydroxide Nanoflake Arrays: A Self-Activated and Robust Electrocatalyst for Oxygen Evolution

This chapter is included as it appears as a journal paper published by **Jinlong Liu**, Yao Zheng, Zhenyu Wang, Zhouguang Lu, Anthony Vasileff, and Shi-Zhang Qiao, Free-Standing Single-Crystalline NiFe-Hydroxide Nanoflake Arrays: A Self-Activated and Robust Electrocatalyst for Oxygen Evolution, ***Chemical Communications***, 2018, 54, 463–466.

Statement of Authorship

Title of Paper	Free-standing single-crystalline NiFe-hydroxide nanoflake arrays: a self-activated and robust electrocatalyst for oxygen evolution
Publication Status	☑ Published ☐ Accepted for Publication ☐ Submitted for Publication ☐ Unpublished and Unsubmitted work written in manuscript style
Publication Details	Jinlong Liu, Yao Zheng, Zhenyu Wang, Zhouguang Lu, Anthony Vasileff and Shi-Zhang Qiao, Free-standing single-crystalline NiFe-hydroxide nanoflake arrays: a self-activated and robust electrocatalyst for oxygen evolution, Chemical Communications, 2018, 54, 463–466.

Principal Author

Name of Principal Author (Candidate)	Jinlong Liu
Contribution to the Paper	Research plan, material synthesis, most of the characterizations and data analysis, electrochemical measurements, and manuscript drafting.
Overall percentage (%)	
Certification:	This paper reports on original research I conducted during the period of my Higher Degree by Research candidature and is not subject to any obligations or contractual agreements with a third party that would constrain its inclusion in this thesis. I am the primary author of this paper.
Signature	Date 4/02/2018

Co-Author Contributions

By signing the Statement of Authorship, each author certifies that:

  i. the candidate's stated contribution to the publication is accurate (as detailed above);
  ii. permission is granted for the candidate in include the publication in the thesis; and
  iii. the sum of all co-author contributions is equal to 100% less the candidate's stated contribution.

Name of Co-Author	Yao Zheng
Contribution to the Paper	Discussion of research plan, data analysis, and manuscript revision.
Signature	Date 5 Feb 2018

Name of Co-Author	Zhenyu Wang
Contribution to the Paper	Assistance with TEM characterization.
Signature	Date 4 Feb 2018

Name of Co-Author	Zhouguang Lu		
Contribution to the Paper	Assistance with TEM characterization.		
Signature		Date	Feb 5, 2018

Name of Co-Author	Anthony Vasileff		
Contribution to the Paper	Assistance with manuscript editing and polishing.		
Signature		Date	05/02/2018

Name of Co-Author	Shi-Zhang Qiao		
Contribution to the Paper	Supervision of the work, data interpretation, and manuscript evaluation.		
Signature		Date	15/02/2018

Free-standing single-crystalline NiFe-hydroxide nanoflake arrays: a self-activated and robust electrocatalyst for oxygen evolution†

Jinlong Liu,[a] Yao Zheng,[a] Zhenyu Wang,[b] Zhouguang Lu, [ID][b] Anthony Vasileff [ID][a] and Shi-Zhang Qiao [ID]*[ac]

Free-standing single-crystalline NiFe-hydroxide nanoflake arrays grown *in situ* on nickel foam are synthesized using a simple hydrothermal method and they exhibit remarkable activity and durability for oxygen evolution in 1.0 M KOH, achieving a decreased overpotential of 235 mV to produce 10 mA cm^{-2} current density after long-term operation up to 100 h.

Water electrolysis, especially using electricity derived from renewable sources (*e.g.*, sunlight, wind, and tides), is being pursued as one of the most promising technologies towards sustainable development.[1] In order to improve the reaction rate and energy conversion efficiency, electrocatalysts for the anodic oxygen evolution reaction (OER) and the cathodic hydrogen evolution reaction (HER) are critical.[1–3] In particular, the overall rate is heavily dependent on the OER catalyst, due to the sluggish kinetics and complex reaction pathway of the OER.[4,5] Currently, state-of-the-art OER catalysts are based on scarce and expensive precious metals (*e.g.*, RuO$_2$ and IrO$_2$).[5,6] Despite the prominent OER activities, they generally suffer from short lifetimes due to dissolution into the electrolyte under oxidizing potentials.[5,7,8] Therefore, it is highly desirable to develop earth-abundant, efficient, and robust OER catalysts for water splitting.[2–5,9]

Since the discovery of the induced effects that Fe impurities have on catalysing the OER in Ni-based alkaline batteries, NiFe-based materials have stimulated great interest in water oxidation over the past few decades.[4,10–12] Specifically, NiFe-hydroxide, *i.e.*, Ni–Fe layered double hydroxide (LDH), materials are found to be ideal OER electrocatalysts amongst all noble-metal-free alternatives, owing to their high abundance and significant activity.[4,12,13]

Their biggest disadvantage, however, is their poor electrical conductivity.[14] In general, conductive carbon nanomaterials, such as carbon nanotubes (CNTs) and reduced graphene oxide (rGO), have been hybridized with two-dimensional (2D) NiFe-hydroxide nanosheets to overcome this issue.[14,15] For instance, Gong and co-workers reported a NiFe-LDH nanoplate/CNT complex as an advanced OER electrocatalyst.[14] Recently, Ma *et al.* fabricated a hetero-assembly composed of exfoliated Ni–Fe LDH nanosheets and rGO, which exhibited significantly enhanced OER performance compared to bare Ni–Fe LDH nanosheets.[15] Although these nanocomposites afforded improved OER activity and conductivity, they exhibited unsatisfactory long-term stability, evidenced by the gradual increase in overpotential during prolonged operation. Corrosion of the carbon (C + 2H$_2$O → CO$_2$ + 4H$^+$ + 4e$^-$, E° = 0.207 V *versus* reversible hydrogen electrode (*vs.* RHE)) under the harsh potential conditions might be responsible for the aggravated performance attenuation.[7,16] Additionally, by loading the powdery catalysts on nickel foam (NF) to prepare the working electrode, increased overpotentials are required. This can be attributed to higher contact resistance and inferior structural properties. Therefore, addressing the issues of poor intrinsic conductivity and stability of NiFe-hydroxide materials remains a fundamental challenge in designing better OER electrocatalysts.

Herein, we propose a versatile strategy to resolve the aforementioned issues by constructing single-crystalline NiFe-hydroxide nanoflake arrays vertically grown on NF (Fe–Ni(OH)$_2$/NF) as a self-supported OER electrocatalyst. The following advantages are predicted for an electrode developed in this way: (1) the self-supported catalyst can be directly used as an OER working electrode, avoiding the undesired issues involved with powder catalysts, such as elaborate electrode preparation, the use of a binder and a carbon support, high contact resistance, and exfoliation off of the substrate; (2) the *in situ* growth of NiFe-hydroxide nanoflakes on NF, using NF as the Ni source, results in a robust structure and facilitates rapid electron transfer between the substrate and the active material; (3) the single-crystalline NiFe-hydroxide nanoflakes contribute to electrode durability due to their rigid and defect-free structure; and (4) the well-aligned nanoflake arrays with vertical orientation allow

[a] School of Chemical Engineering, The University of Adelaide, Adelaide, SA 5005, Australia. E-mail: s.qiao@adelaide.edu.au

[b] Department of Materials Science and Engineering, Southern University of Science and Technology, Shenzhen 518055, P. R. China

[c] School of Materials Science and Engineering, Tianjin University, Tianjin 300072, P. R. China

† Electronic supplementary information (ESI) available: Experimental section, supplementary figures and tables as described in the text. See DOI: 10.1039/c7cc08843d
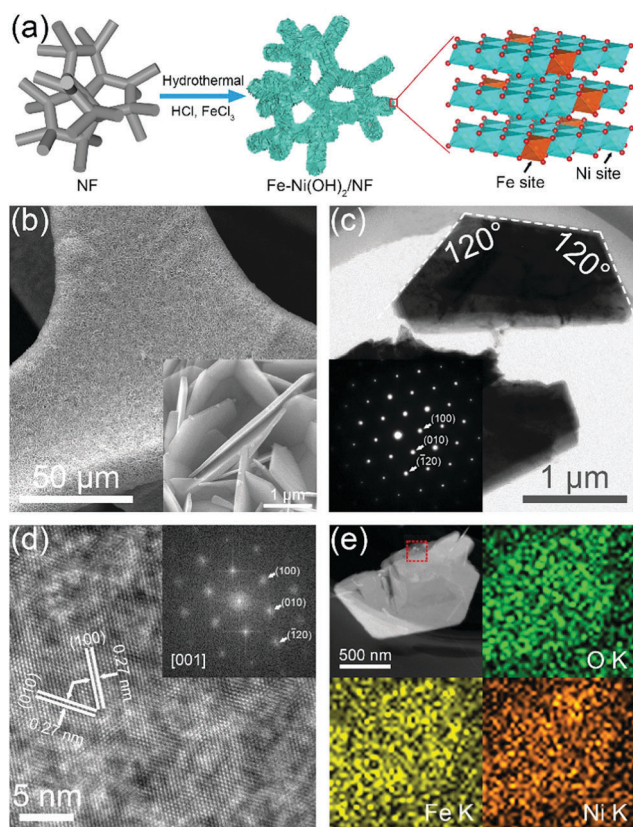
for full contact between active sites and the electrolyte, and promote mass transfer and bubble release. For NiFe-hydroxide, significant effort has been devoted to achieving high activity through creating various defects or by reducing the primary particle size for greater exposure of active sites.[14,17] However, very few studies focus on balancing high activity with good stability (crystallinity), as catalytic activity is often enhanced at the expense of structural stability.[18] In this regard, this is the first report on well-defined single-crystalline NiFe-hydroxide for the OER. Benefitting from the above advantages, the as-designed Fe–Ni(OH)$_2$/NF electrode can efficiently catalyse the OER with low overpotential and significant long-term durability, even outperforming the benchmark IrO$_2$ OER catalyst. The developed strategy in this work provides a foundation for designing active and robust OER electrocatalysts for practical alkaline water electrocatalysis.

As illustrated in Fig. 1a, single-crystalline Fe–Ni(OH)$_2$/NF nanoflake arrays were grown on NF via a simple hydrothermal method using NF as both the substrate and the Ni source. According to Tian et al.,[19] the growth of the nanoflake arrays follows a dissolution–precipitation mechanism, whereby the HCl etches the NF surface, forming Ni^{2+} ions. Once the HCl is consumed, the generated Ni^{2+} ions co-precipitate in situ with the Fe^{3+} ions

Fig. 1 (a) Schematic illustration of the synthesis of Fe–Ni(OH)$_2$/NF. (b) SEM image of Fe–Ni(OH)$_2$ nanoflakes grown on NF. Inset: Magnified SEM image of Fe–Ni(OH)$_2$ nanoflakes. (c) TEM image of a single Fe–Ni(OH)$_2$ nanoflake. Inset: Corresponding SAED pattern. (d) HRTEM image of a single Fe–Ni(OH)$_2$ nanoflake. Inset: Corresponding FFT pattern. (e) HADDF-STEM image of a single Fe–Ni(OH)$_2$ nanoflake and elemental mapping of the selected area (red).

to form robust and well-aligned arrays of single-crystalline Fe–Ni(OH)$_2$ on the NF. For comparison, single-crystalline Ni(OH)$_2$ nanoflake arrays on NF (Ni(OH)$_2$/NF) were fabricated using the same procedure, but in the absence of FeCl$_3$.

The X-ray diffraction (XRD) patterns of Fe–Ni(OH)$_2$/NF and Ni(OH)$_2$/NF (Fig. S1, ESI†) are almost identical, and can be indexed to the hexagonal Ni(OH)$_2$ (JCPDS Card No. 03-0177) and cubic Ni (JCPDS Card No. 04-0850). Therefore, the presence of the Fe precursor has no significant influence on the crystal structure and phase purity of the final product. The morphology of the as-obtained samples was first characterized using scanning electron microscopy (SEM). As shown in Fig. 1b, the surface of the NF is completely covered with vertically aligned Fe–Ni(OH)$_2$ nanoflake arrays. A close observation using transmission electron microscopy (TEM) shows that the Fe–Ni(OH)$_2$ nanoflake is a perfect single crystal with a hexagonal phase, demonstrated by the 120° dihedral angle and the corresponding selected area electron diffraction (SAED) spots (Fig. 1c). Meanwhile, it can be seen that the hexagonal side length of the Fe–Ni(OH)$_2$ nanoflakes is about 1.5 μm, while the thickness is about 100 nm (Fig. S2a, ESI†). High-resolution TEM (HRTEM) was also performed to investigate the detailed crystal structure of a single Fe–Ni(OH)$_2$ nanoflake. In Fig. 1d, the distinct and consecutive lattice fringes with an interplanar spacing of 0.27 nm correspond well to the d-spacing of the (100) and (010) planes of hexagonal Ni(OH)$_2$. No obvious crystal defects can be observed, suggesting a perfect crystal structure. The corresponding fast Fourier transform (FFT) pattern is consistent with the SAED result, further confirming the single crystalline nature of the resultant Fe–Ni(OH)$_2$ nanoflake. High-angle annular dark-field scanning transmission electron microscopy (HAADF-STEM) and energy dispersive spectroscopy (EDS) elemental analyses reveal the presence of O, Fe, and Ni, as well as their uniform distribution throughout the Fe–Ni(OH)$_2$ nanoflake (Fig. 1e and Fig. S2b, ESI†). Likewise, Ni(OH)$_2$/NF shows a similar morphology and single-crystalline structure to Fe–Ni(OH)$_2$/NF (Fig. S3, ESI†). This is due to their identical growth mechanism.

X-ray photoelectron spectroscopy (XPS) measurements were carried out to probe the surface element content and chemical valence states. As depicted in Fig. S4a (ESI†), the wide survey XPS spectrum of Fe–Ni(OH)$_2$/NF shows the presence of O, Fe, and Ni near the surface, in accordance with the EDS result. Quantitative analysis indicates that the surface composition of O, Fe, and Ni is 74.64, 22.72, and 2.64 at%, respectively. The deconvoluted Fe 2p region for Fe–Ni(OH)$_2$/NF (Fig. S4b, ESI†) exhibits two main peaks, namely Fe 2p$_{3/2}$ (712.5 eV) and Fe 2p$_{1/2}$ (724.6 eV), together with a satellite peak (718.9 eV), implying the +3 oxidation state of the Fe species.[20] In Fig. S4c (ESI†), the Ni 2p region of both Fe–Ni(OH)$_2$/NF and Ni(OH)$_2$/NF is fitted to five peaks: Ni^0 (852.9 eV) emanating from the underlying NF substrate (Fig. S5, ESI†), two spin–orbit doublets (Ni 2p$_{3/2}$ and Ni 2p$_{1/2}$), and the corresponding shakeup satellites, indicating the presence of Ni^{2+} in the materials.[20–22] In contrast, the Ni 2p$_{3/2}$ and Ni 2p$_{1/2}$ peaks in Fe–Ni(OH)$_2$/NF shift to a higher binding energy by ∼0.4 eV, which is indicative of electron transfer from the Ni d band to the Fe d band, demonstrating a strong interaction between the Fe^{3+} and Ni^{2+} species. In the O 1s region (Fig. S4d, ESI†), the peaks located at 529.1, 530.4, and 532.1 eV can be assigned to Fe–O, Ni–O, and adsorbed water, respectively.

The positive shift of the Ni–O peak in Fe–Ni(OH)$_2$/NF also provides evidence of the electronic interaction. It is very likely that such electronic interaction could increase charge transfer and improve the OER activity of Fe–Ni(OH)$_2$/NF.

The electrocatalytic properties of the single-crystalline Fe–Ni(OH)$_2$/NF towards OER were evaluated in 1.0 M KOH using a three-electrode cell, and compared with the IrO$_2$/NF benchmark and control samples (*i.e.*, Ni(OH)$_2$/NF and bare NF). Fig. 2a presents their linear sweep voltammetry (LSV) curves at a very slow scan rate of 1 mV s^{-1} to minimize capacitance behaviour. A characteristic oxidation peak, originating from Ni(OH)$_2$ to NiOOH,[12,23] is observed in the potential range of 1.4–1.47 V *vs.* RHE for both Fe–Ni(OH)$_2$/NF and Ni(OH)$_2$/NF. It is widely acknowledged that the potential-induced NiOOH is the active species for the OER.[12,23] Interestingly, cyclic voltammetry (CV) curves at different scan rates show that the oxidation is reversible (Fig. S6, ESI†). Based on previous studies, the asymmetric and broadened oxidation peak in the CV curves contains two processes, namely transformation from α-Ni(OH)$_2$ to γ-NiOOH and β-Ni(OH)$_2$ to β-NiOOH,[23] which can be verified by the two separated reduction peaks on the reverse sweep. It is interesting to note that the redox transformation between Ni(OH)$_2$ and NiOOH is relatively more reversible for Fe–Ni(OH)$_2$/NF with smaller polarization, suggesting easier formation of active NiOOH species. As a result, Fe–Ni(OH)$_2$/NF exhibits a much smaller onset overpotential than IrO$_2$/NF, Ni(OH)$_2$/NF, and NF, indicating excellent electrocatalytic activity for the OER. As can be seen from the inset in Fig. 2a, Fe–Ni(OH)$_2$/NF requires only an overpotential of 267 mV to achieve a current density of 10 mA cm^{-2}, which is about 50, 60, and 112 mV smaller than those of IrO$_2$/NF, Ni(OH)$_2$/NF, and NF, respectively. More importantly, the Tafel slope of Fe–Ni(OH)$_2$/NF is 51.5 mV dec^{-1}, whereas IrO$_2$/NF, Ni(OH)$_2$/NF, and NF show Tafel slopes of 52.6, 61.4, and 66.3 mV dec^{-1}, respectively (Fig. 2b), suggesting more favourable OER kinetics on Fe–Ni(OH)$_2$/NF. Note that both the overpotential and Tafel slope of the as-designed

Fe–Ni(OH)$_2$/NF are also superior to many recently reported OER electrocatalysts (Table S1, ESI†).

To get more insight into the intrinsic OER activity of the single-crystalline Fe–Ni(OH)$_2$ nanoflake arrays, it is necessary to decouple the contribution of the increased active surface area to the improvement in activity. As an effective approach to estimate the electrochemically active surface area, the double-layer capacitance (C_{dl}) of Fe–Ni(OH)$_2$/NF, Ni(OH)$_2$/NF, and the NF electrode was determined *via* CV measurements prior to self-oxidation and OER (in the potential window of 0.85–0.9 V *vs.* RHE without apparent Faradaic processes). As given in Fig. S7 (ESI†), the average C_{dl} values calculated from the scan-rate dependent CVs are 712, 757, and 453.6 μF cm^{-2} for the Fe–Ni(OH)$_2$/NF, Ni(OH)$_2$/NF, and NF, respectively. Given that a smooth electrode surface has a C_{dl} value of 60 μF cm^{-2},[24] the relative roughness factor (R_f) of each electrode is thereby estimated to be 11.87, 12.62, and 7.56, respectively. The specific OER current density ($j_{specific}$) (Fig. 2c) can then be obtained by dividing the OER current density at 1.53 V *vs.* RHE by the corresponding R_f. The $j_{specific}$ value of Fe–Ni(OH)$_2$/NF is about 14.1 and 126.5 times higher than those of Ni(OH)$_2$/NF and NF, respectively (Table S2, ESI†). This evidence shows that the intrinsic OER activity of Fe–Ni(OH)$_2$/NF is significantly greater than those of Ni(OH)$_2$/NF and NF. Viewing the binding energy shift in the Ni 2p region, the higher intrinsic OER activity is likely related to the strong electronic interaction between Fe^{3+} and Ni^{2+} in Fe–Ni(OH)$_2$/NF. As discussed above, the advantageous electrode configuration and unique electronic interaction of Fe–Ni(OH)$_2$/NF are predicted to facilitate charge transfer. In the electrochemical impedance spectra of various samples, Fe–Ni(OH)$_2$/NF shows the smallest charge transfer resistance (R_{ct}, Fig. 2d), which may be the main reason for its enhanced OER activity.

From the prospective of practical application, long-term stability is of paramount importance for an electrocatalyst, yet only a few studies have investigated prolonged operation up to 100 h. To this end, the operational durability of Fe–Ni(OH)$_2$/NF was tested under different overpotentials at 25 h intervals, as shown in Fig. 3a. Remarkably, throughout each 25 h interval, an extremely stable current density of 10, 50, and 100 mA cm^{-2} is achieved at an overpotential of 267, 276, and 288 mV, respectively. More interestingly, after long-term operation at high current densities, a dramatically decreased overpotential of 235 mV is required for Fe–Ni(OH)$_2$/NF to afford a constant 10 mA cm^{-2} current density, suggesting the occurrence of self-activation during the prolonged stability test. When comparing the OER polarization curves of Fe–Ni(OH)$_2$/NF before and after each interval (Fig. 3b–e), it is noted that the oxidation peak assigned to the Ni(OH)$_2$/NiOOH transition increases continuously during the first three intervals. This either indicates the formation of more active NiOOH species or the oxidation into deeper layers of single-crystalline Fe–Ni(OH)$_2$ nanoflakes at a very slow rate, finally reaching a limit, which agrees with previous studies.[12,25] Consequently, it is safe to conclude that the accumulated active NiOOH species during long-term operation leads to further improved OER activity. All these results strongly demonstrate that the developed strategy for constructing self-supported single-crystalline nanoflake arrays is successful in balancing high activity and excellent durability, making the as-synthesized Fe–Ni(OH)$_2$/NF very attractive for practical use.
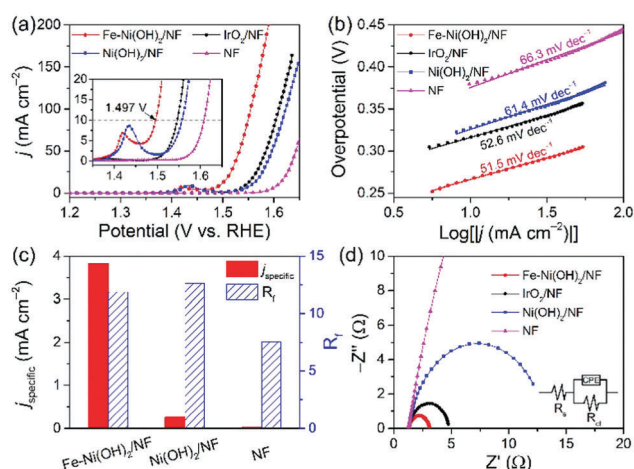

Fig. 2 (a) OER polarization curves of Fe–Ni(OH)$_2$/NF, IrO$_2$/NF, Ni(OH)$_2$/NF, and NF with a scan rate of 1 mV s^{-1} in 1.0 M KOH. Inset: Magnified polarization curves. (b) Corresponding OER Tafel plots. (c) Comparison of $j_{specific}$ at 1.53 V *vs.* RHE and R_f for Fe–Ni(OH)$_2$/NF, Ni(OH)$_2$/NF, and NF. (d) Nyquist plots of various samples, along with fitted curves represented by solid lines. Inset: The equivalent circuit.
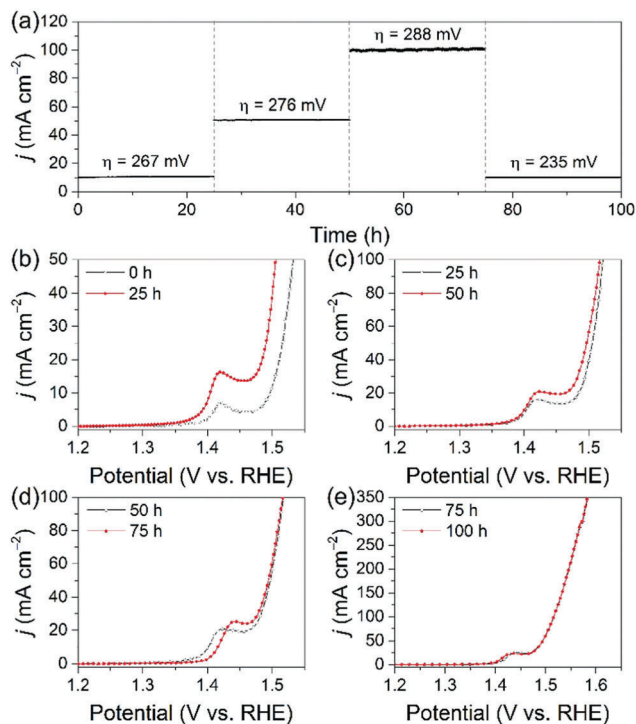
Fig. 3 (a) Current–time chronoamperometric curves of Fe–Ni(OH)$_2$/NF in 1.0 M KOH at overpotentials of 267, 276, 288, and 235 mV during 25 h intervals. (b–e) OER polarization curves of Fe–Ni(OH)$_2$/NF recorded before and after each step at a scan rate of 1 mV s^{-1}.

Some other important factors, including chemical stability and structural robustness of Fe–Ni(OH)$_2$/NF, were also taken into account in order to demonstrate its potential as a high-performance OER catalyst. Accordingly, the electrolyte was collected during the long-term stability test before and after each interval, and analysed using inductively coupled plasma mass spectrometry (ICP-MS). Surprisingly, no signals for Ni^{2+}/Ni^{3+} and Fe^{3+} were detected throughout the whole test, that is, the concentration of both Ni and Fe ions was below the detection limit of ICP-MS (<1 ppb). Hence, Fe–Ni(OH)$_2$/NF demonstrates extraordinary chemical stability without dissolution, even under harsh oxidizing potential conditions. It may also be that any dissolved Ni^{2+}/Ni^{3+} and Fe^{3+} could re-precipitate on the single crystal surface with readily available OH$^-$ and undergo dynamic surface reconstruction.[26] XPS results after long-term operation also demonstrated the excellent chemical stability of Fe–Ni(OH)$_2$/NF (Fig. S8, ESI†). In addition, as shown in the SEM images of Fe–Ni(OH)$_2$/NF after long-term OER electrolysis (Fig. S9, ESI†), the well-aligned nanoflake arrays were well preserved, implying strong structural durability. All these features are closely correlated with the single-crystalline nature of the Fe–Ni(OH)$_2$ nanoflakes as well as their self-supported and robust electrode configuration.

In summary, a simple hydrothermal method was developed to realize the *in situ* growth of single-crystalline Fe–Ni(OH)$_2$ nanoflake arrays. As a self-supported electrode, Fe–Ni(OH)$_2$/NF can efficiently catalyse the OER under alkaline electrolyte conditions with higher catalytic activity and more favourable kinetics, outperforming the benchmark IrO$_2$/NF as well as the control catalysts (*i.e.*, Ni(OH)$_2$/NF and NF). Moreover, it exhibits high stability and enhanced activity

during long-term operation. The outstanding electrochemical performance can be attributed to the single-crystalline Fe–Ni(OH)$_2$ nanoflakes and the advantageous electrode configuration, affording great potential for practical applications in water electrolysis. It is believed that the proposed strategy in this work may inspire the development of other free-standing single-crystalline nanoarrays as high-performance electrocatalysts for a diverse range of energy-conversion reactions, such as the hydrogen evolution reaction, oxygen reduction reaction, CO$_2$ reduction, and so on.

Conflicts of interest

There are no conflicts to declare.

Notes and references

1 Z. W. Seh, J. Kibsgaard, C. F. Dickens, I. Chorkendorff, J. K. Nørskov and T. F. Jaramillo, *Science*, 2017, **355**, eaad4998.
2 I. Roger, M. A. Shipman and M. D. Symes, *Nat. Rev. Chem.*, 2017, **1**, 0003.
3 M. I. Jamesh, *J. Power Sources*, 2016, **333**, 213–236.
4 M. Gong and H. Dai, *Nano Res.*, 2015, **8**, 23–39.
5 E. Fabbri, A. Habereder, K. Waltar, R. Kotz and T. J. Schmidt, *Catal. Sci. Technol.*, 2014, **4**, 3800–3821.
6 Y. Lee, J. Suntivich, K. J. May, E. E. Perry and Y. Shao-Horn, *J. Phys. Chem. Lett.*, 2012, **3**, 399–404.
7 I. Katsounaros, S. Cherevko, A. R. Zeradjanin and K. J. J. Mayrhofer, *Angew. Chem., Int. Ed.*, 2014, **53**, 102–121.
8 S. Cherevko, S. Geiger, O. Kasian, N. Kulyk, J.-P. Grote, A. Savan, B. R. Shrestha, S. Merzlikin, B. Breitbach, A. Ludwig and K. J. J. Mayrhofer, *Catal. Today*, 2016, **262**, 170–180.
9 J. Liu, D. Zhu, C. Guo, A. Vasileff and S.-Z. Qiao, *Adv. Energy Mater.*, 2017, **7**, 1700518.
10 M. S. Burke, L. J. Enman, A. S. Batchellor, S. Zou and S. W. Boettcher, *Chem. Mater.*, 2015, **27**, 7549–7558.
11 J. Liu, D. Zhu, T. Ling, A. Vasileff and S.-Z. Qiao, *Nano Energy*, 2017, **40**, 264–273.
12 L. Trotochaud, S. L. Young, J. K. Ranney and S. W. Boettcher, *J. Am. Chem. Soc.*, 2014, **136**, 6744–6753.
13 F. Dionigi and P. Strasser, *Adv. Energy Mater.*, 2016, **6**, 1600621.
14 M. Gong, Y. Li, H. Wang, Y. Liang, J. Z. Wu, J. Zhou, J. Wang, T. Regier, F. Wei and H. Dai, *J. Am. Chem. Soc.*, 2013, **135**, 8452–8455.
15 W. Ma, R. Ma, C. Wang, J. Liang, X. Liu, K. Zhou and T. Sasaki, *ACS Nano*, 2015, **9**, 1977–1984.
16 B. J. Eastwood, P. A. Christensen, R. D. Armstrong and N. R. Bates, *J. Solid State Electrochem.*, 1999, **3**, 179–186.
17 R. Gao and D. Yan, *Nano Res.*, 2017, DOI: 10.1007/s12274-017-1806-x.
18 C.-W. Tung, Y.-Y. Hsu, Y.-P. Shen, Y. Zheng, T.-S. Chan, H.-S. Sheu, Y.-C. Cheng and H. M. Chen, *Nat. Commun.*, 2015, **6**, 8106.
19 J. Tian, Z. Xing, Q. Chu, Q. Liu, A. M. Asiri, A. H. Qusti, A. O. Al-Youbi and X. Sun, *CrystEngComm*, 2013, **15**, 8300–8305.
20 H. Chen, X. Huang, L.-J. Zhou, G.-D. Li, M. Fan and X. Zou, *ChemCatChem*, 2016, **8**, 992–1000.
21 Y. Ma, X. Dai, M. Liu, J. Yong, H. Qiao, A. Jin, Z. Li, X. Huang, H. Wang and X. Zhang, *ACS Appl. Mater. Interfaces*, 2016, **8**, 34396–34404.
22 A. N. Mansour and C. A. Melendres, *Surf. Sci. Spectra*, 1994, **3**, 255–262.
23 M. E. G. Lyons, A. Cakara, P. O'Brien, I. Godwin and R. L. Doyle, *Int. J. Electrochem. Sci.*, 2012, **7**, 11768–11795.
24 S. Levine and A. L. Smith, *Discuss. Faraday Soc.*, 1971, **52**, 290–301.
25 H. Wang, H.-W. Lee, Y. Deng, Z. Lu, P.-C. Hsu, Y. Liu, D. Lin and Y. Cui, *Nat. Commun.*, 2015, **6**, 7261.
26 E. Fabbri, M. Nachtegaal, T. Binninger, X. Cheng, B.-J. Kim, J. Durst, F. Bozza, T. Graule, R. Schaublin, L. Wiles, M. Pertoso, N. Danilovic, K. E. Ayers and T. J. Schmidt, *Nat. Mater.*, 2017, **16**, 925–931.

Supporting Information

Free-standing single-crystalline NiFe-hydroxide nanoflake arrays: a self-activated and robust electrocatalyst for oxygen evolution

Jinlong Liu,[a] Yao Zheng,[a] Yan Jiao,[a] Zhenyu Wang,[b] Zhouguang Lu,[b] Anthony Vasileff,[a] and Shi-Zhang Qiao[*,a,c]

[a]School of Chemical Engineering, The University of Adelaide, Adelaide, SA 5005, Australia

[b]Department of Materials Science and Engineering, South University of Science and Technology, Shenzhen 518005, P.R. China

[c]School of Materials Science and Engineering, Tianjin University, Tianjin 300072, P.R. China

Corresponding Author: Shi-Zhang Qiao, E-mail address: s.qiao@adelaide.edu.au

I. Experimental Section

1.1 Materials

Nickel foam (NF, thickness 1.6 mm, bulk density 0.45 g cm^{-3}), iron (III) chloride hexahydrate (FeCl$_3$·6H$_2$O), hydrochloric acid (HCl, 37%), iridium (IV) oxide (IrO$_2$), and potassium hydroxide (KOH) were purchased from Sigma-Aldrich and used without further purification. The water used in all experiments was ultra-pure water (18.2 MΩ·cm) produced using a PURELAB Option-Q purification system.

1.2 Synthesis of Electrocatalysts

Preparation of Fe-Ni(OH)$_2$/NF: Single-crystalline Fe-Ni(OH)$_2$ nanoflake arrays were grown in situ under hydrothermal conditions. Typically, a piece of NF (1 cm × 4.5 cm) was pre-cleaned in 3 M HCl and ethanol under sonication, and then rinsed with water. To prepare the precursor solution, 0.5 mL of FeCl$_3$·6H$_2$O (2mg mL^{-1}) and 42 μL of HCl (3 M) were added into 40 mL of water and stirred for 30 min. The solution was then transferred into a 50 mL Teflon-lined stainless steel autoclave, and the pre-cleaned NF was immersed into the reaction solution. The autoclave was then sealed for hydrothermal reaction at 180 ºC for 6 h. The final product was collected and rinsed with water and ethanol several times, and dried in a vacuum oven at 50 ºC for 12 h.

Preparation of Ni(OH)$_2$/NF: To prepare Ni(OH)$_2$/NF, the same hydrothermal procedure for the preparation of Fe-Ni(OH)$_2$/NF was also used but with the absence of FeCl$_3$ in the reaction solution.

Preparation of IrO$_2$/NF: 10 mg of IrO$_2$ was dispersed in 2 mL of ethanol containing 0.15 wt. % of Nafion under sonication for 1 h. 400 μL of the dispersion was loaded onto a piece of pre-cleaned NF (1 cm × 1 cm) and dried using an infrared lamp to obtain the IrO$_2$/NF electrode.

1.3 Characterizations

X-ray diffraction (XRD) patterns were recorded on a Bruker D8 Advance powder diffractometer with Cu Kα radiation (λ = 1.540598 Å). The morphology and crystal structure of the samples were studied using a QUANTA 450 field emission scanning electron microscope and a Tecnai G^2 F30 scanning transmission electron microscope (S/TEM) with

high-angle annular dark-field (HADDF) detector. X-ray photoelectron spectroscopy (XPS) measurements were performed on an ESCALab250 XPS spectrometer. An Agilent 8900 triple quadrupole inductively coupled plasma mass spectrometer (ICP-MS) was used to analyze the trace amounts of Ni and Fe ions in the electrolyte during the long-term stability test.

1.4 Electrochemical Measurements

Electrochemical measurements were performed on a 760D electrochemical workstation (CH Instruments, Inc., USA) using a standard three-electrode glass cell (Pine Research Instruments, USA) with an Ag/AgCl (4 M KCl) electrode as the reference electrode, a carbon rod as the counter electrode, and 1.0 M KOH aqueous solution as the electrolyte. 1 cm × 1 cm Fe-Ni(OH)$_2$/NF, IrO$_2$/NF, Ni(OH)$_2$/NF and bare NF were investigated as the working electrode. All potentials were referenced to the reversible hydrogen electrode (RHE) using the following equation: E(RHE) = E(Ag/AgCl) + 0.205 + 0.059 × pH. Prior to all measurements, the electrolyte was purged with N$_2$ for 30 mins to remove dissolved O$_2$. The linear sweep voltammetry (LSV) curves were collected at a scan rate of 1 mV s^{-1}. Electrochemical impedance spectroscopy (EIS) was recorded in the frequency range of 0.1 Hz to 100 kHz with an amplitude of 5 mV. The C$_{dl}$ of the various samples was measured using CV technique in a small potential range of 0.85−0.90 V vs. RHE. The long-term stability test was evaluated using a chronoamperometric method. All electrochemical measurements were carried out at ambient temperature, and all data were corrected for the iR contribution within the cell.
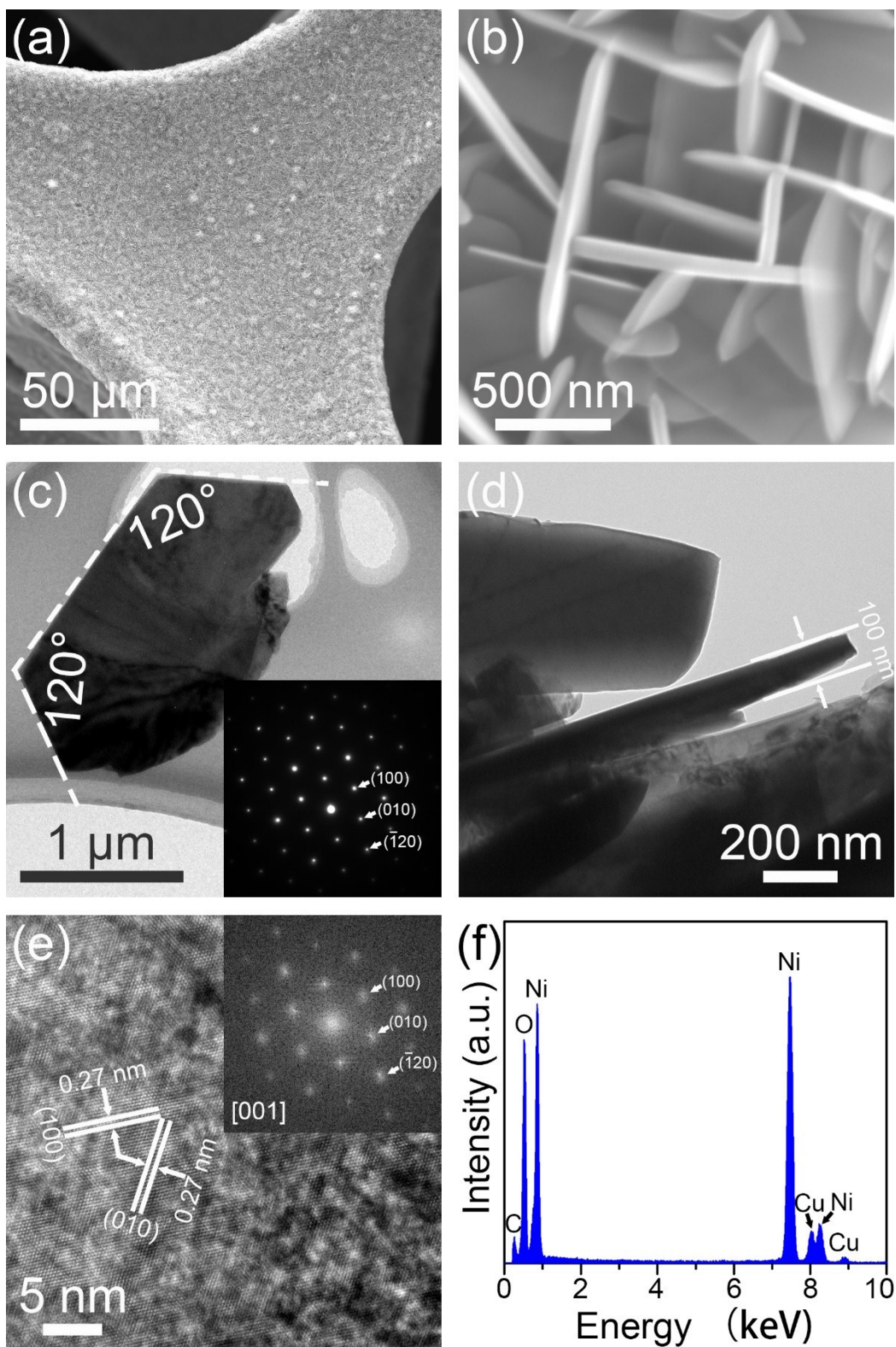
II. Supplementary Figures and Tables
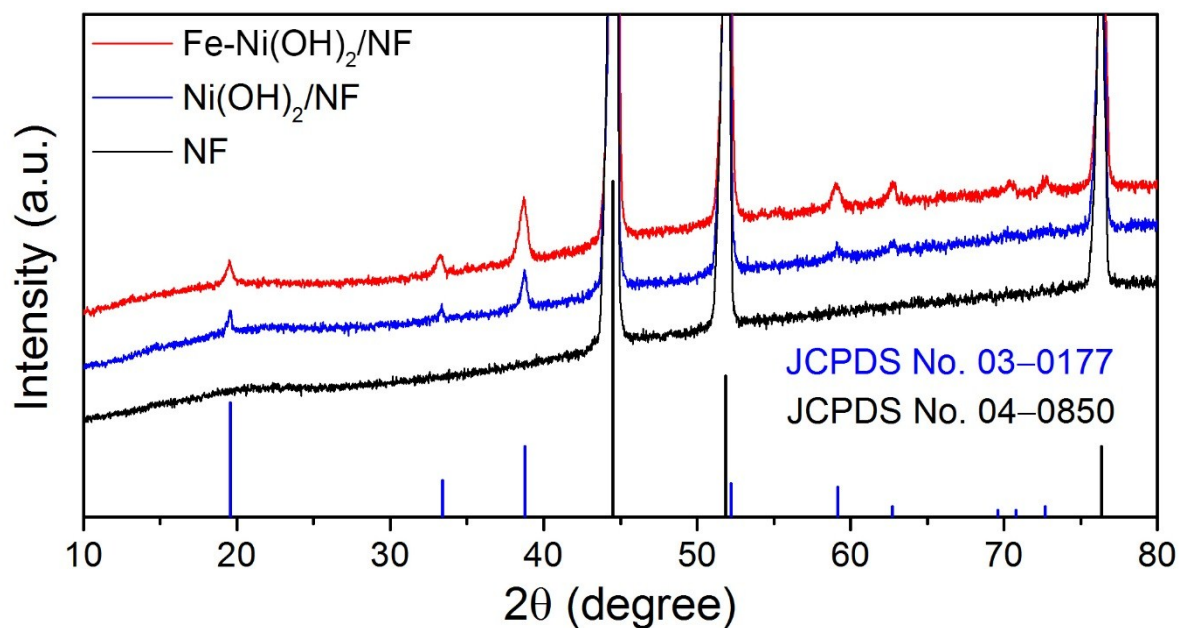
Fig. S1 XRD patterns of Fe-Ni(OH)$_2$/NF, Ni(OH)$_2$/NF, and bare NF, along with standard XRD patterns of Ni(OH)$_2$ and Ni for reference.
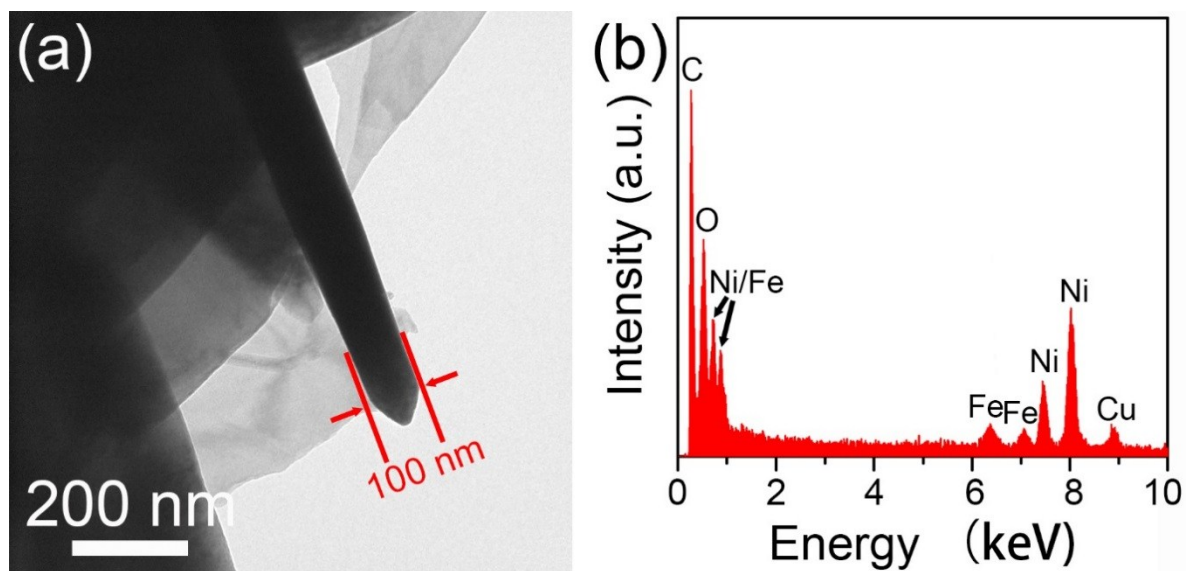
Fig. S2 (a) TEM cross-sectional view of an individual Fe-Ni(OH)$_2$ nanoflake showing a thickness of ~100 nm. (b) EDX spectrum of the Fe-Ni(OH)$_2$ nanoflakes from the TEM image. The signals for C and Cu originate from the TEM grid.

Fig. S3 (a,b) SEM images of Ni(OH)$_2$/NF. (c) TEM image of an individual Ni(OH)$_2$ nanoflake. Inset: corresponding SAED pattern. (d) TEM cross-sectional view of an individual Ni(OH)$_2$ nanoflake showing a thickness of ~100 nm. (e) HRTEM image of Ni(OH)$_2$ nanoflake. Inset: corresponding FFT pattern. (e) EDX spectrum of Ni(OH)$_2$ nanoflakes from the TEM image. The signals for C and Cu originate from the TEM grid.
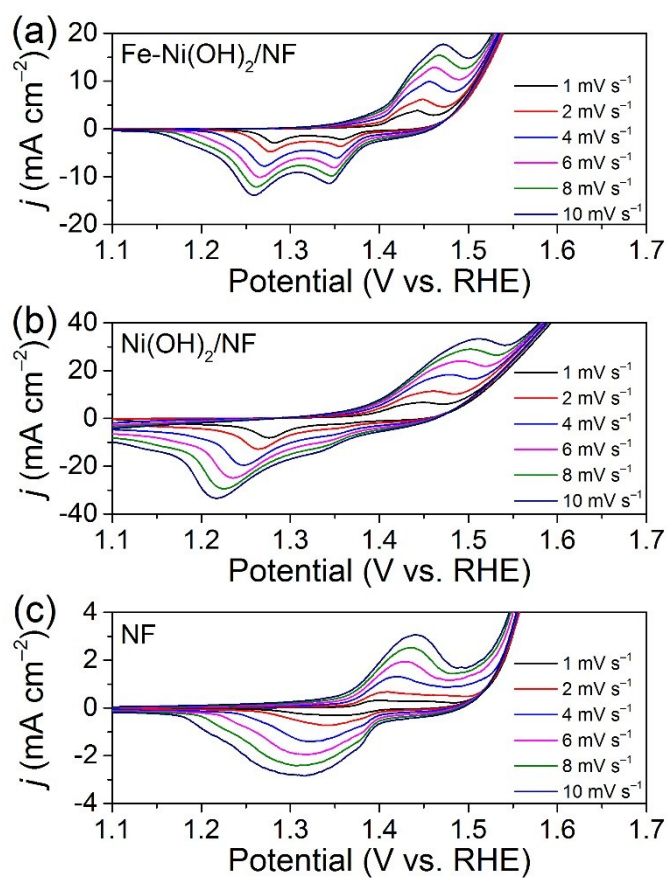
120
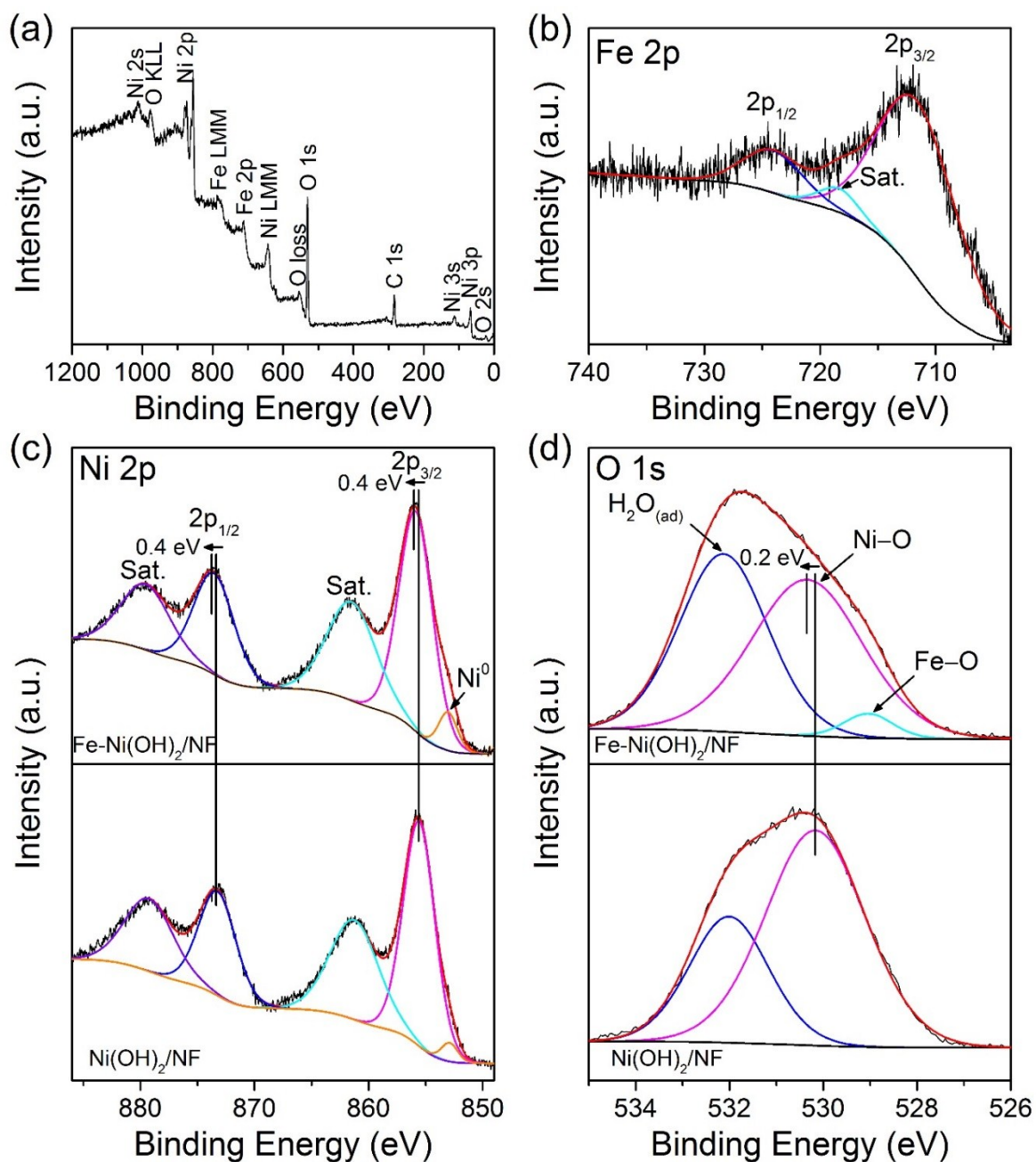
Fig. S4 (a) XPS survey spectrum of Fe-Ni(OH)$_2$/NF. (b) Deconvoluted high-resolution Fe 2p spectrum of Fe-Ni(OH)$_2$/NF. (c) Deconvoluted high-resolution Ni 2p spectra of Fe-Ni(OH)$_2$/NF and Ni(OH)$_2$/NF. (d) Deconvoluted high-resolution O 1s spectra of Fe-Ni(OH)$_2$/NF and Ni(OH)$_2$/NF.
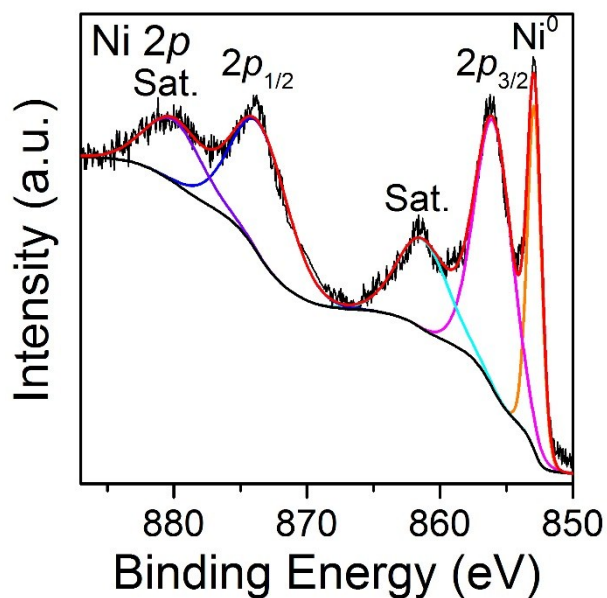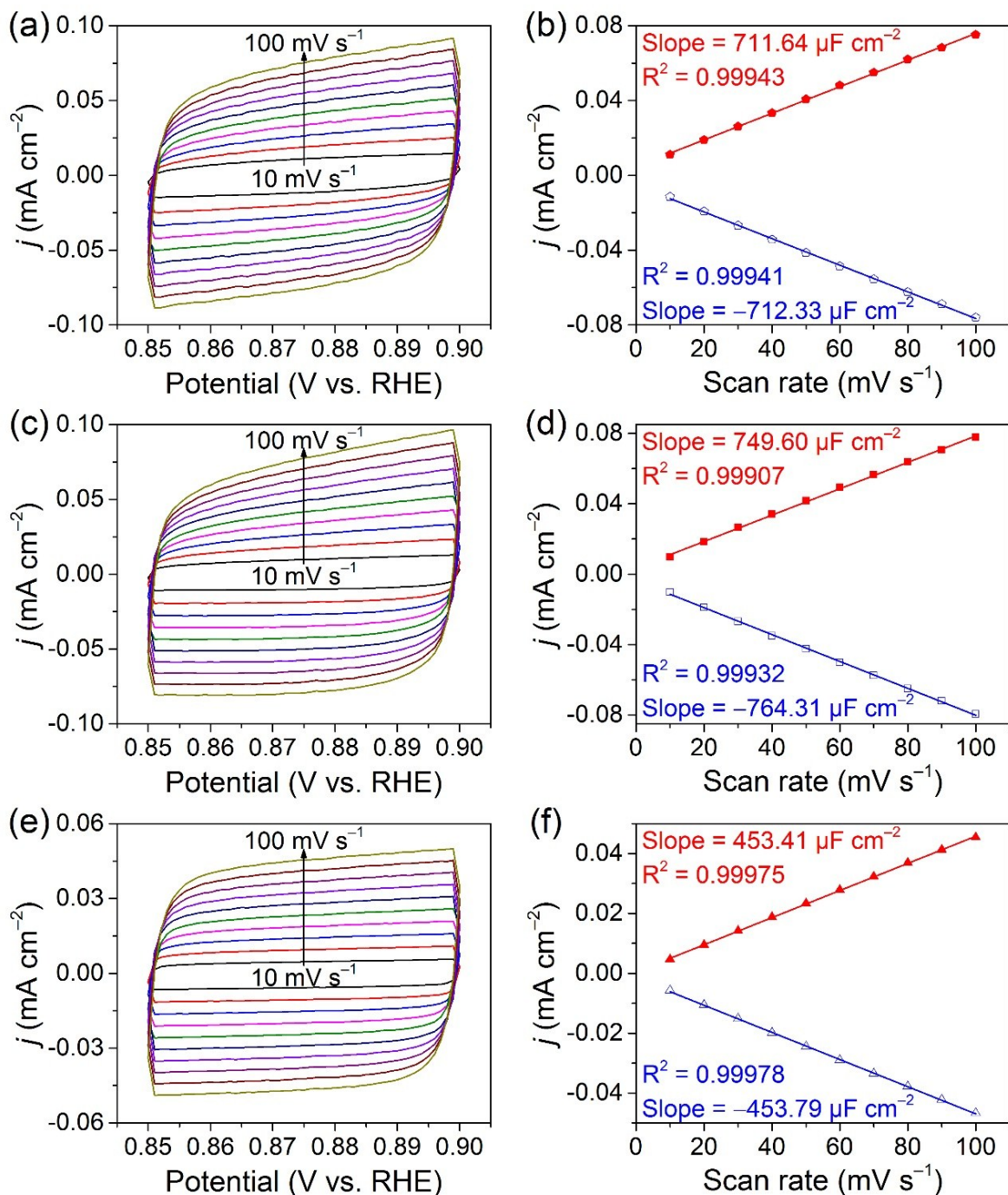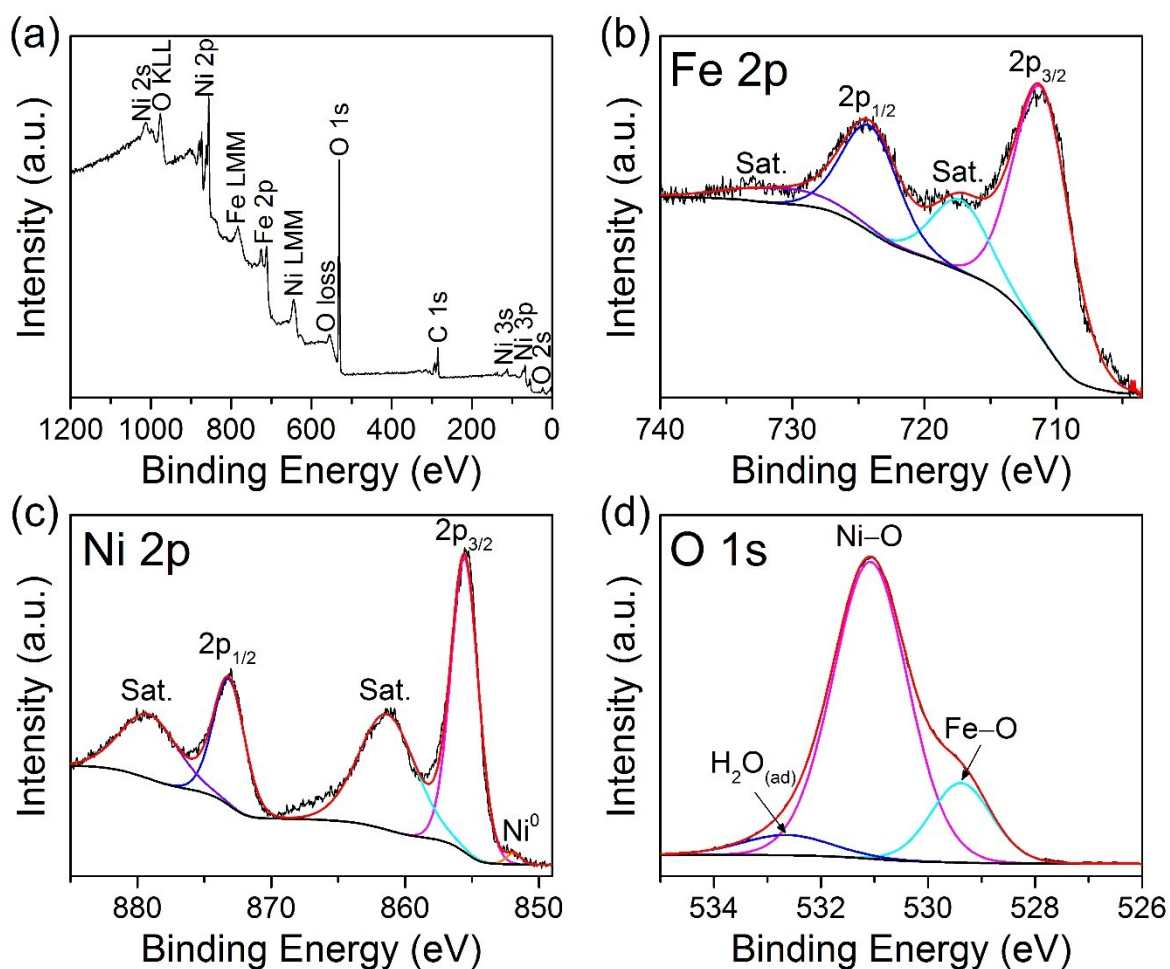
Fig. S5 Deconvoluted high-resolution XPS spectrum for Ni 2p of bare NF. The peak at 852.9 eV originates from the metallic Ni substrate, and the other peaks are attributed to the native oxides on the NF surface.

Fig. S6 CV curves of (a) Fe-Ni(OH)$_2$/NF, (b) Ni(OH)$_2$/NF, and (c) NF in 1.0 M KOH at various scan rates from 1 to 10 mV s^{-1}.

Fig. S7 CV curves at various scan rates from 10 to 100 mV s^{-1} in a non-Faradaic region and corresponding currents measured at 0.875 V vs. RHE plotted as a function of scan rate for (a,b) Fe-Ni(OH)$_2$/NF, (c,d) Ni(OH)$_2$/NF, and (e,f) NF. The determined C$_{dl}$ is taken as the average absolute value of the slopes of both cathodic and anodic linear fits.

Fig. S8 (a) XPS survey spectrum and deconvoluted high-resolution (b) Fe 2p, (c) Ni 2p, (d) O 1s spectra of Fe-Ni(OH)$_2$/NF after long-term stability testing.

Compared with the XPS results of pristine Fe-Ni(OH)$_2$/NF (Fig. S4), the Fe-Ni(OH)$_2$/NF after long-term stability testing showed similar chemical states. It is noted that the intensity of the O 1s in the XPS survey spectrum increased significantly. In the corresponding high-resolution O 1s spectrum (Fig. S8d), the Ni–O species dominated among all components of the O 1s. This result supports the increased Ni(OH)$_2$/NiOOH redox oxidation peak observed in the CV curve of Fe-Ni(OH)$_2$/NF after prolonged operation. This also provides evidence for the generation of more active NiOOH species during long-term stability testing.
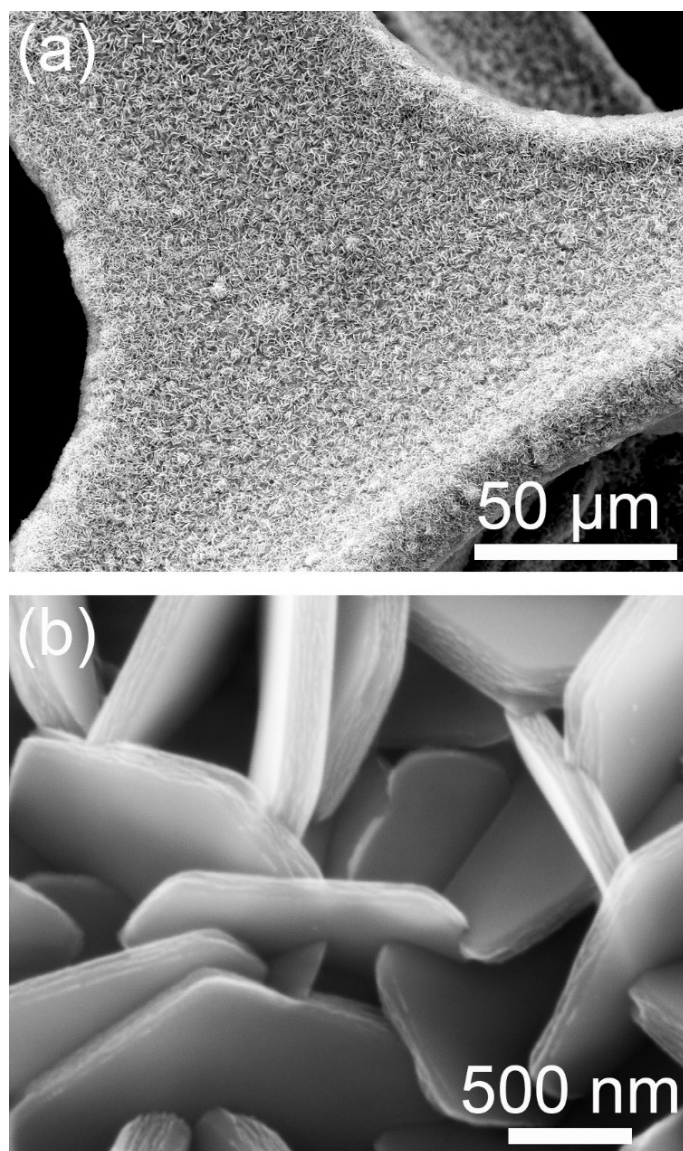
Fig. S9 (a) SEM image and (b) magnified SEM image of Fe-Ni(OH)$_2$/NF after long-term stability testing.

Table S1. Comparison of recently reported OER electrocatalysts in alkaline electrolyte.

Catalysts	Electrolyte	OER η_{10} (mV)	OER Tafel slop (mV dec^{-1})	Ref.
Fe-Ni(OH)$_2$/NF	1.0 M KOH	267 235 after stability test	51.5	This work
NiO/Ni	1.0 M KOH	294	41	1
FeB$_2$-NF	1.0 M KOH	296	52.4	2
Co(S$_x$Se$_{1-x}$)$_2$	1.0 M KOH	283	65.6	3
RuO$_2$/Co$_3$O$_4$	1.0 M KOH	305	69	4
Ni$_{2.0}$Mo$_{0.26}$@NC	1.0 M KOH	310	62.7	5
Cu$_2$O-Cu foams	1.0 M KOH	350	67.52	6
CuO/Cu foam	1.0 M NaOH	290	64	7
Fe$_3$O$_4$/Co$_3$S$_4$	1.0 M KOH	270	56	8
ZnCo$_2$O$_4$/Au/CNTs	1.0 M KOH	440	46.2	9
NiCo$_2$O$_4$	1.0 M NaOH	290	53	10
CoFePO/NF	1.0 M KOH	274.5	51.7	11
NiFeOOH/CNT-47%	1.0 M KOH	278	58	12
NiO/Ni	1.0 M KOH	345	53	13
Ni1Fe2-250	1.0 M KOH	310	42	14
Fe$_{0.5}$Ni$_{0.5}$O$_x$	0.1 M KOH	584	72	15
FeNi/NiFe$_2$O$_4$@NC-800	1.0 M KOH	316	60	16
NiO/NiFe$_2$O$_4$	1.0 M KOH	302	42	17
Fe$_{0.1}$Ni$_{0.9}$O	0.5 M KOH	297	37	18
Fe$_6$Ni$_{10}$O$_x$	1 M KOH	286	48	19
Ni$_{0.69}$Fe$_{0.31}$O$_x$/C	1.0 M KOH	280	30	20

Table S2. Electrochemical analysis of Fe-Ni(OH)$_2$/NF, Ni(OH)$_2$/NF, and NF.

Sample	C_{dl} (µF cm^{-2})	R_f	j @ 1.53 V vs. RHE	$j_{specific}$ @ 1.53 V vs. RHE[a]
Fe-Ni(OH)$_2$/NF	712	11.87	45.4	3.825
Ni(OH)$_2$/NF	757	12.62	3.2	0.254
NF	453.6	7.56	0.23	0.03

[a] $j_{specific}$ is calculated using $$j_{specific} = \frac{j}{R_f}.$$

REFERENCES

1   G. Ou, P. Fan, H. Zhang, K. Huang, C. Yang, W. Yu, H. Wei, M. Zhong, H. Wu and Y. Li, *Nano Energy*, 2017, **35**, 207−214.

2   H. Li, P. Wen, Q. Li, C. Dun, J. Xing, C. Lu, S. Adhikari, L. Jiang, D. L. Carroll and S. M. Geyer, *Adv. Energy Mater.*, 2017, DOI: 10.1002/aenm.201700513.

3   L. Fang, W. Li, Y. Guan, Y. Feng, H. Zhang, S. Wang and Y. Wang, *Adv. Funct. Mater.*, 2017, **27**, 1701008.

4   H. Liu, G. Xia, R. Zhang, P. Jiang, J. Chen and Q. Chen, *RSC Adv.*, 2017, **7**, 3686−3694.

5   X. Zhang, L. Huang, Y. Han, M. Xu and S. Dong, *Nanoscale*, 2017, **9**, 5583−5588.

6   H. Xu, J.-X. Feng, Y.-X. Tong and G.-R. Li, *ACS Catal.*, 2017, **7**, 986−991.

7   T. N. Huan, G. Rousse, S. Zanna, I. T. Lucas, X. Xu, N. Menguy, V. Mougel and M. Fontecave, *Angew. Chem. Int. Ed.*, 2017, **56**, 4792−4796.

8   J. Du, T. Zhang, J. Xing and C. Xu, *J. Mater. Chem. A*, 2017, **5**, 9210−9216.

9   H. Cheng, C.-Y. Su, Z.-Y. Tan, S.-Z. Tai and Z.-Q. Liu, *J. Power Sources*, 2017, **357**, 1−10.

10   X. Gao, H. Zhang, Q. Li, X. Yu, Z. Hong, X. Zhang, C. Liang and Z. Lin, *Angew. Chem. Int. Ed.*, 2016, **55**, 6290−6294.

11   J. Duan, S. Chen, A. Vasileff and S. Z. Qiao, *ACS Nano*, 2016, **10**, 8738−8745.

12   F. Rong, J. Zhao, Q. Yang and C. Li, *RSC Adv.*, 2016, **6**, 74536−74544.

13   J. Liang, Y.-Z. Wang, C.-C. Wang and S.-Y. Lu, *J. Mater. Chem. A*, 2016, **4**, 9797−9806.

14   H. Chen, X. Huang, L.-J. Zhou, G.-D. Li, M. Fan and X. Zou, *ChemCatChem*, 2016, **8**, 992−1000.

15   J. Jiang, C. Zhang and L. Ai, *Electrochim. Acta*, 2016, **208**, 17−24.

16   Y. Ma, X. Dai, M. Liu, J. Yong, H. Qiao, A. Jin, Z. Li, X. Huang, H. Wang and X. Zhang, *ACS Appl. Mater. Interfaces*, 2016, **8**, 34396−34404.

17   G. Liu, X. Gao, K. Wang, D. He and J. Li, *Int. J. Hydrogen Energy*, 2016, **41**, 17976−17986.

18   K. Fominykh, P. Chernev, I. Zaharieva, J. Sicklinger, G. Stefanic, M. Döblinger, A. Müller, A. Pokharel, S. Böcklein, C. Scheu, T. Bein and D. Fattakhova-Rohlfing, *ACS Nano*, 2015, **9**, 5180−5188.

19   L. Kuai, J. Geng, C. Chen, E. Kan, Y. Liu, Q. Wang and B. Geng, *Angew. Chem. Int. Ed.*, 2014, **53**, 7547−7551.

20   Y. Qiu, L. Xin and W. Li, *Langmuir*, 2014, **30**, 7893−7901.

Chapter 5: S-NiFe$_2$O$_4$ Ultra-Small Nanoparticle Built Nanosheets for Efficient Water Splitting in Alkaline and Neutral pH

5.1 Introduction and Significance

Earth-abundant bifunctional electrocatalysts have been keenly pursued towards overall water splitting in recent years. In particular, a substantial OER overpotential is mainly responsible for the energy loss during water electrolysis. As one of the most efficient OER electrocatalysts, NiFe-based oxides hold great potential in this demand. However, they generally exhibit poor HER activity and unsatisfactory durability for overall water splitting, especially in neutral electrolyte, due to their low conductivity and limited active sites. In this chapter, a brand new self-supported electrode, consisting of S-doped NiFe$_2$O$_4$ ultra-small nanoparticle built nanosheets on nickel foam (S-NiFe$_2$O$_4$/NF), was developed as an efficient bifunctional electrocatalyst for overall water splitting. Thanks to the chemical modification and nanostructure engineering, the optimized S-NiFe$_2$O$_4$/NF performed well as both OER and HER catalysts in alkaline and neutral pH. The highlights in this work include:

1. A novel and general synthesis strategy of confined growth was proposed to realize hierarchical nanostructure and uniform S incorporation via the thiourea-assisted electrodeposition, giving the optimized S-NiFe$_2$O$_4$/NF with ultra-small primary nanoparticles (~2 nm) with abundant grain boundaries and defects, interconnected nanosheet network with rich porosity, robust 3D nickel foam framework as a conductive substrate, and homogeneous S doping throughout the NiFe$_2$O$_4$ nanosheets.

2. The optimized S-NiFe$_2$O$_4$/NF showed outstanding OER and HER activity for overall water splitting under alkaline and neutral conditions, with low overpotentials, fast kinetics, excellent durability, and high Faradaic efficiency, even outperforming precious Pt/C and most of the recently reported electrocatalysts.

3. The impressive electrocatalytic activity is associated with three aspects: (i) numerous active sites related to the ultra-small nanoparticles with plentiful grain boundaries and defects, (ii) accelerated mass transport in a highly-developed porous network, and (iii) improved electrical conductivity originating from uniform S doping and conductive nickel foam.

5.2 S-NiFe$_2$O$_4$ Ultra-Small Nanoparticle Built Nanosheets for Efficient Water Splitting in Alkaline and Neutral pH

This chapter is included as it appears as a journal paper published by **Jinlong Liu**, Dongdong Zhu, Tao Ling, Anthony Vasileff, and Shi-Zhang Qiao, S-NiFe$_2$O$_4$ Ultra-Small Nanoparticle Built Nanosheets for Efficient Water Splitting in Alkaline and Neutral pH, ***Nano Energy***, 2017, 40, 264–273.

Statement of Authorship

Title of Paper	S-NiFe$_2$O$_4$ ultra-small nanoparticle built nanosheets for efficient water splitting in alkaline and neutral pH
Publication Status	☑ Published ☐ Accepted for Publication ☐ Submitted for Publication ☐ Unpublished and Unsubmitted work written in manuscript style
Publication Details	Jinlong Liu, Dongdong Zhu, Tao Ling, Anthony Vasileff, Shi-Zhang Qiao, S-NiFe$_2$O$_4$ ultra-small nanoparticle built nanosheets for efficient water splitting in alkaline and neutral pH, Nano Energy, 2017, 40, 264–273.

Principal Author

Name of Principal Author (Candidate)	Jinlong Liu
Contribution to the Paper	Research plan, material synthesis, most of the characterizations and data analysis, electrochemical measurements, and manuscript drafting.
Overall percentage (%)	
Certification:	This paper reports on original research I conducted during the period of my Higher Degree by Research candidature and is not subject to any obligations or contractual agreements with a third party that would constrain its inclusion in this thesis. I am the primary author of this paper.
Signature	Date 4/02/2018

Co-Author Contributions

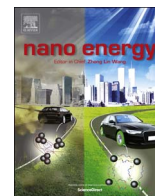By signing the Statement of Authorship, each author certifies that:

  i. the candidate's stated contribution to the publication is accurate (as detailed above);

  ii. permission is granted for the candidate in include the publication in the thesis; and

  iii. the sum of all co-author contributions is equal to 100% less the candidate's stated contribution.

Name of Co-Author	Dongdong Zhu
Contribution to the Paper	Discussion of research plan, data analysis, and manuscript revision.
Signature	Date 4/02/2018

Name of Co-Author	Tao Ling
Contribution to the Paper	Assistance with TEM characterization.
Signature	Date 04/02/2018

Name of Co-Author	Anthony Vasileff			
Contribution to the Paper	Assistance with manuscript editing and polishing.			
Signature			Date	05/02/2018

Name of Co-Author	Shi-Zhang Qiao			
Contribution to the Paper	Supervision of the work, data interpretation, and manuscript evaluation.			
Signature			Date	15/02/2018

Contents lists available at ScienceDirect

Nano Energy

Full paper

S-NiFe$_2$O$_4$ ultra-small nanoparticle built nanosheets for efficient water splitting in alkaline and neutral pH

Jinlong Liu[a], Dongdong Zhu[a], Tao Ling[b], Anthony Vasileff[a], Shi-Zhang Qiao[a,b,*]

[a] *School of Chemical Engineering, The University of Adelaide, Adelaide, SA 5005, Australia*
[b] *School of Materials Science and Engineering, Tianjin University, Tianjin 300072, PR China*

ARTICLE INFO

ABSTRACT

Efficient electrocatalyst is essential to develop water splitting technology for large-scale hydrogen production, especially using bifunctional earth-abundant alternative catalysts under alkaline and neutral conditions. NiFe-based oxides have promising activity towards the oxygen evolution (OER). However, they usually show unsatisfactory performance for the hydrogen evolution reaction (HER), due to their large particle size with limited active sites and poor conductivity. Herein, we report the synthesis of sulfur-incorporated NiFe$_2$O$_4$ nanosheets on nickel foam (S-NiFe$_2$O$_4$/NF), composed of ultra-small nanoparticles (~ 2 nm), by a facile confined growth strategy with the assistance of thiourea. Due to the favorable 3D hierarchical structure, the self-supported electrocatalyst endows abundant active sites, high electrical conductivity and rapid mass transfer, thereby achieving remarkable catalytic performance for overall water splitting under alkaline and neutral conditions. Specifically, the optimal S-NiFe$_2$O$_4$/NF electrode requires only 1.65 and 1.95 V to deliver a current density of 10 mA cm^{-2} in 1.0 M KOH and 1.0 M PBS, respectively, outperforming that of the commercial Pt/C as well as its counterparts (i.e. S-NiO/NF, S-Fe$_3$O$_4$/NF and pure NiFe$_2$O$_4$/NF). In addition, the synthesis strategy developed here can be applied to other mixed transition metal oxides with similar morphology and structure for various applications, such as supercapacitors, metal-air batteries, and photocatalysis.

1. Introduction

Hydrogen (H$_2$) is considered to be an appealing alternative energy carrier to conventional fossil fuels, and can address current issues related to them such as global warming and long-term energy security [1,2]. In this respect, water electrolysis is of particular interest, as it can make full use of renewable energy to produce H$_2$ [3]. However, the key challenge to developing such a technology lies in the exploration of earth-abundant, cost-effective, and environmentally friendly electrocatalysts with comparable catalytic activity to that of state-of-the-art precious metal based catalysts (i.e. Pt, IrO$_2$ and RuO$_2$) [4–6]. During past decades, a great number of transition metal based materials, including alloys [7,8], carbides [9,10], nitrides [11,12], oxides [13,14], phosphides [15,16], and chalcogenides [17,18], have been intensively investigated as electrocatalysts for water splitting. It should be noted that most of the emerging hydrogen evolution reaction (HER) electrocatalysts achieve high activities in acidic electrolytes [7,9,16–18]. However, almost all contemporary oxygen evolution reaction (OER) electrocatalysts perform well only under alkaline or neutral conditions, as almost all non-precious metal catalysts show drastic degradation

under oxidizing potentials in acidic media [19]. Currently, industrial water electrolysis is mainly carried out in alkaline electrolyte, but the harsh alkaline operating conditions often cause serious corrosion and related environmental problems. In the long run, the splitting of ocean or river water in neutral pH is the ultimate goal to satisfy a sustainable future hydrogen economy [20]. Given these facts, it is of great importance to develop earth-abundant, efficient, and durable bifunctional electrocatalysts that can simultaneously catalyse both the HER and OER under alkaline and/or neutral conditions for overall water splitting. Further, bifunctional electrocatalysts can not only reduce cost by utilizing only one electrode material, but also by simplyfing water electrolyzer design and operating conditions by using the same electrolyte [21,22]. Yet it remains a great challenge to screen suitable bifunctional catalysts with these requirements.

Among various electrocatalysts for water splitting, NiFe-based compounds have shown great potential for replacing noble metal based catalysts for the OER, owing to their unique physicochemical properties, earth abundance, and low cost [23]. In recent years, with the rising demand for H$_2$ as a renewable commodity, NiFe-based compounds have also been employed as electrocatalysts towards the HER [24–26]. For

---

* Corresponding author at: School of Chemical Engineering, The University of Adelaide, Adelaide, SA 5005, Australia.
  E-mail address: s.qiao@adelaide.edu.au (S.-Z. Qiao).

instance, Xia and co-workers synthesized iron-nickel sulfide (INS) ultrathin nanosheets by topotactic transition of its hydroxide precursor, which showed excellent HER activity and stability, but the electrochemical measurements were still conducted in acidic media [24]. Wang et al. demonstrated that the ultra-small NiFeO$_x$ nanoparticles with large surface area and abundant grain boundaries, synthesized by lithiation and de-lithiation processes through assembling lithium-ion battery, were effective in enhancing the catalytic activity and stability for both the OER and HER in alkaline electrolyte [25]. However, the lithium-induced conversion reaction was rather complicated and time-consuming. Further, the as-synthesized NiFeO$_x$ exhibited poor activity in neutral electrolyte. Consequently, it is essential to fabricate NiFe-based materials with well-defined nanostructures to fully exploit their catalytic properties towards both the HER and OER in both alkaline and neutral media.

Given that NiFe-based compounds are regarded as one of the most promising OER candidates [19], the key to exploit NiFe-based materials as bifunctional electrocatalysts hinges on the enhancement of their HER performance. From the perspective of catalyst design, an ideal HER electrocatalyst should meet the following criteria. First, a HER catalyst must possess multiple active sites to attain desirable catalytic activity. In this aspect, nanotechnology is favorable for significantly enlarging surface area and thus exposing abundant active sites [27]. Second, the catalyst should be conductive to promote electron transfer. Generally, element doping or incorporation has been demonstrated as a useful strategy to regulate the electronic structure for improving intrinsic conductivity [28], while integrating active materials with conductive substrates such as carbon cloth and nickel foam (NF) provides another option to increase charge transfer [20,21]. Third, the catalyst should have excellent durability for practical operation. To this end, the preparation of three-dimensional (3D) self-supported electrodes using robust substrates like NF is expected to facilitate product transfer and boost mechanical strength, aiming at the enhancement of long-term stability [21]. Additionally, the catalyst should be synthesized using facile techniques and based on inexpensive raw materials for large-scale application [26]. As two earth-abundant elements, Fe and Ni are very attractive non-noble metal candidates. When designing rational NiFe-based electrocatalysts in alkaline and neutral electrolytes, these considerations are important to realize superior activity, conductivity, stability, and viability for the HER.

Inspired by these criteria, we herein highlight the synthesis of sulfur-incorporated nickel ferrite ultra-small nanoparticle built nanosheets grown on NF (denoted S-NiFe$_2$O$_4$/NF) via in situ thiourea-assisted electrodeposition and subsequent low-temperature calcination. As a free-standing electrode, S-NiFe$_2$O$_4$/NF exhibits remarkable catalytic activity and durability for overall water splitting in both alkaline and neutral pH, outperforming its counterparts (i.e. S-NiO/NF, S-Fe$_3$O$_4$/NF and pure NiFe$_2$O$_4$/NF) as well as many recently reported electrocatalysts [22,29–33]. Moreover, the facile synthetic method proposed in this study can be easily extended as a general approach for producing other mixed metal oxides with ultra-small nanoparticles as primary building units for diverse applications, such as supercapacitor and lithium/sodium-ion batteries.

2. Experimental section

2.1. Materials and synthesis of electrocatalysts

All chemicals used in this work, including Ni(NO$_3$)$_2$·6H$_2$O, Fe(NO$_3$)$_3$·9H$_2$O, Co(NO$_3$)$_2$·6H$_2$O, thiourea, urea, KOH, phosphate buffer solution (1.0 M, pH 7.4), Pt/C (20 wt% of Pt on Vulcan XC72), Nafion (15 wt%) and nickel foam (thickness 1.6 mm, bulk density 0.45 g cm^{-3}), were purchased from Sigma-Aldrich and used without further purification. All chemicals were of analytical reagent grade and ultrapure water (18.2 MΩ cm, P.LAB Option-Q) was used in all experiments. S-NiFe$_2$O$_4$/NF was synthesized through thiourea-assisted

electrodeposition followed by low-temperature calcination. In a typical experiment, nickel foam (NF, 1 cm × 4 cm) was cleaned thoroughly with 3 M HCl, ethanol, and water in sequence under sonication for 10 min each time. 1 mM nickel nitrate (Ni(NO$_3$)$_2$·6H$_2$O), 2 mM iron nitrate (Fe(NO$_3$)$_3$·9H$_2$O), and 60 mM thiourea were dissolved in 100 mL of deionized water to obtain the precursor solution. The electrodeposition was performed with a CHI 760D electrochemical workstation using a three-electrode configuration, in which the cleaned NF, carbon rod and Ag/AgCl electrode were used as the working electrode, counter electrode, and reference electrode, respectively. The electrodeposition was conducted at a constant potential of − 1.1 V vs. Ag/AgCl for 600 s in a single-compartment glass cell (125 mL) at ambient temperature. After electrodeposition, the sample was removed and washed with deionized water several times to remove remaining electrolyte, and then dried in a vacuum oven at 60 °C overnight. Under Ar atmosphere, the obtained NiFe-precursor was heated to 250 °C in a tube furnace at a rate of 2 °C min^{-1} and held at that temperature for 2 h. After cooling naturally to room temperature, the target S-NiFe$_2$O$_4$/NF sample was collected. To investigate the effect of applied potential, the electrodeposition was also performed at − 0.9, − 1, − 1.2, and − 1.4 V vs. Ag/AgCl for 600 s. The influence of electrodeposition time was investigated by varying the time from 150 s to 1200 s at − 1.1 V vs. Ag/AgCl. Moreover, the typical NiFe-precursor/NF obtained above was treated under 400 °C for 2 h to investigate the influence of calcination temperature. For comparison, S-NiO/NF, S-Fe$_3$O$_4$/NF and NiFe$_2$O$_4$/NF were also prepared as control groups under the same conditions (electrodeposition at − 1.1 V vs. Ag/AgCl for 600 s and calcination in Ar under 250 °C for 2 h) except for the absence of Fe^{3+}, Ni^{2+} and thiourea, respectively. For benchmark comparison, 10 mg of 20 wt% Pt/C was dispersed in 2 mL of ethanol containing 0.15 wt% of Nafion under ultrasound for 1 h. Next, 200 μL of the Pt/C dispersion (5 mg mL^{-1}) was loaded onto a piece of NF (1 cm × 1 cm) to produce the PtC/NF electrode. To confirm the general applicability of the proposed synthesis strategy, S-NiCo$_2$O$_4$/NF and S-CoFe$_2$O$_4$/NF were further prepared by same approach using corresponding nitrates.

2.2. Characterizations

The morphologies of the as-synthesized samples were directly observed on field emission scanning electron microscopy (SEM, QUANTA 450). The electrodeposited S-NiFe$_2$O$_4$, S-NiFe$_2$O$_4$ (400 °C), NiFe$_2$O$_4$, S-NiO, and S-Fe$_3$O$_4$ were flaked off the electrodes via ultrasonication for further characterizations. The microstructure and elemental distribution were analyzed by transmission electron microscopy (TEM, Tecnai G2 Spirit and JEOL 2100 Cryo) equipped with EDS. The crystal structures were tested using powder X-ray diffractometer (XRD, Cu-target Bruker D8 Advance). Fourier transform infrared (FTIR) spectroscopy and X-ray photoelectron spectroscopy (XPS) data were collected using a Nicolet 6700 spectrometer and an ESCALab250 spectrometer, respectively. The produced H$_2$ and O$_2$ were assessed by gas chromatograph (GC, Clarus 480, PerkinElmer, USA with Ar as a carrier gas and 5 Å molecular sieve column).

2.3. Electrochemical measurements

Electrochemical measurements were conducted in a standard three-electrode glass cell and a two-electrode glass cell on a 760D workstation (Pine Research Instruments, US). For the HER and OER tests, a carbon rod and a Ag/AgCl (4 M KCl) electrode were used as the counter electrode and the reference electrode, respectively. Before measurements, the cells were purged with N$_2$ for 30 min to remove dissolved O$_2$. After repetitive cyclic voltammetry (CV) scan for 20 cycles, the linear sweep voltammetry (LSV) curves were collected with a scan rate of 5 and 1 mV s^{-1} for the HER and OER, respectively, and all polarization curves were corrected for the iR contribution within the cell. The onset overpotential is defined as the overpotential at which HER or OER current
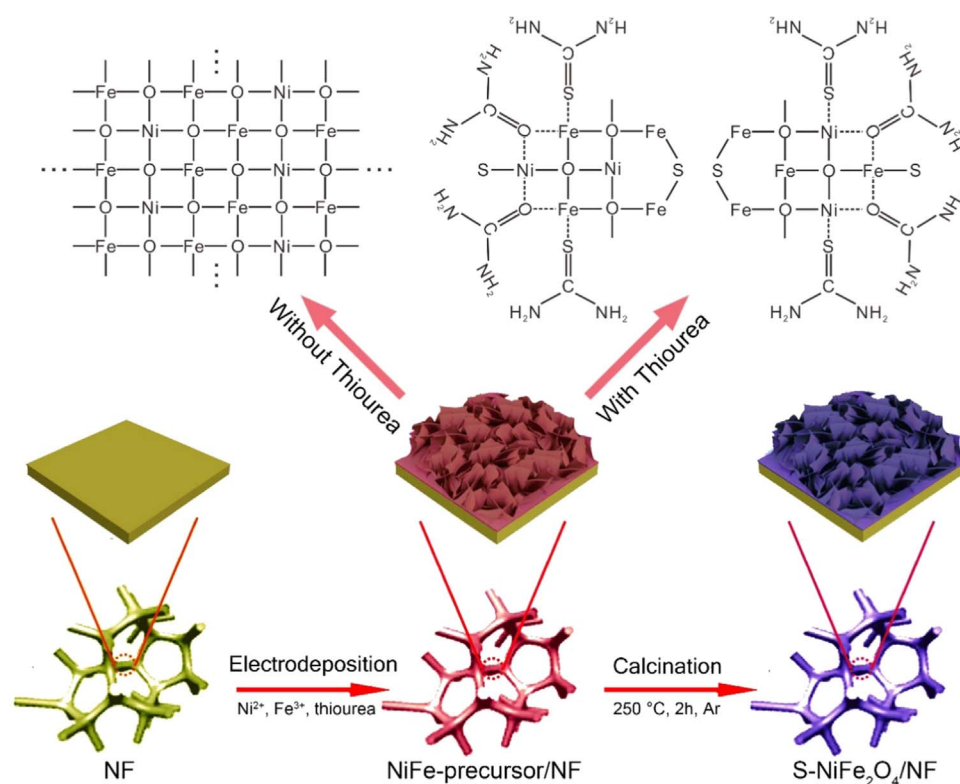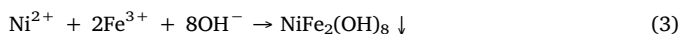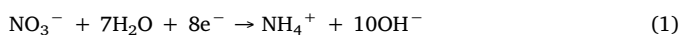
Fig. 1. Schematic illustration of the confined growth for the fabrication of S-NiFe$_2$O$_4$/NF with the assistance of thiourea.

density is at 1.0 mA cm^{-2}. Electrochemical impedance spectroscopy (EIS) was carried out in the frequency range from 0.1 Hz to 100 kHz with an amplitude of 5 mV. In the case of overall water splitting, electrodes constructed with the same material were employed as both the anode and cathode. All potentials were calibrated to a reversible hydrogen electrode (RHE) by adding a value of (0.205 + 0.059 × pH).

3. Results and discussion

As illustrated in Fig. 1, the fabrication of S-NiFe$_2$O$_4$/NF involves two main steps, that is, thiourea-assisted electrodeposition and low-temperature calcination in Ar atmosphere. First, NiFe-based layered double hydroxide (denoted NiFe-precursor) is deposited onto the surface of cleaned NF (Fig. S1 in the Supporting information) using a potentiostatic technique in an aqueous electrolyte containing Ni^{2+} and Fe^{3+} (mole ratio 1:2) according to the following reactions [34,35].

$$NO_3^- + 7H_2O + 8e^- \rightarrow NH_4^+ + 10OH^- \tag{1}$$

$$2H_2O + 2e^- \rightarrow H_2 \uparrow + 2OH^- (HER) \tag{2}$$

$$Ni^{2+} + 2Fe^{3+} + 8OH^- \rightarrow NiFe_2(OH)_8 \downarrow \tag{3}$$

Notably, the addition of excess thiourea plays a significant role in tuning the micro-structure of the NiFe-precursor, because the thiourea can be adsorbed on the freshly generated primary nanocrystallites to avoid their rapid growth (Fig. S2 in the Supporting information) [36,37]. Meanwhile, part of the adsorbed thiourea can serve as a source of sulfide through the decomposition reaction ($SC(NH_2)_2 + H_2O \rightarrow S^{2-} + OC(NH_2)_2 + 2H^+$) under the applied negative potential [37], in which the produced urea is coordinated with fringe metal ions (Fig. S2 in the Supporting information) and the sulfide ions are able to terminate the nanocrystal growth. In contrast, the absence of thiourea leads to the rapid co-deposition of Ni^{2+} and Fe^{3+} due to the drastic generation of hydroxide ions, resulting in the rapid extension of NiFe-precursor nanoparticles. Afterwards, the as-obtained NiFe-precursor/NF is calcinated in Ar atmosphere for 2 h, during which the NiFe-precursor is converted into S-NiFe$_2$O$_4$ with low crystallinity. For the NiFe-

precursor synthesized without the assistance of thiourea, NiFe$_2$O$_4$/NF is obtained after calcination.

In such a developed strategy, the applied potential, electrodeposition time and calcination temperature have a significant effect on the morphology and structure of the resultant S-NiFe$_2$O$_4$/NF (see Figs. S3–S5 in the Supporting information for details). Specifically, the cathodic current increases continuously with a decrease in the applied potential (Fig. S6 and S7 in the Supporting information), leading to faster electrodeposition of NiFe-precursor. On the other hand, longer electrodeposition times give rise to thicker coatings of NiFe-precursor on NF. In general, too much or too little mass loading of a catalyst can hardly achieve the optimal catalytic activity [28]. Correspondingly, the applied potential and electrodeposition time should be well controlled to reach the optimal deposition of NiFe-based compound. In terms of thermal treatment, the calcination temperature is crucial to realize the balance between amorphousness and crystallinity, as amorphousness is essential to achieve high activity with abundant active sites, whereas appropriate crystallinity plays an indispensable role in stabilizing the structure for excellent durability [23]. High temperature is likely to cause the further growth or even aggregation of primary nanoparticles, so an appropriate low-temperature calcination is beneficial to maintain ultra-small nanoparticles with abundant defects, grain boundaries, and preferable crystallinity. For comparison, S-NiO/NF, S-Fe$_3$O$_4$/NF, and pure NiFe$_2$O$_4$/NF, synthesized with the absence of Fe^{3+}, Ni^{2+}, and thiourea, respectively, were also prepared as control groups under the same conditions. Additionally, commercial 20 wt% Pt/C was loaded onto NF (denoted PtC/NF) using Nafion as a binder, and the proposed strategy was extended to fabricate S-NiCo$_2$O$_4$/NF and S-CoFe$_2$O$_4$/NF, in order to validate its general applicability.

The low magnification scanning electron microscopy (SEM) image of S-NiFe$_2$O$_4$/NF (Fig. 2a) reveals that the surface of NF was completely covered by uniform S-NiFe$_2$O$_4$ nanosheets. As shown in Fig. 2b, the high magnification SEM image indicates the interconnection of well-defined S-NiFe$_2$O$_4$ nanosheets with porous architecture, constructing an advantageous network structure for both charge and mass transfer. The interconnected porous S-NiFe$_2$O$_4$ network was further confirmed by the
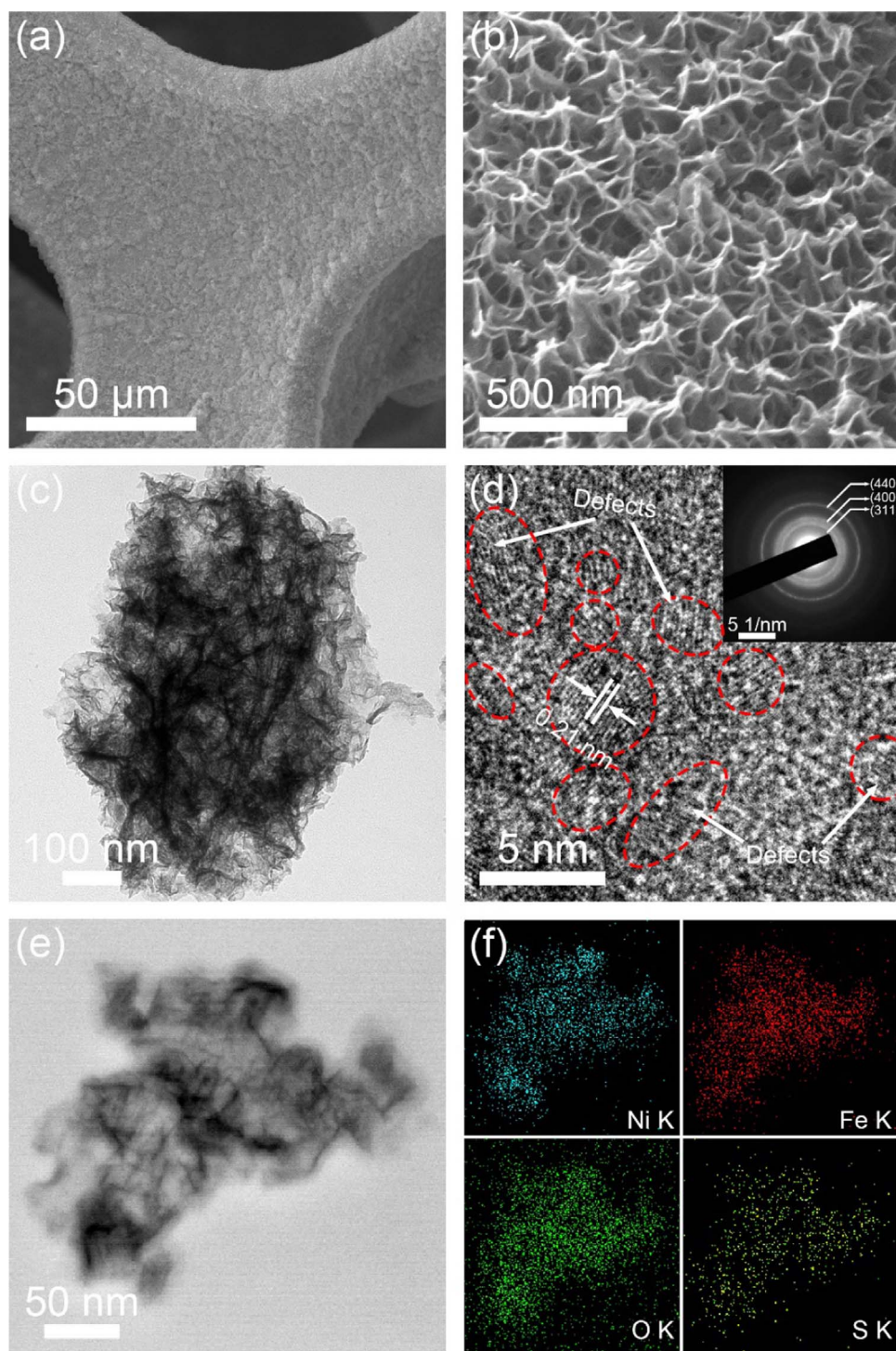
Fig. 2. Morphology and structure characterizations of S-NiFe$_2$O$_4$/NF. (a) Low magnification SEM image and (b) high magnification SEM image of S-NiFe$_2$O$_4$/NF. (c) TEM image, (d) HRTEM image (Inset: SAED of S-NiFe$_2$O$_4$ nanosheets), (e) HAADF-STEM image and (f) corresponding element mapping of S-NiFe$_2$O$_4$ nanosheets.

transmission electron microscopy (TEM) image (Fig. 2c). The high resolution TEM (HRTEM) image (Fig. 2d) demonstrates that the nanosheets were composed of interconnected nanocrystals with ultra-small sizes of ~ 2 nm, creating numerous grain boundaries between nanoparticles. Well-resolved lattice fringes show an interlayer distance of 0.21 nm, consistent with the theoretical interplanar spacing of (400) planes for spinel NiFe$_2$O$_4$. Notably, as indexed in the HRTEM image, distortions and dislocations can be observed among the crystal lattices, implying the existence of rich defects. The selected-area electron diffraction (SAED) pattern (inset in Fig. 2d) indicates the polycrystalline nature of S-NiFe$_2$O$_4$ nanosheets due to the ultra-small nanoparticle assembly. To verify the incorporation of S species and their uniform

distribution in the S-NiFe$_2$O$_4$ nanosheets, scanning TEM (STEM) equipped with energy dispersive X-ray (EDX) detector was employed to get more insightful structure information. Fig. 2e gives a typical high-angle annular dark field (HAADF) STEM image of S-NiFe$_2$O$_4$ nanosheets. Corresponding EDX mapping indicates that the Ni, Fe, O, and S elements were uniformly distributed throughout the network, suggesting the successful incorporation of S as well as the homogeneous distribution of all elements. In comparison, the as-synthesized S-NiO/NF was composed of nanosheet arrays, while massive nanosheet clusters were observed in S-Fe$_3$O$_4$/NF. Both S-NiO and S-Fe$_3$O$_4$ nanosheets consisted of a large number of nanoparticles with size of ~ 5 nm (Figs. S8 and S9 in the Supporting information). NiFe$_2$O$_4$/NF exhibited a

similar morphology to S-Fe$_3$O$_4$/NF and noticeable aggregation can be observed. Significantly, no obvious grain boundary was seen on the pure NiFe$_2$O$_4$ nanosheets, evidence of continuous crystal growth without the confinement of thiourea (Fig. S10 in the Supporting information). In addition, S-NiCo$_2$O$_4$/NF and S-CoFe$_2$O$_4$/NF were made up of well-defined nanosheets grown on NF (Fig. S11 in the Supporting information). Especially in S-NiCo$_2$O$_4$/NF, the NF was homogeneously covered by interconnected nanosheet arrays with perpendicular orientation. All these results provide strong support for the confined growth strategy and its general feasibility.

The structural information of the as-fabricated S-NiFe$_2$O$_4$ and its counterparts was investigated by X-ray diffraction (XRD, Fig. S12 in the Supporting information). Intriguingly, the XRD spectroscopy of S-NiFe$_2$O$_4$ nanosheets showed no characteristic peaks of spinel NiFe$_2$O$_4$, suggesting that the size of the primary nanoparticles is under the coherence length of the X-ray [38]. In contrast, the XRD pattern of pristine NiFe$_2$O$_4$ displayed distinct peaks which are well indexed to crystalline reflections of spinel NiFe$_2$O$_4$ (JCPDS card no. 54−0964). Evidently, the assistance of thiourea can prevent oriented crystal growth in accordance with the above analysis. Meanwhile, S-Fe$_3$O$_4$ and S-NiO showed very weak signals assigned to spinel Fe$_3$O$_4$ (JCPDS card no. 19−0629) and cubic NiO (JCPDS card no. 47−1049), respectively, indicating the presence of larger nanoparticle sizes compared to that of S-NiFe$_2$O$_4$. On the basis of the HRTEM observations and XRD patterns, it is likely that single metal ions tend to grow quickly after nucleation

during the electrodeposition, whereas mixed metal ions are inclined to rapid nucleation.

For more insight into the elemental composition and oxidation state of all samples, X-ray photoelectron spectroscopy (XPS) measurements were further performed. The XPS survey spectrum of S-NiFe$_2$O$_4$/NF (Fig. 3a) showed the presence of Ni, Fe, O, and S atoms on the surface of the nanosheets, which agrees with the element mapping results. In the Ni 2p and Fe 2p spectra of S-NiFe$_2$O$_4$/NF (Fig. 3b and c), two spin-orbit peaks, namely 2p$_{3/2}$ and 2p$_{1/2}$, accompanied with two shake-up satellites (denoted Sat.) were observed. By using a Gaussian fitting method, all spin-orbit peaks in Ni 2p and Fe 2p regions were best fitted into two characteristic peaks which were attributed to the coexistence of Ni^{2+}/Ni^{3+} and Fe^{2+}/Fe^{3+} cations [11,24,35]. For comparison, a Ni 2p XPS spectrum of bare NF was also obtained (Fig. S13 in the Supporting information). In addition to the peaks originating from oxides on the surface of bare the NF, the distinct peak located at 852.9 eV can be assigned to Ni^0 or metallic Ni [8]. This indicates that the surface oxide layer is non-uniform or too thin to completely mask the underlying metallic Ni signal. It is worth noting that no peak representing the metallic state of Ni was detected in the Ni 2p spectrum of S-NiFe$_2$O$_4$/NF [8,26], verifying the full coverage of NF by the S-NiFe$_2$O$_4$ nanosheets. The deconvolution peaks of the O 1 s spectrum are centered at 530, 531.8, and 533.2 eV (Fig. 3d), which are usually ascribed to metal-oxygen bonds, low-coordinated oxygen ions at the surface and defect sites, and adsorbed water, respectively [35].
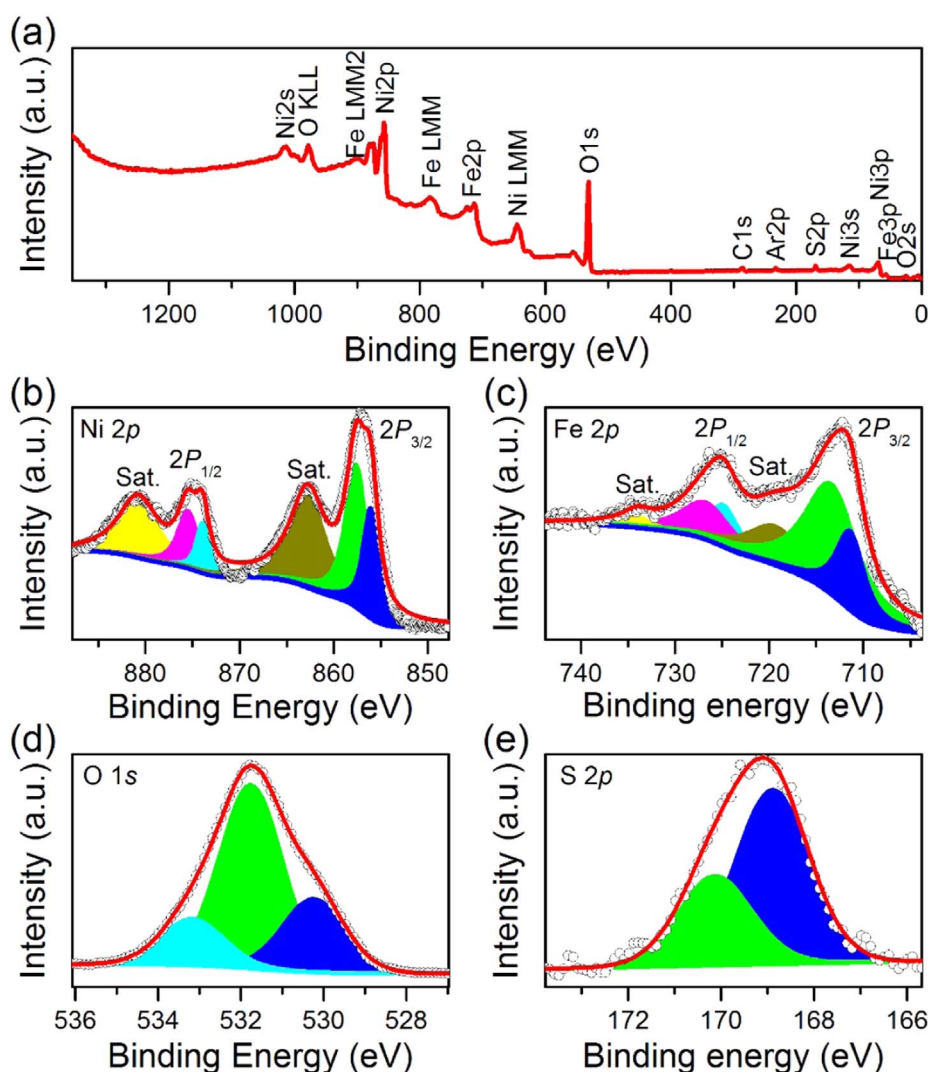

Fig. 3. Surface chemistry of S-NiFe$_2$O$_4$/NF. (a) XPS survey spectrum and high-resolution XPS spectra of (b) Ni 2p, (c) Fe 2p, (d) O 1s, and (e) S 2p of S-NiFe$_2$O$_4$/NF.
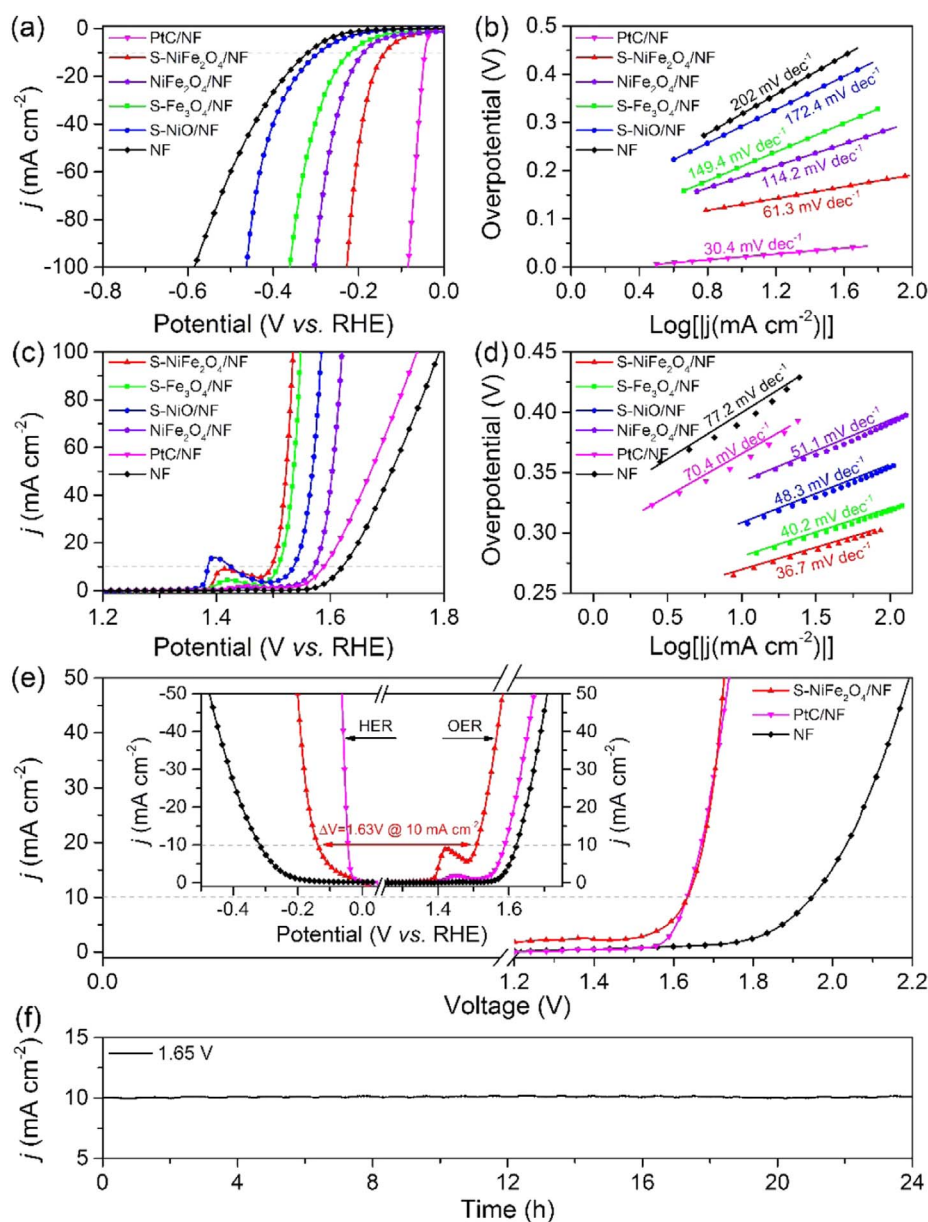
Fig. 4. Bifunctional S-NiFe₂O₄/NF for alkaline water splitting. (a) HER polarization curves and (b) corresponding HER Tafel plots, (c) OER polarization curves and (d) corresponding OER Tafel plots of S-NiFe₂O₄/NF, S-Fe₃O₄/NF, S-NiO/NF, NiFe₂O₄/NF, PtC/NF and NF in 1.0 M KOH. (e) Polarization curves of S-NiFe₂O₄/NF, PtC/NF and NF for overall alkaline water splitting in a two-electrode configuration (Inset: Polarization curves of S-NiFe₂O₄/NF, PtC/NF and NF for HER and OER from Figs. 4a and 4c). (f) Chronoamperometric curve of S-NiFe₂O₄/NF for water electrolysis in 1.0 M KOH at 1.65 V.

Similarly, the S 2p XPS spectrum was deconvoluted into two peaks at 168.9 and 170.1 eV (Fig. 3e), corresponding to metal-sulfur bonds and coordinatively unsaturated sulfur ions at the surface and defect sites, respectively [39]. In parallel, S-NiO/NF, S-Fe₃O₄/NF, and NiFe₂O₄/NF had similar oxidation states (Figs. S14–S16 in the Supporting information). Specifically, the large amount of low-coordinated oxygen and sulfur ions at the surface and defect sites may give important implications in providing abundant active sites for water splitting.

To highlight the as-prepared S-NiFe₂O₄/NF as an efficient bifunctional electrocatalyst for water splitting, S-NiFe₂O₄/NF, along with S-Fe₃O₄/NF, S-NiO/NF, NiFe₂O₄/NF, PtC/NF, and NF, were firstly investigated and compared as an integrated electrode in 1.0 M KOH using a three-electrode configuration (Fig. S17 in the Supporting information). Taking alkaline HER as a proof-of-concept, among a series of S-NiFe₂O₄/NF samples, the sample synthesized at − 1.1 V vs. Ag/AgCl for 600 s and calcinated under 250 ℃ showed the best catalytic activity and the most favorable charge transfer resistance (R_{ct}, Fig. S18 in the Supporting information). Therefore, S-NiFe₂O₄/NF refers to this sample unless otherwise noted. Fig. 4a gives the linear sweep voltammetry (LSV) curves of various samples for the HER. As expected, S-NiFe₂O₄/

NF exhibited remarkably superior HER activity with much lower onset potential and greater current density than NiFe₂O₄/NF, S-Fe₃O₄/NF, S-NiO/NF, and NF. To be specific, S-NiFe₂O₄/NF achieved an earlier onset potential of − 0.029 V vs. RHE and delivered a current density of 10 mA cm⁻² at an overpotential (η_{10}) of 138 mV, which is 50, 81, 155, and 180 mV smaller than that for NiFe₂O₄/NF, S-Fe₃O₄/NF, S-NiO/NF, and NF, respectively. More importantly, the corresponding HER Tafel plots show that S-NiFe₂O₄/NF had a Tafel slope of 61.3 mV dec⁻¹ which was much smaller than the control groups (Fig. 4b). Evidently, the lower Tafel slope of S-NiFe₂O₄/NF affords more favorable kinetics to drive a large current density towards HER at low overpotential.

At the same time, all freshly prepared samples were evaluated as catalytic electrodes for the OER. The OER polarization curves are depicted in Fig. 4c. Before the onset of OER, distinct oxidation peaks centered at 1.40 and 1.41 V vs. RHE are observed for S-NiO/NF and S-NiFe₂O₄/NF, respectively, originating from the pre-oxidation of Ni^{2+} to Ni^{3+} [40–42]. The slight positive shift of oxidation peak in S-NiFe₂O₄/NF was induced by the introduction of Fe, which is consistent with previous reports [41,42]. It is noted that S-NiO/NF featured a bigger Ni^{2+}/Ni^{3+} oxidation peak but inferior OER activity to that of S-

$NiFe_2O_4/NF$, indicating that the introduced Fe ions in spinel $NiFe_2O_4$ may serve as the main active centers for the OER. Clearly, the S-$NiFe_2O_4/NF$ electrode showed the highest OER activity among all samples. After the pre-oxidation process, the anodic current increased rapidly, generating the lowest η_{10} of 267 mV. In comparison, an η_{10} of 279, 306, 343, 359, and 392 mV was required for S-Fe_3O_4/NF, S-NiO/NF, $NiFe_2O_4/NF$, PtC/NF, and NF, respectively. Although Pt is currently an unbeatable HER electrocatalyst, the poor OER activity of Pt will definitely impair its advantage as a bifunctional electrocatalyst for overall water splitting. Similarly, the corresponding Tafel plots (Fig. 4d) indicate that S-$NiFe_2O_4/NF$ had the lowest OER Tafel slope of 36.7 mV dec^{-1}, implying appreciable kinetics for the OER. It should be mentioned that the prominent performance of S-$NiFe_2O_4/NF$ towards the HER and OER in alkaline pH is not only associated with its abundant active sites, but also closely related to the significant improvements in its conductivity that can be explained by its smaller R_{ct} (Fig. S19 in the Supporting information).

Furthermore, S-$NiFe_2O_4/NF$, PtC/NF, and NF were evaluated as bifunctional electrodes for overall water splitting in 1.0 M KOH using a two-electrode configuration (Fig. S20 in the Supporting information), and their polarization curves are presented in Fig. 4e. It can be seen that

S-$NiFe_2O_4/NF$ exhibited comparable performance to PtC/NF for alkaline water splitting under voltages less than 1.7 V, while surpasses it with further increases in cell voltage. Granted, PtC/NF achieves superior HER activity to S-$NiFe_2O_4/NF$, however, this is largely outweighed by its poor OER activity. Correspondingly, S-$NiFe_2O_4/NF$ is the superior electrode at higher voltages due to its remarkable OER activity. Theoretically, the voltage for overall water splitting in a two-electrode configuration can be calculated from the potential difference (ΔV) between HER and OER at the same current density in a three-electrode system. Taking S-$NiFe_2O_4/NF$ for example, it should require a voltage of 1.63 V to produce 10 mA cm^{-2} in 1.0 M KOH (Inset of Fig. 4e). S-$NiFe_2O_4/NF$ actually reaches 10 mA cm^{-2} at 1.65 V for overall water splitting, almost identical to the calculated value. The catalytic performance of S-$NiFe_2O_4/NF$ in alkaline electrolyte is comparable to most of the recently reported electrocatalysts under similar conditions (Tables S1–S3 in the Supporting information). To fulfil practical application, chronoamperometry was adopted to investigate the durability of S-$NiFe_2O_4/NF$. Impressively, S-$NiFe_2O_4/NF$ displays excellent stability for 24 h, achieving steady 10 mA cm^{-2} at 1.65 V with negligible decay. During the long-term stability test, H_2 and O_2 bubbles were visibly observed (see Fig. S20 and Video S1 in the
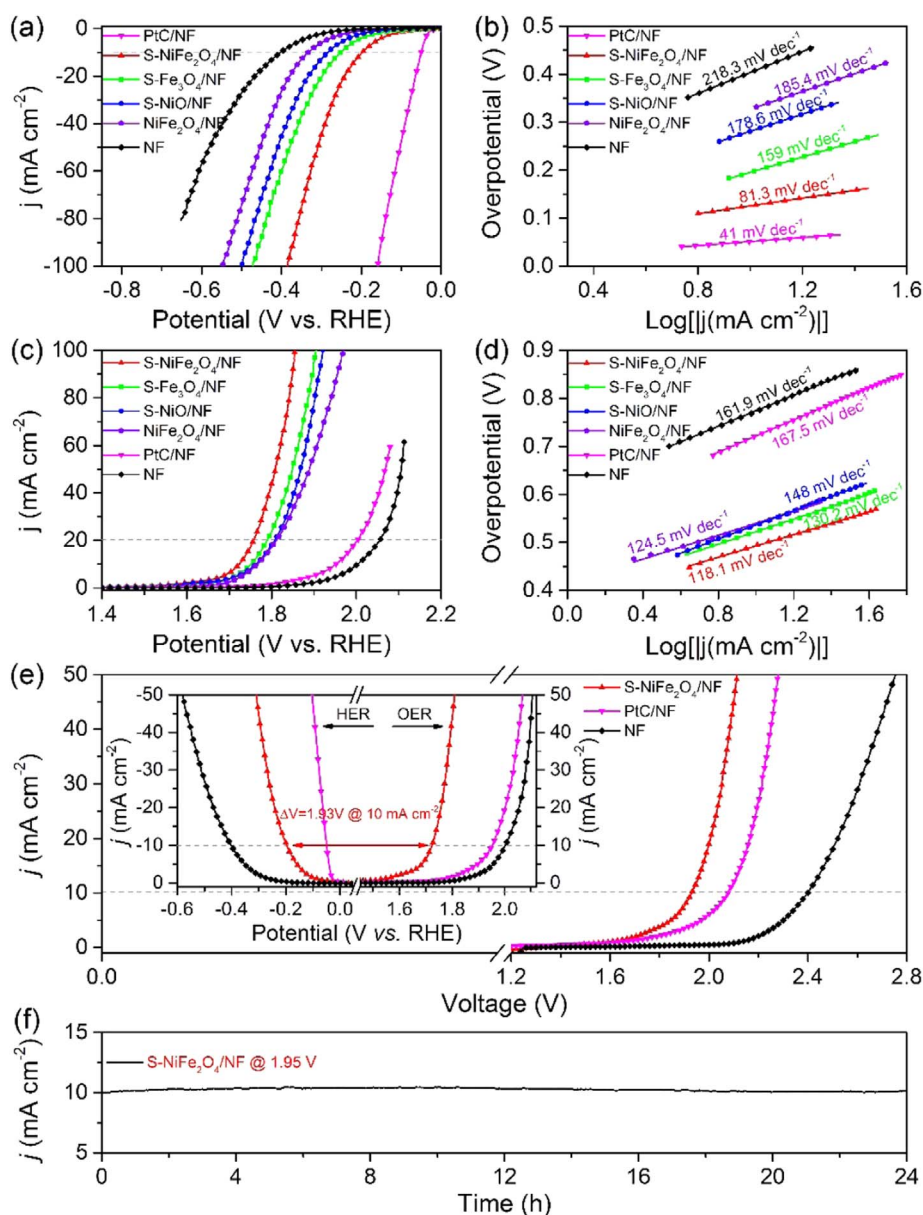
Fig. 5. Bifunctional S-$NiFe_2O_4/NF$ for neutral water splitting. (a) HER polarization curves and (b) corresponding HER Tafel plots, (c) OER polarization curves and (d) corresponding OER Tafel plots of S-$NiFe_2O_4/NF$, S-Fe_3O_4/NF, S-NiO/NF, $NiFe_2O_4/NF$, PtC/NF and NF in 1.0 M PBS. (e) Polarization curves of S-$NiFe_2O_4/NF$, PtC/NF and NF for overall neutral water splitting in a two-electrode configuration (Inset: Polarization curves of S-$NiFe_2O_4/NF$, PtC/NF and NF for HER and OER from Figs. 5a and 5c). (f) Chronoamperometric curve of S-$NiFe_2O_4/NF$ for water electrolysis in 1.0 M PBS at 1.95 V.

Supporting information). The evolved H_2 and O_2 were further assessed quantitatively using gas chromatography (GC). The generation of H_2 and O_2 over time is close to the ideal mole ratio of 2:1, reflecting a near 100% Faradaic efficiency (FE) towards H_2 and O_2 (Fig. S21 in the Supporting information). Regarding the stability of doped S, XPS was employed to analyse the S content before and after stability testing (Fig. S22 in the Supporting information). Compared to the electrode before the test, the S content of both HER and OER electrodes after long-term operation shows little decrease, demonstrating considerable stability of the doped S. These results strongly demonstrate that the as-synthesized S-NiFe$_2$O$_4$/NF is capable of promoting overall alkaline water splitting with good catalytic activity, remarkable durability, and high FE.

Supplementary material related to this article can be found online at http://dx.doi.org/10.1016/j.nanoen.2017.08.031.

Apart from alkaline water splitting, S-NiFe$_2$O$_4$/NF was also investigated and compared with its control group in neutral electrolyte to demonstrate our original intention for realistic application. As seen in Fig. 5a, all samples require higher overpotential to drive HER in 1.0 M phosphate buffer solution (PBS) with a pH of 7.4, due to the relatively impaired kinetics in neutral pH. Nevertheless, they display a similar polarization trend to that performed in alkaline solution, and S-NiFe$_2$O$_4$/NF still exhibited the best activity towards HER over its counterparts, achieving an η_{10} of 197 mV. This value is 55, 87, 136, and 206 mV lower than that of S-Fe$_3$O$_4$/NF, S-NiO/NF, NiFe$_2$O$_4$/NF, and NF, respectively. The small Tafel slope (81.3 mV dec^{-1}, Fig. 5b) and R_{ct} (6.26 Ω, Fig. S23a and b in the Supporting information) of S-NiFe$_2$O$_4$/NF enabled enhanced intrinsic activity and conductivity for better HER performance. Likewise, increased polarization towards the OER is also observed in neutral electrolyte (Fig. 5c). Yet S-NiFe$_2$O$_4$/NF retained the highest OER catalytic activity with a considerably small η_{10} of 494 mV. Note that the pre-oxidation peaks observed under alkaline condition completely disappeared in neutral electrolyte. This is likely owing to the significantly smaller OH$^-$ concentration ($\sim 1 \times 10^{-7}$ M) in neutral pH, causing less oxidation of Ni^{2+} to Ni^{3+} (generally from Ni(OH)$_2$ or NiO to NiOOH) [40,42]. Among all studied samples, S-NiFe$_2$O$_4$/NF shows the smallest Tafel slope of 118.1 mV dec^{-1} (Fig. 5d) and lowest R_{ct} of 9.85 Ω (Fig. S23c and d in the Supporting information). When using S-NiFe$_2$O$_4$/NF as a bifunctional electrocatalyst in a two-electrode configuration containing 1.0 M PBS, the neutral water splitting performance of S-NiFe$_2$O$_4$/NF outperforms that of PtC/NF and NF, in which 10 mA cm^{-2} is produced at 1.95 V, correlating significantly close to the calculated voltage of 1.93 V in a three-electrode system (Fig. 5e). Again, the electrocatalytic performance of S-NiFe$_2$O$_4$/NF are remarkable when compared with a series of recent electrocatalysts in neutral electrolytes (Tables S4–S6 in the Supporting information). Moreover, the excellent durability of S-NiFe$_2$O$_4$/NF under neutral condition is further confirmed by the steady chronoamperometric curve over 24 h at 1.95 V (Fig. 5f). Continuous gas bubbling was still observed for both the HER and OER electrodes during the test (see Video S2 in the Supporting information). According to the above results, the as-developed S-NiFe$_2$O$_4$/NF, as a bifunctional electrocatalyst for overall water splitting, is versatile in a wide pH range from alkaline to neutral.

Supplementary material related to this article can be found online at http://dx.doi.org/10.1016/j.nanoen.2017.08.031.

Based on the above results, the water splitting mechanism on the S-NiFe$_2$O$_4$/NF electrode originates from its optimized composition and well-defined 3D hierarchical structure. Firstly, as a NiFe-based composite, S-NiFe$_2$O$_4$ is intrinsically active towards the OER. The ultra-small nanoparticles with rich defects and grain boundaries can provide abundant active sites, leading to improved OER activity as well as appreciable activity for the HER. Besides, anion doping has been demonstrated to be an effective strategy for modifying the electronic structure, which is beneficial in optimizing the hydrogen adsorption energy ($|\Delta G_{H*}|$) and improving intrinsic conductivity [28,43–45]. Accordingly, the uniform S incorporation throughout the nanosheets contributes to regulating $|\Delta G_{H*}|$, making it close to zero and offering

additional active sites for the HER. Combining the significantly reduced R_{ct} and previous reports [28,45], the doped S can further improve the intrinsic conductivity of S-NiFe$_2$O$_4$ nanosheets. Secondly, the interconnected nanosheet networks create plentiful pores, enabling full access of the electrolyte to numerous active sites and thereby accelerating mass transfer, especially reactant diffusion and product transfer away from the active sites. Thirdly, the highly conductive 3D NF facilitates rapid charge transport to the S-NiFe$_2$O$_4$ nanosheets, and the porous nanosheet network further promotes the charge transfer to active sites. In addition, the robustness of the 3D NF framework and its strong interaction with S-NiFe$_2$O$_4$ nanosheets are in favor of long-term stability. Thanks to these unique physiochemical features, S-NiFe$_2$O$_4$/NF as an integrated electrode affords superior catalytic activity and durability for both alkaline and neutral water splitting.

4. Conclusions

In conclusion, a facile and reliable strategy was proposed and successfully demonstrated to synthesize S-NiFe$_2$O$_4$/NF via thiourea-assisted electrodeposition and subsequent low-temperature calcination. Benefitting from the rationally designed 3D hierarchical structure and optimized composition with favorable conductivity, the as-synthesized S-NiFe$_2$O$_4$/NF as an integrated bifunctional electrode exhibited fascinating catalytic properties for both the HER and OER, achieving 10 mA cm^{-2} for overall alkaline and neutral water splitting at a cell voltage of 1.65 and 1.95 V, respectively. The excellent catalytic activity, remarkable stability, and facile synthesis technique make S-NiFe$_2$O$_4$/NF one of the most promising bifunctional electrocatalysts for overall water splitting, especially under neutral conditions. The strategy developed in this work can be extended to other mixed transition metal oxides with similar structure, and may be extended to other applications such as supercapacitors, metal-air batteries, and photocatalysis.

Acknowledgements

Appendix A. Supplementary material

Supplementary data associated with this article can be found in the online version at http://dx.doi.org/10.1016/j.nanoen.2017.08.031.

References

[1] J.A. Turner, Sustainable hydrogen production, Science 305 (2004) 972–974.
[2] S. Singh, S. Jain, V. Ps, A.K. Tiwari, M.R. Nouni, J.K. Pandey, S. Goel, Hydrogen: a sustainable fuel for future of the transport sector, Renew. Sustain. Energy Rev. 51 (2015) 623–633.
[3] R. Eisenberg, Rethinking water splitting, Science 324 (2009) 44–45.
[4] M.S. Faber, S. Jin, Earth-abundant inorganic electrocatalysts and their nanostructures for energy conversion applications, Energy Environ. Sci. 7 (11) (2014) 3519–3542.
[5] X. Zou, Y. Zhang, Noble metal-free hydrogen evolution catalysts for water splitting, Chem. Soc. Rev. 44 (2015) 5148–5180.
[6] I. Roger, M.A. Shipman, M.D. Symes, Earth-abundant catalysts for electrochemical and photoelectrochemical water splitting, Nat. Rev. Chem. 1 (2017) 0003.
[7] X. Wang, R. Su, H. Aslan, J. Kibsgaard, S. Wendt, L. Meng, M. Dong, Y. Huang, F. Besenbacher, Tweaking the composition of NiMoZn alloy electrocatalyst for enhanced hydrogen evolution reaction performance, Nano Energy 12 (2015) 9–18.
[8] Y. Yang, Z. Lin, S. Gao, J. Su, Z. Lun, G. Xia, J. Chen, R. Zhang, Q. Chen, Tuning electronic structures of nonprecious ternary alloys encapsulated in graphene layers for optimizing overall water splitting activity, ACS Catal. 7 (2017) 469–479.
[9] M. Zeng, Y. Chen, J. Li, H. Xue, R.G. Mendes, J. Liu, T. Zhang, M.H. Rümmeli, L. Fu, 2D WC single crystal embedded in graphene for enhancing hydrogen evolution reaction, Nano Energy 33 (2017) 356–362.
[10] J. Zhu, K. Sakaushi, G. Clavel, M. Shalom, M. Antonietti, T.P. Fellinger, A general salt-templating method to fabricate vertically aligned graphitic carbon nanosheets

and their metal carbide hybrids for superior lithium ion batteries and water splitting, J. Am. Chem. Soc. 137 (2015) 5480–5485.

[11] B. Zhang, C. Xiao, S. Xie, J. Liang, X. Chen, Y. Tang, Iron–nickel nitride nanostructures in situ grown on surface-redox-etching nickel foam: efficient and ultra-sustainable electrocatalysts for overall water splitting, Chem. Mater. 28 (2016) 6934–6941.

[12] Y. Wang, D. Liu, Z. Liu, C. Xie, J. Huo, S. Wang, Porous cobalt-iron nitride nanowires as excellent bifunctional electrocatalysts for overall water splitting, Chem. Commun. 52 (2016) 12614–12617.

[13] G. Ou, P. Fan, H. Zhang, K. Huang, C. Yang, W. Yu, H. Wei, M. Zhong, H. Wu, Y. Li, Large-scale hierarchical oxide nanostructures for high-performance electrocatalytic water splitting, Nano Energy 35 (2017) 207–214.

[14] X. Gao, H. Zhang, Q. Li, X. Yu, Z. Hong, X. Zhang, C. Liang, Z. Lin, Hierarchical $NiCo_2O_4$ hollow microcuboids as bifunctional electrocatalysts for overall water-splitting, Angew. Chem. Int. Ed. 55 (2016) 6290–6294.

[15] D.H. Ha, B. Han, M. Risch, L. Giordano, K.P.C. Yao, P. Karayaylali, Y. Shao-Horn, Activity and stability of cobalt phosphides for hydrogen evolution upon water splitting, Nano Energy 29 (2016) 37–45.

[16] Z. Huang, Z. Chen, Z. Chen, C. Lv, M.G. Humphrey, C. Zhang, Cobalt phosphide nanorods as an efficient electrocatalyst for the hydrogen evolution reaction, Nano Energy 9 (2014) 373–382.

[17] B. Konkena, J. Masa, W. Xia, M. Muhler, W. Schuhmann, MoSSe@reduced graphene oxide nanocomposite heterostructures as efficient and stable electrocatalysts for the hydrogen evolution reaction, Nano Energy 11 (2015) 46–53.

[18] M.R. Gao, J.X. Liang, Y.R. Zheng, Y.F. Xu, J. Jiang, Q. Gao, J. Li, S.H. Yu, An efficient molybdenum disulfide/cobalt diselenide hybrid catalyst for electrochemical hydrogen generation, Nat. Commun. 6 (2015) 5982.

[19] C.C.L. McCrory, S. Jung, J.C. Peters, T.F. Jaramillo, Benchmarking heterogeneous electrocatalysts for the oxygen evolution reaction, J. Am. Chem. Soc. 135 (2013) 16977–16987.

[20] J. Miao, F.X. Xiao, H.B. Yang, S.Y. Khoo, J. Chen, Z. Fan, Y.Y. Hsu, H.M. Chen, H. Zhang, B. Liu, Hierarchical Ni-Mo-S nanosheets on carbon fiber cloth: a flexible electrode for efficient hydrogen generation in neutral electrolyte, Sci. Adv. 1 (2015) 1500259.

[21] S.H. Ahn, A. Manthiram, Direct growth of ternary Ni-Fe-P porous nanorods onto nickel foam as a highly active, robust bi-functional electrocatalyst for overall water splitting, J. Mater. Chem. A 5 (2017) 2496–2503.

[22] K. Li, J. Zhang, R. Wu, Y. Yu, B. Zhang, Anchoring CoO domains on $CoSe_2$ nanobelts as bifunctional electrocatalysts for overall water splitting in neutral media, Adv. Sci. 3 (2016) 1500426.

[23] M. Gong, H. Dai, A mini review of NiFe-based materials as highly active oxygen evolution reaction electrocatalysts, Nano Res. 8 (2015) 23–39.

[24] X. Long, G. Li, Z. Wang, H. Zhu, T. Zhang, S. Xiao, W. Guo, S. Yang, Metallic iron–nickel sulfide ultrathin nanosheets as a highly active electrocatalyst for hydrogen evolution reaction in acidic media, J. Am. Chem. Soc. 137 (2015) 11900–11903.

[25] H. Wang, H.W. Lee, Y. Deng, Z. Lu, P.C. Hsu, Y. Liu, D. Lin, Y. Cui, Bifunctional non-noble metal oxide nanoparticle electrocatalysts through lithium-induced conversion for overall water splitting, Nat. Commun. 6 (2015) 7261.

[26] X. Zhang, H. Xu, X. Li, Y. Li, T. Yang, Y. Liang, Facile synthesis of nickel–iron/nanocarbon hybrids as advanced electrocatalysts for efficient water splitting, ACS Catal. 6 (2016) 580–588.

[27] Z.W. Seh, J. Kibsgaard, C.F. Dickens, I. Chorkendorff, J.K. Nørskov, T.F. Jaramillo, Combining theory and experiment in electrocatalysis: insights into materials design, Science 355 (2017) 4998.

[28] J. Xie, J. Zhang, S. Li, F. Grote, X. Zhang, H. Zhang, R. Wang, Y. Lei, B. Pan, Y. Xie, Controllable disorder engineering in oxygen-incorporated MoS_2 ultrathin nanosheets for efficient hydrogen evolution, J. Am. Chem. Soc. 135 (2013) 17881–17888.

[29] P. Chen, K. Xu, S. Tao, T. Zhou, Y. Tong, H. Ding, L. Zhang, W. Chu, C. Wu, Y. Xie, Phase-transformation engineering in cobalt diselenide realizing enhanced catalytic activity for hydrogen evolution in an alkaline medium, Adv. Mater. 28 (2016) 7527–7532.

[30] J. Wang, L. Ji, Z. Chen, In situ rapid formation of a nickel–iron-based electrocatalyst for water oxidation, ACS Catal. 6 (2016) 6987–6992.

[31] L.L. Feng, G. Yu, Y. Wu, G.D. Li, H. Li, Y. Sun, T. Asefa, W. Chen, X. Zou, High-index faceted Ni_3S_2 nanosheet arrays as highly active and ultrastable electrocatalysts for water splitting, J. Am. Chem. Soc. 137 (2015) 14023–14026.

[32] X. Zou, X. Huang, A. Goswami, R. Silva, B.R. Sathe, E. Mikmeková, T. Asefa, Cobalt-embedded nitrogen-rich carbon nanotubes efficiently catalyze hydrogen evolution reaction at all pH values, Angew. Chem. 126 (2014) 4461–4465.

[33] K. Xu, H. Cheng, L. Liu, H. Lv, X. Wu, C. Wu, Y. Xie, Promoting active species generation by electrochemical activation in alkaline media for efficient electrocatalytic oxygen evolution in neutral media, Nano Lett. 17 (2017) 578–583.

[34] P.K. Ng, E.W. Schneider, Distribution of nickel hydroxide in sintered nickel plaques measured by radiotracer method during electroimpregnation, J. Electrochem. Soc. 133 (1986) 17–21.

[35] C. Yuan, J. Li, L. Hou, X. Zhang, L. Shen, X.W. Lou, Ultrathin mesoporous $NiCo_2O_4$ nanosheets supported on Ni foam as advanced electrodes for supercapacitors, Adv. Funct. Mater. 22 (2012) 4592–4597.

[36] J. Xie, H. Zhang, S. Li, R. Wang, X. Sun, M. Zhou, J. Zhou, X.W. Lou, Y. Xie, Defect-rich MoS_2 ultrathin nanosheets with additional active edge sites for enhanced electrocatalytic hydrogen evolution, Adv. Mater. 25 (2013) 5807–5813.

[37] H. Sun, D. Qin, S. Huang, X. Guo, D. Li, Y. Luo, Q. Meng, Dye-sensitized solar cells with NiS counter electrodes electrodeposited by a potential reversal technique, Energy Environ. Sci. 4 (2011) 2630–2637.

[38] P. Poizot, S. Laruelle, S. Grugeon, L. Dupont, J.M. Tarascon, Nano-sized transition-metal oxides as negative-electrode materials for lithium-ion batteries, Nature 407 (2000) 496–499.

[39] H. Chen, J. Jiang, L. Zhang, H. Wan, T. Qi, D. Xia, Highly conductive $NiCo_2S_4$ urchin-like nanostructures for high-rate pseudocapacitors, Nanoscale 5 (2013) 8879–8883.

[40] R.D.L. Smith, M.S. Prévot, R.D. Fagan, S. Trudel, C.P. Berlinguette, Water oxidation catalysis: electrocatalytic response to metal stoichiometry in amorphous metal oxide films containing iron, cobalt, and nickel, J. Am. Chem. Soc. 135 (2013) 11580–11586.

[41] J.Y.C. Chen, L. Dang, H. Liang, W. Bi, J.B. Gerken, S. Jin, E.E. Alp, S.S. Stahl, Operando analysis of NiFe and Fe oxyhydroxide electrocatalysts for water oxidation: detection of Fe^{4+} by Mössbauer spectroscopy, J. Am. Chem. Soc. 137 (2015) 15090–15093.

[42] M. Görlin, P. Chernev, J. Ferreira de Araújo, T. Reier, S. Dresp, B. Paul, R. Krähnert, H. Dau, P. Strasser, Oxygen evolution reaction dynamics, Faradaic charge efficiency, and the active metal redox states of Ni–Fe oxide water splitting electrocatalysts, J. Am. Chem. Soc. 138 (2016) 5603–5614.

[43] Q. Gong, L. Cheng, C. Liu, M. Zhang, Q. Feng, H. Ye, M. Zeng, L. Xie, Z. Liu, Y. Li, Ultrathin $MoS_{2(1-x)}Se_{2x}$ alloy nanoflakes for electrocatalytic hydrogen evolution reaction, ACS Catal. 5 (2015) 2213–2219.

[44] J. Zhuo, M. Cabán-Acevedo, H. Liang, L. Samad, Q. Ding, Y. Fu, M. Li, S. Jin, High-performance electrocatalysis for hydrogen evolution reaction using Se-doped pyrite-phase nickel diphosphide nanostructures, ACS Catal. 5 (2015) 6355–6361.

[45] K. Wang, C. Zhou, D. Xi, Z. Shi, C. He, H. Xia, G. Liu, G. Qiao, Component-controllable synthesis of $Co(S_xSe_{1-x})_2$ nanowires supported by carbon fiber paper as high-performance electrode for hydrogen evolution reaction, Nano Energy 18 (2015) 1–11.

Jinlong Liu received his BE and ME degrees in Applied Chemistry from Central South University in 2011 and 2014, respectively. He is currently a Ph.D. candidate in Chemical Engineering under the supervision of Prof. Shi-Zhang Qiao at The University of Adelaide. His current research is focused on the design and synthesis of functional materials for energy storage and catalysis.
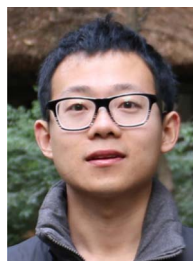
Dongdong Zhu received his BE and ME degrees in Materials Science and Engineering and Materials Science and Engineering from Nanjing University of Science and Technology in 2011 and 2014, respectively. He is currently a Ph.D. candidate in Chemical Engineering under the supervision of Professor Shi-Zhang Qiao at The University of Adelaide. His current research is focused on the development of nanostructured materials for electrocatalysis.

Tao Ling received her Ph.D. degree in Materials Science and Engineering from Tsinghua University, China in 2009. She was a visiting scholar in The University of Adelaide, Australia from 2015 to 2016. Now she is an associate professor in School of Materials Science and Engineering, Tianjin University, China. Her research focuses on developing newly catalytic materials for sustainable clean energy generation and conversion (electrocatalysis, photocatalysis, and photoelectrocatalysis).

Anthony Vasileff is a Ph.D. candidate in the School of Chemical Engineering at The University of Adelaide. Anthony received his Bachelor's degree in Chemical Engineering at The University of Adelaide. His graduate research is focused on developing novel non-metal electrocatalysts and supports, particularly nanostructured carbon, for electrochemical processes. Currently, he is working on developing new nanomaterials for carbon dioxide reduction in order to advance clean energy storage technologies.

Shi-Zhang Qiao is currently a Chair Professor at the School of Chemical Engineering of the University of Adelaide, Australia. His research expertise is in nanomaterials for new energy technologies (electrocatalysis, photocatalysis, batteries, fuel cell, supercapacitors). He has co-authored more than 300 papers in refereed journals with over 23,000 citations and h-index ~ 80.

140

S-NiFe$_2$O$_4$ ultra-small nanoparticle built nanosheets for efficient water splitting in alkaline and neutral pH

Jinlong Liu[a], Dongdong Zhu[a], Tao Ling[b], Anthony Vasileff[a], and Shi-Zhang Qiao[a,b,*]

[a] School of Chemical Engineering, The University of Adelaide, Adelaide, SA 5005, Australia

[b] School of Materials Science and Engineering, Tianjin University, Tianjin, 300072, P.R. China

Corresponding Author: Shi-Zhang Qiao, E-mail address: s.qiao@adelaide.edu.au

I. Supplementary Results
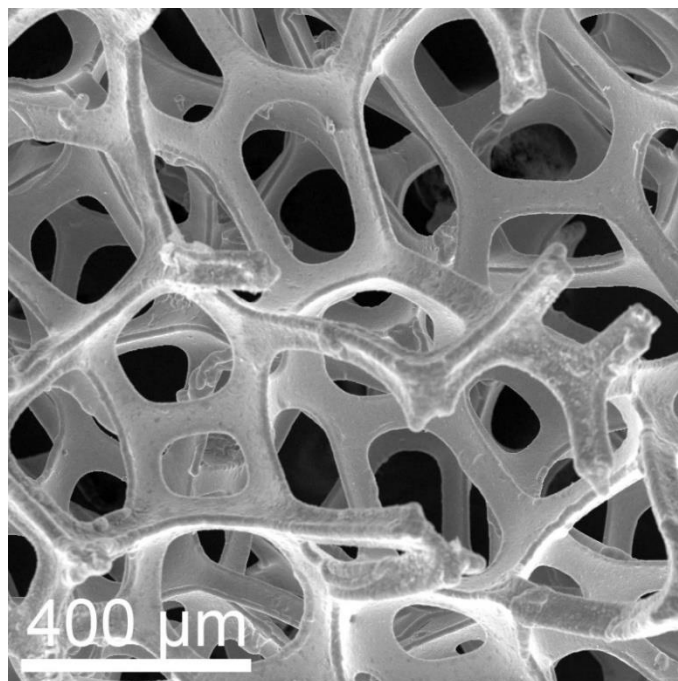
Fig. S1. SEM image of nickel foam (NF) cleaned by 3 M HCl, ethanol, and water sequentially.
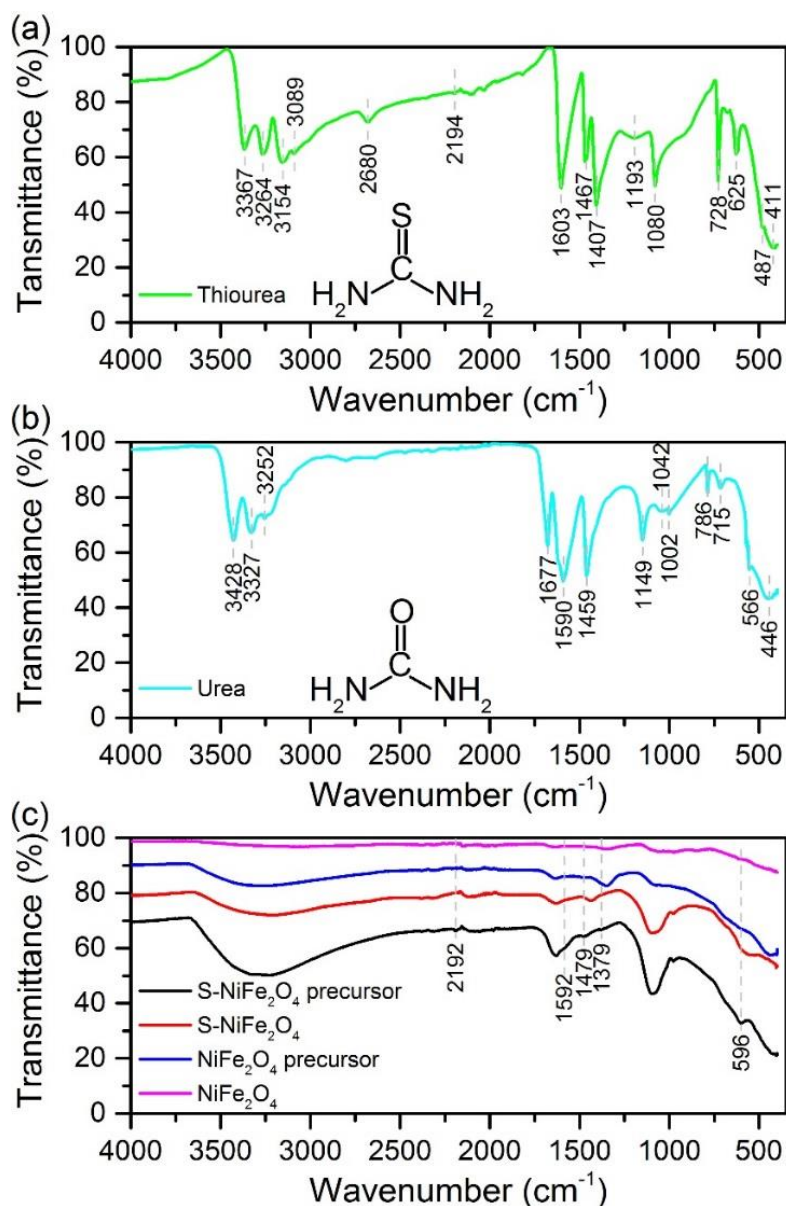
Fig. S2. Fourier transform infrared (FTIR) spectra of (a) thiourea, (b) urea, (c) S-NiFe$_2$O$_4$ precursor, S-NiFe$_2$O$_4$, NiFe$_2$O$_4$ precursor and S-NiFe$_2$O$_4$.

As can be seen in the FTIR spectrum of S-NiFe$_2$O$_4$ precursor, the exclusive vibration bands at 1592, 1479, 1379 and 596 cm^{-1} can be assigned to the in-plane bending of the −NH$_2$ groups (i.e. δ(NH$_2$)), the asymmetric stretching of C−N and/or symmetric twisting of N−C−N (i.e. v_a(CN) and/or γ_s(N−C−N)), the asymmetric twisting of C=S (i.e. γ_{as}(C=S)), and the scissoring of N−C−N and/or the symmetric in-plane bending of C=O (i.e. π(N−C−N) and/or δ_s(C=O)), respectively, indicating the presence of thiourea and urea in the S-NiFe$_2$O$_4$ precursor.[1,2] Besides, the vibration band observed at 2192 cm^{-1} can be correlated with the twisting of N=C=S (i.e. γ(N=C=S)) in the

thiourea molecule,[2] and the significantly intensified absorption around 3300 cm^{-1} for the S-NiFe$_2$O$_4$ precursor should be attributed to the stretching and twisting of abundant −NH$_2$ groups (i.e. ν(NH$_2$) and γ(NH$_2$)).[1,2] By contrast, no characteristic absorption bands associated with thiourea and urea were found in the NiFe$_2$O$_4$ precursor, NiFe$_2$O$_4$ and S-NiFe$_2$O$_4$. This evidence suggests that the added thiourea and generated urea could co-deposit with Ni^{2+} and Fe^{3+} as coordination agents, and they can be removed completely by thermal decomposition under low-temperature calcination.
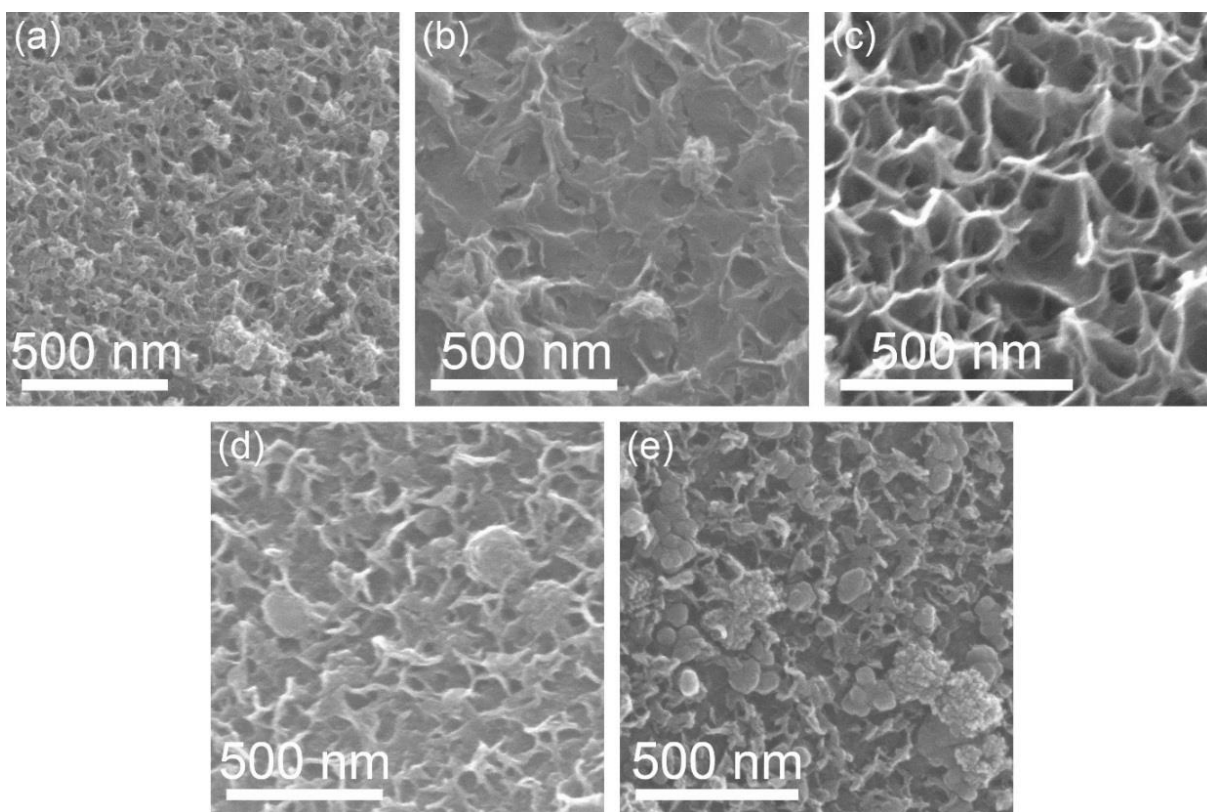
Fig. S3. SEM images of S-NiFe$_2$O$_4$/NF synthesized at different applied potentials for 600 s: (a) −0.9 V, (b) −1 V, (c) −1.1 V, (d) −1.2 V, (e) −1.4 V vs. Ag/AgCl.

Under relatively high applied potential, the fast nucleation resulted in dense small S-NiFe$_2$O$_4$ nanosheets. While with more negative applied potential, the substantial hydroxide ions resulted in rapid growth of NiFe-precursor nanoparticles, leading to the appearance of S-NiFe$_2$O$_4$ nanoparticles among the nanosheet architect, and even the severe aggregation of S-NiFe$_2$O$_4$ nanoparticles. Only at moderate applied potentials, a compromise between nucleation and crystal growth can be achieved to generate well-defined S-NiFe$_2$O$_4$ nanosheets with porous structure.
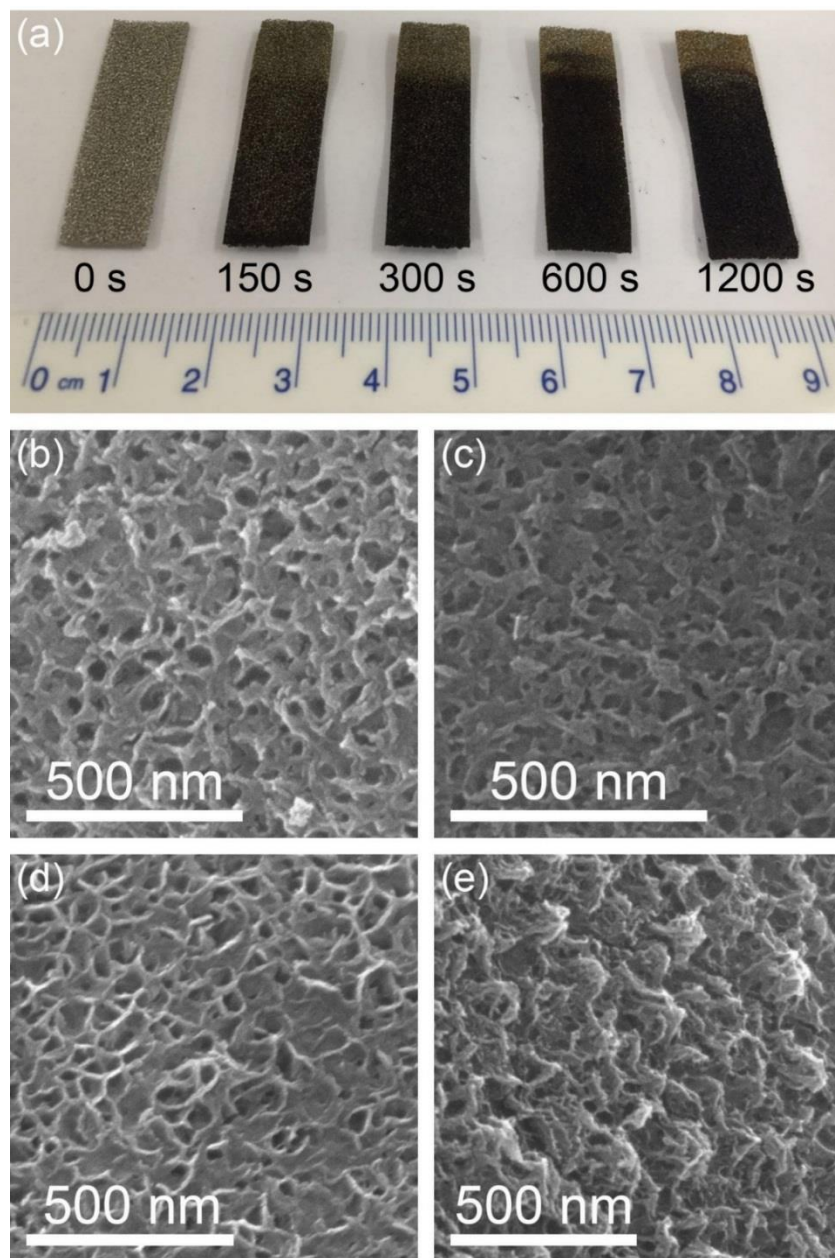
Fig. S4. (a) Optical image of typical NF and S-NiFe$_2$O$_4$/NF electrode synthesized at −1.1 V vs. Ag/AgCl for different electrodeposition time, and SEM images of S-NiFe$_2$O$_4$/NF synthesized at −1.1 V vs. Ag/AgCl for (b) 150 s, (c) 300 s, (d) 600 s, (e) 1200s.

When the electrodeposition time is too short, the NF can hardly be completely covered by S-NiFe$_2$O$_4$ nanosheets. With prolonged reaction time, excessive electrodeposition occurred in the pores of S-NiFe$_2$O$_4$ nanosheets, ruining the porous structure. Therefore, both situations resulted in adverse effects on catalytic activity and stability.
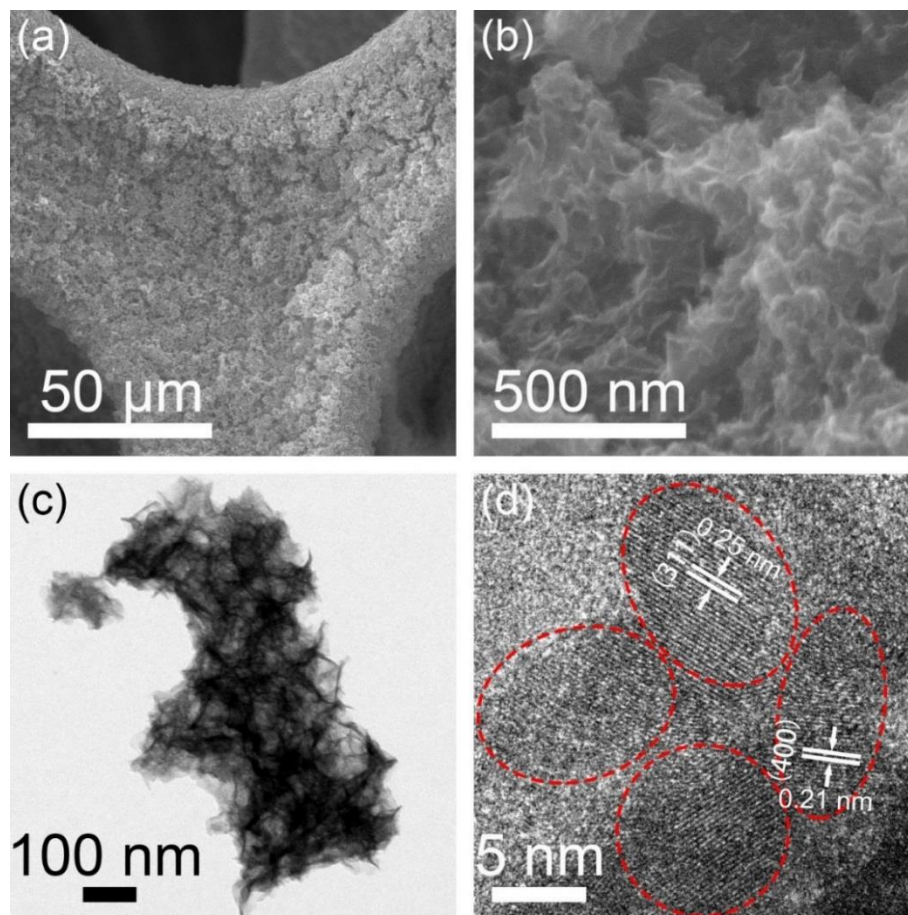
Fig. S5. (a) Low magnification SEM and (b) high magnification SEM images of S-NiFe$_2$O$_4$/NF calcinated at 400 ºC for 2 h. (c) TEM and (d) HRTEM images of corresponding S-NiFe$_2$O$_4$ nanosheets.

Due to the higher temperature, the S-NiFe$_2$O$_4$/NF calcinated at 400 ºC suffers evident structural shrinkage and the primary nanoparticle grows to about 10 nm with less grain boundaries and improved crystallinity, compared with S-NiFe$_2$O$_4$/NF obtained at 250 ºC. Further, the interplanar distances of 0.21 and 0.25 nm corresponded well to the (400) and (311) planes of spinel NiFe$_2$O$_4$ (JCPDS card No. 54−0964).
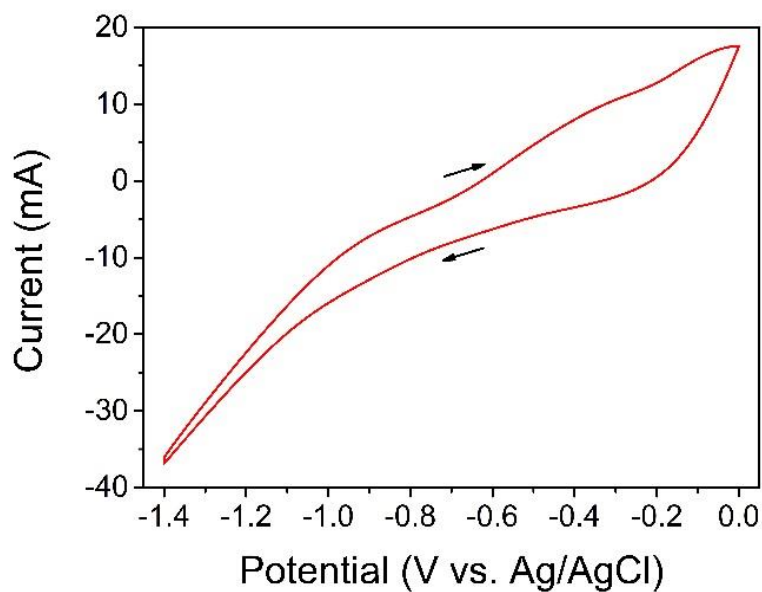
Fig. S6. Cyclic voltammetry (CV) curve of the typical electrodeposition system in aqueous electrolyte containing 10 mM $Ni(NO_3)_2$, 20 mM $Fe(NO_3)_3$ and 0.6 M thiourea.
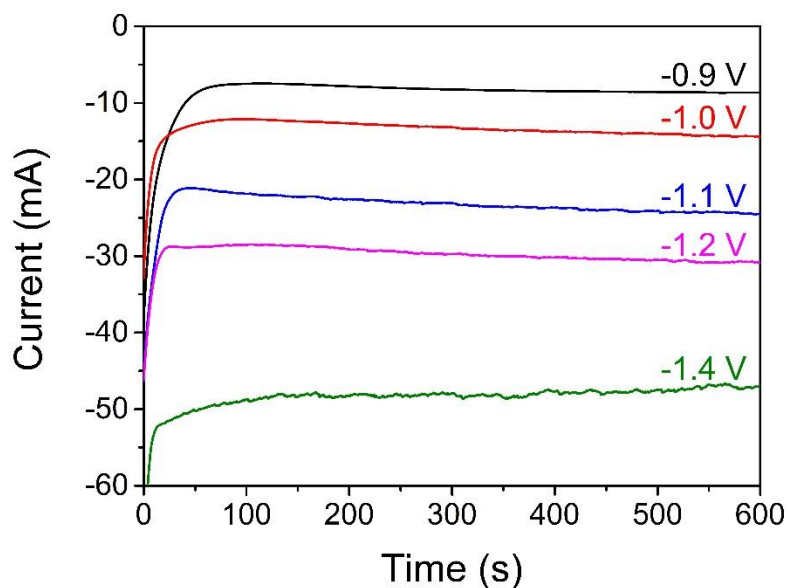
Fig. S7. I-t curves of $S-NiFe_2O_4/NF$ during the electrodeposition under different applied potentials (vs. Ag/AgCl) for 600 s.
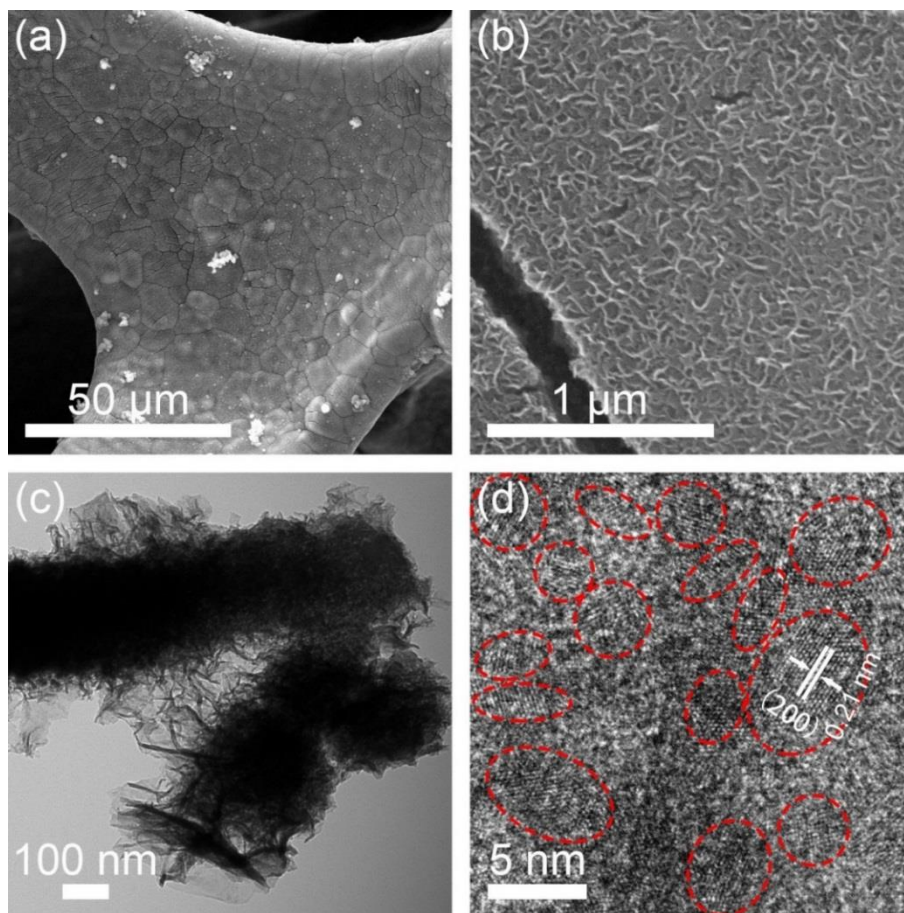
Fig. S8. (a) Low magnification SEM and (b) high magnification SEM images of S-NiO/NF. (c) TEM and (d) HRTEM images S-NiO nanosheets.
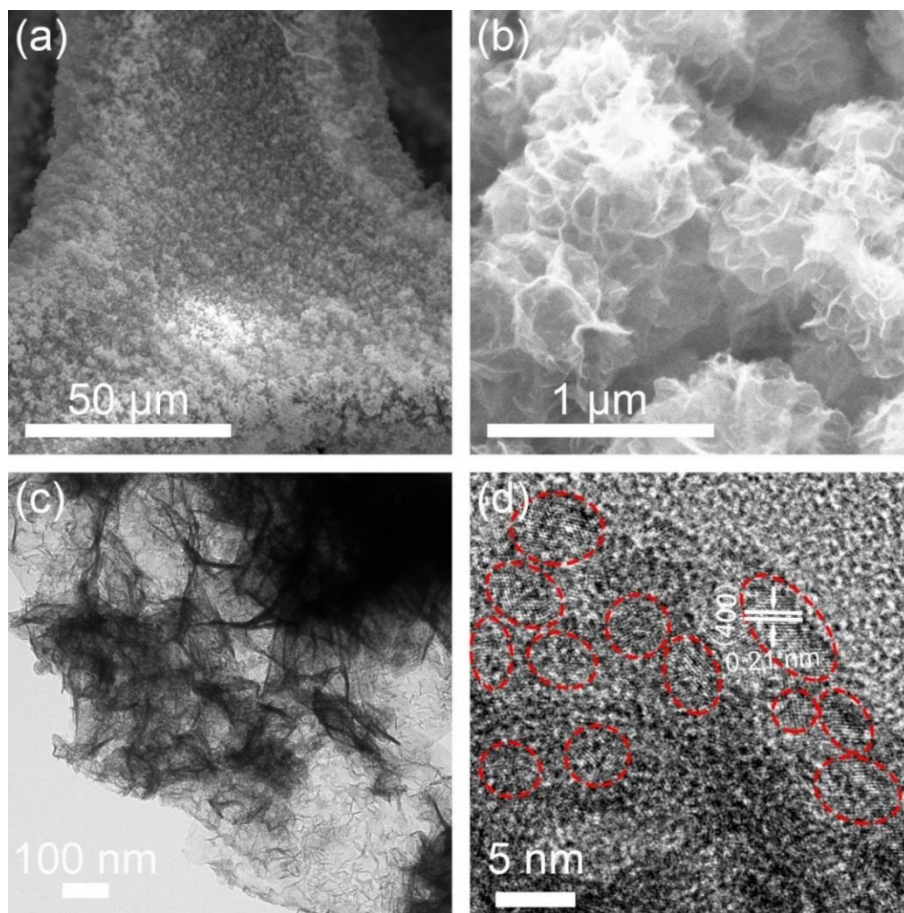
Fig. S9. (a) Low magnification SEM and (b) high magnification SEM images of S-Fe$_3$O$_4$/NF. (c) TEM and (d) HRTEM images of S-Fe$_3$O$_4$ nanosheets.
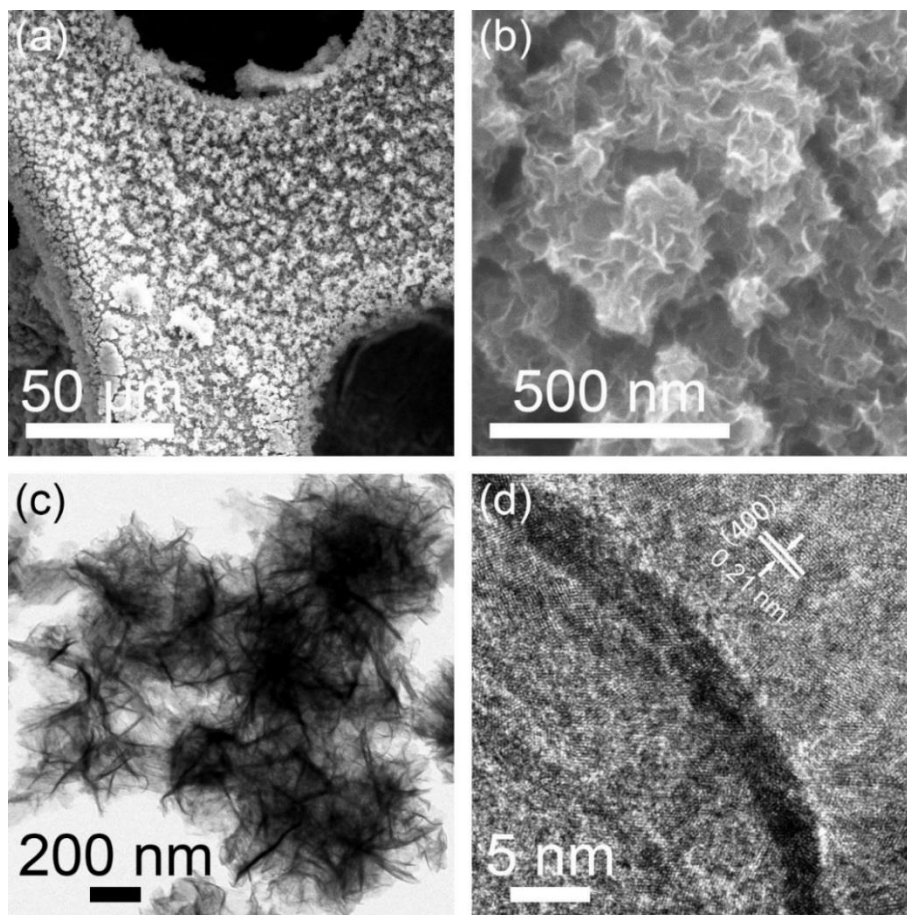
Fig. S10. (a) Low magnification SEM and (b) high magnification SEM images of NiFe$_2$O$_4$/NF. (c) TEM and (d) HRTEM images of pristine NiFe$_2$O$_4$ nanosheets.
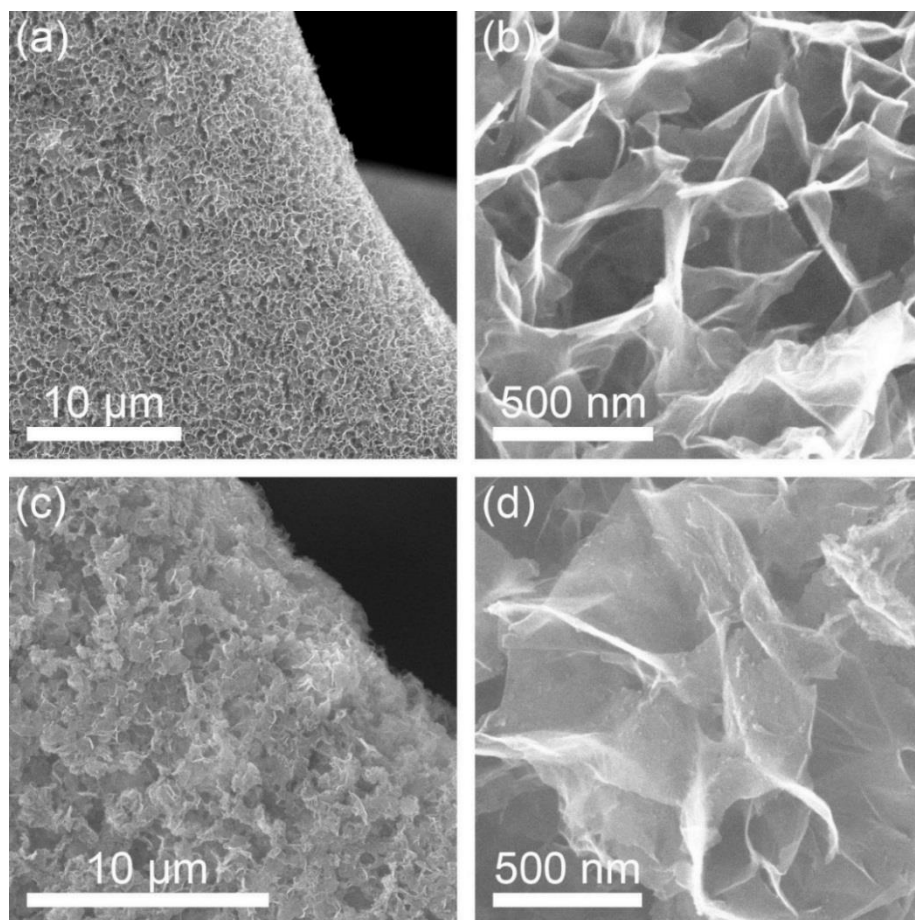
Fig. S11. (a) Low magnification SEM and (b) high magnification SEM images of S-NiCo$_2$O$_4$/NF.
(c) Low magnification SEM and (d) high magnification SEM images of S-CoFe$_2$O$_4$/NF.
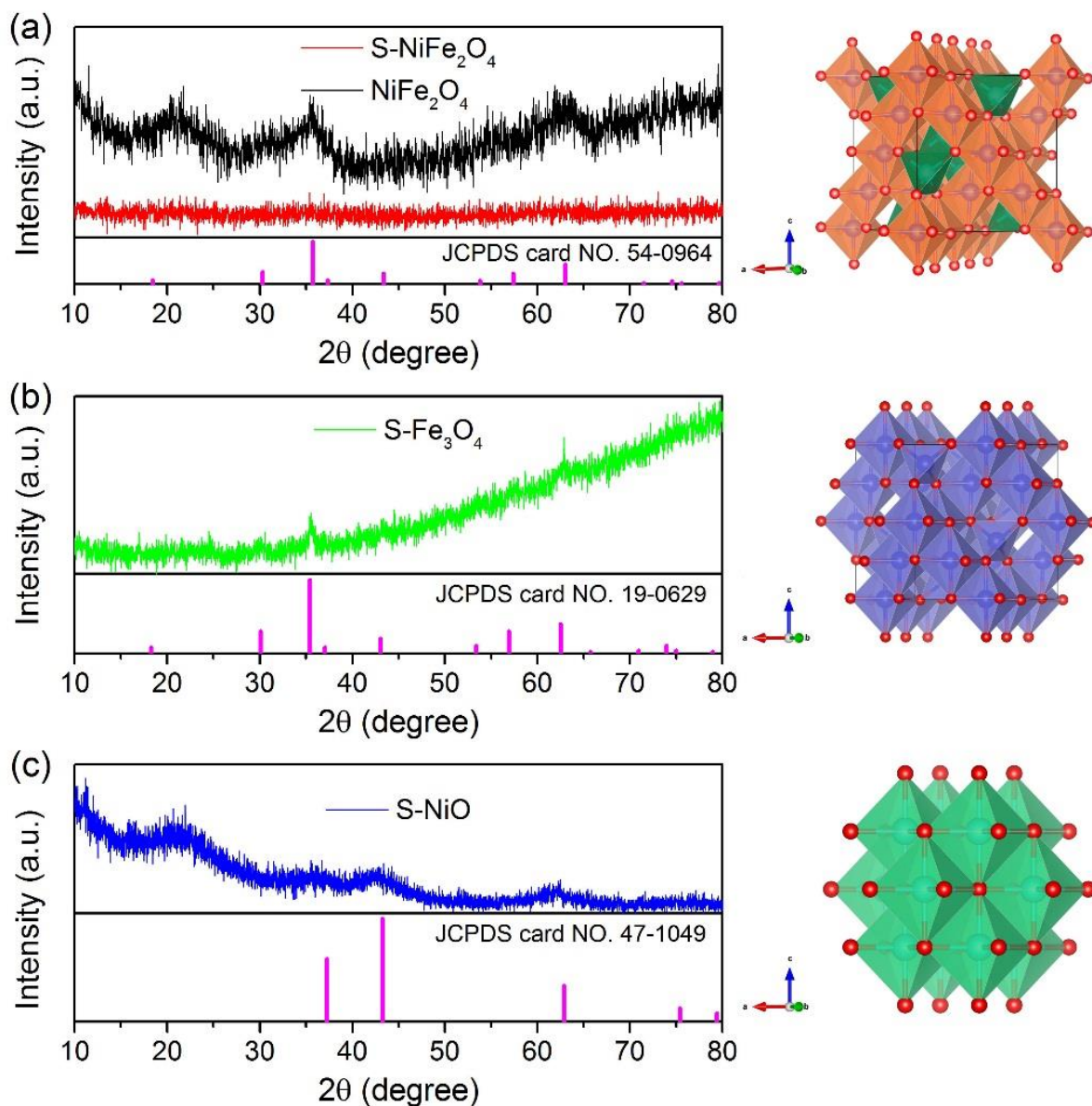
Fig. S12. (a) XRD spectra of S-NiFe₂O₄ (red) and pristine NiFe₂O₄ (black) with standard XRD pattern of spinel NiFe₂O₄ (JCPDS card No. 54−0964) and corresponding unit cell. (b) XRD spectrum of S-Fe₃O₄ (green) with standard XRD pattern of spinel Fe₃O₄ (JCPDS card No. 19−0629) and corresponding unit cell. (c) XRD spectrum of S-NiO (blue) with standard XRD pattern of cubic NiO (JCPDS card No. 47−1049) and corresponding unit cell.
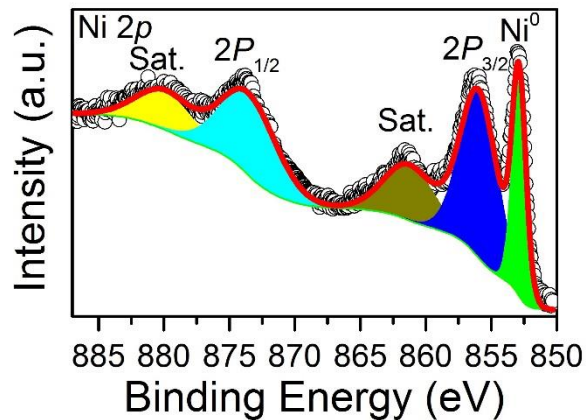
Fig. S13. High-resolution XPS spectrum of Ni 2p of bare NF.
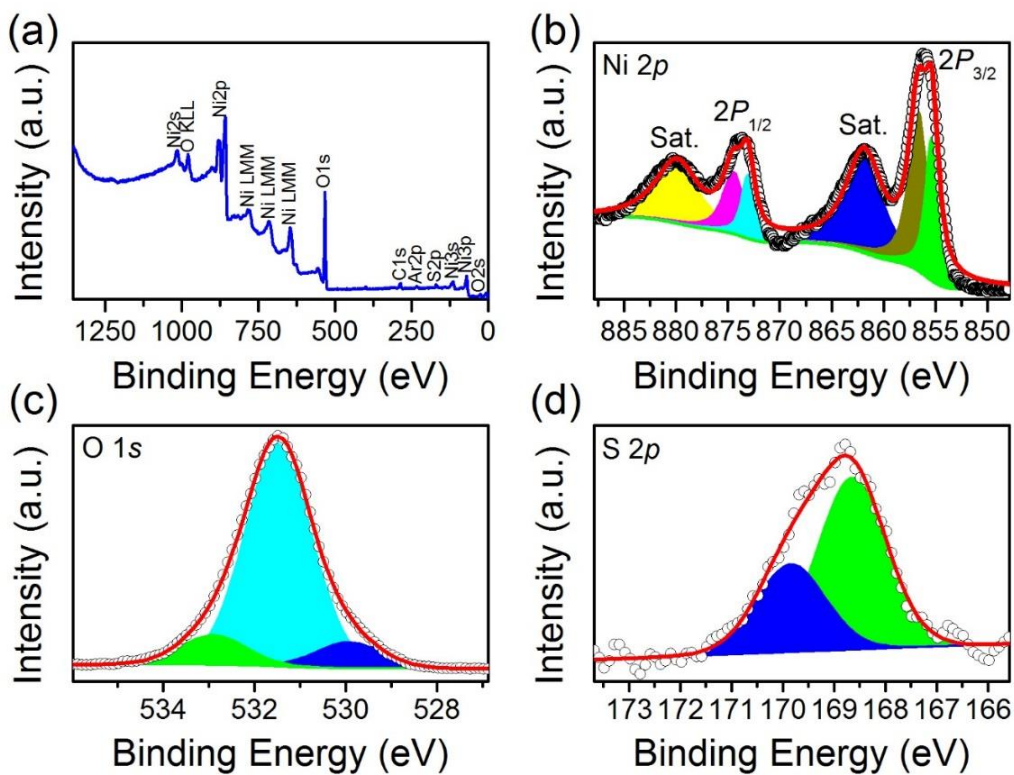
Fig. S14. (a) XPS survey spectrum and high-resolution XPS spectra of (b) Ni 2p, (c) O 1s, and (d) S 2p of S-NiO/NF.
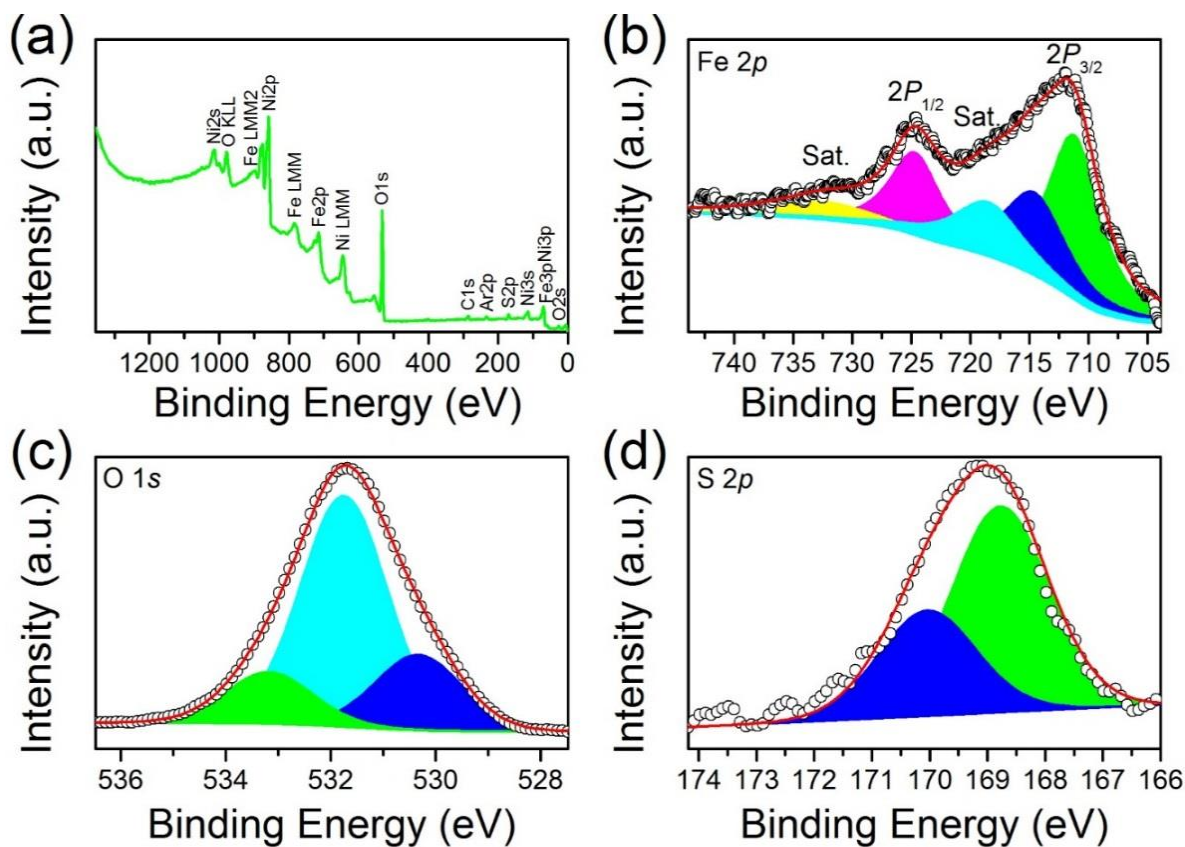
Fig. S15. (a) XPS survey spectrum and high-resolution XPS spectra of (b) Fe 2p, (c) O 1s, and (d) S 2p of S-Fe$_3$O$_4$/NF.
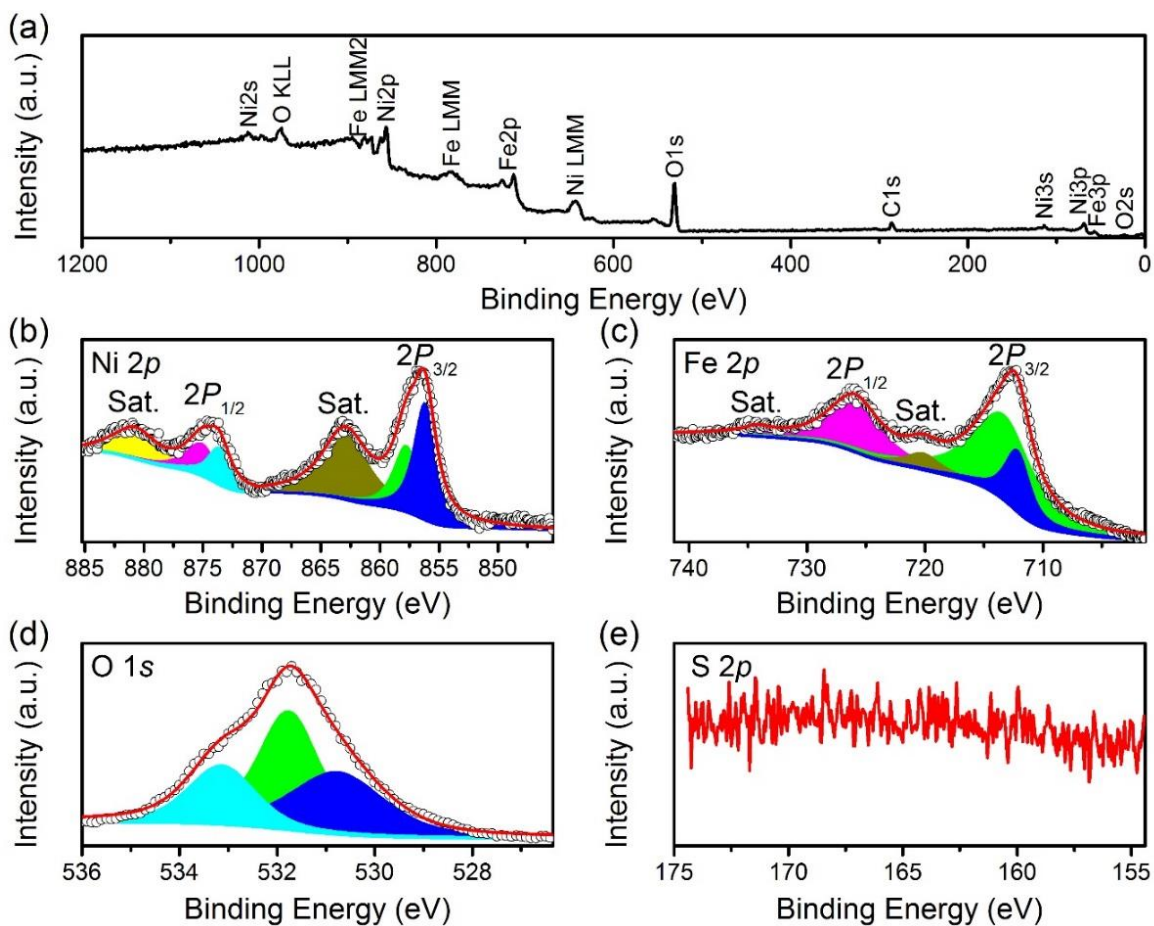
Fig. S16. (a) XPS survey spectrum and high-resolution XPS spectra of (b) Ni 2p, (c) Fe 2p, (d) O 1s, and (e) S 2p of NiFe$_2$O$_4$/NF. No S was detected in the NiFe$_2$O$_4$/NF due to the absence of thiourea during the electrodeposition.
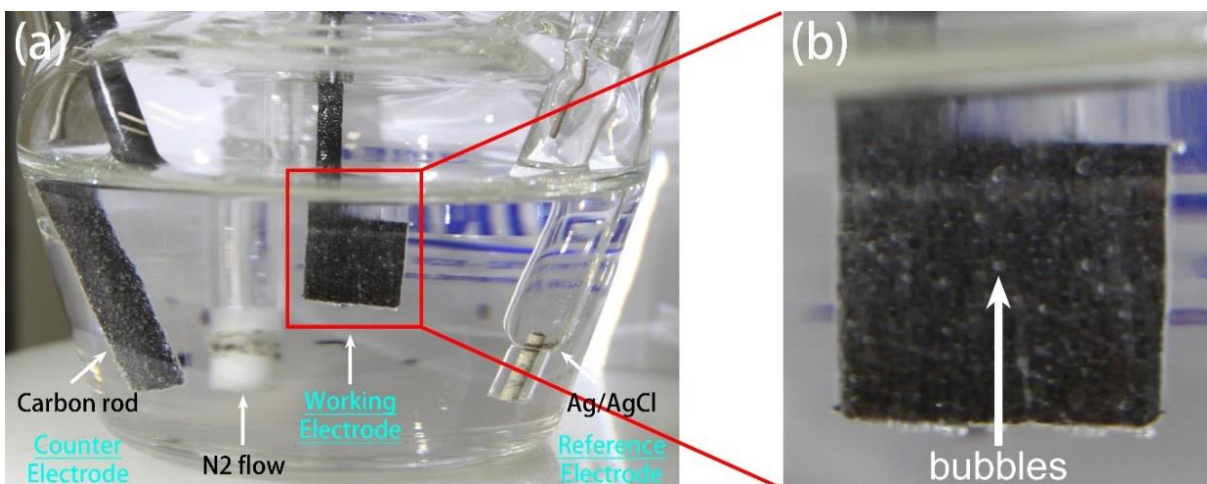
Fig. S17. (a) Digital photograph of the three-electrode glass cell for HER and OER measurements and (b) the magnified image of gas bubbles formed on the surface of S-NiFe$_2$O$_4$/NF electrode during the test.
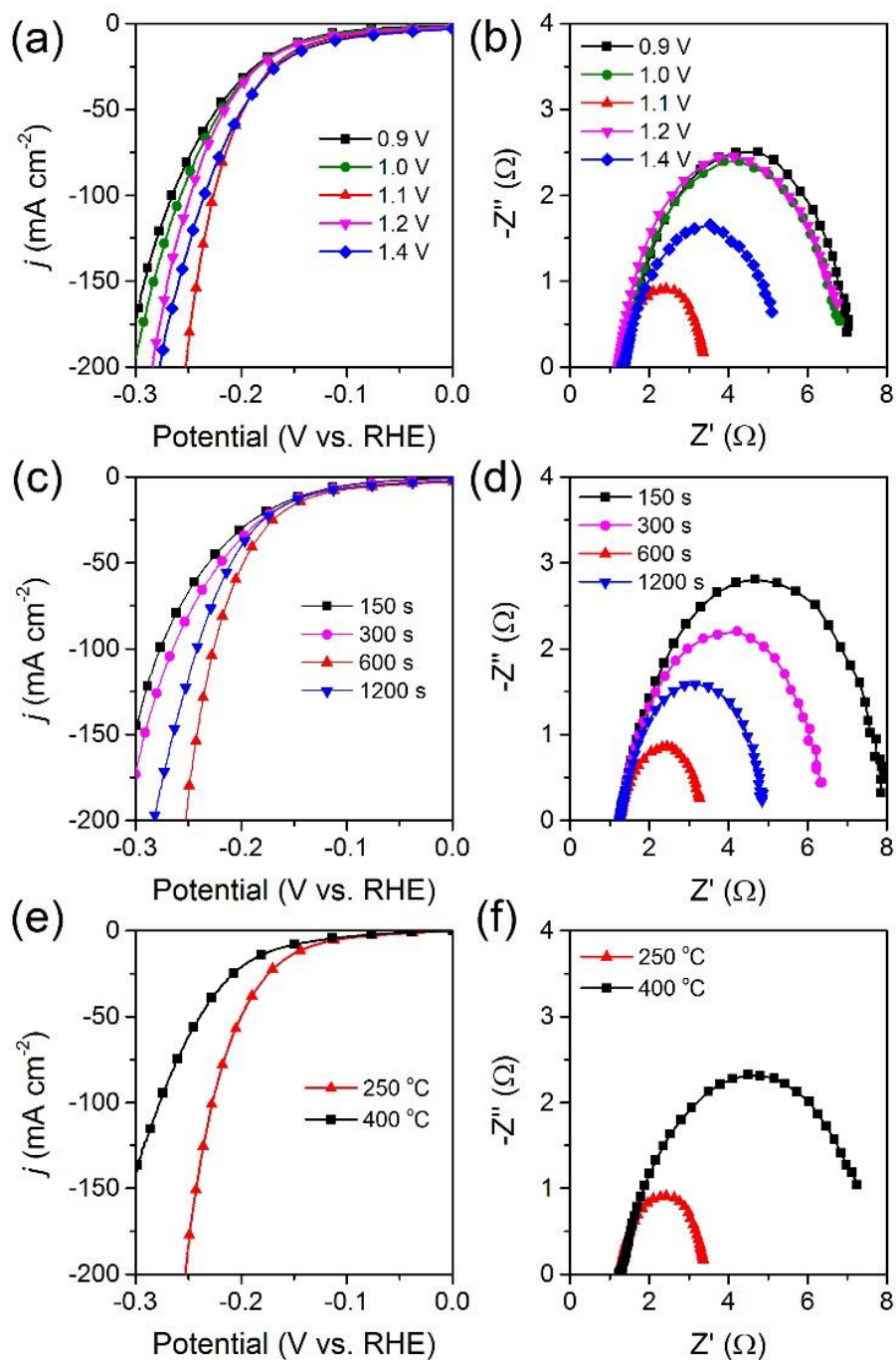
Fig. S18. (a) Polarization curves and (b) Nyquist plots of S-NiFe$_2$O$_4$/NF prepared at different applied potentials (vs. Ag/AgCl) for 600 s; (c) polarization curves and (d) Nyquist plots of S-NiFe$_2$O$_4$/NF prepared at −1.1 V vs. Ag/AgCl for various electrodeposition time ranging from 150 to 1200 s; (e) polarization curves and (f) Nyquist plots of S-NiFe$_2$O$_4$/NF prepared at 250 and 400 °C.
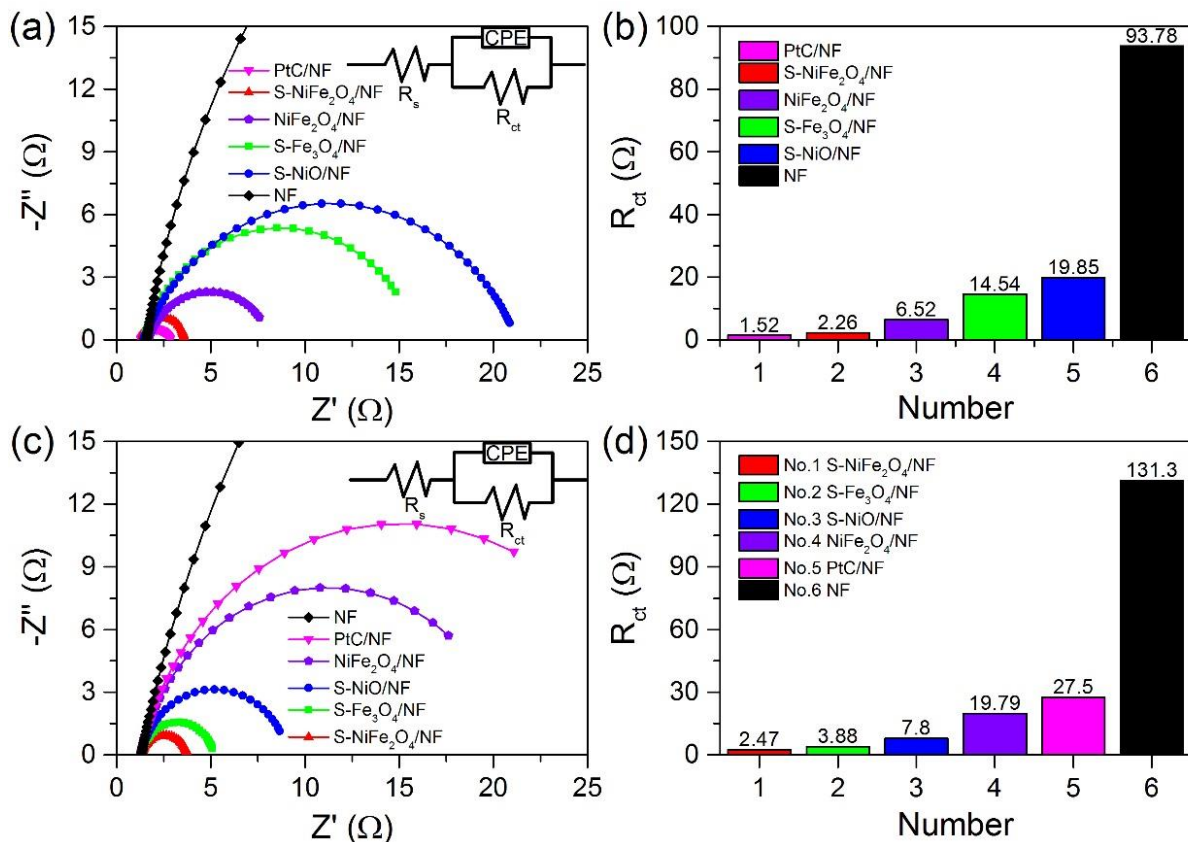
Fig. S19. (a) Nyquist plots and (b) simulated R_{ct} of various electrodes at -0.15 V vs. RHE in 1.0 M KOH. (c) Nyquist plots and (d) simulated R_{ct} of various electrodes at 1.5 V vs. RHE in 1.0 M KOH. The fitted curves using the equivalent circuit (inset) are presented by solid lines.

158
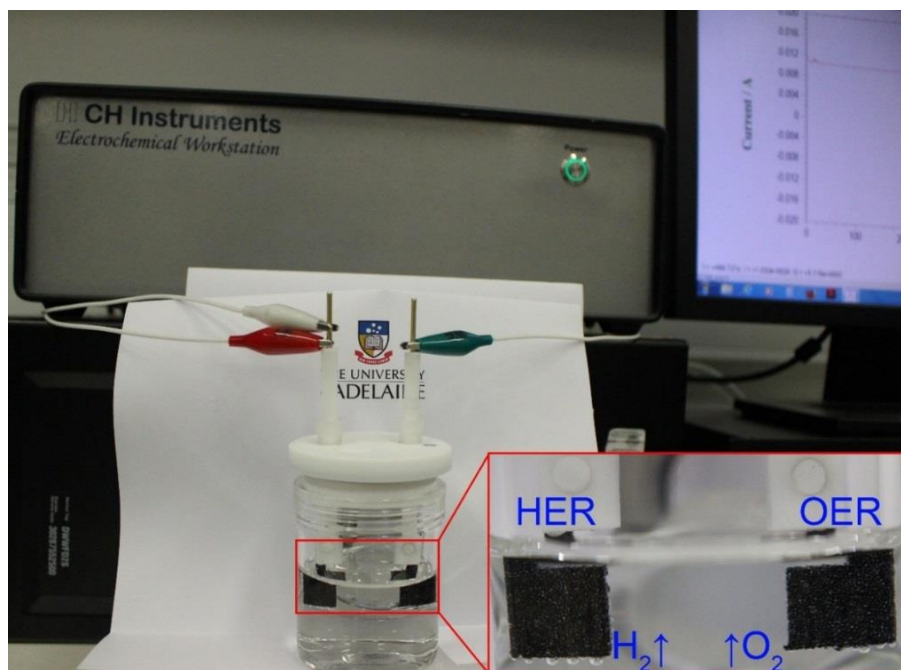
Fig. S20. Digital photograph of the two-electrode cell connected with a CHI 760D electrochemical workstation for overall water splitting. Inset: Enlarged view showing the obvious evolution of H_2 and O_2 bubbles on the S-NiFe$_2$O$_4$/NF electrodes.
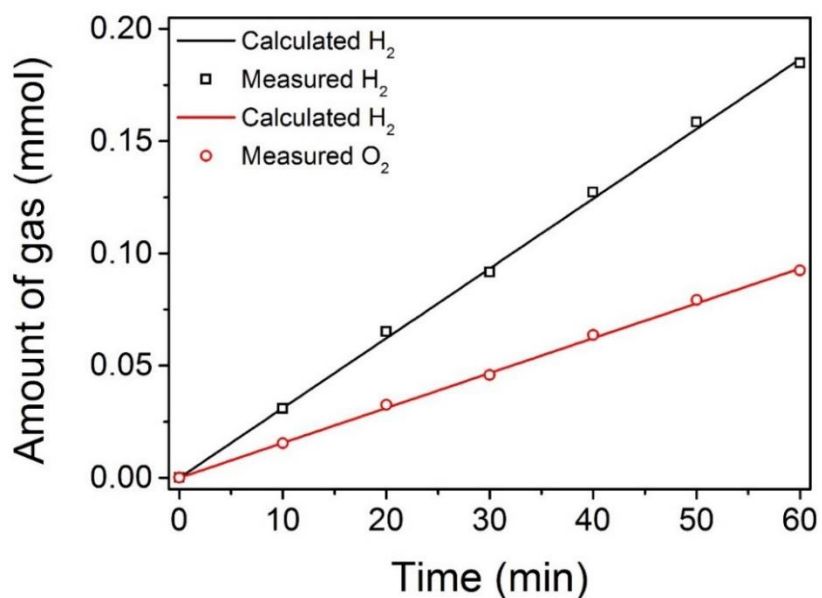
Fig. S21. The amount of H_2 and O_2 experimentally measured and theoretically calculated versus time for overall water splitting of S-NiFe$_2$O$_4$/NF in 1.0 M KOH.
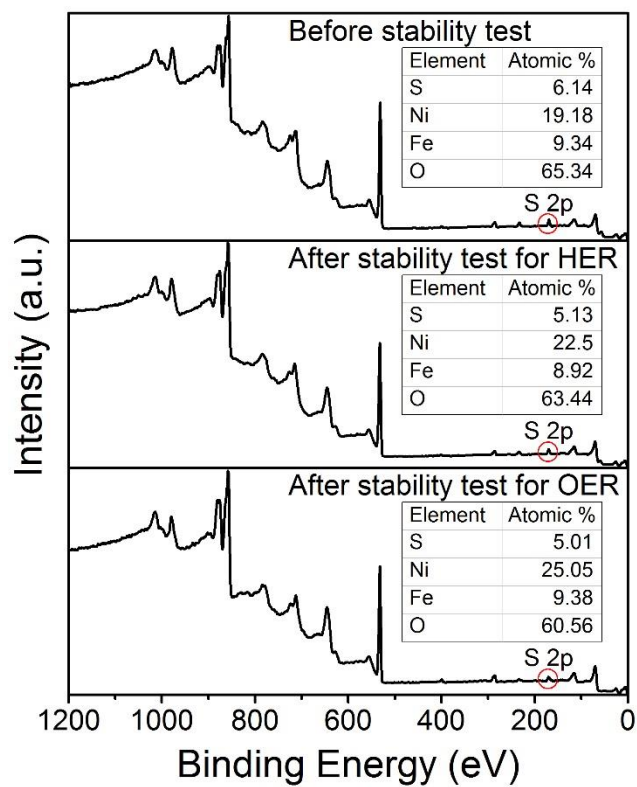
Fig. S22. XPS survey spectra of S-NiFe$_2$O$_4$/NF (a) before stability test, (b) after stability test for HER, and (c) after stability test for OER. Inset: Atomic percentages of S, Ni, Fe, and O.
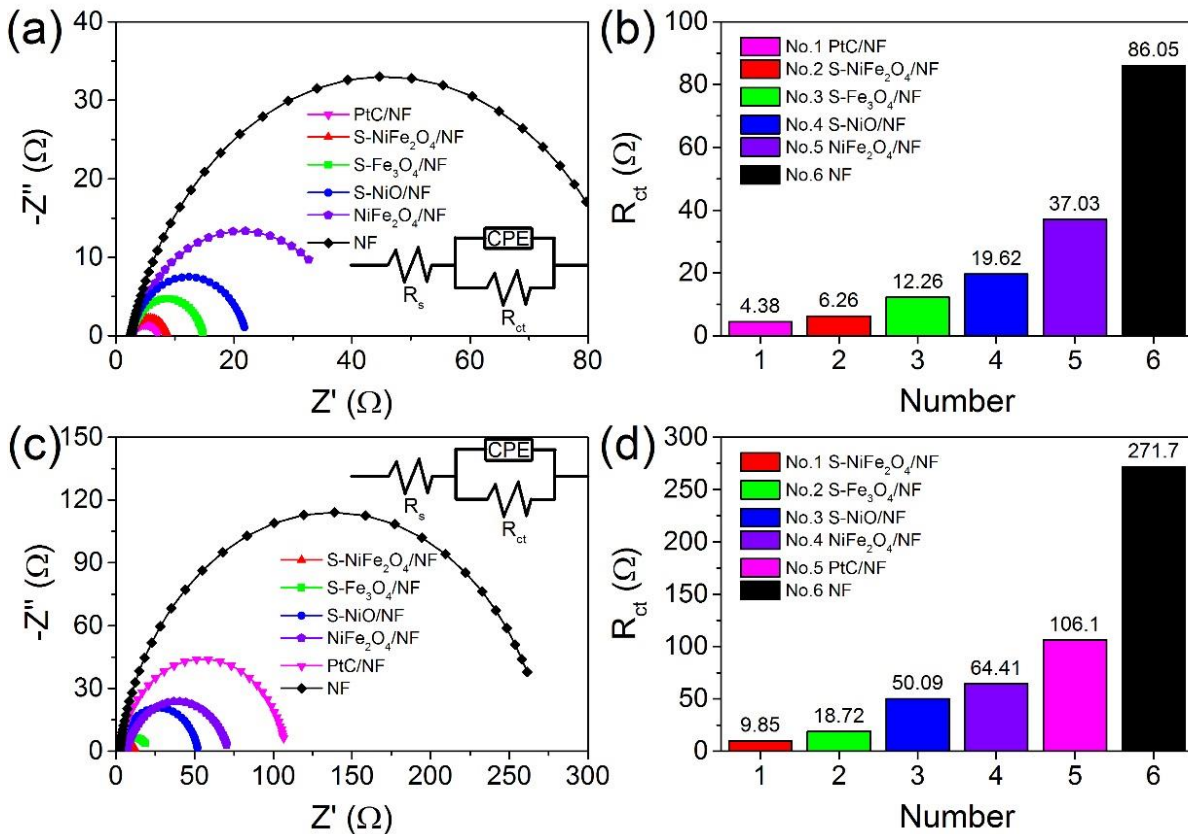
Fig. S23. (a) Nyquist plots and (b) simulated R_{ct} of various electrodes at -0.2 V vs. RHE in 1.0 M PBS. (c) Nyquist plots and (d) simulated R_{ct} of various electrodes at 1.75 V vs. RHE in 1.0 M PBS. The fitted curves using the equivalent circuit (inset) are presented by solid lines.

Table S1. Comparison of recent electrocatalysts for HER in alkaline electrolytes.

Catalyst	Electrolyte	η_{onset} (mV)	η_{10} (mV)	Tafel slope (mV dec^{-1})	Ref.
S-NiFe$_2$O$_4$/NF	1 M KOH	29	138	61.3	This work
Fe$_{0.5}$Co$_{0.5}$@NC/NCNS-800	1 M KOH	0.63	150	49.1	[3]
c-CoSe$_2$/CC	1 M KOH	-	190	85	[4]
Pr0.5BSCF	1 M KOH	179	237	45	[5]
Ni$_3$S$_2$	1 M KOH	-	335	97	[6]
Co-Mo$_2$C-0.020	1 M KOH	25	118	44	[7]
Mo$_2$C-GNR	1 M NaOH	116	217	64	[8]
Ni$_3$S$_2$/AT-NF	1 M KOH	-	200	107	[9]
Co-NRCNTs	1 M KOH	160	370	-	[10]
CoP/CC	1 M KOH	115	209	129	[11]
Mo$_2$C	1 M KOH	~135[a]	~190[a]	54	[12]

[a] Values estimated from polarization curve found in Ref [12].

Table S2. Comparison of recent NiFe-based electrocatalysts for OER in alkaline electrolytes.

Catalyst	Nanoparticle size (nm)	Electrolyte	η_{10} (mV)	Tafel slope (mV dec^{-1})	Ref.
S-NiFe$_2$O$_4$/NF	~2	1 M KOH	267	36.7	This work
Ni$_{0.53}$Fe$_{0.47}$O$_x$/ITO	6	1 M KOH	310	28	[13]
Ni1Fe2-250	~100	1 M KOH	310	42	[14]
Fe$_{0.5}$Ni$_{0.5}$O$_x$	10–15	0.1 M KOH	~584	72	[15]
NiO/NiFe$_2$O$_4$	6.4	1 M KOH	302	42	[16]
FeNi/NiFe$_2$O$_4$@NC-800	11.1±2.2	1 M KOH	~316	60	[17]
Fe$_{0.1}$Ni$_{0.9}$O	2.0±0.4	0.5 M KOH	297	37	[18]
Ni-85-200 (Ni-Fe oxide)	~5[a]	0.1 M KOH	328	42	[19]
Ni$_{0.88}$Fe$_{0.12}$O$_x$/ITO	~8	0.1 M KOH	300	42	[20]
Fe$_6$Ni$_{10}$O$_x$	≥200	1 M KOH	286	48	[21]
NiFeO$_x$	-	1 M NaOH	350±10	-	[22]

[a] Value estimated from HRTEM image found in Ref [19].

162

Table S3. Comparison of recent bifunctional electrocatalysts for overall water splitting in alkaline electrolytes.

Catalysts	Electrolyte	HER η_{10} (mV)	HER Tafel slop (mV dec^{-2})	OER η_{10} (mV)	OER Tafel slop (mV dec^{-1})	E_{10} (V)	Ref.
S-NiFe$_2$O$_4$/NF	1 M KOH	138	61.3	267	36.7	1.65	This work
RuO$_2$/Co$_3$O$_4$	1 M KOH	89	91	305	69	1.645	[23]
Co-NC/CNT	1 M KOH	203	125	354	78	1.625	[24]
CoO/MoO$_x$	1 M KOH	163	44	310mV @ 20 mA cm^{-2}	-	~1.72	[25]
Ni$_3$FeN-NPs	1 M KOH	158	42	280	46	-	[26]
NiCo$_2$O$_4$	1 M NaOH	110	49.7	290	53	1.65	[27]
Ni$_{0.9}$Fe$_{0.1}$/NC	1 M KOH	85	111	270	45	1.58	[28]
Co-P/NC	1 M KOH	154	51	319	52	>1.7	[29]
NiCo$_2$S$_4$/CC	1 M KOH	230 (onset)	141	270 (onset)	89	1.68	[30]
Ni$_3$S$_2$/NF	1 M KOH	223	-	260	-	~1.76V @ ~13 mA cm^{-2}	[31]
Co-P films	1 M KOH	94	42	345	47	~1.65[a]	[32]
2-cycle NiFeO$_x$/CFP	1 M KOH	88	150.2	250	31.5	1.55	[33]
NiSe/NF	1 M KOH	96	120	-	64	1.63	[34]
NiFe LDH/NF	1 M NaOH	210	-	240	-	1.7	[35]

[a] Value estimated from polarization curve found in Ref [32].

Table S4. Comparison of recent electrocatalysts for HER in neutral electrolytes.

Catalyst	Electrolyte	η_{onset} (mV)	η_{10} (mV)	Tafel slope (mV dec^{-1})	Ref.
S-NiFe$_2$O$_4$/NF	1 M PBS	81	197	81.3	This work
Co$_9$S$_8$/CC-2	PBS (pH=7)	25	175	-	[36]
Γ-Cu$_2$S/CF	1 M PBS	105	190	98.8	[37]
Mo$_2$C-GNR	1 M PBS	124	266	74	[8]
Ni-Mo-S/CFC	0.5 M PBS (pH 6.9)	132	200	85.3	[38]
WP$_2$ SMPs	1 M PBS (pH=7)	~120[a]	244	92	[39]
Co-B	0.5 M PBS (pH 7)	~150[a]	251	75	[40]
Ni$_3$S$_2$/NF	1 M PBS	180	220	108	[41]
Co-NRCNTs	0.1 M PBS (pH=7)	330	540	-	[10]
Ni-S/FTO	PBS (pH7)	227	330	77	[42]

[a] Values estimated from polarization curves found in Ref [39] and [40].

Table S5. Comparison of recent electrocatalysts for OER in neutral electrolytes.

Catalyst	Electrolyte	η_{onset} (mV)	η_{10} (mV)	Tafel slope (mV dec^{-1})	Ref.
S-NiFe$_2$O$_4$/NF	1 M PBS	307	494	118.1	This work
a-Co$_2$P	0.1 M PBS	320	592	94.4	[43]
1-D CoHCF	PBS (pH7)	474	880	-	[44]
Co-Bi NS/G	PBS (pH7)	235	570mV @ 14.4 mA cm^{-2}	160	[45]
Bi$_2$WO$_6$ CNPs	0.5 M Na$_2$SO$_4$ (pH6.6)	370	540	-	[46]
Co$_3$S$_4$ ultrathin nanosheets	PBS	310	700mV @ 3.97 mA cm^{-2}	151	[47]
CuCo$_2$O$_4$/NrGO	0.1 M PBS (pH7.6)	-	540	79	[48]

Table S6. Comparison of recent bifunctional electrocatalysts for overall water splitting in neutral electrolytes.

Catalysts	Electrolyte	HER η_{10} (mV)	HER Tafel slope (mV dec^{-1})	OER η_{10} (mV)	OER Tafel slope (mV dec^{-1})	E_{10} (V)	Ref.
S-NiFe$_2$O$_4$/NF	1 M PBS	197	81.3	494	118.1	1.95	This work
CoO/CoSe$_2$-Ti	0.5 M PBS	337	131	510	137	2.18	[49]
Fe$_{10}$Co$_{40}$Ni$_{40}$P/NF	1 M PBS	88	62	466	246	-	[50]

III. Supplementary Videos

Supplementary Video 1.

H_2 and O_2 evolution of water splitting on S-NiFe$_2$O$_4$/NF electrode in 1.0 M KOH at an applied voltage of 1.65 V.

Supplementary Video 2.

H_2 and O_2 evolution of water splitting on S-NiFe$_2$O$_4$/NF electrode in 1.0 M PBS at an applied voltage of 1.95 V.

References

[1] P. Hermet, P. Ghosez, First-principles study of the dynamical and nonlinear optical properties of urea single crystals, Phys. Chem. Chem. Phys. 12 (2010) 835−843.

[2] B. Ravindran, G. Madhurambal, M. Mariappan, S.C. Mojumdar, Synthesis and characterization of some single crystals of thiourea urea zinc chloride, J. Therm. Anal. Calorim. 104 (2011) 893−899.

[3] M. Li, T. Liu, X. Bo, M. Zhou, L. Guo, A novel flower-like architecture of FeCo@NC functionalized ultra-thin carbon nanosheets as highly efficient 3D bifunctional electrocatalyst for full water splitting, J. Mater. Chem. A 5 (2017) 5413−5425.

[4] P. Chen, K. Xu, S. Tao, T. Zhou, Y. Tong, H. Ding, L. Zhang, W. Chu, C. Wu, Y. Xie, Phase-transformation engineering in cobalt diselenide realizing enhanced catalytic activity for hydrogen evolution in an alkaline medium, Adv. Mater. 28 (2016) 7527−7532.

[5] X. Xu, Y. Chen, W. Zhou, Z. Zhu, C. Su, M. Liu, Z. Shao, A perovskite electrocatalyst for efficient hydrogen evolution reaction, Adv. Mater. 28 (2016) 6442−6448.

[6] N. Jiang, Q. Tang, M. Sheng, B. You, D. E. Jiang, Y. Sun, Nickel sulfides for electrocatalytic hydrogen evolution under alkaline conditions: a case study of crystalline NiS, NiS$_2$, and Ni$_3$S$_2$ nanoparticles, Catal. Sci. Technol. 6 (2016) 1077−1084.

[7] H. Lin, N. Liu, Z. Shi, Y. Guo, Y. Tang, Q. Gao, Cobalt-doping in molybdenum-carbide nanowires toward efficient electrocatalytic hydrogen evolution, Adv. Funct. Mater. 26 (2016) 5590−5598.

[8] W. Gao, Y. Shi, Y. Zhang, L. Zuo, H. Lu, Y. Huang, W. Fan, T. Liu, Molybdenum carbide anchored on graphene nanoribbons as highly efficient all-pH hydrogen evolution reaction electrocatalyst, ACS Sustainable Chem. Eng. 4 (2016) 6313−6321.

[9] C. Ouyang, X. Wang, C. Wang, X. Zhang, J. Wu, Z. Ma, S. Dou, S. Wang, Hierarchically porous Ni_3S_2 nanorod array foam as highly efficient electrocatalyst for hydrogen evolution reaction and oxygen evolution reaction, Electrochim. Acta 174 (2015) 297−301.

[10] X. Zou, X. Huang, A. Goswami, R. Silva, B.R. Sathe, E. Mikmeková, T. Asefa, Cobalt-embedded nitrogen-rich carbon nanotubes efficiently catalyze hydrogen evolution reaction at all pH values, Angew. Chem. 126 (2014) 4461−4465.

[11] J. Tian, Q. Liu, A.M. Asiri, X. Sun, Self-supported nanoporous cobalt phosphide nanowire arrays: an efficient 3D hydrogen-evolving cathode over the wide range of pH 0–14, J. Am. Chem. Soc. 136 (2014) 7587−7590.

[12] H. Vrubel, X. Hu, Molybdenum boride and carbide catalyze hydrogen evolution in both acidic and basic solutions, Angew. Chem. Int. Ed. 51 (2012) 12703−12706.

[13] J. Wang, L. Ji, Z. Chen, In situ rapid formation of a nickel–iron-based electrocatalyst for water oxidation, ACS Catal. 6 (2016) 6987−6992.

[14] H. Chen, X. Huang, L. J. Zhou, G. D. Li, M. Fan, X. Zou, Electrospinning synthesis of bimetallic nickel–iron oxide/carbon composite nanofibers for efficient water oxidation electrocatalysis, ChemCatChem 8 (2016) 992−1000.

[15] J. Jiang, C. Zhang, L. Ai, Hierarchical iron nickel oxide architectures derived from metal-organic frameworks as efficient electrocatalysts for oxygen evolution reaction, Electrochim. Acta 208 (2016) 17−24.

[16] G. Liu, X. Gao, K. Wang, D. He, J. Li, Uniformly mesoporous $NiO/NiFe_2O_4$ biphasic nanorods as efficient oxygen evolving catalyst for water splitting, Int. J. Hydrogen Energy 41 (2016) 17976−17986.

[17] Y. Ma, X. Dai, M. Liu, J. Yong, H. Qiao, A. Jin, Z. Li, X. Huang, H. Wang, X. Zhang, Strongly coupled FeNi alloys/$NiFe_2O_4$@carbonitride layers-assembled microboxes for enhanced oxygen evolution reaction, ACS Appl. Mater. Interfaces 8 (2016) 34396−34404.

[18] K. Fominykh, P. Chernev, I. Zaharieva, J. Sicklinger, G. Stefanic, M. Döblinger, A. Müller, A. Pokharel, S. Böcklein, C. Scheu, T. Bein, D. Fattakhova-Rohlfing, Iron-doped nickel oxide nanocrystals as highly efficient electrocatalysts for alkaline water splitting, ACS Nano 9 (2015) 5180−5188.

[19] J. Qi, W. Zhang, R. Xiang, K. Liu, H. Y. Wang, M. Chen, Y. Han, R. Cao, Porous nickel–iron oxide as a highly efficient electrocatalyst for oxygen evolution reaction, Adv. Sci. 2 (2015) 1500199.

[20] J.A. Bau, E.J. Luber, J.M. Buriak, Oxygen evolution catalyzed by nickel–iron oxide nanocrystals with a nonequilibrium phase, ACS Appl. Mater. Interfaces 7 (2015) 19755−19763.

[21] L. Kuai, J. Geng, C. Chen, E. Kan, Y. Liu, Q. Wang, B. Geng, A reliable aerosol-spray-assisted approach to produce and optimize amorphous metal oxide catalysts for electrochemical water splitting, Angew. Chem. Int. Ed. 53 (2014) 7547−7551.

[22] C.C.L. McCrory, S. Jung, J.C. Peters, T.F. Jaramillo, Benchmarking heterogeneous electrocatalysts for the oxygen evolution reaction, J. Am. Chem. Soc. 135 (2013) 16977−16987.

[23] H. Liu, G. Xia, R. Zhang, P. Jiang, J. Chen, Q. Chen, MOF-derived RuO_2/Co_3O_4 heterojunctions as highly efficient bifunctional electrocatalysts for HER and OER in alkaline solutions, RSC Adv. 7 (2017) 3686−3694.

[24] F. Yang, P. Zhao, X. Hua, W. Luo, G. Cheng, W. Xing, S. Chen, A cobalt-based hybrid electrocatalyst derived from a carbon nanotube inserted metal-organic framework for efficient water-splitting, J. Mater. Chem. A 4 (2016) 16057−16063.

[25] X. Yan, L. Tian, S. Atkins, Y. Liu, J. Murowchick, X. Chen, Converting $CoMoO_4$ into CoO/MoO_x for overall water splitting by hydrogenation, ACS Sustainable Chem. Eng. 4 (2016) 3743−3749.

[26] X. Jia, Y. Zhao, G. Chen, L. Shang, R. Shi, X. Kang, G.I.N. Waterhouse, L. Z. Wu, C. H. Tung, T. Zhang, Ni_3FeN nanoparticles derived from ultrathin NiFe-layered double hydroxide nanosheets: an efficient overall water splitting electrocatalyst, Adv. Energy Mater. 6 (2016) 1502585.

[27] X. Gao, H. Zhang, Q. Li, X. Yu, Z. Hong, X. Zhang, C. Liang, Z. Lin, Hierarchical $NiCo_2O_4$ hollow microcuboids as bifunctional electrocatalysts for overall water-splitting, Angew. Chem. Int. Ed. 55 (2016) 6290−6294.

[28] X. Zhang, H. Xu, X. Li, Y. Li, T. Yang, Y. Liang, Facile synthesis of nickel–iron/nanocarbon hybrids as advanced electrocatalysts for efficient water splitting, ACS Catal. 6 (2016) 580−588.

[29] B. You, N. Jiang, M. Sheng, S. Gul, J. Yano, Y. Sun, High-performance overall water splitting electrocatalysts derived from cobalt-based metal–organic frameworks, Chem. Mater. 27 (2015) 7636−7642.

[30] D. Liu, Q. Lu, Y. Luo, X. Sun, A.M. Asiri, $NiCo_2S_4$ nanowires array as an efficient bifunctional electrocatalyst for full water splitting with superior activity, Nanoscale 7 (2015) 15122−15126.

[31] L.L. Feng, G. Yu, Y. Wu, G.D. Li, H. Li, Y. Sun, T. Asefa, W. Chen, X. Zou, High-index faceted Ni_3S_2 nanosheet arrays as highly active and ultrastable electrocatalysts for water splitting, J. Am. Chem. Soc. 137 (2015) 14023−14026.

[32] N. Jiang, B. You, M. Sheng, Y. Sun, Electrodeposited cobalt-phosphorous-derived films as competent bifunctional catalysts for overall water splitting, Angew. Chem. Int. Ed. 54 (2015) 6251−6254.

[33] H. Wang, H.W. Lee, Y. Deng, Z. Lu, P.C. Hsu, Y. Liu, D. Lin, Y. Cui, Bifunctional non-noble metal oxide nanoparticle electrocatalysts through lithium-induced conversion for overall water splitting, Nat. Commun. 6 (2015) 7261.

[34] C. Tang, N. Cheng, Z. Pu, W. Xing, X. Sun, NiSe nanowire film supported on nickel foam: an efficient and stable 3D bifunctional electrode for full water splitting, Angew. Chem. Int. Ed. 54 (2015) 9351−9355.

[35] J. Luo, J. H. Im, M.T. Mayer, M. Schreier, M.K. Nazeeruddin, N. G. Park, S.D. Tilley, H.J. Fan, M. Grätzel, Water photolysis at 12.3% efficiency via perovskite photovoltaics and earth-abundant catalysts, Science 345 (2014) 1593−1596.

[36] L. L. Feng, M. Fan, Y. Wu, Y. Liu, G. D. Li, H. Chen, W. Chen, D. Wang, X. Zou, Metallic Co_9S_8 nanosheets grown on carbon cloth as efficient binder-free electrocatalysts for the hydrogen evolution reaction in neutral media, J. Mater. Chem. A 4 (2016) 6860−6867.

[37] M. Fan, R. Gao, Y. C. Zou, D. Wang, N. Bai, G. D. Li, X. Zou, An efficient nanostructured copper(I) sulfide-based hydrogen evolution electrocatalyst at neutral pH, Electrochim. Acta 215 (2016) 366−373.

[38] J. Miao, F.X. Xiao, H.B. Yang, S.Y. Khoo, J. Chen, Z. Fan, Y.Y. Hsu, H.M. Chen, H. Zhang, B. Liu, Hierarchical Ni-Mo-S nanosheets on carbon fiber cloth: a flexible electrode for efficient hydrogen generation in neutral electrolyte, Sci. Adv. 1 (2015) 1500259.

[39] Z. Xing, Q. Liu, A.M. Asiri, X. Sun, High-efficiency electrochemical hydrogen evolution catalyzed by tungsten phosphide submicroparticles, ACS Catal. 5 (2015) 145−149.

[40] S. Gupta, N. Patel, A. Miotello, D.C. Kothari, Cobalt-boride: an efficient and robust electrocatalyst for hydrogen evolution reaction, J. Power Sources 279 (2015) 620−625.

[41] C. Tang, Z. Pu, Q. Liu, A.M. Asiri, Y. Luo, X. Sun, Ni_3S_2 nanosheets array supported on Ni foam: a novel efficient three-dimensional hydrogen-evolving electrocatalyst in both neutral and basic solutions, Int. J. Hydrogen Energy 40 (2015) 4727−4732.

[42] N. Jiang, L. Bogoev, M. Popova, S. Gul, J. Yano, Y. Sun, Electrodeposited nickel-sulfide films as competent hydrogen evolution catalysts in neutral water, J. Mater. Chem. A 2 (2014) 19407−19414.

[43] K. Xu, H. Cheng, L. Liu, H. Lv, X. Wu, C. Wu, Y. Xie, Promoting active species generation by electrochemical activation in alkaline media for efficient electrocatalytic oxygen evolution in neutral media, Nano Lett. 17 (2017) 578−583.

[44] H.T. Bui, D.Y. Ahn, N.K. Shrestha, M.M. Sung, J.K. Lee, S. H. Han, Self-assembly of cobalt hexacyanoferrate crystals in 1-D array using ion exchange transformation route for enhanced electrocatalytic oxidation of alkaline and neutral water, J. Mater. Chem. A 4 (2016) 9781−9788.

[45] P. Chen, K. Xu, T. Zhou, Y. Tong, J. Wu, H. Cheng, X. Lu, H. Ding, C. Wu, Y. Xie, Strong-coupled cobalt borate nanosheets/graphene hybrid as electrocatalyst for water oxidation under both alkaline and neutral conditions, Angew. Chem. Int. Ed. 55 (2016) 2488−2492.

[46] Z. P. Nie, D. K. Ma, G. Y. Fang, W. Chen, S. M. Huang, Concave Bi_2WO_6 nanoplates with oxygen vacancies achieving enhanced electrocatalytic oxygen evolution in near-neutral water, J. Mater. Chem. A 4 (2016) 2438−2444.

[47] Y. Liu, C. Xiao, M. Lyu, Y. Lin, W. Cai, P. Huang, W. Tong, Y. Zou, Y. Xie, Ultrathin Co_3S_4 nanosheets that synergistically engineer spin states and exposed polyhedra that promote water oxidation under neutral conditions, Angew. Chem. 127 (2015) 11383−11387.

[48] S.K. Bikkarolla, P. Papakonstantinou, $CuCo_2O_4$ nanoparticles on nitrogenated graphene as highly efficient oxygen evolution catalyst, J. Power Sources 281 (2015) 243−251.

[49] K. Li, J. Zhang, R. Wu, Y. Yu, B. Zhang, Anchoring CoO domains on $CoSe_2$ nanobelts as bifunctional electrocatalysts for overall water splitting in neutral media, Adv. Sci. 3 (2016) 1500426.

[50] Z. Zhang, J. Hao, W. Yang, J. Tang, Iron triad (Fe, co, Ni) trinary phosphide nanosheet arrays as high-performance bifunctional electrodes for full water splitting in basic and neutral conditions, RSC Adv. 6 (2016) 9647−9655.

Chapter 6: NiO as a Bifunctional Promoter for RuO$_2$ toward Superior Overall Water Splitting

6.1 Introduction and Significance

The ever-increasing advances in computational quantum chemistry allow for in-depth understanding of fundamental reaction kinetics on various electrocatalysts at the atomic and/or molecular level, thus guide the design of more advanced bifunctional electrocatalysts. According to previous computational studies, RuO$_2$ is found close to the top of OER volcano and is predicted to be a better OER electrocatalyst by strengthening oxygen binding. Meanwhile, Ru is a promising HER electrocatalyst, due to the favourable hydrogen adsorption. Interestingly, the RuO$_2$ surface can be reduced to Ru under applied HER potentials. Therefore, RuO$_2$ provides an idea platform for a proof-of-concept study of engineering bifunctional electrocatalyst towards water electrolysis. In this chapter, NiO was proposed as a suitable promoter to modify RuO$_2$ for such a goal. Hierarchical RuO$_2$/NiO nanosheet arrays, designed with rational in situ interfacial engineering, revealed unique potential-induced synergies that dramatically improved OER and HER activities. The highlights in this work include:

1. Rationally designed porous nanosheet arrays, consisting of strongly interacting RuO$_2$ and NiO nanoparticles, were grown vertically on three-dimensional nickel foam (RuO$_2$/NiO/NF) through a simple hydrothermal reaction, chemical etching and thermal treatment process. As a promotor, NiO can not only reinforce the oxygen binding energy of RuO$_2$, approaching the OER volcano peak, but also promote the prior water dissociation step by cleaving the HO−H bond.

2. The RuO$_2$/NiO/NF displayed significantly enhanced activity, favourable kinetics, and strong long-term/cyclic durability for both OER and HER compared to its counterparts (i.e. RuO$_2$/NF, NiO/NF, and bare NF), even outperforming commercial 20 wt.% Pt/C and IrO$_2$. More impressively, this bifunctional electrode assured remarkable activity and stability for overall water splitting with a constant 10 mA cm^{-2} at a cell voltage of 1.5 V in 1.0 M KOH, which was superior to the PtC/NF||IrO$_2$/NF couple (1.56 V) and most of recently reported bifunctional electrocatalysts.

3. Reasonable mechanism analysis revealed the origins of such electrocatalytic reactivity from several merits: (i) enhanced electrical conductivity for rapid charge transport; (ii)

enlarged electrochemical active surface to expose abundant active sites; (iii) porous vertically aligned nanosheet arrays enabling fast mass transfer; (iv) most importantly, advantageous potential-induced interfacial synergy toward enhanced intrinsic OER and HER under alkaline conditions; (v) excellent chemical and structural robustness for long-term operation.

6.2 NiO as a Bifunctional Promoter for RuO$_2$ toward Superior Overall Water Splitting

This chapter is included in this thesis as it appears as a research paper published by **Jinlong Liu**, Yao Zheng, Yan Jiao, Zhenyu Wang, Zhouguang Lu, Anthony Vasileff, and Shi-Zhang Qiao, NiO as a Bifunctional Promoter for RuO$_2$ toward Superior Overall Water Splitting, ***Small***, 2018, 14, 1704073.

Statement of Authorship

Title of Paper	NiO as an efficient bifunctional promotor for RuO_2 towards superior alkaline water splitting

Publication Status	☐ Published ☑ Accepted for Publication ☐ Submitted for Publication ☐ Unpublished and Unsubmitted work written in manuscript style
Publication Details	Jinlong Liu, Yao Zheng, Yan Jiao, Zhenyu Wang, Zhouguang Lu, Anthony Vasileff, and Shi-Zhang Qiao, NiO as an efficient bifunctional promotor for RuO_2 towards superior alkaline water splitting, Small, 2018, accepted.

Principal Author

Name of Principal Author (Candidate)	Jinlong Liu		
Contribution to the Paper	Research plan, material synthesis, most of the characterizations and data analysis, electrochemical measurements, and manuscript drafting.		
Overall percentage (%)			
Certification:	This paper reports on original research I conducted during the period of my Higher Degree by Research candidature and is not subject to any obligations or contractual agreements with a third party that would constrain its inclusion in this thesis. I am the primary author of this paper.		
Signature		Date	4/02/2018

Co-Author Contributions

By signing the Statement of Authorship, each author certifies that:

 i. the candidate's stated contribution to the publication is accurate (as detailed above);

 ii. permission is granted for the candidate in include the publication in the thesis; and

 iii. the sum of all co-author contributions is equal to 100% less the candidate's stated contribution.

Name of Co-Author	Yao Zheng		
Contribution to the Paper	Discussion of research plan, data analysis, and manuscript revision.		
Signature		Date	5 Feb 2018

Name of Co-Author	Yan Jiao		
Contribution to the Paper	Discussion of research plan and data analysis.		
Signature		Date	5 Feb 2018

Name of Co-Author	Zhenyu Wang
Contribution to the Paper	Assistance with TEM characterization.
Signature	Date 4 Feb 2018

Name of Co-Author	Zhouguang Lu
Contribution to the Paper	Assistance with TEM characterization.
Signature	Date Feb 5, 2018

Name of Co-Author	Anthony Vasileff
Contribution to the Paper	Assistance with manuscript editing and polishing.
Signature	Date 05/02/2018

Name of Co-Author	Shi-Zhang Qiao
Contribution to the Paper	Supervision of the work, data interpretation, and manuscript evaluation.
Signature	Date 15/02/2018

NiO as a Bifunctional Promoter for RuO_2 toward Superior Overall Water Splitting

Jinlong Liu, Yao Zheng, Yan Jiao, Zhenyu Wang, Zhouguang Lu, Anthony Vasileff, and Shi-Zhang Qiao*

Conventional development of nanomaterials for efficient electrocatalysis is largely based on performance-oriented trial-and-error/iterative approaches, while a rational design approach at the atomic/molecular level is yet to be found. Here, inspired by a fundamental understanding of the mechanism for both oxygen and hydrogen evolution half reactions (OER/HER), a unique strategy is presented to engineer RuO_2 for superior alkaline water electrolysis through coupling with NiO as an efficient bifunctional promoter. Benefitting from desired potential-induced interfacial synergies, NiO-derived NiOOH improves the oxygen binding energy of RuO_2 for enhanced OER, and NiO also promotes water dissociation for enhanced HER on RuO_2-derived Ru. The resulting hybrid material exhibits remarkable bifunctional activities, affording 2.6 times higher OER activity than that of RuO_2 and an HER activity comparable to Pt/C. As a result, the simple system requires only 1.5 V to deliver 10 mA cm^{-2} for overall alkaline water splitting, outperforming the benchmark PtC/NF‖IrO_2/NF couple with high mass loading. Comprehensive electrochemical investigation reveals the unique and critical role of NiO on the optimized RuO_2/NiO interface for synergistically enhanced activities, which may be extended to broader (electro)catalytic systems.

1. Introduction

Developing water electrolysis toward sustainable H_2 production, especially using clean and renewable energy sources (solar, wind, and hydro power etc.), requires efficient catalysts. Efficient catalysts increase reaction rate by improving the kinetics for both the cathodic hydrogen evolution reaction (HER) and the anodic oxygen evolution reaction (OER), and by reducing the energy input through smaller overpotentials.[1–6] In general, platinum (Pt) and iridium dioxide (IrO_2) are regarded as the benchmark electrocatalysts for the HER and OER, respectively.[7,8] From the perspective of device simplification and cost reduction, it is highly desirable to develop effective bifunctional electrocatalysts for both the HER and OER using the same electrolyte.[9–12] Although there have been some relevant studies in recent years, such as transition metal alloys,[13,14] oxides,[10,12,15–18] nitrides,[19] chalcogenides,[20–22] and phosphides,[11,23] most of these studies have been guided by a trial-and-error and/or iterative approach. However, few reports have focused on the rational design of bifunctional electrocatalysts based on an in-depth understanding of the reaction mechanism at a molecular level, particularly when substantial experimental and theoretical insights into water electrolysis on many well-studied catalysts has been accumulated.[24]

Among various model catalysts, ruthenium dioxide (RuO_2) is known to be the most active OER electrocatalyst, with an optimal oxygen binding energy close to the top of volcano plot, even surpassing IrO_2 with lower overpotential.[25,26] For example, Lee et al. demonstrated that RuO_2 nanoparticles have slightly higher intrinsic and mass OER activities than IrO_2 nanoparticles with similar size.[27] For the HER, Ru-based catalysts possess considerable activity, due to the favorable hydrogen adsorption of Ru.[28,29] Notably, RuO_2 surfaces, at least several atomic layers, are reduced to metallic Ru, if the applied potential is more negative than ≈0.04 V versus the reversible hydrogen electrode (vs RHE),[30] i.e., RuO_2 surface is converted into Ru under HER potentials. As a result, RuO_2 is believed to be an ideal platform for constructing more advanced bifunctional electrocatalysts for overall water splitting. In this aspect, 1D RuO_2 nanowires on carbon nitride (1D RuO_2-CN$_x$) and MOF-derived RuO_2/Co_3O_4 heterojunctions have recently been reported as efficient bifunctional electrocatalysts for OER and HER in alkaline environments.[16,31] Regardless of the enhanced OER/HER activities, these performance-oriented studies fail to reveal the rational design principle of RuO_2 based bifunctional electrocatalysts. Hence, modification of RuO_2 with a suitable promoter is still a great challenge, whereby further improved OER and HER activity can be simultaneously achieved.

J. L. Liu, Dr. Y. Zheng, Dr. Y. Jiao, A. Vasileff, Prof. S.-Z. Qiao
School of Chemical Engineering
The University of Adelaide
Adelaide, SA 5005, Australia
E-mail: s.qiao@adelaide.edu.au
Z. Y. Wang, Prof. Z. G. Lu
Department of Materials Science and Engineering
South University of Science and Technology
Shenzhen 518005, P. R. China
Prof. S.-Z. Qiao
School of Materials Science and Engineering
Tianjin University
Tianjin 300072, P. R. China

The ORCID identification number(s) for the author(s) of this article can be found under https://doi.org/10.1002/smll.201704073.

173

**ADVANCED
SCIENCE NEWS**

www.advancedsciencenews.com

small

NANO MICRO

www.small-journal.com

Fundamentally, in order to realize such a goal, there remains several major issues needed to be addressed: (i) RuO_2 approaches the top of OER volcano plot from the weak oxygen binding branch, and theoretical predictions indicate that improvements can be made by slightly increasing the oxygen adsorption of RuO_2;[25] accordingly, the target promoter should possess strong capability of binding oxygen intermediates. (ii) Regarding the HER in alkaline electrolyte, it involves the initial water dissociation step to cleave H_2O molecule into H and OH, which is found to be crucial for the overall alkaline HER rate;[32] consequently, the selected promoter should also be able to facilitate the cleavage of HO—H bonds, thus accelerating subsequent hydrogen adsorption on RuO_2-derived Ru for further recombination into molecular hydrogen.[32] (iii) Also, it is preferable to choose promoter candidate with high earth abundance and corrosion resistance, aiming to lower the cost and improve the stability.

Given these criteria, NiO is selected as a potential cocatalyst for engineering hybrid catalyst with RuO_2 to testify the above hypotheses. According to previous studies, individual NiO bind OH too strongly, leading to a higher overpotential for the OER.[8,26] Due to the strong adsorption of OH, it has appreciable capability for water dissociation, but its unfavorable hydrogen adsorption limits the alkaline HER activity.[33] Interestingly, fruitful synergy is expected to achieve superior overall water electrolysis through hybridizing NiO with RuO_2. To be specific, under applied oxidizing potentials before the OER onset, NiO and/or $Ni(OH)_2$ are oxidized into NiOOH as the actual active species.[24,34–37] As such, the formed RuO_2/NiOOH interface enables reinforced oxygen adsorption approaching the OER volcano peak, and optimizing the OER catalyst system by satisfying the Sabatier principle.[24,25] Meanwhile, the coupling of NiO and RuO_2 can experience enhanced alkaline HER activity via bifunctional interaction, where NiO promotes the cleavage of HO—H bonds and the nearby RuO_2-derived Ru facilitates the hydrogen adsorption and recombination into molecular hydrogen. Note that under HER potentials, RuO_2 can be reduced to Ru, while NiO is electrochemically stable (Note S1, Supporting Information). For these reasons, although NiO itself is a poor bifunctional electrocatalyst, it holds great potential to serve as a bifunctional promoter for RuO_2 toward superior overall water splitting. Yet this remains to be seen.

To this end, we herein report the fabrication of hybrid porous nanosheet arrays composed of strongly coupled RuO_2 and NiO nanoparticles vertically aligned on nickel foam (denoted RuO_2/NiO/NF). The resultant RuO_2/NiO/NF, synthesized by a simple wet chemistry method, features numerous well-defined RuO_2/NiO interfaces with homogeneous distribution of RuO_2 nanoparticles on the NiO surface. This not only offers abundant active sites, but also provides the targeted interfacial synergy. Remarkably, this nanostructured hybrid material shows significantly enhanced bifunctional catalytic activities toward both the OER and HER. The correlation of mechanism analysis results demonstrates that NiO is a versatile cocatalyst to promote RuO_2 as a highly efficient bifunctional electrocatalysts for superior overall alkaline water splitting. Further, the RuO_2/NiO assembly also exhibits excellent long-term stability due to its favorable electrode configuration. As an example of "theory

guides practice," this work may provide valuable strategies for developing multicomponent catalyst systems toward advanced water electrolysis.

2. Results and Discussions

The synthetic strategy used for fabricating hierarchical RuO_2/NiO/NF is illustrated in **Figure 1**a. Typically, well-defined $Ni(OH)_2$ nanoflake arrays were first grown on NF using a simple hydrothermal reaction in aqueous HCl solution reported by Tian et al.[38] As can be seen in the X-ray diffraction (XRD) pattern of $Ni(OH)_2$/NF (Figure S1, Supporting Information), all the diffraction peaks can be indexed to hexagonal $Ni(OH)_2$ (JCPDS card No. 03-0177), except for the background peaks originating from the cubic NF substrate (JCPDS card No. 04-0850). The scanning electron microscopy (SEM) images in Figure S2a,b in the Supporting Information show the full coverage of NF with vertically aligned $Ni(OH)_2$ nanoflake arrays, and corresponding energy dispersive X-ray (EDX) analysis shows the presence of Ni and O without any impurity elements (Figure S2c, Supporting Information). Transmission electron microscopy (TEM) image and selected area electron diffraction (SAED) patterns demonstrate that the anisotropic 2D nanoflakes correspond to hexagonal $Ni(OH)_2$ single crystals oriented along the [001] direction (Figure S3a–c, Supporting Information). High-resolution TEM (HRTEM) images further confirm the single crystal nature of the hexagonal $Ni(OH)_2$ nanoflakes, with a distinct hexagonal fast Fourier transform (FFT) pattern and a clear (101) interplanar spacing of 0.235 nm (Figure S3d–f, Supporting Information).

The as-obtained $Ni(OH)_2$/NF was subsequently decorated with amorphous $Ru(OH)_3$ by a chemical etching process in 5×10^{-3} M $RuCl_3$. The etching preferentially occurs on the surface of the $Ni(OH)_2$ nanoflakes, leading to the in situ formation of amorphous $Ru(OH)_3$ deposited on $Ni(OH)_2$ nanoflakes. SEM images show that the nanoflake arrays are well preserved, though the smooth surfaces of the $Ni(OH)_2$ nanoflakes become rougher after the chemical etching (Figure S4a,b, Supporting Information). From TEM imaging (Figure S4c, Supporting Information), it can be seen that the $Ni(OH)_2$ nanoflakes crack into multiple blocks due to the etching process. However, the corresponding SAED pattern shows evidence that the $Ni(OH)_2$ nanoflakes retain their single crystal nature, which is also shown by HRTEM image and corresponding FFT pattern (Figure S4d,e, Supporting Information). No diffraction pattern or lattice fringe associated with $Ru(OH)_3$ nanocrystals can be found, suggesting that the deposited $Ru(OH)_3$ is amorphous. The uniform deposition of $Ru(OH)_3$ throughout the $Ni(OH)_2$ nanoflakes is confirmed by high-angle annular dark-field scanning transmission electron microscope (HAADF-STEM) imaging, element mapping, and corresponding EDX spectrum (Figure S5, Supporting Information).

After thermal treatment at 300 °C in Ar atmosphere, the $Ru(OH)_3$/$Ni(OH)_2$ nanoflake arrays were decomposed and converted into porous RuO_2/NiO nanosheet arrays. As reflected in the XRD pattern (Figure 1b), the resultant RuO_2/NiO/NF contains tetragonal RuO_2 (JCPDS card No. 21-1172) and cubic NiO (JCPDS card No. 04-0835). Meanwhile, it was found that
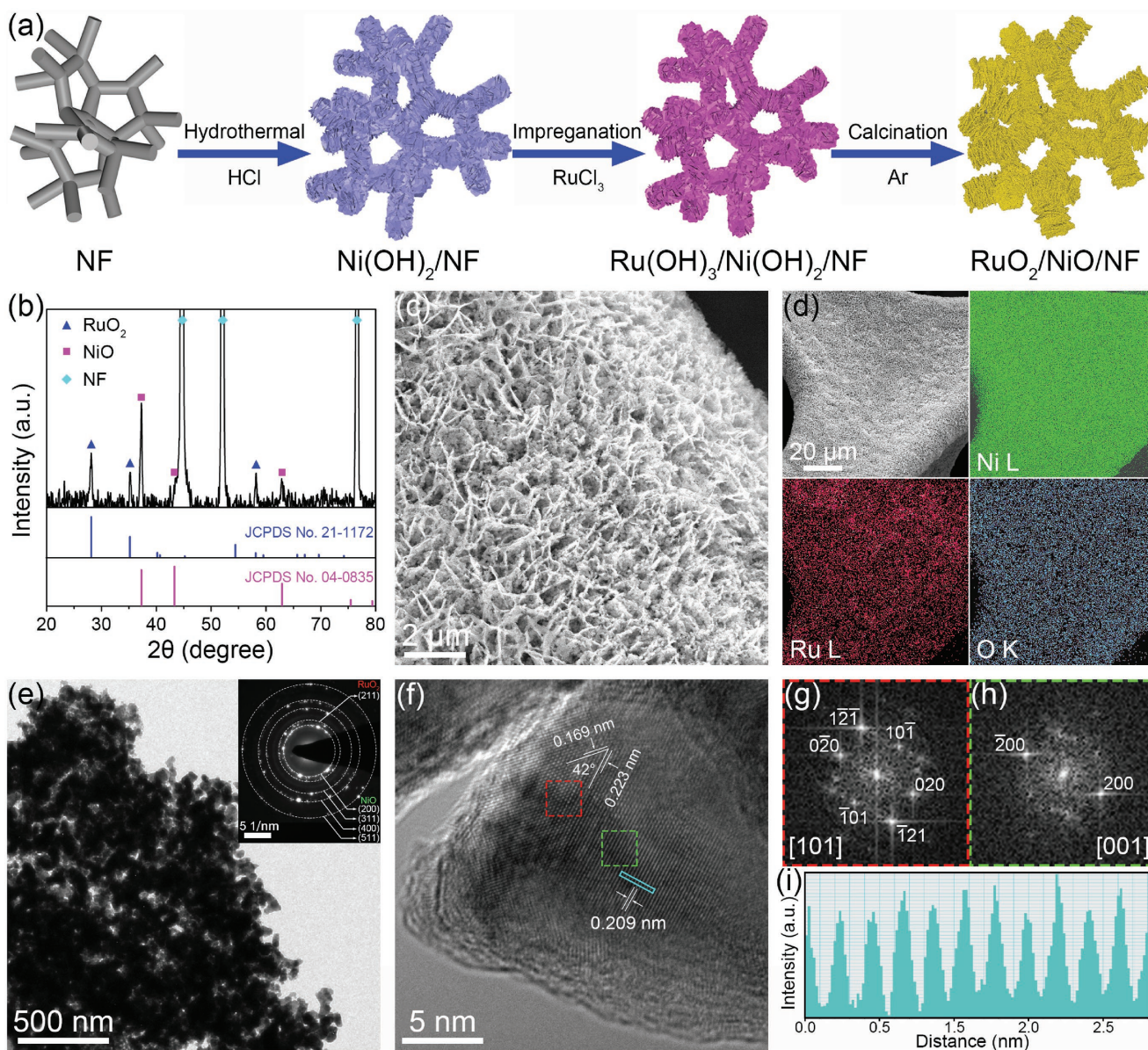
Figure 1. a) Schematic illustration for the fabrication process of hierarchical RuO$_2$/NiO/NF. b) XRD pattern, c,d) SEM images, and element mapping of Ni, Ru, O on RuO$_2$/NiO/NF. e) TEM image (inset in panel (e) showing the corresponding SAED pattern) and f) HRTEM image of RuO$_2$/NiO. g,h) FFT patterns and i) the lattice spacing corresponding to the selected areas in panel (f).

thermal annealing effect improved the HER activity (Figure S6, Supporting Information). Typical SEM images (Figure 1c,d) indicate that the solid nanoflake arrays are converted into porous nanosheet arrays after thermal treatment. EDX mapping analysis displays the uniform distribution of Ni, Ru, and O on the surface of the NF. Further, it is observed in the TEM image (Figure 1e) that the porous nanosheet is composed of numerous interconnected nanoparticles. The corresponding SAED pattern can be indexed to polycrystalline RuO$_2$ and NiO as marked. The nanoparticle built nanosheet with porous structure and homogeneous element distribution is also verified by HAADF-STEM and corresponding elemental analysis (Figure S7, Supporting Information). The HRTEM image of RuO$_2$/NiO nanoparticles provides more structural information about the

RuO$_2$/NiO interface. Two different domains are observed. Specifically, the lattice fringe spaces of 0.169 and 0.223 nm with a dihedral angle of 42° are attributed to the (211) and (200) planes of tetragonal RuO$_2$, respectively; the clear lattice with a spacing of 0.209 nm corresponds to the (200) plane of cubic NiO (Figure 1f,i). This is further supported by the indexed FFT diffractograms given in Figure 1g,h. From the domain corresponding to the RuO$_2$ nanoparticle (Figure 1f), it is estimated that the size of RuO$_2$ is about 5 nm. Based on these results, the hierarchical RuO$_2$/NiO/NF electrode, namely, the 3D NF framework, 2D porous nanosheet arrays, and interconnected RuO$_2$/NiO nanoparticles with strong interfacial interaction, is expected to facilitate charge/mass transport, increase electrolyte contact, expose abundant active sites, and most importantly,

**ADVANCED
SCIENCE NEWS**
www.advancedsciencenews.com

NANO MICRO

small

www.small-journal.com

achieve the desired synergistic effect for significantly improved activity toward the OER and HER.

To clarify the surface element contents and chemical states of RuO$_2$/NiO/NF, X-ray photoelectron spectroscopy (XPS) measurements were also conducted. The XPS survey spectrum of RuO$_2$/NiO/NF indicates the presence of Ru, Ni, and O elements on the surface of the as-synthesized electrode (**Figure 2**a), in agreement with the elemental mapping results. Quantification analysis shows that the atomic percentage of Ru, Ni, and O are estimated to be 21.47%, 17.45%, and 61.08%, respectively. In this synthesis strategy, the amount of Ru used is relatively low, thus significantly reducing the overall price of the as-designed RuO$_2$/NiO/NF. As shown in Figure 2b, the Ru 3d spectrum gives two spin-orbit peaks, which can be fitted to characteristic Ru 3d$_{3/2}$ (284.9 eV) and Ru 3d$_{5/2}$ of RuO$_2$ (280.5 eV) with a pair of satellites (denoted Sat.).[39,40] The deconvoluted peak located at 285 eV is attributed to the C 1s for energy calibration.[41] The Ni 2p

spectrum (Figure 2c) is divided into Ni 3p$_{3/2}$ (853.9 and 855.6 eV) and its satellite (861.4 eV), and Ni 2p$_{1/2}$ (872.8 eV) and its satellite (879.5 eV), suggesting the presence of NiO with Ni^{2+}.[42,43] For comparison, the Ni 2p spectrum of bare NF is also carried out, in which a sharp peak located at (852.6 eV) is assigned to metallic Ni, and the other peaks are related to the NiO$_x$ due to surface oxidization (Figure S8, Supporting Information).[44] In the O 1s spectrum (Figure 2d), the peaks at 529.5 and 531.1 eV are ascribed to Ru–O and Ni–O,[40,43–45] respectively, whereas the peak at 532.4 eV is attributed to the O–H from adsorbed water.[46] Moreover, no Cl 2p signal is detected (Figure 2e), implying that there are no Cl species remaining in RuO$_2$/NiO/ NF after the synthetic process. Therefore, this surface chemical information further demonstrates the successful preparation of RuO$_2$/NiO nanosheet arrays on NF.

As a self-supported electrode, RuO$_2$/NiO/NF was first investigated as an OER electrocatalyst in a typical three-electrode
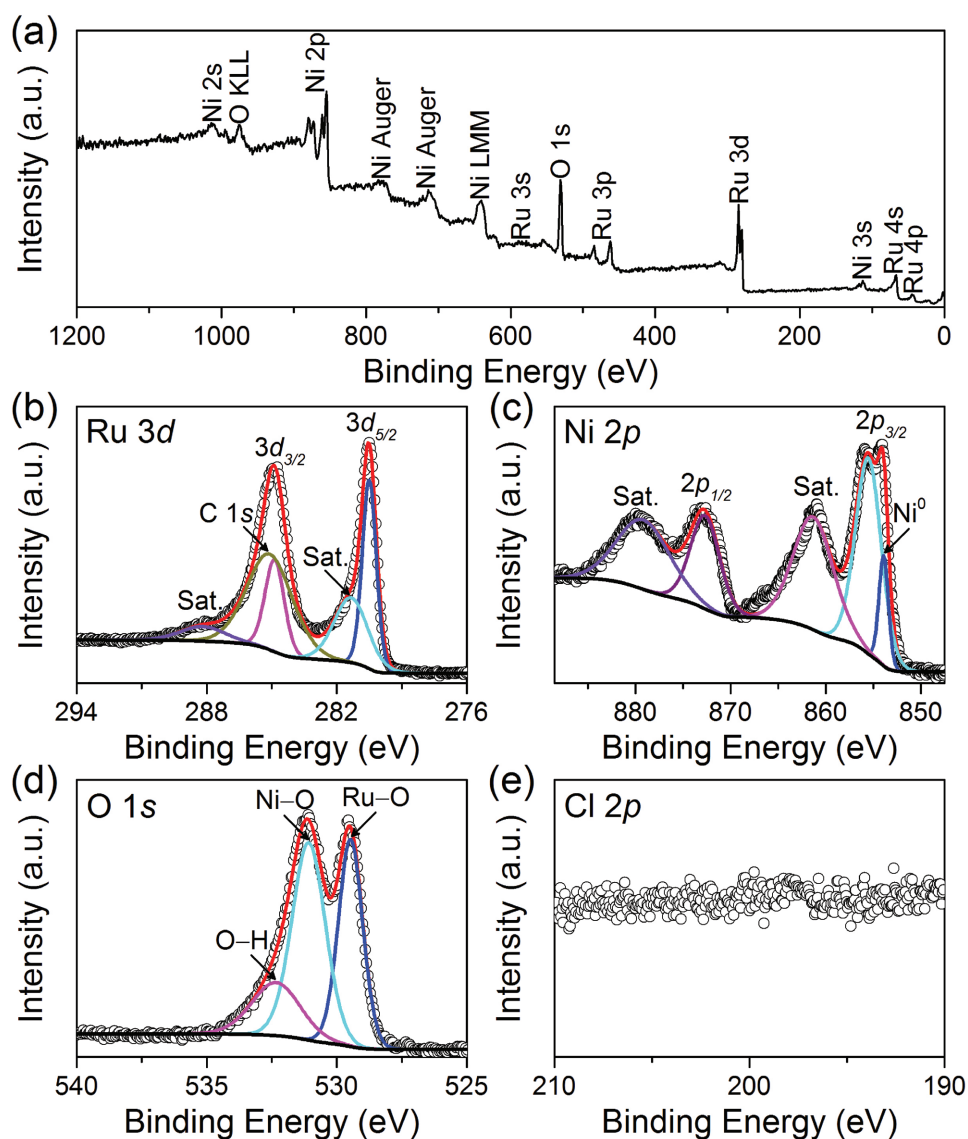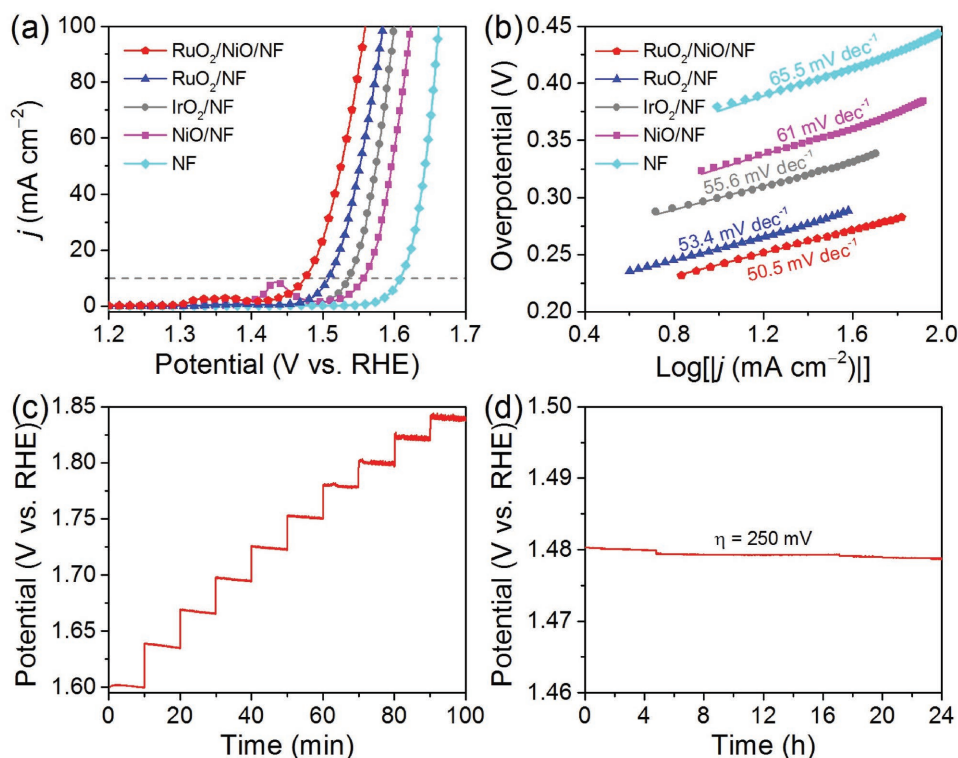

Figure 2. a) XPS survey spectrum and high-resolution XPS spectra of b) Ru 3d, c) Ni 2p, d) O 1s, and e) Cl 2p for RuO$_2$/NiO/NF.
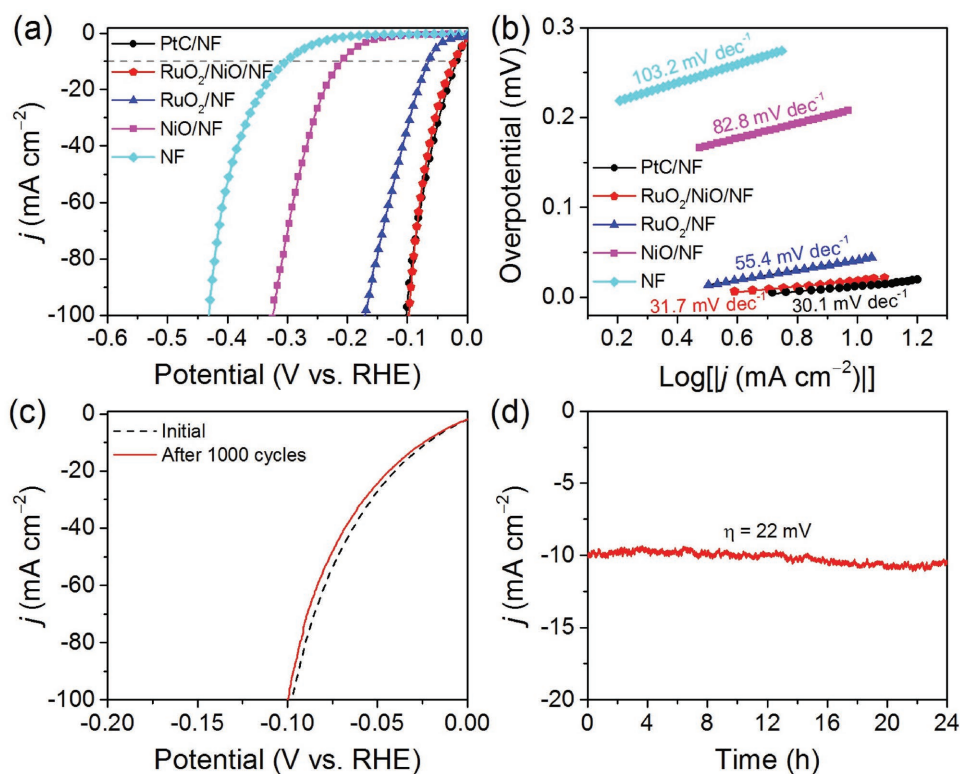
**ADVANCED
SCIENCE NEWS**

www.advancedsciencenews.com

NANO MICRO

small

www.small-journal.com

Figure 3. a) OER polarization curves and b) corresponding OER Tafel plots of $RuO_2/NiO/NF$, IrO_2/NF, RuO_2/NF, NiO/NF, and NF. c) Multicurrent process of $RuO_2/NiO/NF$ from 50 to 500 mA cm^{-2} with an increment of 50 mA cm^{-2} per 10 min (IR uncorrected). d) Chronoamperometric curve of $RuO_2/NiO/NF$ to deliver 10 mA cm^{-2}.

system. The OER activity of IrO_2/NF, RuO_2/NF, NiO/NF, and bare NF were also tested and compared under the same conditions. From the polarization curves (**Figure 3**a), $RuO_2/NiO/NF$ showed the lowest onset potential, indicating the highest OER activity among all samples. It is worth noting that there are distinct oxidation peaks before the OER onset for $RuO_2/NiO/NF$ and NiO/NF, which is attributed to the oxidation of NiO into active NiOOH.[36] To deliver a current density of 10 mA cm^{-2}, $RuO_2/NiO/NF$ only required an overpotential (η) of 250 mV, which is 33, 61, 83, and 134 mV lower than that of RuO_2/NF, IrO_2/NF, NiO/NF, and bare NF, respectively. At a potential of 1.5 V versus RHE, $RuO_2/NiO/NF$ affords an OER current density of 24 mA cm^{-2}, 2.6 and 17 times higher than that for RuO_2/NF and IrO_2/NF, respectively. By calculating the corresponding Tafel slopes of all samples (Figure 3b), it was found that $RuO_2/NiO/NF$ also exhibited the most favorable reaction kinetics with a Tafel slope of 50.5 mV dec^{-1}, outperforming that of RuO_2/NF (53.4 mV dec^{-1}), IrO_2/NF (55.6 mV dec^{-1}), NiO/NF (61 mV dec^{-1}), and bare NF (65.5 mV dec^{-1}). In particular, $RuO_2/NiO/NF$ has significantly higher OER activity than RuO_2/NF and NiO/NF, likely resulting from the synergistic effect between RuO_2 and NiO toward the OER (discussed later). In addition to activity, stability is another important property of efficient electrocatalysts. Figure 3c displays the chronopotentiometric curve for $RuO_2/NiO/NF$ at different current densities from 50 to 500 mA cm^{-2} without IR-correction. Interestingly, the overpotential decreases slightly to maintain a given current density at each step. In a prolonged stability test (Figure 3d), the

overpotential to afford a current density of 10 mA cm^{-2} (η_{10}) starts at 253 mV and reduces to 248 mV after 24 h. This phenomenon is probably caused by the gradual increase of active NiOOH during operation.[36] Meanwhile, the OER polarization curve of $RuO_2/NiO/NF$ after 1000 cycles (Figure S9, Supporting Information) shows an obvious negative shift with a much higher Ni^{2+}/Ni^{3+} oxidation peak, consistent with the chronoamperometric stability result. Evidently, its remarkable OER activity and stability make $RuO_2/NiO/NF$ a significantly improved OER electrocatalyst.

The electrocatalytic HER performance of freshly prepared $RuO_2/NiO/NF$, along with PtC/NF, RuO_2/NF, NiO/NF, and bare NF were also evaluated and compared using a three-electrode configuration. As presented in **Figure 4**a, $RuO_2/NiO/NF$ shows a very small onset overpotential comparable to PtC/NF ($\eta_{onset} = \approx 0$ mV). Impressively, $RuO_2/NiO/NF$ only needs an η_{10} of 22 mV. Compared to RuO_2/NF, NiO/NF, and bare NF, this overpotential is smaller by 43, 189, and 281 mV, respectively, implying a prominent synergistic effect for alkaline HER as expected. Similarly, $RuO_2/NiO/NF$ has a small HER Tafel slope of 31.7 mV dec^{-1}, resulting in faster HER kinetics than RuO_2/NF (55.4 mV dec^{-1}), NiO/NF (82.8 mV dec^{-1}), and bare NF (103.2 mV dec^{-1}, Figure 4b). In terms of alkaline HER stability, $RuO_2/NiO/NF$ was first tested by employing cyclic voltammetry (CV). In Figure 4c, it can be seen that the HER polarization curve for $RuO_2/NiO/NF$ shows negligible attenuation after 1000 CV cycles. Moreover, during 24 h operation at $\eta = 22$ mV, $RuO_2/NiO/NF$ affords an almost constant 10 mA cm^{-2} catalytic

ADVANCED
SCIENCE NEWS
www.advancedsciencenews.com

NANO MICRO
small
www.small-journal.com

Figure 4. a) HER polarization curves and b) corresponding HER Tafel plots of RuO₂/NiO/NF, PtC/NF, RuO₂/NF, NiO/NF, and NF. c) Polarization curves of RuO₂/NiO/NF before and after 1000 CV cycles. d) Chronoamperometric curve of RuO₂/NiO/NF for HER at η = 22 mV.

current output (Figure 4d), suggesting that the material is highly stable for alkaline HER. This evidence demonstrates that the RuO₂/NiO/NF is highly active and stable for both the OER and HER in alkaline electrolyte.

To further highlight RuO₂/NiO/NF as a bifunctional electrode for overall alkaline water electrolysis, a two-electrode electrolyzer setup using RuO₂/NiO/NF as both anode and cathode was constructed as shown in **Figure 5**a. Of all configurations tested, this water electrolyzer displayed the highest performance with a current density of 10 mA cm⁻² at a cell voltage of 1.5 V in 1.0 M KOH (Figure 5b). This performance was even better than the commercial PtC/NF‖IrO₂/NF couple (1.56 V), NiO/NF‖NiO/NF couple (1.77 V), bare NF‖NF couple (1.92 V), and almost all recently reported bifunctional electrocatalysts (Table S1, Supporting Information). Additionally, the electrolyzer based exclusively on RuO₂/NiO/NF is stable for overall water splitting, as both chronoamperometric and chronopotentiometric curves show that the cell produces a constant 10 mA cm⁻² at 1.5 V over 24 h continuous operation (Figure 5c).

The significantly enhanced bifunctional activity and stability of RuO₂/NiO/NF are correlated with its unique components and hierarchical structure. First, RuO₂/NiO/NF has good electrical conductivity due to the highly conductive 3D NF substrate, metallic RuO₂, and strong interaction between the NF and RuO₂/NiO nanosheet arrays. This is supported by the electrochemical impedance spectra, in which RuO₂/NiO/NF shows the smallest charge transfer resistance of all samples tested (R_{ct}, Figure S10, Supporting Information). Second, the catalytic efficiency is expected to be proportional to the

electrochemical surface area (ECSA),[47] and the interconnected RuO₂/NiO nanoparticle built nanosheet arrays are beneficial to expose the abundant active sites. Generally, the double-layer capacitance (C_{dl}) is a good approach to assess the ECSA.[48] As shown in Figure S11 in the Supporting Information, the C_{dl} of RuO₂/NiO/NF is 4.1 mF cm⁻². In contrast, the C_{dl} of RuO₂/NF, NiO/NF, and bare NF is 2.23 mF cm⁻², 802.2 μF cm⁻², and 467.8 μF cm⁻², respectively. Undoubtedly, the large active surface area of RuO₂/NiO/NF, originating from the favorable hierarchical architecture, makes considerable contribution to its high catalytic activity. Of course, to decouple the geometric effect associated with an enhanced ECSA, the specific OER/HER current densities of RuO₂/NiO/NF were further analyzed and compared with other control samples. Table S2 in the Supporting Information demonstrates that RuO₂/NiO/NF has significantly greater intrinsic OER/HER activities compared to that of the other samples. Third, the porous vertically aligned nanosheet arrays enable full penetration of the electrolyte to the active sites and promote the release of generated bubbles, thereby facilitating mass transfer for improved reaction kinetics.[49] Most importantly, the greatly enhanced activity is closely related to the potential-induced interfacial synergy between the RuO₂ and NiO nanoparticles illustrated in **Figure 6**. As mentioned earlier, NiOOH (converted from NiO under applied potentials) has a capability of dissociating water molecule,[26] while RuO₂ can efficiently dissociate OH due to the strong affinity of bridging oxygen (O^br) for H and the neighboring coordinatively unsaturated ruthenium (Ru^cus) for O.[50,51] On individual RuO₂ and NiOOH surfaces, it is difficult to achieve optimal dissociation

ADVANCED
SCIENCE NEWS
www.advancedsciencenews.com

NANO MICRO
small
www.small-journal.com
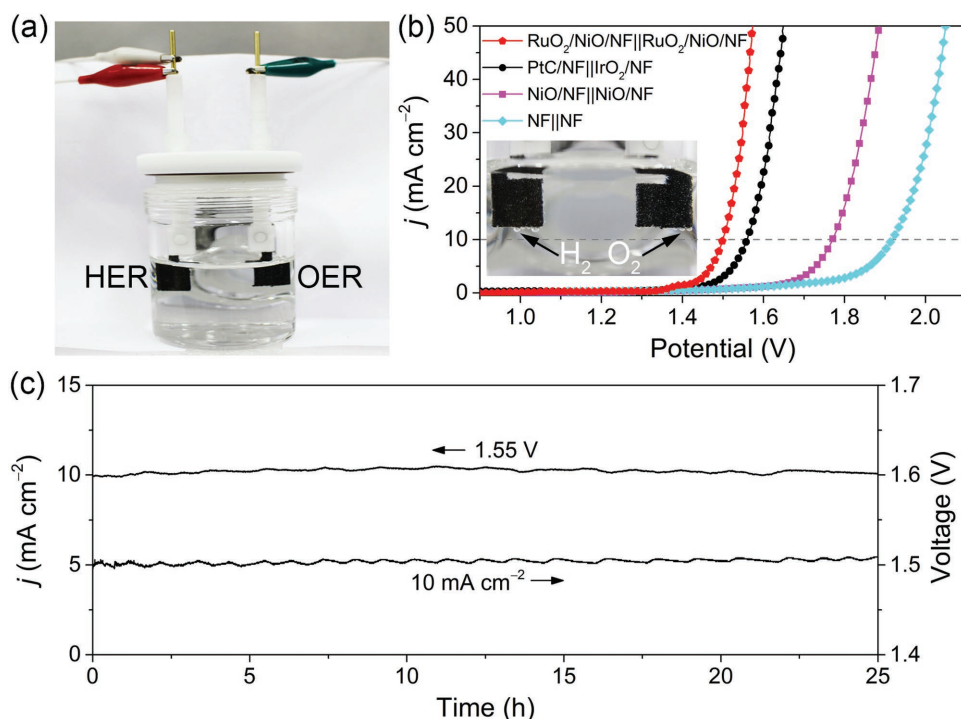
Figure 5. a) Digital photograph of the two-electrode electrolyzer. b) Polarization curves of $RuO_2/NiO/NF\|$ $RuO_2/NiO/NF$, $PtC/NF\|IrO_2/NF$, NiO/NF$\|$NiO/NF, and NF$\|$NF in 1.0 M KOH (inset in panel (b) showing the H_2 and O_2 evolution on $RuO_2/NiO/NF$). c) Chronoamperometric and chronopotentiometric curves of $RuO_2/NiO/NF$ in the two-electrode configuration for overall water splitting.

of H_2O and OH^-, respectively. However, at in situ formed $RuO_2/NiOOH$ interfaces, (i) dissociation of H_2O and (ii) dissociation of OH^- can be coupled and optimized to produce the OOH^- intermediate. The highly active OOH^- intermediate can further deprotonate and be released as (iii) molecular O_2, thus realizing the synergistic effect for alkaline OER (Figure 6a). On the cathodic side, an in situ Ru/NiO interface can be generated considering the electrochemical reduction of RuO_2 at applied negative potentials. Given the stronger affinity for OH^- on the NiO surface,[26] NiO is able to promote the dissociation of water into OH^- and H. The produced H can then be immediately absorbed by nearby Ru and further recombined into molecule H_2. As shown in Figure 6b, such a reaction pathway provides the Ru/NiO interface with significantly improved HER rate. It is well-known that the Tafel slope is an inherent property of a specific catalyst determined by the reaction mechanism. To further verify the above hypothesis, theoretical analysis of the OER and HER mechanism, along with corresponding Tafel slope, has been provided in Notes 2 and 3 in the Supporting Information. Evidently, the self-consistent interpretations of the Tafel slopes support the OER and HER mechanisms with interfacial synergy. Finally, the robust NF framework, strong coupling of RuO_2 and NiO, together with excellent intrinsic corrosion resistance of each component, provide long-term durability of the as-fabricated $RuO_2/NiO/NF$ for practical applications. As observed in Figure S12 in the Supporting Information, the nanosheet arrays of $RuO_2/NiO/NF$ were preserved after long-term operation. Benefitting from these advantageous features, $RuO_2/NiO/NF$ as a self-supported electrode affords superior activity and stability for overall alkaline water electrolysis.

3. Conclusion

In summary, hybrid RuO_2/NiO nanosheet arrays on NF exhibit remarkable activity, favorable kinetics, and excellent durability for both the OER and HER under alkaline conditions. As a bifunctional electrocatalyst, $RuO_2/NiO/NF$ is efficient and stable toward overall alkaline water splitting, and is even better than the commercial $PtC/NF\|IrO_2/NF$ couple and almost all recently reported bifunctional electrocatalysts. The significantly enhanced performance can be attributed to the unique nanostructure and functional components of the as-synthesized electrode, giving rise to good conductivity, enlarged active surface area, improved mass transport, strong structural stability, and potential-induced interfacial synergy. All these results confirm NiO as an effective bifunctional promoter to tailor RuO_2 toward superior overall alkaline water splitting. It is believed that the design strategy developed in this work may provide a new perspective for designing other advanced nanocomposite catalysts for various applications, such as fuel cells, metal–air batteries, and photoelectrocatalysis.

4. Experimental Section

Chemicals: All chemicals (analytical reagent grade) used in this work, including HCl, ethanol, KOH, $RuCl_3\cdot xH_2O$, RuO_2, IrO_2, nickel foam (NF, thickness 1.6 mm, bulk density 0.45 g cm^{-3}), Pt/C (20 wt% of Pt on Vulcan XC72), Nafion (15 wt%) were purchased from Sigma-Aldrich and used without further purification. Ultrapure water (18.2 MΩ cm, PURELAB Option-Q) was used in all the experiments.

Preparation of Ni(OH)$_2$/NF: Ni(OH)$_2$ nanoflake arrays were synthesized on NF by a simple hydrothermal reaction according to

ADVANCED
SCIENCE NEWS
www.advancedsciencenews.com

NANO · MICRO
small
www.small-journal.com
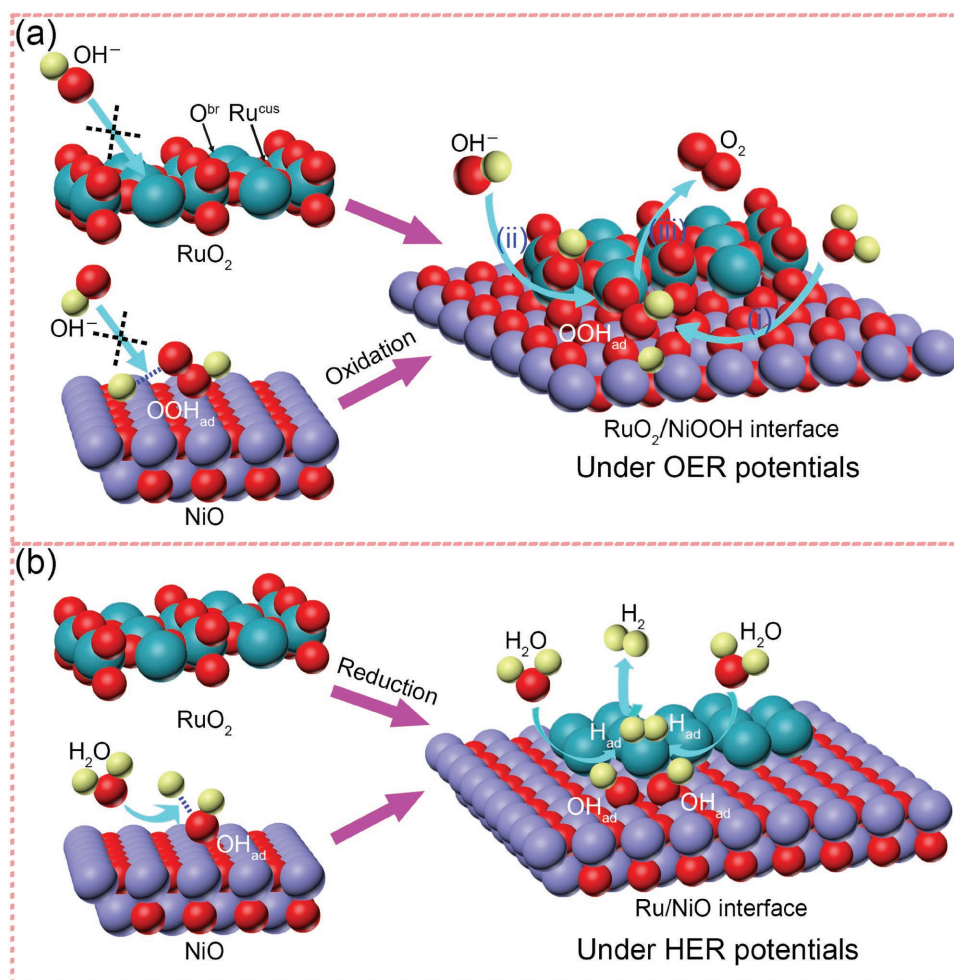
Figure 6. Schematic illustration of potential-induced interfacial synergy between RuO_2 and NiO for enhanced a) OER and b) HER under alkaline conditions.

Tian et al.[38] In detail, a piece of NF (1 cm × 4 cm) was ultrasonically cleaned in 3 M HCl and ethanol, and then rinsed with water. The cleaned NF was immersed into 40 mL of HCl solution with pH of 2.5, which was then transferred into a 50 mL Teflon-lined stainless steel autoclave. The autoclave was sealed and maintained at 180 °C for 6 h. After cooling naturally to room temperature, the sample was collected and rinsed with water and ethanol several times, and further dried in Ar flow.

Preparation of $RuO_2/NiO/NF$: Typically, the $Ni(OH)_2/NF$ obtained as above was immersed into 20 mL of 5 × 10^{-3} M $RuCl_3$ aqueous solution overnight. Afterward, the sample was collected and dried in a vacuum oven at 60 °C for 12 h to give $Ru(OH)_3/Ni(OH)_2/NF$. Under Ar atmosphere, the obtained precursor was heated to 300 °C in a tube furnace at a rate of 2 °C min^{-1} and kept at that temperature for 2 h. The mass loading of NiO and RuO_2 on NF was calculated as follows. The mass increment of NF was directly weighed after preparation, which was found to be about 1.1 mg cm^{-2}. EDX quantification analysis of the RuO_2/NiO nanosheet then revealed that the mass percentage of Ru was ≈13.6%, thus mass loading of RuO_2 was (M_{RuO2}/M_{Ru}) × 13.6% × 1.1 mg cm^{-2} = (133.07/101.07) × 13.6% × 1.1 mg cm^{-2} ≈ 0.2 mg cm^{-2}, and the mass loading of NiO was (1.1–0.2) mg cm^{-2} = 0.9 mg cm^{-2}.

Preparation of NiO/NF: To fabricate NiO/NF for comparison, the same calcination procedure for the preparation of $RuO_2/NiO/NF$ was also performed on the $Ni(OH)_2/NF$ obtained as above.

Preparation of RuO_2/NF: 5 mg of commercial RuO_2 was dispersed in 1 mL of ethanol containing 0.15 wt% of Nafion under sonication for 1 h.

200 μL of the dispersion was loaded onto a piece of precleaned NF (1 cm × 1 cm) to obtain RuO_2/NF electrode.

Preparation of IrO_2/NF: IrO_2/NF electrode was prepared by the same approach as the preparation of RuO_2/NF, except that the commercial RuO_2 was replaced with commercial IrO_2.

Preparation of PtC/NF: PtC/NF electrode was prepared by the same approach as the preparation of RuO_2/NF, except that the commercial RuO_2 was replaced with commercial 20 wt% Pt/C.

Characterizations: XRD patterns were recorded on a Cu-target Bruker D8 Advance powder diffractometer (λ = 1.540598 Å). SEM images, TEM images, HRTEM images, element mappings, EDX spectra, SAED patterns were collected on a QUANTA 450 field emission scanning electron microscope equipped with EDX detector and a Tecnai G^2 F30 scanning transmission electron microscope with high-angle annular dark-field detector. XPS measurements were carried out on an ESCALab250 XPS spectrometer.

Electrochemical Measurements: Electrochemical measurements were performed on a 760D electrochemical workstation (CH Instruments, Inc., USA) using a standard three-electrode glass cell (Pine Research Instruments, USA). 1 cm × 1 cm $RuO_2/NiO/NF$, NiO/NF, RuO_2/NF, IrO_2/NF, PtC/NF, and bare NF were directly used as the working electrode. A carbon rod and an Ag/AgCl (4 M KCl) electrode were employed as the counter electrode and the reference electrode, respectively. All potentials were referenced to the RHE using the following equation: $E(RHE) = E(Ag/AgCl) + 0.205 + 0.059 \times pH$. All the electrolytes were purged with N_2 for 30 min before measurements

to remove dissolved O_2. The linear sweep voltammetry curves were collected at a scan rate of 1 and 5 mV s^{-1} for the OER and HER, respectively. IR compensation of polarization curves was performed using the solution resistance (R_s) estimated from electrochemical impedance spectroscopy (EIS) measurements. EIS was measured in the frequency range from 0.1 Hz to 100 kHz with an amplitude of 5 mV. The C_{dl} of various samples was evaluated using CV technique in a small potential range of 0.85–0.90 V versus RHE. The long-term stability test was carried out by repetitive CV scans, chronoamperometric and chronopotentiometric tests. For overall water electrolysis, a two-electrode setup was used during the electrochemical investigation. All electrochemical measurements were conducted at ambient temperature, and all data were corrected for the IR contribution within the cell unless otherwise noted.

Supporting Information

Supporting Information is available from the Wiley Online Library or from the author.

Acknowledgements

Conflict of Interest

The authors declare no conflict of interest.

Keywords

[1] Z. W. Seh, J. Kibsgaard, C. F. Dickens, I. Chorkendorff, J. K. Nørskov, T. F. Jaramillo, *Science* **2017**, *355*, eaad4998.

[2] S. Anantharaj, S. R. Ede, K. Sakthikumar, K. Karthick, S. Mishra, S. Kundu, *ACS Catal.* **2016**, *6*, 8069.

[3] L. Han, S. Dong, E. Wang, *Adv. Mater.* **2016**, *28*, 9266.

[4] M. I. Jamesh, *J. Power Sources* **2016**, *333*, 213.

[5] T. Y. Ma, S. Dai, S. Z. Qiao, *Mater. Today* **2016**, *19*, 265.

[6] J. Liu, D. Zhu, C. Guo, A. Vasileff, S. Z. Qiao, *Adv. Energy Mater.* **2017**, *7*, 1700518.

[7] C. C. L. McCrory, S. Jung, I. M. Ferrer, S. M. Chatman, J. C. Peters, T. F. Jaramillo, *J. Am. Chem. Soc.* **2015**, *137*, 4347.

[8] C. C. L. McCrory, S. Jung, J. C. Peters, T. F. Jaramillo, *J. Am. Chem. Soc.* **2013**, *135*, 16977.

[9] C. Tang, N. Cheng, Z. Pu, W. Xing, X. Sun, *Angew. Chem., Int. Ed.* **2015**, *54*, 9351.

[10] H. Wang, H.-W. Lee, Y. Deng, Z. Lu, P.-C. Hsu, Y. Liu, D. Lin, Y. Cui, *Nat. Commun.* **2015**, *6*, 7261.

[11] J. Duan, S. Chen, A. Vasileff, S. Z. Qiao, *ACS Nano* **2016**, *10*, 8738.

[12] Y. Jin, H. Wang, J. Li, X. Yue, Y. Han, P. K. Shen, Y. Cui, *Adv. Mater.* **2016**, *28*, 3785.

[13] J. Tian, N. Cheng, Q. Liu, X. Sun, Y. He, A. M. Asiri, *J. Mater. Chem. A* **2015**, *3*, 20056.

[14] M. Y. Gao, C. Yang, Q. B. Zhang, J. R. Zeng, X. T. Li, Y. X. Hua, C. Y. Xu, P. Dong, *J. Mater. Chem. A* **2017**, *5*, 5797.

[15] X. Gao, H. Zhang, Q. Li, X. Yu, Z. Hong, X. Zhang, C. Liang, Z. Lin, *Angew. Chem., Int. Ed.* **2016**, *55*, 6290.

[16] H. Liu, G. Xia, R. Zhang, P. Jiang, J. Chen, Q. Chen, *RSC Adv.* **2017**, *7*, 3686.

[17] G. Ou, P. Fan, H. Zhang, K. Huang, C. Yang, W. Yu, H. Wei, M. Zhong, H. Wu, Y. Li, *Nano Energy* **2017**, *35*, 207.

[18] X. Yan, L. Tian, S. Atkins, Y. Liu, J. Murowchick, X. Chen, *ACS Sustainable Chem. Eng.* **2016**, *4*, 3743.

[19] B. Zhang, C. Xiao, S. Xie, J. Liang, X. Chen, Y. Tang, *Chem. Mater.* **2016**, *28*, 6934.

[20] L. Fang, W. Li, Y. Guan, Y. Feng, H. Zhang, S. Wang, Y. Wang, *Adv. Funct. Mater.* **2017**, *27*, 1701008.

[21] Y. Yang, K. Zhang, H. Lin, X. Li, H. C. Chan, L. Yang, Q. Gao, *ACS Catal.* **2017**, *7*, 2357.

[22] J. Zhang, T. Wang, D. Pohl, B. Rellinghaus, R. Dong, S. Liu, X. Zhuang, X. Feng, *Angew. Chem., Int. Ed.* **2016**, *55*, 6702.

[23] J. Li, G. Wei, Y. Zhu, Y. Xi, X. Pan, Y. Ji, I. V. Zatovsky, W. Han, *J. Mater. Chem. A* **2017**, *5*, 14828.

[24] R. Subbaraman, D. Tripkovic, K.-C. Chang, D. Strmcnik, A. P. Paulikas, P. Hirunsit, M. Chan, J. Greeley, V. Stamenkovic, N. M. Markovic, *Nat. Mater.* **2012**, *11*, 550.

[25] J. Rossmeisl, Z. W. Qu, H. Zhu, G. J. Kroes, J. K. Nørskov, *J. Electroanal. Chem.* **2007**, *607*, 83.

[26] I. C. Man, H.-Y. Su, F. Calle-Vallejo, H. A. Hansen, J. I. Martínez, N. G. Inoglu, J. Kitchin, T. F. Jaramillo, J. K. Nørskov, J. Rossmeisl, *ChemCatChem* **2011**, *3*, 1159.

[27] Y. Lee, J. Suntivich, K. J. May, E. E. Perry, Y. Shao-Horn, *J. Phys. Chem. Lett.* **2012**, *3*, 399.

[28] X. Kong, K. Xu, C. Zhang, J. Dai, S. Norooz Oliaee, L. Li, X. Zeng, C. Wu, Z. Peng, *ACS Catal.* **2016**, *6*, 1487.

[29] J. Greeley, M. Mavrikakis, *J. Phys. Chem. B* **2005**, *109*, 3460.

[30] M. T. M. Koper, *Electrochim. Acta* **2011**, *56*, 10645.

[31] T. Bhowmik, M. K. Kundu, S. Barman, *ACS Appl. Mater. Interfaces* **2016**, *8*, 28678.

[32] R. Subbaraman, D. Tripkovic, D. Strmcnik, K. C. Chang, M. Uchimura, A. P. Paulikas, V. Stamenkovic, N. M. Markovic, *Science* **2011**, *334*, 1256.

[33] J. Wang, S. Mao, Z. Liu, Z. Wei, H. Wang, Y. Chen, Y. Wang, *ACS Appl. Mater. Interfaces* **2017**, *9*, 7139.

[34] O. Diaz-Morales, I. Ledezma-Yanez, M. T. M. Koper, F. Calle-Vallejo, *ACS Catal.* **2015**, *5*, 5380.

[35] E. Fabbri, A. Habereder, K. Waltar, R. Kotz, T. J. Schmidt, *Catal. Sci. Technol.* **2014**, *4*, 3800.

[36] L. Trotochaud, J. K. Ranney, K. N. Williams, S. W. Boettcher, *J. Am. Chem. Soc.* **2012**, *134*, 17253.

[37] M. E. G. Lyons, A. Cakara, P. O'Brien, I. Godwin, R. L. Doyle, *Int. J. Electrochem. Sci.* **2012**, *7*, 11768.

[38] J. Tian, Z. Xing, Q. Chu, Q. Liu, A. M. Asiri, A. H. Qusti, A. O. Al-Youbi, X. Sun, *CrystEngComm* **2013**, *15*, 8300.

[39] D. J. Morgan, *Surf. Interface Anal.* **2015**, *47*, 1072.

[40] K.-H. Kwak, D. W. Kim, Y. Kang, J. Suk, *J. Mater. Chem. A* **2016**, *4*, 16356.

[41] C. Liu, C. Li, K. Ahmed, W. Wang, I. Lee, F. Zaera, C. S. Ozkan, M. Ozkan, *Adv. Mater. Interfaces* **2016**, *3*, 1500503.

[42] M. A. Peck, M. A. Langell, *Chem. Mater.* **2012**, *24*, 4483.

[43] A. G. Marrani, V. Novelli, S. Sheehan, D. P. Dowling, D. Dini, *ACS Appl. Mater. Interfaces* **2014**, *6*, 143.

**ADVANCED
SCIENCE NEWS**

www.advancedsciencenews.com

NANO MICRO

small

www.small-journal.com

[44] E. Symianakis, S. Ladas, G. A. Evangelakis, *Appl. Surf. Sci.* **2003**, *217*, 239.

[45] H. Boris, H. Kristína, R. Alica, Š. Ján, R. Raul, K. Aarne, U. Teet, M. Matej, O. Mária, A. Jaan, F. Karol, *J. Phys. D: Appl. Phys.* **2013**, *46*, 385304.

[46] H. S. Casalongue, S. Kaya, V. Viswanathan, D. J. Miller, D. Friebel, H. A. Hansen, J. K. Nørskov, A. Nilsson, H. Ogasawara, *Nat. Commun.* **2013**, *4*, 2817.

[47] D. Kong, H. Wang, Z. Lu, Y. Cui, *J. Am. Chem. Soc.* **2014**, *136*, 4897.

[48] J. Kibsgaard, Z. Chen, B. N. Reinecke, T. F. Jaramillo, *Nat. Mater.* **2012**, *11*, 963.

[49] J. Duan, S. Chen, C. Zhao, *Nat. Commun.* **2017**, *8*, 15341.

[50] Q. Sun, K. Reuter, M. Scheffler, *Phys. Rev. B* **2004**, *70*, 235402.

[51] Y. D. Kim, A. P. Seitsonen, S. Wendt, J. Wang, C. Fan, K. Jacobi, H. Over, G. Ertl, *J. Phys. Chem. B* **2001**, *105*, 3752.

NANO | MICRO

small

Supporting Information

NiO as a Bifunctional Promoter for RuO$_2$ toward Superior Overall Water Splitting

Jinlong Liu, Yao Zheng, Yan Jiao, Zhenyu Wang, Zhouguang Lu, Anthony Vasileff, and Shi-Zhang Qiao*

Supporting Information

NiO as a Bifunctional Promotor for RuO₂ toward Superior Overall Water Splitting

Jinlong Liu,[†] Yao Zheng,[†] Yan Jiao,[†] Zhenyu Wang,[‡] Zhouguang Lu,[‡] Anthony Vasileff,[†] and Shi-Zhang Qiao[,†,§]*

[†]School of Chemical Engineering, The University of Adelaide, Adelaide, SA 5005, Australia

[‡]Department of Materials Science and Engineering, South University of Science and Technology, Shenzhen 518005, P.R. China

[§]School of Materials Science and Engineering, Tianjin University, Tianjin 300072, P.R. China

Corresponding Author: Shi-Zhang Qiao, E-mail address: s.qiao@adelaide.edu.au
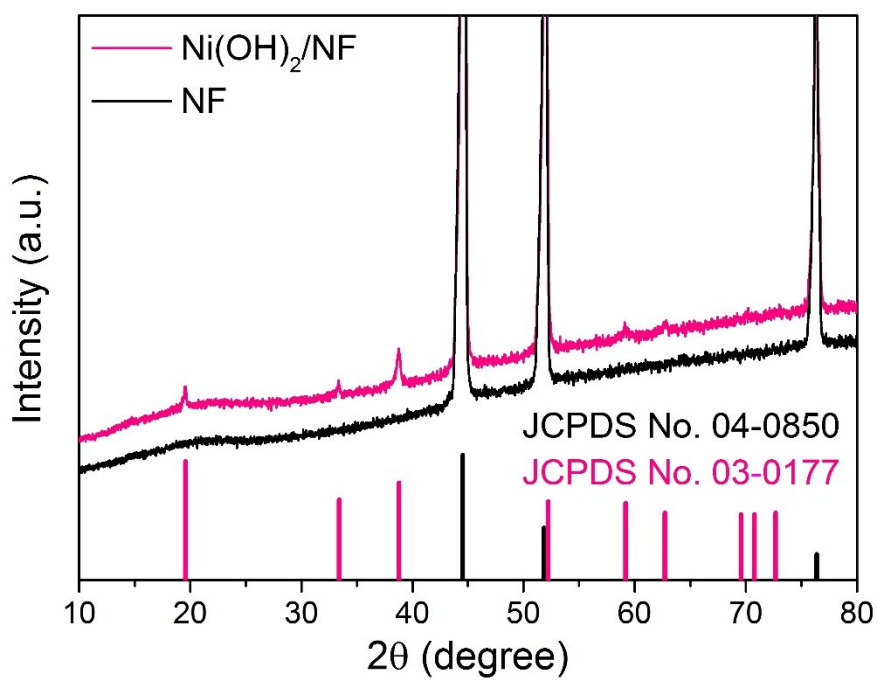
Figure S1. Experimental XRD patterns of bare NF and $Ni(OH)_2$/NF, along with standard XRD patterns of cubic Ni (JCPDS card No. 04-0850) and hexagonal $Ni(OH)_2$ (JCPDS card No. 03-0177).
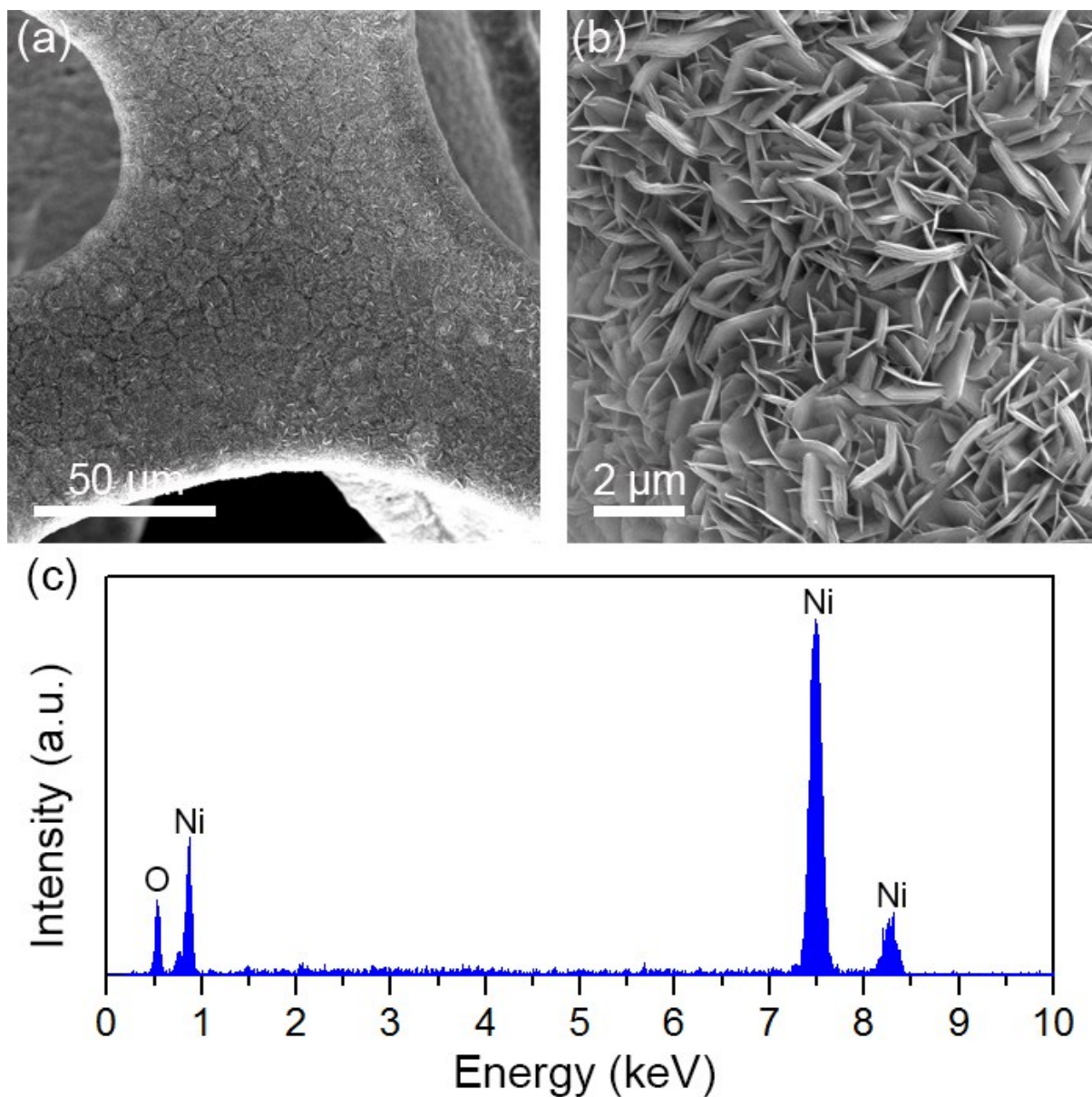
Figure S2. (a, b) SEM images and (c) EDX spectrum of Ni(OH)$_2$/NF.
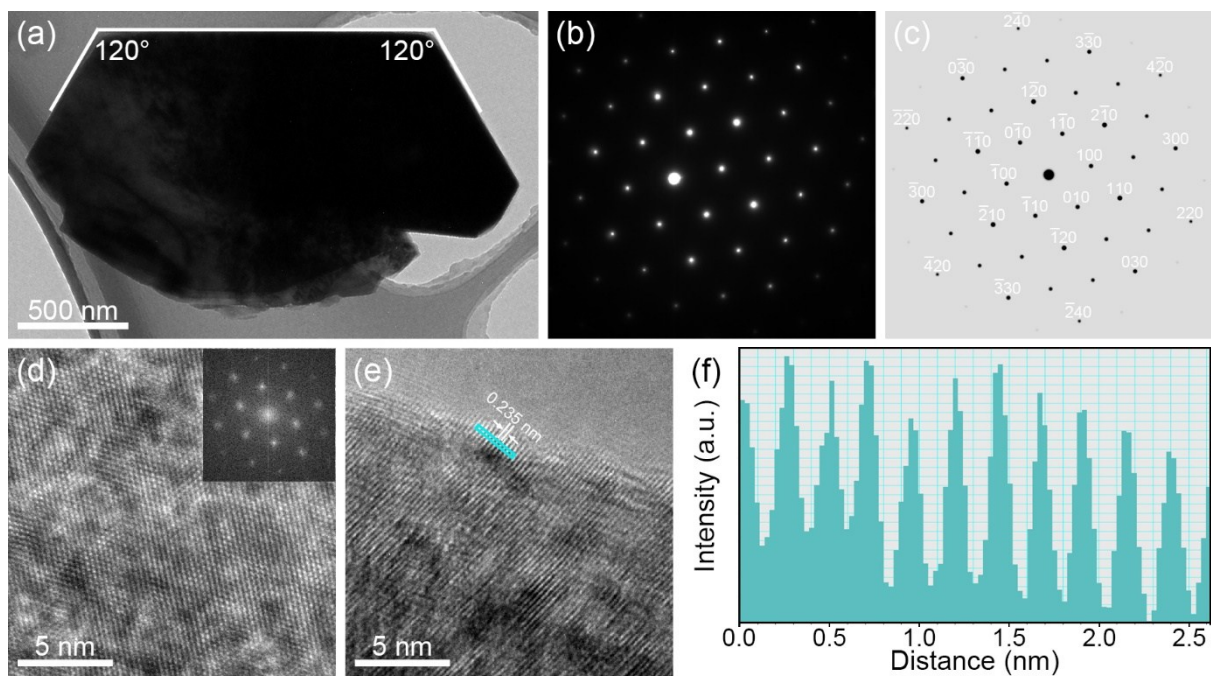
Figure S3. (a) TEM image, (b) SAED pattern, (c) simulated [001] diffraction pattern, (d, e) HRTEM images of Ni(OH)$_2$ nanoflakes (Inset in panel (d) showing the corresponding FFT pattern), and (f) the lattice spacing along the cyan rectangle in panel (e).
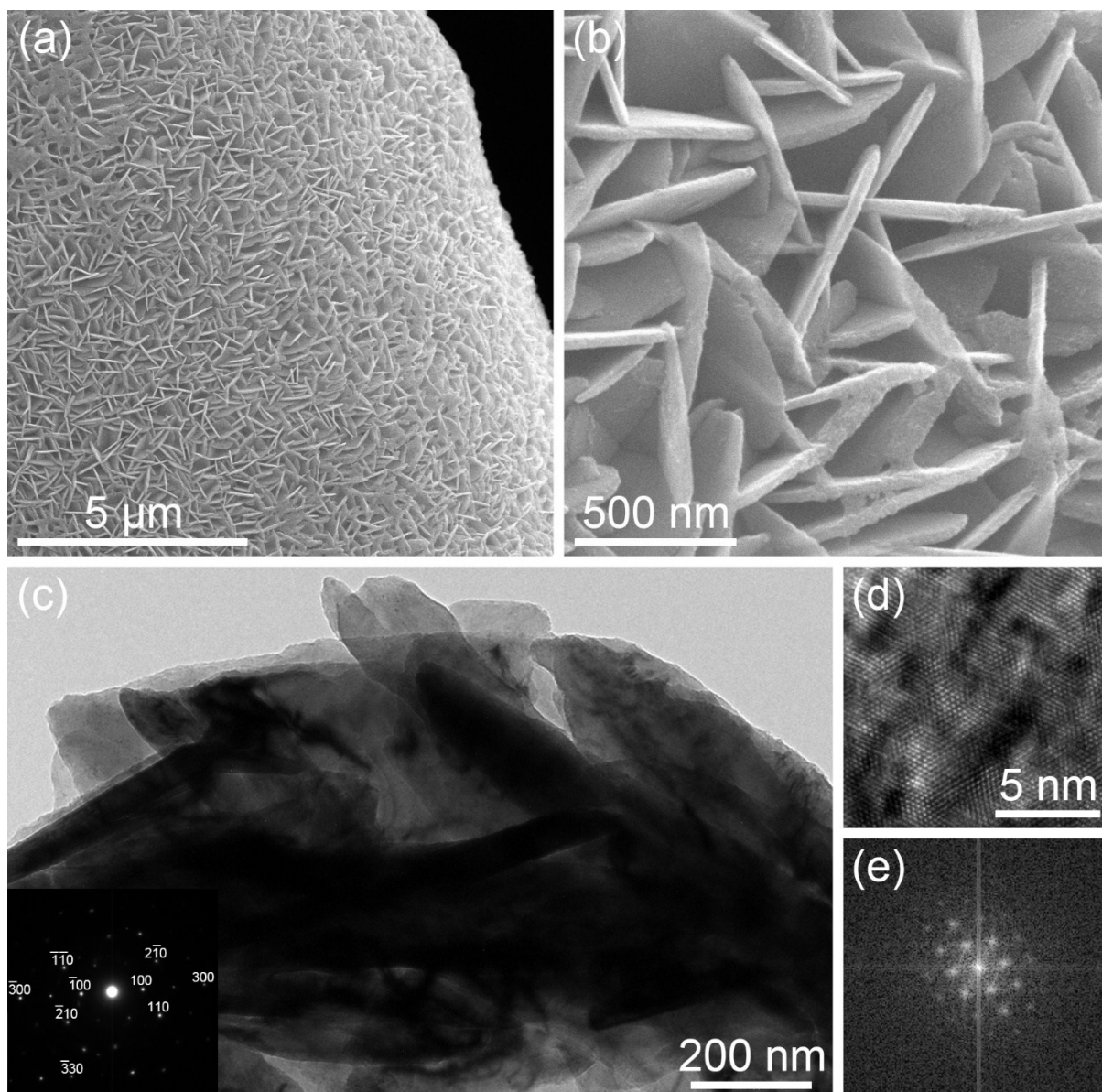
Figure S4. (a, b) SEM images of Ru(OH)$_3$/Ni(OH)$_2$/NF, (c) TEM image (Inset in panel (c) showing the corresponding SAED pattern), (d) HRTEM image and (e) corresponding FFT pattern of Ru(OH)$_3$/Ni(OH)$_2$ nanoflakes.
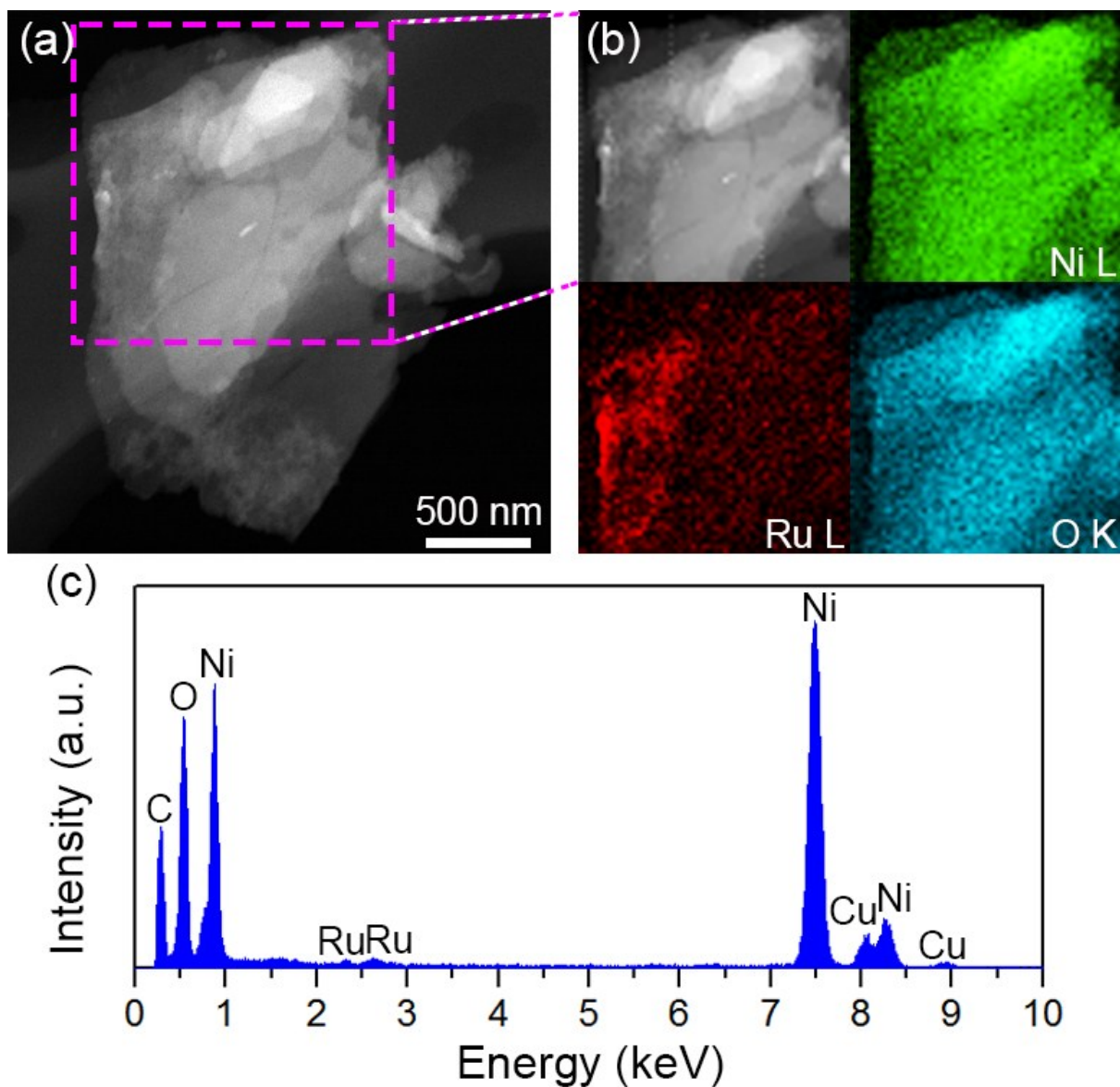
Figure S5. (a) HAADF-STEM image, (b) element mappings of selected area in panel (a), and (c) EDX spectrum of $Ru(OH)_3/Ni(OH)_2$ nanoflakes.
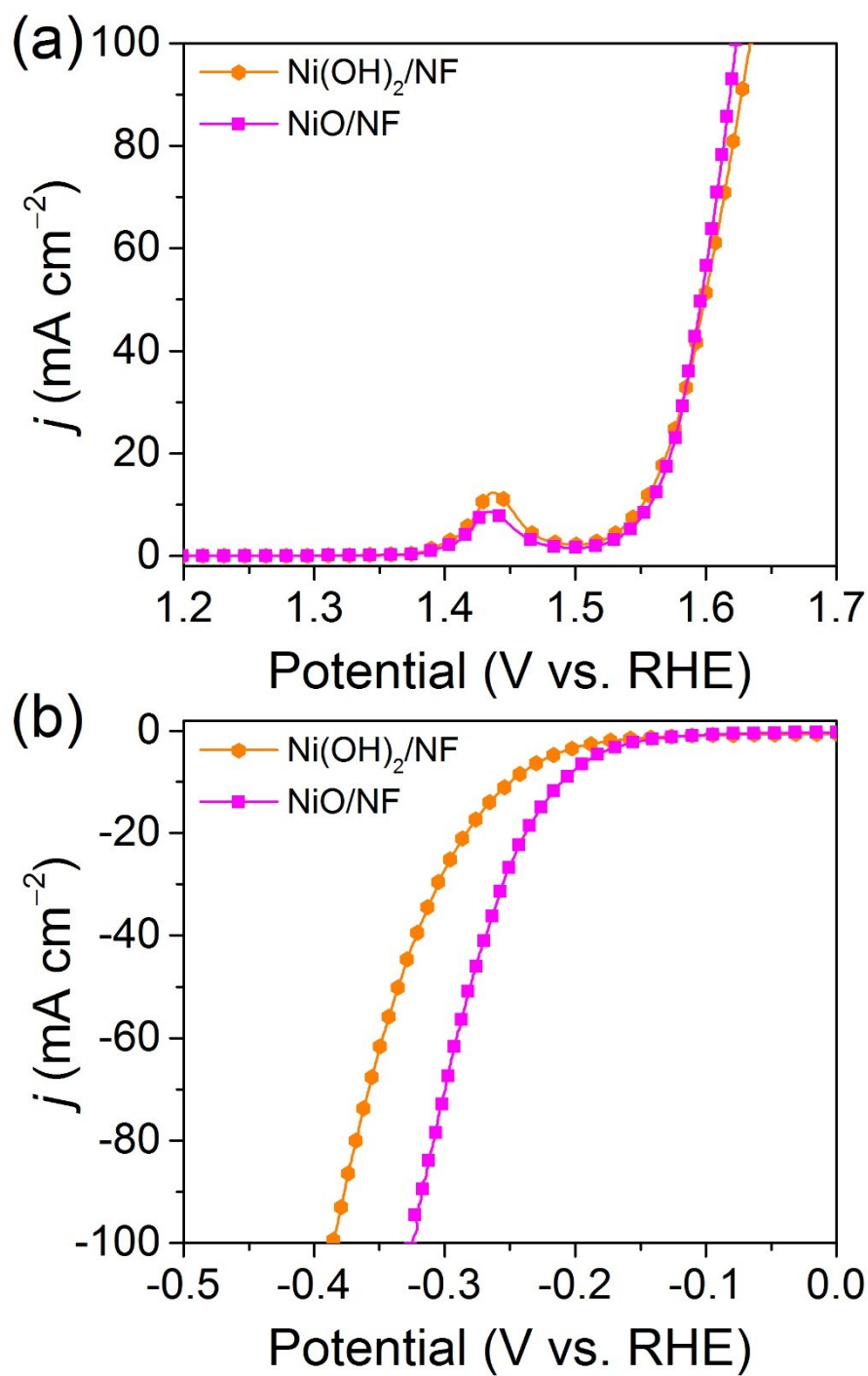
Figure S6. (a) OER and (b) HER polarization curves of Ni(OH)$_2$/NF and NiO/NF, indicating the favourable effect of thermal annealing on HER activity.
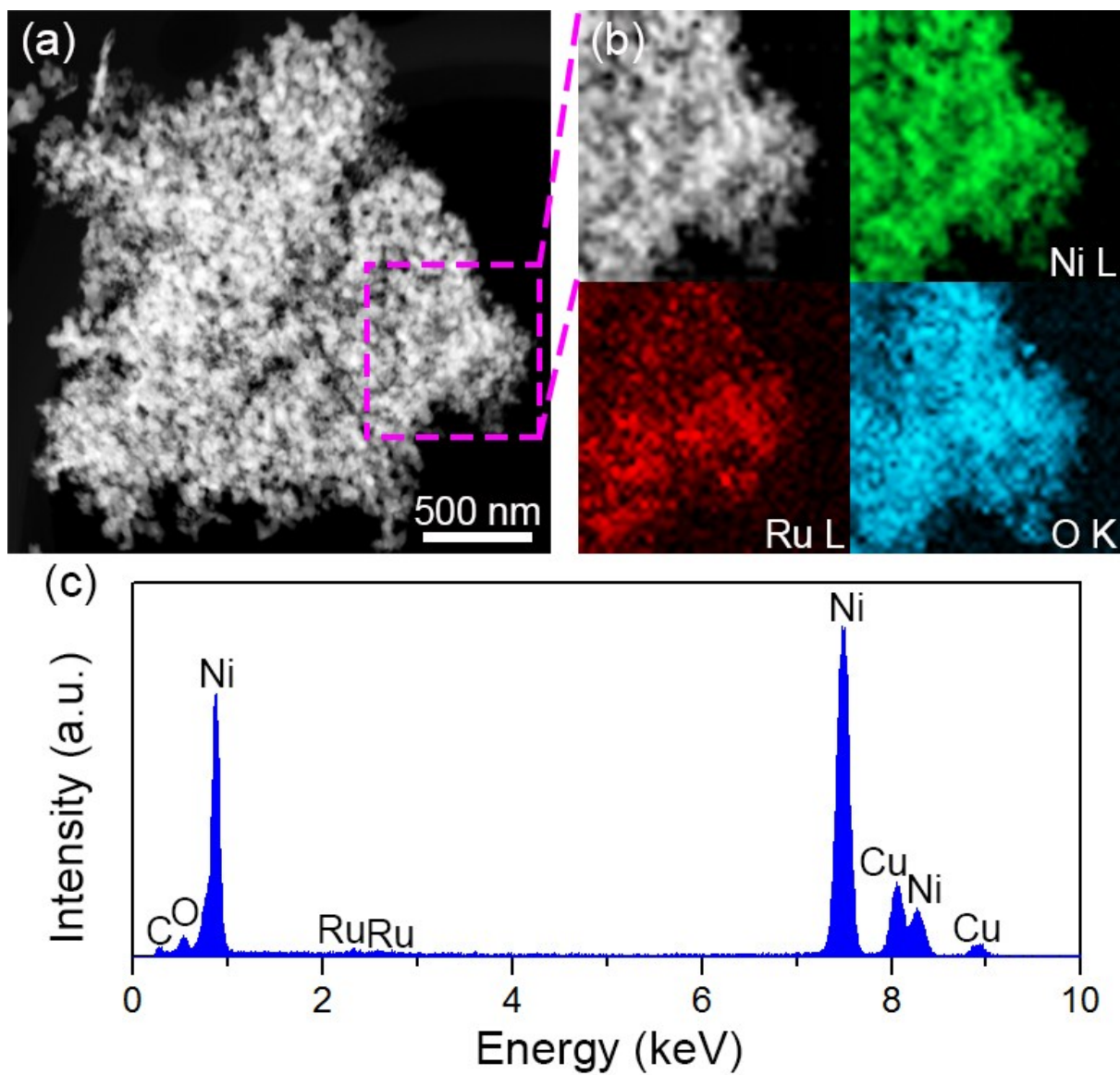
Figure S7. (a) HAADF-STEM image, (b) element mappings for selected area in panel (a), and (c) EDX spectrum of RuO_2/NiO nanosheet.
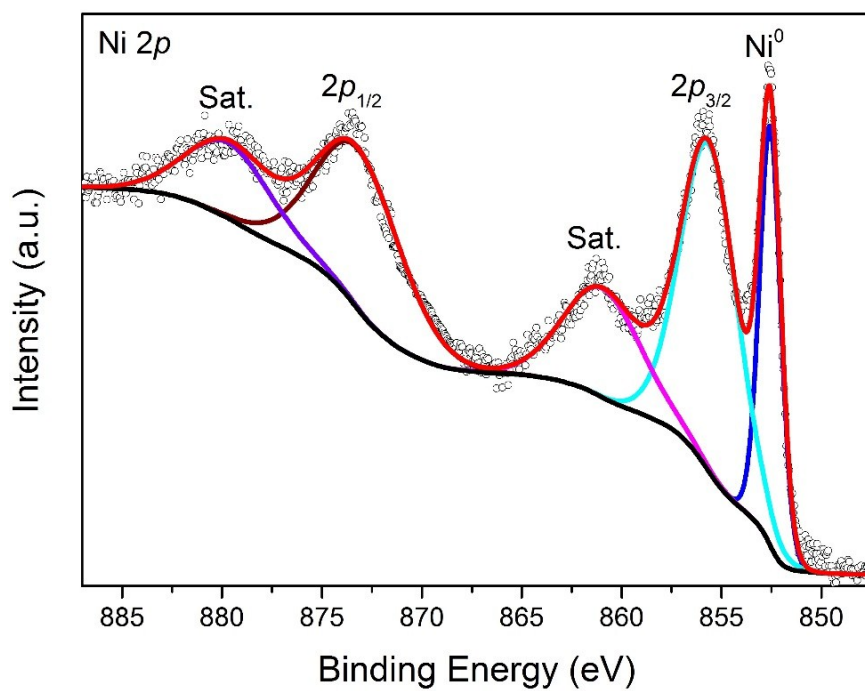
Figure S8. High-resolution XPS spectrum for Ni 2p of bare NF.
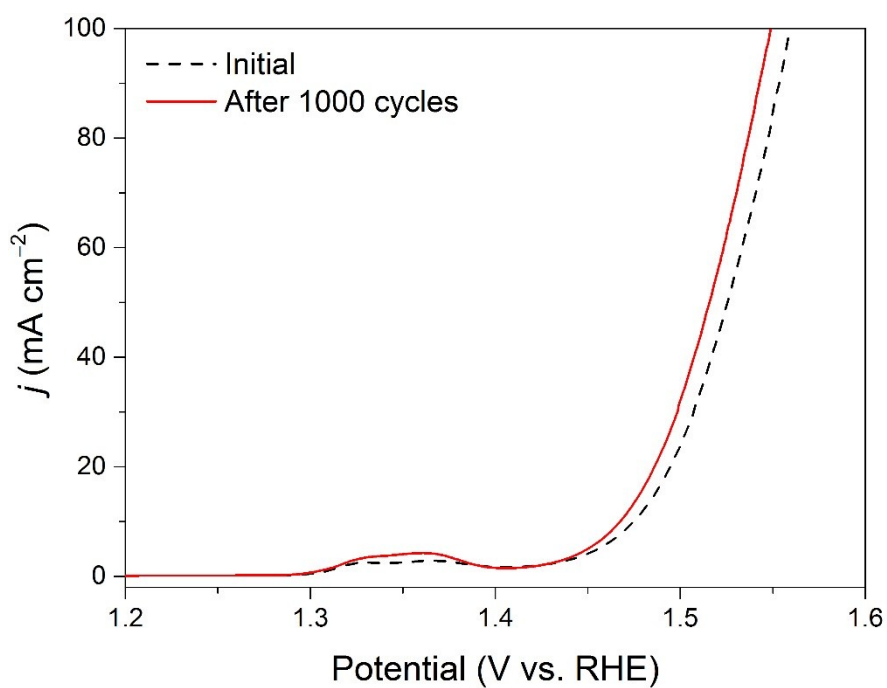
Figure S9. OER polarization curves of $RuO_2/NiO/NF$ before test and after 1000 cycles.
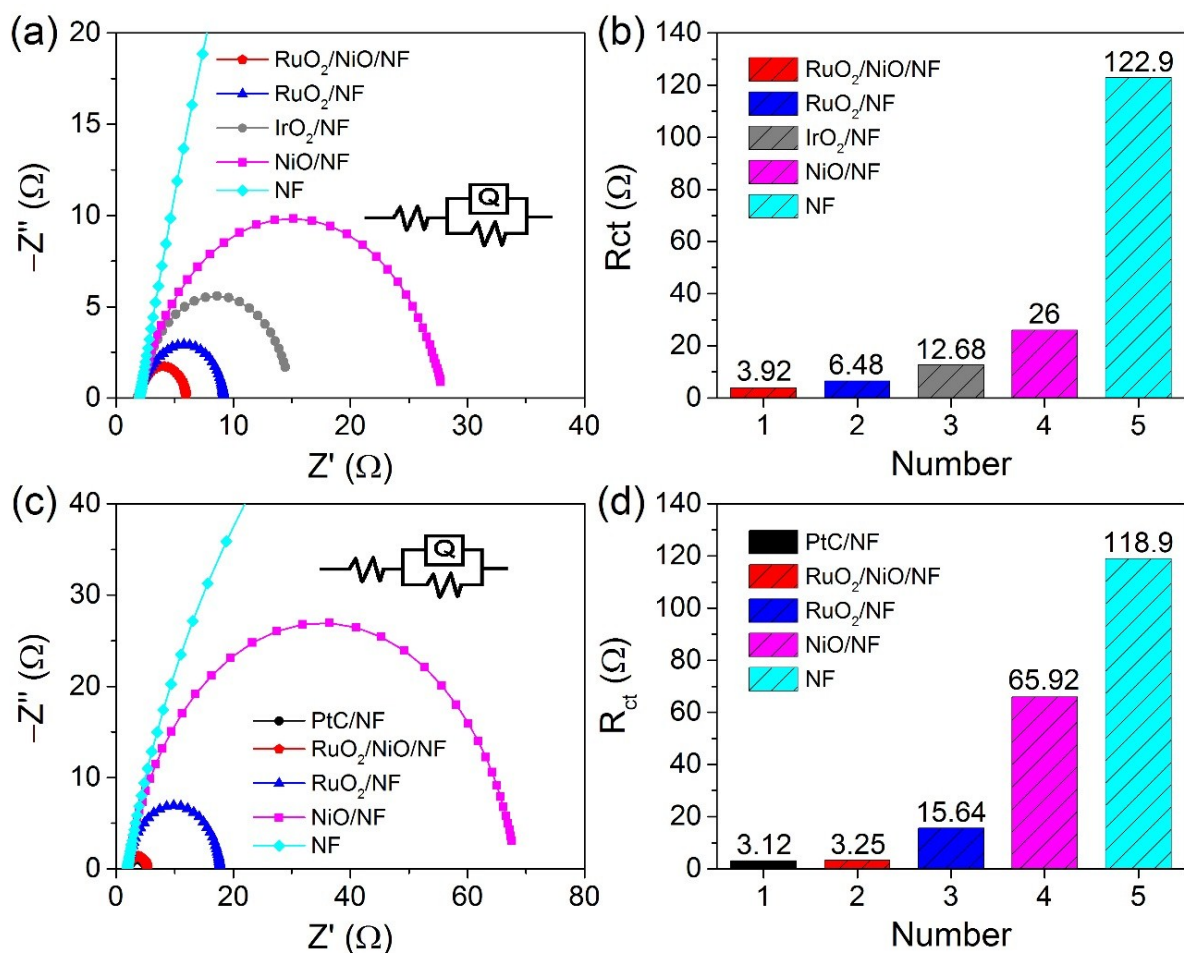
Figure S10. (a) Nyquist plots and (b) simulated R_{ct} of various electrodes at 1.53 V vs. RHE in 1.0 M KOH. (c) Nyquist plots and (d) simulated R_{ct} of various electrodes at −0.1 V vs. RHE in 1.0 M KOH. The fitted curves using the equivalent circuit (inset) are presented by solid lines.
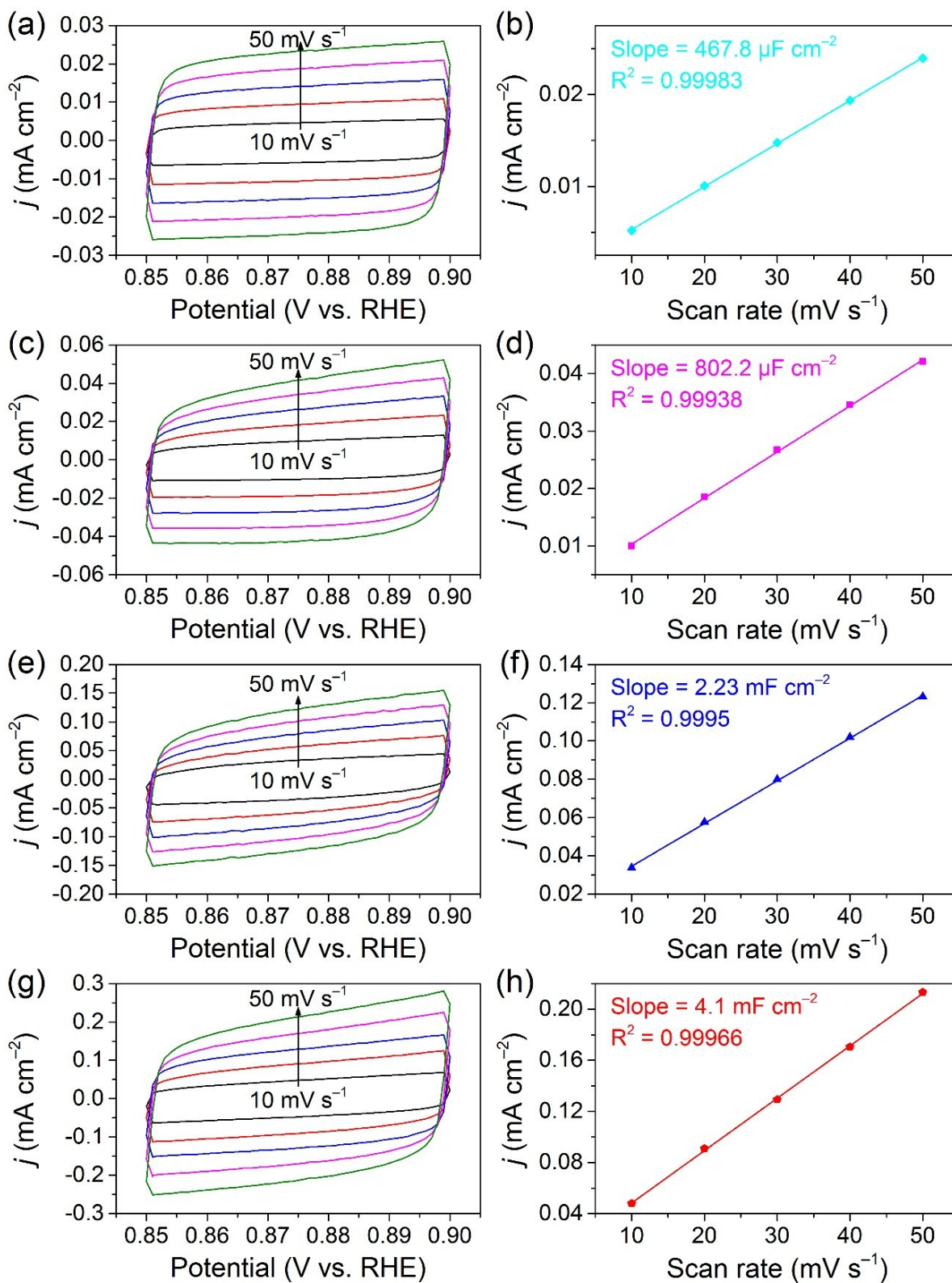
Figure S11. CV curves and the capacitive currents at 0.875 V vs. RHE against scan rate of (a, b) bare NF, (c, d) NiO/NF, (e, f) RuO$_2$/NF, and (g, h) RuO$_2$/NiO/NF.
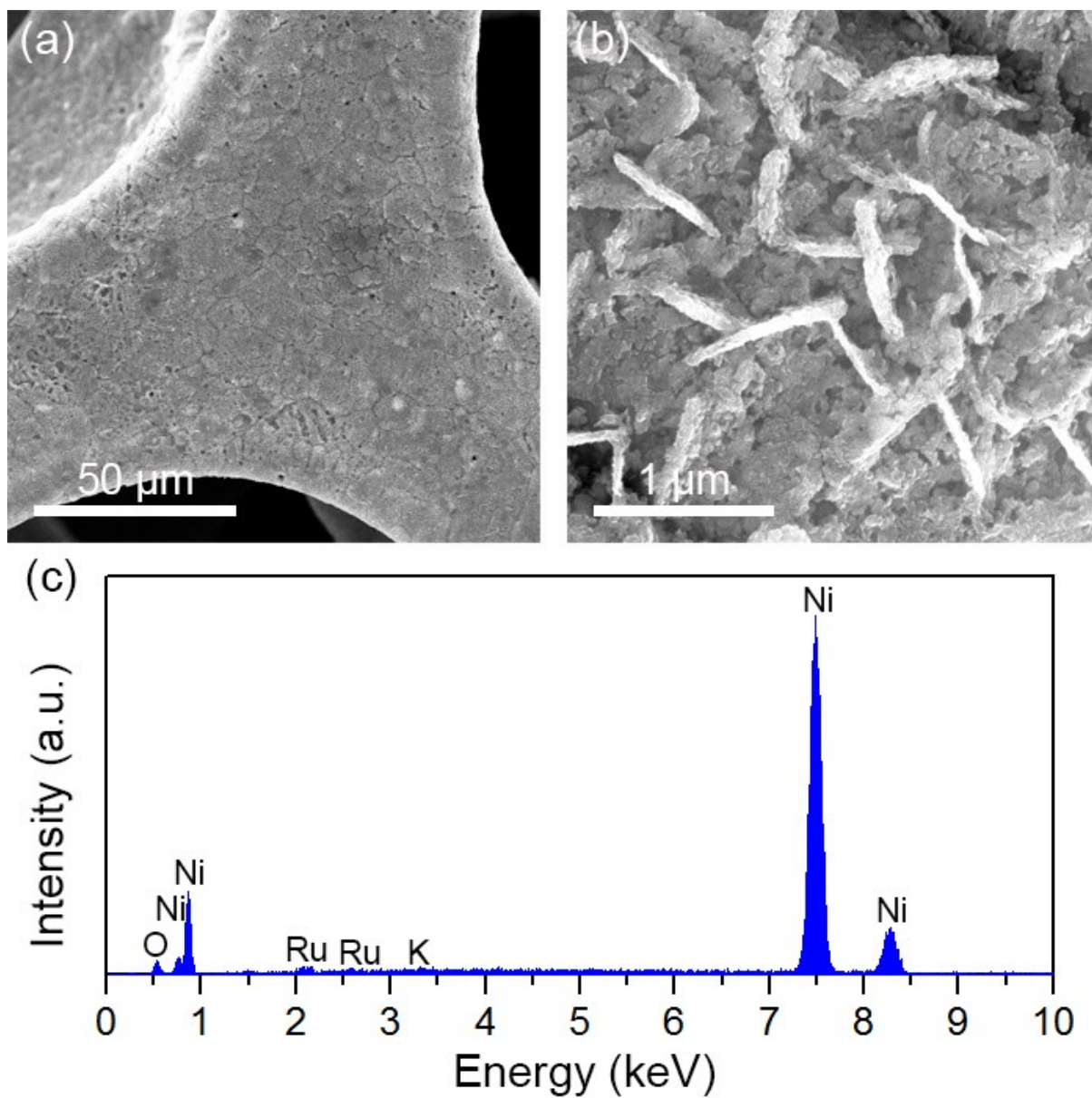
Figure S12. (a, b) SEM images and (c) EDX spectrum of RuO$_2$/NiO/NF after 24 h stability test.

Table S1. Comparison of recent bifunctional electrocatalysts for overall water splitting in alkaline electrolytes.

Catalysts	Electrolyte	HER η_{onset} (mV)[a]	HER η_{10} (mV)	HER Tafel slop (mV dec^{-1})	OER η_{onset} (mV)[a]	OER η_{10} (mV)	OER Tafel slop (mV dec^{-1})	E_{10} (V)	Ref.
RuO$_2$/NiO/NF	1.0 M KOH	0	22	31.7	-	250	50.5	1.5	This work
NiFe-MOF/NF	0.1 M KOH	-	134	-	-	240	34	1.55	Nat. Commun. **2017**, *8*, 15341
MoS$_2$-Ni$_3$S$_2$ HNRs/NF	1.0 M KOH	31*	98	61	195*	249	57	1.5	ACS Catal. **2017**, *7*, 2357
Ni$_x$Co$_{3-x}$S$_4$/Ni$_3$S$_2$/NF	1.0 M KOH	-	136	107	-	160	95	1.53	Nano Energy **2017**, *35*, 161
Co$_1$Mo$_1$CH/NF	1.0 M KOH	-	180	-	-	η_{30} = 294 mV	-	1.68	J. Am. Chem. Soc. **2017**, *139*, 8320
NiO/Ni	1.0 M KOH	-	121	88	-	294	41	1.7	Nano Energy **2017**, *35*, 207
NiCoP NWAs/NF	1.0 M KOH	-	104	54	-	η_{20} = 270 mV	116	E_{20} =1.64 V	J. Mater. Chem. A **2017**, *5*, 14838
Co(S$_x$Se$_{1-x}$)$_2$	1.0 M KOH	-	122	85.7	-	283	65.6	1.63	Adv. Funct. Mater. **2017**, *27*, 1701008
FeB$_2$-NF	1.0 M KOH	~0*	61	87.5	250*	296	52.4	1.57	Adv. Energy. Mater. **2017**, 1700513
RuO$_2$/Co$_3$O$_4$	1.0 M KOH	-	89	91	-	305	69	1.645	RSC Adv. **2017**, *7*, 3686
1D-RuO$_2$-CN$_x$	0.5 M KOH	16*	95	70	190*	260	56	-	ACS Appl. Mater. Interfaces **2016**, *8*, 28678
CoFePO/NF	1.0 M KOH	-	87.5	38.1	-	274.5	51.7	1.566	ACS Nano 2016, *10*, 8738
CoO/MoO$_x$	1.0 M KOH	40*	163	44	230*	η_{20} = 310 mV	-	1.72	ACS Sustainable Chem. Eng. **2016**, *4*, 3743
FeNi$_3$N/NF	1.0 M KOH	-	75	98	200*	202	40	1.62	Chem. Mater. **2016**, *28*, 6934
NF-Ni$_3$Se$_2$/Ni	1.0 M KOH	97	203	79	-	239	144	1.612	Nano Energy **2016**, *24*, 103
NiCoFe LTHs/CFC	1.0 M KOH	180*	200	70	220*	239	32	1.55	ACS Energy Lett. **2016**, *1*, 445
Ni$_x$P$_y$-325	1.0 M KOH	-	η_{20} = 160 mV	107.3	-	320	72.2	1.57	ACS Appl. Mater. Interfaces **2016**, *8*, 10826

Porous MoO₂/NF	1.0 M KOH	0	27	200*	41	260	54	1.53	Adv. Mater. **2016**, 28, 3785
NiCo₂O₄	1.0 M NaOH	50	110	230	49.7	290	53	1.65	Angew. Chem. Int. Ed. **2016**, 55, 6290
2-cycle NiFeOₓ/CFP	1.0 M KOH	40*	88	200*	150.2	250	31.5	1.55	Nat. Commun., **2015**, 6, 7261
Ni₃S₂/NF	1.0 M KOH	-	223	-	-	260	-	$E_{13} = 1.76V$	J. Am. Chem. Soc. **2015**, 137, 14023
NiSe/NF	1.0 M KOH	-	96	-	120	η_{20} = 270 mV	64	1.63	Angew. Chem. Int. Ed. **2015**, 54, 9351

[a] Here we define the onset overpotential (η_{onset}) as the overpotential at an absolute current density of 1 mA cm^{-2}. Values marked with a "*" have been interpolated from presented data and are not clearly defined by the authors.

Table S2. Electrochemical analysis of various samples and their intrinsic activities toward OER and HER

Sample	C_{dl} (μF cm^{-2})[a]	R_f[b]	OER		HER	
			j @ 1.50 V vs. RHE (mA cm^{-2})	$j_{specific}$ @ 1.50 V vs. RHE (mA cm^{-2})[c]	j @ −0.05 V vs. RHE (mA cm^{-2})	$j_{specific}$ @ −0.05 V vs. RHE (mA cm^{-2})[c]
RuO₂/NiO/NF	4100	68.33	24	0.351	−27.29	−0.399
RuO₂/NF	2230	37.17	6.7	0.180	−4.76	−0.128
NiO/NF	802.2	13.37	1.56	0.117	−0.4	−0.03
NF	467.8	7.80	0.21	0.027	−0.22	−0.028

[a] The double-layer capacitance (C_{dl}) is estimated by applying the equation: $C_{dl} = \frac{\Delta j}{2 \cdot v} = \frac{(j_a - j_c)}{2 \cdot v}$ [1], where j_a and j_c are the anodic and cathodic current densities, respectively, recorded at a potential of 0.875 V vs. RHE, and v is the scan rate (Figure. S10).

[b] According to Ref. [2], an ideal plane electrode has a C_{dl} of 60 μF cm^{-2}, and the roughness factor (R_f) can be calculated using the equation: $R_f = \frac{C_{dl}}{60} \times 1000$.

[c] According to Ref. [3,4], the specific current density ($j_{specific}$) is calculated by the following equation: $j_{specific} = \frac{j}{R_f}$, where j is the OER and HER current density at a potential of 1.50 and −0.05 V vs. RHE, respectively.

Supplementary Note 1. Electrochemical stability of RuO_2 and NiO

Half-reaction	E^o (V vs. RHE)
$Ni^{2+} + 2e^- \rightleftharpoons Ni$	-0.257
$Ni(OH)_2 + 2e^- \rightleftharpoons Ni + 2OH^-$	-0.72
$2H^+ + 2e^- \rightleftharpoons H_2$ (HER)	0
$Ru^{2+} + 2e^- \rightleftharpoons Ru$	0.455
$RuO_2 + 4H^+ + 2e^- \rightleftharpoons Ru^{2+} + 2H_2O$	1.12

From the above standard reduction potentials (E^o at T = 298.15 K and P = 101.325 kPa),[5] it can be seen that prior to the HER onset, RuO_2 reduction to Ru (overall reaction: $RuO_2 + 4H^+ + 4e^- \rightleftharpoons Ru + 2H_2O$, E^o = 0.7875 V vs. RHE) is thermodynamically preferable in a two-step process. Considering the reduction overpotentials, Marc observed two obvious reduction peaks corresponding to RuO_2/Ru^{2+} at ~0.47 V vs. RHE and Ru^{2+}/Ru at ~0.18 V vs. RHE.[6] However, NiO or $Ni(OH)_2$ reduction to Ni is thermodynamically unfavorable under the conducted HER conditions. Likewise, given the reduction overpotentials, surface reduction of NiO to Ni is impossible for $RuO_2/NiO/NF$ in the potential window from 0 to -0.2 V vs. RHE. Therefore, under the conducted HER potentials, RuO_2 is electrochemically unstable and reduced to target Ru, whereas NiO is electrochemically stable without reduction.

Supplementary Note 2. OER reaction mechanism and Tafel slope

Considering that in situ formed NiOOH has appreciable capability of dissociating water molecules by cleaving the H−OH bond, the OER mechanism on $RuO_2/NiO/NF$ is deemed to initiate with water dissociation on a Ni site. In alkaline solution, Ru^{cus} on the RuO_2 surface exists in the form of Ru^{cus}−OH^- (denoted as M(Ru)−OH^-). According to well-established models, M(Ru)−OH^- can be oxidized into a high chemical state by deprotonation under OER potentials.[7] If the interfacial synergy is assumed to be involved in the OER on $RuO_2/NiO/NF$, the as-formed M(Ni)−OH and M(Ru)−O should react with each other as the rate-determining step (RDS) to generate the key intermediate M(Ni/Ru)−OOH. Following the commonly accepted pathway,[7−9] the M(Ni/Ru)−OOH intermediate undertakes further deprotonation to finally release O_2 from the catalyst surface. With these considerations, we suggest the OER pathway at the potential-induced $RuO_2/NiOOH$ interface by the following reaction sequence:

M(Ni) + H_2O $\rightleftharpoons$ M(Ni)−OH +H^+ +e^-
(a)

M(Ru)−OH⁻ ⇌ M(Ru)−O + H⁺ +e⁻

(b)

M(Ni)−OH + M(Ru)−O ⇌ M(Ni/Ru)−OOH (c)

M(Ni/Ru)−OOH + OH⁻ ⇌ M(Ni/Ru)−OO + H₂O + e⁻

(d)

M(Ni/Ru)−OO + OH⁻ ⇌ M(Ni) + M(Ru)−OH⁻ + O₂ + e⁻ (e)
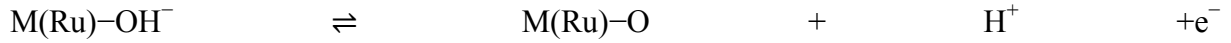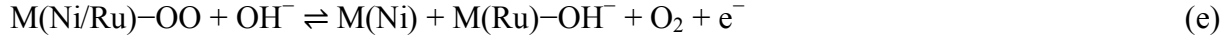
where M represents corresponding metal catalytic center/interface.

For step (a), the reaction fluxes j in the forward (+) or backward (−) directions can be respectively expressed as:

$$j_{+a} = k_{+a} \cdot (1 - \theta_{Ni}) \cdot e^{\frac{\alpha \cdot \eta \cdot F}{R \cdot T}}$$

(1)

$$j_{-a} = k_{-a} \cdot a_{H^+} \cdot \theta_{Ni} \cdot e^{-\frac{(1-\alpha) \cdot \eta \cdot F}{R \cdot T}}$$

(2)

Here, θ is the fractional occupancy of the electrode surface by corresponding active sites, and α is the electron transfer symmetry factor. At low overpotentials, we assume that reaction (a) precedes in quasi-equilibrium (i.e. $j_{+a} = j_{-a}$), we can get the following equation:

$$\theta_{Ni} = \frac{k_{+a} \cdot e^{\frac{\eta \cdot F}{R \cdot T}}}{k_{+a} \cdot e^{\frac{\eta \cdot F}{R \cdot T}} + k_{-a} \cdot a_{H^+}}$$

(3)

Similarly, for reaction (b), we obtain:

$$j_{+b} = k_{+b} \cdot (1 - \theta_{Ru}) \cdot e^{\frac{\alpha \cdot \eta \cdot F}{R \cdot T}}$$

(4)

$$j_{-b} = k_{-b} \cdot a_{H^+} \cdot \theta_{Ru} \cdot e^{-\frac{(1-\alpha) \cdot \eta \cdot F}{R \cdot T}}$$

(5)

$$\theta_{Ru} = \frac{k_{+b} \cdot e^{\frac{\eta \cdot F}{R \cdot T}}}{k_{+b} \cdot e^{\frac{\eta \cdot F}{R \cdot T}} + k_{-b} \cdot a_{H^+}}$$

(6)

The rate equation for reaction (c) is:

$$j_{+c} = k_{+c} \cdot \theta_{Ni} \cdot \theta_{Ru} \cdot e^{\frac{\alpha \cdot \eta \cdot F}{R \cdot T}}$$

(7)

If reaction (c) is the RDS, the overall OER current density is equal to:

$$i = 2 \cdot F \cdot j_{+c} = 2 \cdot F \cdot k_{+c} \cdot \theta_{Ni} \cdot \theta_{Ru} \cdot e^{\frac{\alpha \cdot \eta \cdot F}{R \cdot T}} \tag{8}$$

Unlike common OER kinetic analyses involving single active sites, reaction (c) occurs at the RuO_2/NiOOH interface, implying that a more complicated model including dual active sites is required. In this case, the dual barrier model proposed by MacDonald and Conway is more applicable for analyzing the RDS.[10] Specifically, they developed a general form with the following rate equation:

$$i = W \cdot e^{\frac{(1+\alpha_t) \cdot E \cdot F}{R \cdot T}} \tag{9}$$

$$\alpha_t = \frac{\alpha_f \cdot \alpha_s}{\alpha_f + \alpha_s} \tag{10}$$

where α_t is the overall symmetry factor, α_f is the symmetry factor for field dependent charge transport and α_s is that for the electrochemical charge transfer. Using this dual barrier model, we assume that the RDS at the RuO_2/NiOOH interface has the same expression, except that the overall symmetry factor α_t is determined by two symmetry factors, accounting for the Ni site and Ru site. Thus, we get:

$$\alpha_t = \frac{\alpha_{Ni} \cdot \alpha_{Ru}}{\alpha_{Ni} + \alpha_{Ru}} \tag{11}$$

The rate equation for the RDS (9) is thus given by:

$$i = W \cdot e^{\frac{(1+\frac{\alpha_{Ni} \cdot \alpha_{Ru}}{\alpha_{Ni} + \alpha_{Ru}}) \cdot E \cdot F}{R \cdot T}} \tag{12}$$

Therefore, the OER Tafel slope is:

$$b = \left(\frac{\partial \log i}{\partial \log a_s}\right)_E = 2.303 \times \frac{\cdot R \cdot T}{(1+\frac{\alpha_{Ni} \cdot \alpha_{Ru}}{\alpha_{Ni} + \alpha_{Ru}}) \cdot F} \tag{13}$$

For $T = 298.15$ K, R = 8.3145 J mol^{-1} K^{-1}, and F = 96485.33 C mol^{-1}, assuming the potential barriers on Ni site and Ru site are symmetrical (i.e. $\alpha_{Ni} = \alpha_{Ru} = 0.5$), the theoretical Tafel slope is:

$$b = 2.303 \times \frac{4 \cdot R \cdot T}{5 \cdot F} = 47.3 \text{ mV dec}^{-1} \tag{14}$$

Evidently, the observed OER Tafel slope of 50.5 mV dec^{-1} for RuO_2/NiO/NF is in good agreement with the theoretical value, supporting the OER mechanism with synergistic effect at the RuO_2/NiOOH interface as illustrated in Figure 6(a).

Supplementary Note 3. HER reaction mechanism and Tafel slope

Regarding the HER mechanism at the potential-induced Ru/NiO interface in 1.0 M KOH, the first step is water dissociation to form electrochemically adsorbed hydrogen (H_{ads}, Volmer reaction), where the produced H_{ads} binds on the Ru site.[11] In the next step, two H_{ads} recombine to generate a hydrogen molecule (H_2, Tafel reaction), and the H_2 is finally released

from the catalyst surface.[11] Overall, the Volmer-Tafel mechanism is operative for the HER catalyzed by $RuO_2/NiO/NF$. As illustrated in Figure 6(b), the HER mechanism is represented by the following reaction sequence:

$$M(Ni/Ru) + H_2O + e^- \rightleftharpoons OH^- + M(Ru)-H_{ads} \tag{f}$$

$$M(Ru)-H_{ads} + M(Ru)-H_{ads} \rightleftharpoons M(Ru)-H_2 \tag{g}$$

$$M(Ru)-H_2 \rightleftharpoons M(Ru) + H_2 \tag{h}$$

For reaction (f), we can get the following rate equations:

$$j_{+f} = k_{+f} \cdot (1 - \theta) \cdot e^{-\frac{\beta \cdot F \cdot E}{R \cdot T}}$$

(15)

$$j_{-f} = k_{-f} \cdot c(OH^-) \cdot \theta \cdot e^{\frac{(1-\beta) \cdot F \cdot E}{R \cdot T}}$$

(16)

where β is the symmetry factor, and θ is the fractional occupancy of H-adsorption sites on Ru. If reaction (g) representing the key intermediate H_{ads} recombination into H_2 is the RDS, the preceding reaction (f) should be in steady-state, so the reaction fluxes in the forward (+) or backward (−) directions are equal (i.e. $j_{+f} = j_{-f}$), and we can get:

$$k_{+f} \cdot (1 - \theta) \cdot e^{-\frac{\beta \cdot F \cdot E}{R \cdot T}} = k_{-f} \cdot c(OH^-) \cdot \theta \cdot e^{\frac{(1-\beta) \cdot F \cdot E}{R \cdot T}}$$

(17)

At low overpotentials, θ is close to 0, then it can be approximated that $(1 - \theta(Ru)) \to 1$. Hence, Eq. (17) is simplified as follows:

$$\theta = \frac{k_{+f}}{k_{-f}} \cdot \frac{1}{c(OH^-)} \cdot e^{-\frac{F \cdot E}{R \cdot T}} \tag{18}$$

For reaction (g) as the RDS, the overall HER current density is equal to:

$$-i = -2 \cdot F \cdot j_{+g} = -2 \cdot F \cdot k_{+g} \cdot \theta^2 = -2 \cdot F \cdot k_{+g} \cdot \left(\frac{k_{+f}}{k_{-f}}\right)^2 \cdot \left(\frac{1}{c(OH^-)}\right)^2 e^{-\frac{2 \cdot F \cdot E}{R \cdot T}}$$

(19)

Therefore, the HER Tafel slope is:

$$b = \left(\frac{\partial \log i}{\partial \log a_s}\right)_E = 2.303 \times \frac{R \cdot T}{2 \cdot F} \approx 30 \text{ mV dec}^{-1} \tag{20}$$

Again, the observed HER Tafel slope of 31.7 mV dec^{-1} for $RuO_2/NiO/NF$ is in agreement with the calculated value. This demonstrates the HER mechanism with synergistic effect at the Ru/NiO interface as illustrated in Figure 6(b).

In summary, the mechanism analyses illustrated in Figure 6 are supported by self-consistent interpretations of the Tafel slopes.

References

[1]   C. C. L. McCrory, S. Jung, J. C. Peters, T. F. Jaramillo, *J. Am. Chem. Soc.* **2013**, *135*, 16977.

[2]   S. Levine, A. L. Smith, *Discuss. Faraday Soc.* **1971**, *52*, 290.

[3]   B. M. Jović, V. D. Jović, U. Č. Lačnjevac, L. Gajić-Krstajić, N. V. Krstajić, *Int. J. Hydrogen Energy* **2015**, *40*, 10480.

[4]   B. M. Jović, V. D. Jović, U. Č. Lačnjevac, S. I. Stevanović, J. Kovač, M. Radović, N. V. Krstajić, *J. Electroanal. Chem.* **2016**, *766*, 78.

[5]   P. Vanysek, *Electrochemical Series. In CRC Handbook of Chemistry and Physics, 96th ed.* CRC Press: Boca Raton, **2015**.

[6]   M. T. M. Koper, *Electrochim. Acta* **2011**, *56*, 10645.

[7]   R. Kötz, H. J. Lewerenz, S. Stucki, *J. Electrochem. Soc.* **1983**, *130*, 825.

[8]   M. E. G. Lyons, R. L. Doyle, *Int. J. Electrochem. Sci.* **2012**, *7*, 9488.

[9]   M. E. G. Lyons, M. P. Brandon, *J. Electroanal. Chem.* **2010**, *641*, 119.

[10]   J. J. MacDonald, B. E. Conway, *Proc. R. Soc. London, Ser. A* **1962**, *269*, 419.

[11]   Y. Zheng, Y. Jiao, M. Jaroniec, S. Z. Qiao, *Angew. Chem. Int. Ed.* **2015**, *54*, 52.

Chapter 7: Conclusions and Perspectives

7.1 Conclusions

This thesis is devoted to deepening insights into the reaction rates and mechanisms of key energy conversion reactions relating to water electrocatalysis, and developing a series of improved electrocatalysts as alternatives to benchmark noble metal based catalysts. Based on the works in this thesis, the following conclusions can be drawn:

1. Having established a catalyst model on Ru and MoS_2, the pH-dependent HER mechanisms have been identified. Different from the acidic HER that can be perfectly described by the hydrogen adsorption free energy (ΔG_{H*}), the HER in alkaline media involves an essential step of water dissociation prior to hydrogen adsorption. Combining two functional materials like Ru/MoS_2, one enabling efficient cleaving of HO−H bond and the other allowing for favourable hydrogen adsorption, offers a new strategy to explore enhanced HER catalysts for the alkaline HER. Despite that only unsaturated edge atoms of MoS_2 are active towards the HER, defect engineering of MoS_2 has been demonstrated as an effective approach to creating plenty of in-plane active sites.

2. In situ growth of single-crystalline nanoarrays on conductive substrate can effectively improve the electrical conductivity and structural stability of resultant electrode, due to the strong connection between active materials and underlying current collector and minimal structural disorder. As a result, single-crystalline Fe-Ni(OH)$_2$ nanoflake arrays on nickel foam manifested remarkable OER activity with ultra-stable durability. On account of the increase of active oxyhydroxide species during long-term operation, the Fe-Ni(OH)$_2$/NF enabled self-activation to further reduce the OER overpotential.

3. Thiourea-assisted electrodeposition has been put forward to synthesize catalysts with well controlled nanostructure and chemical modification, where thiourea confines the growth of primary nanoparticles and serves as S source to realize S doping. As a general synthesis strategy, it can be applied to various S-doped transition metal oxides nanosheets consisting of ultra-small nanoparticles. The effect of synthesis parameters on the catalytic activity was systematically studied. The optimized S-NiFe$_2$O$_4$ nanosheets on nickel foam assured ultra-small nanoparticles (~2 nm) as building units to expose a great number of active sites and uniform S-incorporation to achieve excellent conductivity, resulting in prominent bifunctional reactivity for overall water splitting in both alkaline and neutral pH.

4. Systematic understanding of the catalytic properties of well-studied materials represents a fundamental step towards rational design of bifunctional electrocatalysts for water electrolysis. On the basis of previous studies, both experimental and theoretical, NiO was predicted to be a bifunctional promotor for RuO_2 favouring synergistic water splitting. As a proof-of-concept, porous nanosheet arrays consisting of strongly interacting RuO_2 and NiO nanoparticles were grown vertically on nickel foam, which exhibited superior OER activity to pristine RuO_2 and IrO_2 catalysts as well as Pt-like HER activity. The correlation of experimental and computational results regarding reaction kinetics analysis proved the potential-induced interfacial synergies for improved alkaline OER and HER.

In summary, the insightful understanding of these electrochemical reaction mechanisms can lay a solid foundation for rational design of more efficient electrocatalysts, and the developed synthetic strategies are effective to construct nanostructured materials with well-controlled composition, morphology, structure and size, therefore collectively paving a new way for developing advanced catalysts in water electrolysis.

7.2 Perspectives

Although considerable progress has been made in the research area of nanostructured electrocatalysts for energy conversion technologies, more efforts are needed to accelerate the advent of sustainable energy future.

1. The catalytic reactivity of a catalyst/system depends heavily on the number of active sites and the intrinsic physiochemical properties. In this aspect, nanostructure engineering has been demonstrated as an effective strategy to expose more electrochemically active surface area, while the intrinsic catalytic activity can be tuned by combining with other materials. Accordingly, it is highly desirable to hybridize different nanomaterials with fine-tuned interfaces, aiming to bring some new functionalities via synergistic effect. Extending established synthetic strategies in this thesis to construct a variety of new nanocomposites remains to be explored in the near future.

2. In addition to water electrolysis, HER and OER are also critical electrochemical reactions for other energy conversion technologies. For example, HER is a half reaction in urea electrolysis, and OER is a half reaction in CO_2 reduction and also involved in the charging process of rechargeable metal-air batteries. Undoubtedly, the developed nanostructured electrocatalysts in this thesis have great potential to be applied in those emerged electrocatalysis research. Moreover, bifunctional electrocatalysts, such as $S-NiFe_2O_4$ and

RuO$_2$/NiO, might be readily applicable for other electrochemical reactions like urea oxidation, which yet remains to be seen.

3. The atomistic and molecular level understanding of the mechanisms of key electrochemical reactions and the origin of so-called synergistic effects are still uncertain or ambiguous, which severely limit insights into materials design. In this regard, it is necessary to carry out more studies combining theory and experiment in electrocatalysis. Particularly, in situ characterization techniques, such as in situ TEM, XAESE, XPS, Raman spectroscopy, and infrared spectroscopy, are powerful for probing the reaction processes, which open up a new avenue to ascertain proposed reaction mechanisms. Further, the development of efficient computational screening is anticipated to speed up the pace of materials discovery for advanced electrocatalysts.

To sum up, it is believed that more and more breakthroughs in this promising research area are to be expected through further exploration of nanostructured electrocatalysts.

Appendix I: Publications during PhD Candidature

[1] Dongdong Zhu[†], **Jinlong Liu**[†], and Shi Zhang Qiao[*], Recent Advances in Inorganic Heterogeneous Electrocatalysts for Reduction of Carbon Dioxide, *Advanced Materials*, 2016, 28, 3423–3452. ([†]**Equal contribution**)

[2] **Jinlong Liu**, Chunxian Guo, Anthony Vasileff, and Shizhang Qiao[*], Nanostructured 2D Materials: Perspective Catalysts for Electrochemical CO_2 Reduction, *Small Methods*, 2017, 1, 1600006.

[3] **Jinlong Liu**, Dongdong Zhu, Chunxian Guo, Anthony Vasileff, and Shi-Zhang Qiao[*], Design Strategies toward Advanced MOF-Derived Electrocatalysts for Energy-Conversion Reactions, *Advanced Energy Materials*, 2017, 7, 1700518.

[4] **Jinlong Liu**, Dongdong Zhu, Tao Ling, Anthony Vasileff, and Shi-Zhang Qiao[*], S-$NiFe_2O_4$ Ultra-Small Nanoparticle Built Nanosheets for Efficient Water Splitting in Alkaline and Neutral pH, *Nano Energy*, 2017, 40, 264–273.

[5] **Jinlong Liu**, Yao Zheng, Dongdong Zhu, Anthony Vasileff, Tao Ling, and Shi-Zhang Qiao[*], Identification of pH-Dependent Synergy on Ru/MoS_2 Interface: A Comparison of Alkaline and Acidic Hydrogen Evolution, *Nanoscale*, 2017, 9, 16616–16621.

[6] **Jinlong Liu**, Yao Zheng, Zhenyu Wang, Zhouguang Lu, Anthony Vasileff, and Shi-Zhang Qiao[*], Free-Standing Single-Crystalline NiFe-Hydroxide Nanoflake Arrays: A Self-Activated, Efficient, and Robust Electrocatalyst for Oxygen Evolution, *Chemical Communications*, 2018, 54, 463–466.

[7] **Jinlong Liu**, Yao Zheng, Yan Jiao, Zhenyu Wang, Zhouguang Lu, Anthony Vasileff, and Shi-Zhang Qiao[*], NiO as an Efficient Bifunctional Promotor for RuO_2 towards Superior Alkaline Water Splitting, *Small*, 2018, 14, 1704073.

[8] **Jinlong Liu**, Dongdong Zhu, Yao Zheng, Anthony Vasileff, and Shi-Zhang Qiao[*], Self-Supported Earth-Abundant Nanoarrays as Efficient and Robust Electrocatalysts for Energy-Related Reactions, *ACS Catalysis*, submitted.

[9] Dongdong Zhu, Chunxian Guo, **Jinlong Liu,** Liang Wang, Yi Du, and Shi-Zhang Qiao[*], Two-Dimensional Metal-Organic Frameworks with High Oxidation States for Efficient Electrocatalytic Urea Oxidation, *Chemical Communications*, 2017, 53, 10906–10909.

[10] Huanyu Jin, Chunxian Guo, Xin Liu, **Jinlong Liu**, Anthony Vasileff, Yan Jiao, Yao Zheng[*], and Shi-Zhang Qiao[*], Emerging Two-Dimensional Nanomaterials for Electrocatalysis, *Chemical Reviews*, 2018, DOI: 10.1021/acs.chemrev.7b00689.

Appendix II: Other First-Author Papers in their Journal Styles

REVIEW

Electrocatalysts

ADVANCED
ENERGY
MATERIALS

www.advenergymat.de

Design Strategies toward Advanced MOF-Derived Electrocatalysts for Energy-Conversion Reactions

Jinlong Liu, Dongdong Zhu, Chunxian Guo, Anthony Vasileff, and Shi-Zhang Qiao*

The key challenge to developing renewable and clean energy technologies lies in the rational design and synthesis of efficient and earth-abundant catalysts for a wide variety of electrochemical reactions. This review presents materials design strategies for constructing improved electrocatalysts based on MOF precursors/templates, with special emphasis on component manipulation, morphology control, and structure engineering. Guided by these strategies, recently developed MOF-derived materials have exhibited remarkable activity, selectivity, and stability for various energy-conversion processes, manifesting great potential for replacing precious-metal-based catalysts in next-generation energy devices. Existing challenges and opportunities regarding MOF-derived electrocatalysts are also discussed. It is anticipated that by extending current materials design strategies to a wider range of MOF precursors for various energy-related electrocatalytic reactions, significant advances toward achieving highly efficient electrocatalysts can be made.

1. Introduction

Energy supply is a key issue for the sustainable development of modern society.[1,2] Especially when confronted with continuing population growth, increasing depletion of fossil fuels, and worsening effects of climate change, it is paramount to develop new clean and sustainable sources of energy.[2,3] During the past decades, tremendous research efforts, both in academic and industrial communities, have been devoted to seeking advanced techniques in harvesting renewable energy sources (including biofuels, wind, sunlight, geothermal heat, hydroelectricity, etc.).[2,4] In the pursuit of energy security, energy-conversion and storage technologies are essential to expedite the large-scale exploitation of these energy resources.[4,5] Among various next-generation energy technologies, fuel cells, metal–air batteries, electrochemical water splitting, and CO_2 reduction show

great potential to meet our ever-growing demand for energy. These devices appear most promising due to their high energy-conversion and storage efficiencies, portability, which can mitigate the intermittent distribution of the aforementioned energy in space and time, and environmental benignancy.[6–10] Fundamentally, these electrochemical systems or devices involve different energy-conversion reactions, such as the oxygen reduction reaction (ORR), oxygen evolution reaction (OER), hydrogen evolution reaction (HER) and electrochemical CO_2 reduction (ECR), which provide energy by directly converting chemical energy (e.g., methanol, ethanol, zinc, and hydrogen) into electrical energy, or store energy vice versa.[6–12] The intrinsically sluggish kinetics of these reactions highlights the critical role of electrocatalysts. In this regard, the development of advanced electrocatalysts has always been the technological bottleneck that hinders the practical applications of these energy techniques at any appreciable scale.[7–12]

Currently, noble-metal-based materials (e.g., Pt, IrO_2, RuO_2, and Au) are considered to be state-of-the-art catalysts for a variety of energy devices,[13–16] such as proton exchange membrane fuel cells (PEMFCs).[13] In spite of their outstanding catalytic performance for many electrochemical reactions, the high cost and scarcity of these noble metals severely hamper their large-scale commercialization.[17] Further, precious metal catalysts face issues with poisoning when exposed to a range of chemical compounds like methaol and carbon monoxide, leading to significant activity loss.[18] Therefore, extensive studies have focused on the development of alternative electrocatalysts with high activity, long stability, low cost, widespread availability, and facile synthesis.[8–10,19,20]

To replace precious-metal-based catalysts, a wide range of non-noble-metal materials, especially transition-metal-based materials and metal-free carbon materials, have been intensively investigated as electrocatalysts for different applications.[21] Most of these electrocatalyst candidates show great promise in energy-conversion reactions. Nevertheless, very few alternative materials have yet to achieve superior electrochemical properties to those of noble-metal-based catalysts. Fortunately, the accumulation of experimental and theoretical studies have significantly advanced our knowledge on the chemical and physical nature of various candidate materials.[10–12] For example, our group has shed light on the activity origin of

J. L. Liu, D. D. Zhu, Dr. C. X. Guo, A. Vasileff, Prof. S.-Z. Qiao
School of Chemical Engineering
University of Adelaide
Adelaide, SA 5005, Australia
E-mail: s.qiao@adelaide.edu.au
Prof. S.-Z. Qiao
School of Materials Science and Engineering
Tianjin University
Tianjin 300072, China

The ORCID identification number(s) for the author(s) of this article can be found under https://doi.org/10.1002/aenm.201700518.

209

**ADVANCED
SCIENCE NEWS**

www.advancedsciencenews.com

**ADVANCED
ENERGY
MATERIALS**

www.advenergymat.de

heteroatom (e.g., B, N, S, and P)-doped carbon materials for the HER.[22] Similarly, some researchers have demonstrated that N-coordinated metals on a carbon matrix (M−N−C, M=Fe, Co, Ni, etc.) serve as a highly active configuration for the ORR.[23,24] On the basis of these gained knowledge, it is anticipated that rational design of efficient electrocatalysts is possible.

As an emerging type of compound material, metal–organic frameworks (MOFs), composed of metal ions and organic ligands by strong coordination bonds, have stimulated huge research interest due to their unique properties.[25] First of all, diversity in metal centers and organic linkers has led to the synthesis of thousands of different MOFs. Until now, more than 20000 MOFs have been reported, and the number of MOFs is still increasing exponentially.[25] Secondly, MOF structures can be well controlled in one-, two-, or three-dimensions simply by varying the constituent geometry. Meanwhile, the size, morphology, and porosity of MOFs can also be tuned precisely through diverse synthetic procedures,[25] and their ultrahigh surface areas (from 1000 to 10000 m^2 $g^{−1}$) makes them extremely attractive over traditional porous materials like zeolites and mesoporous carbons.[25] By virtue of these favourable features, MOFs exhibit promising applications in an ever-increasing variety of areas, such as gas storage and separation,[26] catalysis,[27] sensors,[28] water treatment,[29] and drug delivery.[30] To better understand the theory behind the chemistry and applications of MOFs, the readers can refer to Furukawa et al.'s review article (ref. [25]).

In recent years, advanced materials derived from MOFs through effective post-treatments, especially high-temperature calcination, have brought unimaginable opportunities to expand their functionalities. On the one hand, MOFs contain both inorganic metal source and organic source, thus can serve as an ideal precursor to prepare composite materials with functional species. On the other hand, they can also work as a template to control the resultant morphology and structure. When used as electrode materials in energy-conversion reactions, MOF-derived materials have displayed appealing performance in electrochemical systems, and comprehensive studies indicate that MOF-derived materials have several advantageous characteristics for electrochemical energy generation and storage. These are: 1) the carbon matrix obtained from the organic framework is able to act as a highly conductive network, promoting fast electron transfer;[31–36] 2) various heteroatoms (e.g., N, O, S, and P) contained in the organic ligands can be directly doped into the carbon framework, which can not only provide more active sites, but also create a favourable microenvironment for the growth of functional nanoparticles (NPs, e.g., transition metal carbides, nitrides, and oxides);[24,36–41] 3) the metal atoms in MOFs can form corresponding metals and/or compounds and homogeneously distribute in the carbon network, leading to the in situ synthesis of a carbon framework decorated with transition metals and/or transition metal compounds;[24,41–43] 4) a well-defined morphology, size, and structure can be obtained by adjusting synthesis parameters;[42–45] 5) many of the features (e.g., large surface area and high porosity) inherited from the MOF precursors can be preserved in the resultant materials after post-treatments.[46–48]

Unsurprisingly, owing to the advantages discussed above, these MOF-derived materials have stimulated much interest

Jinlong Liu received his B.E. and M.E. degrees in applied chemistry from Central South University in 2011 and 2014, respectively. He is currently a Ph.D. candidate in chemical engineering under the supervision of Prof. Shi-Zhang Qiao at The University of Adelaide. His current research is focused on the design and synthesis of functional materials for energy storage and catalysis.

Anthony Vasileff is a Ph.D. student in the School of Chemical Engineering at The University of Adelaide. Anthony received his Bachelor's degree in chemical engineering at The University of Adelaide. His graduate research is focused on developing novel nonmetal electrocatalysts and supports, particularly nanostructured carbon, for electrochemical processes. Currently, he is working on developing new nanomaterials for carbon dioxide reduction in order to advance clean energy-storage technologies.

Shi-Zhang Qiao received his Ph.D. degree in chemical engineering from Hong Kong University of Science and Technology in 2000. He is currently a Chair Professor in the School of Chemical Engineering at The University of Adelaide, Australia. His research expertise is in nanomaterials for catalysis, drug and gene delivery, and energy storage and conversion.

in energy fields,[49–51] and have been studied as electrode materials in batteries and supercapacitors.[49,50] Recent progress in these two attractive technologies has been comprehensively reviewed by Lu et al.[50] Another very important application is electrocatalysis.[51] In particular, as promising substitutes for noble-metal-based electrocatalysts, MOF-derived materials have been extensively investigated as alternative electrocatalysts for the ORR, OER, and HER, and have made many great achievements during the past decade.[51,52] Notably, some MOF-derived materials have shown significantly enhanced performances,

**ADVANCED
SCIENCE NEWS**
www.advancedsciencenews.com

**ADVANCED
ENERGY
MATERIALS**
www.advenergymat.de

even superior to noble-metal-based electrocatalysts.[51,52] A few reviews have summarized the progress of MOF-derived materials in electrocatalysis, but have mainly focused on the application of MOF-derived materials as ORR electrocatalysts in fuel cells.[51,52] Regardless of recent advances in this field, the exploration of MOF-derived electrocatalysts is still in its infancy. Accordingly, an updated perspective on the general and effective strategies toward materials design and synthesis from newly emerged MOF-derived materials has far-reaching significance, which offers valuable guidance and inspiration for further development of improved MOF-derived catalysts as well as extended applications in diverse, emerging, energy-related reactions. Therefore, a timely review with emphasis on the materials design strategies toward advanced MOF-derived catalysts will expand our knowledge on rational synthesis of improved electrocatalysts in energy-conversion reactions.

In this review, we first focus on the design strategies of MOF-derived materials with desirable composition, morphology, and structure. The effective synthetic strategies, including component manipulation, morphology control, and structure engineering, along with decisive reaction parameters to optimize target properties are summarized. Furthermore, their applications as electrocatalysts for the ORR, OER, HER, ECR, and other reactions, as well as bifunctional electrocatalysts in energy devices, are discussed through recent case studies and a table summary. The significant improvements in electrocatalytic performance achieved by MOF-derived materials have highlighted their potential in replacing noble-metal-based electrocatalysts. Finally, we conclude this review with the challenges surrounding MOF-derived materials and provide a perspective to promote their future development in advanced electrocatalysis for energy-conversion reactions.

2. Strategies for Designing Efficient MOF-Derived Electrocatalysts

To begin with, it is necessary to define "MOF-derived materials" to limit the scope of discussion. Herein, "MOF-derived materials" will refer to materials converted from MOF-based precursors/templates by a series of post-processing, such as high temperature thermal treatment, surface decoration, and chemical modification. In short, the synthesis of MOF-derived materials involves two major steps, that is, the selective preparation of a MOF precursor and deliberate post-treatments of this precursor. Typically, MOFs are almost exclusively prepared by traditional solution-based approaches or by a hydrothermal/solvothermal approach. The fabrication of MOF precursors has been widely reported in many reports,[25] so this step will not be discussed in detail. Instead, we will mainly focus on the post-processing of MOF precursors used to obtain target materials with tailored compositions, morphologies, and structures.

Since the purpose of post-treatment is to obtain a material with specific properties that improve electrochemical performance, it is essential to clarify the general relationship between material physicochemical properties and electrocatalytic performance. Firstly, the intrinsic properties of a component determine its activity and conductivity. Rational selection of components is beneficial in reducing overpotentials, reducing

Tafel slopes, and increasing catalytic current density. Meanwhile, the incorporation of conductive components facilitates fast electron transfer. Secondly, modification of the material's morphology can expose a greater number of active sites, especially specific crystal faces with high activity. Thirdly, structure is closely related to the number of active sites and durability because favourable structures contribute to preventing agglomeration and promoting mass transfer (i.e., reactant diffusion and product release). With these ideas in mind, discussion of the design of MOF-derived materials will focus on these three aspects. Of course, one has to account for all of them in comprehensive electrocatalyst design.

2.1. Component Manipulation

The versatility of the inorganic and organic building units for MOFs has led to increased growth in MOF research during the past few decades.[25] Accordingly, the large number of MOF precursors has provided plentiful options for constructing MOF-derived materials with desired compositions. By means of annealing under a controlled temperature and atmosphere, the organic units can be transformed into heteroatom-doped carbon materials, while metal-containing units are simultaneously converted into the corresponding transition-metal-based NPs supported on the as-formed carbon substrate.[24,38,41,42,44,53] More importantly, the advancement of chemical modification allows the precise manipulation of the component for the resultant composites.[41] From the view of composition, MOF-derived composites could offer strong synergistic effects between the carbon framework and metal component, which is highly preferable in enhancing electrocatalytic performance.

2.1.1. Nitrogen Doping

Electroactivity is highly dependent on the electronic properties of the electrocatalyst.[11,12] Pristine carbon materials show little to no electrocatalytic activity toward the aforementioned energy-conversion reactions because a pure carbon matrix consists of sp^2-bonded carbon atoms without polarization.[54] As a result, this perfectly uniform electron and charge density throughout the carbon network cannot accomodate the chemical adsorption of reactants or the electronic attack of intermediates.[54] However, both theoretical calculations and experimental results demonstrate that the introduction of heteroatoms with different electronegativity (χ), especially N, into the sp^2 lattice of graphitic carbon can significantly modify the electronic structure of the carbon matrix, thus restructuring their electron-donor properties to create active sites for chemical adsorption and intermediate reactions.[55] More importantly, the doped N can interact with other functional components via coordination, to stabilize transition metal atoms/compounds or induce synergistic effects.[40b,41,67f] As expected, heteroatom-doped carbon materials have emerged as a new class of advanced metal-free electrocatalysts, due to their extraordinary electrocatalytic performance, better defined reaction mechanisms, low cost, simple preparation, and easy scale-up.[33,56–63]

**ADVANCED
SCIENCE NEWS**

www.advancedsciencenews.com

**ADVANCED
ENERGY
MATERIALS**

www.advenergymat.de

Among the single heteroatom-doped carbon materials, one of the most widely studied cases is the substitution of partial C (χ = 2.55) with more electronegative N (χ = 3.04).[33,56,58,60,63] In particular, MOF precursors with N-containing ligands can be directly converted into N-doped electrocatalysts after pyrolysis under inert atmosphere.[58,60] For instance, in order to fabricate N-doped MOF-derived materials, zeolitic imiazolate frameworks (ZIFs), a subclass of MOFs composed of tetrahedrally coordinated transition metal ions (e.g., Zn, Fe, Co, Cu) and imidazolate (IM) ligands, are frequently utilized as the precursor and/or template because of their high N content and other preferred properties, such as large surface area and uniform particle size.[24,33,34,36,38–41,44,53,64–69]

Recently, You et al. reported the conversion of ZIF-67 (Co(MIM)$_2$, MIM = methylimidazole) to Co- and N-doped carbon (CoNC) via direct pyrolysis, producing a N-doped material with high N content.[39] Similarly, Chen and co-workers studied porous carbon materials derived from a series of bimetallic ZIFs (BMZIFs), which are based on ZIF-8 and ZIF-67 with varied Zn/Co ratio.[53] Uniform N doping was readily carried out within the skeleton of the derived porous carbons. Shortly after, Sun's group also reported self-supported porous cobalt−nitrogen−carbon (Co−N−C) composite by the facile carbonization of self-adjusted Zn and Co bimetal–organic frameworks (bi-MOF).[38] Note that BMZIFs and bi-MOF are materials of similar concept but with different designations. As illustrated in **Figure 1**a, using both Zn^{2+} and Co^{2+} as metal centers and 2-methylimidazole (MeIM) as organic linkers, a series of Zn$_x$Co$_{1−x}$(MeIM)$_2$ were prepared as precursor MOFs, wherein x (x = 0–1) represents the molar ratio of Zn^{2+} in the initial reactants. The carbonization of Zn$_x$Co$_{1−x}$(MeIM)$_2$ resulted in the target Co−N−C-x composites with no other post-treatments required. Among these materials, Co−N−C-0.8 was found to be the most active toward the ORR. Inductively coupled plasma-atomic emission spectrometry and element analysis revealed that 8.5 wt% of N was doped in Co−N−C-0.8. Corresponding X-ray photoelectron spectroscopy (XPS) results further indicated that the doped N existed in three configurations, namely, pyridicnic N (47%), pyrrolic N (43%), and oxidized N (10%), respectively.

In addition to ZIF-based MOF precursors, other MOFs with N-containing organic ligands can also be carbonized to produce N-doped electrocatalysts.[42,58,70–73] Taking MIL-88B-NH$_3$ (Fe$_3$O(H$_2$N-BDC)$_3$, H$_2$N-BDC = 2-aminoterephtalic acid) for example, Zhao et al. prepared well-defined N-doped carbonized nanoparticles (CNPs) by pyrolyzing spindle-like MIL-88B-NH$_3$ NPs.[42] Notably, unlike IM-based ligands in ZIFs, which already contain N atoms in pyridine/pyrrole configurations, H$_2$N-BDC only contains amino-type N atoms. Despite this difference, the results from Zhao et al. found that the amino-type N in MIL-88B-NH$_3$ were converted into pyridine and quaternary N after carbonization.[42] Evidently, amino-type N atoms in organic ligands can serve as good N dopants, rather than decompose into ammonia. In another example, Zhao et al. introduced N-rich ligands (1H-1,2,3-triaole) into ZIF-8 using a solvent-assistant-linker-exchange (SALE) approach, thereby fabricating a new MOF with rich N atoms for N doping.[67c] Hence, the carbonization of N-containing MOFs is a preminent strategy to realize N doping. Even for those MOF precursors with no

N-containing organic ligands, N doping can also be performed by annealing the target MOFs with extrinsic N sources (e.g., urea, melamine, triethylamine, etc.).[63,74–77] As an example of this, Li et al. designed and synthesized Fe$_3$C/Mo$_2$C containing N, P co-doped graphitic carbon (Fe$_3$C/Mo$_2$C@NPGC) by employing PMo$_{12}$@MIL-100 (Fe) and melamine as the starting materials, in which melamine provided a source of N (Figure 1b).[74] Accordingly, this N-doping strategy (i.e., mixing an external N source with MOF precursors) could be extended to other MOF-derived materials.

As an effective way to change the electronic properties of a carbon matrix, N doping can be integrated into the carbon framework by quite a few bonding configurations: pyridinic, pyrrolic, graphitic N (also known as quaternary N), metal-coordinated N, and N-oxide.[53] Different N doping configurations have different binding energies with distinguishing hybridizations (Figure 1c). As a consequence, specific binding configurations are exceptionally advantageous for certain applications. Generally, it has been widely reported that all N configurations, except for N-oxidize, improve electrocatalytic properties.[53] Specifically, pyridinic N is able to improve the capacity for accepting protons owing to its charge neutralization effect;[39] pyrrolic and pyridinic N can reduce the energy barrier of O$_2$ adsorption, thus facilitating the first rate-limiting step in the ORR by increasing electron transfer;[38] and graphitic N has shown to provide more valence electrons for increasing the conductivity and catalytic activity.[39] Metal-coordinated N usually withdraws electrons from the metal center and thus lower its electron density, which is beneficial for reducing the redox potential of the metal center by optimizing the bond strength between the metal center and intermediate.[38] In effect, doping N by pyrolysis always results in a mixture of different N species, whereas theoretical calculations often point out that one N configuration will dominate in a specific catalytic reaction. Hence, tuning the N configurations and their content is of particular interest in the implementation of a N-doping strategy.

To this end, it is essential to control the thermal pyrolysis by optimizing relevant synthesis parameters, such as the precursor MOFs and calcination temperatures.[38,39,65] For precursor MOFs, You et al. indicated that pyrolysis of ZIF-67 at 900 °C for 3 h under Ar generated carbonized ZIF-67 with a N content of only 1.1 wt%.[38] By contrast, carbonized ZIF-8 obtained by using the same pyrolysis conditions contained 8.6 wt% N, in which the percentage of pyrrolic and pyridinic N was 78.3%. The aforementioned Co−N−C-0.8, derived from Zn$_{0.8}$Co$_{0.2}$(MeIM)$_2$ under identical conditions, had almost the same N content (8.5 wt%) as carbonized ZIF-8, but the percentage of active pyridinic and pyrrolic N increased significantly up to 90%. This is much higher than those of carbonized ZIF-8 and ZIF-67, despite being synthesized using the same carbonization process. It can thus be concluded that the selection of precursor MOFs is the first priority in determining not only the total N-doping content but also the resultant percentage of N configurations. Additionally, carbonization temperature is also crucial for the optimization of N content and configurations. In this respect, You et al. investigated the influence of the annealing temperature on N content and distribution of N configurations.[39] To obtain ZIF-67-derived catalysts as a function of pyrolysis temperature, they calcinated the precursor
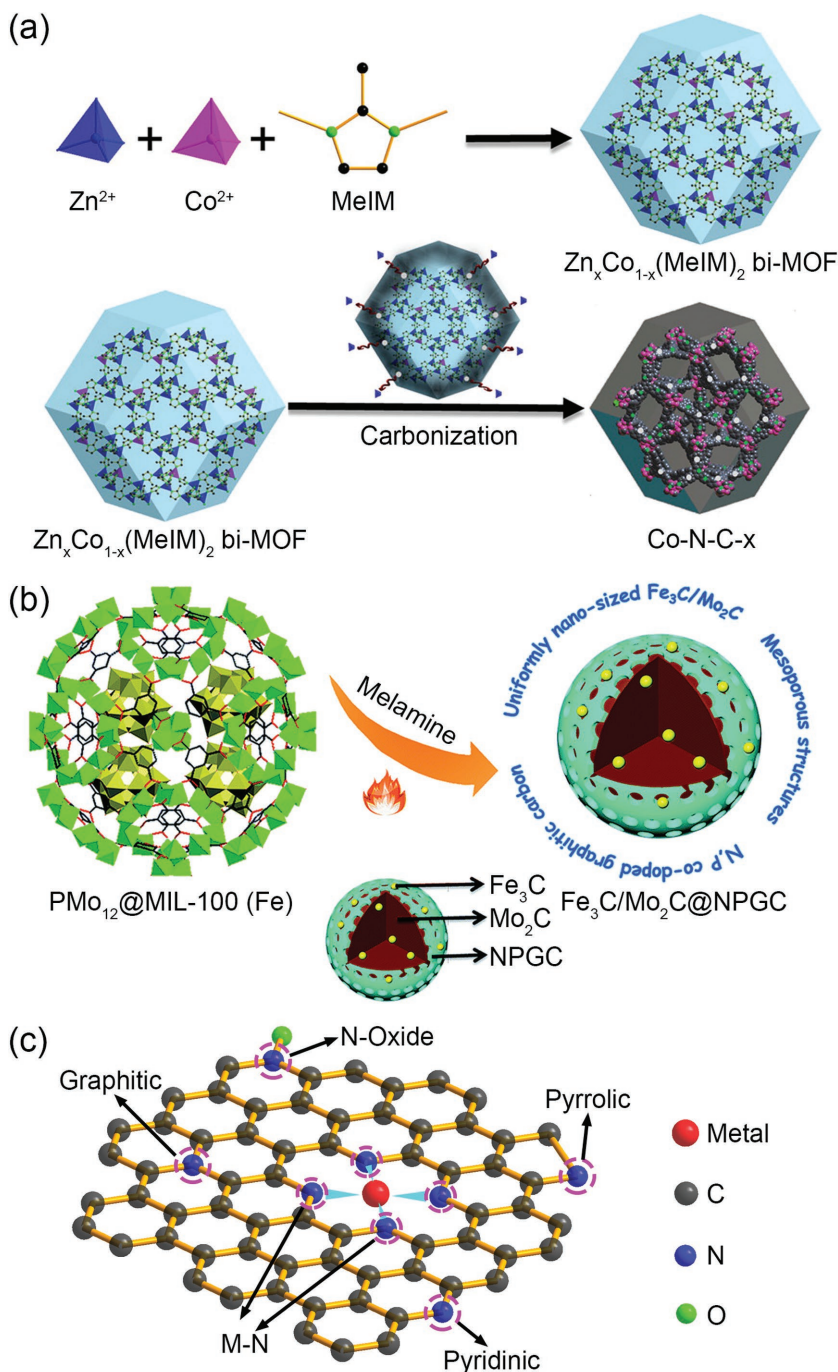
Figure 1. a) Illustration of the formation of Zn,Co bi-MOF $Zn_xCo_{1-x}(MeIM)_2$ and its carbonization to produce self-supported Co—N—C-x without any additional procedures, during which Zn evaporation occurs. Adapted with permission.[38] Copyright 2015, American Chemical Society. b) Preparation of the $Fe_3C/Mo_2C@NPGC$ nanocomposite derived from POM-based MOFs. Adapted with permission.[74] Copyright 2015, The Royal Society of Chemistry. c) Schematic of N configurations in various chemical environments of N—C catalysts.

at a peak temperature in the range of 600 to 1000 °C for 2 h. It was found that the content of N in the carbonized ZIF-67 decreased rapidly with increasing temperature. Specifically, from 16.49 at% at 600 °C to 1.36 at% at 1000 °C. Interestingly, the N species in terms of pyridinic N, pyrrolic N, and graphitic

N displayed different trends. The fraction of pyridinic N declined markedly from 90.56 to 36.06%, while pyrrolic N rose from 3.43 to 17.77% and graphitic N went up dramatically from 6 to 46.17%. Note that there was a volcano-type relationship between the ORR activity of the as-derived catalysts and the pyrolysis temperature, and the best performance was achieved for materials pyrolized at 900 °C. This suggests that the distribution of N configurations is the dominant factor at relatively low pyrolysis temperatures, while at higher temperatures which limit the total N content, total N content becomes the key factor. Therefore, calcination temperature is of critical importance in optimising the balance between total N content and the distribution of N configurations.

2.1.2. Multiple Heteroatom Co-Doping

The success of N doping has triggered experimentation with other dopants, such as B, S, and P, for tuning the electronic structure of a carbon matrix.[22,59,61,62,64,74,78,79] During the past decade, synergistic coupling effects by the chemical substitution of some carbon atoms with two or more different kinds of heteroatoms have been shown. This is because the co-doping of two or more elements with reverse electronegativity into the carbon matrix can induce unique electron-donor properties.[22,79] Compared with single-heteroatom-doped carbon materials, multiple-heteroatom-doped carbon materials are much more effective for activating carbon atoms, leading to more defects and active sites for further enhanced electrochemical properties.[22,79] In the case of MOF-derived electrocatalysts, dual and ternary heteroatom doping strategies have also been explored by performing N doping together with one or two other elements (e.g., B, S, and P).[59,61,62,64,74] Therefore, multiple heteroatom doping can be another feasible solution for optimizing the composition of MOF-derived electrocatalysts. Morever, other heteroatoms can be doped through similar strategies to N doping.

N, S Co-Doping: In 2014, Li et al. prepared MOF-templated N and S co-doped porous carbons as an efficient ORR electrocatalyst for the first time.[61] As shown in **Figure 2**a, MOF-5 $[Zn_4O(O_2CC_6H_4CO_2)_3]$ was utilized as the template. Urea and dimethyl sulfoxide (DMSO) were chosen to provide extrinsic N and S sources, respectively, and the synthesis procedure included two main steps. Firstly, urea and DMSO were encapsulated into porous MOF-5 by soaking dried MOF-5 in

**ADVANCED
SCIENCE NEWS**
www.advancedsciencenews.com

**ADVANCED
ENERGY
MATERIALS**
www.advenergymat.de
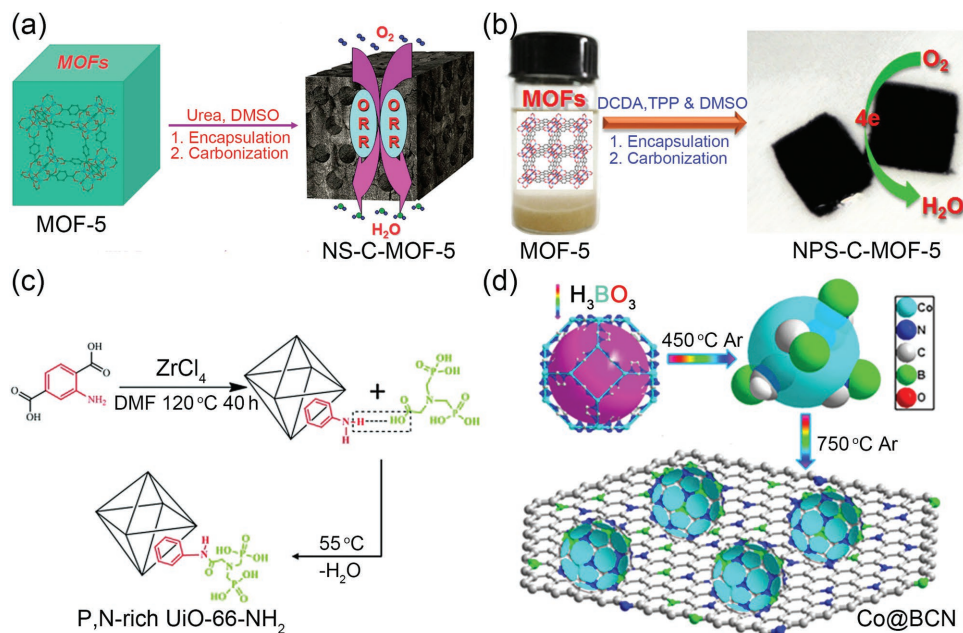
Figure 2. a) Synthesis procedure for MOF-5 templated N and S co-doped porous carbons as metal-free electrocatalysts. Adapted with permission.[61] Copyright 2014, The Royal Society of Chemistry. b) Schematic illustration of the synthesis of N, P, and S ternary-doped porous carbons using MOF-5 as template. Adapted with permission.[59] Copyright 2014, Nature Publishing Group. c) The preparation of the P,N-rich carbon precursor. Adapted with permission.[62] Copyright 2016, WILEY-VCH. d) Basic structural units of ZIF-67 and the two-step preparation for the N,B-doped core–shell Co@BCN. Adapted with permission.[64] Copyright 2016, American Chemcial Society.

a solution of them dissolved in methanol. Then, the filtered MOFs were used as a precursor, which were carbonized in ultra-pure N_2. The final products were obtained after washing the carbonized materials with dilute hydrochloric acid (HCl) and distilled water. The resultant samples were named NS(A:B)-C-MOF-5, where A:B is the feed ratio of urea to DMSO. It is worth mentioning that the ratio of N to S poses a direct influence on electrocatalytic performance. Specifically, when the urea feed was larger than that of DMSO, the catalytic activity of the as-obtained dual-doped carbon materials was positively related to the N/S ratio, which was superior to those of pristine and N-doped porous carbons (i.e., C-MOF-5 and N-C-MOF-5). However, the N and S co-doped carbons with N/S ratio lower than one exhibited poor ORR performance than C-MOF-5. From this trend, it is speculated that an enhanced synergistic effect depends on the simultaneous doping of N and S with N as the dominant dopant. However, the N and S content in the synthesized samples were not mentioned in the report, neither were the percentages of N and S configurations. Further research work should be conducted to get more insight into the N- and S-doping model, as well as their interaction mechanism.

N, P, S Ternary Doping: Based on the above study, Li and coworkers further investigated the N, P, and S ternary-doping effect by employing MOFs as templates to derive multiple doped porous carbon materials.[59] As given in Figure 2b, under a similar synthesis process for preparing N and S co-doped porous carbons, N, P and S ternary-doped porous carbon materials were also fabricated using MOF-5 as the template and dicyandiamide (DCDA), triarylphosphine (TPP), and dimethyl sulfoxide (DMSO) as N, P, and S precursors, respectively. The synthesized materials were denoted NPS-C-MOF-5, in which

the contents of N, P, and S were 4.5%, 0.27%, and 0.75%, respectively. Meanwhile, control experiments were systematically carried out by investigating undoped, N-doped, N,S or N,P co-doped porous carbons, denoted C–MOF-5, N–C–MOF-5, NS–C–MOF-5 or NP–C–MOF-5, respectively. The results showed that NPS–C–MOF-5 and NP–C–MOF-5 achieved better ORR performances than C–MOF-5, verifying the synergistic effect caused by multiple heteroatom doping. Conversely, NS–C–MOF-5 and N–C–MOF-5 displayed poorer activity when compared with that of C–MOF-5. This result is not consistent with their previous report on MOF-5-templated N and S co-doped porous carbons, in which N-doped and NS co-doped carbons showed improved catalytic activity. Careful comparison indicates that the only difference lies in the N precursors. One was DCDA, and the other was urea. Following this discrepancy, it is likely that the selection of extrinsic dopant precursors has a direct impact on the doping effect. Besides MOF-5, MOF-177 ($Zn_4O(BTB)$, BTB = benzene-1,3,5-tribenzoate) and UMCM-1 ($Zn_4O(BDC)(BTB)_{4/3}$, BDC = benzene-1,4-dicarboxylic acid) were also pyrolyzed to produce porous carbon materials. Intriguingly, the original morphologies of the precursor MOFs remained relatively unchanged after high temperature pyrolysis. Moreover, the influence of carbonization temperature was also evaluated on MOF-5 by varying the temperature from 700 to 1000 °C. Again, in this report, a volcano-type relationship between the ORR activity of the as-derived catalysts and the pyrolysis temperature was confirmed.

N, P Co-Doping: P is another significant dopant with an electronegativity of 2.19. Since N and P have reverse electronegativity, it appears appropriate to make full use of their synergistic coupling effect by N, P co-doping. For example,

**ADVANCED
SCIENCE NEWS**

www.advancedsciencenews.com

**ADVANCED
ENERGY
MATERIALS**

www.advenergymat.de

using PMo_{12}@MIL-100 (Fe) and melamine as precursors, Li et al. fabricated Fe_3C/Mo_2C@NPGC.[74] In their study, the co-doping of N and P was realized in as-derived graphitic carbon frameworks, which afforded increased conductivity and an increased number of active sites. To obtain N and P co-doped MOF-derived carbon materials, Fu et al. proposed an inspiring strategy by focusing on the preparation of modified MOF precursors with high content of N and P.[62] Briefly, as illustrated in Figure 2c, the initial precursor MOF (UiO-66-NH_2) was first synthesized via a solvothermal approach using zirconium chloride ($ZrCl_4$) and 2-aminoterephthalic acid (H_2ATA) as building units. Then, postsynthetic modification (PSM) of the MOF precursor was performed via the dehydration reaction between the $-NH_2$ group in UiO-66-NH_2 and the $-OH$ groups in glyphosine. Through this PSM, a target precursor framework with homogeneous N and P distribution was obtained for effective co-doping of N and P. Subsequently, a N, P co-doped carbon material was prepared via a facile one-step pyrolysis process. In the N, P co-doped carbon matrix derived under 950 °C, 1.73 at% N and 1.09 at% P were detected by XPS. Uniform distributions of N and P were also observed by element mapping. Unlike typical co-doping through the introduction of extrinsic heteroatom precursors into the reaction mixture, this work laid a solid foundation for seeking alternative precursors via functionalized MOFs by the PSM method. Significantly, such a strategy is beneficial for achieving several things: 1) effective co-doping by grafting the initial MOF precursor with suitable small molecules contaning desired heteroatoms; 2) better control over resultant dopant content and the uniformity of their distribution; 3) tuning the bonding configurations of the heteroatoms in the carbon matrix. Undoubtedly, these attractive features are definitely advantageous for improving the electrochemical properties of the synthesized electrocatalysts.
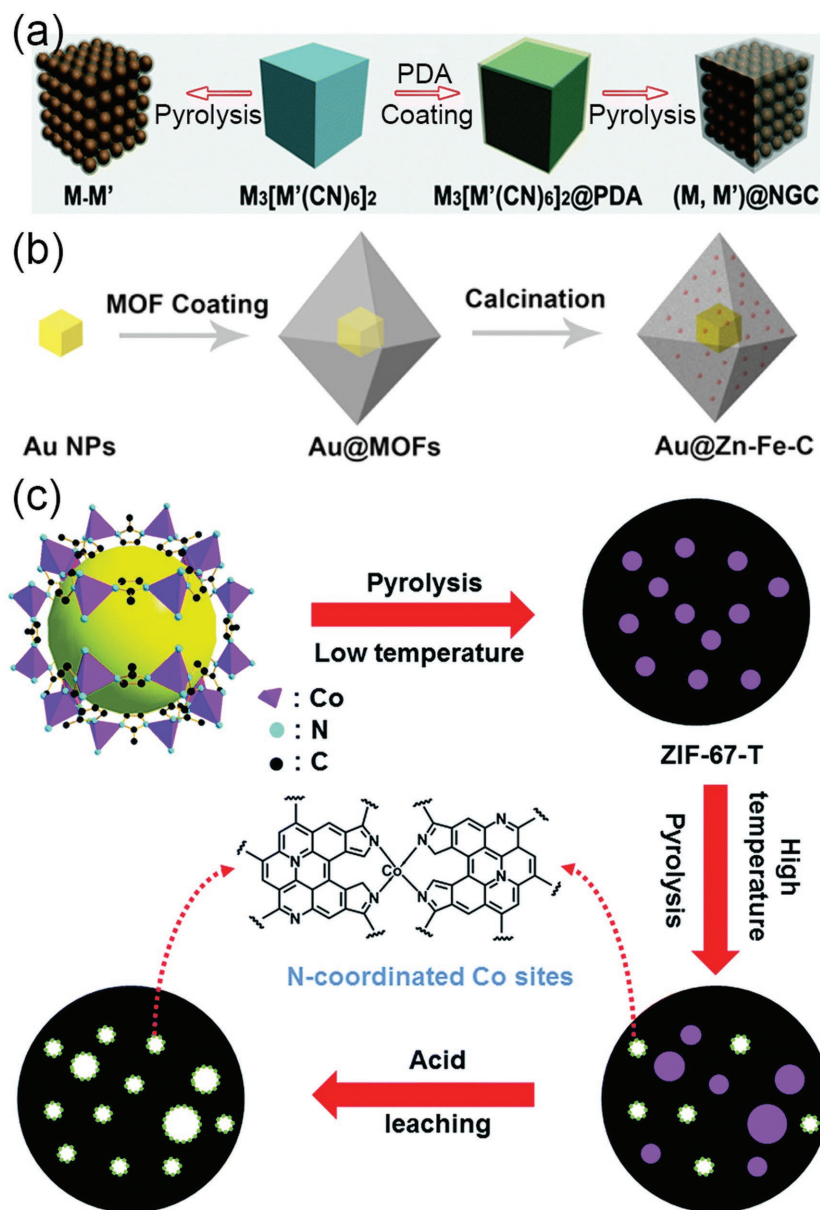
N, B Co-Doping: Recently, Zhang et al. reported the hybrid of cobalt encapsulated by N, B co-doped ultrathin carbon cages (denoted Co@BCN) through a bottom-up approach using MOFs as a precursor and self-sacrificing template.[64] Figure 2d depicts the preparation process for Co@BCN. It can be seen that the bottom-up strategy involves two calcination steps using ZIF-67 and H_3BO_3 as the precursors. In the first step, the mixture of ZIF-67 and H_3BO_3 was annealed at 450 °C in Ar, resulting in the collapse of the ZIF-67 framework and the formation of new components. In the second calcination step, the temperature was increased to 750 °C, under which ZIF-67 was pyrolyzed into N-doped carbon sheets and carbon shells with encapsulated Co NPs, accompanied by B doping via the diffusion of B atoms from the decomposition of H_3BO_3. For the as-assembled Co@BCN, N and B atoms were homogeneously doped into the carbon framework, and their contents were analysed to be about 3.0 at% and 0.7 at%, respectively. Owing to the distinct electronegativities of B ($\chi = 2.04$) and N ($\chi = 3.04$), the 2p orbital of the C atom ($\chi = 2.55$) can be first polarized by a B dopant and then the polarized C atom is capable of donating extra electons to an adjacent N atom. Accordingly, the asymmetrical spin and charge density originating from the dual-doped B−C−N hetero-ring contributes greatly to improving catalytic activity. More recently, the synergistic effects of N, B co-doping was also demonstrated by Hassina et al.[67e]

2.1.3. Transition Metal Incorporation

Considering that MOFs contain abundant metal ions and that pyrolytic carbon originating from organic ligands is able to create reductive conditions under high temperature, transition metal NPs are usually incorporated into the MOF-derived composites after pyrolysis.[40,53,64,68,70,77,80] Since the metal ions distribute homogeneously among the framework, most of the generated transition metal NPs are encapsulated by the carbon materials. According to previous literature, metal NPs alone display minimal electrocatalytic activity toward energy-conversion reactions.[81] By contrast, the construction of hybrids based on transition metal NPs and doped carbon materials with tailored structures, such as core–shell structures, has proven to be an effective way of improving catalytic performance.[64,81] Generally speaking, metal NPs embedded in carbon shells cannot only increase electron transport, but also change the local work function for tuning the adsorption of intermediates.[64,82] For example, the pioneering work reported by Deng et al. indicated that CoNi NPs coated by ultrathin graphene shells (carbon layers < 3) enabled enhanced electron penetration from the metal cores to the carbon shells, thereby modulating the electron density and the electronic structure of the graphene surface.[82] This effect further tuned free energy for the adsorption of intermediates to enhance catalytic activity. At the same time, their study demonstrated the synergistic effect between N dopants and enclosed metal clusters for further enhanced activity. The structural advantages of core–shell materials will be discussed further later. Hence, organizing components in specific structures is vital for constructing highly efficient catalysts. Inspired by Deng et al.'s research, similar strategies have been successfully implemented in MOF-derived composites.[64] As illustrated in Figure 2d, uniform Co NPs were implanted in N, B co-doped carbon matrixes.

Aside from the incorporation of single transition metals, multiple transition metals can be easily introduced into the MOF-derived composites by choosing suitable MOF precursors.[81] Using polydopamine (PDA)-encapsulated $Fe_3[Co(CN)_6]_2$ nanocubes as the precursor, Xi et al. fabricated core–shell (Fe,Co)@nitrogen-doped graphitic carbon ((Fe, Co)@NGC) nanocubes via the approach illustrated in **Figure 3**a.[81] In detail, $Fe_3[Co(CN)_6]_2$ nanocubes were initially prepared by the precipitation reaction between Fe^{2+} cations and $[Co(CN)_6]^{3-}$ anions with the assistance of polyvineypirrolydone (PVP). PDA was then coated on the surface of $Fe_3[Co(CN)_6]_2$ nanocubes through immersion. The PDA-encapsulated $Fe_3[Co(CN)_6]_2$ nanocubes were decomposed into the target (Fe, Co)@NGC. Even though Fe nanocubes, Co nanocubes and (Fe, Co) nanocubes were prepared as control experiments by thermal decomposition of $Fe_4[Fe(CN)_6]_2$, $Co_3[Co(CN)_6]_2$, and $Fe_3[Co(CN)_6]_2$, respectively, it is difficult to comment on the significance of bimetallic cores without considering the role of the NGC shell. In such a study, if Fe@NGC and Co@NGC were synthesized and compared under the same criteria, the role of multiple metals incorporation should be evidently distinguished from that of the single metals.

Interestingly, in addition to self-incorporation of metal NPs as core components, exotic metal NPs can also be coated by MOFs and form transition-metal-incorporated nanocomposites

**ADVANCED
SCIENCE NEWS**
www.advancedsciencenews.com

**ADVANCED
ENERGY
MATERIALS**
www.advenergymat.de

Figure 3. a) Schematic of the formation process of the (M, M')@NGC nanocubes. Adapted with permission.[81] Copyright 2015, The Royal Society of Chemistry. b) Schematic illustration of the synthetic process of Au@Zn−Fe−C core–shell nanostructures. Adapted with permission.[83] Copyright 2016, American Chemcial Society. c) Schematic illustration of the synthesis process for the ZIF-67-T catalysts. The coordination environment of Co in the product (a proposed structure) is also shown. Adapted with permission.[24] Copyright 2014, The Royal Society of Chemistry.

facile calcination at controlled temperatures. Likewise, the Au core had intimate electronic interactions with the carbon shell, which facilitated electron transfer from the core to the shell, thereby tuning the electron density of the carbon shell and reducing the local work function. The strategy developed in this study might be a general approach for incorporating pre-synthesized non-precious metal cores such as Fe, Co, and Ni.

Of course, the incorporation of transition metals is not limited to providing core components. Apart from the core–shell structure described above, another important configuration is porphyrin-like MN_x (M=Fe, Co, etc.), consisting of transition metal centers and N dopants linked by coordination bonds.[24,39,53] Especially, the well-defined coordination between metal ions and N-containing ligands (e.g., MeIM) in MOFs makes it viable to derive porphyrin-like MN_x. To illustrate this protocol, Wang et al. prepared CoN_x by a two-step pyrolysis of ZIF-67 and subsequent acid leaching.[24] From Figure 3c, the Co NPs embedded in the carbon matrix could be deliberately removed by acid leaching, leaving voids in their original location and creating a nanoporous structure. Nevertheless, the Co atoms directly bonded to pyrrolic/pyridinic N were preserved on the walls of the open nanopores. These N-coordinated Co sites were believed to be the active sites for energy-conversion reactions.

2.1.4. Transition Metal Compounds Composition

With the development of various electrocatalysts based on transition metal compounds, such as transition metal oxides, carbides, nitrides, sulphides, selenides, and phosphides,[84] it is logical to derive functional nanocomposites involving these compounds by using MOFs as precursors and/or templates. Although the metal ions in MOFs are inclined to be reduced to metal NPs during carbonization, it is still likely to convert the metal ions into compounds directly by selecting appropriate precursors and controlling the annealing conditions.[36,42,43,45,73,74,76,85–98] The most easily obtained compound is transition metal carbides due to the availability of carbon originating from the decomposition of organic ligands.[36,42,43,45,73,74,76,88,93] The case depicted in Figure 1b supports this point. Not only transition metal carbides, but nitrides and many other compounds are theoretically formed with the presence of corresponding heteroatoms in organic ligands.

After incorporating transition metals into the MOF-derived composites, the metal component can be converted to the

via post-treatment processes. In this regard, Lu et al. studied Au NPs@zinc-iron-embedded porous carbons (Au@Zn-Fe-C) derived from MOFs.[83] As shown in Figure 3b, the preparation process involves three steps: i) monodisperse Au NPs with diameter of 50–100 nm were initially synthesized by chemical reduction of $HAuCl_4$; ii) the obtained Au NPs were utilized as heterogeneous nuclei for the epitaxial growth of Zn−Fe−MOF; iii) the Zn−Fe−MOF shell was then pyrolyzed into porous carbons embedded with zinc–iron compounds (Zn−Fe−C) via

**ADVANCED
SCIENCE NEWS**
www.advancedsciencenews.com

**ADVANCED
ENERGY
MATERIALS**
www.advenergymat.de

desired transition metal compounds via simple chemical modification.[85,94,97,98] As an illustration, You and co-workers synthesized CoP_x (a mixture of CoP and Co_2P) NPs embedded in N-doped carbon matrices (Co-P/NC) using ZIF-67 as the precursor and template.[98] As can be seen in **Figure 4**a, upon carbonization, ZIF-67 nanopolyhedrons were transformed to Co NPs embedded in porous N-doped carbon matrices (Co/NC). Subsequently, the metallic Co in Co/NC was phosphatized to CoP_x through annealing with sodium hypophosphite monohydrate ($NaPO_2H_2 \cdot H_2O$), giving rise to polyhedron-like Co-P/NC. Indeed, this facile two-step route can be expanded to produce many other MOF-derived composites based on transition metal compounds and carbon materials. For instance, Chaikittisilp et al. prepared a carbon–cobalt-oxide hybrid by annealing ZIF-9 ($Co(PhIM)_2$, PhIM = benzimidazolate) in a N_2 atmosphere and air, successively.[97]

Another applicable approach for incorporating transition metal compounds into MOF-derived composites involves the chemical decoration of MOF-derived porous carbons, in which target chemicals are implanted in the MOF precursors or MOF-derived carbon substrates by an impregnation method.[48,99] This strategy can not only make full use of the electrochemical properties of integrated active compounds, but also exploits the unique characteristics of MOF-derived carbons, including high surface area, uniform porosity, good conductivity, and well-defined structure. For example, Liu et al. prepared a MoS_2-based 3D nanoporous composite ($MoS_2/3D$-NPC).[48] The step-by-step construction of this composite is illustrated in Figure 4b. First, an Al-based porous coordination polymer (Al-PCP) was assembled into a MOF precursor. Then, 3D nanoporous carbon (3D-NPC) was derived from the MOF precursor by calcination at 800 °C and subsequent HF etching to eliminate the residue Al. Finally, the confined growth of MoS_2 nanosheets in the pores of 3D-NPC was carried out via the in situ solvothermal reduction of $(NH_4)_2MoS_4$, resulting in a 3D hierarchical structured MOF-derived composite. In another study, Zhu et al. reported the synthesis of N and S dual-doped honeycomb-like porous carbons with Co_9S_8 NPs (denoted Co_9S_8@CNST; where T is the pyrolysis temperature), in which MIL-101-NH_2 was employed as the MOF framework, and thiourea and $CoCl_2$ were introduced as secondary precursors in the MOF via a chemical impregnation approach.[99]
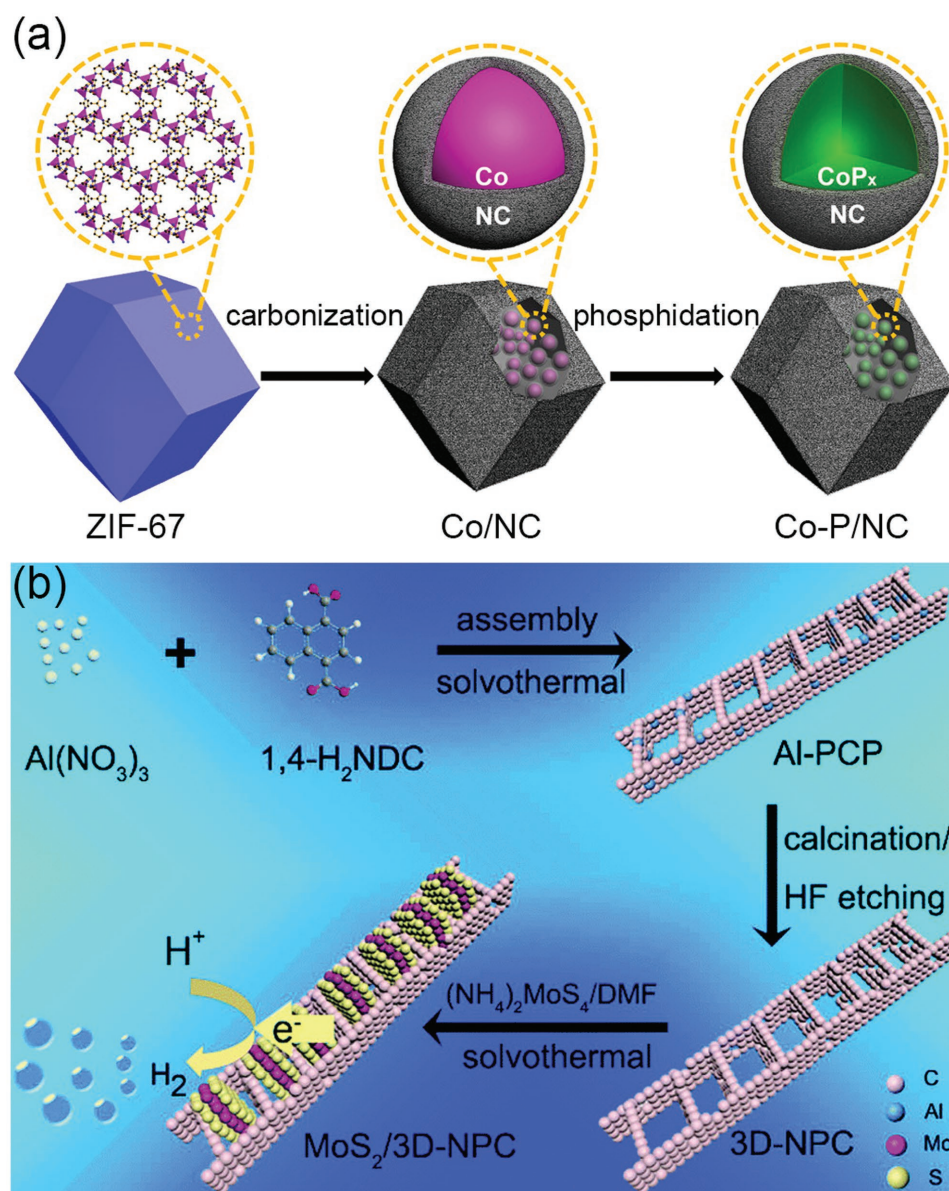
2.2. Morphology Control

In addition to constituent components, morphology is another crucial factor in designing high-performance MOF-derived catalysts, as it closely correlates with exposed facets and active sites.[85,89,91] It is well-known that the catalytic activity of each facet varies significantly due to their different electronic structures.[10] For instance, it has been demonstrated that the ORR activity on the low index surfaces of Pt decreases by the following trend: (110) > (111) > (100).[100] For this reason, controlling well-defined morphology is a considerable strategy for increasing the intrinsic activity through exposing active facets and/or sites. Moreover, as mentioned previously, precursor MOFs usually possess specific morphologies with high surface area and porosity, which are favourable properties for

electrocatalysis.[45,89] Unfortunately, in most cases, the morphology of the precursor MOFs is destroyed after pyrolysis at high temperature, owing to severe and irreversible shrinkage, fusion, pulverization, and aggregation.[44] Undoubtedly, these changes can adversely affect catalytic performance.[44] To be specific, aggregation often results in a dramatic decrease in the number of active sites and poor dispersability, impairing activity and fast mass transfer. Also, the shrinkage and fusion of MOF precursors typically give rise to the degradation of their porous structure, which impedes the rapid access of reactants to active sites and the diffusion of reaction products. In view of these circumstances, morphology control represents a significant strategy to prepare highly efficient electrocatalysts derived from MOFs. However, it remains a great challenge to preserve the morphology of precursor MOFs during thermal treatment.

Introducing an external material as a protective coating has been commonly used in nanotechnology to avoid aggregation, especially when high-temperature calcination is involved. Inspired by this, Shang et al. reported a protected calcination strategy through coating with mesoporous silica ($mSiO_2$).[44] In this work, monodispersed bimetallic MOF (i.e., Zn,Co-ZIF), with well-defined dodecahedral shape, was employed to test the strategy (**Figure 5**a). As evidenced by Figure 5b,c, the Zn,Co-ZIF was effectively coated by a layer of $mSiO_2$ without structural changes. More importantly, after the thermal treatment and removal of the $mSiO_2$ shell, the final Co,N co-doped carbon nanoframework (denoted Co,N-CNF) retained the morphology of ZIF, the hierarchical pore structure, and high dispersity (Figure 5d,f). By contrast, severe aggregation was observed in the absence of the $mSiO_2$ coating. As expected, the as-synthesized Co,N-CNF retained a large specific surface area and rich porosity, and when compared with the sample subjected to direct pyrolysis, the specific surface area and cumulative pore volume of Co,N-CNF improved by a factor of more than 2 and 3, respectively. The well-protected morphology with its inherent qualities not only allows for an increased number of active sites, but also facilitates mass transfer processes, thereby contributing to remarkable catalytic activity and excellent stability. However, the complicated synthesis procedure and the utilization of corrosive and toxic HF during etching of the $mSiO_2$ shell make it difficult for practical applications. Therefore, developing facile and effective methods for controlling morphology is still a great challenge that needs to be addressed.

To circumvent the disadvantages pertaining to the SiO_2 coating, an appropriate solution has been to replace SiO_2 with another coating material that can be incorporated into the final catalyst material. For instance, Xi and co-workers demonstrated the feasibility of polydopamine encapsulation for conserving the MOF morphology.[81] Using Prussian blue analogues (PBA) as the precursor, a polydopamine shell can be facilely formed on the surface of $Fe_3[Co(CN)_6]_2$ nanocubes via the self-polymerization of dopamine (Figure 3a). Similarly, the nanocube morphology can be preserved after pyrolysis in the temperature range of 600–900 °C. Meanwhile, the polydopamine coating pyrolyzed into N-doped graphitic carbon (NGC) shells, wrapping the generated (Fe,Co) nanocubes. Obviously, the NGC is able to act as a carbon support to confer improved electrical conductivity. Further, as N-doped carbon, the NGC shell itself

**ADVANCED
SCIENCE NEWS**
www.advancedsciencenews.com

**ADVANCED
ENERGY
MATERIALS**
www.advenergymat.de

Figure 4. a) Illustration of the two-step synthesis of Co—P/NC nanopolyhedrons. Adapted with permission.[98] Copyright 2015, American Chemcial Society. b) Schematic illustration of the synthesis of a MoS₂/3D-NPC composite. Adapted with permission.[48] Copyright 2015, The Royal Society of Chemistry.

can induce catalytic activity to some extent by creating charge delocalization. Therefore, the success of polydopamine encapsulation provides a new method of controlling the morphology of MOF-derived catalysts.

Interestingly, choosing a suitable temperature during postprocessing can also maintain the well-defined morphology of some MOF precursors. Almost concurrently, Hao et al. synthesized well-defined $Co_xFe_{1-x}P$ nanocubes by a general phosphorization of PBAs, in which NaH_2PO_2 was decomposed under N_2 in the temperature range of 350–550 °C.[91] Due to the relatively low temperatures, the as-derived catalysts showed poor crystallinity,which is a detrimental factor to catalyst stability for various reactions, such as the HER. This reason is the likely cause of a noticeable decay in current density observed during

the durability tests. Nevertheless, the study offers some guidance for morphology control, but further efforts should be invested to overcome its drawbacks.

2.3. Structure Engineering

From the prospective of heterogeneous catalysis, catalytic activity essentially hinges on the number of accessible active sites and the intrinsic activity of each active site.[10] For this purpose, rational catalyst design lies in constructing novel electrocatalysts with favourable structures.[33,35,41,64,83,101] Structure engineering is a promising and indispensable strategy to develop improved catalysts in this respect,[102] and plays
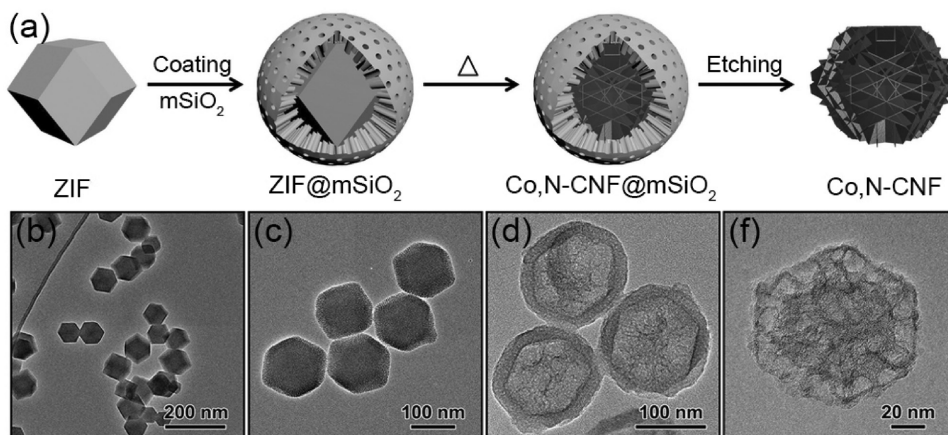
Figure 5. a) Synthetic procedure of the Co,N-CNF by the mSiO$_2$-protected calcination strategy. TEM images of b) Co,Zn-ZIF, c) Co,Zn-ZIF@mSiO$_2$, d) Co,N-CNF@mSiO$_2$, and f) Co,N-CNF. Adapted with permission.[44] Copyright 2015, WILEY-VCH.

a critical role in integrating all components to make full use of their functionalities. Until now, a variety of nanostructures or architectures based on MOF-derived materials, such as edge-rich strucutures,[48] core–shell structures,[64,83] sandwich structures,[33] porous nanowire array structures,[35] and three-dimensional hierarchical structures,[101] have been synthesized and widely investigated. These attempts have proven successful for validating this strategy. More significantly, with the advances of synthetic methods and characterization techniques, the microstructure at the atomic level can also be tuned to explore highly efficient catalysts.[41] Unlike conventional structure engineering, fine tuning of structures at the atomic or molecular level provides a more effective approach to increasing the intrinsic catalytic activity. To distinguish these, the former will be referred to as nanostructure engineering, while structural tuning at the atomic will be defined as atom-structure engineering herein.
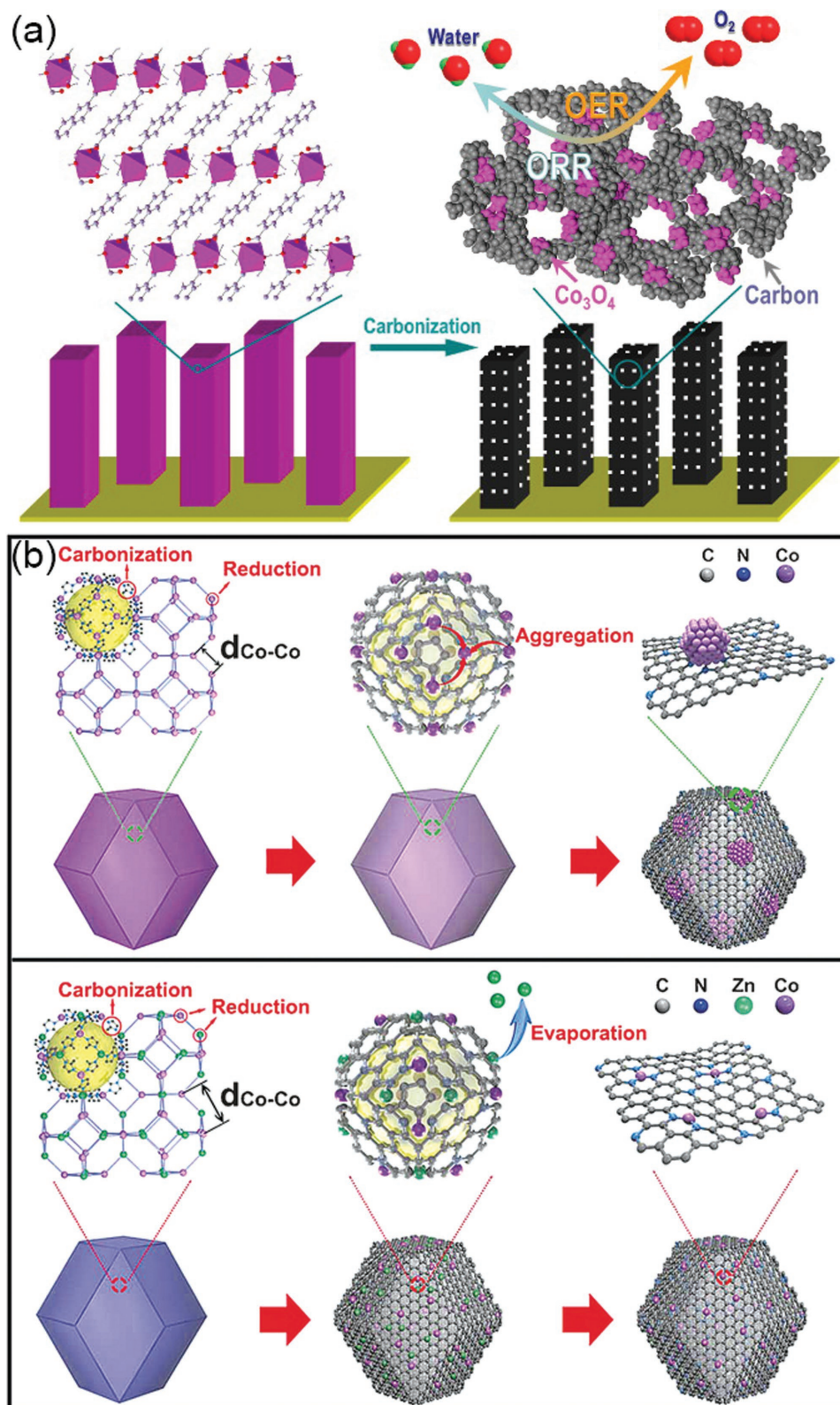
In general, nanostructure engineering enables the substantial exposure of active sites, and expedites electrolyte penetration and mass transfer. As illustrated in Figure 4b, the in situ and confined growth of MoS$_2$ nanosheets in porous 3D-NPC resulted in an edge-rich structure, which allowed for the exposure of significantly more egdes as active sites.[48] For different nanostructures, however, many other features and properties can be introduced to further enhance catalytic performance. Co@BCN with core–shell structure,[64] for example, has a carbon shell which could protect the inner metal NPs from corrosion and oxidization by external electrolytes, especially strong acid and base. Further, such a core–shell architecture provides an ideal way to regulate the electronic structure of the electrocatalyst, and thus compromises adsorption free energy or local work function for beneficial adsorption and desorption of reaction intermediates.[64] As for the HER in this study, the free energy for H adsorption is too strong on the Co metal and too weak on the carbon, whereas it can reach a moderate, more optimal result on the core–shell Co@BCN because of the electron transfer from Co core to carbon shell. It should be noted that the N and B dopants can greatly reinforce the modification of electronic structure. Consequently, the unique electron donation character associated with the core–shell structure accounts

significantly for the highly improved HER performance. Unsurprisingly, the effect has also been demonstrated by the study reported by Lu et al. regarding ORR and HER, in which different metal (Au and Pt) NPs were implanted into MOF-derived shells (Figure 3b).[83] Due to the electron-donor effect, the electrocatalytic activity appears insensitive to different core metals.

To maximize the persistent exposure of active sites, another attractive strategy is to assemble interconnected porous nanostructures with continuous conducting networks. For instance, compositing MOF precursors with conductive supports, such as CNTs,[69,95] graphene,[33,34,92] and carbon fabric,[94] has been widely explored to enhance catalytic activity. Recently, Lai et al. reported ZIF-8-derived N-enriched meso-microporous carbon (NEMC) frameworks.[33] Composites of 2D NEMC on graphene (NEMC/G) with sandwich structure were especially promising, exhibiting significantly improved catalytic performance.

Although combining MOF-derived NPs with carbon supports is favourable for improving electronic conductivity, the utilization of binders hinders fast charge transfer. Accordingly, it is highly desirable to assemble MOF-derived nanomaterials into integrated electrodes with well-preserved nanostructures. With this in mind, our group proposed the direct growth of MOF precursors on metal substrates to produce electrodes composed of porous nanowire arrays (**Figure 6**a).[35] Specifically, the Co-naphthalenedicarboxylate MOF on Cu foil was converted into porous nanowire arrays consist of strongly interacting Co$_3$O$_4$ and carbon (Co$_3$O$_4$C-NA). The as-designed electrode with porous nanowire arrays featured abundant active sites, highly improved conductivity, and extremely strong stability, and thus performed excellently as an OER electrocatalyst. Very recently, Ming and co-workers fabricated 3D hybrid electrode composed of Co-doped nickel selenide and Ni foam through a similar structure strategy.[101] Due to its advantageous 3D herarchical structure, the as-prepared electrode afforded excellent activity and very good long-term durability for overall water splitting. Ultimately, structure engineering for constructing such integrated electrodes holds vast potential for practical applications.

In the last decade, heteroatom-doped carbon materials have been broadly explored as metal-free catalysts,[11] and for our purposes, heteroatom doping in carbon matrices can be classified

**ADVANCED
SCIENCE NEWS**

www.advancedsciencenews.com

**ADVANCED
ENERGY
MATERIALS**

www.advenergymat.de

Figure 6. a) Schematic illustration of the fabrication of hybrid Co_3O_4C-NA. Adapted with permission.[35] Copyright 2014, American Chemcial Society. b) Schematic illustration of the formation of Co NPs-N/C (top) and Co SAs/N-C (bottom). Adapted with permission.[41] Copyright 2016, WILEY-VCH.

**ADVANCED
SCIENCE NEWS**

www.advancedsciencenews.com

**ADVANCED
ENERGY
MATERIALS**

www.advenergymat.de

as atom-structure engineering. However, their catalytic performances are still inferior to most electrocatalysts containing metal elements. In this regard, one of the most promising strategies is to prepare atomically-dispersed metal atoms on robust conductive supports, that is, to develop single atom catalysts. Even though single atom catalysts in biomolecules, such as heme, were discovered in the last century, the synthesis of inorganic single atom catalysts is greatly hindered by the lack of techniques to effectively disperse and stabilize single metal atoms. Thanks to the rapid progress of nanotechnology, nanostructure engineering has emerged as a powerful strategy in the design of single metal atom catalysts. For example, Yin et al. recently synthesized single Co atoms on N-doped porous carbon via the pyrolysis of predesigned Zn,Co-ZIF, in which the atom loading was up to 4 wt%.[41] As shown in Figure 6b, the success of this strategy relied significantly on the homogeneous distribution of Zn ions in the precursor MOF, leading to an enlarged distance of adjacent Co atoms and preventing the formation of Co−Co bonds during the subsequent calcination. Extended X-ray absorption fine structure (EXAFS) spectra indicated that the dominant Co single atoms existed as planar Co−N$_4$ or Co−N$_2$. Atom-structure engineering opens up a profound procedure for the precise control of single metal atoms, aiming at the enhancement of catalytic properties. More significantly, the successful synthesis of single atom catalysts endows great possibilities for elucidating the underlying reaction mechanisms of various energy-conversion processes, as the mechanisms can be studied exclusively on single, well-defined active site.

3. Applications of MOF-Derived Materials for Energy-Conversion Reactions

The ultimate goal of rational catalyst design is to improve catalytic performance as much as possible for certain applications. Benefitting from functional components, well-defined morphology, and favourable structure, many MOF-derived materials have been highlighted as electrocatalysts toward different energy-conversion processes, including the ORR, OER, HER, etc.[35,36,41] In addition, owing to their rich diversity and versatility, MOF derivatives have huge potential in emerging energy-conversion reactions like the ECR.[103] Very importantly, well-designed MOF-derived materials exhibit desirable bifunctional features, allowing for application in next-generation energy devices such as rechargeable metal-air batteries and overall water electrolyzers.[104–106] Despite several reviews having introduced MOF-derived catalysts for electrocatalysis,[51,52] some remarkable progress has been made very recently. Therefore, a timely progress report in this field would provide a more comprehensive account of the design strategies toward improved MOF-derived electrocatalysts.

3.1. ORR

The ORR is a key process in fuel cells and metal–air batteries, and Pt has been regarded as the benchmark electrocatalyst for this process. As an important alternative to Pt catalysts, MOF-derived materials exhibit remarkable ORR

performance in terms of activity, durability, and tolerance to methanol.[24,32–34,38–44,47,53,58–63,65–73,75–77,81,83,97,99,107–109] In particular, some newly developed MOF derivatives achieved highly improved activity that is comparable and even superior to Pt catalysts under identical experimental conditions. **Table 1** summarizes the catalytic performances of representative MOF-derived electrocatalysts for the ORR. Among them, Yin et al.'s report on Co SAs/N−C, synthesized by annealing Zn$_1$Co$_1$–BMOF (Zn/Co = 1:1) at a desired temperature (800, 900, and 1000 °C) for 3 h in a N$_2$ atomsphere, represents the rational strategies discussed above in designing MOF-derived catalysts (Figure 6b).[41] Specifically, component manipulation was reflected in N-doping to create a coordination structure and Zn incorporation to expand the adjacent distance between Co atoms, whereas morphology control and structure engineering were verified by the reserved initial rhombododecahedral shape and homogeneous generation of Co single atoms on N-doped carbon in the final product (**Figure 7**a–c). Strikingly, the optimized Co SAs/N-C(900) showed more positive half-wave potential (E$_{1/2}$, 0.881 V vs RHE) than that of Pt/C (Figure 7d). Also, it promoted the ORR by efficient four-proton–electron transfer with improved kinetic current density (Figure 7e,f). More significantly, no noticeable decay in activity was observed after 5000 potential cycles (Figure 7g), due to the extraordinary robustness of the catalyst. This study shows that N-coordinated Co single atoms among a carbon matrix are highly active toward ORR, and that atom-structure engineering is capable of significantly increasing active sites. In addition, being able to preserve morphology and porous structure is highly advantageous for enhancing mass transfer as well as long-term stability.

Very recently, Li et al. designed a lamellar MOF-derived Fe−N−C nanocomposite with bimodal porosity for efficient ORR.[110] Notably, it is critical to control component distribution, morphology, and structure of MOF precursors for desirable features. Unlike most MOF-derived ORR catalysts based on 3D MOF crystals, a lamellar MOF named DCI–Fe was prepared by solvothermal synthesis from 4.5-dicyanoimidazole (DCI) and iron acetate in N,N-dimethylformamide (DMF), whereby N-rich DCI interacted with iron ions through strong coordination. After high-temperature pyrolysis (600, 700, and 800 °C in N$_2$ for 2 h), the as-formed DCI–Fe converted into iron carbide nanospheres interlaminated in N-doped carbon shells on N-doped carbon nanosheets (Fe$_3$C@NC/NCS, **Figure 8**a). It can be clearly observed that the lamellar structure was well preserved, and the core–shell structured Fe$_3$C@NC were evenly distributed on the 2D carbon nanosheets (Figure 8b–d). As an ORR electrocatalyst, the optimized DCI–Fe-700 showed superior activity and durability to commercial Pt/C, with a more positive E$_{1/2}$ of 17 mV, significantly improved tolerance to methanol, and prolonged stability (Figure 8e–g). Consistent with our discussion and previous reports,[111] the surpassing electrocatalytic performance of DCI–Fe-700 over its counterparts was a result of the balance between N doping (to obtain increased N content with high fraction of active pyrrolic N), specific surface area (to expose more active sites), and appropriate pyrolysis temperature. The enhanced ORR activity was also closely related to its bimodal porosity, that is, mesopores (≈50 nm) between FeC$_3$-spaced carbon sheet layers in favor of rapid mass transfer, and nanopores (≈4 nm) among encapsulated FeC$_3$ nanospheres

**ADVANCED
SCIENCE NEWS** _____
www.advancedsciencenews.com

**ADVANCED
ENERGY
MATERIALS**
www.advenergymat.de

Table 1. Summary of the MOF-derived ORR electrocatalysts with comparable/superior activity to commercial Pt/C.

No.	Catalyst	MOF used	Electrolyte	E_{onset}[a] (V vs RHE)	$E_{1/2}$[a] (V vs RHE)	Ref.	Year
1	MOF-253–Fe–phen-C	MOF-253	0.1 M KOH	0.98 (0.98)	0.84 (0.82)	[109]	2017
2	PNPC-1000	Al(OH)(BPYDC)	0.1 M KOH	0.89 (–)	0.76 (–)	[58]	2017
3	LDH@ZIF-67-800	ZIF-67	0.1 M KOH	0.94 (0.94)	0.83 (0.805)	[107]	2016
			0.1 M HClO$_4$	0.875 (0.892)	0.675 (0.693)		
4	Fe$_3$C@N–CNT assemblies	MIL-88B & ZIF-8	0.1 M KOH	0.97 (–)	0.85 (0.83)	[43]	2016
5	Co SAs/N–C(900)	Zn,Co-ZIF	0.1 M KOH	0.982 (0.982)	0.881 (0.811)	[41]	2016
6	C$_3$N$_4$@NH$_2$–MIL-101-700	NH$_2$–MIL-101	0.1 M KOH	0.99 (–)	0.84 (–)	[73]	2016
			0.5 M H$_2$SO$_4$	0.92 (–)	0.67 (–)		
			0.1 M PBS	0.90 (–)	0.65 (–)		
7	NGPC/NCNT-900	MOF-5	0.1 M KOH	–0.051 (–0.59) vs Ag/AgCl	–0.171 (–0.172) vs Ag/AgCl	[75]	2015
8	Co–N–C	Zn,Co-ZIF	0.1 M KOH?	0.982 (0.982)	0.871 (0.841)	[38]	2015
			0.1 M HClO$_4$		0.761 (0.82)		
			0.1 M PBS		0.731 (0.768)		
9	P–CNCo-20	Zn,Co–ZIF	0.1 M KOH	0.93 (0.93)	0.85 (0.81)	[53]	2015
10	Fe/Fe$_3$C–C	MIL-88B–NH$_3$	0.1 M KOH	1.03 (1.01)	0.92 (–)	[42]	2014
11	N–Fe–MOF	Cage-containing MOF	0.5 M H$_2$SO$_4$		0.79 (0.85)	[71]	2014
			0.1 M KOH		0.88 (≈0.86)		
12	GNPCSs-800	ZIF-8	0.1 M KOH	0.957 (–)		[34]	2014
13	ZIF-67-900-AL	ZIF-67	0.1 M KOH	0.93 (0.92)	0.85 (0.84)	[24]	2014
			0.5 M H$_2$SO$_4$	0.85 (0.88)			
14	P-Z8–Te-1000	ZIF-8	0.1 M KOH	0.881 (0.871)	0.79 (0.759)	[66]	2014

[a]Reported values are presented vs RHE unless otherwise noted, and the values in parentheses are corresponding data for commercial Pt/C.; (–): No data presented for commercial Pt/C.
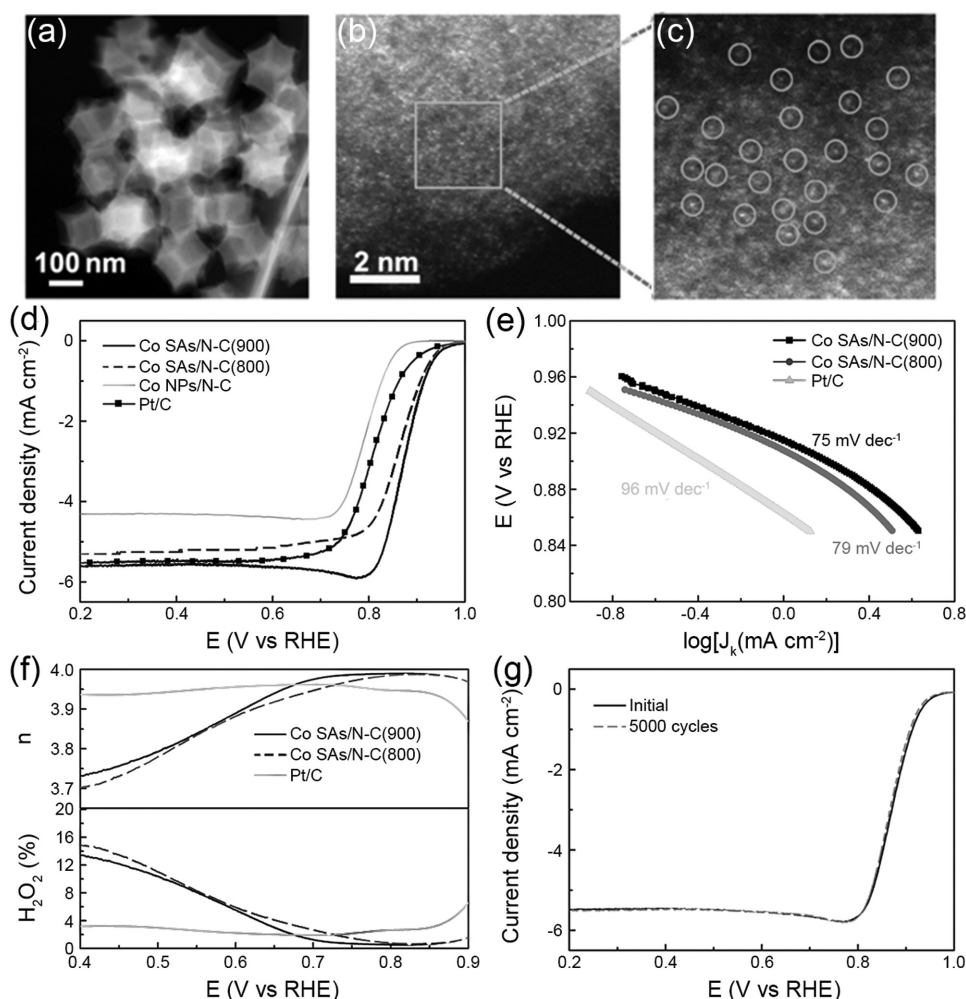
contributing to abundant accessible active sites. Moreover, the core–shell FeC$_3$@NC with unique host–guest eletronic interaction and robust structure was advantageous to ameliorate ORR activity and durability. The success of this study may provide new opportunities in designing advanced electrocatalysts from lamellar MOF precursors.

Although the majority of MOF-derived catalysts have achieved prominent performance for the ORR in alkaline electrolyte, much effort is needed to advance both theory and experiment toward the ORR in acidic media, aiming to meet the requirment of specific energy technologies such as PEMFCs. So far, some MOF-derived materials especially M–N–C catalysts have been investigated as ORR electrocatalysts in acidic conditions, which exhibited promising activity to satifiy practical demand.[24,38,71,73,107] However, few studies have elucidated the catalytic ORR mechanism on particular M–N–C configurations in order to understand the structure–performance relationship. Until recently, Lai and co-workers synthesized an Fe–N/C electrocatalyst derived from Fe-mIm nanoclusters (guest) in ZIF-8 (host) via pyrolysis (900 °C in N$_2$ for 2 h), acid (0.5 M H$_2$SO$_4$) etching, and a second heat treatment (same conditions as pyrolysis), and studied different types of Fe–N$_x$ sites with two-, four-, and five-coordinated configurations on a porous carbon matrix.[112] By varying the molar ratio of the host and the guest components (R% from 5 to 25%), a series of R% Fe–N/C samples were obtained, among which 5% Fe–N/C exhibited the best ORR performance in 0.1 M HClO$_4$.

The characterizations by X-ray absorption near edge structure (XANES) and Fourier transform (FT) extended X-ray absorption fine structure (EXAFS) indicated that the improved acidic ORR activity of 5% Fe–N/C could be ascribed to the high oxidation state of Fe maintained in highly coordinated N–Fe–N$_4$ configuration, whereas the coordiantion number was reduced gradually from five to two, due to the weakened confinement effect with higher R%. The higher ORR activity of five-coordianted Fe–N$_x$ configuration in acid media was further verified by spin-polarized DFT calculations. Compared with Fe–N$_4$ and Fe–N$_2$ structures, the N–Fe–N$_4$ configuration associated with 5% Fe–N/C possessed both a decreased reaction energy barrier and reduced adsorption energy for intermediate OH, in accordance with the experimental results. The definite establishment of a relationship between the Fe–N$_x$ configurations and ORR catalytic performance provided a deeper insight into the design of more efficient M–N–C electrocatalysts under acid conditions. Evidently, MOF-derived materials represent a class of promising candidates for high-performance ORR electrocatalysts.
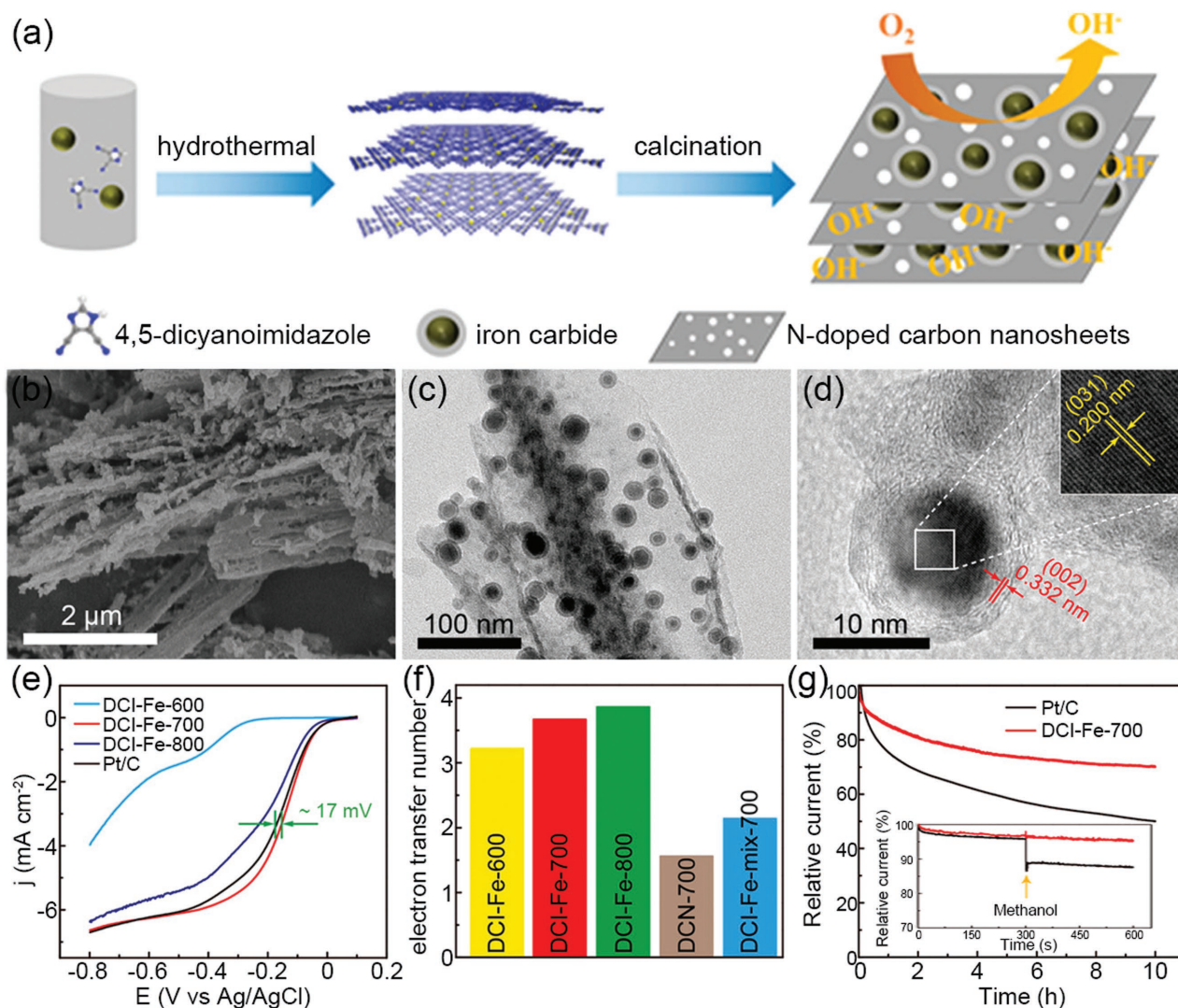
3.2. OER

As the reverse reaction to the ORR, the OER is another important process in many energy-conversion devices, such as metal–air batteries and water electrolyzers. Due to the intrinsically

ADVANCED
SCIENCE NEWS
www.advancedsciencenews.com

ADVANCED
ENERGY
MATERIALS
www.advenergymat.de

Figure 7. a) HAADF-STEM and b,c) magified HAADF-STEM images of Co SAs/N—C(800), showing that only Co single atoms are present in Co SAs/N—C. d) RDE polarization curves of Co SAs/N—C(900), Co SAs/N—C(800), Co NPs/N—C, and Pt/C in O₂-saturaed 0.1 M KOH with a sweep rate of 10 mV s⁻¹ and 1600 rpm. e) Corresponding Tafel plots obtained from the RDE polarization curves. f) Electron transfer number (n; top) and H₂O₂ yield (bottom) vs potential. g) LSV curves of Co SAs/N-C(900) before and after 5000 potential cycles. Adapted with permission.[41] Copyright 2016, WILEY-VCH.

sluggish kinetics of the OER, it often requires considerable overpotential to promote the reaction, resulting in poor energy efficiency.[16] Currently, precious-metal-based catalysts (i.e., Ir, IrO₂, and RuO₂) are the benchmark electrocatalysts for the OER.[15,16] Again, rationally designed materials derived from MOFs have been widely reported as alternative OER electrocatalysts,[35,80,94–96,98,101,113–116] and a summary of the OER performances of recent MOF-derived catalysts is listed in **Table 2**. In this respect, Co₃O₄C-NA on Cu foil, fabricated by carbonization of Co–MOF NA precursor (Figure 6a) under N₂ protection (400 °C for 2 h and 600 °C for 4 h), displayed high OER activity (10 mA cm⁻² at 1.5 V vs RHE), favourable kinetics (70 mV dec⁻¹) and outstanding stability (6.5% current loss at 30 h and 96.7% current retention after 3000 cycles), which surpassed that of state-of-the-art IrO₂/C (**Figure 9**).[35] As stated previously, the improved OER performance can be attributed to the high surface area, excellent electron conductivity, and advanced electrode configuration associated with the structure of the porous nanowire arrays.[35]

Similarly, Zhou et al. recently fabricated hierarchically structured Co₃O₄@X (X = Co₃O₄, CoS, C, and CoP) integrated electrodes, which were derived from cobalt carbonatehydroxide@ZIF-67 (CCH@ZIF-67) precursors via chemical modifications (**Figure 10**a).[117] Specifically, Co₃O₄@Co₃O₄ was prepared by calcination of CCH@ZIF-67 in air, Co₃O₄@CoS was obtained by sulfurization of as-prepared Co₃O₄@Co₃O₄ in thioacetamide and ethanol solution, Co₃O₄@C was fabricated by pyrolysis of CCH@ZIF-67 under N₂ atmosphere, and Co₃O₄@CoP was synthesized through the phosphorization of Co₃O₄@Co₃O₄ using NaH₂PO₂·H₂O as the P source. As given in Figure 10b–e, the as-obtained Co₃O₄@X retained the structure of the well-aligned nanorod arrays on Ni foil substrates, and Co₃O₄@CoS and Co₃O₄@CoP, in particular, inherited the original morphology of ZIF-67. Impressively, all of the Co₃O₄@X electrodes displayed superior OER performance to commercial Ir/C, in terms of OER acitivity, kinetics, and stability (Figure 10f–h). Particularly, the Co₃O₄@CoP electrode achieved the highest OER activity with a much lower

ADVANCED
SCIENCE NEWS
www.advancedsciencenews.com

ADVANCED
ENERGY
MATERIALS
www.advenergymat.de

Figure 8. a) Schematic illustration of the preparation of Fe₃C@NC/NCS nanohybrides. b) SEM and c) TEM images of DCI-Fe-700 catalyst. d) HRTEM image of Fe₃C@C nanosphere in DCI-Fe-700 catalyst. (Inset) HRTEM image showing lattice fringes of the Fe₃C core. e) LSV curves of DCI–Fe-600, -700, and -800, and Pt/C at a rotation rate of 1600 rpm. f) Chronoamperometric responses of DCI–Fe-700 and Pt/C catalysts to the addition of methanol. g) Chronoamperometric responses of DCI–Fe-700 and Pt/C catalysts in O₂-saturated 0.1 M KOH. Adapted with permission.[110] Copyright 2017, American Chemcial Society.

Table 2. Summary of representative MOF-derived materials for the OER.

No.	Catalyst	MOF used	Electrolyte	η_{onset} [mV]	η_{10} [mV]	Tafel slope [mV dec⁻¹]	Ref.	Year
1	Co₃O₄@CoP	ZIF-67	1 M KOH		238	51.4	[117]	2017
2	Ni1Co₄S@C-1000	ZIF-67	0.1 M KOH	200	280	64	[96]	2016
3	Co–MOF@CNTs (5 wt%)	Co(PhIm)₂·(DMF)·(H₂O)	1 M KOH	280	340	69	[113]	2016
4	Zn-doped CoSe₂/CFC	Zn,Co–ZIF	1 M KOH		356	88	[94]	2016
5	CoP hollow polydedrons	ZIF-67	1 M KOH	300	400	57	[89]	2016
6	FeNi@N–CNT	Zn/Fe/Ni–ZIF	1 M KOH		300	47.7	[114]	2016
7	Co–CNT–PC	ZIF-67	0.1 M KOH	260	315	73.8	[80]	2016
8	CoP/rGO-400	ZIF-67	1 M KOH		340	66	[92]	2016
9	Co₃O₄@C–MWCNTs	ZIF-9	1 M KOH	270	320	62	[95]	2015
10	Co₃O₄C–NA	Co-naphthalenedicarboxylate	0.1 M KOH	240	290	70	[35]	2014

**ADVANCED
SCIENCE NEWS**

www.advancedsciencenews.com

**ADVANCED
ENERGY
MATERIALS**

www.advenergymat.de
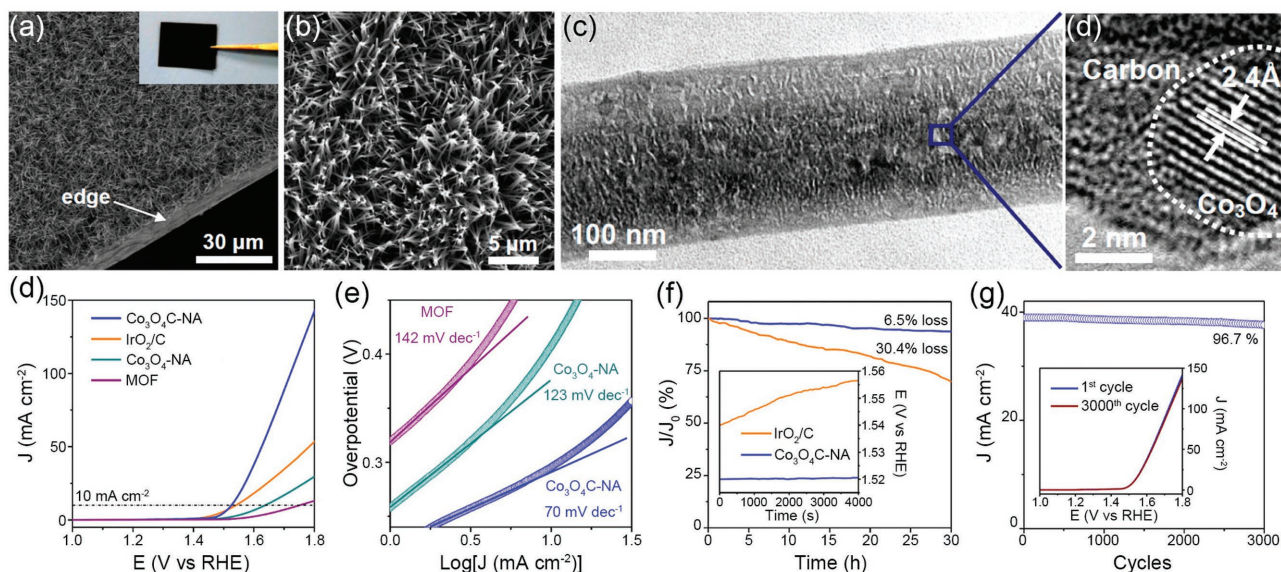
Figure 9. a,b) SEM, c) TEM, and d) HRTEM images of Co_3O_4C-NA. Inset in (a): optical image of Co_3O_4C-NA. d) Polarization curves and e) Tafel plots of Co_3O_4–NA, IrO_2/C, Co_3O_4–NA, and the Co–MOF in an O_2-saturated 0.1 M KOH solution (scan rate 0.5 mV s^{-1}). f) Chronoamperometric response at a constant potential of 1.52 V ($E_{j=10}$). Inset in (e): chronopotentiometric response at a constant current density of 10 mA cm^{-2} of Co_3O_4–NA in comparison to that of IrO_2/C. g) Plot of the current density at 1.60 V recorded from the polarization curve of Co_3O_4C–NA vs. the cycle number. Inset in (f): polarization curves of Co_3O_4C–NA before and after 3000 potential cycles (scan rate 100 mV s^{-1}). Adapted with permission.[35] Copyright 2014, American Chemcial Society.

overpotential of 238 mV to afford 10 mA cm^{-2}. It should be mentioned that the high catalytic properties of the Co_3O_4@CoP electrode was further demonstrated by its efficient electro-oxidation of small organic molecules including glycerol, methanol, and ethanol. Aside from the features of the nanorod array structure similar to that of Co_3O_4C–NA on Cu foil, such as accessible and sustainable diffusion channels between nanorods for mass transfer, and high specific surface area with abundant active sites, the superior catalytic performance of the Co_3O_4@CoP electrode is attributed to the intrinsic properties of CoP. Even though the authors did not explain why the Co_3O_4@CoP electrode was superior to the other Co_3O_4@X electrodes, this study demonstrates the advantages of MOF-derived electrocatalysts with hierarchical structure for the OER and versatile component manipulation based on MOFs. It is obvious that MOF-derived materials offer great potential as a new category of efficient OER electrocatalysts.

3.3. HER

In order to develop a hydrogen economy, tremendous efforts have been directed to search for efficient and earth-abundant HER electrocatalysts.[8,19] The HER performances of many recently developed MOF-derived catalysts have been summarized in **Table 3**. As an ideal prototype for designing MOF-derived HER electrocatalyst using the above strategies, Zhang and co-workers synthesized ultrafine Mo_xC NPs embedded into a 3D N-doped carbon matrix (MoCN-3D, **Figure 11**a–c).[36] Particularly, a hybrid ZIF (HZIF) precursor was designed by substituting the $Zn(im)_4^{2-}$ units in ZIF-8 with MoO_4^{2-} nodes via a one-pot solvothermal (DMF) approach to tailor the functional component. Carbonization of HZIF (700 °C in Ar for 2 h) and

acid (0.5 M H_2SO_4) treatment were then conducted to construct a 3D hierarchical porous structure. These features endowed the as-obtained MoCN-3D with abundant highly active β-Mo_2C NPs, large surface area, high electrical conductivity, and a strong 3D porous carbon framework. As a consequence, the MoCN-3D exhibited remarkable activity toward the HER in acidic media, achieving 10 mA cm^{-2} at an overpotential of 89 mV (Figure 11d). Moreover, the improved activity of MoCN-3D was further supported by its favourable Tafel slope of 51.4 mV dec^{-1} and high turnover frequency of 0.017 s^{-1} (Figure 11e). This enhanced HER activity originated from the effective coupling effect between the Mo_2C NPs and the N-doped carbon matrix, which was further confirmed by DFT calculations.

Although intensive research has been devoted to developing alternative HER electrocatalysts, unlike the ORR and OER, few noble-metal-free catalysts can outperform the benchmark Pt electrocatalysts for the HER because Pt metal is located on the peak of the activity volcano plot with the smallest ΔG_{H^*} and the largest exchange current (j_0).[12,118] Accordingly, another approach is to minimize the required use of Pt by alloying with earth-abundant transition metals. For example, by annealing Pt-incorporated $Co_3[Fe(CN)_6]_2$ precursor obtained through a hydrothermal process, Chen et al. prepared N-doped carbon encapsulated ternary PtCoFe alloy (PtCoFe@CN, **Figure 12**a).[119] The HRTEM image in Figure 12b shows that the as-prepared PtCoFe@CN possessed a well-defend core–shell structure. In addition, component analysis revealed that the content of Pt in the alloy was only 4.6%. Remarkably, the PtCoFe@CN exhibited high activity for the HER with a very low overpotential of 45 mV at 10 mA cm^{-2} and a favorable Tafel slope of 32 mV dec^{-1}, which is comparable to commercial 20% Pt/C (Figure 12c,d). As expected, the core–shell structured PtCoFe@CN displayed excellent stability after 10000 cycles
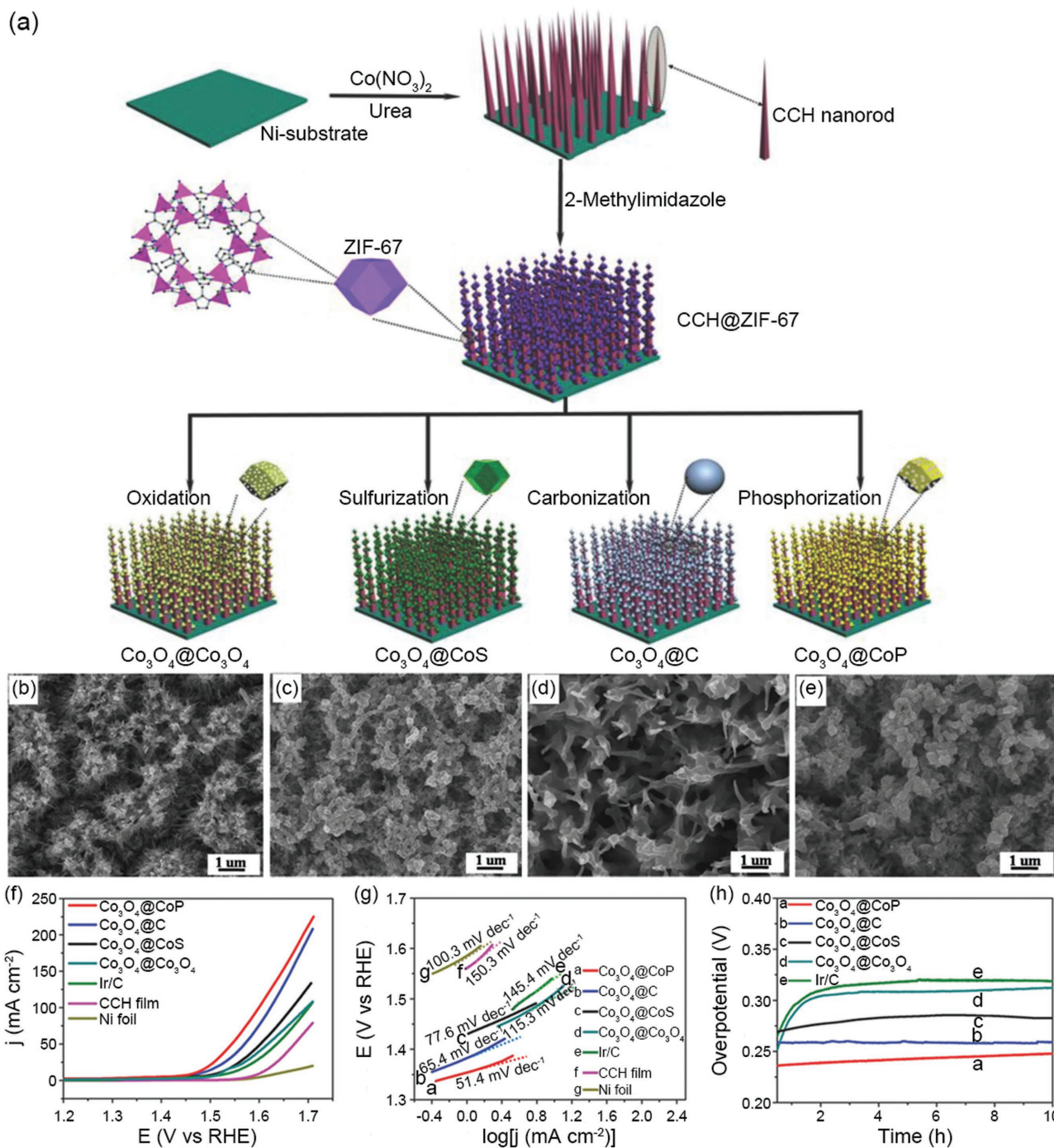
Figure 10. a) Schematic illustration of the fabrication of hierarchically structured $Co_3O_4@X$ (X = Co_3O_4, CoS, C, and CoP) derived from CCH@ZIF-67 for high performance OER. SEM images of b) $Co_3O_4@Co_3O_4$, c) $Co_3O_4@CoS$, d) $Co_3O_4@C$, and e) $Co_3O_4@CoP$. f) LSV curves and g) corresponding Tafel plots of various samples for OER. h) Chronopotentiometric curves at 10 mA cm^{-2} for $Co_3O_4@X$ and commercial Ir/C over 10 h. Adapted with permission.[117] Copyright 2017, WILEY-VCH.

(Figure 12e). DFT calculations show that electron transfer occurs from the alloy core to the N-doped carbon shell in the PtCoFe@CN, leading to the lowest ΔG_{H*} of 0.14 eV (Figure 12f). Overall, much of this superior HER performance originates from the MOF-derived synthesis techniques with rational control of the components and microstructure.

3.4. Other Energy-Conversion Reactions

Beyond these commonly studied electrochemical processes, MOF-derived materials have also been applied to other emerging energy-conversion reactions.[103,120] One important reaction is the electrochemical reduction of CO_2 to useful fuels

**ADVANCED
SCIENCE NEWS**

www.advancedsciencenews.com

**ADVANCED
ENERGY
MATERIALS**

www.advenergymat.de

Table 3. Summary of representative MOF-derived materials for the HER.

No.	Catalyst	MOF used	Electrolyte	η_{onset} [mV]	η_{10} [mV]	Tafel slope [mV dec^{-1}]	Ref.	Year
1	PtFeCo@CN	Co$_3$[Fe(CN)$_6$]$_2$	0.5 M H$_2$SO$_4$		45	32	[119]	2017
2	CoP$_3$	ZIF-67	0.5 M H$_2$SO$_4$		78	53	[116]	2016
3	MoCN-3D	ZIF-8	0.5 M H$_2$SO$_4$		89	51.4	[36]	2016
			1 M KOH		122	78.4		
4	Zn$_{0.3}$Co$_{2.7}$S$_4$	Zn,Co–ZIF	0.5 M H$_2$SO$_4$	35	80	47.5	[87]	2016
5	CoPd@NC	Co$_3$[Co(CN)$_6$]$_2$	0.5 M H$_2$SO$_4$		80	31	[121]	2016
6	CoP hollow polydedrons	ZIF-67	0.5 M H$_2$SO$_4$	35	159	59	[89]	2016
7	Ni–NPs@NC	Ni$_2$(bdc)$_2$(ted)	1 M KOH		77 mV at 20 mA cm^{-2}	68	[114]	2016
8	CoP/rGO-400	ZIF-67	0.5 M H$_2$SO$_4$	13	105	50	[92]	2016
			1 M KOH		150	38		
9	Fe$_3$C/Mo$_2$C@NPGC	MIL-100 (Fe)	0.5 M H$_2$SO$_4$	18	98	45.2	[74]	2016
10	Mo$_2$C/C	MIL-53 (Al)	1 M KOH		165	63.6	[93]	2016
11	nanoMoC@GS(700)	Mo$_3$(BTC)$_2$	0.5 M H$_2$SO$_4$		132	46	[88]	2016
12	Ni$_2$P	Ni–BTC	0.5 M H$_2$SO$_4$	75	172	62	[86]	2015
13	CoP–N–C-400	ZIF-67	0.5 M H$_2$SO$_4$	31	91	42	[90]	2015
14	MoCx nano-octahedrons	NENU-5	0.5 M H$_2$SO$_4$	≈25	142	53	[45]	2015
			1 M KOH	≈80	151	59		
15	CoP CPHs	ZIF-67	0.5 M H$_2$SO$_4$	≈30	133	51	[85]	2015
16	Co$_{0.59}$Fe$_{0.41}$P	Co/Fe–PBAs	0.5 M H$_2$SO$_4$	31	72	52	[91]	2015
17	MoS$_2$/3D-NPC	Al–PCP	0.5 M H$_2$SO$_4$	180	210	51	[48]	2015

and chemicals, which can simultaneously reduce anthropological greenhouse gases and store energy from renewable sources. Very recently, Zhao et al. prepared Cu-based MOF

(HKUST-1) using Cu(NO$_3$)$_2$ and benzene-1,3,5-tricarboxylate under hydrothermal condition and obtained oxide-derived Cu/carbon (OD Cu/C) via a facile pyrolysis method (**Figure 13**a).[103]
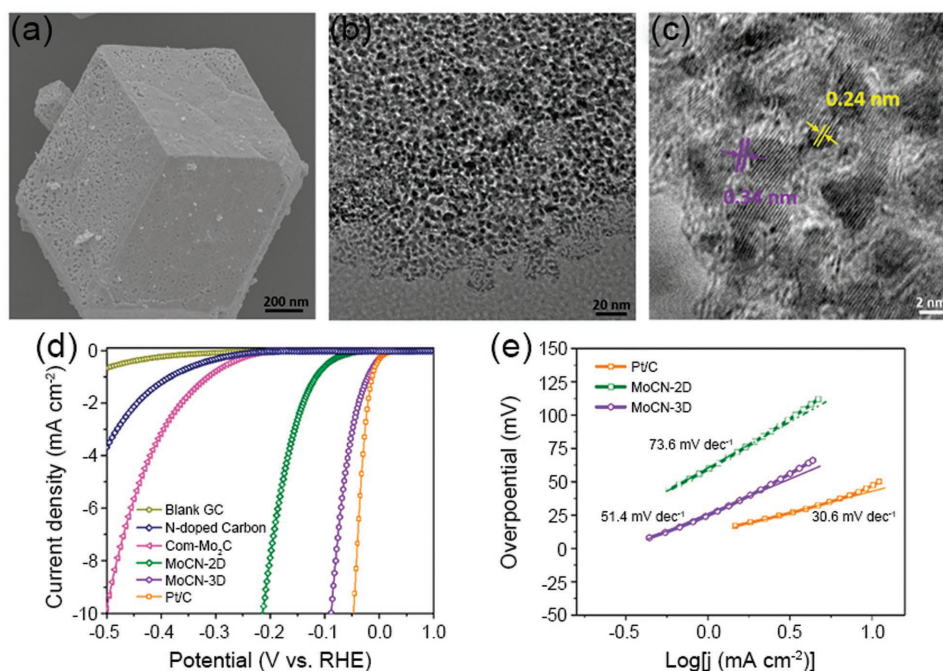
Figure 11. a) SEM, b) TEM, and c) HERTEM images of MoCN-3D. d) The HER polarization curves of various catalysts in 0.5 M H$_2$SO$_4$, and e) corresponding Tafel plots. Adapted with permission.[36] Copyright 2016, Nature Publishing Group.
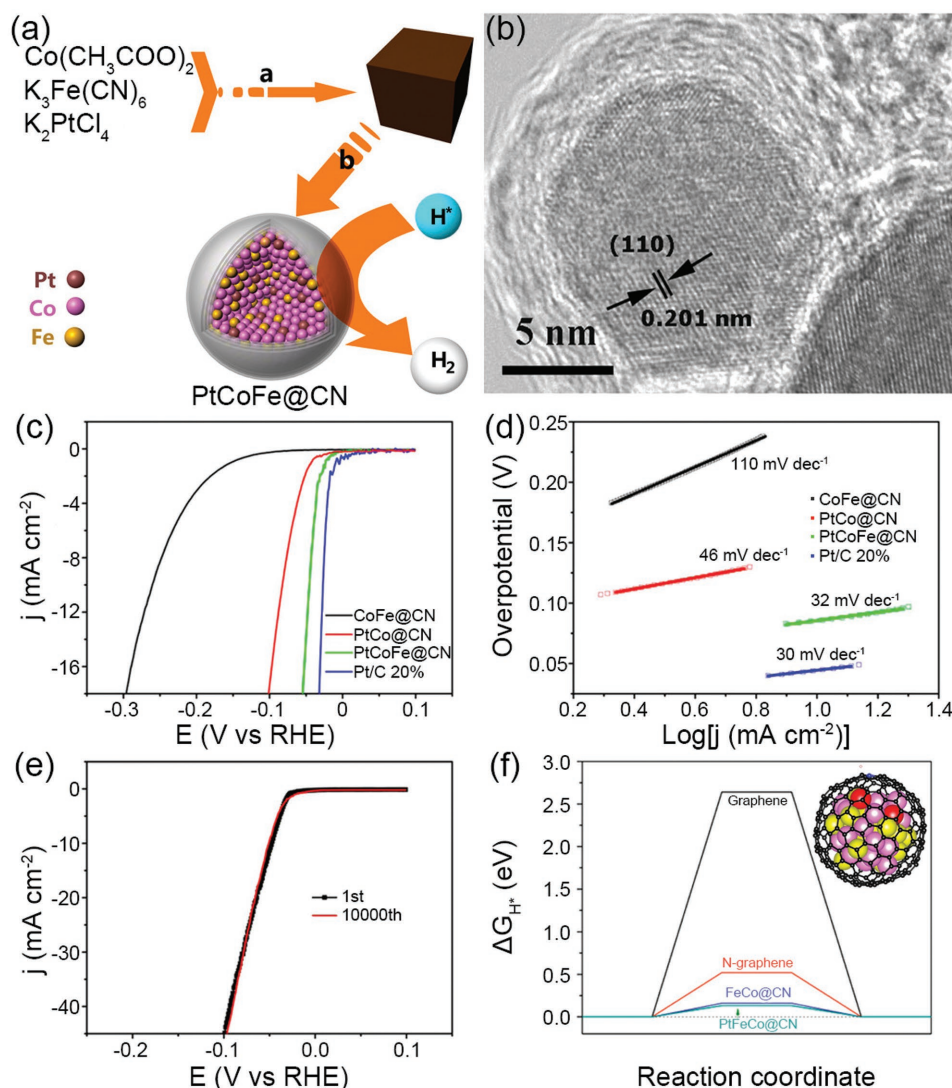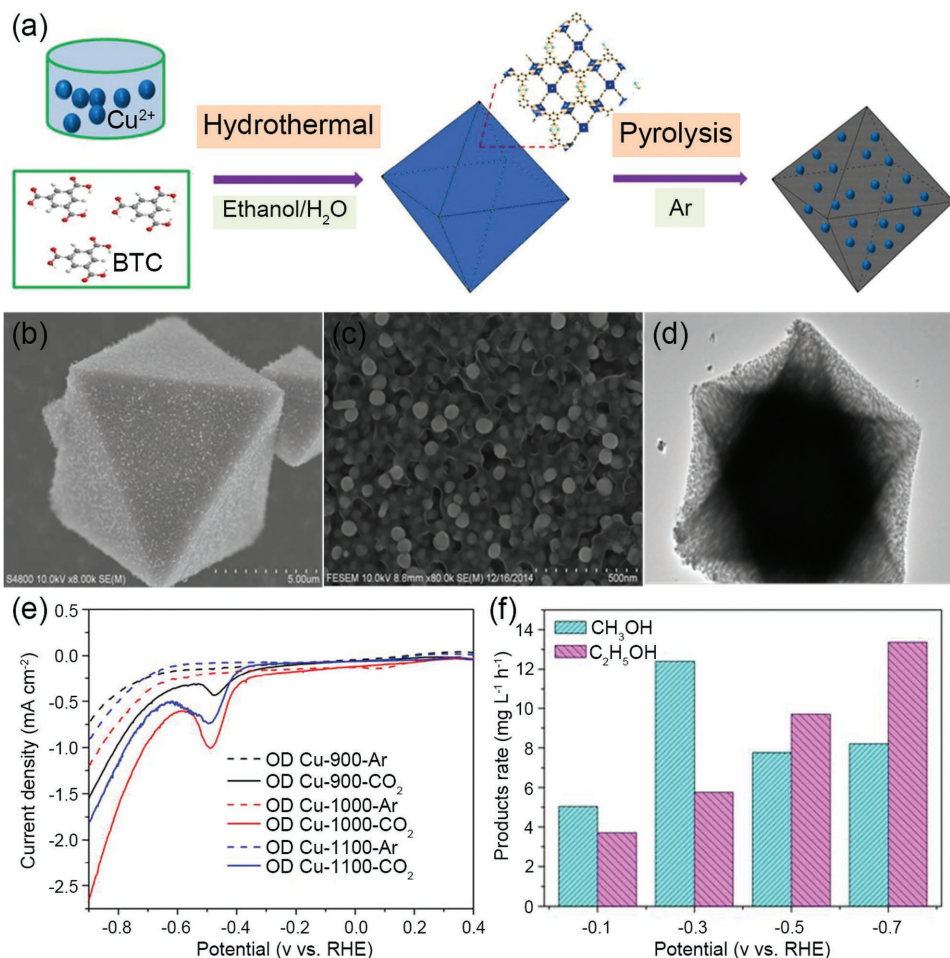
Figure 12. a) Synthetic illustration of graphene encapsulated PtCoFe ternary alloys. b) HRTEM image and the lattice spacing of PtCoFe alloy. c) Polarization curves and d) Tafel plots of various samples. e) Polarization curves of PtCoFe@CN 1st and 10000th cycles. f) Calculated ΔG_{H*} on different models. (Inset) Optimized structure of H* adsorbed on PtFeCo@CN. The yellow, pink, and red spheres refer to Fe, Co, and Pt atoms, respectively. Adapted with permission.[119] Copyright 2017, American Chemical Society.

By choosing a suitable carbonization temperature, the optimized OD Cu/C-1000, composed of Cu NPs on a porous carbon framework, retained the morphology and size of the precursor HKUST-1 (Figure 13b–d). Because of the beneficial component, morphology, and structure, the OD Cu/C-1000 exhibited high activity and selectivity for the ECR, achieving a very low overpotential of ≈190 mV for ethanol formation, as well as high production rates for methanol and ethanol up to 12.4 and 13.4 mg L^{-1} h^{-1}, respectively (Figure 13e,f). Aside from the ECR, MOF-derived materials have also been applied to diverse electrocatalysis processes, such as BH^{4-} electro-oxidation, nicotinamide adenine dinucleotide (NADH) electro-oxidation, H$_2$O$_2$ electro-reduction, and the electrosynthesis of dimethyl carbonate.[120] Although these areas are relatively less explored, the development of these reactions may totally restructure the future landscape of the energy and chemical industries.

3.5. Bifunctional Electrocatalysts for Energy Devices

In general, many energy devices involve more than one energy-conversion reaction. Specifically, rechargeable metal–air batteries involve the ORR and OER,[104,105] and water electrolysis involves the OER and HER.[106] In particular, rechargeable metal–air batteries require the electrocatalyst be efficient for both the ORR and OER, which means a bifunctional electrocatalyst is necessary. Under such circumstances, noble-metal-based electrocatalysts seem to no longer be competitive, as they are poor bifunctional electrocatalysts.[104,105] For water electrolyzers, even though individual OER and HER electrocatalysts can form a pair of working electrodes, this usually creates some operating obstacles, such as the utilization of ion-exchange membranes because of the different electrolytes required for the OER and HER. In contrast, it is highly

**ADVANCED
SCIENCE NEWS**
www.advancedsciencenews.com
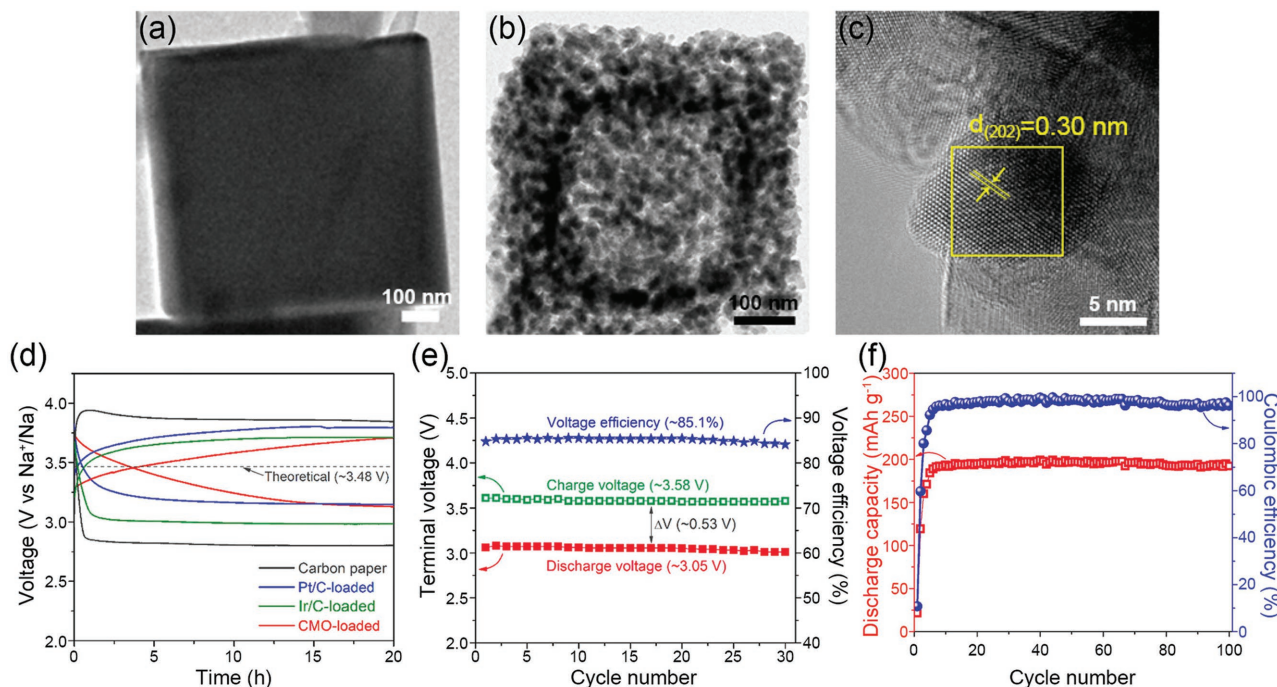
**ADVANCED
ENERGY
MATERIALS**
www.advenergymat.de

Figure 13. a) Schematic illustration of the synthesis process of oxide-derived Cu/carbon catalysts. b,c) SEM and d) TEM images of the OD Cu/C-1000. e) Linear sweep voltammetry curves of OD Cu/C materials in Ar- or CO_2-saturated solution with a scan rate of 5 mV s^{-1}. f) Methanol and ethanol production rate of OD Cu/C-1000 for electrochemical CO_2 reduction (applied potential from −0.1 to −0.7 vs RHE and electrolyte concentration 0.1 M KHCO$_3$). Adapted with permission.[103] Copyright 2017, American Chemical Society.

desirable to use bifunctional electrocatalysts in the same electrolyte, which greatly simplifies the water splitting system for practical applications.[106] Therefore, the concept of exploring bifunctional electrocatalysts is of paramount importance to realizing functional energy devices.

Thanks to the versatility of MOFs in tuning components, morphology, and structure, the advantages of MOF-derived materials can be fully embodied as bifunctional electrocatalysts in energy devices. As a proof-of-concept, Wang et al. designed highly graphitic carbon on N-doped carbon (NC@GC) as an efficient oxygen bifunctional electrocatalyst, which was synthesized by the carbonization of core–shell structured ZIF-8@ZIF-67 precursor.[104] To produce core–shell structured ZIF-8@ZIF-67, a two-step hydrothermal method was adopted, in which ZIF-8 was first prepared as core and then ZIF-67 was coated on the ZIF-8. The NC@GC retained the dodecahedral shape of ZIF-67 and showed a distinct hollow structure with graphitic carbon and nanotubes. Strikingly, the NC@GC exhibited superior ORR and OER performances to commercial Pt/C and Ir/C, respectively. As

expected, the NC@GC-based primary Zn–air battery achieved high discharge voltage and stability, even at increased discharge current densities. Furthermore, rechargeable Zn–air batteries containing NC@GC showed good cycle-life with steady charge and discharge voltage. The excellent catalytic performance of NC@GC for Zn–air batteries originated from the synergistic interaction of NC and GC in the core–shell structure, where NC provided high surface area, Co doping, and high N content, and GC contributed high crystallinity, good conducivity, and durability.

In addition to Zn–air batteries, MOF-derived electrocatalysts have also been applied to rechargeable hybrid Na–air/seawater batteries. Taking the recent study by Abirami et al. as an example,[105] spinel-type cobalt manganese oxide ($Co_xMn_{3-x}O_4$, CMO) nanocubes consisted of substantial nanoparticles were derived from PBA precursor $Mn_3[Co(CN)_6]_2 \cdot nH_2O$ (**Figure 14**a–c). It should be noted that the resultant CMO had a porous and hollow structure, which created a huge surface area with large number of actives sites. When investigated as a bifunctional oxygen electrocatalyst, the cell using the CMO

ADVANCED
SCIENCE NEWS

www.advancedsciencenews.com

ADVANCED
ENERGY
MATERIALS

www.advenergymat.de

Figure 14. a) TEM image of as-prepared $Mn_3[Co(CN)_6]_2$ nanocubes. b) TEM and c) HRTEM images of porous CMO nanocubes. d) Initial charge–discharge voltage profiles of a seawater battery (Nalseawater) with different electrocatalysts at a current density of 0.01 mA cm^{-2}. e) The terminal voltages and voltage efficiency during cycling. f) Variations of the discharge capacity and Coulombic efficiency of the full cell with cycle number to 100 cycles. Adapted with permission.[105] Copyright 2016, American Chemical Society.
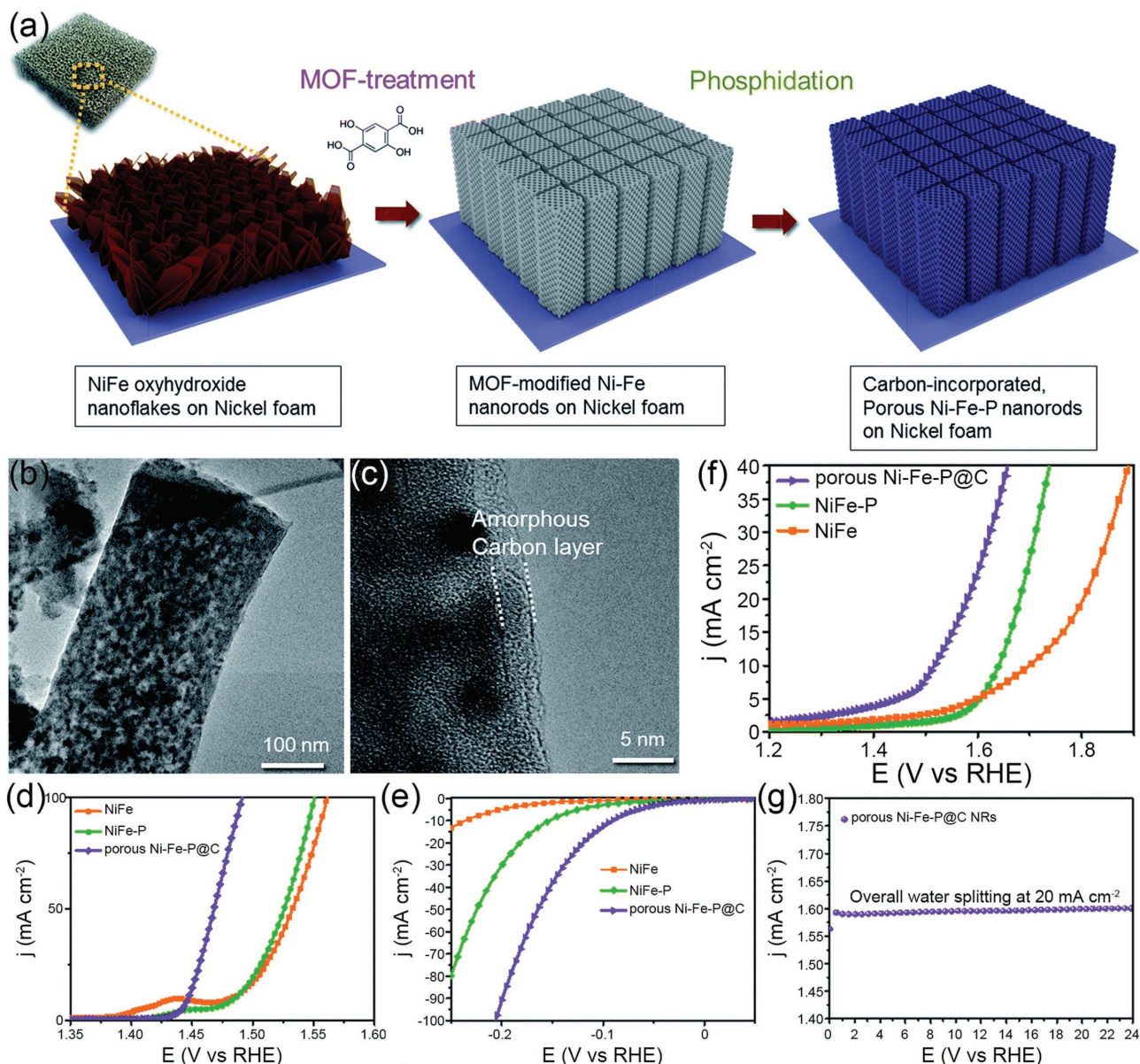
catalyst showed the smallest voltage gap (ΔV, $\approx$0.58 V) between charging and discharging processes, lower than that of Pt/C ($\approx$0.64 V) and Ir/C ($\approx$0.73 V, Figure 14d). In Figure 14e, the terminal voltage was rather stable during cycling and the discharge capacity of the CMO cell was up to $\approx$195 mA h g^{-1}, even with prolonged cycling (Figure 14f). These results are a direct result of the excellent bifunctional electrocatalytic activity and stability of CMO toward both the OER and ORR.

Parallel to their application in metal–air batteries, MOF-derived materials have also been used as bifunctional electrocatalysts for overall water splitting.[98,101,106,114–116] Among recent studies, Ahn and co-workers' report is one of the highest bifunctional catalysts for water electrolysis.[106] As presented in **Figure 15**a, a typical two-step approach was employed to derive carbon-incorporated porous Ni-Fe-P nanorods grown on nickel foams (porous Ni$-$Fe$-$P@C). Typically, the hydrothermally grown Ni$_{0.7}$Fe$_{0.3}$ oxyhydroxide nanoflakes on nickel foam were converted into Ni$-$Fe$-$MOF nanorods through solvothermal reaction with 2,5-dihydroxyterephthalic acid in DMF, which were further pyrolyzed with NaH$_2$PO$_2$ to perform phosphorization. The nanorod morphology and porous structure of the Ni$-$Fe$-$P@C was confirmed from TEM and HRTEM images (Figure 15b,c). As an integrated electrode with 3D porous architecture, the as-derived porous Ni$-$Fe$-$P@C exhibited remarkable OER and HER activity, achieving 10 mA cm^{-2} at overpotential of 217 and 70 mV, respectively (Figure 15d,e). When assembling a water electrolyzer with two porous Ni$-$Fe$-$P@C electrodes in 1 M KOH, it only required a voltage of 1.52 V to deliver 10 mA cm^{-2} for overall water splitting

(Figure 15f). As well, the robust structure of the integrated electrode provided the porous Ni$-$Fe$-$P@C with very good stability during long-term water splitting (Figure 15g). Therefore, it can be concluded that the bifunctional properties of MOF-derived materials make them extremely attractive for real application in next-generation energy devices.

4. Perspective and Conclusion

To date, a large number of MOF-derived materials have been developed under the guidance of design strategies highlighted above. Although some recently emerged MOF-derived electrocatalysts have achieved remarkably improved performances in various energy-conversion reactions, there are still some challenges for future exploration of more advanced MOF-based catalysts. First, although thousands of MOFs have been reported and the number continues to increase, only several typical MOFs, such as ZIF-8, ZIF-67, PBA, and MIL-88B-NH$_3$, have been widely investigated as precursors and/or templates to derive improved electrocatalysts. It is believed that the extension of materials design strategies highlighted in this review will lead to the discovery of many novel electrocatalysts. Remarkably, the majority of pristine MOFs are poor conductors, whereas graphitic carbon produced from calcinated MOFs possesses a conductivity (σ) of 2–4 × 10^5 S m^{-1},[122] higher than the best conductive MOF (Cu$_3$(BHT)$_2$, σ = 1.58 × 10^5 S m^{-1}).[123] Accordingly, poor conductivity might be the main restrictive factor in designing pristine MOFs with high electroactivity.

**ADVANCED
SCIENCE NEWS**
www.advancedsciencenews.com

**ADVANCED
ENERGY
MATERIALS**
www.advenergymat.de

Figure 15. a) Schematic illustration of the preparation of porous Ni−Fe−P nanorods directly grown onto nickel foam via a subsequent two-step post-treatment. b) TEM and c) HRTEM images of the porous Ni-Fe-P@C NRs with a 3-nm-thick amorphous carbon coating layer. d,e) Steady-state polarization curves of various samples toward OER and HER in a 1 M KOH electrolyte with a sweep rate of 0.5 mV s^{-1}. f) Steady-state polarization curves for overall water splitting of various samples in a two-electrode configuration in a 1 M KOH electrolyte with a sweep rate of 0.5 mV s^{-1}. g) Chronopotentiometric curve for the overall water splitting with the porous Ni−Fe−P@C NRs at 20 mA cm^{-2}. Adapted with permission.[106] Copyright 2017, The Royal Society of Chemistry.

The development of highly conductive MOFs is anticipated to create new opportunities to design highly efficient MOF electrocatalysts.[124] Second, compared with the profound progress of MOF-derived materials for the ORR, OER, and HER, more efforts are needed to promote their applications in other emerging and promising clean energy reactions, especially the ECR, because breakthroughs in frontier research are anticipated to provide solutions to current environmental and energy crises. For practical requirements, stability in long operation is of great importance, because the materials are likely prone

to significant changes in composition, morphology and structure during long-term cycling. Unfortunately, few studies have given much attention to materials characterization after long stability tests, whereby uncovering the possible migration and disordering of functional components may elucidate stability trends of MOF-derived materials after long operation. Last but not least, it remains a great challenge to understand the reaction mechanisms of various energy-conversion processes, and deep insight into these mechanisms could lay a solid foundation for electrocatalysts design. With the advances of

computer science and quantum chemistry, it is predicted that the combination of theory and experiment will provide new opportunities for the construction of high-performance MOF-derived catalysts for various energy-conversion reactions.

In summary, rational strategies have been highlighted in the development of efficient MOF-derived electrocatalysts, in terms of component manipulation, morphology control, and structure engineering. The as-developed MOF-derived materials, possessing functional components, well-defined morphology, and favourable structure, show great potential in a wide range of energy-conversion reactions (e.g., ORR, OER, HER, ECR, etc.) and real energy devices (e.g., rechargeable metal–air batteries and water electrolyzers) as improved electrocatalysts. Particularly, some representative MOF-derived electrocatalysts outperform state-of-the-art noble metal based catalysts (e.g., Pt and IrO_2) owing to their rational design and unique properties. Hopefully, further exploration of MOF-derived materials, especially through the combination of experiment and theory, will create many new opportunities for discovery and breakthroughs in advanced electrocatalysis.

Conflict of Interest

The authors declare no conflict of interest.

[1] S. Chu, A. Majumdar, *Nature* **2012**, *488*, 294.

[2] Z. Yang, J. Zhang, M. C. W. Kintner-Meyer, X. Lu, D. Choi, J. P. Lemmon, J. Liu, *Chem. Rev.* **2011**, *111*, 3577.

[3] P. C. Stern, B. K. Sovacool, T. Dietz, *Nat. Clim. Change* **2016**, *6*, 547.

[4] a) M. S. Dresselhaus, I. L. Thomas, *Nature* **2001**, *414*, 332; b) S. Chu, Y. Cui, N. Liu, *Nat. Mater.* **2017**, *16*, 16.

[5] B. Dunn, H. Kamath, J. M. Tarascon, *Science* **2011**, *334*, 928.

[6] T. Sadhasivam, K. Dhanabalan, S. H. Roh, T. H. Kim, K. W. Park, S. Jung, M. D. Kurkuri, H. Y. Jung, *Int. J. Hydrogen Energy* **2016**, *42*, 4415.

[7] D. Aurbach, B. D. McCloskey, L. F. Nazar, P. G. Bruce, *Nat. Energy* **2016**, *1*, 16128.

[8] I. Roger, M. A. Shipman, M. D. Symes, *Nat. Rev. Chem.* **2017**, *1*, 0003.

[9] D. D. Zhu, J. L. Liu, S. Z. Qiao, *Adv. Mater.* **2016**, *28*, 3423.

[10] Z. W. Seh, J. Kibsgaard, C. F. Dickens, I. Chorkendorff, J. K. Nørskov, T. F. Jaramillo, *Science* **2017**, *355*, eaad4998.

[11] J. Duan, S. Chen, M. Jaroniec, S. Z. Qiao, *ACS Catal.* **2015**, *5*, 5207.

[12] Y. Zheng, Y. Jiao, M. Jaroniec, S. Z. Qiao, *Angew. Chem., Int. Ed.* **2015**, *54*, 52.

[13] V. R. Stamenkovic, B. Fowler, B. S. Mun, G. Wang, P. N. Ross, C. A. Lucas, N. M. Marković, *Science* **2007**, *315*, 493.

[14] a) J. Zhang, K. Sasaki, E. Sutter, R. R. Adzic, *Science* **2007**, *315*, 220; b) B. Lim, M. Jiang, P. H. C. Camargo, E. C. Cho, J. Tao, X. Lu, Y. Zhu, Y. Xia, *Science* **2009**, *324*, 1302; c) L. C. Seitz, C. F. Dickens, K. Nishio, Y. Hikita, J. Montoya, A. Doyle, C. Kirk, A. Vojvodic, H. Y. Hwang, J. K. Norskov, T. F. Jaramillo, *Science* **2016**, *353*, 1011; d) Y. Chen, C. W. Li, M. W. Kanan, *J. Am. Chem. Soc.* **2012**, *134*, 19969; e) D. Kim, J. Resasco, Y. Yu, A. M. Asiri, P. Yang, *Nat. Commun.* **2014**, *5*, 4948.

[15] Y. Lee, J. Suntivich, K. J. May, E. E. Perry, Y. Shao-Horn, *J. Phys. Chem. Lett.* **2012**, *3*, 399.

[16] C. C. L. McCrory, S. Jung, J. C. Peters, T. F. Jaramillo, *J. Am. Chem. Soc.* **2013**, *135*, 16977.

[17] Z. Chen, D. Higgins, A. Yu, L. Zhang, J. Zhang, *Energy Environ. Sci.* **2011**, *4*, 3167.

[18] a) N. Jung, Y. H. Cho, M. Ahn, J. W. Lim, Y. S. Kang, D. Y. Chung, J. Kim, Y. H. Cho, Y. E. Sung, *Int. J. Hydrogen Energy* **2011**, *36*, 15731; b) X. Cheng, Z. Shi, N. Glass, L. Zhang, J. Zhang, D. Song, Z. S. Liu, H. Wang, J. Shen, *J. Power Sources* **2007**, *165*, 739; c) E. Christoffersen, P. Liu, A. Ruban, H. L. Skriver, J. K. Nørskov, *J. Catal.* **2001**, *199*, 123.

[19] M. S. Faber, S. Jin, *Energy Environ. Sci.* **2014**, *7*, 3519.

[20] a) M. Shao, Q. Chang, J. P. Dodelet, R. Chenitz, *Chem. Rev.* **2016**, *116*, 3594; b) M. Gong, H. Dai, *Nano Res.* **2015**, *8*, 23.

[21] a) G. Wu, K. L. More, C. M. Johnston, P. Zelenay, *Science* **2011**, *332*, 443; b) M. Lefèvre, E. Proietti, F. Jaouen, J. P. Dodelet, *Science* **2009**, *324*, 71; c) J. Shui, C. Chen, L. Grabstanowicz, D. Zhao, D. J. Liu, *Proc. Natl. Acad. Sci.* **2015**, *112*, 10629; d) Z. Q. Liu, H. Cheng, N. Li, T. Y. Ma, Y. Z. Su, *Adv. Mater.* **2016**, *28*, 3777; e) G. F. Chen, T. Y. Ma, Z. Q. Liu, N. Li, Y. Z. Su, K. Davey, S. Z. Qiao, *Adv. Funct. Mater.* **2016**, *26*, 3314; f) H. Cheng, Y. Z. Su, P. Y. Kuang, G. F. Chen, Z. Q. Liu, *J. Mater. Chem. A* **2015**, *3*, 19314; g) Y. Zheng, Y. Jiao, Y. Zhu, L. H. Li, Y. Han, Y. Chen, A. Du, M. Jaroniec, S. Z. Qiao, *Nat. Commun.* **2014**, *5*, 3783.

[22] Y. Zheng, Y. Jiao, L. H. Li, T. Xing, Y. Chen, M. Jaroniec, S. Z. Qiao, *ACS Nano* **2014**, *8*, 5290.

[23] N. Ramaswamy, U. Tylus, Q. Jia, S. Mukerjee, *J. Am. Chem. Soc.* **2013**, *135*, 15443.

[24] X. Wang, J. Zhou, H. Fu, W. Li, X. Fan, G. Xin, J. Zheng, X. Li, *J. Mater. Chem. A* **2014**, *2*, 14064.

[25] H. Furukawa, K. E. Cordova, M. O'Keeffe, O. M. Yaghi, *Science* **2013**, *341*, 1230444.

[26] a) B. Chen, N. W. Ockwig, A. R. Millward, D. S. Contreras, O. M. Yaghi, *Angew. Chem.* **2005**, *117*, 4823; b) T. H. Bae, J. S. Lee, W. Qiu, W. J. Koros, C. W. Jones, S. Nair, *Angew. Chem., Int. Ed.* **2010**, *49*, 9863; c) J. A. Mason, M. Veenstra, J. R. Long, *Chem. Sci.* **2014**, *5*, 32; d) X. Zhao, B. Xiao, A. J. Fletcher, K. M. Thomas, D. Bradshaw, M. J. Rosseinsky, *Science* **2004**, *306*, 1012; e) N. L. Rosi, J. Eckert, M. Eddaoudi, D. T. Vodak, J. Kim, M. O'Keeffe, O. M. Yaghi, *Science* **2003**, *300*, 1127; f) T. Rodenas, I. Luz, G. Prieto, B. Seoane, H. Miro, A. Corma, F. Kapteijn, F. X. Llabrés i Xamena, J. Gascon, *Nat. Mater.* **2015**, *14*, 48; g) O. K. Farha, A. Özgür Yazaydın, I. Eryazici, C. D. Malliakas, B. G. Hauser, M. G. Kanatzidis, S. T. Nguyen, R. Q. Snurr, J. T. Hupp, *Nat. Chem.* **2010**, *2*, 944; h) S. Bourrelly, P. L. Llewellyn, C. Serre, F. Millange, T. Loiseau, G. Férey, *J. Am. Chem. Soc.* **2005**, *127*, 13519.

[27] a) L. Yang, S. Kinoshita, T. Yamada, S. Kanda, H. Kitagawa, M. Tokunaga, T. Ishimoto, T. Ogura, R. Nagumo, A. Miyamoto,

M. Koyama, *Angew. Chem., Int. Ed.* **2010**, *49*, 5348; b) Y. Gong, T. Wu, P. G. Jiang, J. H. Lin, Y. X. Yang, *Inorg. Chem.* **2013**, *52*, 777; c) M. Jiang, L. Li, D. Zhu, H. Zhang, X. Zhao, *J. Mater. Chem. A* **2014**, *2*, 5323; d) B. Li, K. Leng, Y. Zhang, J. J. Dynes, J. Wang, Y. Hu, D. Ma, Z. Shi, L. Zhu, D. Zhang, Y. Sun, M. Chrzanowski, S. Ma, *J. Am. Chem. Soc.* **2015**, *137*, 4243; e) N. Kornienko, Y. Zhao, C. S. Kley, C. Zhu, D. Kim, S. Lin, C. J. Chang, O. M. Yaghi, P. Yang, *J. Am. Chem. Soc.* **2015**, *137*, 14129.

[28] a) B. Chen, Y. Yang, F. Zapata, G. Lin, G. Qian, E. B. Lobkovsky, *Adv. Mater.* **2007**, *19*, 1693; b) Z. Guo, H. Xu, S. Su, J. Cai, S. Dang, S. Xiang, G. Qian, H. Zhang, M. O'Keeffe, B. Chen, *Chem. Commun.* **2011**, *47*, 5551; c) C. W. Kung, Y. S. Li, M. H. Lee, S. Y. Wang, W. H. Chiang, K. C. Ho, *J. Mater. Chem. A* **2016**, *4*, 10673.

[29] N. L. Torad, M. Hu, S. Ishihara, H. Sukegawa, A. A. Belik, M. Imura, K. Ariga, Y. Sakka, Y. Yamauchi, *Small* **2014**, *10*, 2096.

[30] a) P. Horcajada, T. Chalati, C. Serre, B. Gillet, C. Sebrie, T. Baati, J. F. Eubank, D. Heurtaux, P. Clayette, C. Kreuz, J. S. Chang, Y. K. Hwang, V. Marsaud, P. N. Bories, L. Cynober, S. Gil, G. Ferey, P. Couvreur, R. Gref, *Nat. Mater.* **2010**, *9*, 172; b) K. M. L. Taylor-Pashow, J. D. Rocca, Z. Xie, S. Tran, W. Lin, *J. Am. Chem. Soc.* **2009**, *131*, 14261.

[31] A. Aijaz, N. Fujiwara, Q. Xu, *J. Am. Chem. Soc.* **2014**, *136*, 6790.

[32] I. A. Khan, Y. Qian, A. Badshah, M. A. Nadeem, D. Zhao, *ACS Appl. Mater. Interfaces* **2016**, *8*, 17268.

[33] Q. Lai, Y. Zhao, Y. Liang, J. He, J. Chen, *Adv. Funct. Mater.* **2016**, *26*, 8334.

[34] H. X. Zhong, J. Wang, Y. W. Zhang, W. L. Xu, W. Xing, D. Xu, Y. F. Zhang, X. B. Zhang, *Angew. Chem., Int. Ed.* **2014**, *53*, 14235.

[35] T. Y. Ma, S. Dai, M. Jaroniec, S. Z. Qiao, *J. Am. Chem. Soc.* **2014**, *136*, 13925.

[36] H. Zhang, Z. Ma, G. Liu, L. Shi, J. Tang, H. Pang, K. Wu, T. Takei, J. Zhang, Y. Yamauchi, J. Ye, *NPG Asia Mater.* **2016**, *8*, e293.

[37] F. Meng, H. Zhong, D. Bao, J. Yan, X. Zhang, *J. Am. Chem. Soc.* **2016**, *138*, 10226.

[38] B. You, N. Jiang, M. Sheng, W. S. Drisdell, J. Yano, Y. Sun, *ACS Catal.* **2015**, *5*, 7068.

[39] S. You, X. Gong, W. Wang, D. Qi, X. Wang, X. Chen, N. Ren, *Adv. Energy Mater.* **2016**, *6*, 1501497.

[40] a) H. Tang, S. Cai, S. Xie, Z. Wang, Y. Tong, M. Pan, X. Lu, *Adv. Sci.* **2016**, *3*, 1500265; b) T. Zhou, Y. Du, S. Yin, X. Tian, H. Yang, X. Wang, B. Liu, H. Zheng, S. Qiao, R. Xu, *Energy Environ. Sci.* **2016**, *9*, 2563; c) L. Zhou, J. Meng, P. Li, Z. Tao, L. Mai, J. Chen, *Mater. Horiz.* **2017**, *4*, 268.

[41] P. Yin, T. Yao, Y. Wu, L. Zheng, Y. Lin, W. Liu, H. Ju, J. Zhu, X. Hong, Z. Deng, G. Zhou, S. Wei, Y. Li, *Angew. Chem., Int. Ed.* **2016**, *55*, 10800.

[42] S. Zhao, H. Yin, L. Du, L. He, K. Zhao, L. Chang, G. Yin, H. Zhao, S. Liu, Z. Tang, *ACS Nano* **2014**, *8*, 12660.

[43] B. Y. Guan, L. Yu, X. W. Lou, *Energy Environ. Sci.* **2016**, *9*, 3092.

[44] L. Shang, H. Yu, X. Huang, T. Bian, R. Shi, Y. Zhao, G. I. N. Waterhouse, L. Z. Wu, C. H. Tung, T. Zhang, *Adv. Mater.* **2016**, *28*, 1668.

[45] H. B. Wu, B. Y. Xia, L. Yu, X. Y. Yu, X. W. Lou, *Nat. Commun.* **2015**, *6*, 6512.

[46] a) M. Hu, J. Reboul, S. Furukawa, N. L. Torad, Q. Ji, P. Srinivasu, K. Ariga, S. Kitagawa, Y. Yamauchi, *J. Am. Chem. Soc.* **2012**, *134*, 2864; b) H. L. Jiang, B. Liu, Y. Q. Lan, K. Kuratani, T. Akita, H. Shioyama, F. Zong, Q. Xu, *J. Am. Chem. Soc.* **2011**, *133*, 11854; c) B. Liu, H. Shioyama, T. Akita, Q. Xu, *J. Am. Chem. Soc.* **2008**, *130*, 5390.

[47] X. Wang, X. Li, C. Ouyang, Z. Li, S. Dou, Z. Ma, L. Tao, J. Huo, S. Wang, *J. Mater. Chem. A* **2016**, *4*, 9370.

[48] Y. Liu, X. Zhou, T. Ding, C. Wang, Q. Yang, *Nanoscale* **2015**, *7*, 18004.

[49] a) F. S. Ke, Y. S. Wu, H. Deng, *J. Solid State Chem.* **2015**, *223*, 109; b) Y. Zhao, Z. Song, X. Li, Q. Sun, N. Cheng, S. Lawes, X. Sun, *Energy Storage Mater.* **2016**, *2*, 35; c) W. Xia, A. Mahmood, R. Zou, Q. Xu, *Energy Environ. Sci.* **2015**, *8*, 1837.

[50] L. Wang, Y. Han, X. Feng, J. Zhou, P. Qi, B. Wang, *Coord. Chem. Rev.* **2016**, *307*, 361.

[51] a) A. Mahmood, W. Guo, H. Tabassum, R. Zou, *Adv. Energy Mater.* **2016**, *6*, 1600423; b) H. M. Barkholtz, D. J. Liu, *Mater. Horiz.* **2017**, *4*, 20; c) K. Shen, X. Chen, J. Chen, Y. Li, *ACS Catal.* **2016**, *6*, 5887; d) Z. Song, N. Cheng, A. Lushington, X. Sun, *Catalysts* **2016**, *6*, 116.

[52] H. Zhang, H. Osgood, X. Xie, Y. Shao, G. Wu, *Nano Energy* **2017**, *31*, 331.

[53] Y. Z. Chen, C. Wang, Z. Y. Wu, Y. Xiong, Q. Xu, S. H. Yu, H. L. Jiang, *Adv. Mater.* **2015**, *27*, 5010.

[54] a) L. Zhang, Z. Xia, *J. Phys. Chem. C* **2011**, *115*, 11170; b) X. Kong, Q. Liu, D. Chen, G. Chen, *ChemCatChem* **2017**, *9*, 846.

[55] K. H. Wu, D. W. Wang, D. S. Su, I. R. Gentle, *ChemSusChem* **2015**, *8*, 2772.

[56] a) W. Hao, C. Kai, C. Yingjie, Z. Juntong, J. Yining, F. Lai, D. Xiao, Z. Guifu, *Nanotechnology* **2016**, *27*, 405401; b) L. Qu, Y. Liu, J. B. Baek, L. Dai, *ACS Nano* **2010**, *4*, 1321; c) Z. Xiang, D. Cao, L. Huang, J. Shui, M. Wang, L. Dai, *Adv. Mater.* **2014**, *26*, 3315; d) Q. Wei, X. Tong, G. Zhang, J. Qiao, Q. Gong, S. Sun, *Catalysts* **2015**, *5*, 1574; e) G. A. Ferrero, A. B. Fuertes, M. Sevilla, M. M. Titirici, *Carbon* **2016**, *106*, 179; f) L. Ye, G. Chai, Z. Wen, *Adv. Funct. Mater.* **2017**, 1606190.

[57] Y. Qian, Z. Hu, X. Ge, S. Yang, Y. Peng, Z. Kang, Z. Liu, J. Y. Lee, D. Zhao, *Carbon* **2017**, *111*, 641.

[58] L. Li, P. Dai, X. Gu, Y. Wang, L. Yan, X. Zhao, *J. Mater. Chem. A* **2017**, *5*, 789.

[59] J. S. Li, S. L. Li, Y. J. Tang, K. Li, L. Zhou, N. Kong, Y. Q. Lan, J. C. Bao, Z. H. Dai, *Sci. Rep.* **2014**, *4*, 5130.

[60] L. Zhang, Z. Su, F. Jiang, L. Yang, J. Qian, Y. Zhou, W. Li, M. Hong, *Nanoscale* **2014**, *6*, 6590.

[61] J. Li, Y. Chen, Y. Tang, S. Li, H. Dong, K. Li, M. Han, Y. Q. Lan, J. Bao, Z. Dai, *J. Mater. Chem. A* **2014**, *2*, 6316.

[62] Y. A. Fu, Y. Huang, Z. Xiang, G. Liu, D. Cao, *Eur. J. Inorg. Chem.* **2016**, *2016*, 2100.

[63] S. Pandiaraj, H. B. Aiyappa, R. Banerjee, S. Kurungot, *Chem. Commun.* **2014**, *50*, 3363.

[64] H. Zhang, Z. Ma, J. Duan, H. Liu, G. Liu, T. Wang, K. Chang, M. Li, L. Shi, X. Meng, K. Wu, J. Ye, *ACS Nano* **2016**, *10*, 684.

[65] D. Zhao, J. L. Shui, L. R. Grabstanowicz, C. Chen, S. M. Commet, T. Xu, J. Lu, D. J. Liu, *Adv. Mater.* **2014**, *26*, 1093.

[66] W. Zhang, Z. Y. Wu, H. L. Jiang, S. H. Yu, *J. Am. Chem. Soc.* **2014**, *136*, 14385.

[67] a) W. Xia, J. Zhu, W. Guo, L. An, D. Xia, R. Zou, *J. Mater. Chem. A* **2014**, *2*, 11606; b) C. Liu, J. Wang, J. Li, J. Liu, C. Wang, X. Sun, J. Shen, W. Han, L. Wang, *J. Mater. Chem. A* **2017**, *5*, 1211; c) R. Zhao, W. Xia, C. Lin, J. Sun, A. Mahmood, Q. Wang, B. Qiu, H. Tabassum, R. Zou, *Carbon* **2017**, *114*, 284; d) A. Aijaz, J. Masa, C. Rösler, W. Xia, P. Weide, A. J. R. Botz, R. A. Fischer, W. Schuhmann, M. Muhler, *Angew. Chem., Int. Ed.* **2016**, *55*, 4087; e) H. Tabassum, W. Guo, W. Meng, A. Mahmood, R. Zhao, Q. Wang, R. Zou, *Adv. Energy Mater.* **2017**, 1601671; f) S. H. Ahn, M. J. Klein, A. Manthiram, *Adv. Energy Mater.* **2016**, 1601979.

[68] W. Xia, R. Zou, L. An, D. Xia, S. Guo, *Energy Environ. Sci.* **2015**, *8*, 568.

[69] L. Ge, Y. Yang, L. Wang, W. Zhou, R. De Marco, Z. Chen, J. Zou, Z. Zhu, *Carbon* **2015**, *82*, 417.

[70] A. Kong, C. Mao, Q. Lin, X. Wei, X. Bu, P. Feng, *Dalton Trans.* **2015**, *44*, 6748.

[71] Q. Li, P. Xu, W. Gao, S. Ma, G. Zhang, R. Cao, J. Cho, H. L. Wang, G. Wu, *Adv. Mater.* **2014**, *26*, 1378.

**ADVANCED
SCIENCE NEWS**

www.advancedsciencenews.com

**ADVANCED
ENERGY
MATERIALS**

www.advenergymat.de

[72] H. Zhong, Y. Luo, S. He, P. Tang, D. Li, N. Alonso-Vante, Y. Feng, *ACS Appl. Mater. Interfaces* **2017**, *9*, 2541.

[73] W. Gu, L. Hu, J. Li, E. Wang, *ACS Appl. Mater. Interfaces* **2016**, *8*, 35281.

[74] J. S. Li, Y. J. Tang, C. H. Liu, S. L. Li, R. H. Li, L. Z. Dong, Z. H. Dai, J. C. Bao, Y. Q. Lan, *J. Mater. Chem. A* **2016**, *4*, 1202.

[75] L. Zhang, X. Wang, R. Wang, M. Hong, *Chem. Mater.* **2015**, *27*, 7610.

[76] J. S. Li, S. L. Li, Y. J. Tang, M. Han, Z. H. Dai, J. C. Bao, Y. Q. Lan, *Chem. Commun.* **2015**, *51*, 2710.

[77] H. S. Lu, H. Zhang, R. Liu, X. Zhang, H. Zhao, G. Wang, *Appl. Surf. Sci.* **2017**, *392*, 402.

[78] a) J. Liang, Y. Jiao, M. Jaroniec, S. Z. Qiao, *Angew. Chem., Int. Ed.* **2012**, *51*, 11496; b) S. Chen, J. Duan, Y. Zheng, X. Chen, X. W. Du, M. Jaroniec, S. Z. Qiao, *Energy Storage Mater.* **2015**, *1*, 17; c) K. Qu, Y. Zheng, S. Dai, S. Z. Qiao, *Nano Energy* **2016**, *19*, 373; d) H. Tabassum, R. Zou, A. Mahmood, Z. Liang, S. Guo, *J. Mater. Chem. A* **2016**, *4*, 16469; e) L. Yang, S. Jiang, Y. Zhao, L. Zhu, S. Chen, X. Wang, Q. Wu, J. Ma, Y. Ma, Z. Hu, *Angew. Chem., Int. Ed.* **2011**, *50*, 7132; f) S. Dou, A. Shen, Z. Ma, J. Wu, L. Tao, S. Wang, *J. Electroanal. Chem.* **2015**, *753*, 21; g) C. Hu, L. Dai, *Adv. Mater.* **2016**, 1604942; h) J. Zhang, Z. Zhao, Z. Xia, L. Dai, *Nat. Nanotechnol.* **2015**, *10*, 444.

[79] Y. Zheng, Y. Jiao, L. Ge, M. Jaroniec, S. Z. Qiao, *Angew. Chem., Int. Ed.* **2013**, *52*, 3110.

[80] S. Dou, X. Li, L. Tao, J. Huo, S. Wang, *Chem. Commun.* **2016**, *52*, 9727.

[81] J. Xi, Y. Xia, Y. Xu, J. Xiao, S. Wang, *Chem. Commun.* **2015**, *51*, 10479.

[82] J. Deng, P. Ren, D. Deng, X. Bao, *Angew. Chem., Int. Ed.* **2015**, *54*, 2100.

[83] J. Lu, W. Zhou, L. Wang, J. Jia, Y. Ke, L. Yang, K. Zhou, X. Liu, Z. Tang, L. Li, S. Chen, *ACS Catal.* **2016**, 1045.

[84] a) M. S. Burke, L. J. Enman, A. S. Batchellor, S. Zou, S. W. Boettcher, *Chem. Mater.* **2015**, *27*, 7549; b) W. F. Chen, J. T. Muckerman, E. Fujita, *Chem. Commun.* **2013**, *49*, 8896; c) Y. Zhong, X. Xia, F. Shi, J. Zhan, J. Tu, H. J. Fan, *Adv. Sci.* **2016**, *3*, 1500286; d) Y. Yan, B. Xia, Z. Xu, X. Wang, *ACS Catal.* **2014**, *4*, 1693; e) X. Zou, Y. Zhang, *Chem. Soc. Rev.* **2015**, *44*, 5148; f) P. Xiao, W. Chen, X. Wang, *Adv. Energy Mater.* **2015**, *5*, 1500985; g) A. Dutta, N. Pradhan, *J. Phys. Chem. Lett.* **2017**, *8*, 144; h) J. F. Callejas, C. G. Read, C. W. Roske, N. S. Lewis, R. E. Schaak, *Chem. Mater.* **2016**, *28*, 6017.

[85] M. Xu, L. Han, Y. Han, Y. Yu, J. Zhai, S. Dong, *J. Mater. Chem. A* **2015**, *3*, 21471.

[86] T. Tian, L. Ai, J. Jiang, *RSC Adv.* **2015**, *5*, 10290.

[87] Z. F. Huang, J. Song, K. Li, M. Tahir, Y. T. Wang, L. Pan, L. Wang, X. Zhang, J. J. Zou, *J. Am. Chem. Soc.* **2016**, *138*, 1359.

[88] Z. Shi, Y. Wang, H. Lin, H. Zhang, M. Shen, S. Xie, Y. Zhang, Q. Gao, Y. Tang, *J. Mater. Chem. A* **2016**, *4*, 6006.

[89] M. Liu, J. Li, *ACS Appl. Mater. Interfaces* **2016**, *8*, 2158.

[90] Z. Zhang, J. Hao, W. Yang, J. Tang, *ChemCatChem* **2015**, *7*, 1920.

[91] J. Hao, W. Yang, Z. Zhang, J. Tang, *Nanoscale* **2015**, *7*, 11055.

[92] L. Jiao, Y. X. Zhou, H. L. Jiang, *Chem. Sci.* **2016**, *7*, 1690.

[93] M. Qamar, A. Adam, B. Merzougui, A. Helal, O. Abdulhamid, M. N. Siddiqui, *J. Mater. Chem. A* **2016**, *4*, 16225.

[94] Q. Dong, Q. Wang, Z. Dai, H. Qiu, X. Dong, *ACS Appl. Mater. Interfaces* **2016**, *8*, 26902.

[95] X. Li, Y. Fang, X. Lin, M. Tian, X. An, Y. Fu, R. Li, J. Jin, J. Ma, *J. Mater. Chem. A* **2015**, *3*, 17392.

[96] B. Chen, G. Ma, Y. Zhu, J. Wang, W. Xiong, Y. Xia, *J. Power Sources* **2016**, *334*, 112.

[97] W. Chaikittisilp, N. L. Torad, C. Li, M. Imura, N. Suzuki, S. Ishihara, K. Ariga, Y. Yamauchi, *Chem. - Eur. J.* **2014**, *20*, 4217.

[98] B. You, N. Jiang, M. Sheng, S. Gul, J. Yano, Y. Sun, *Chem. Mater.* **2015**, *27*, 7636.

[99] Q. L. Zhu, W. Xia, T. Akita, R. Zou, Q. Xu, *Adv. Mater.* **2016**, *28*, 6391.

[100] N. M. Marković, R. R. Adžić, B. D. Cahan, E. B. Yeager, *J. Electroanal. Chem.* **1994**, *377*, 249.

[101] F. Ming, H. Liang, H. Shi, X. Xu, G. Mei, Z. Wang, *J. Mater. Chem. A* **2016**, *4*, 15148.

[102] a) Y. Zheng, Y. Jiao, S. Z. Qiao, *Adv. Mater.* **2015**, *27*, 5372; b) J. Xie, Y. Xie, *ChemCatChem* **2015**, *7*, 2568.

[103] K. Zhao, Y. Liu, X. Quan, S. Chen, H. Yu, *ACS Appl. Mater. Interfaces* **2017**, *9*, 5302.

[104] Z. Wang, Y. Lu, Y. Yan, T. Y. P. Larissa, X. Zhang, D. Wuu, H. Zhang, Y. Yang, X. Wang, *Nano Energy* **2016**, *30*, 368.

[105] M. Abirami, S. M. Hwang, J. Yang, S. T. Senthilkumar, J. Kim, W. S. Go, B. Senthilkumar, H. K. Song, Y. Kim, *ACS Appl. Mater. Interfaces* **2016**, *8*, 32778.

[106] S. H. Ahn, A. Manthiram, *J. Mater. Chem. A* **2017**, *5*, 2496.

[107] Z. Li, M. Shao, L. Zhou, R. Zhang, C. Zhang, M. Wei, D. G. Evans, X. Duan, *Adv. Mater.* **2016**, *28*, 2337.

[108] a) Y. Luo, L. Calvillo, C. Daiguebonne, M. K. Daletou, G. Granozzi, N. Alonso-Vante, *Appl. Catal. B* **2016**, *189*, 39; b) Y. Luo, L. A. Estudillo-Wong, L. Cavillo, G. Granozzi, N. Alonso-Vante, *J. Catal.* **2016**, *338*, 135; c) F. Afsahi, S. Kaliaguine, *J. Mater. Chem. A* **2014**, *2*, 12270; d) M. Jahan, Q. Bao, K. P. Loh, *J. Am. Chem. Soc.* **2012**, *134*, 6707; e) B. Y. Xia, Y. Yan, N. Li, H. B. Wu, X. W. Lou, X. Wang, *Nat. Energy* **2016**, *1*, 15006; f) F. Bai, H. Huang, C. Hou, P. Zhang, *New J. Chem.* **2016**, *40*, 1679; g) J. Xue, L. Zhao, Z. Dou, Y. Yang, Y. Guan, Z. Zhu, L. Cui, *RSC Adv.* **2016**, *6*, 110820.

[109] Y. Wang, X. Chen, Q. Lin, A. Kong, Q. G. Zhai, S. Xie, P. Feng, *Nanoscale* **2017**, *9*, 862.

[110] Z. Li, H. Sun, L. Wei, W. J. Jiang, M. Wu, J. S. Hu, *ACS Appl. Mater. Interfaces* **2017**, *9*, 5272.

[111] W. J. Jiang, J. S. Hu, X. Zhang, Y. Jiang, B. B. Yu, Z. D. Wei, L. J. Wan, *J. Mater. Chem. A* **2014**, *2*, 10154.

[112] Q. Lai, L. Zheng, Y. Liang, J. He, J. Zhao, J. Chen, *ACS Catal.* **2017**, *7*, 1655.

[113] Y. Fang, X. Li, F. Li, X. Lin, M. Tian, X. Long, X. An, Y. Fu, J. Jin, J. Ma, *J. Power Sources* **2016**, *326*, 50.

[114] Z. Tao, T. Wang, X. Wang, J. Zheng, X. Li, *ACS Appl. Mater. Interfaces* **2016**, *8*, 35390.

[115] a) F. Yang, P. Zhao, X. Hua, W. Luo, G. Cheng, W. Xing, S. Chen, *J. Mater. Chem. A* **2016**, *4*, 16057; b) H. Liu, G. Xia, R. Zhang, P. Jiang, J. Chen, Q. Chen, *RSC Adv.* **2017**, *7*, 3686.

[116] T. Wu, M. Pi, X. Wang, D. Zhang, S. Chen, *Phys. Chem. Chem. Phys.* **2016**, *19*, 2104.

[117] J. Zhou, Y. Dou, A. Zhou, R. M. Guo, M. J. Zhao, J. R. Li, *Adv. Energy Mater.* **2017**, 1602643.

[118] J. K. Nørskov, T. Bligaard, A. Logadottir, J. R. Kitchin, J. G. Chen, S. Pandelov, U. Stimming, *J. Electrochem. Soc.* **2005**, *152*, J23.

[119] J. Chen, Y. Yang, J. Su, P. Jiang, G. Xia, Q. Chen, *ACS Appl. Mater. Interfaces* **2017**, *9*, 3596.

[120] a) Y. Zhang, X. Bo, C. Luhana, H. Wang, M. Li, L. Guo, *Chem. Commun.* **2013**, *49*, 6885; b) G. Jia, W. Zhang, W. Jin, W. An, Y. Gao, X. Zhang, J. Liu, *Electrochim. Acta* **2014**, *144*, 1; c) J. Liu, H. Wang, C. Wu, Q. Zhao, X. Wang, L. Yi, *Int. J. Hydrogen Energy* **2014**, *39*, 6729; d) J. Liu, Q. Zhao, C. Wu, Y. Wang, W. wei, X. Wang, L. Yi, *RSC Adv.* **2014**, *4*, 17129.

[121] J. Chen, G. Xia, P. Jiang, Y. Yang, R. Li, R. Shi, J. Su, Q. Chen, *ACS Appl. Mater. Interfaces* **2016**, *8*, 13378.

[122] H. O. Pierson, *Handbook of Carbon, Graphite, Diamond and Fullerenes: Properties, Processing, and Applications*, Noyes Publications, Park Ridge, NJ, USA **1993**.

[123] X. Huang, P. Sheng, Z. Tu, F. Zhang, J. Wang, H. Geng, Y. Zou, C. A. Di, Y. Yi, Y. Sun, W. Xu, D. Zhu, *Nat. Commun.* **2015**, *6*, 7408.

[124] L. Sun, M. G. Campbell, M. Dincă, *Angew. Chem., Int. Ed.* **2016**, *55*, 3566.

ADVANCED
SCIENCE NEWS
www.advancedsciencenews.com

small
methods
www.small-methods.com

REVIEW

Nanostructured 2D Materials: Prospective Catalysts for Electrochemical CO$_2$ Reduction

Jinlong Liu, Chunxian Guo, Anthony Vasileff, and Shizhang Qiao*

Electrochemical CO$_2$ reduction to useful fuels and chemicals, driven by renewable energy from intermittent sources such as solar and wind, has been keenly pursued in recent years as a means to resolving energy security and environmental issues associated with conventional fossil fuels. Nanostructured two-dimensional (2D) materials, possessing abundant active sites in the form of surface atoms and edge sites, and providing better electrical conductivity along 2D conducting channels, represent promising candidates for high-performance CO$_2$-reduction electrocatalysts. Here, newly developed nanostructured 2D materials, including atomically thin transition-metal/metal oxides, transition-metal dichalcogenides, and metal-free 2D materials, are highlighted as state-of-the-art catalysts toward electrochemical CO$_2$ reduction. Through further exploration of new nanostructured 2D materials and their nanocomposites, more and more breakthroughs in this field of research are to be expected.

1. Introduction

Anthropogenic carbon dioxide (CO$_2$) emissions, arising from the unprecedented consumption of fossil fuels since the industrial revolution, pose a severe threat to the global environment and consequently cause much concern in conventional energy production practices.[1,2] Fixation and conversion of greenhouse CO$_2$ are of paramount importance in realizing energy and environmental sustainability.[3,4] Particularly, electrochemical CO$_2$ reduction (ECR) to useful fuels and chemicals, using electricity generated from renewable sources, such as sunlight and wind, provides a highly desirable solution to artificial carbon recycling.[5–7] However, this promising technique is challenged by the lack of efficient ECR electrocatalysts with high activity, good selectivity, and durability, due to the thermodynamic stability of the CO$_2$ molecule.[8] During the past few decades, tremendous efforts have been devoted to the exploration of suitable materials for efficient CO$_2$ electrolysis.[3,9] Early work focused on bulk metals, which possess some activity for ECR. One example is bulk copper (Cu), which is able to reduce

CO$_2$ into a variety of hydrocarbons (e.g., methane, ethylene etc.).[3] However, bulk materials used for ECR suffer from low activity with low current density, high overpotential, and poor product selectivity. Beyond that, fast deactivation is another unavoidable and serious drawback of metal electrodes. Several different explanations for this phenomenon have been proposed, but no definitive answers have been found that accurately account for the rapid loss of CO$_2$ reduction activity. Generally, it is ascribed to the presence of impurities (e.g., heavy-metal ions and organic pollutants) or the contamination of some carbonaceous intermediates, which can poison active sites by electrodeposition or irreversible adsorption.[3] For a more detailed explanation, readers can refer to ref. [3]. Undoubtedly, all these issues restrict their practical application inevitably. With significant advances in nanoscience and nanotechnology in the past two decades, a series of nanostructured electrocatalysts have been synthesized and investigated to address these problems.[5–7,9–11] Owing to the high surface area and unique possibility of tailoring rich active sites, nanostructured electrocatalysts generally exhibit dramatically improved tolerance to impurities in electrolytes. Additionally, nanomaterials allow well-controlled exposure of specific crystal facets, which in turn allows structural fine tuning, resulting in higher activity, better selectivity, and enhanced stability. In this regard, our previous work summarizes the recent progress in inorganic heterogeneous electrocatalysts for ECR, including transition metals (TMs), transition-metal oxides (TMOs), transition-metal dichalcogenides (TMDs), and carbon-based materials.[9] Notably, recently developed nanostructured electrocatalysts have made encouraging accomplishments in ECR, compared with traditional bulk metal catalysts.[6,7,11]

Nanostructured two-dimensional (2D) materials refer to a class of materials with thickness of one or a few atoms and intrinsically layered materials like TMDs have attracted increasing attention. Very recently, 2D nanomaterials, especially partially oxidized Co 4-atom-thick layers,[6] tungsten diselenide (WSe$_2$) nanoflakes,[7] and nitrogen-doped graphene (N-graphene),[11,12] have emerged as promising candidates for ECR electrocatalysts and represent state-of-the-art ECR catalysts among various others reported to date. Owing to their distinct 2D structure and ultrathin layer dimension, 2D nanomaterials offer many advantages toward ECR. Particularly, their robust layered structures with ultralarge surface area and substantial number of active sites contribute to a great enhancement in

J. L. Liu, Dr. C. X. Guo, A. Vasileff, Prof. S. Z. Qiao
School of Chemical Engineering
University of Adelaide
Adelaide, SA 5005, Australia
E-mail: s.qiao@adelaide.edu.au
Prof. S. Z. Qiao
School of Materials Science and Engineering
Tianjin University
Tianjin 300072, China

small
methods
www.small-methods.com

ADVANCED
SCIENCE NEWS
www.advancedsciencenews.com

REVIEW

stability compared with bulk and other nanostructured materials. In addition, the well-defined structure of 2D nanomaterials can serve as the ideal medium for understanding the relationship between electrochemical performance and physicochemical properties. Our purpose here is to highlight three representative categories of 2D nanostructured ECR catalysts, namely; atomically thin TMs/TMOs, nanostructured TMDs and metal-free 2D materials. Furthermore, based on the characteristics of 2D materials and the current status of research on ECR, the challenges and opportunities of 2D materials as prospective ECR electrocatalysts will also be discussed.

## 2. Nanostructured 2D Materials as Efficient Electrocatalysts for ECR

2.1. Atomically Thin TMs/TMOs

Since the great success of metal/metal oxide composites (e.g., Sn/SnO_x)[4] and oxide-derived (OD) metals (e.g., OD Cu and OD Au)[5,8] in ECR discovered by Kanan and co-workers, TMs/TMOs have attracted much attention as potential ECR catalysts. Despite their enhanced performance for ECR, TMOs still suffer from a low number of active sites and poor electrical conductivity. Previous research suggested that low-coordinated surface metal cations can ensure a larger degree of CO_2 adsorption during heterogeneous catalysis. More interestingly, density functional theory (DFT) calculations indicated that reducing the thickness of TMOs to atomic level thickness can significantly enhance both the density of states (DOS) and the charge density around the conduction-band edges. In doing this, it is anticipated that the rapid carrier transport improves the electronic conductivity along the 2D ultrathin layer.[13] Moreover, it is expected that atomically thin layers are capable of exposing plenty of coordinatively unsaturated surface atoms as active centers. In light of these benefits, ultrathin Co_3O_4 layers with thicknesses of 1.72 and 3.51 nm were successfully synthesized via solvothermal reaction and fast-heating treatment to test these predictions.[13] As expected, the ultrathin Co_3O_4 layer exhibited much better electrocatalytic activity toward ECR. In particular, the 1.72 nm-thick Co_3O_4 layers showed the highest ECR activity with a current density of 0.68 mA cm^{-2} at −0.88 V versus the saturated calomel electrode (vs SCE). This ECR activity is over 1.5 and 20 times higher than those of 3.51 nm-thick Co_3O_4 layers and bulk Co_3O_4 respectively. Moreover, a Faradaic efficiency (FE) of over 60% toward formate in 20 h continuous reaction revealed that the 1.72 nm-thick Co_3O_4 layers had higher selectivity and better stability.

Very recently, Xie's group developed a synthesis technique for producing much thinner Co-based sheets with a thickness of only 4 atoms (≈0.84 nm) using solvothermal growth, as illustrated and characterized in **Figure 1**a–d.[6] By deliberately controlling the reaction time, partial oxidation of the 4-atom-thick Co layer was introduced on its surface (Figure 1e–g). Undoubtedly, such an even thinner 2D Co-based layer was more promising toward ECR, due to more-abundant surface active sites and higher electrical conductivity resulting from the metallic nature of Co. As a result, partially oxidized Co with 4-atom-thick layers showed exceptional ECR performance. From the

Jinlong Liu received his BE and ME degrees in applied chemistry from Central South University, Changsha, China, in 2011 and 2014, respectively. He is currently a Ph.D. candidate in chemical engineering under the supervision of Prof. Shizhang Qiao at the University of Adelaide, Australia. His current research is focused on the design and synthesis of functional materials for energy storage and catalysis.
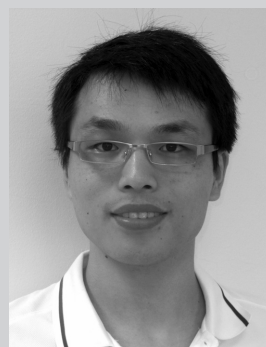
Chunxian Guo works as a DECRA research follow with Prof. Shizhang Qiao in chemical engineering at the University of Adelaide, Australia. His research focuses on the design and fabrication of efficient and stable electrocatalysts by surface atomic engineering of new nanostructured materials, in particular novel two-dimensional nanomaterials.

Shizhang Qiao received his Ph.D. degree in chemical engineering from Hong Kong University of Science and Technology in 2000; he is currently a Chair Professor at the School of Chemical Engineering of the University of Adelaide, Australia. His research expertise is in nanomaterials for catalysis, drug and gene delivery, and energy storage and conversion.

linear-sweep voltammetric (LSV) curves in Figure 1h, it can be seen that partially oxidized Co 4-atom-thick layers showed a distinct CO_2 reduction peak at −0.85 V versus SCE, with a current density of 10.59 mA cm^{-2} in a CO_2-saturated 0.1 M Na_2SO_4 aqueous solution. When compared with pure Co 4-atom-thick layers, partially oxidized bulk Co, and bulk Co, this is an increase of about 10, 40, and 260 times, respectively. Moreover, the as-obtained partially oxidized Co 4-atom-thick layers achieved a stable reduction current density up to 10 mA cm^{-2} over 40 h and a high FE toward formate production of approximately 90% at a very low overpotential of only 0.24 V. This level of performance is superior to previously reported TMs or TMOs electrodes investigated under comparable conditions. This remarkably enhanced activity is partly attributed to increased

ADVANCED
SCIENCE NEWS

www.advancedsciencenews.com

small
methods

www.small-methods.com

REVIEW
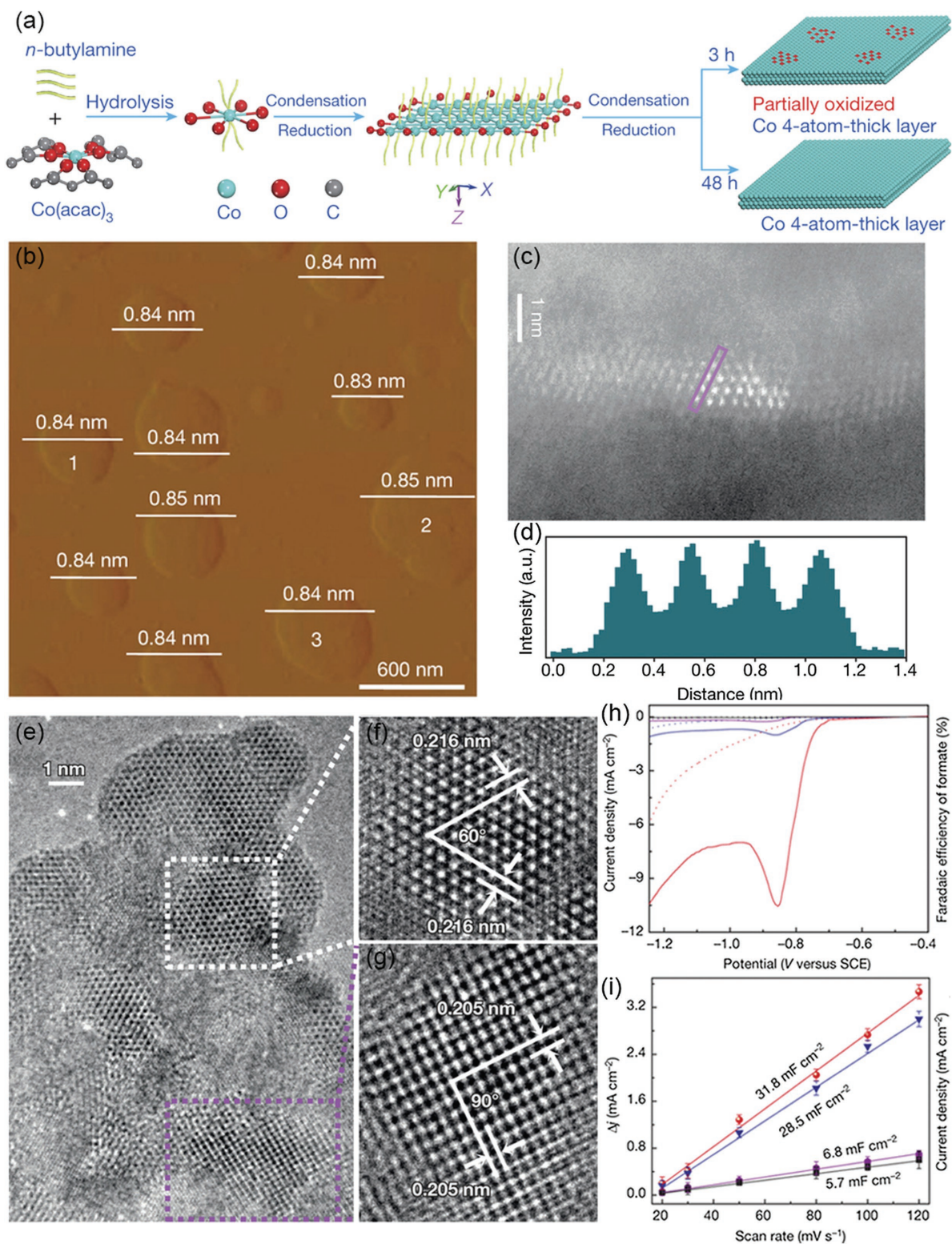
Figure 1. a) Schematic formation process of the partially oxidized and pure Co 4-atomic-layer, respectively. b–g) Atomic force microscopy (AFM) image (b), lateral high-angle annular dark-field scanning transmission electron microscopy (HAADF-STEM) image (c), the corresponding intensity profile along the purple rectangle in Figure 1c (d), high-resolution transmission electron microscopy (HR-TEM) image (e), and enlarged HR-TEM images for the partially oxidized Co 4-atom-thick layers (f,g). h,i) Linear-sweep voltammetric (LSV) curves in a CO_2-saturated (solid line) and N_2-saturated (dashed line) 0.1 M Na_2SO_4 aqueous solution (h) and charging current density differences $\triangle j$ plotted against scan rates for partially oxidized Co 4-atom-thick layers (red), Co 4-atom-thick layers (blue), partially oxidized bulk Co (violet), and bulk Co (black) (i). Adapted with permission.[6] Copyright 2016, Nature Publishing Group.

small
methods
www.small-methods.com

ADVANCED
SCIENCE NEWS
www.advancedsciencenews.com

REVIEW

electrochemical surface area (ECSA) as depicted in Figure 1i. Importantly, the partially oxidized Co 4-atom-thick layers possessed almost the same ECSA as the pure Co 4-atom-thick layers (Figure 1i), whereas it exhibited a tenfold higher catalytic activity. Such a result demonstrated that atomic Co_3O_4 exhibits much higher intrinsic activity and selectivity than atomic Co for the CO_2 electroreduction to formate. This enlightening work indicates that the nanostructure construction at the 2D atomic level and the controlled manipulation of oxidation states open up a new way to develop highly efficient and robust ECR catalysts based on TMs/TMOs.

2.2. Nanostructured TMDs

TMDs, represented by molybdenum disulfide (MoS_2), are another class of layered materials, which are composed of one layer of metal cations and two layers of chalcogen anions with a sandwich-like structure. MoS_2 has been intensively studied as an electrocatalyst candidate for the hydrogen evolution reaction (HER) because of its rich edge sites as active centers toward HER.[14] Given that the HER is a primary competing reaction to ECR, MoS_2 does not represent an efficient catalyst for ECR, in theory. Surprisingly, with the assistance of an ionic liquid (IL), 1-ethyl-3-methylimidazolium tetrafluoroborate (EMIM-BF_4), as a co-catalyst in the electrolyte, Asadi et al. found that CO_2 reduction to carbon monoxide (CO) could be carried out efficiently on Mo-terminated edges of bulk MoS_2, due to their metallic character, high d-electron density and relatively low work function (3.9 eV).[1] Also, the IL played a critical role in stabilizing the CO_2 molecule by forming the [EMIM–CO_2]$^+$ complex in acidic environments (**Figure 2**a,b). Furthermore, the EMIM–CO_2 complex could effectively suppress the HER.
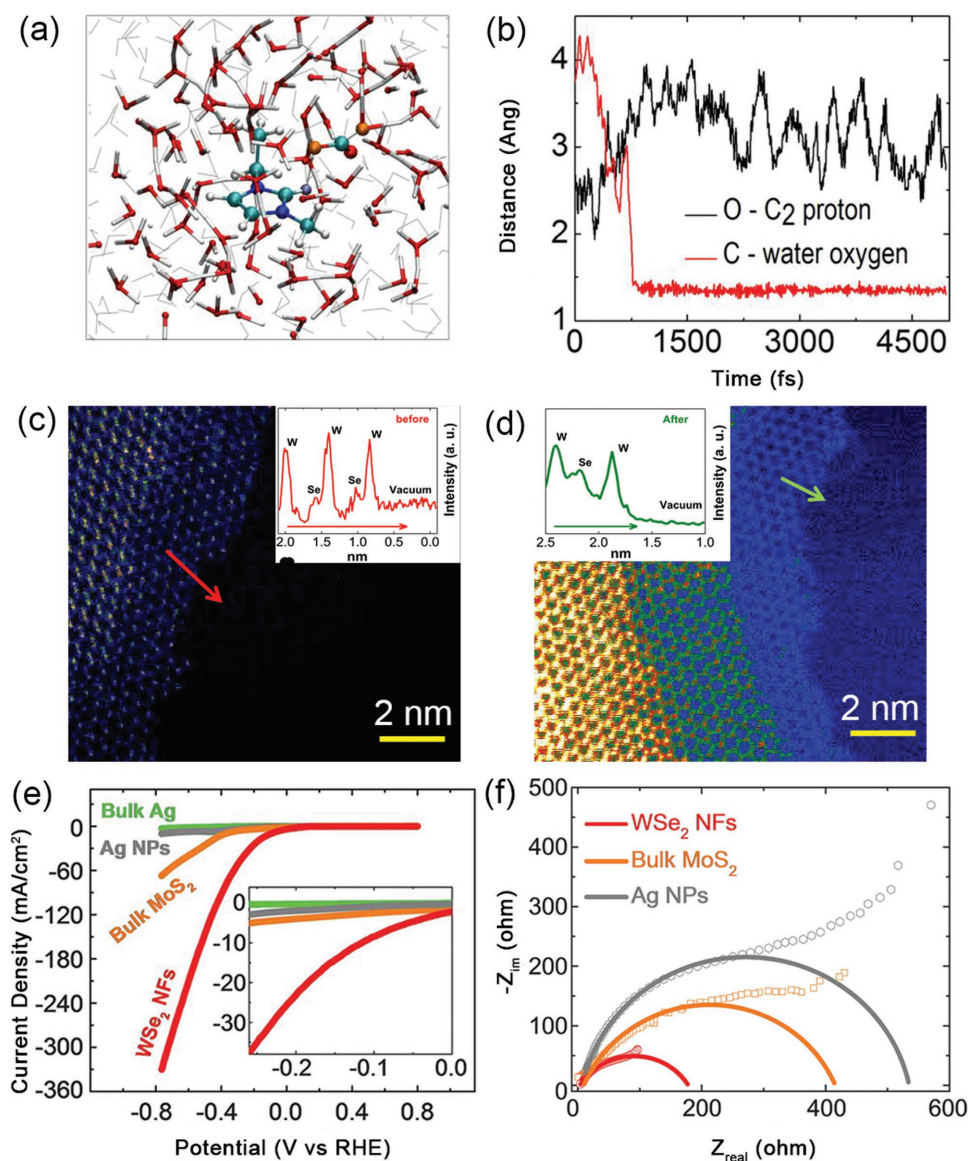
Followed by this earlier work, Asadi and co-workers further prepared a series of nanostructured TMDs, including MoS_2, WS_2, $MoSe_2$, and WSe_2 nanoflakes (NFs), and evaluated their catalytic performance toward ECR in aqueous electrolyte containing 50 vol% EMIM-BF_4.[7] Similarly, all the TMD-based NFs represented by WSe_2 NFs exhibited better ECR catalysis than previously reported bulk MoS_2 and other reported catalysts (Figure 2e), resulting from a greater number of exposed edge sites in the 2D nanoarchitecture. Especially, WSe_2 NFs terminated with W atoms (Figure 2c) displayed the best performance in catalyzing CO_2 reduction to CO, realizing a current density of 18.95 mA cm^{-2}, an FE toward CO of 24%, and a CO formation turnover frequency of 0.28 s^{-1} at −0.164 V versus reversible hydrogen electrode (RHE) (overpotential of 54 mV). Likewise, according to theoretical calculations and related characterizations, the superior properties of WSe_2 NFs were attributed to their much lower charge-transfer resistance (R_{ct}) (Figure 2f) and considerably lower work function (3.52 eV). In addition, the extremely stable W edge atoms (Figure 2d) provided WSe_2 NFs with outstanding durability over 27 h of chronoamperometry. It is noteworthy that the WSe_2/IL co-catalyst system could be effectively integrated in a light-harvesting artificial-leaf platform, which was able to reduce CO_2 into CO and concurrently oxidize H_2O into O_2 in the absence of any external potential. From the studies of Asadi and co-workers,[1,7] the

intrinsically high activity and stability of metal atoms at the edge sites make nanostructured TMDs another class of exceptional ECR catalysts, but it seems that IL is a necessary co-catalyst to inhibit undesirable HER.

2.3. Metal-Free 2D Materials

By virtue of their extremely high surface area, excellent mechanical stability and flexibility, good electrical conductivity, cost effectiveness, environmental friendliness, and, more importantly, the adjustable doping of heteroatoms (e.g., B, N etc.), a great number of graphene-based materials have been extensively employed as metal-free functional materials for various energy-conversion reactions, such as the oxygen reduction reaction (ORR), the oxygen evolution reaction (OER), and the HER. Very recently, heteroatom-doped graphene has been explored for ECR. Phani and co-workers studied the electrocatalytic activity of boron-doped graphene (B-graphene) for ECR in 0.1 M $KHCO_3$ aqueous solution, which exhibited an FE of 66% toward formate at −1.4 V (vs SCE).[10] DFT calculations suggested that the presence of B in the graphene matrices resulted in an asymmetric charge and spin density, thus affording active B and C atoms for chemisorption and facilitating CO_2 reduction to formate. More recently, N-doped graphene has also been reported as an efficient electrocatalyst for the reduction of CO_2 to CO and formate in aqueous electrolytes. For instance, Ajayan and co-workers demonstrated CO production with an FE up to 85% at a low overpotential of 0.47 V using N-doped graphene foam as the ECR catalyst.[12] Combining experimental investigation and DFT calculations, pyridinic N is believed to be the most active site for the adsorption of intermediate COOH* and further formation of CO. Intriguingly, the N-doped graphene (**Figure 3**a,b) developed by Tan and co-workers using carefully screened melamine as the N precursor, could selectively reduce CO_2 to formate in 0.5 M $KHCO_3$ aqueous solution, even though most of the reduction products of N-doped carbon electrocatalysts were limited to CO.[11] In general, the amount and configuration of N dopants, especially pyridinic N atoms, are considered to be responsible for the improvement in activity and selectivity. In this instance, XPS has been carried out to analyze the N configurations, in which pyridinic N had the highest concentration of 3 at% (Figure 3c,d). It should be mentioned that near-edge X-ray absorption fine-structure (NEXAFS) might be a better way to reveal the graphitic properties and N incorporation into the graphene structure. However, little effort has been made to characterize the electronic structure of these ECR catalysts. As can be seen from the LSV scans in Figure 3e, the as-synthesized N-doped graphene displayed obvious activity toward CO_2 reduction in the potential range from −0.3 to −1 V versus RHE. When operated at a moderate negative potential (−0.84 V vs RHE), the N-doped graphene remained highly selective to formate (maximum FE of 73%) for 12 h (Figure 3f). Obviously, heteroatom doping can be a powerful strategy to regulate the structural, electrical, and physicochemical properties of graphene, thereby fully exploiting its potential for ECR.

Graphitic carbon nitride (g-C_3N_4) is another important metal-free 2D material that has received increasing attention in

ADVANCED
SCIENCE NEWS
www.advancedsciencenews.com

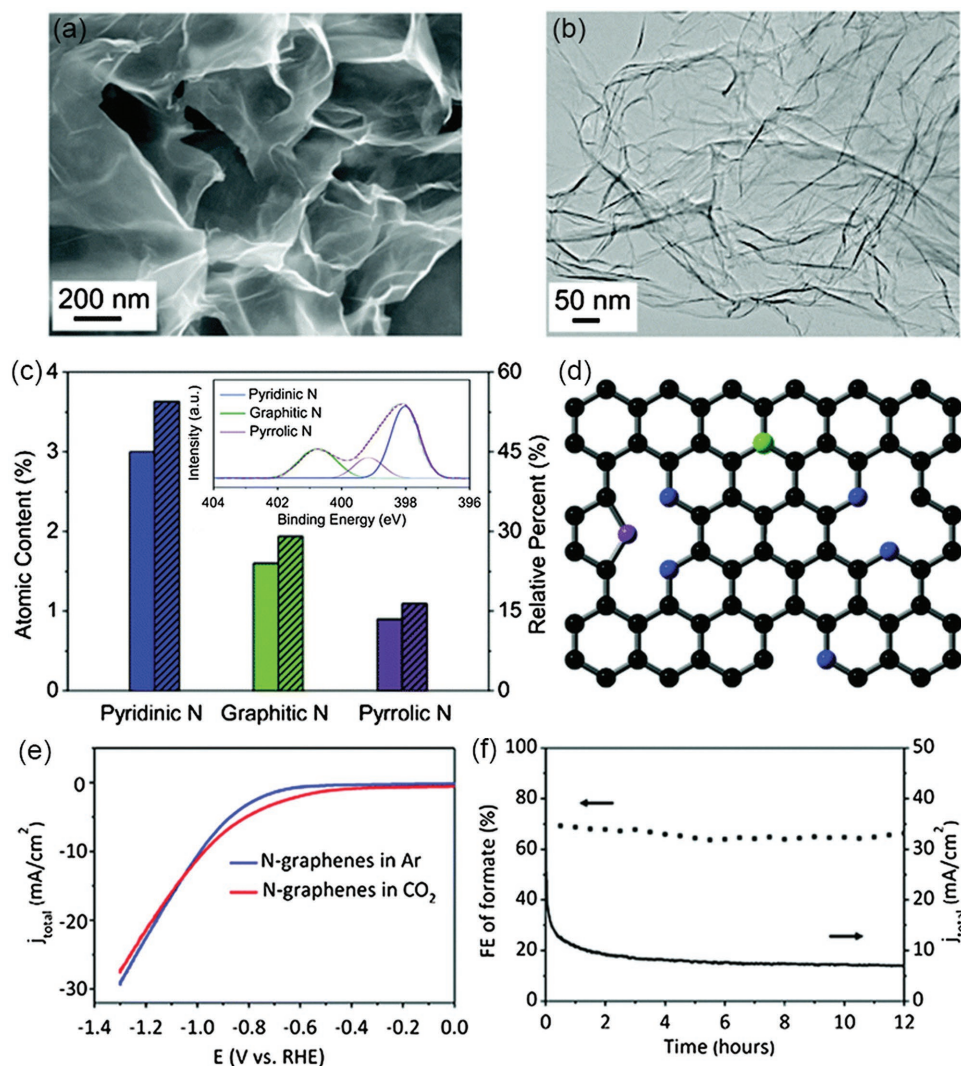small
methods
www.small-methods.com

REVIEW

Figure 2. a) Formation and stabilization of the [EMIM–CO$_2$] complex with an additional coordination of CO$_2$ and a water molecule (the oxygen is highlighted in orange). b) Time dependence of the hydrogen-bond length between CO$_2$ and EMIM$^+$ and the C—O bond length between the CO$_2$ and an adjacent water molecule. a,b) Adapted with permission.[1] Copyright 2014, Nature Publishing Group. c) STEM image of WSe$_2$ NFs. The inset shows the corresponding intensity profile of the flake before electrochemical tests. d) STEM image of WSe$_2$ NFs. The inset shows the corresponding intensity profile of the flake after 27 h chronoamperometry testing. e) Cyclic voltammetry (CV) curves for WSe$_2$ NFs, bulk MoS$_2$, Ag nanoparticles (Ag NPs), and bulk Ag in a CO$_2$ atmosphere. The inset shows the current densities in low overpotentials. f) Electrochemical impedance spectroscopy of CO$_2$ reduction using WSe$_2$ NFs, bulk MoS$_2$, and Ag NPs at 150 mV overpotential. c–f) Adapted with permission.[7] Copyright 2016, American Association for the Advancement of Science.

both photocatalysis and electrocatalysis.[15] Despite its low electrical conductivity, g-C$_3$N$_4$ is able to liberate its electrochemical properties by compositing with other carbon-based materials. As for ECR, Amal and co-workers recently reported a g-C$_3$N$_4$/carbon nanotube (CNT) composite as a highly selective and stable electrocatalyst for CO$_2$ reduction to CO, in which the strongly formed C—N bonds could become active sites to promote ECR, giving rise to a FE of 60% and remarkable durability over 50 h.[15] Therefore, g-C$_3$N$_4$ based materials may be another new class of metal-free 2D electrocatalysts for efficient ECR.

3. Challenges and Opportunities of Nanostructured 2D Materials for ECR

Among various electrocatalysts documented in the past few decades, recently emerging nanostructured 2D materials have made profound progress in the electrocatalytic reduction of CO$_2$, yet there are still some challenges in their practical application. First, the large-scale production of 2D nanomaterials with well-controlled nanostructures is very challenging, because strong in-plane bonds, electrostatic interaction, and π–π stacking

small
methods
www.small-methods.com

REVIEW

ADVANCED
SCIENCE NEWS
www.advancedsciencenews.com

Figure 3. a,b) Scanning electron microscopy (SEM) image (a) and TEM image (b) of N-graphene. c) Statistical N atomic content and relative percentage in N-graphene (the insert is the representative X-ray photoelectron spectroscopy (XPS) of N 1s for N-graphene). d) Schematic of pyridinic (blue), graphitic (green), and pyrrolic (purple) N configurations in N-graphene. e) 15 mV s^{-1} LSV scans for the N-graphene catalyst in Ar- and CO$_2$-saturated 0.5 M KHCO$_3$. f) Long-term durability of different forms of N-graphene operated at −0.84 V for 12 h. Adapted with permission.[11] Copyright 2016, The Royal Society of Chemistry.

within the atomic layers often result in severe agglomeration, and the yield of currently developed methods, such as solvothermal growth and liquid exfoliation, is too low to satisfy commercial demand. Secondly, it is still difficult to realize specific component modification and structural manipulation at the atomic level for further optimization of catalytic activity, selectivity, and stability, especially with the aim of attaining significantly high CO$_2$-reduction current density, reduction of CO$_2$ to larger-chain hydrocarbons, and long operating life-cycles for industrial application. Thirdly, other factors such as electrolytes, substrates, catalyst loading, and ion-exchange membranes, are essential to improve the overall performance of ECR for practical application. This is because aqueous solutions are unfavorable for CO$_2$ dissolution and facilitate competing HER, it is difficult for conventional glassy carbon to serve as a catalyst support for large-scale applications, and the predominant membrane

resistance imposes severe limitations to charge and mass transfer.[16] Nevertheless, much less effort has been invested toward these aspects. Finally, the ECR reaction mechanism still remains uncertain or ambiguous, and this is severely limited by effective in situ characterizations at the atomic level and/or within several femtoseconds. This last point is most important, because attaining an in-depth understanding of the reaction pathways is vital to lay a solid foundation for future ECR technology.

Fortunately, the rapid advances in the field of material science, chemistry, computer science, and related technologies provide great opportunities to explore more efficient ECR catalysts based on nanostructured 2D materials. On the one hand, along with the development of synthetic technology, an increasing number of 2D nanostructured materials have been readily prepared with high yield. For example, inspired by a traditional Chinese

**ADVANCED
SCIENCE NEWS**
www.advancedsciencenews.com

**small
methods**
www.small-methods.com

REVIEW

food called "thousand-layer pie", Wu and co-workers recently reported the large fabrication of 2D metallic nanosheets, with a thickness as small as 1 nm and size in the micrometer range, by a facile, efficient, and cost-effective general mechanical rolling method under ambient conditions.[17] Besides, the tailored assembly of different nanostructured 2D materials will promote the development of 2D nanocomposite electrocatalysts.[18] Furthermore, the utilization of IL as electrolytes facilitates the integrated research of ECR. Simultaneously, the comprehensiveness of current theoretical calculations is able to offer valuable predictions and guidelines for screening and optimizing ECR catalysts. Taking the recent calculations of Nørskov and co-workers as an example, their DFT study indicated that doped MoS_2 could break transition-metal scaling relations for ECR due to the presence of dual binding sites after the doping of another metal.[19] According to their calculations, nickel (Ni) was predicted to be the most promising dopant in terms of scaling and cost. On the other hand, the improvement of in situ characterization techniques, such as in situ infrared spectroscopy and X-ray absorption spectroscopy,[2,20,21] together with theoretical calculations will definitely provide more insight into the mechanisms of ECR. It is believed that the increasing interest and huge efforts made in ECR research will accelerate technological breakthroughs and eventually advance this research field enough to where commercial application is realizable.

4. Conclusion and Outlook

In summary, we have briefly discussed nanostructured 2D materials with peculiar structural, electrical, and physicochemical properties as efficient electrode materials for ECR. Recently emerging nanostructured 2D electrocatalysts, represented by atomically thin TMs/TMOs, nanostructured TMDs, and metal-free 2D materials, have achieved fascinating activity, selectivity, and durability toward ECR. Challenges still exist for the large-scale fabrication of nanostructured 2D materials. Nevertheless, new approaches, including surface atomic engineering, will be explored to synthesize 2D nanomaterials and their nanocomposites with tailored properties. Moreover, a combination of experimental and theoretical investigations will greatly advance this research field.

Acknowledgements

[1] M. Asadi, B. Kumar, A. Behranginia, B. A. Rosen, A. Baskin, N. Repnin, D. Pisasale, P. Phillips, W. Zhu, R. Haasch, R. F. Klie, P. Král, J. Abiade, A. Salehi-Khojin, *Nat. Commun.* **2014**, *5*, 4470.

[2] Y. Liu, S. Chen, X. Quan, H. Yu, *J. Am. Chem. Soc.* **2015**, *137*, 11631.

[3] Y. Hori, *Modern Aspects of Electrochemistry*, Springer, New York **2008**.

[4] Y. Chen, M. W. Kanan, *J. Am. Chem. Soc.* **2012**, *134*, 1986.

[5] Y. Chen, C. W. Li, M. W. Kanan, *J. Am. Chem. Soc.* **2012**, *134*, 19969.

[6] S. Gao, Y. Lin, X. Jiao, Y. Sun, Q. Luo, W. Zhang, D. Li, J. Yang, Y. Xie, *Nature* **2016**, *529*, 68.

[7] M. Asadi, K. Kim, C. Liu, A. V. Addepalli, P. Abbasi, P. Yasaei, P. Phillips, A. Behranginia, J. M. Cerrato, R. Haasch, P. Zapol, B. Kumar, R. F. Klie, J. Abiade, L. A. Curtiss, A. Salehi-Khojin, *Science* **2016**, *353*, 467.

[8] C. W. Li, M. W. Kanan, *J. Am. Chem. Soc.* **2012**, *134*, 7231.

[9] D. D. Zhu, J. L. Liu, S. Z. Qiao, *Adv. Mater.* **2016**, *28*, 3423.

[10] N. Sreekanth, M. A. Nazrulla, T. V. Vineesh, K. Sailaja, K. L. Phani, *Chem. Commun.* **2015**, *51*, 16061.

[11] H. Wang, Y. Chen, X. Hou, C. Ma, T. Tan, *Green Chem.* **2016**, *18*, 3250.

[12] J. Wu, M. Liu, P. P. Sharma, R. M. Yadav, L. Ma, Y. Yang, X. Zou, X. D. Zhou, R. Vajtai, B. I. Yakobson, J. Lou, P. M. Ajayan, *Nano Lett.* **2016**, *16*, 466.

[13] S. Gao, X. Jiao, Z. Sun, W. Zhang, Y. Sun, C. Wang, Q. Hu, X. Zu, F. Yang, S. Yang, L. Liang, J. Wu, Y. Xie, *Angew. Chem., Int. Ed.* **2016**, *55*, 698.

[14] T. F. Jaramillo, K. P. Jørgensen, J. Bonde, J. H. Nielsen, S. Horch, I. Chorkendorff, *Science* **2007**, *317*, 100.

[15] X. Lu, T. H. Tan, Y. H. Ng, R. Amal, *Chem. – Eur. J.* **2016**, *22*, 11991.

[16] B. A. Rosen, A. Salehi-Khojin, M. R. Thorson, W. Zhu, D. T. Whipple, P. J. A. Kenis, R. I. Masel, *Science* **2011**, *334*, 643.

[17] H. Liu, H. Tang, M. Fang, W. Si, Q. Zhang, Z. Huang, L. Gu, W. Pan, J. Yao, C. Nan, H. Wu, *Adv. Mater.* **2016**, *28*, 8170.

[18] F. Li, S. F. Zhao, L. Chen, A. Khan, D. R. MacFarlane, J. Zhang, *Energy Environ. Sci.* **2016**, *9*, 216.

[19] X. Hong, K. Chan, C. Tsai, J. K. Nørskov, *ACS Catal.* **2016**, *6*, 4428.

[20] M. F. Baruch, J. E. Pander, J. L. White, A. B. Bocarsly, *ACS Catal.* **2015**, *5*, 3148.

[21] J. Rosen, G. S. Hutchings, Q. Lu, R. V. Forest, A. Moore, F. Jiao, *ACS Catal.* **2015**, *5*, 4586.